Rheinland-Pfälzische Technische Universität Kaiserslautern Landau

Mononuclear Fe(III)-Hydroxide- and Fe(II)-Aqua-Complexes as Reactive, Structural Analogues for the Active Site of Rabbit-Lipoxygenase

Mononukleare Fe(III)-Hydroxid- und Fe(II)-Aqua-Komplexe als Reaktive, Strukturelle Analoge für das Aktive Zentrum der Kaninchen-Lipoxygenase

Vom Fachbereich Chemie

der Rheinland-Pfälzischen Technischen Universität (RPTU) Kaiserslautern-Landau

zur Verleihung des akademischen Grades

'Doktor der Naturwissenschaften'

Dr. rer. nat.

genehmigte Dissertation

DE-386

Vorgelegt von

Emiel Dobbelaar, M. Sc.

Betreuer der Dissertation: Prof. H.-J. Krüger, PhD

Datum der wissenschaftlichen Aussprache: 01.06.2023

Kaiserslautern 2023

Doctoral Committee

The research reported in this thesis was conducted from January 2019 to November 2022 in the group of Prof. Hans-Jörg Krüger, PhD in the department of chemistry, subject area of inorganic chemistry, at the Technical University of Kaiserslautern (now Rheinland-Pfälzische Technische Universität Kaiserslautern-Landau) according to the doctoral examination regulations that were in place on 01.01.2019.

Day of the thesis defense: 01.06.2023

Committee:

Chair:	Prof. Dr. Antonio Pierik
Referee:	Prof. Dr. Hans-Jörg Krüger
Referee:	Prof. Dr. Helmut Sitzmann

Statutory Declaration

I, Emiel Dobbelaar, hereby confirm that I have completed this thesis independently in accordance with the doctoral examination regulations of the Department of Chemistry at the Technical University of Kaiserslautern. No other aids than those specified were used; passages taken from other sources are marked as such. Parts of this work have already been published in a scientific journal; permission to reproduce, reprint and adapt the complete article for the dissertation was obtained from the respective publisher. It has been marked for which sections this is relevant and author contribution statements as well as a link to the journal publication are provided.

Kaiserslautern, _____ _____

Emiel Dobbelaar

“Nature is our biggest ally and our greatest inspiration.

We just have to do what nature has always done.

It worked out the secret of life long ago.

In this world, a species can only thrive… when everything else around it thrives, too.

We can solve the problems we now face by embracing this reality.

If we take care of nature, nature will take care of us.”

Sir David F. Attenborough

A Life On Our Planet: My Witness Statement and a Vision for the Future

2020.

Dedicated to my parents Jan & Sarianne Dobbelaar

Abstract

This thesis describes the synthesis and extensive characterization of mononuclear *cis*-(carboxylato)(hydroxo)iron(III) and *cis*-(carboxylato)(aqua)iron(II) complexes among others and illuminates their capability to engage in hydrogen atom transfer reactions via reactivity studies with suitable substrates. The employed carboxylates include benzoate, *p*-nitrobenzoate, and *p*-methoxybenzoate. Additionally, the first example for a solution-stable mononuclear *cis*-di(hydroxo)iron(III) complex is presented, the extensive characterization of which aims to contribute to the identification of spectroscopic markers and a better understanding of the role of the carboxylate ligand in the above-mentioned complexes.

The *cis*-(carboxylato)(hydroxo/aqua)iron(III/II) complexes match the coordination environment and the electronic properties of the active iron site in the resting state of rabbit lipoxygenase as well as of the reaction intermediates postulated for the enzymatic mechanism. In addition to being excellent structural and electronic models, the *cis*-(carboxylato)(hydroxo)iron(III) complexes display reactivity in abstracting hydrogen atoms from (weak) O–H and C–H bonds of suitable substrates, thus proving themselves to be worthy functional model complexes for lipoxygenases. The findings are supported with extensive structural, spectroscopic, spectrometric, magnetic, and electrochemical investigations as well as with quantified thermodynamic and kinetic parameters to allow for an adequate comparison between the derivatives with varying carboxylate ligands and to other works. Moreover, the reactivity investigation for the *cis*-(benzoato)(hydroxo)iron(III) (the first example found) was exemplary accompanied by a thorough theoretical study (done by external cooperation partners), which validates the experimental results and identifies an underlying concerted proton-coupled-electron-transfer (cPCET) mechanism for the *cis*-(carboxylato)(hydroxo)iron(III) complexes – analogous to the one suggested for the enzyme.

The synthesis and study of a functional structural model complex is extremely challenging and rarely successful. Thus, this result alone represents a significant scientific advancement for the field, as no such model for lipoxygenases had been precedented prior to this project. The in-depth studies with derivatives of the initial

cis-(benzoato)(hydroxo/aqua)iron(III/II) complexes further contribute to this advancement by illuminating structure-function relations.

German translation

Diese Arbeit beschreibt u.a. die Synthese und umfangreiche Charakterisierung von *mononuklearen* *cis*-(carboxylato)(hydroxo)Eisen(III)- und *cis*-(carboxylato)(aqua)Eisen(II)-Komplexen und beleuchtet deren Fähigkeit, H-atom Transferreaktionen mit geeigneten Substraten durchzuführen. Zu den verwendeten Carboxylatliganden im Rahmen dieser Untersuchungen gehören Benzoat, *p*-Nitrobenzoat und *p*-Methoxybenzoat. Weiterhin wird in dieser Arbeit das erste Beispiel für einen mononuklearen *cis*-Di(hydroxo)eisen(III)-Komplex vorgestellt, welcher in Lösung nachweislich stabil ist. Dessen umfangreiche Charakterisierung trägt nicht nur zum besseren Verständnis der Rolle des Carboxylatliganden in den o.g. Komplexen bei, sondern beschreibt außerdem seine spektroskopischen Eigenschaften, welche der Identifikation solcher Spezies in zukünftigen Studien dienlich sein könnten.

Die *cis*-(carboxylato)(hydroxo/aqua)eisen(III/II)-Komplexe entsprechen der Koordinationsumgebung und den elektronischen Eigenschaften des aktiven Zentrums der Kaninchen-Lipoxygenase. Dies gilt sowohl für den Ruhezustand als auch für die, für den enzymatischen Mechanismus postulierten, reaktiven Zwischenprodukte. Die genannten Komplexe sind nicht nur hervorragende strukturelle und elektronische Modelle, sondern zeigen auch eine Reaktivität mit (schwachen) O–H und C–H Bindungen geeigneter Substrate und erweisen sich damit als würdige funktionale Modellkomplexe für Lipoxygenasen. Die Ergebnisse dieser Arbeit werden durch umfangreiche strukturelle, spektroskopische, spektrometrische, magnetische und elektrochemische Untersuchungen sowie durch quantifizierte thermodynamische und kinetische Daten unterstützt, um einen adäquaten Vergleich zwischen den Derivaten mit verschiedenen Carboxylat-Liganden und anderen Arbeiten zu ermöglichen. Für die Reaktivitätsstudien des *cis*(-benzoato)(hydroxo)Eisen(III) Komplexes wurde weiterhin in externer Kooperationsarbeit eine gründliche theoretische Studie durchgeführt, die die experimentellen Ergebnisse validiert und einen zugrunde liegenden konzertierten

protonengekoppelten Elektronentransfermechanismus (cPCET) für die Reaktivität dieser Komplexe identifiziert – analog zu dem Mechanismus, der für das Enzym vorgeschlagen wird.

Die Synthese und Untersuchung eines funktionalen strukturellen Modellkomplexes ist äußerst herausfordernd und gelingt nur selten. Daher stellt dieses Ergebnis allein schon einen bedeutenden wissenschaftlichen Fortschritt für das Gebiet dar, besonders da es vor dem Abschluss dieses Projekts noch kein solches Modell gab. Die weiterführenden Synthesen von Derivaten der initialen *cis*(-benzoato)(hydroxo/aqua)eisen(III/II)-Komplexe und deren Untersuchungen tragen weiter zu diesem Fortschritt bei, indem sie die Struktur-Funktions-Beziehungen vertieft herausstellen.

Transparency note: The German translation of this abstract was initially generated by the translator tool embedded in Microsoft Word (Office 365, latest version, 01.04.2023) from the English abstract above and then corrected and revised for improved readability.

Table of Contents

Synopsis

This thesis contains previously published work that has been reprinted (adapted) with permission from “E. Dobbelaar, C. Rauber, T. Bonck, H. Kelm, M. Schmitz, M. E. de Waal Malefijt, J. E. M. N. Klein, and H.-J. Krüger, “Combining Structural with Functional Model Properties in Iron Synthetic Analogue Complexes for the Active Site in Rabbit Lipoxygenase” *Journal of the American Chemical Society* **2021**, 143 (33), 13145-13155, DOI: 10.1021/jacs.1c04422”.[1] This material is excerpted from a work that was published as mentioned above, copyright © 2021 American Chemical Society after peer review. To access the final edited and published work see the DOI link above.

The previously published work is described mostly in chapter 2 and referenced multiple times throughout the thesis. Additionally, the introduction, motivation and objectives, conclusion, and outlook partially contain statements that were reproduced and/or adapted for the compilation of this monography. Any revised or updated data are explicitly noted with reference to the original work. Wording of e.g. figure and table descriptions/captions as well as some discussions and experimental descriptions in other chapters of this thesis are partially adapted/reproduced for consistency within the monography. Method, instrument, and experimental descriptions in chapter 7 and 8 which pertain the contents of previously published results described in chapter 2 are reproduced and only adapted if necessary for a more accurate description. Wording for analogous synthetic descriptions of unpublished results may in part also be adapted from published descriptions for consistency. A description of all author contributions and differentiation statements from previous works are contained where appropriate.

Abbreviations

General

A	Acceptor
ATR	attenuated total reflection
a.u.	arbitrary units
BDE	bond dissociation energy
BDFE	bond dissociation free energy
br	broad
ca.	circa
calc’d	calculated
catal.	catalytic
CCDC	Cambridge Crystallographic Data Centre
COSY	correlated spectroscopy
cPCET	concerted proton-coupled electron transfer
CT	charge transfer
CV	cyclic voltammetry
D	Donor
dev.	Deviation
DFT	density functional theory
e.g.	for example
EPR	electron paramagnetic resonance
ESD	estimated standard deviation
ESI	electrospray ionization
ESI-MS	electrospray ionization mass spectrometry
etc.	et cetera
EXAFS	extended X-ray absorption fine structure (spectroscopy)
EXSY	exchange correlated spectroscopy

FID	free induction decay
FTIR	Fourier transformation infrared
GOE	great oxidation event
Gya	gigayears ago
HAT	hydrogen atom transfer
hLOX	human lipoxygenase
IBO	intrinsic bond orbital
ic	inversion center
I-effect	inductive effect
IR	infrared
IRC	intrinsic reaction coordinate
iso	isotropic
KIE	kinetic isotope effect
λ	reorganization energy
LOX	lipoxygenase
max.	maximal
M-effect	mesomeric effect
min.	minimum
n.d.	not determined
NHE	normal hydrogen electrode
NIR	near infrared
NMR	nuclear magnetic resonance
PCET	proton-coupled electron transfer
ppm	parts per million
Ref	reference
rLOX	rabbit lipoxygenase
rmsd	root mean square deviation
ROI	region of interest

RT	room temperature
SCE	standard calomel electrode
sh	shoulder
SHE	standard hydrogen electrode
SO	spin-only
SQUID	superconducting quantum interference device
UV	ultraviolet
vis	visible
vs	versus
XRD	X-ray diffraction
ZFS	zero-field splitting

Chemicals

BHT	butylated hydroxytoluene
CHD	1,4-cyclohexadiene
d5-$PhCO_2$	pentadeuterated benzoate
DHA	9,10-dihydroanthracene
DMF	*N*,*N*-dimethylformamide
DNA	desoxyribonucleic acid
Et	ethyl
Fc/Fc^+	ferrocene/ferrocenium
H_2bim	2,2′-bis-imidazoline
His	Histidine (protein side chain residue)
Ile	Isoleucine/Isoleucinate (protein side chain residue)
L-$N_4{}^t Bu_2$	*N*,*N*'-di(*tert*-butyl)-2,11-diaza[3.3](2,6)-pyridinophane
Me	methyl
MeCN-d3	deuterated acetonitrile
O_2CPh^{pNO2}	*p*-nitrobenzoate

O_2CPh^{pOMe}	*p*-methoxybenzoate
$O^{Me2}N_4$(tren)	3-((2-(bis(2-aminoethyl)amino)ethyl)imino)2-methylbutan-2-olate)
OTf	triflate
O_w	oxygen atom of a water molecule
Ph	phenyl
py	pyridine
PY5	2,6-bis-(bis(2-pyridyl)methoxymethyl)pyridine
PyPz	tetramethyl-2,3-pyridinoporphyrazine
R	organic residue
RNA	ribonucleic acid
TBAP	tetrabutylammonium perchlorate
^{t}Bu	*tert*-butyl
TEMPOH	2,2,6,6-tetramethylpiperidin-*N*-hydroxid
TEMPO	2,2,6,6-tetramethylpiperidin-*N*-oxyl
tnpa	tris(6-neopentylamino-2-pyridylmethyl)amine
TTBP	2,4,6-tri(*tert*-butyl)phenol
X, Y	placeholders for organic groups/ligands or atoms

In NMR-spectroscopy

δ	chemical shift
s	singlet
d	doublet
t	triplet
m	multiplet
sh	shoulder
br	broad

Chemicals Directory

Structures of the metal complexes

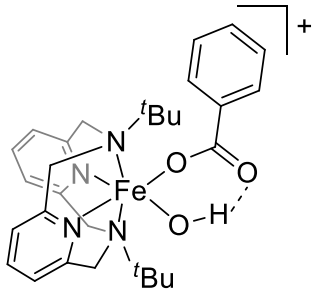

1

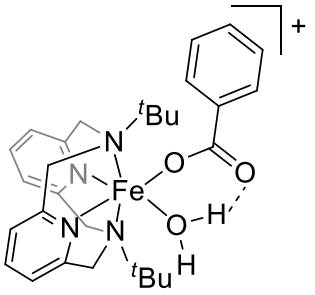

2

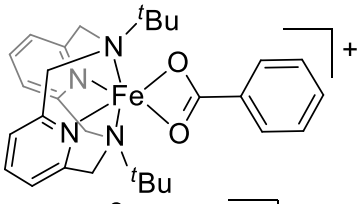

3

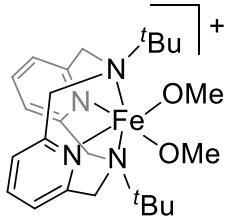

4

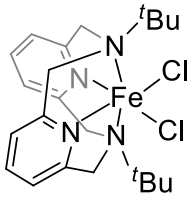

5

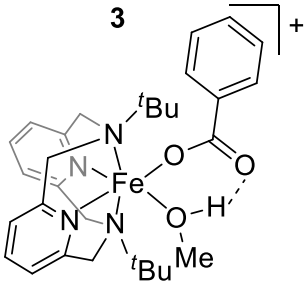

6

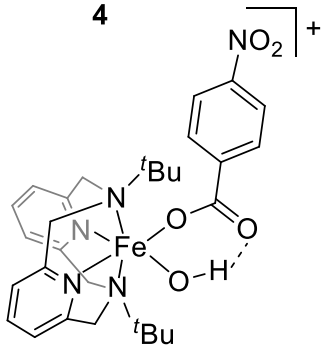

7

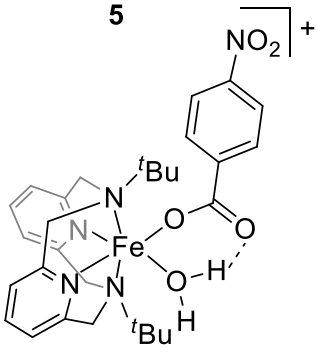

8

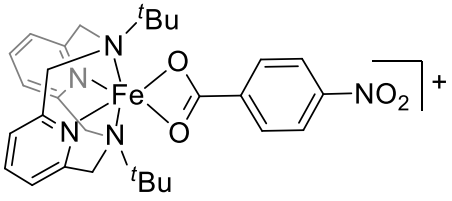

9

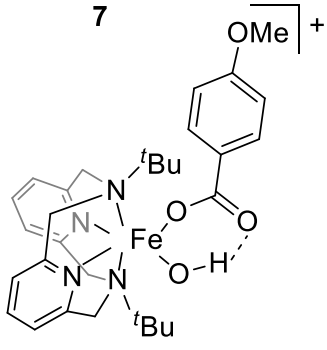

10

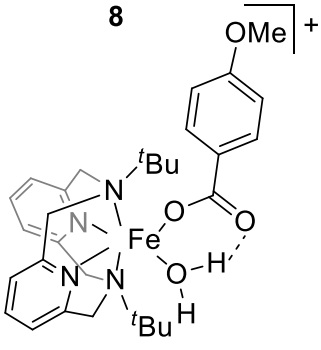

11

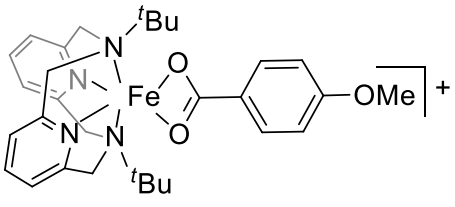

12

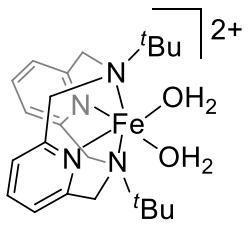

13

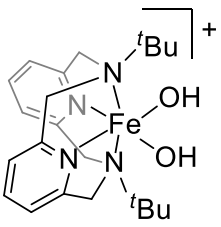

14

Compounds containing the above-mentioned metal complexes

1a	$[Fe^{III}(L\text{-}N_4{}^tBu_2)(O_2CPh)(OH)]BPh_4$
1b	$[Fe^{III}(L\text{-}N_4{}^tBu_2)(O_2CPh)(OH)]BPh_4 \cdot MeCN$
1c	$[Fe^{III}(L\text{-}N_4{}^tBu_2)(O_2CPh)(OH)]PF_6$
2a	$[Fe^{II}(L\text{-}N_4{}^tBu_2)(O_2CPh)(OH_2)]ClO_4$
2b	$[Fe^{II}(L\text{-}N_4{}^tBu_2)(O_2CPh)(OH_2)]CF_3SO_3$
2c	$[Fe^{II}(L\text{-}N_4{}^tBu_2)(O_2CPh)(OH_2)]PF_6$
2e	$[Fe^{II}(L\text{-}N_4{}^tBu_2)(O_2CPh)(OH_2)]_2(BPh_4)_2 \cdot 2H_2O \cdot 2Et_2O \cdot MeCN$
3a	$[Fe^{II}(L\text{-}N_4{}^tBu_2)(O_2CPh)(OH_2)]ClO_4 \cdot MeCN$
4a	$[Fe^{III}(L\text{-}N_4{}^tBu_2)(OMe)_2]BPh_4$
4b	$[Fe^{III}(L\text{-}N_4{}^tBu_2)(OMe)_2]PF_6$
4c	$[Fe^{III}(L\text{-}N_4{}^tBu_2)(OMe)_2]ClO_4$
5	$[Fe^{II}(L\text{-}N_4{}^tBu_2)(Cl)_2]$
6a	$[Fe^{II}(L\text{-}N_4{}^tBu_2)(O_2CPh)(HOMe)]ClO_4$
7a	$[Fe^{III}(L\text{-}N_4{}^tBu_2)(O_2CPh^{pNO2})(OH)]BPh_4$
7b	$[Fe^{III}(L\text{-}N_4{}^tBu_2)(O_2CPh^{pNO2})(OH)]ClO_4$
9a	$[Fe^{II}(L\text{-}N_4{}^tBu_2)(O_2CPh^{pNO2})(OH_2)]ClO_4 \cdot MeCN$
10a	$[Fe^{III}(L\text{-}N_4{}^tBu_2)(O_2CPh^{pOMe})(OH)]BPh_4$
10b	$[Fe^{III}(L\text{-}N_4{}^tBu_2)(O_2CPh^{pOMe})(OH)]ClO_4 \cdot 1H_2O$
10c	$[Fe^{III}(L\text{-}N_4{}^tBu_2)(O_2CPh^{pOMe})(OH)]PF6 \cdot 1Et_2O$
11a	$[Fe^{II}(L\text{-}N_4{}^tBu_2)(O_2CPh^{pOMe})(OH_2)]CF_3SO_3$
11a*	$[Fe^{II}(L\text{-}N_4{}^tBu_2)(O_2CPh^{pOMe})(OH_2)]CF_3SO_3 \cdot xH_2O$
12a	$[Fe^{II}(L\text{-}N_4{}^tBu_2)(O_2CPh^{pOMe})(OH_2)]ClO_4 \cdot MeCN$
13a	$[Fe^{II}(L\text{-}N_4{}^tBu_2)(OH_2)_2](OTs)_2$
13b	$[Fe^{II}(L\text{-}N_4{}^tBu_2)(OH_2)_2](OTf)_2$
14a	$[Fe^{II}(L\text{-}N_4{}^tBu_2)(OH)_2]PF_6 \cdot 1H_2O$
14b	$[Fe^{II}(L\text{-}N_4{}^tBu_2)(OH)_2]_3(PF_6)_3 \cdot 5H_2O$
14c	$[Fe^{II}(L\text{-}N_4{}^tBu_2)(OH)_2]PF_6$

*Notes: **6a** is not discussed in this thesis and is only given as a reference to keep the numbering consistent with the original publication.[1,2] **13b** was not produced in this work. However, some data analysis was done for comparison with **13a** with permission from Pascal Peter, who collected the data.[3] No compound containing **8** could be isolated with sufficient purity.*

Isotope marked compounds

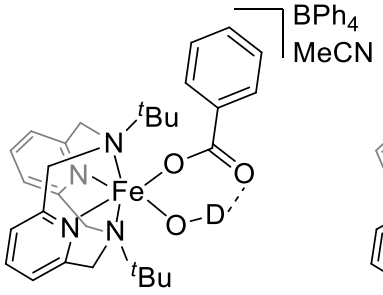

1d

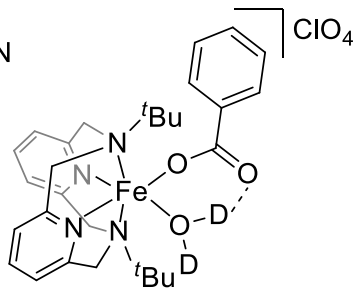

2d

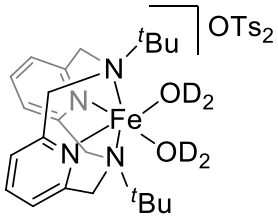

13d

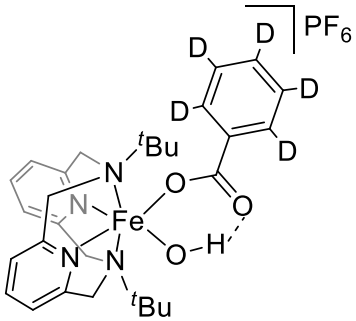

1^{D}c

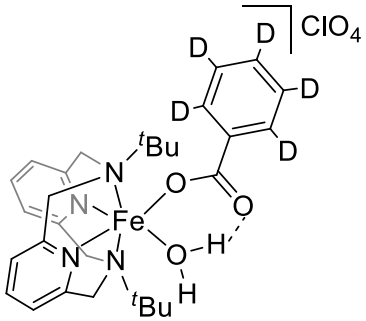

2^{D}a

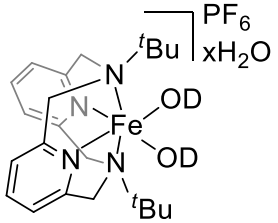

14d

Special structural arrangements

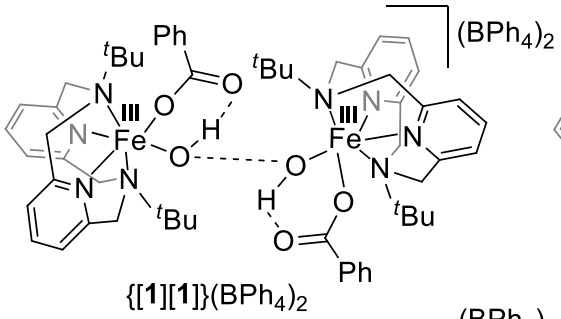

{[**1**][**1**]}$(BPh_4)_2$

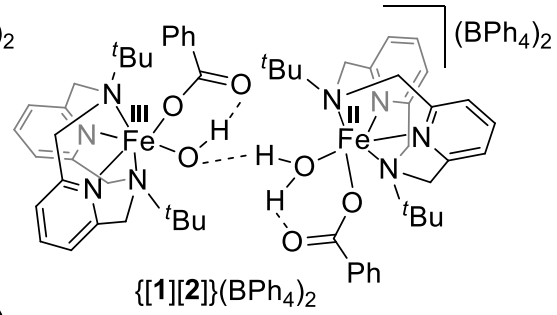

{[**1**][**2**]}$(BPh_4)_2$

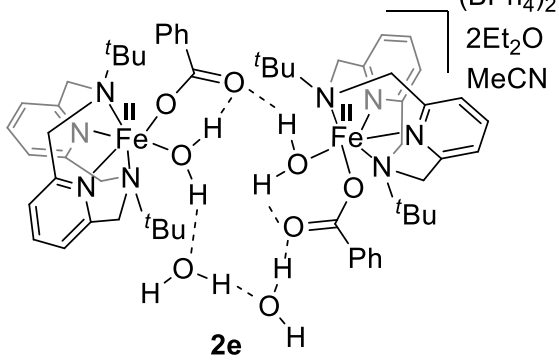

2e

*Note: The association of complexes **1** and **2** as {[**1**][**2**]}$^{2+}$, {[**1**][**1**]}$^{2+}$, {[**2**][**2**]}$^{2+}$ units via short distance interactions found in the structures of the depicted compounds are discussed separately in chapter 4. {[**1**][**1**]}$(BPh_4)_2$ is equivalent to **1a**.*

Introduction

1. Introduction

1.1. General Introduction

1.1.1. An Introduction to Bioinorganic Chemistry

Although it has long been known that typical inorganic ions and molecules such as Na^+, K^+, Ca^{2+}, $Fe^{2+/3+}$, O_2, HCO_3^-, or HPO_4^{2-} are essential for life as we know it, our deeper knowledge about their biological relevance is mostly based on research of the last ~60 years.[4,5] The rather recently evolved interdisciplinary field that contributes to the advancement of this knowledge and aims to apply it in bioinspired and biological systems is called “bioinorganic chemistry”. It was pioneered by analytical efforts of e.g., Robert J. P. Williams around 1950, with first formal meetings on bioinorganic chemistry happening in the 1960s.[5] To grasp where biological processes are investigated under the aspect of bioinorganic chemistry, we first need to overview which elements are essential for life in general (Figure 1).

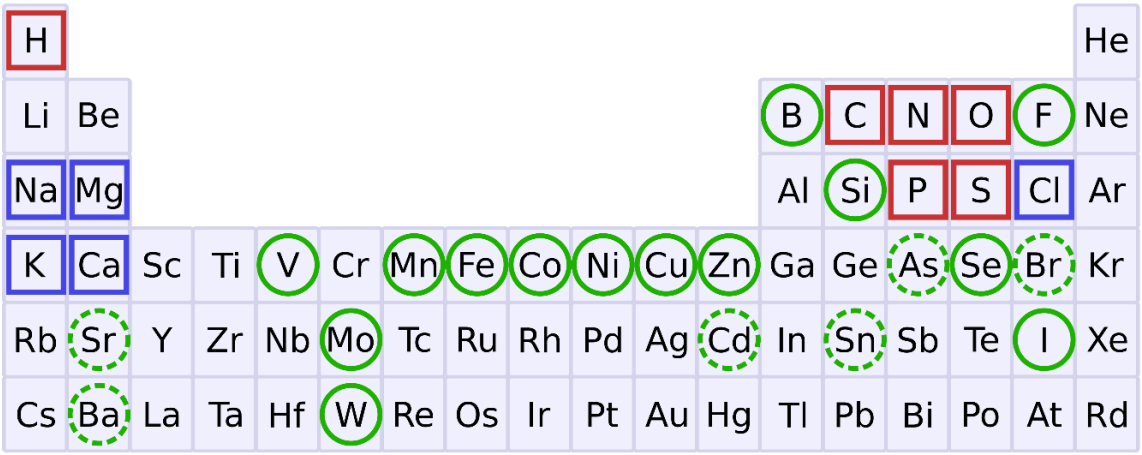

Figure 1. Biologically essential and potentially essential elements (adapted from D. Rehder, *Bioinorganic Chemistry*, Oxford University Press, 2014).[4,6] Red squares: bulk biological elements; blue squares: bulk biological elements found as elemental ions; green circles: essential trace elements; dashed green circles: potentially essential elements for some life forms. Although chromium (Cr) is listed as an essential trace element in the original source and others, the study by *Schwarz* and *Mertz* (1959) that this refers to was methodologically flawed.[7] More recent studies suggest that Cr is not a biologically essential element.[8]

When we look at the elemental composition of the human body as an example for a (multi-)cellular lifeform, we find that ~99 % of its weight comes from oxygen, carbon, hydrogen, nitrogen, calcium, and phosphorus.[9,10] Oxygen itself makes up over half of our mass, largely as part of cellular water. The hydrogen that is not contained in cellular water is mostly covalently bound to carbon and nitrogen in organic molecules (carbohydrates/fats, amino acids/proteins, DNA), while calcium and phosphorus add to our weight as inorganic calcium e.g., in our bones, and phosphates, e.g. in phospholipids and our DNA. The remaining 1 % is made up of sulfur in proteins and molecular ions, anionic chlorine, cationic potassium, sodium, and magnesium, and essential trace elements such as 3d transition metals.

The interest of most bioinorganic chemists lies in the metals of the final 1 %, particularly trace transition metals, although some studies are also dedicated to the role of metal-free small molecules. The main topics concern 1) metalloproteins/-enzymes 2) metal transport and storage, 3) ion channels, 4) medicinal applications (metallodrugs, radiopharmaceuticals), 5) DNA and RNA metal interactions and toxicology/diseases particularly related to metals, 6) metal-free small inorganic molecules (H_2O_2, $HO^{\cdot}$, NO, CO, …).[11]

Among these, the study of metalloproteins/-enzymes has arguably gained the most attention to date and is a research field that is especially popular with synthetic metalorganic chemists.[12] A common approach in synthetic bioinorganic chemistry is to develop simple models of (enzymatic) metalloproteins for detailed investigations. Here, five main aspects or stages from fundamental research to application are explored:[11]

1) **Fundamental research**: The feasibility to model features of a metalloprotein in the first place as a fundamental challenge.
2) **Structural models**: Modelling structural and electronic properties of a metalloprotein to establish e.g., spectroscopic markers for distinct features and to study interactions with surrounding molecules and ions.
3) **Functional models**: Modelling the functionality of a metalloprotein to investigate e.g., reaction mechanisms.
4) **Complete synthetic analogues**: The combination of 1 & 2 in one model to elucidate e.g., structure-function relations.

5) **Biomimetic/Bioinspired Applications (“Bionics”)**: The application of the newly acquired knowledge for technological or medicinal advancements.

In this work, the approach to achieve a complete synthetic analogue was taken. A more detailed description of this is described in section 1.2.1.

1.1.2. A Brief History of Transition Metals in Biology

As soon as one takes a closer look at metalloproteins such as enzymes, one must realize the ingenuity of these complex molecules. Although we appreciate natural evolution for the development of complex and efficient organisms, metalloproteins do raise the question how nature came to develop complicated pathways to use biologically poorly available trace elements. As an example, two enzymatic catalytic pathways exist for the catalytic aldolization of carbonyls: Class I aldolases function through metal-free organocatalysis (enolate pathway) while class II aldolases use a zinc cofactor to realize the same reaction.[13] Organic building blocks are bioavailable but zinc, like many other transition metals, needs to be enriched to be utilized for this reaction and requires complicated uptake, storage, and transport mechanisms for a safe and targeted use. This becomes especially clear when comparing the elemental composition of e.g., a human, to the abundance of metals in seawater as a measure of element solubility (as ions) and natural bioavailability (Figure 2).

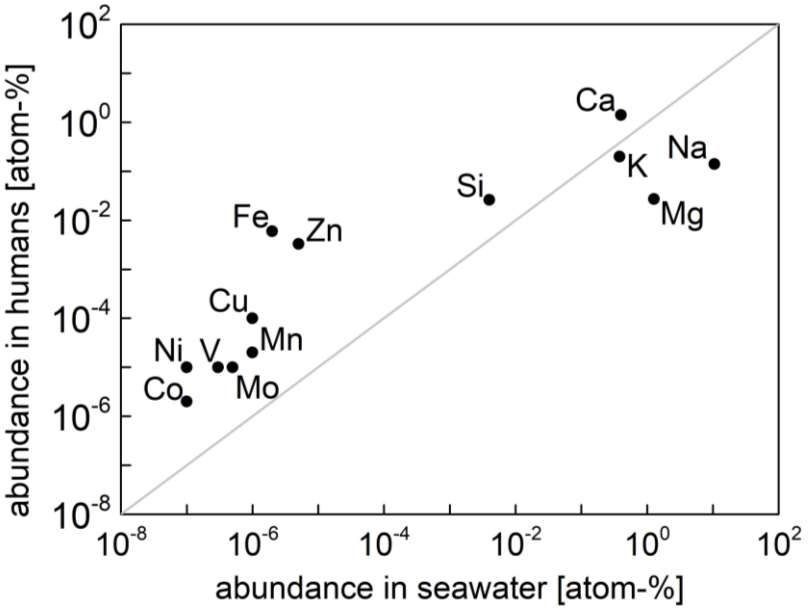

Figure 2. Abundance of biologically relevant main group and transition metals in the human body compared to their abundance in seawater of today's oceans in atom-%. Underlying data were obtained from *Nature's Building Blocks* (Emsley, 2011),[10] *The Oceans, Their Physics, Chemistry, and General Biology* (Sverdrup, Johnson, Fleming, 1942)[14] and *MacMillans Chemical and Physical Data* (James, Lord, 1992).[15] Lower concentrations are subject to higher inaccuracies, especially in the case of oceanic concentrations of Cobalt due to limited data availability.[16]

It seems odd that nature would choose to develop complicated mechanisms and pathways to achieve metalloenzymes, only to catalyze a reaction that could also be catalyzed with a purely organic active enzymatic site. To understand the fundamental origin of this, we need to regard the bioavailability of elements in the early evolutionary stages of life rather than today's environmental conditions. Many chemical strategies and pathways that organisms use today are reminiscent of those that were developed by early single-celled life under primeval environmental conditions. Thus, the answer to the question why and how nature developed mechanisms to enrich and use transition metals, lies in the distant history of life itself.

The availability of metals in primeval oceans

Although the bioavailability of transition metals such as iron is poor nowadays, this was not always the case. When life first emerged in primordial oceans after the Hadean period approximately 3.5 – 4 billion years ago, earth likely had a reducing, hydrosulfuric atmosphere.[17] Because Fe^{2+} is well-soluble in water and the atmosphere was largely anoxic, easily oxidizable Fe^{2+} was probably well-available next to main group metal ions such as Na^{+}, K^{+}, Ca^{2+}, and Mg^{2+}.[18,19] Even more so, iron-sulfur minerals such as pyrite were abundant and Fe^{2+} ions likely played an important role as reducing agents in early biotic or even prebiotic chemical pathways in proximity to the hydrothermal vents they were emitted from ("black smokers").[20] Such a hypothesis is supported by the occurrence of iron-sulfur clusters as integral part of many enzymatic pathways even in modern day enzymes and their facility to assist in challenging oxidoreductive chemical transformations.[21]

Changing environmental conditions

Eventually, approximately 3 – 3.5 billion years ago, the most important (metal-based) chemical pathway for the evolution of modern complex lifeforms emerged: Photosynthesis.[22] With the ability to harness energy from sunlight, the triumph of procaryotic lifeforms that used photosynthesis was inevitable. When oxygenic photosynthesis became relevant, the environment changed drastically because of the release of dioxygen as a waste product which triggered further developments. This so called "great oxidation event" (GOE) happened approximately 2 – 2.5 billion years ago (Figure 3).[18,20,23] At first, the oxygen was consumed by the dissolved, easily oxidizable ions especially in shallow oceans. This led to the oxidation of e.g., Fe^{2+} to Fe^{3+} and its

sedimentation as insoluble metal-oxides (banded iron formations) at the now much more positive potentials present in the oceans.[24] At the same time, however, oxidative weathering of sulfides to sulfates released cations such as Zn^{2+} and Cu^{2+} from sulfide minerals into primeval oceans that then became more biologically available.[18,25,26]

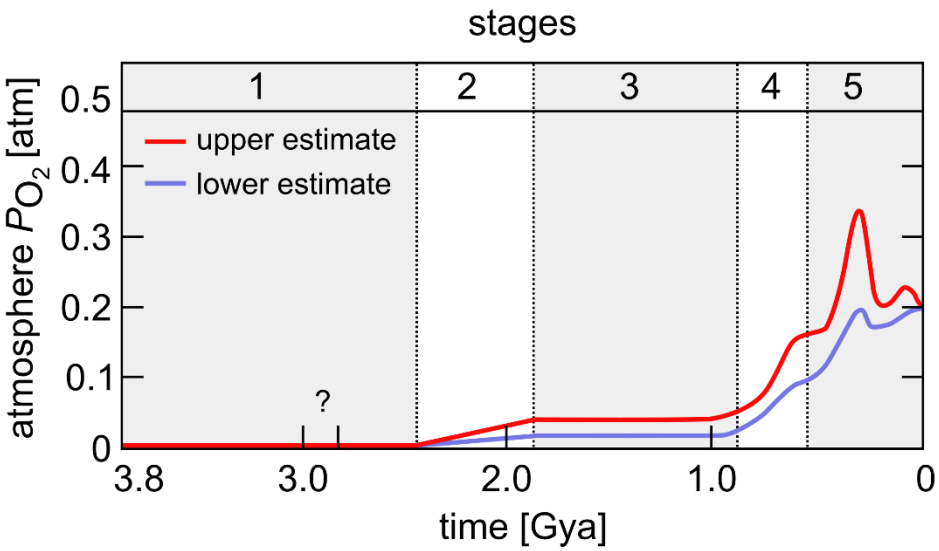

Figure 3. Evolution of atmospheric oxygen versus time in gigayears ago (gya). The figure was qualitatively retraced from the work of Holland (2006) as no original data were available.[23] The proposed stages by Holland are: 3.85 – 2.45 Gya (1), 2.45 – 1.85 Gya (2), 1.85 – 0.85 Gya (3), 0.85 – 0.54 Gya (4), and 0.54 Gya – present (5). Stage 2 represents the GOE. For the period between 3.0 and 2.8 Gya it is not ascertained that the oxygen levels were in a ppm range, thus a question mark is given to highlight this uncertainty. The red and blue lines indicate the upper and lower estimated values in atm, respectively. *Note: The original reference gives further graphs for shallow and deep ocean oxygen concentrations. The shallow ocean concentrations follow similar trends as the atmospheric concentration. The deep oceans are suggested to have been anoxic until stage 3 and exhibit delayed trends.*

The adaptation of early life to oxidizing conditions

The changing conditions from a reductive atmosphere to an oxidizing one forced early life to adapt. On the one hand, the new situation required ways to accumulate, transport, and store easily oxidizable (Fe^{2+}) and poorly soluble (e.g. Fe^{3+}) ions, that were becoming less available, as a precious, depleting resource.[27] On the other hand, it also allowed for diversification through the development of new metal-based chemical pathways with metal ions that were becoming increasingly available.[26]

Additionally, some cells developed mechanisms to benefit from the new dioxygen resources by harnessing significant amounts of energy from oxidative chemistry through respiration, which ultimately became the counterpart to balance photosynthetic oxygen production to an equilibrium state.[28]

Consequences of the "great oxidation event"

When the shallow oceans were no longer able to consume and buffer the oxygen as most of the easily oxidizable ions such as Fe^{2+} and S^{2-} had depleted, the atmospheric oxygen began to build up even more and even deep oceans became oxidized.[18,23] As many lifeforms were still adapted to a reducing atmosphere, the oxidizing reactivity of molecular oxygen was toxic to all those that did not develop ways to use it and/or protect their chemical pathways and transport mechanisms from this threat e.g. by compartmentalization.[29] The single-celled lifeforms that did survive the great oxygen event further evolved to become the ancestors of modern life. The atmospheric increase of free oxygen further led to the build-up of the ozone layer which provided a blanket that protected lifeforms even on land from harsh high-energy ultraviolet radiation. When eucaryotic and multi-cellular lifeforms occurred, they continued to further develop their mechanisms and establish pathways to accumulate, transport, store, and use metals in their metabolism in an oxygen-rich environment. This was accompanied by rising atmospheric oxygen contents until it peaked approximately 500 million years ago before it decreased to today's levels (Figure 3).[23]

Notably, the rising availability of phosphate that was increasingly weathered from apatite minerals during and after the GOE not only provided important resources for genetic material (nucleotides) but also for photosynthesis and respiration which heralded the success of complex life on earth.[18] Eventually, the prosperity of life and the production of organic chelators lead to biological scavenging and a depletion of transition metal ions such as Cu^{2+} and Zn^{2+} that were initially released e.g. from metal sulfides in course of the GOE. Thus, today, they are bound in sediments and again scarce in surface water areas, making them poorly bioavailable.[30]

Metal metabolism as an established part of modern life

Because of this history, even today all lifeforms use transition metals in their metabolism and saline water as a solvent.[4,21] The role of transition metals is, thus, crucial for biology, and intricate mechanisms to facilitate their biological use even at

today's poorer bioavailability have evolved.[12] This may be best demonstrated by the example of the most common trace element in our bodies, iron (~50 mg/kg).[4] Today, most lifeforms use either siderophores, which have a high affinity to iron(III) ions, or ferric reductases that reduce the iron(III) to more soluble iron(II), to compensate for the poor bioavailability and to take up iron.[27,31] In our bodies, transport proteins such as transferrin then escort the iron to the protein ferritin which encapsulates the iron in an amorphous cluster until it is needed.[32] For the biosynthesis of a metalloprotein, chaperones mobilize the iron and ensure a safe transport from ferritin to the exact cellular medium where the respective proteinogenesis (or synthesis of a metal cofactor) takes place.[33] Finally, in metalloproteins, the iron sites are inserted into a specific organic protein environment designed to ensure controlled functionality and prohibit undesired side reactions, e.g. of Fe(II) sites with oxidizing agents such as O_2.[34]

The relevance of bioinorganic chemistry

In summary, the changing environmental conditions in earth's history led to diverse chemical pathways that made metals essential for today's life. The contribution of inorganic components to life as we know it is large and an understanding of biology is only possible if we can grasp the roles of all components – also the inorganic ones and the trace elements. The study of biological processes that involve metals promises advancements in medicine and technology through the application of newly uncovered knowledge via bioinspired and biomimetic principles (section 1.1.1).

The target of this thesis, which aims to contribute to the understanding of the relevance of metals in biology, is to uncover the mechanism and structure-function relations of the active site of a specific metalloenzyme (rabbit lipoxygenase, rLOX) to explore alternative, biomimetic oxidative catalytical pathways using iron complexes (section 1.3). For this, the toolbox of bioinorganic chemistry offers the "synthetic analogue approach"; a challenging but potentially rewarding approach that will be further described in the following.

1.2. Theoretical Background

Note: The theoretical background contains previously published work that was reproduced/adapted from "E. Dobbelaar, C. Rauber, T. Bonck, H. Kelm, M. Schmitz, M. E. de Waal Malefijt, J. E. M. N. Klein, and H.-J. Krüger, "Combining Structural with Functional Model Properties in Iron Synthetic Analogue Complexes for the Active Site in Rabbit Lipoxygenase" Journal of the American Chemical Society ***2021****, 143 (33), 13145-13155, DOI: 10.1021/jacs.1c04422". Copyright 2021 American Chemical Society.*[1]

1.2.1. Synthetic Analogue Approach

In bioinorganic studies, a “synthetic analogue” of an enzymatic (active) site describes the accurate modelling of its structural, electronic, and/or functional properties (Scheme 1). A complete synthetic analogue can be described as a combination of the synthetic approaches for structural modelling and for functional modelling of an enzymatic site (see section 1.1.1). Consequently, this “structural-functional modelling” entails the synthesis of small inorganic model complexes that can provide a rational basis to understanding the structural, electronic, or mechanistic properties of the metal sites in metalloproteins. Ultimately, the elegancy of the approach lies in the simplification of the complicated, large metalloprotein to allow for more facile studies about important chemical properties of the enzyme on a single, synthetically accessible metal complex without the need of elaborate protein isolation practices.

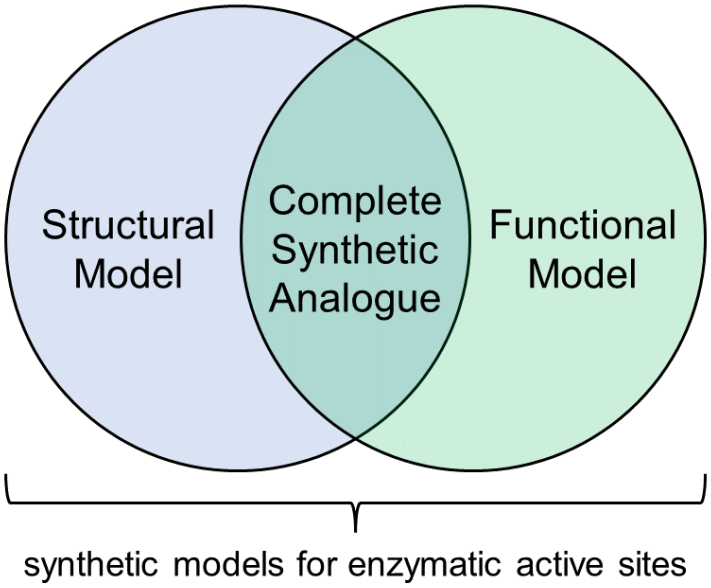

Scheme 1. Synthetic bioinorganic approaches towards modelling enzymatic active sites with small metalorganic complexes. The synthetic analogue approach combines functional and structural/electronic modelling.

Complete synthetic analogues are, however, extremely rare and challenging to achieve.[35] The complexity of metalloproteins offer significantly more control over the coordination environment, reactivity, and selectivity via the encapsulation of the metal site with a large and evolutionary designed protein matrix than a small molecule with simple ligands could ever provide. Very rarely, a synthetic analogue complex is a good model for the structural and/or electronic properties and, at the same time, a good

model for the reactivity of an enzyme.[1] Nonetheless, the potential value of the synthetic analogue approach, if successful, is very high: The results of such a study promise to reward researchers not only with gains in knowledge of bioinorganic issues but also with information about the features that are essential to achieve desired, bioinspired reactivities in e.g., novel catalysts. This goes beyond what can be achieved with structural *or* functional models which can only provide limited information and do not fully reflect the chemical properties of an enzymatic site. In contrast to these simpler approaches, a complete synthetic analogue can help in identifying those intrinsic properties of the enzyme associated with the metal site and its first coordination sphere and those contributed by the protein matrix.[1,35–37]

Here, it should also be noted that recent endeavours in bioinorganic chemistry have touched on synthesizing so called artificial metalloenzymes (ARMs), also termed *de novo* enzymes, to better understand and utilize the concept of a proteinogenic ligand system that encompasses a catalytically active metal complex to achieve, e.g., high selectivity.[38] This represents somewhat of a middle ground between enzymatic examples and their small molecule analogues.[39] Although intriguing and somewhat related to synthetic analogues, as both approaches strive for utilizing bioinspired structural properties of enzymes to understand and manipulate reactivities, this will not be further discussed as it is not relevant for this work.

1.2.2. Non-Heme Iron Enzymes as Oxidation Catalysts

Iron metalloproteins are among the most popular ones studied by bioinorganic chemists.[12] This is not only motivated by the manifold of examples nature has to offer, but also incentivized by the exciting opportunities that are promised by their understanding: Achieving challenging catalytic transformations under ambient conditions with the abundant and rather benign 3d transition metal. Thus, although investigations with model compounds to e.g., better understand iron transport proteins and siderophores exist,[40] the focus of most studies lies on iron metalloenzymes. Metalloenzymes utilize iron in various ways, e.g., as Lewis acid and/or as redoxactive component to facilitate one-, two-, or multi-electron transfer pathways. Common examples are iron-sulfur proteins (e.g. Rubredoxin),[41] heme-iron proteins (e.g. Cytochrom P450),[42] and non-heme iron enzymes.

Because non-heme iron enzymes are rather common and show a wide range of interesting oxidation reactivities, many bioinorganic chemists have attempted to model and better understand them.[39,43–45] However, there are different levels of complexity with respect to the involved species and mechanisms of these enzymes. To start simply: Most mononuclear non-heme iron oxidases and oxygenases contain a facial triad of two histidine residues and one aspartate or glutamate ligand around the iron core, paired with three additional water molecules that complete the distorted octahedral environment (Figure 4).[46] For transformations that require few electron-transfers, the active site itself is sufficient to achieve catalytic turnovers (e.g. Isopenicillin-*N*-Synthase).[45,47] However, more challenging reactions often require additional electron equivalents. Thus, some non-heme iron enzymes employ complimenting redoxactive cofactors, such as Rieske-iron-sulfur-proteins,[48] which provide additional opportunities for electron transfer reactions within their catalytic cycles. This allows for a relatively simple modulation of the reactivity of a standard active *fac*-tri(aqua)-di(histidine)-monocarboxylatoiron(II) motif and creates a diverse set of accessible catalytic oxidation reactions in nature (Figure 4).[45,49–51] To achieve even more challenging oxidations where this strategy does not suffice, nature has furthermore developed non-heme diiron enzymes (e.g. soluble methane monooxygenase) that can also provide additional electron equivalents.[39,44,52] However, to keep it simple, diiron enzymes are not further discussed in this section.

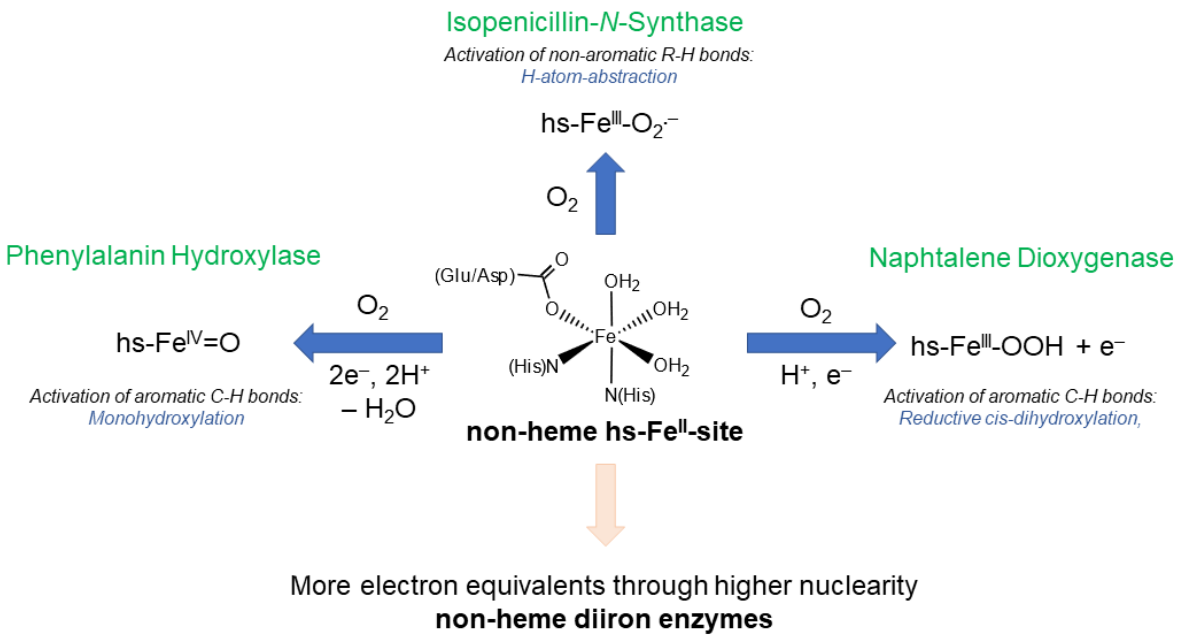

Figure 4. Typical reoccurring active site in non-heme iron oxygenases/oxidases and different reactivities achieved with or without a supplemental redox-active cofactor. Examples given: Isopenicillin-*N*-synthase (no cofactor), phenylalanin hydroxylase (tetrahydrobiopterin cofactor), naphtalene dioxygenase (Rieske-cofactor).[45,49,50] hs = high-spin. (*This figure was inspired by S. Becker, Bioanorganische Chemie, Lecture, TU Kaiserslautern, **2021**.)*

When looking at the initial steps of the reactions of typical mononuclear non-heme iron enzymes, two things become apparent: 1) The spin state does not change, and 2) almost all non-heme iron oxidases and oxygenases activate molecular oxygen from air first, before activating the target R-H bonds (selected examples given in Figure 4).

The first aspect can be explained from an entropic, energetic, and kinetic standpoint: A spin-state change would require the expense of a large reorganization energy to accompany large bond length changes. This would significantly increase the activation barrier for the initiation reaction and decrease the reaction rate. Thus, maintaining the same spin state is beneficial for the enzymes and they have evolved accordingly. The second aspect is more intriguing. Although most of these enzymes activate oxygen first in order to activate the target R–H bond,[53] some enzymes are also capable of direct substrate activation to allow the reaction of a substrate radical with triplet O_2.[54] The differences between these two distinct pathways will be discussed in the following.

1.2.3. Oxygen Activation vs Substrate Activation

As discussed above, non-heme iron enzymes are mostly known and appreciated for their biocatalytic oxidation of substrates with triplet O_2. They achieve such reactions by overcoming the spin-barrier between a singlet substrate and triplet dioxygen (selection rule for reactivity: $\Delta S \leq 0.5$).[46,55] To do this, two pathways are feasible: Either an oxygen activation or a substrate activation pathway (Figure 5).

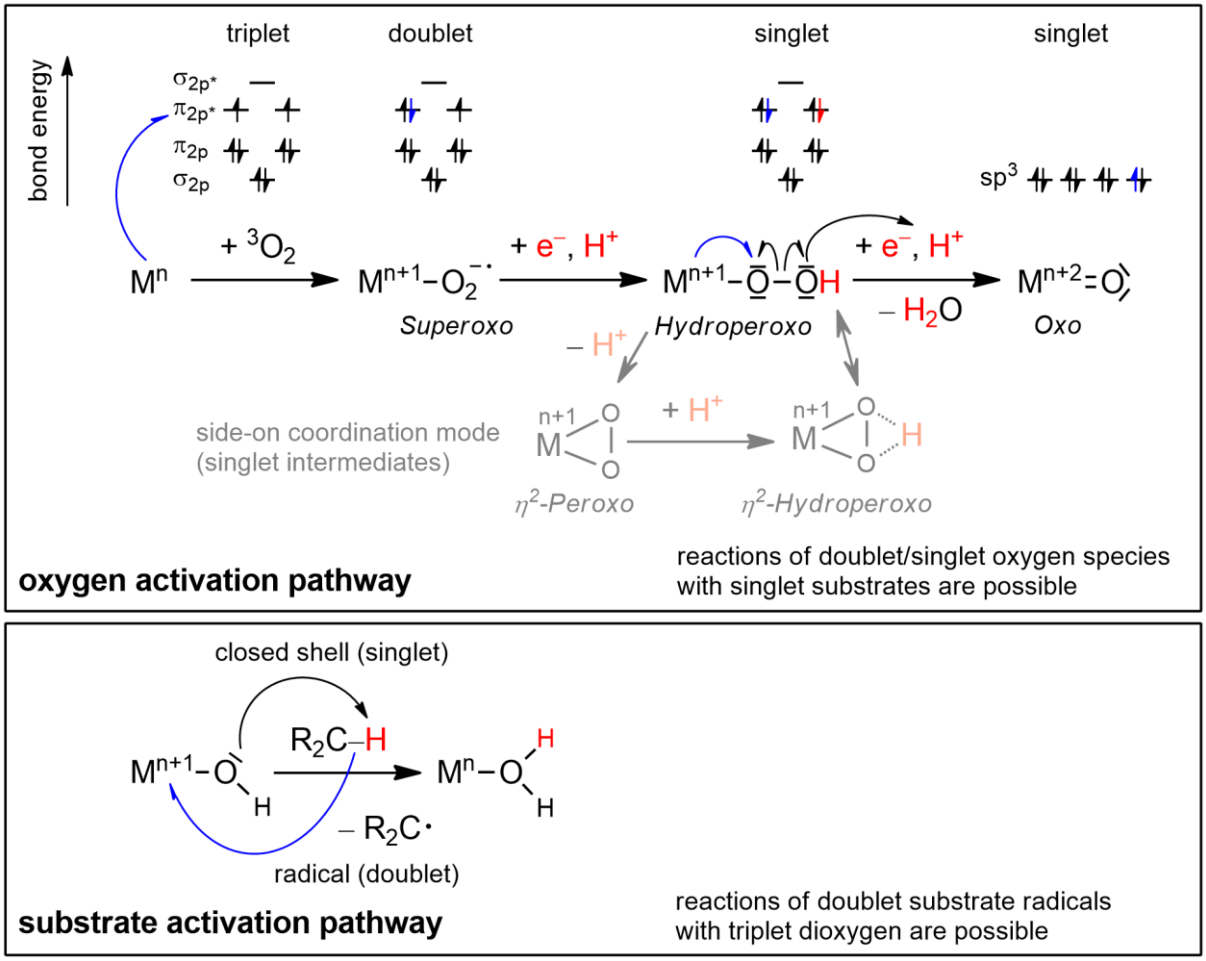

Figure 5. Two pathways to overcome the spin barrier between triplet oxygen (depicted as $^3O_2$ for simplicity) and singlet substrates.[54,56] Indicated bond energies / orbital occupancies do not consider metal-ligand interactions but solely refer to the oxygen ligands. Electron transfer processes with metal involvement are illustrated in blue, proton and electron processes with external partners (e.g. cofactors or substrates) are illustrated in red. The end-on coordination of dioxygen is used as the main example, the side-on coordination modes also discussed in literature are depicted in grey for additional reference.[49,57]

In the case of oxygen activation, e.g., mononuclear iron complexes react with oxygen to form doublet superoxo-, or singlet peroxo-/hydroperoxo-/oxo-iron intermediates which can then further react with a singlet substrate. In the case of substrate activation, the iron site performs a simple hydrogen atom abstraction from a substrate, forming a doublet organic radical which can then react directly with triplet oxygen from air. Although it is not ascertained why nature favors oxygen activation, it appears that the impressive control over oxygen activated species that biological systems have evolved by using cofactors has made this pathway more attractive, because it allows for targeted and versatile oxidation, monooxygenation, or dioxygenation reactions. Additionally, because of their positive reduction potentials, e.g. Fe(IV)=O species are able to achieve driving forces for R–H activation that are unparalleled for a simple substrate activation pathway with e.g. a Fe(III)-OH species, making more challenging transformations accessible.[1,58,59]

Probably because oxygen activation is much more common in enzymes than substrate activation, and because the versatility of iron-oxygen intermediates with different reactivities (nucleophilic deformylation, electrophilic oxidation)[57] is academically very interesting, most efforts have explored this pathway and multiple model complexes for the reactive, oxygen activated intermediates (oxo, superoxo, hydroperoxo, peroxo,…) have been reported.[44,53,57,60,61,62] However, although model complexes for the highly reactive iron-oxygen intermediates are achievable, all of them are thermally very unstable and efforts to utilize them as catalytically active species have only provided conceptual examples with poor turnover numbers.[62,63] Thus, the applicability of biomimetic oxidation catalysts that follow the example of such oxygen activation pathways is currently far from realistic.

Considering this, studying alternative, more robust pathways exemplified in biology that avoid these highly unstable intermediates appears attractive, even if this would entail some drawbacks in versatility and activity towards R–H bond activation. As has been discussed above, the substrate activation pathway suits this description and could bear a large, untapped potential for biomimetic, more sustainable oxidation catalysts. However, the number of studies on this is limited and further research is required to potentially make such an approach accessible.

A unique class of non-heme iron enzymes that employ substrate activation pathways to peroxidize unsaturated fatty acids and have attracted some attention in literature are iron-containing Lipoxygenases.[64] Since these enzymes provide a suitable example to study the substrate activation pathway for efficient oxidation catalysis, the enhancement of their understanding through a synthetic analogue approach became the focus of this work. To provide a good background on this specific topic, the following sections aim to briefly summarize their structure and relevance (1.2.4), the challenges of modelling their active sites (1.2.5), and the current state of research (1.2.6).

1.2.4. Lipoxygenases – A Unique Class of Enzymes

Most lipoxygenases (LOX) are non-heme iron oxidoreductases found in plants and animals that contain a mononuclear *cis*-(carboxylato)(hydroxo)iron(III) coordination unit as the catalytically active site for the hydroperoxidation of (*Z*,*Z*)-1,4-pentadiene moeties with molecular oxygen.[64,65,66] Hereby, the carboxylate ligand is provided by a C-terminal isoleucinate (Ile) residue rather than a deprotonated acidic amino acid side chain (aspartate or glutamate), which is unusual.[67,68] Structural investigations (EXAFS) of the reduced *cis*-(carboxylato)(aqua)iron(II) state indicate the existence of a hydrogen bonding interaction between the oxygen atoms deriving from the water ligand and the carbonyl group of the carboxylate ligand.[66,69] While the residual distorted octahedral coordination sphere of the active non-heme iron(III) unit is completed by four histidine nitrogen donors in rabbit and human 15-lipoxygenases (rLOX[67,68] and hLOX[66], Figure 6), the composition of the protein-derived ligand environment in lipoxygenases from other sources varies by substitution of one of the histidine residues, e.g. by an asparagine carbonyl oxygen donor.[64,67–69,70] Generally, these environments structurally distinguish this class of oxygenases from typical non-heme iron enzymes as they lack the typical facial triade of two histidine residues and one glutamate/aspartate ligand (see section 1.2.2). The most notable differentiation, however, lies in their substrate activating reactivity (see below).

Through the hydroperoxidation of fatty acids (e.g. arachidonic acid or linoleic acid), Lipoxygenases play a major role, for example, in controlling cellular differentiation and growth, and in initiating inflammatory or allergic processes in mammals.[71,72] They do this, by regulating the metabolism of eicosanoid polyunsaturated fatty acids and by initiating the production of leukotrienes (from e.g., linoleate and arachidonate), which are part of a larger group of autocrine/paracrine tissue hormones that also include prostaglandines and thromboxanes.[73,74]

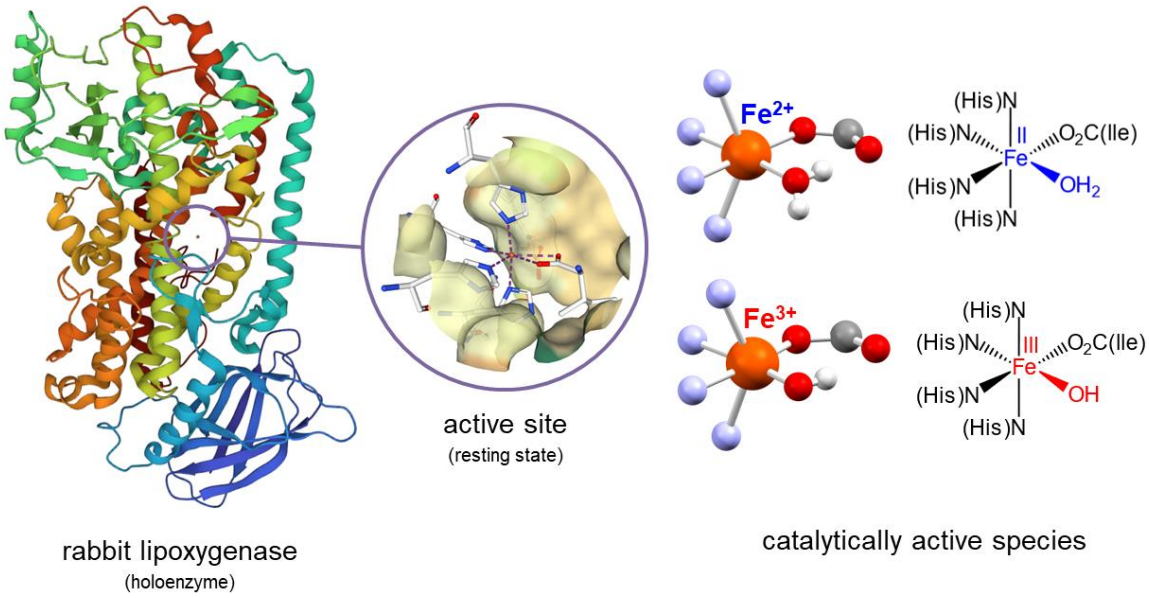

Figure 6. Depictions of the holoenzyme, the active site, and the catalytically active ferric/ferrous species in rabbit lipoxygenase. The aqua ligand in the crystal structure of the resting state could not be resolved to date, no structure for the active state is available.[67,68]

The first step in the production of leukotrienes entails the hydroperoxidation of arachidonic acid which is facilitated by lipoxygenases via a substrate activation mechanism (Scheme 2).[73] This distinguishes this unique enzyme class from other non-heme iron oxygenases and oxidases that usually employ oxygen activation mechanisms (see section 1.2.2). The most widely accepted mechanism for this reaction involves two states for the active iron site of the enzyme: a high-spin ferric hydroxide and a high-spin ferrous aqua complex (Figure 6).[64,75] In the initial step of the reaction cycle, the ferric hydroxide (regio-)selectively converts the methylene carbon in 7-position of arachidonic acid (that is contained in a pentadiene moeity) into a “pentadienyl” radical via an overall H-atom abstraction (Scheme 2). Subsequently, molecular triplet oxygen selectively reacts with the mesomeric structure where the carbon radical is rearranged to the 5-position. Finally, the resulting peroxyl radical abstracts a hydrogen atom from the intermediate aquairon(II) species which regenerates the hydroxoiron(III) biocatalyst and produces the selectively hydroperoxidized product.

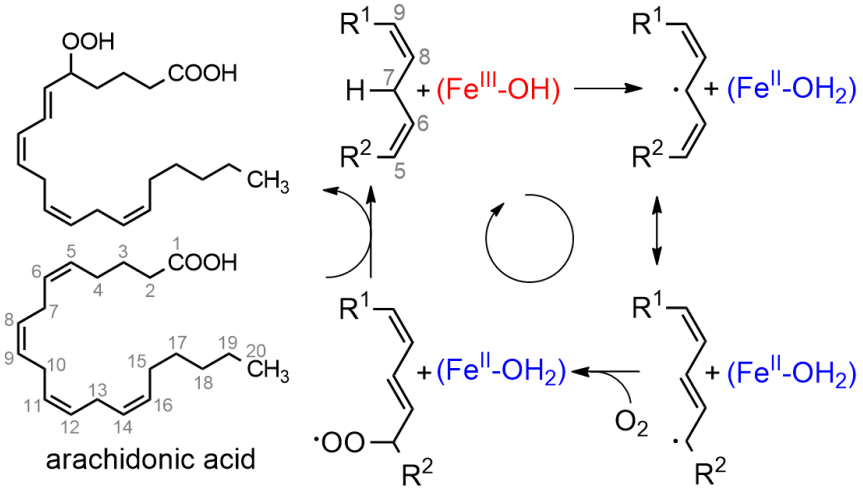

Scheme 2. Generally accepted radical mechanism for the peroxidation of the 1,4-pentadiene units in polyunsaturated fatty acids by rLOX. The regioselectivity of the enzymatic catalysis is exemplified with the natural substrate arachidonic acid.

Simply stated, the enzymatic active site of lipoxygenase is only responsible for activating the substrate via an initial hydrogen atom abstraction, which is mechanistically described as a concerted proton-coupled electron transfer (cPCET) in current research.[1,54,64,76,77] After this initial reaction, the activated substrate itself performs the radical rearrangement and reaction with molecular oxygen without further assistance from the active site, although the protein scaffold of the enzyme still ensures regioselectivity by providing a substrate binding channel.[69] Even the regeneration of the catalyst is initiated by a hydrogen atom abstraction by the peroxyl radical substrate. Thus, fundamentally, it appears likely that a small molecule synthetic analogue could achieve the same C–H activation and oxidizing reactivity.

The unique substrate activation pathway, the rather simple catalytic cycle, and the mononuclear active iron core promise an interesting research opportunity towards novel biomimetic oxygenation catalysts. However, because the modelling of the hydroxoiron(III) core is very challenging, the feasibility of a complete small-molecule analogue (combining structural and functional properties) had not been proven prior to this work and only limited examples for structural or functional analogues existed. Thus, a review of the challenges in achieving model complexes for lipoxygenase active sites (section 1.2.5) and the current state of research (section 1.2.6) is important to understand the strategies that this work aims to employ to achieve such an analogue.

1.2.5. The Challenges of Stabilizing Ferric Hydroxide Complexes

Probably the most challenging part of generating a structural model for the active site in rabbit lipoxygenase is the preparation of a mononuclear (hydroxo)iron(III) complex that maintains its mononuclearity in solution and does not undergo the usually observed formation of μ-oxo- or μ-hydroxo bridged multinuclear iron(III) species.[78,79] Until recently, reports of mononuclear (hydroxo)iron(III) complexes that had been structurally characterized were rare. However, an increasing number of new examples have been published over the last few years, providing evidence of a developing interest in such compounds.[78,80,81,82,83–91] Strategies to achieve mononuclearity are listed in the following:[1]

1. Sterical shielding of the Fe^{III}–OH site.[83,84]
2. Increased electron donating capabilities of the ancillary ligands by incorporating negatively charged donor groups.[89–91]
3. Large overall positive charge of the metal complex to increase the affinity of the iron core to the anionic hydroxide.[75,92]
4. High coordination number of the iron(III) ion.[85]
5. Hydrogen bond donor or acceptor groups in ancillary ligands for secondary stabilizing interactions with either the electron lone pair or the proton of the coordinated hydroxide ligand.[80,81,86]

Because of the well-known characteristic Fe(III)–OH moiety in lipoxygenase enzymes as biological example, most reported synthetic mononuclear ferric hydroxide complexes claim to be biomimetic at least to some degree. In the following, an overview over the (subjectively) most important synthetic modelling efforts for the lipoxygenase active sites prior to this work and their findings is provided.

1.2.6. Previous Efforts to Model Lipoxygenase Active Sites

Both functional and structural model complexes for lipoxygenases have previously been reported. However, prior to this work, none of the structural models could reproduce both catalytically relevant redox states and demonstrate functionality towards R–H bond activation. Likewise, the previously reported functional model complexes for lipoxygenases are limited to stoichiometric R–H activation rather than catalytic R–H bond oxidation and differ significantly from the enzymatic active sites with respect to their immediate ligand environment and electronic properties.

The most important advances in structural modelling were probably made by the groups of Watanabe (1998) and Kovacs (2015) for the catalytically relevant ferric hydroxide and ferrous aqua species, respectively (Figure 7).[79,80]

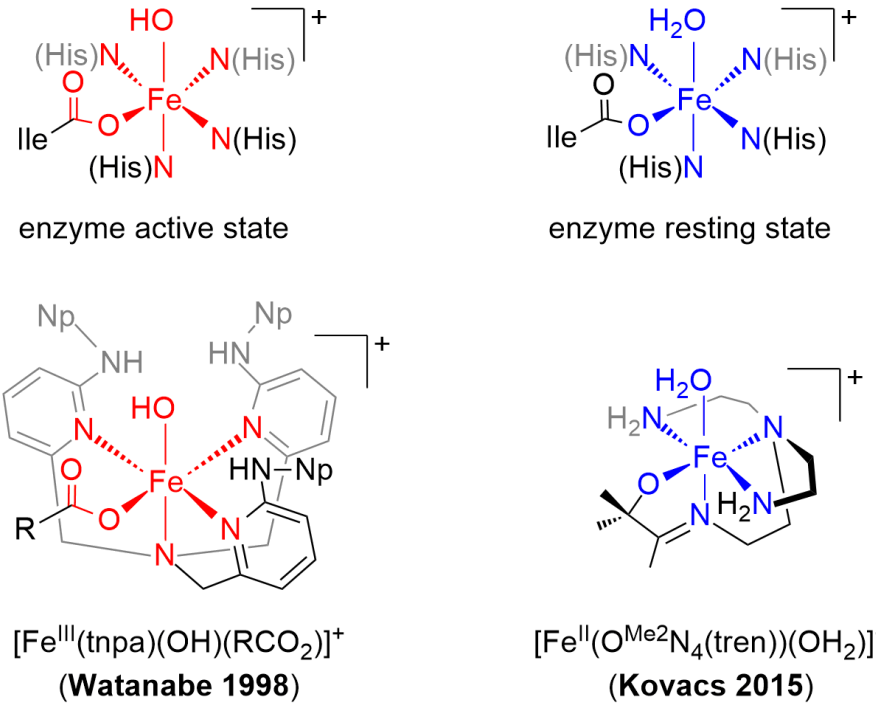

Figure 7. Structural model complexes for the active site of rabbit lipoxygenase by Watanabe and Kovacs,[79,80] respectively. tnpa = tris(6-neopentylamino-2-pyridylmethyl)amine, R = C_6H_5 (1998),[80] CH_3, H (2002);[81] $O^{Me2}N_4$(tren) = 3-((2-(bis(2-aminoethyl)amino)ethyl)imino)2-methylbutan-2-olate); Ile = C-terminal isoleucine residue; His = Histidine residue.

Although Watanabe *et al.* succeeded in the stabilization of a mononuclear ferric hydroxide complex and in the reproduction of the first coordination sphere, neither the

original model complex nor the derivatives reported four years later showed any reactivity.[80,81] Nonetheless, Watanabe and his group were the first to demonstrated that the electronic and spectroscopic properties of the enzymatic active site of lipoxygenases could be reproduced by a *cis*-(carboxylate)(hydroxo)iron(III) complex with four ancillary nitrogen donors, supporting the generally accepted theory of such an active species in spite of lacking crystallographic evidence for the active enzyme. Additionally, they found that, in such a configuration, the carboxylate ligand takes part in an intramolecular hydrogen bonding interaction with the hydroxide – a key feature that will be further elaborated on in this work.

Although Kovacs *et al.* did not reproduce the carboxylate moiety and the intramolecular hydrogen bond in the ferrous species, they succeeded in stabilizing a high-spin, monocationic *cis*-(alcoholato)(aqua)iron(II) complex with four ancillary nitrogen donors, thus modelling the first coordination sphere of the resting state of rabbit lipoxygenase.[79] Even more importantly, this structural model was shown to be capable of hydrogen atom donor reactivity similar to the catalytic step in lipoxygenases that regenerates the active ferric hydroxide species (see above). However, in this example, the ferric hydroxide product is immediately deactivated and converted to a diferric oxygen bridged species. Despite the reactivity of the ferrous complex, it cannot be considered a true functional model as it does not reproduce the fundamental substrate R–H activation reactivity of the active enzyme species even though the demonstration of O–H bond breaking in the ferrous complex species is a notable advancement.

In terms of functional models, the example by Stack *et al.* (2006) was long considered to be the state of the art.[75] Although this ferric hydroxide complex is dicationic and contains five ancillary nitrogen donors and no carboxylate, Stack *et al.* were able to maintain the reactivity and achieve hydrogen atom abstraction from weak C–H bonds (Cyclohexadiene, Dihydroanthracene). This was the first time that such a reactivity was precedented for synthetic ferric hydroxide complexes. Nonetheless, Stack *et al.* failed to demonstrate any catalytic reactivity and the regeneration of the active species, as the proposed reduced ferrous aqua species was not evidenced by stability in the same solvent as the ferric hydroxide complex.

In 2017, Groves *et al.* reported on a low spin, tetracationic *trans*-(hydroxo)(aqua)iron(III) porphyrazine complex that performed hydrogen atom abstraction (HAT) in water and exhibited the highest reactivity of any known synthetic

ferric hydroxide complex.[92] Additionally, a large kinetic isotope effect KIE = 20 that comes closer to that of lipoxygenases (KIE = 80) than any other functional model was described.[75,93] The bond dissociation free energy (BDFE) of the corresponding air stable low spin *trans*-di(aqua)iron(II) porphyrazine was determined to be 84 kcal·mol^{-1} (in H_2O) and the kinetics were found to be 5-6 orders of magnitude faster than previous examples. However, the strategy to achieve this high reactivity was likely not motivated by a biomimetic approach but rather by a simple thermodynamic one: The increase of the overall charge of the complex as high as 4+ modulates the electrochemical potential to extremely positive values and thus increases the driving force for HAT driven reduction. The thermodynamic basis for such an approach is provided by the proportionality of the BDFE of the reduced species and the electrochemical reduction potential of the oxidized species as described by the Bordwell equation that is further elaborated on below.[59]

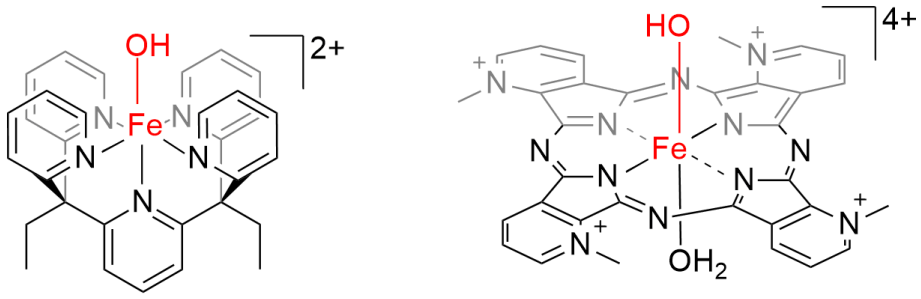

$[Fe^{III}(PY5)(OH)]^{2+}$
(**Stack 2006**)

$BDFE_{DMSO}$ = 80 kcal·mol^{-1}
KIE = 6.3

$[Fe^{III}(PyPz)(OH)(OH_2)]^{4+}$
(**Groves 2017**)

$BDFE_{H2O}$ = 84 kcal·mol^{-1}
KIE = 20.2

Figure 8. Functional model complexes for the active species of rabbit lipoxygenase by Stack and Groves.[75,92] The BDFEs describe the estimated bond strength of the formed O-H bond upon H-atom abstraction in the respective solvent. The KIE value represents the H/D kinetic isotope effect observed for a C–H abstraction from 9,10-dihydroanthracene (Stack) or xanthene (Groves) substrates. PY5 = 2,6-bis-(bis(2-pyridyl)methoxymethyl)pyridine, PyPz = tetramethyl-2,3-pyridinoporphyrazine.

The demonstration of such a high BDFE and reactivity by the Groves group is an important finding of what is achievable through the modulation of the electrochemical potential, although the structural/electronic resemblance of the enzymatic active site is limited to the ferric hydroxide/aqua moiety in the wrong spin state. Yet again, however,

no catalytic activity was reported. Moreover, no crystallographic evidence was provided for either of the two species (*trans*-(aqua)(hydroxo)iron(III) and *trans*-di(aqua)iron(II)).

In addition to the biomimetic modelling approaches and synthetic advances in stabilizing reactive mononuclear ferric hydroxide complexes, the mechanistics of the oxidative reactivity of lipoxygenases were elucidated by the Solomon group (2003) and the initial step was described as a concerted proton-coupled electron transfer.[54] Complimentary to this, the advances of the Mayer group to unify PCET with the Marcus-Theory (2011) and their further studies in the field led to a much better understanding of the lipoxygenase reactivity.[94–98] Thus, a summary of the most important aspects of current cPCET theory relevant to lipoxygenase is additionally given in the following section.

1.2.7. Hydrogen Atom Abstractions as Proton-Coupled Electron Transfer Reactions

Hydrogen atom transfer (HAT) reactions describe the most common elementary reactions that transfer two elemental particles: A proton and an electron.[94] Contrary to past assumptions, a hydrogen atom transfer is not only described by the transfer of a single hydrogen atom entity but can also entail concerted or stepwise transfers of the distinct particles.[99]

In transition metal chemistry, the electron transfer is often paramount, thus allowing for a description of HAT reactions as proton-coupled electron transfers (PCET) where the proton transfer accompanies a fundamental electron transfer.[99] This can be understood as a consequence of the transport of the electron and the proton to different localities: The electron is transferred to/from a metal site while the proton is accepted or dissociated to/from a ligand.

In the first decade of the millennium, James M. Mayer showed that standard electron transfer theory can be applied to describe the kinetics of a PCET reaction by applying the Marcus-Hush theory.[94,96,98,100–102] Here, predictions of cross-reaction kinetics from self-exchange kinetic constants were proven to be successful under the assumption of an ideal adiabatic system (equation 1).[94,100]

(1) $k_{AH/B} = \sqrt{k_{AH/A} k_{BH/B} K_{eq/B} f}$ k: rate constant, $f = \frac{(lnK_{12})^2}{4 \ln\left(\frac{k_{11}k_{22}}{Z^2}\right)}$, simplified $f = 1$

As can be expected from the applicability of the Marcus-Hush theory, transition state theory is also a very important aspect for the accurate description of PCET reactions.

The first and most obvious additional component to be considered for this is the mechanism of the coupled proton transfer which can occur in a concerted or sequential manner before or after the electron transfer, respectively.[99] However, as the proton can either be transferred along a reaction coordinate or via a tunneling mechanism in both cases, any experimental attempts to distinguish between a stepwise and a concerted PCET mechanism, e.g. via kinetic isotope effect (KIE) studies, are ambiguous. Thus, a distinction is practically only possible with *in silico* methods.[103]

The second component to transition state theory lies in the intrinsic properties of the reaction partners in agreement with the Hammond postulate that the kinetics are influenced by the transition state geometries.[104] On the one hand, there is the reorganization energy of participating metal complexes and, on the other hand, there is the nature of organic R–H bonds that will drastically influence the overall reaction barrier $\Delta G^{\ddagger}$ and, consequently, the rate constant.

The reorganization energy λ, which is practically an activation barrier term derived from Marcus theory (equation 2)[105] of a 3d transition metal complex such as iron is strongly influenced by the spin states of the oxidized and the reduced metal complexes.[98] Simply stated, the more the bond lengths and coordination environment change upon reduction/oxidation, the larger the reorganization energy becomes. The largest changes are hereby expected for a spin-state change, a change in geometry, and/or a change in the coordination number/ligand environment within a PCET reaction.[94] Thus, to maintain a low activation barrier, smaller changes are desirable. This can be achieved, e.g. by maintaining the same spin state and the same geometry and ligand environment (apart from the intrinsically necessary difference of a proton) in both oxidation states of the metal complex.[98]

$$(2)\quad \Delta G^{\ddagger} = \frac{(\Delta G^{0} + \lambda)}{4\,\lambda}$$

$\Delta G^{\ddagger}$: reaction barrier, ΔG^{0}: driving force, λ: reorganization

Similar to differing activation barriers found in metal complexes, organic R–H bonds and their radical counterparts are governed by intrinsic entropic and enthalpic properties that influence their reactivity.[99,106] This is well-described by the Eyring transition state theory and the correlation lines derived from the works of Bell, Evans and Polanyi.[107,108] Although the rate constants correlate linearly with the bond dissociation free energy (BDFE) within one type of R–H bond, e.g. O–H and C–H bonds lie on different correlation lines because of their differing intrinsic activation barriers (Figure 9).[99] Thus, C–H abstraction reactions are known to occur slower by a factor of approximately 10^4 as compared to O–H abstractions with identical BDFEs.[94] Consequently, because C–H abstraction and O–H abstraction reactions follow the same mechanistic principles, it is convenient to study the much more rapid O–H abstractions as model reactions to draw conclusions for C–H abstractions.

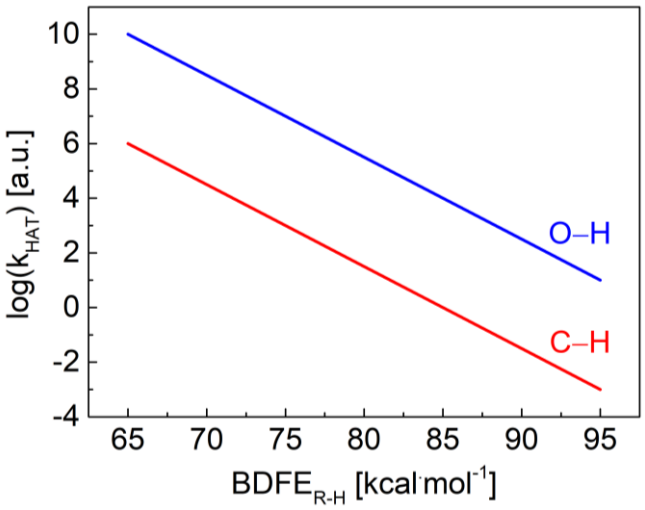

Figure 9. Idealized schematic depiction of relative Evans-Polanyi correlation lines for O–H and C–H abstraction reactions with an arbitrary reaction partner. The arbitrary log(k_{HAT}) magnitude and slope for C–H atom abstractions are roughly oriented towards the experimental rates described for the reaction of [Ru(O)(bipyridine)$_2$pyridine]$^{2+}$ with weak C–H bonds as reported by J. M. Mayer.[94] This example was chosen as a basis because of a relatively large dataset and verified behavior in line with Marcus- and Eyring theory. The log(k_{HAT}) magnitude and slope for O–H abstraction reactions aim to illustrate the approximate theoretical intrinsic kinetic differences (factor ~10^4) between C–H and O–H atom abstraction reactivities which are also described to occur in the original work.

A more detailed and very comprehensive overview about what governs and influences the kinetics in different HAT reactions is given in "*Understanding Hydrogen Atom Transfer: From Bond Strengths to Marcus Theory*" by J. M. Mayer, published in *Acc. Chem. Res.* in 2011.[94] This publication is highly recommended for further theoretical background on the topic.

Because the BDFEs of the partners in a PCET reaction describe the fundamental driving force for the energetics of the reaction, a brief description of how this value is composed in practical terms is given in the following.

1.2.8. Bond Dissociation Free Energies (BDFEs)

When regarding the strength of R–H bonds for HAT reactivity, two main aspects are important: The tendency of the substrate to engage in electron transfer reactions (redox potential) and its tendency to engage in proton transfer reactions (acidity).[96] Additionally, the reaction medium will have an influence on both and, thus, needs to be corrected for. In 1993, Bordwell summarized these fundamental aspects in an equation that is now widely used to determine bond strengths and energetics of HAT reactions:[59]

$$(3)\quad BDFE_{HA} = 1.37pK_{HA} + 23.06E_{ox}(A^{-}) + C_G$$

In this, the numeric factors are derived from thermodynamic and electrochemical considerations, C_G describes a solvent parameter, and the reference potential for E_{ox} is Fc/Fc^{+} for most solvents but SHE for H_2O.[96] A thorough discussion as well as a derivation of the formula are given in a chemical review publication by J. J. Warren, T. A. Tronic, and J. M. Mayer (2010) that is suggested for further details.[96] However, it must also be noted that some corrections of the thermodynamic solvent constants were published recently.[97,109]

Following the notion of sequential or concerted proton-coupled electron transfer reactions (section 1.2.7), a “thermodynamic square” can be drawn that allows for the determination of BDFEs by using the pK_a and $E_{1/2}$ values of different involved species in agreement with Bordwell’s equation.[79,96] An example for a metal complex capable of proton-coupled electron transfer is given in Figure 10.

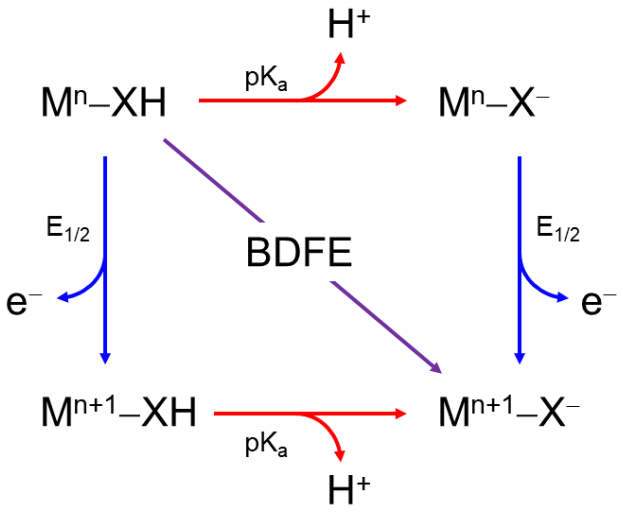

Figure 10. Thermodynamic square exemplified for a metal complex M with a positive charge n (n+1) and a proton donor/acceptor ligand XH (X^-). The BDFE can be calculated by determining the $E_{1/2}$ and pK_a values for one of two paths for a proton-electron ($H^\bullet$) transfer.

As a final statement, it must be noted that a critical review of the literature values is extremely important, as many errors have occurred and carried throughout the literature when it comes to BDFEs and PCET reactions: In the past, BDE was often used as a synonym for BDFE;[75,110] however not all BDE values consider an entropic component, as BDE would accurately only describe the bond dissociation enthalpy. Additionally, many reported BDFEs have relied on erroneous C_G solvent constants that were later reviewed and corrected.[79,97] Furthermore, some works have converted BDFEs between solvents by simply exchanging C_G or compared BDFEs derived from different solvents, which is, however, a flawed method that does not accurately reflect the thermodynamic fundamentals.[96,111] Although J. M. Mayer had attempted to review and correct many of these mistakes in the literature,[96] the erroneous C_G values were reported in his review and only corrected for 10 years later, which has added to the confusion.[97,109]

1.3. Objectives

The overarching goal of this thesis was to synthesize structural/electronic model complexes for the rabbit lipoxygenases and investigate their electronic/structural properties as well as their reactivity towards hydrogen atom transfer (HAT) from weak O–H and C–H bonds. The project was divided into specific, measurable, and achievable (within the time frame of a PhD program) subgoals which are given below as primary and secondary objectives according to their relevance to the main goal of this work. Because parts of this work build on previous, unpublished results obtained in the Krüger group, a differentiation statement is given at the beginning of the first "results & discussion" chapter (chapter 2). The motivation and relevance of the overall study is summarized in section 1.4.

1.3.1. Primary Objectives

1.3.1.1. Synthesis and Characterization of a Structural/Electronic Model for rLOX

The first objective was to develop a synthesis to obtain pure samples of $[Fe(LN_4{}^tBu_2)(O_2CPh)(OH)]^+$ (**1**) and a corresponding $[Fe(LN_4{}^tBu_2)(O_2CPh)(OH)_2]^+$ (**2**) complex and characterize both via a plethora of analytical methods in the solid state and in solution to describe their structural, electronic, magnetic, spectroscopic, spectrometric, and electrochemical properties. This aimed to precedent the first example for a pair of structural/electronic model complexes representing both relevant oxidation states participating in the catalytic cycle of a lipoxygenase (rLOX). The results of this study are given in chapter 2 (section 2.1).

1.3.1.2. Establishing of the Reactivity of the Structural/Electronic Models

As a second objective, the reactivity of the ferric complex **1** was to be studied towards hydrogen atom transfer towards weak O–H bonds under nitrogen atmosphere. In this, the production of **2** should be ascertained and the BDFE of **2** should be determined for comparability to libraries of X–H bond strengths and future reference. Subsequently, the reactivity of **1** towards C–H bonds with thermodynamically suitable bond strengths

should be investigated under nitrogen atmosphere and paired with a kinetic study, ideally including a kinetic isotope effect (KIE) investigation if feasible. Once the nature of the reactivity was established under nitrogen atmosphere, **2** was to be probed for oxidation to **1** with air and, consequently, **1** was to be probed for catalytic activity in the oxidation of weak O–H and C–H bonds. After conclusion of the experimental reactivity studies, a theoretical study to verify the results and determine the mechanism of the HAT reactivity was sought after. For this, a collaborator should be attracted. The reactivity investigation of **1** and **2** aimed to precedent the first reactive structural model complexes of lipoxygenases and provide evidence that the fundamental reactivity can be modelled via small molecule analogues. The results of this study are given in chapter 2 (sections 2.3 and 2.4).

1.3.1.3. Electronic Derivatization of the Complete Synthetic Analogue to Study Structure-Function Relations

As a third objective, building on the precedence of a first structural-functional model system, the ligand environment should be electronically derivatized with electron withdrawing (–NO_2) and electron donating (–OMe) groups in the backbone of the carboxylate ligand as $[Fe(LN_4{}^tBu_2)(O_2CPh^R)(OH)]^+$ and $[Fe(LN_4{}^tBu_2)(O_2CPh^R)(OH_2)]^+$. The influence of electronic variation on the structural, electronic, magnetic, spectroscopic, spectrometric, and electrochemical properties was to be elucidated. Moreover, the reactivity of the resulting ferric complexes was to be compared to the above-mentioned example **1**. In this, the derivatized ferric complexes were to be investigated towards their reactivities with weak O–H and C–H substrates and towards their thermodynamic parameters (BDFEs) and kinetics. The results of this study are given in chapter 3 (sections 3.1 and 3.3).

1.3.2. Secondary Objectives

1.3.2.1. The Study of Aquairon(II)-Hydroxoiron(III) Associates

During the development of the synthetic pathways to attain the first objective (see above), the co-crystallization of the *cis*-(carboxylato)(aqua)iron(II) complex **2** and *cis*-(carboxylato)(aqua)iron(III) complex **1** as $\{[\mathbf{1}][\mathbf{2}]\}^{2+}$ pairs/associates was observed. This sparked interest in a further study of the interactions between these cations and gave rise to an additional, fourth objective that somewhat aligns with the reactivity studies of these types of complexes (sections 2.3 and 3.3). At first, a characterization of the co-crystallized species was to be done to probe for evidence of (magnetic) metal-metal interactions or hydrogen atom self-exchange reactions in the solid state. Secondly, solution-based kinetic studies should be done to determine the hydrogen atom self-exchange rate in solution and clarify if preorganized $\{[\mathbf{1}][\mathbf{2}]\}^{2+}$ associates are present in solution that could influence the kinetics of the hydrogen atom abstraction from organic substrates. The results of this study are described in chapter 4.

1.3.2.2. Synthesis and Characterization of a rare *cis*-Di(hydroxo)iron(III) Complex

Finally, because of the apparent stability of mononuclear ferric hydroxide complexes containing the macrocyclic ligand L-$N_4{}^t Bu_2$, the targeted synthesis and characterization of an extremely rare *cis*-di(hydroxo)iron(III) should be attempted as a fifth objective. Through a thorough characterization in the solid state and in solution, the stability of a *cis*-di(hydroxo)iron(III) complex should be evidenced and precedented. This was found to be of interest as only a single example for the stabilization of such a species in the solid state exists. However, no systematic study was done to investigate the solution stability of such a species and, thus, this gap in the literature should be filled. The results of this study are described in chapter 5.

1.4. Motivation and Relevance

In the first instance, the motivation to pursue the challenge of attaining the first complete synthetic analogues for a lipoxygenase came from promising results that had already been obtained in the Krüger group prior to this work. This includes the demonstrated accessibility of a *cis*-(carboxylato)(hydroxo)iron(III) complex with the tetradentate macrocyclic *N*,*N*'-di-*tert*-butyl-2,11-diaza[3.3](2,6)pyridinophane ligand (L-N$_4$*t*Bu$_2$) and preliminary reactivity studies that indicated its capability to abstract hydrogen atoms from weak O–H and C–H bonds.[2,112,113] However, as is described in the differentiation statement in chapter 2, these results were only preliminary and an additional thorough and complete study was required. In the following, the reasons to further pursue, conclude, and extend this work (primary objectives) are described alongside additional information on the motivation for the secondary objectives.

1.4.1. Primary Objectives

1.4.1.1. The L-N$_4$*t*Bu$_2$ Ligand – A Unique Opportunity

When the project was conceived, it was found that the tetradentate L-N$_4$*t*Bu$_2$ ligand, which has been employed in the Krüger group for decades,[3,114,115] is particularly suitable for the approach to synthesize reactive small molecule analogues of the rabbit lipoxygenase (rLOX) active site. Because of its small ring size and rigidity, an equatorial coordination of this ligand cannot be achieved for 3d metal ions such as iron. Thus, the tetradentate macrocycle folds along the N$_{amine}$-N$_{amine}$ axis to coordinate the pyridine nitrogen donors equatorially and the amine nitrogen donors axially, leaving room for two additional equatorial ligands in *cis*-position in a (pseudo-)octahedral coordination environment around e.g. Fe^{3+} and Fe^{2+} ions (Scheme 3).[114] With four nitrogen donors this macrocycle can facilitate the accurate reproduction of the first coordination sphere of the active site of the enzyme when the open coordination sites are populated with a carboxylate and a hydroxide/aqua ligand. The folding of the macrocycle has two additional consequences that are highly important for this project: Firstly, the sterically demanding *tert*-butyl groups are positioned above and below the equatorial plane which prevents the formation of undesired μ-oxo bridged dinuclear

metal complexes while maintaining an open channel for the important interaction of a substrate with an equatorial hydroxide ligand (the proton acceptor in the HAT reaction). Secondly, the rigidity of the macrocycle imposes a steric stress on the folded ligand which consequently elongates the metal-N_{amine} bonds and distorts the octahedral environment. This raises the electrochemical potential, increasing the driving force for a $Fe^{3+/2+}$ reduction that occurs in the desired HAT reaction. In summary, the L-$N_4{}^t Bu_2$ ligand provides a unique opportunity to not only stabilize rare mononuclear iron(III) hydroxide complexes but also accurately model the active site of rLOX while supporting the desired HAT reactivity. Preliminary results have already indicated that this may allow forthe unification of structural and functional properties in a single model complex.

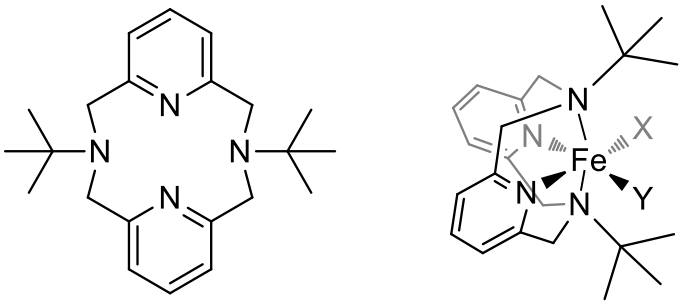

L-$N_4{}^t Bu_2$ [Fe(L-$N_4{}^t Bu_2$)(X)(Y)]

Scheme 3. Schematic depiction of the tetradentate macrocyclic ligand L-$N_4{}^t Bu_2$ (left) and its coordination mode (right). The coordination mode is exemplary shown with iron and two placeholder ligands (X, Y) that complete the (pseudo-)octahedral coordination environment. An overall neutral charge is assumed in the complex example.

1.4.1.2. Lipoxygenases as Biological Paragons

Lipoxygenases are an interesting class of enzymes that are unique in their mechanism to catalyze the oxygenation of biological substrates.[54] Although non-heme iron oxidases and oxygenases have gained significant attention in bioinorganic research, most studies have dealt with the more common “oxygen-activating” enzymes and the field around modelling the “substrate-activating” lipoxygenases is underdeveloped, as described in the introduction.[53,64] The outlook to model the function of a lipoxygenase by reproducing its structural/electronic properties therefore promises a notable advancement and could demonstrate the feasibility of functional small molecule

analogues capable of direct substrate activation. Moreover, such complete synthetic analogues would allow for structure-function studies through targeted electronic derivatization which are not accessible for the metalloprotein itself. In general, an advancement in modelling lipoxygenase active sites promises to elucidate the fundamental principles that govern their reactivity which could assist in the development of e.g., new biomimetic oxidation catalysts and targeted therapeutics.[72]

1.4.1.3. The Relevance for Biomimetic Oxidation Catalysis

Iron-based biomimetic oxidation catalysis is of interest because it bears the potential to increase energy efficiency, safety, and sustainability while optimizing cost for commercially relevant transformations with a cheap and well-available metal ion that works under atmospheric conditions.[63] Current efforts are based on enzymes models that utilize an initial oxygen activation to facilitate the catalysis. However, so far, these catalysts have fallen far behind expectations with only conceptual examples and low turnover numbers that thwart their commercial application.[62,63] Precedenting a complete synthetic analogue for a lipoxygenase would highlight an alternative route towards biomimetic oxidation catalysts that function through a substrate activation as the initial step. The fact that such a pathway avoids thermally unstable iron peroxo/hydroperoxo/superoxol/oxo intermediates may promise more robust biomimetic iron oxidation catalysts which could outperform current examples.

1.4.1.4. The Feasibility of a Complete Synthetic Analogue for rLOX

Synthetic analogue approaches aiming for structural-functional models are rarely successful, because e.g., second coordination sphere interactions and three-dimensional substrate channels provided by the protein matrix cannot be well-modelled by small molecules.[35,36] Moreover, complex reaction mechanisms and additional cofactors present in the biological examples further complicate the reproduction of all relevant functional, structural, and electronic features in most cases. In the case of rLOX, the simple pseudo-octahedral iron(III) complex active site fundamentally only performs an initial hydrogen atom abstraction to catalyze the reaction of a substrate with triplet oxygen. This works without a cofactor or the apparent need of secondary protein interactions beyond regioselectivity.[54] Because of the

simplicity of the iron core, the mechanism, and the ubiquitous availability of triplet oxygen under atmospheric conditions, the modelling of a functional-structural analogue appears feasible for rLOX.

1.4.2. Secondary Objectives

1.4.2.1. The Curious Co-Crystallization of *cis*-(carboxylato)(aqua)iron(II) and *cis*-(carboxylato)(hydroxo)iron(III) Complexes

Because it was found that the monocationic *cis*-(carboxylato)(aqua)iron(II) complex **2** and the *cis*-(carboxylato)(aqua)iron(III) complex **1** could co-crystallize with a short hydrogen bridge between the aqua ligand of **2** and the hydroxide ligand of **1**, two ideas arose that motivated further studies. Firstly, the short hydrogen-bridged distance between the two complexes sparked speculations about potential magnetic interactions and hydrogen atom self-exchange reactions in the solid state. Thus, studies were done to explore such a potential reactivity in the solid state. Secondly, the association of the cationic complexes in the crystal lattice gave rise to the idea that such associates could also exist in solution and describe a self-inhibition pathway in solution especially at high complex concentrations. Thus, a kinetic study of the self-exchange kinetics was motivated by the idea that this could provide further information on the reactivity of the model complexes in solution.

1.4.2.2. Precedenting Solution-Stability of a *cis*-Di(hydroxo)iron(III) Complex

Because it appeared feasible to stabilize an extremely rare *cis*-di(hydroxo)iron(III) complex with the L-N$_4$^{t}Bu$_2$ ligand scaffold, this was first attempted out of pure academic curiosity. However, as the only reported example for such a species was reported without a systematic study on solution stability and lacked a thorough characterization, it was found that this work could contribute to identifying analytical markers and precedent the solution stability of a *cis*-di(hydroxo)iron(III) species.[78] This is considered relevant for fundamental research and may provide a basis for the future spectroscopic identification of such species e.g. in catalytic cycles.

Results

&

Discussion

2. The First Structural Functional Model for the Active Site of Rabbit Lipoxygenase

This chapter describes the synthesis and characterization of the first complete synthetic analogue metal complexes of the active iron site in rabbit lipoxygenase (rLOX) which accurately model the structural and electronic properties of the enzyme as well as its reactivity.

In section 2.1, a mononuclear pseudo-octahedral *cis*-(carboxylato)(hydroxo)iron(III) complex with a tetraazamacrocyclic ligand is presented (**1**) alongside the corresponding (carboxylato)(aqua)iron(II) (**2**) and η^2-(carboxylato)iron(II) complexes (**3**). All three compounds were derived from suitable iron(III) (**4**) and iron(II) (**5**) complex precursors (Scheme 4). A thorough investigation of the electronic and structural properties of the complexes **1**-**3** reveals that both the hydroxoiron(III) and the aquairon(II) complex accurately model the first coordination shell of the only two essential states found in the enzymatic mechanism of peroxidation of polyunsaturated fatty acids while **3** might represent a previously not discussed chelated resting state of the enzyme that is present in an equilibrium with the aquairon(II) complex.

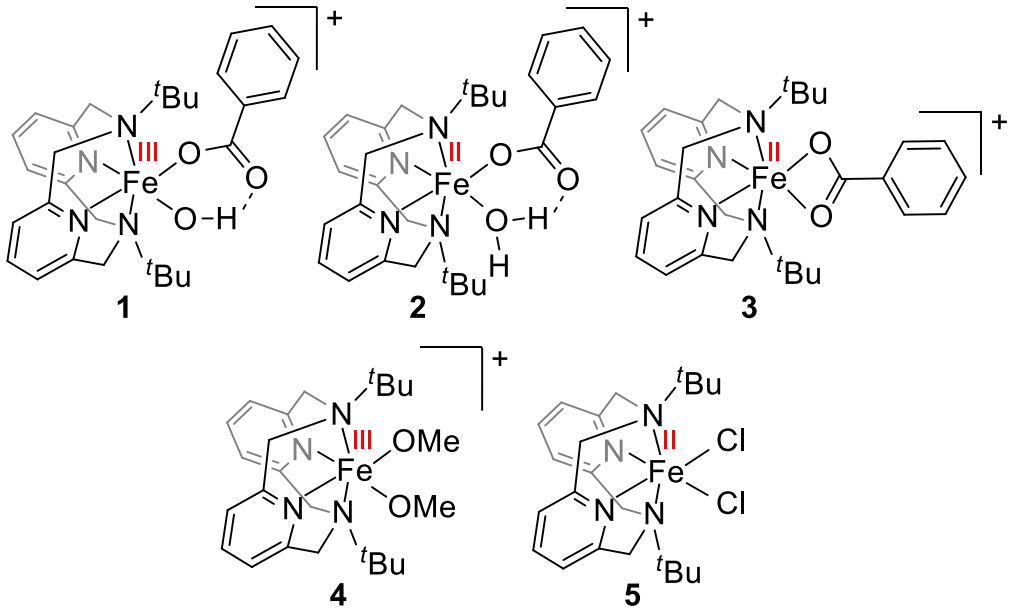

Scheme 4. Depiction of the complex cations to be discussed in this chapter.

In section 2.3, the reactivity studies of complexes **1** and **4** with weak X–H bonds are described alongside evidence for the capability of **2** (and **3**) to be oxidized to **1** under aerobic conditions. The studies reveal that **1** is capable of hydrogen atom abstraction from weak O–H and C–H bonds to produce **2** while **4** does not show such a reactivity under the same conditions. The fundamental reactivity of **1** with selected substrates is supported by an experimental determination of the driving force and bond dissociation free energy (BDFE) of the O–H bond in **2** that is formed upon hydrogen atom abstraction with **1**. Moreover, the results of preliminary kinetic studies are provided to compare the differences in activation barriers between O–H and C–H abstraction reactions with theoretical considerations. The capability of **2** to produce **1** under aerobic conditions concludes that **1** can function as an oxidation catalyst which is demonstrated with 2,4,6-tri-*tert*-butylphenol as a substrate. The results of complementing theoretical investigations that are provided in section 2.4 support a concerted proton-coupled electron transfer (cPCET) mechanism for the initial step which is in close analogy to the enzymatic mechanism.[54]

Differentiation from Previous Works

For clarity, it is stated that the iron(II) precursor **5** and its synthesis have been previously described by *Krüger*.[114] Secondly, while this work builds on previous results by *Rauber*, *Bonck*, and my own master thesis, a clear distinction can be made. Notably, all previous works relied on the oxidation of a ferrous precursor with air or a pure oxygen atmosphere to the generate the ferric complex **1**.[2,112,113,116] However, over the course of this thesis it was found that this is an impractical method that does not yield the pure product as the reaction is not quantitative. The supposed reason for this is the affinity of the hydroxoiron(III) and the aquairon(II) complexes to co-crystallize (see chapter 4). This had probably gone unnoticed as impurities of an aquairon(II) species in the hydroxoiron(III) product are near impossible to identify with most spectroscopic methods: The error in combustion analysis is too large if the impurity only differs in one hydrogen atom, IR spectroscopy, UV-vis-NIR and cyclic voltammetry are barely sensitive enough to detect such an impurity if it falls below a certain percentage, $S = 2$ species are not observed with X-band EPR spectroscopy and reduced species observed with ESI-mass spectrometry conditions are obscured by artificially generated ferrous species by the ionizing conditions of the measurement. Only Mößbauer spectroscopic analysis can meet the requirements to probe for such an impurity, a

method that had not been applied in the previous works and now revealed variable amounts of ferrous impurities (~10 %) in the “ferric” compounds directly synthesized by oxidation of a ferrous precursor with O_2. Importantly, the ferric product can also be reduced by the stabilizing agent 2,6-di-*tert*-butyl-4-methyl-hydroxyphenol (commonly known as butylated hydroxytoluene BHT) present in commercial Et_2O. As the crystallization and isolation of the ferric complex had been done using Et_2O in previous works and no cautionary statement was added, the thought of further impurities imported from such a source can also not be excluded. Therefore, all previous results obtained with respect to **1** can only be viewed as preliminary. In this work, an alternative route was found to yield analytically pure bulk material of **1** and careful attention was directed to the purity of the ferric species. All characterizations, investigations and studies were conducted on verified pure compounds.

Notably, while the crystal structure of **3** was previously reported in my master thesis, no further reliable characterizations were done, as the described IR-spectrum was not matched with an elemental analysis that fit the theory. Thus, the synthesis was repeated and all characterizations described in this chapter are unique results obtained over the course of this work.

Additionally, while the triflate salt of **4** had been previously reported by *Mirica et al.*,[117] the compounds that contain **4** as the complex cation described in this thesis were synthesized with a vastly different procedure and are unique with respect to the different counterions employed. All described investigations pertaining **4** were done independently and within this work.

With respect to the reactivity studies, preliminary results could be obtained in all previous theses on the topic. In the work of *Rauber*, the oxidation of a variety of substrates with weak O–H bonds was investigated with *in situ* generated **1**.[112] In the work of Bonck, C–H activation studies were done with isolated **1**.[113] However, as stated above, the purity of the complexes cannot be verified due to the synthetic procedure through which they were obtained. The same is true for the reactivity studies conducted in my own master thesis.[2] Thus, while the preliminary results were promising even before the investigations of this work, the reactivity studies appeared unreliable and were revisited with verified pure compounds.

Author Contributions

This chapter contains previously published work that has been reproduced (adapted) with permission from “E. Dobbelaar, C. Rauber, T. Bonck, H. Kelm, M. Schmitz, M. E. de Waal Malefijt, J. E. M. N. Klein, and H.-J. Krüger, “Combining Structural with Functional Model Properties in Iron Synthetic Analogue Complexes for the Active Site in Rabbit Lipoxygenase” *Journal of the American Chemical Society* **2021**, 143 (33), 13145-13155, DOI: 10.1021/jacs.1c04422”. Copyright 2021 American Chemical Society and the supporting information, respectively.[1] In the interest of consistency, the numbering of the compounds is kept analogous to that of the original manuscript.

All synthetic developments, syntheses, crystallizations, data collections, structural, spectroscopic, spectrometric, magnetometric, and electrochemical characterizations and analyses as well as all data workup, reactivity studies and nearly all interpretations described in the published manuscript, the supplementary information, and this thesis, respectively, were done during this work if not stated otherwise. X-Ray diffraction data and Mößbauer spectroscopic data were collected and interpreted by Dr. Harald Kelm and SQUID magnetometric data was collected by Dr. Markus Schmitz. Theoretical calculations were performed and interpreted by Johannes E. M. N. Klein and Matina E. de Waal Malefijt, B.Sc. The manuscript, figures, tables, and the supplementary information that are reproduced (adapted) in this work were written and prepared by Emiel Dobbelaar under the supervision of Hans-Jörg Krüger, and with help from Johannes E. M. N. Klein with respect to the theoretical calculations as indicated (section 2.4). Intellectual credit must be attributed to previous works that provided preliminary results and the motivation for the project as mentioned above in the differentiation statement.

2.1. Synthesis and Characterization

2.1.1. Synthesis

The most convenient way to synthesize iron(II) complexes with a macrocyclic diazapyridinophane ligand such as *N*,*N*'-di-*tert*-butyl-2,11-diaza[3.3](2,6)pyridinophane (L-$N_4{}^tBu_2$) is to utilize an established $[Fe(L\text{-}N_4{}^tBu_2)(X)_2]^{n+}$ complex precursor and exchange the monodentate coligands X to obtain the target material. In this case, the chloride ligands of the dichloroiron(II) complex $[Fe(L\text{-}N_4{}^tBu_2)Cl_2]$ (**5**), first reported by Krüger,[114] were exchanged by a benzoate ligand through a salt metathesis reaction with sodium benzoate and a suitable counterion (Scheme 5). Under dry, anaerobic conditions, this yields the ferrous complex $[Fe(L\text{-}N_4{}^tBu_2)(O_2CPh)]^+$ (**3**) where the benzoate acts as a bidentate chelating ligand. In the presence of small amounts of water, the aquairon(II) complex $[Fe(L\text{-}N_4{}^tBu_2)(O_2CPh)(OH_2)]^+$ (**2**) can be obtained where the benzoate acts as a monodentate ligand and engages in an intramolecular hydrogen bond with the aqua ligand in *cis* position.

Synthesizing a mononuclear hydroxo-iron(III) complex is more challenging, as such species usually tend to form thermodynamically more favourable dinuclear μ-oxo bridged complexes. The strategy to inhibit such a formation endowed the steric shielding with the bulky *tert*-butyl substituents of the macrocyclic ligand and hydroxide ligand stabilization via an intramolecular hydrogen bond with the carboxylate ligand in *cis*-position. Under air, complex **2** indeed forms the mononuclear complex $[Fe(L\text{-}N_4{}^tBu_2)(O_2CPh)(OH)]^+$ (**1**) as an oxidation product, but this reaction is not fully quantitative and is, therefore, an impractical method of obtaining complex **1** as an analytically pure material (also see chapter 4). Thus, although the proof of principle is valuable, a suitable iron(III) precursor has to be identified for the synthesis of analytically pure **1**. Such a precursor can conveniently be obtained by the aerobic oxidation of **5** in alkaline methanol in the presence of a suitable counterion, yielding $[Fe(L\text{-}N_4{}^tBu_2)(OMe)_2]^+$ (**4**). The treatment of **4** with one equivalent of benzoic acid in acetonitrile containing small amounts of water results in the formation of the hydroxoiron(III) complex **1**.

Overall, complex cations **1**, **2**, and **4** were isolated with a variety of counterions as described in Scheme 5. Further synthetic details can be found in the experimental section.

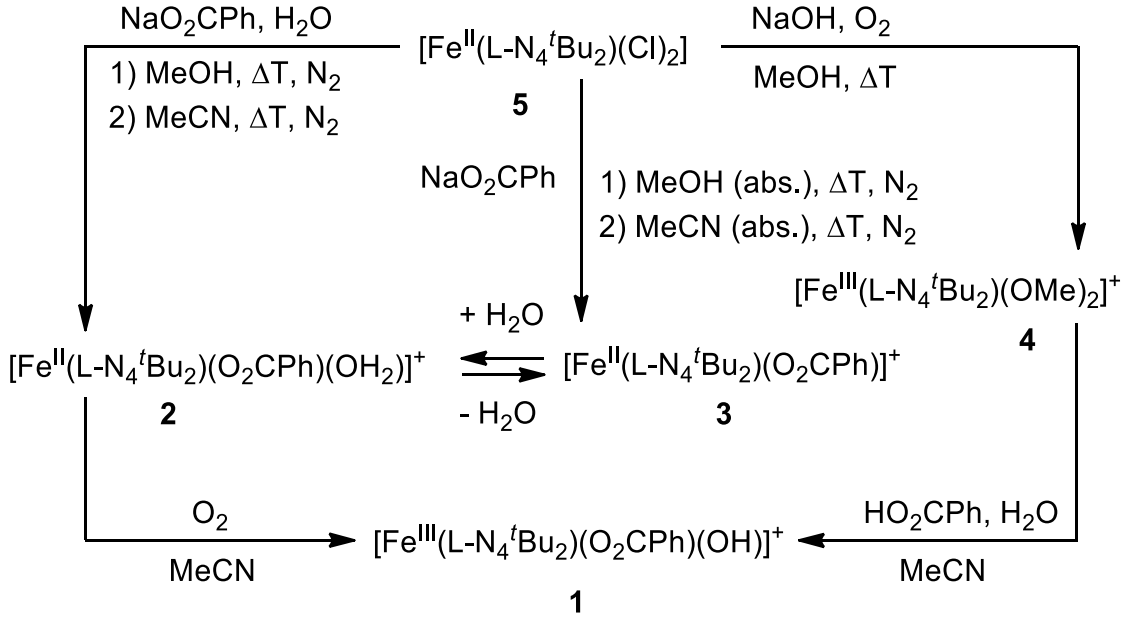

Scheme 5. Synthetic reactions. The cationic complexes were crystallized and isolated as [**1**](BPh_4) (**1a**), [**1**](BPh_4)•MeCN (**1b**), [**1**](PF_6) (**1c**), [**2**](ClO_4) (**2a**), [**2**](PF_6) (**2b(1)**, *P2₁/n* and **2b(2)**, *C2/c*), [**2**](CF_3SO_3) (**2c**), [**3**](ClO_4•MeCN) (**3a**), [**4**](BPh_4) (**4a**), [**4**](PF_6) (**4b**), [**4**](ClO_4) (**4c**).

Starting with the previously described precursor **5**, all syntheses were designed to follow the principles of *green chemistry*.[118] Reagents with rather low hazard or even non-hazardous reagents such as water were used, and all transformations resulted in good atom economy and high yields with respect to the products. As by-products, only non-hazardous substances such as sodium chloride or water, or common solvent molecules such as methanol were produced. When feasible, the transformations were done at room temperature to increase energy efficiency. Although the use of acetonitrile as a solvent is not ideal from a green chemistry perspective, it is necessary as an aprotic polar solvent and has the advantage of very high solubility such that only small quantities (~10 mL) are required for e.g. the synthesis of significant amounts of **1** from **4** for further studies. Methanol is required as a reagent and coordinating solvent and is, thus, imperative for the synthesis, although ethanol may be a feasible, greener alternative.

Generally, attentive work is important in the synthesis of complexes **1**-**4**. While the analytically pure complex **1** can be crystallized with various counterions upon the slow addition or diffusion of diethylether, it is very important to remove any butylated hydroxytoluene (BHT) residues by distillation prior to use. This is because this frequently used stabilizing agent can reduce **1** to **2** via H-atom transfer as suggested by the preliminary reactivity studies conducted by *Rauber* and in agreement with the results of this work (section 2.3).[112] Additionally, detailed attention is to be paid to the mass spectra of **1** during product analysis to ensure the conversion of **4** to **1** is complete and that no methoxide ligands are present in the bulk product (section 2.1.9). For **2**, it has been shown that the coordinated water molecule in **2** can be replaced by a variety of alcohol molecules (e.g. by MeOH or EtOH to form $[Fe(L\text{-}N_4{}^tBu_2)(O_2CPh)(MeOH)]^+$ and $[Fe(L\text{-}N_4{}^tBu_2)(O_2CPh)(EtOH)]^+$, respectively).[2,112,116] Thus, it is important to remove any alcoholic solvent residues prior to crystallization efforts of **2** or **3**. For **3**, the additional exclusion of water is equally important.

Different counterions were employed for **1** and **2** because differences in bond lengths, angles and hydrogen bonding interactions were observed in the crystal structures (section 2.1.2). This variation and the subsequent averaging of the bond lengths obtained from multiple structures allowed for a better contemplation of the complex cations' bond lengths by reducing the influence of packing effects, contacts, and secondary interactions present in single examples. In addition, in the investigation by some physical methods (NMR, electrochemistry), the utilization of some specific counter ions is less opportune and, therefore, variations in the counterion are helpful.

It is noteworthy to point out that the triflate salt of **4** has been described by *Khusnutdinova et al.*, however, the above described synthetic approach represents a much more facile and efficient pathway.[117] Thus, this approach should be favoured in the future.

All substances were generally characterized by structural analysis, elemental analysis, ESI-mass spectrometry, and IR spectroscopy (see experimental section). The complete physical characterization was, however, only performed with selected substances: The plethora of different physical methods was applied just to compound **2a** in the case of the (benzoato)(aqua)iron(II) complex **2**, on the other hand, compounds **1a**, **1b**, and **1c** were used for characterization of the (benzoato)(hydroxo)iron(III) complex **1**. It should be emphasized here, that substances

1a and **1b** have the same counterion but differ in the presence of an acetonitrile molecule in the crystal lattice. The synthesis of the (benzoato)(hydroxo)iron(III) complex with the BPh_4^- anion sometimes resulted in the crystallization of compound **1a** and other times of **1b**. It is speculated that the rate of crystallization plays a role in determining which crystalline material is actually formed. Many factors, such as the speed of ether addition and even the numbers of scratches in the employed glassware, can influence the formation of crystallization seeds that eventually determine the rate of crystallization of each form. Thus, a controlled synthesis of the one or the other compound appears to be unfeasible. Each batch of preparation was therefore carefully analyzed by elemental analysis and, additionally, the crystalline material was surveyed by structure analytical methods for the crystal cell parameters of a number of single crystals selected at random. Both methods indicated apparent uniformity of the material in each batch. However, one must be aware that in an elemental analysis a maximum contamination of 20% by the other substance could still lead to generally acceptable deviation of only 0.3% in the nitrogen content (Table 1). For most physical characterizations, however, a mixture of both compounds will not exert any notable influence on the results. For those experiments where a molar quantity is determined, the error introduced (since it will only concern the presence or absence of an acetonitrile molecule) is estimated to be less than 5% and, therefore, negligible.

Table 1. Exemplary elemental analysis results and maximal deviations in % for the compounds described in Scheme 5. Data is given in the format “calculated (found)”.

	C [%]	**H** [%]	**N** [%]	**S** [%]	max. dev. [%]
1a	73.53 (73.33)	6.75 (6.66)	6.47 (6.56)	-	0.20
1b	72.85 (72.69)	6.78 (6.95)	7.72 (7.52)	-	0.20
1c	50.37 (50.08)	5.54 (5.73)	8.10 (8.03)	-	0.29
2a	53.84 (53.70)	6.08 (6.01)	8.66 (8.62)	-	0.14
2b	50.30 (50.20)	5.68 (5.75)	8.09 (8.12)	-	0.10
2c	51.73 (51.70)	5.64 (5.71)	8.04 (8.13)	4.60 (4.71)	0.11
3a	55.57 (55.31)	6.02 (5.92)	10.45 (10.24)	-	0.26
4a	73.01 (72.83)	7.40 (7.30)	7.09 (7.13)	-	0.18
4b	46.84 (46.76)	6.22 (6.20)	9.10 (9.19)	-	0.09
4c	50.58 (50.32)	6.72 (6.62)	9.83 (9.78)	-	0.26
5	55.13 (54.89)	6.73 (6.96)	11.69 (11.66)	-	0.24

max. dev. = maximal deviation. Method error ≤0.30 %.

2.1.2. Structural Investigation

All compounds of interest to this chapter (**1**-**4**) were crystallized directly from synthetic procedures and structurally characterized by single crystal X-ray structure analyses. Representative perspective views of the complex cations **1**, **2**, **3** and **4** derived from the structures **1a**, **2a**, **3a**, and **4b** are given in Figure 11 and Figure 12, respectively. Representative numbering of the atoms for these cations is indicated and also kept consistent for **1b**, **1c**, **2b(1)**, **2b(2)**, **2c**, and **4a** to facilitate the data analysis and the subsequent discussion. Notably, while **1b** contains two crystallographically distinct cations (**1b(a)**, **1b(b)**) and the numbering is done consecutively within the structure, the numbering of the second cation (**1b(b)**) was adapted to match the numbering scheme of the other iron complexes for the discussion. Structural parameters, a full list of bond lengths, angles, and hydrogen bonds for the structures derived from **1b**, **1c**, **2b(1)**, **2b(2)**, **2c**, and **4a** can be found in the attachment alongside the CCDC accession codes for all previously published structures.[2]

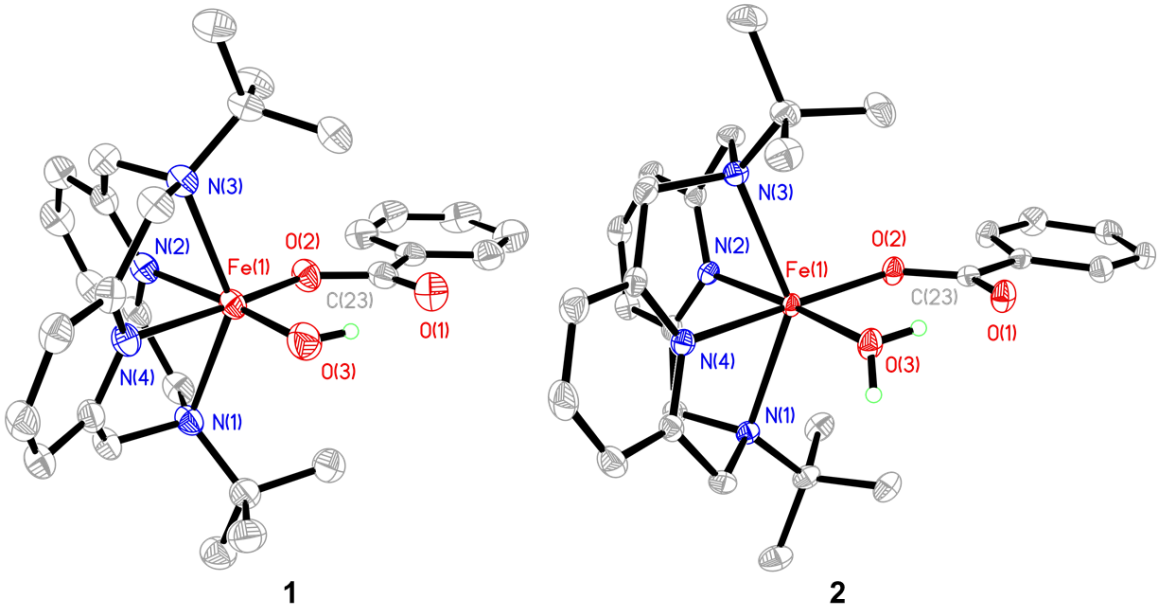

Figure 11. Perspective views of the complex cations in the ferric compound **1a**, and the ferrous compound **2a** with thermal ellipsoids displaying a probability level of 50%. Hydrogen atoms are omitted for clarity with the exception of those bound to O(3).

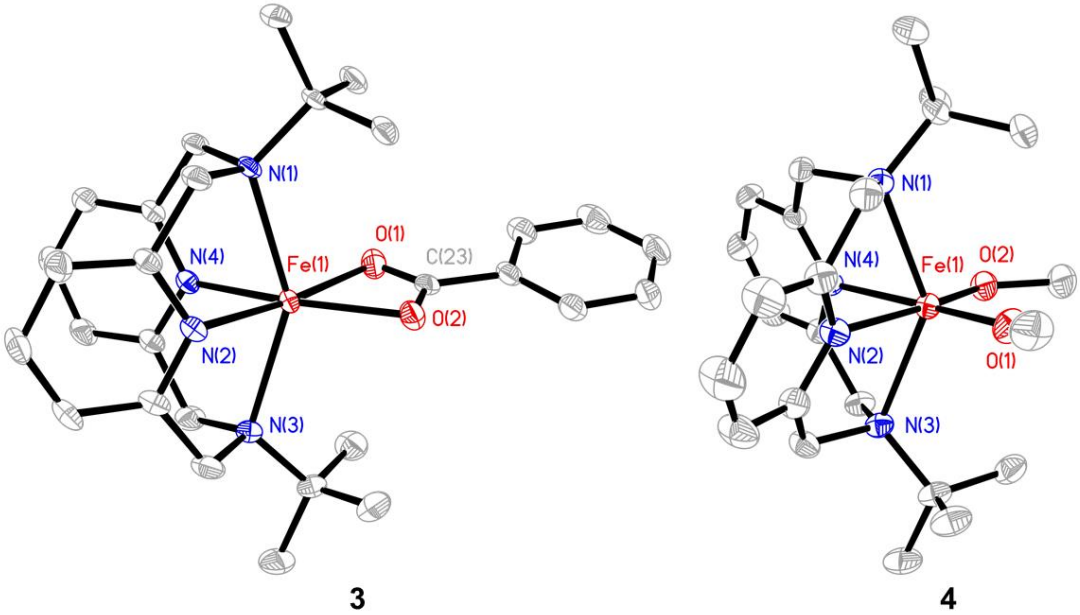

Figure 12. Perspective views of the complex cations in the ferrous compound **3a**, and the ferric compound **4b** with thermal ellipsoids displaying a probability level of 50%. Hydrogen atoms are omitted for clarity.

As evident from the structures, the tetradentate macrocyclic ligand is folded along the N_{amine}–N_{amine} axis upon coordination, leaving two *cis* coordination sites *trans* to the pyridine nitrogen donor atoms to be occupied by the two oxygen donor atoms originating from monodentate benzoate and hydroxide or water ligands in **1** or **2**, from the chelating benzoate ligand in **3**, and from the two methoxide ligands in **4**, respectively. The coordinated tetraazamacrocyclic ligand is slightly twisted, resulting in an idealized C_2-symmetry of the [Fe(L-$N_4{}^t Bu_2$)]-fragment. As usually observed in pseudo-octahedral complexes with diazapyridinophane ligands, the axial Fe-N_{amine} bonds are considerably longer than the Fe-N_{py} bonds in the equatorial coordination plane of the metal ion (Table 2 and Table 3).[115,119]

Since complex cations **1** and **2** and **4** could be structurally investigated with different counterions, the measured lengths for equivalent bonds from these different structure analyses span a range. Especially, due to different hydrogen-bonding patterns of the coordinated water molecule in the individual crystal packings, the spread of bond lengths in **2** is somewhat larger than that in **1**. Thus, in Table 2, the ranges of some selected bond lengths or interatomic distances and their changes between the ferric complex **1** and the ferrous complex **2** are provided alongside the distances of the first

coordination sphere obtained from the structural analysis of **3a**. As the intramolecular hydrogen bonds between O(3)-H(3A)···O(1) in particular are a key feature in the structures of **1** and **2**, the distances of O(3)···O(1) are also provided. As the Fe···O(1) distance characterizes the difference between a chelated benzoate and a singly ligated benzoate, these distances are also given for **1** and **2** for comparison to **3**; selected distances for **4** are given separately in Table 3, also with a range for the bonds obtained from different crystal structures. Though observable, the spread of bond lengths between different structures of **4** is rather small as no hydrogen bond interactions were observed.

Table 2. Selected bond length ranges and interatomar distances (in Å) in the ferric complex cation **1**,[a] and the ferrous complex cations **2**[b] and **3**[c] and differences Δ*d* in lengths/distances.

	3	**2**	**1**	**Δ(*d*(1)-d(2))**
Fe-O(2)	2.08	2.02 – 2.05	1.95 – 1.96	- (0.06 – 0.10)
Fe-O(3)	-	2.08 – 2.12	1.83 – 1.85	- (0.23 – 0.29)
Fe-N(1) or Fe-N(3)	2.38*, 2.40	2.35 – 2.39	2.29 – 2.34	- (0.01 – 0.10)
Fe-N(2)	2.14	2.08 – 2.10	2.10 – 2.11	+ (0 – 0.03)
Fe-N(4)	2.11	2.10 – 2.12	2.08 – 2.10	- (0 – 0.04)
Fe···O(1)	2.24	3.41 – 3.42	3.30 – 3.36	- (0.05 – 0.12)
O(1)···O(3*)*	-	2.58 – 2.63	2.79 – 2.96	+ (0.38 – 0.16)

Selected distances as obtained from the structural analyses of [a] **1a**, **1b**, and **1c**; [b] **2a**, **2b(1)**, **2b(2)**, and **2c**; and [c] **3a**. Despite the higher experimental accuracy, all bond lengths are rounded to a hundredth of an Å for clarity. N(1) and N(3) are the axial amine donors, N(2) is the pyridine nitrogen atom *trans* to the hydroxide/aqua oxygen donor O(3) in **1** and **2**, N(4) is the pyridine nitrogen atom *trans* to the carboxylate oxygen donor O(2). O(1) refers to the carbonyl oxygen atom of the carboxylate ligand. For more details see attachment. **Note: In the main text table of the original publication,[1] this value was erroneously reported as 2.31 Å because of a typing error.*

Table 3. Selected bond length ranges and interatomar distances (in Å) in the ferric complex cation **4**.

	4
Fe-O(1)	1.83 – 1.85
Fe-O(2)	1.84 – 1.86
Fe-N(1)	2.34 – 2.35
Fe-N(2)	2.11 – 2.12
Fe-N(3)	2.33 – 2.34
Fe-N(4)	2.12 – 2.13

Selected distances as obtained from the structural analyses of **4a**, **4b**, and **4c**. For **4b**, structural data obtained by *C. Rauber* were used for the analysis. Despite the higher experimental accuracy, all bond lengths are rounded to a hundredth of an Å for clarity. N(1) and N(3) are the axial amine donors, N(2) is the pyridine nitrogen atom *trans* to the methoxide oxygen donor O(2) that is disordered in the structure of **4a**, N(4) is the pyridine nitrogen atom *trans* to the second methoxide oxygen donor O(1). For more details see attachment.

The Fe-N bond lengths to the macrocyclic ligand can be used to unambiguously identify the spin state of the iron ion. The relatively long Fe–N bonds in complexes **1**, **2**, **3** and **4** are consistent with other high-spin iron complexes containing this macrocyclic ligand.[114] Shorter Fe–N_{amine} bonds in the ferric complexes **1** and **4** as compared to the ferrous complexes **2** and **3** are attributed to the increased charge density at the iron center. The stabilization of a high spin ground state even in the cases of the ferric complexes with an N_4O_2 coordination environment is a result of the strong axial distortion caused by the macrocyclic ligand. The Fe–O bond lengths of 1.83 – 1.85 Å in **1**, 2.08 – 2.12 Å in **2**, and 1.83 – 1.86 in **4** agree well with those reported for other octahedral high-spin iron(III)-hydroxide,[81,87,120] iron(II)-aqua[88,121,122] and iron(III)-methoxide[110] complexes, supporting the assignments as a hydroxide, a water ligand, and a methoxide in **1**, **2**, and **4**, respectively. The stabilization of a rare mononuclear ferric hydroxide complex is achieved through the steric shielding of the *tert*-butyl-substituents at the N_{amine} donors of the macrocyclic ligand and an intramolecular hydrogen bond interaction with the benzoate ligand. A noticeable feature in **3** is the difference of 0.16 Å in the Fe-O bond lengths. This indicates a more

localized charge character in the chelating coordination mode of the carboxylate ligand.

When comparing the bond lengths in complexes **1** and **2**, further characteristic properties of these closely related complexes are revealed. All Fe–N/O bonds decrease in length upon oxidation except for the Fe–N_{py} bond *trans* to the hydroxide/water ligand. The reverse trend for the latter bond is related to the stronger *trans* influence of the anionic hydroxide ligand. Despite this detail, the smallest change in bond length is observed for the Fe–N_{py} bonds; the already quite elongated axial Fe–N_{amine} bonds react to the change in the oxidation state of the metal ion with a somewhat larger alteration of the bond length, probably because these already weak axial bonds are characterized by rather soft vibration modes. In turn, the largest change is observed for the Fe–O bonds to the water/hydroxide and to the carboxylate ligand (0.23 – 0.29 Å and 0.06 – 0.10, respectively). This is understood to relate to the effects of electrostatic attraction between negatively charged ligands and the positively charged metal ion: The Fe–O bond to the monodentate, anionic carboxylate is expected to be more strongly affected by the charge change of the iron center than the neutral amine and pyridine nitrogen donors of the rather rigid macrocyclic ligand. Similarly, the prominent changes in the Fe–O bond to the neutral aqua (**2**) / anionic hydroxide (**1**) ligand can clearly be attributed to the difference of a neutral versus a charged ligand.

The variations in bond length and charge arising at the two oxygen donor ligands in **1** and **2** affect the hydrogen bonding interaction considerably. A list of all hydrogen bonds observed in the crystal structures of **1** and **2** is provided in Table 4 and Table 5. While the hydrogen bonding in **1** is limited to an intramolecular interaction, the coordinated water ligand in **2** engages in various intermolecular hydrogen bonding interactions with either the counterion or a neighbouring complex cation. However, the most relevant interaction in both complexes is the intramolecular one discussed in the following.

Table 4. Selected hydrogen bond lengths and angles found in **1a, 1b** and **1c**. All protons were localized from the difference map of the structural data.

	1a	**1b (a)**	**1b (b)**	**1c**
O(3)-H(3A)…O(1)				
d(D-H) [Å]	0.823(10)	0.848(10)	0.839(10)	0.814(10)
d(H…A) [Å]	2.184(13)	2.11(2)	2.18(2)	2.034(17)
d(D…A) [Å]	2.9552(18)	2.874(3)	2.924(3)	2.785(2)
<(D-H-A)	156(2)°	149(3)°	147(3)°	153(3)°

D = donor, A = acceptor.

Table 5. Selected bond lengths and angles found in the hydrogen bonding between the water ligand and the carbonyl oxygen atom within the (carboxylato)(aqua)iron(II) unit and the coordinated water ligand and other nearby atoms in **2a**, **2b(1)**, **2b(2)**, **2c**. All protons were localized from the difference map of the structural data.

	2a	**2b(1)**	**2b(2)**	**2c**
O(3)-H(3A)…O(1)				
d(D-H) [Å]	0.84(3)	0.89(3)	0.91(3)	0.88(4)
d(H…A) [Å]	1.80(3)	1.71(3)	1.74(3)	1.73(4)
d(D…A) [Å]	2.6192(18)	2.582(2)	2.631(2)	2.608(3)
<(D-H-A)	166(2)°	165(3)°	163(3)°	170(3)°
O(3)-H(3B)…O(1)#1[a]				
d(D-H) [Å]	0.82(3)			
d(H…A) [Å]	1.96(3)			
d(D…A) [Å]	2.7351(18)			
<(D-H-A)	158(2)°			

	2a	2b(1)	2b(2)	2c
O(3)-H(3B)…F(4)[b]				
d(D-H) [Å]		0.834(10)	0.833(10)	
d(H…A) [Å]		2.25(2)	2.49(2)	
d(D…A) [Å]		2.956(5)	3.0046(19)	
<(D-H-A)		143(3)°	121(2)°	
O(3)-H(3B)…F(5)[b]				
d(D-H) [Å]		0.834(10)	0.833(10)	
d(H…A) [Å]		2.118(6)	2.118(10)	
d(D…A) [Å]		2.904(3)	2.951(2)	
<(D-H-A)		157(3)°	178(3)°	
O(3)-H(3B)…O(4)[c]				
d(D-H) [Å]				0.82(4)
d(H…A) [Å]				1.91(4)
d(D…A) [Å]				2.736(3)
<(D-H-A)				174(3)°

D = donor, A = acceptor. [a] Symmetry transformations for equivalent atoms: #**1** -x,-y,-z+2. [b] For structure **2b(1)** the PF_6^- counter anion is disordered. Only one conformation shows hydrogen bonding to the counter anion fluorine atoms F(4) and F(5). [c] For **2c**, O(4) refers to oxygen atom of the $CF_3SO_3^-$ counter anion.

The significantly shorter interatomar distance O(1)···O(3) as well as the larger O(3)-H(3A)-O(1) angle (highlighted in grey in Table 6) indicate the presence of a substantially stronger hydrogen bonding interaction in **2** compared to **1**. This, and the rather long axial Fe-N_{amine} bond changes (see above), contribute to the driving force of **1** to act as a H-atom abstraction reagent as discussed in (sections 2.3 and 2.4).

It is also noteworthy that in both complexes (**1** and **2**) an almost planar hexagon is formed by the iron ion, the coordinated carboxylate group, the hydroxide/water ligand and the hydrogen bonding interaction between carboxylate and hydroxide/water moieties (Figure 11, Table 6, Table 7), retaining the general structural motif in both oxidation states. Crucially, this hexagonal interaction network not only stabilizes the active moiety and maintains the mononuclearity of the ferric complex but also limits further reorientations that would increase the activation barrier for reactions of **1** with suitable substrates. Additionally, this feature orients the lone pairs of the coordinated hydroxo ligand in **1** in such a way that a reaction path for an overall hydrogen abstraction reaction from O–H and C–H bonds is enabled in the first place. The interaction also directs more electron density to the oxygen via partial deprotonation of the O–H bond that is contained in both **1** and **2** and thus, in turn, increases the oxide-character of the hydroxide ligand in **1** and the bond strength of the second O–H bond in **2**. This demonstrates the importance of such an intramolecular hydrogen bonding interaction for the reactivity.

Table 6. Angles within the hexagon formed by the hydrogen bonding in the (carboxylato)(hydroxo)iron(III) unit in **1a**, **1b** and **1c** and in the (carboxylato)(aqua)iron(II) unit in **2a**, **2b(1)**, **2b(2)**, and **2c**. All protons were localized from the difference map of the structural data.

<(L-M-L)	**1a**	**1b (a)**	**1b (b)**	**1c**
O(1)-C(23)-O(2)	124.68(15)°	123.9(2)°	124.8(2)°	124.7(2)°
C(23)-O(2)-Fe(1)	131.20(11)°	130.62(17)°	132.94(17)°	130.5(2)°
O(2)-Fe(1)-O(3)	102.93(6)°	100.33(8)°	100.13(8)°	98.16(7)°
Fe(1)-O(3)-H(3A)	101.7(17)°	107(2)°	110(2)°	108(2)°
O(3)-H(3A)…O(1)	156(2)°	149(3)°	147(3)°	153(3)°
H(3A)-O(1)-C(23)	103.0(6)°	105.2(9)°	104.6(8)°	104.5(8)°
Σ [°]	720(3)°	716(4)°	719(4)°	719(4)°

<(L-M-L)	**2a**	**2b(1)**	**2b(2)**	**2c**
O(1)-C(23)-O(2)	123.98(16)°	124.8(2)°	124.40(17)°	124.5(2)°
C(23)-O(2)-Fe(1)	132.94(11)°	133.09(14)°	133.66(12)°	132.99(17)°
O(2)-Fe(1)-O(3)	89.32(5)°	87.54(6)°	88.76(6)°	88.23(8)°
Fe(1)-O(3)-H(3A)	100.7(16)°	102(2)°	100.3(17)°	99(2)°
O(3)-H(3A)…O(1)	166(2)°	165(3)°	163(3)°	170(3)°
H(3A)-O(1)-C(23)	106.1(8)°	104(1)°	105.0(9)°	104(1)°
Σ [°]	719(2)°	716(4)°	715(4)°	719(4)°

The sum of all angles is given as a measure for planarity. Ideal planarity for a six membered ring would be observed with a sum of all internal angles Σ = 720°. The estimated standard deviation (ESD) for the sum was calculated as the root sum of the squares of each individual angle. The summarized values and ESDs were subsequently rounded to integer numbers.

Table 7. Deviation (in Å) of the position of the atoms from the least-squares planes calculated to pass through the atoms Fe(1), O(3), H(3A), O(1), C(23), and O(2) of the (carboxylato)(hydroxo)iron(III) units in **1a**, **1b** and **1c** and through the atoms Fe(1), O(3, H(3A), O(1), C(23), and O(2) of the (carboxylato)(aqua)iron(II) units in **2a**, **2b(1)**, **2b(2)** and **2c**.

	1a	**1b (a)**	**1b (b)**	**1c**
Fe(1)	-0.0366 (0.0013)	0.0070 (0.0014)	-0.0093 (0.0015)	0.0440 (0.0017)
O(3)	0.0285 (0.0101)	-0.0684 (0.0147)	0.0109 (0.0147)	-0.0382 (0.0138)
H(3A)	0.0029 (0.0142)	0.0582 (0.0210)	-0.0077 (0.0200)	0.0122 (0.0195)
O(1)	-0.0379 (0.0058)	0.0367 (0.0089)	0.0020 (0.0086)	0.0131 (0.0082)
C(23)	0.0256 (0.0011)	-0.0860 (0.0018)	-0.0073 (0.0019)	0.0146 (0.0015)
O(2)	0.0176 (0.0028)	0.0525 (0.0046)	0.0113 (0.0044)	-0.0456 (0.0039)
rmsd[a]	0.0276	0.0572	0.0087	0.0316

	2a	**2b (1)**	**2b (2)**	**2c**
Fe(1)	-0.0010 (0.0011)	-0.0685 (0.0014)	0.0372 (0.0010)	-0.0581 (0.0012)
O(3)	0.0332 (0.0095)	0.0939 (0.0126)	-0.0875 (0.0107)	0.0765 (0.0140)
H(3A)	-0.0306 (0.0144)	-0.0396 (0.0196)	0.0583 (0.0168)	-0.0111 (0.0226)
O(1)	-0.0206 (0.0057)	-0.0720 (0.0080)	0.0607 (0.0069)	-0.0529 (0.0055)
C(23)	0.0470 (0.0012)	0.0517 (0.0016)	-0.0838 (0.0015)	0.0985 (0.0035)
O(2)	-0.0280 (0.0023)	0.0344 (0.0030)	0.0151 (0.0026)	-0.0529 (0.0055)
rmsd[a]	0.0302	0.0634	0.0624	0.0641

[a] root mean square deviation.

2.1.3. SQUID Magnetometric Analysis

Temperature-dependent measurements of the magnetic susceptibility and magnetization at low temperatures in the solid state were done for **1b**, **2a**, and **4a**. Some results are displayed in Figures 13-15 and Table 8. A magnetic field sweep of 0-7 T at 100 K was also done to rule out significant paramagnetic impurities, proven by a linear correlation of *M* vs. *H*. Measurements of **3a** were not done due to the rather limited accuracy and reliability of such data in this study (**3a** was found to rapidly lose its co-crystallized MeCN and to be highly hygroscopic). However, the magnetic ground state at 150 K and at room temperature is expected to be high spin from a thermodynamic perspective and analogy to **2a**, as can also be deduced e.g. from structural analysis (150 K, section 2.1.2) and UV-vis-NIR spectroscopic data (298 K, section 2.1.6), respectively.

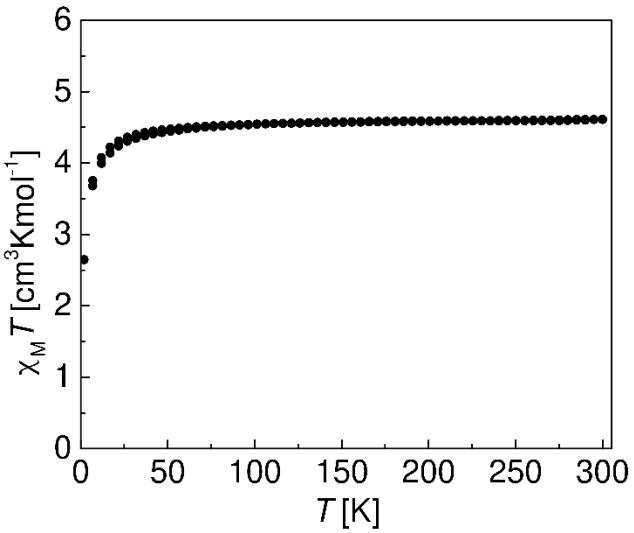

Figure 13. Temperature dependence of $\chi_M T$ for **1b** between 2 and 300 K measured at 0.5 T with a sweep rate of 2 K/min. Data points of cooling mode (300 K → 2 K) and heating mode (2 K → 300 K) are layered on top of each other.

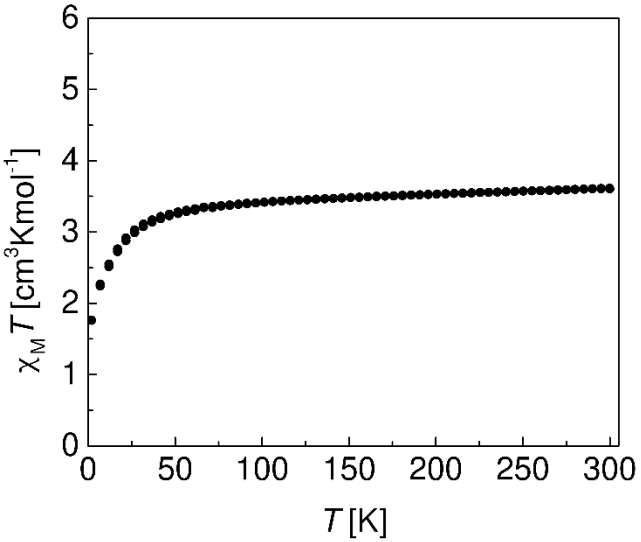

Figure 14. Temperature dependence of $\chi_M T$ for **2a** between 2 and 300 K measured at 0.5 T with a sweep rate of 2 K/min. Data points of cooling mode (300 K → 2 K) and heating mode (2 K → 300 K) are layered on top of each other.

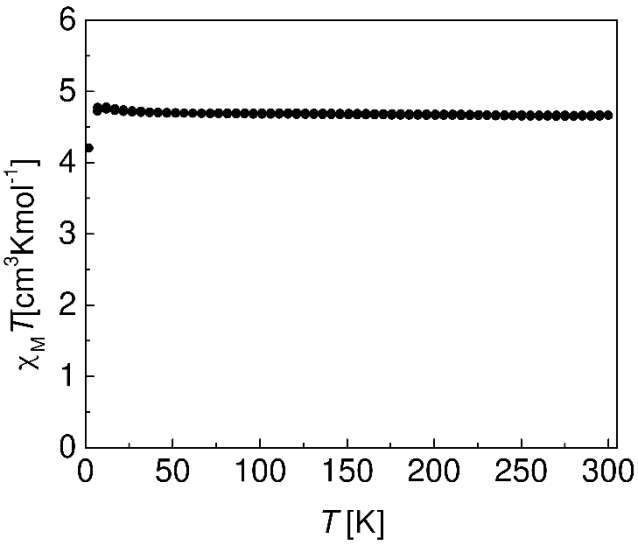

Figure 15. Temperature dependence of $\chi_M T$ for **4a** between 2 and 300 K measured at 0.2 T with a sweep rate of 2 K/min. Data points of cooling mode (300 K → 2 K) and heating mode (2 K → 300 K) are layered on top of each other.

Table 8. Magnetic data (χT) of **1**, **2** and **4** as obtained by SQUID-magnetometric measurements on **1b**, **2a**, and **4a** at 298 K, 50 K, and 2 K.

T [K]	**1b** [cm^3Kmol^{-1}]	**2a** [cm^3Kmol^{-1}]	**4a** [cm^3Kmol^{-1}]
298	4.61 (HS)	3.61 (HS)	4.66 (HS)
50	4.44 (HS)	3.26 (HS)	4.69 (HS)
2	2.64	1.75	4.20

HS = high spin. Data is given at 50 K to represent the low temperature magnetic moment and spin-state without the influence of zero-field splitting effects.

The results show a high spin state across a temperature range between 2 K and 300 K for all complexes. The observed magnetic moments of **1** and **4** concur with the expected values for the ferric complexes; deviations from the spin-only (SO) value (S = 5/2, $\chi_M T_{SO}$ = 4.38 cm^3Kmol^{-1}) are within the range of previously reported high-spin d^5 complexes.[123] The slightly increased magnetic moments as compared to the theoretical SO-value are attributed to mixing of the wavefunctions of excited states and their orbital contributions into the ground state wavefunctions. The magnetic moment of the ferrous compound **2a** shows a magnetic moment higher than the spin only value (S = 2, $\chi_M T_{SO}$ = 3.00 cm^3Kmol^{-1}) which is attributed to the spin-orbit coupling in the ground state and some mixing of the wavefunctions of excited states into the ground state wavefunction. The slight upward slope in the $\chi_M T$ vs. T plot towards higher temperatures can be explained by a temperature-independent paramagnetism (TIP).

The results of the magnetization measurements proved to be more challenging to interpret. Magnetization was measured at temperatures between 2 K and 10 K in 1 K increments with magnetization sweeps from 0 – 7 T to obtain information about the magnitude of zero-field splitting by fitting of the temperature-dependent data. Satisfactory fits for the data obtained on **1b** and **4a** were achieved with the assumption of an isotropic g-value and are represented in Figure 16 and Figure 17.[124] However, satisfactory fits for the magnetization data of **2a** could not be obtained, supposedly due to this simplified assumption. While the fits were not only visibly far off, also the calculated g-values $g \approx 2.7$ and a zero-field splitting energy of -15 or -20 cm^{-1} for the supposedly best fits hardly agree with the low temperature behaviour observed in the

susceptibility measurement. Thus, no zero-field splitting energy could be obtained, and no fitting results are displayed in Figure 18.

At this point it should also be noted that a second, more accurate determination of the zero-field splitting and the individual g_x-, g_y-, and g_z-values was achieved for **1** and **4** with temperature dependent X-band EPR measurements on frozen solutions between 10 and 40 K and discussed in section 2.1.8. Since **2** has an integer spin of S = 2, this method could not be used to investigate **2** and these parameters could not be obtained in this work.

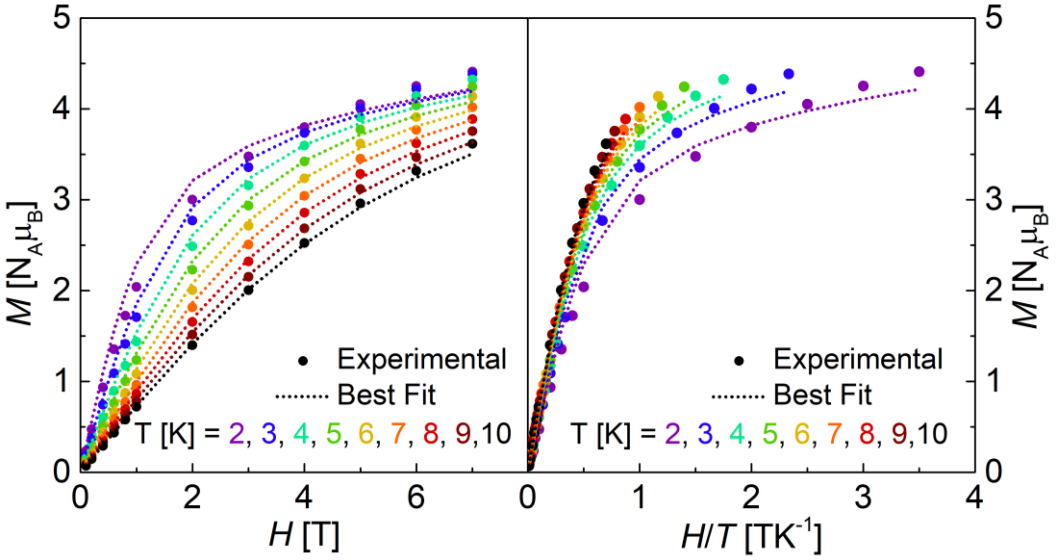

Figure 16. Variable temperature magnetization (left) and reduced magnetization plots (right) for the data (solid circles) and fits (dotted lines) obtained for **1b** between 2 and 10 K in 1 K increments. The fits were done with the PHI software by the Chilton group, assuming an isotropic *g*-value for a powdered sample.[124] Deviations of the fit vs. the experimental data at higher fields and lower temperatures are attributed to the approximation of an isotropic *g*-value. Fitting results (simplex): **1b** *g*-value = 2.008 ± 0.011, zero-field-splitting = 3.23 ± 0.18 cm^{-1} (strong parameter correlation), residual = 0.91.

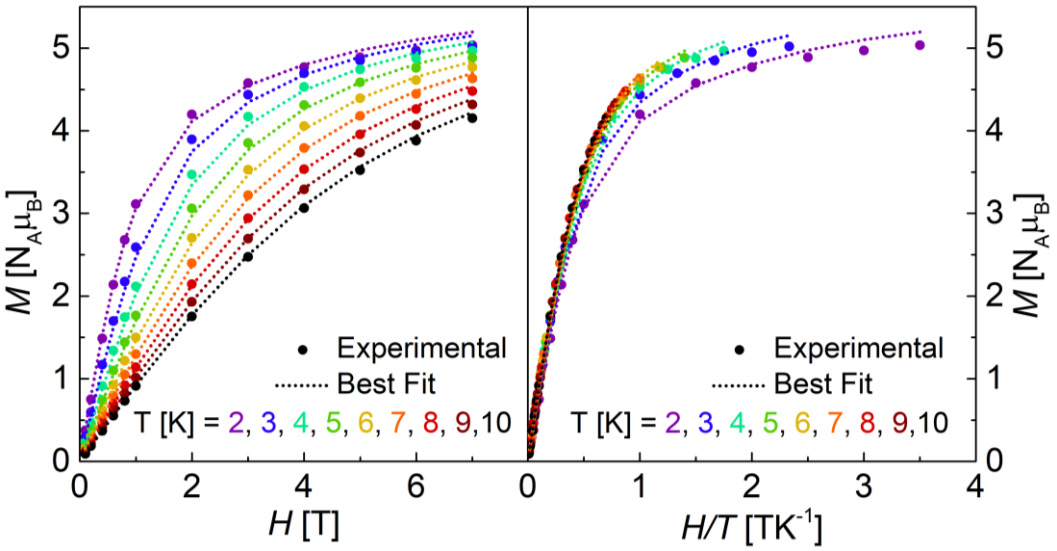

Figure 17. Variable temperature magnetization (left) and reduced magnetization plots (right) for the data (solid circles) and fits (dotted lines) obtained for **4a** between 2 and 10 K in 1 K increments. The fits were done with the PHI software by the Chilton group, assuming an isotropic *g*-value for a powdered sample.[124] Deviations of the fit vs. the experimental data at higher fields and lower temperatures are attributed to the approximation of an isotropic *g*-value. Fitting results (simplex): **4a** *g*-value = 2.073 ± 0.000, zero-field-splitting = 0.90 ± 0.02 cm^{-1} (weak parameter correlation, 0.1), residual = 0.37. *Note: This fit was revisited after the original work was published to achieve better results, thus the values differ from those reported in the journal article.*[1]

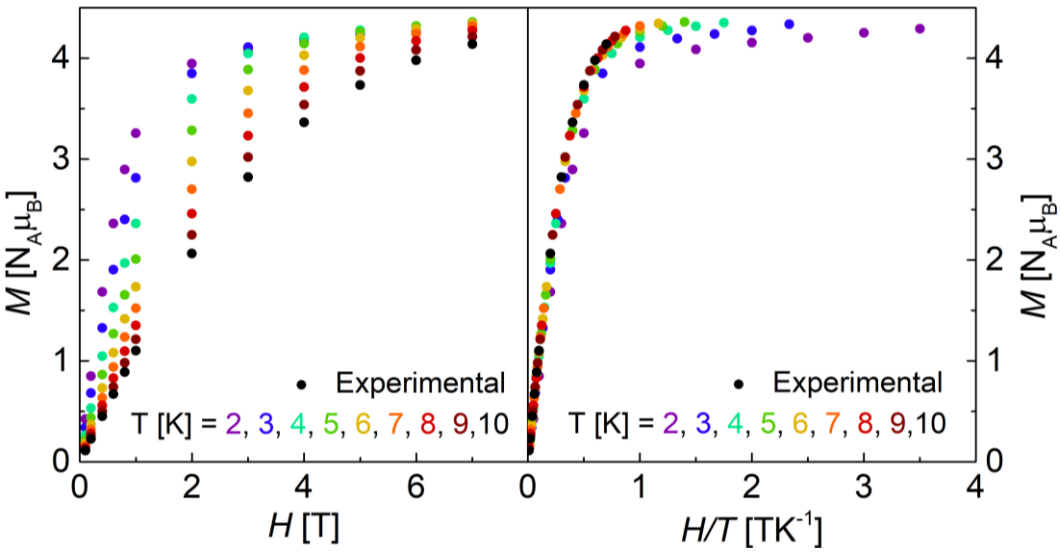

Figure 18. Variable temperature magnetization (left) and reduced magnetization plots (right) for the data (solid circles) obtained for **2a** between 2 and 10 K in 1 K increments. Data are presented as acquired; no satisfactory fits were achieved.

2.1.4. Mößbauer-Spectroscopic Analysis

The Mößbauer spectra of **1a** and **2a** confirm both the spin state and the oxidation state in complexes **1** and **2** to be high-spin d^5 and high-spin d^6, respectively (Figure 19).

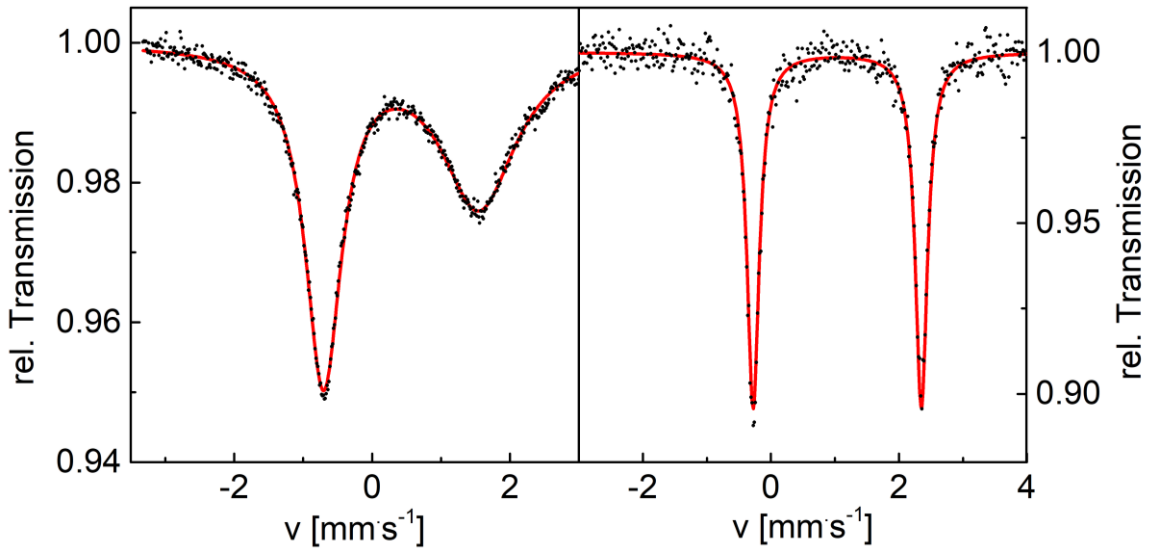

Figure 19. Experimental Mößbauer spectra (black dots) and fits (red trace) of **1a** (left) at 90 K and **2a** (right) at room temperature (RT). Mößbauer parameters for **2** (RT): δ_{IS} = 1.04 mms^{-1}, ΔE = 2.63 mms^{-1}; Fitting quality χ^2 = 1.11. Mößbauer parameters for **1** (90 K): δ_{IS} = 0.42 mms^{-1}, ΔE = 2.25 mms^{-1}; Fitting quality χ^2 = 1.12. The isomeric shift δ_{IS} is given relative to α-Fe foil (δ_{IS}(α-Fe vs source) = 0.107 $mm{\cdot}s^{-1}$).

The ferrous complex **2** produces a doublet signal with a narrow half-width at δ_{IS} = 1.04 mm/s and ΔE_Q = 2.63 mm/s at room temperature. For the ferric complex **1** a considerably broader, asymmetric doublet with an isomeric shift δ_{IS} = 0.42 mm/s and a quadrupole splitting ΔE_Q = 2.25 mm/s is observed at 90 K. The lower measurement temperature for **1** was chosen because of its poor resolution and weak Mößbauer-effect, something that is frequently observed for high-spin iron(III) complexes containing macrocyclic diazapyridinophane ligands.

*Note: At a later stage of this work, a room temperature measurement of **1a** over multiple days was successfully resolved and is reported in chapter 3 (section 3.1.3). For consistency with the originally published work,[1] only the 90 K spectrum is discussed in this chapter.*

In contrast to the still sufficiently well-behaved spectrum of **1** that allows for fitting and the determination of the characteristic Mößbauer parameters δ_{IS} and ΔE_Q, the signal broadening in **4** obtained from **4a** at various temperatures is even more extreme (Figure 20). The spectra of **4** could not be fitted satisfyingly even at very low temperatures and, thus, the characteristic parameters determined can just to be taken as preliminary estimates. This rather strong broadening arises from the internal magnetic field caused by the high-spin state of the d^5-ion resulting in an intermediate relaxation time for the magnetic interaction.

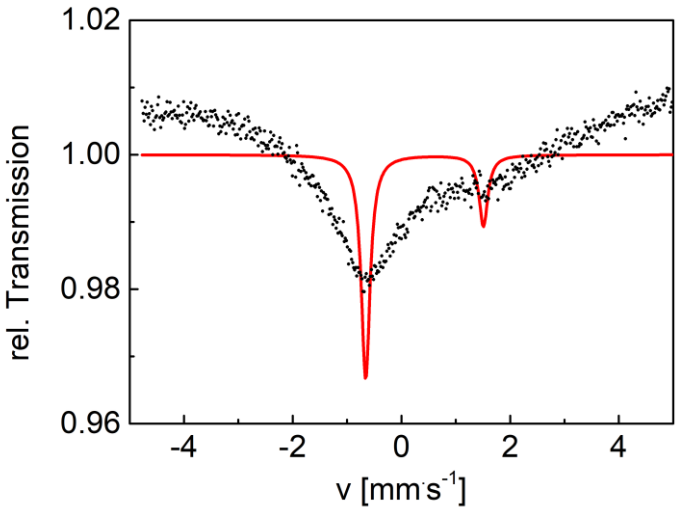

Figure 20. Experimental Mößbauer spectrum (black dots) and preliminary fit (red trace) of **4a** (left) at 10 K (thermometer temperature, sample temperature probably significantly higher). The spectrum was fitted with two singlets at 1.5 mms^{-1} and -0.66 mms^{-1} to allow for the determination of preliminary estimates of the Mößbauer parameters: δ_{IS} = 0.42 mms^{-1}, ΔE = 2.16 mms^{-1}; Fitting quality χ^2 = 30.13. The isomeric shift δ_{IS} is given relative to α-Fe foil (δ_{IS}(a-Fe vs source) = 0.107 $mm{\cdot}s^{-1}$).

The decrease in δ_{IS} in **1** as compared to **2** is consistent with a reduced electron shielding in the ferric compound as opposed to the ferrous compound, and the values for δ_{IS} are in line with the Mößbauer data of other iron complexes.[125] The unusually large quadrupole splitting in the ferric complex is explained by the pronounced differences in bond strength between the axial amine ligands and the equatorial ligands imposed on the complex by the substantial distorting coordination properties of the macrocyclic ligand.[115] This substantial reduction in symmetry of the ligand field results in a high electric field gradient at the only seemingly totally symmetric high-spin d^5 shell

of the high-spin iron(III) ion. This aspect is a frequently observed feature of these types of macrocyclic L-N_4R_2 ligands.[1,115]

In this study, Mößbauer spectroscopy also proved to be a very valuable tool for detecting small contaminations by the iron(II) starting complex in the attempted preparation of pure **1** by oxidation of **2** with molecular oxygen, as described at the beginning of this chapter. The isolation of a pure ferric complex is thwarted by the tendency of small amounts of ferrous impurities to co-crystallize in ferric hydroxide crystals, an aspect that is discussed in chapter 4. As the composition of the ferrous and the ferric complexes differ only by one hydrogen atom, the purity of the sample cannot be unambiguously determined by elemental analysis. In addition, small amounts of ferrous impurities co-crystallized in the ferric hydroxide crystals cause only moderate deviations in bond lengths (see section 4.1.2). Also, ferrous impurities in the ferric hydroxide substance do not generate significantly distinctive features in the IR-, EPR- or UV-vis-NIR-spectra to be recognized. Furthermore, the alteration of the magnetic susceptibility data of the ferric complex by small amounts of the contaminating ferrous complex is not substantial enough and, therefore, barely detectable. Attempts to provide unambiguous evidence of purity by ESI-mass spectrometry fails because a small amount of benzoato iron(II) complex is formed in the transfer of the (benzoato)(hydroxo)iron(III) complex from the solution into the gas phase (section 2.1.9). In contrast, even a very small contribution of the rather narrow Mößbauer doublet of the ferrous complex to the broad spectrum of the ferric hydroxide complex can easily be resolved.

As Mößbauer spectroscopy was seemingly not a part of the previous works by *Rauber*, *Bonck* and *Dobbelaar*, the aspect of ferrous impurities in **1** went undetected and resulted in retrospectively unreliable results since *all* synthetic attempts of **1** involved the oxidation of a ferrous benzoate precursor complex with molecular oxygen (i.e. $[Fe(L\text{-}N_4{}^tBu_2)(O_2CPh)(OR)]^+$ with R = Et, Me and H_2O in the early work of this thesis).[2,112,113]

2.1.5. Infrared-Spectroscopic Analysis

Infrared (IR) spectra were obtained on all reported compounds **1a**, **1b**, **1c**, **2a**, **2b**, **2c** (Figure 21), **3a** (Figure 22), **4a**, **4b** (Figure 23), and **4c**. To ensure that signals arising from O–H stretching vibrations are not overlaid or obscured by absorptions due to atmospheric moisture or adventitious water content in the sample or in a KBr pellet, pure, polycrystalline samples of the compounds were investigated using an ATR accessory. Moreover, deuterated compounds [Fe(L-$N_4{}^tBu_2$)($PhCO_2$)(OD)]BPh_4·MeCN (**1d**) and [Fe(L-$N_4{}^tBu_2$)($PhCO_2$)(OD_2)]$^+$ (**2d**) were synthesized specifically for the purpose of an unambiguous assignment of the O–H / O–D IR-absorptions by the coordinated water/hydroxide ligands in **1** and **2** (Figure 24). As **2b** crystallizes in two polymorphs, it is ambiguous which polymorphs are contained in the bulk material measured, thus no differentiation of **2b(1)** and **2b(2)** is considered in this analysis. Moreover, as spectra are expected to be extremely similar because of the crushing of the material by the used ATR accessory and the consequent extent of lattice destruction prior to the measurement, the error is negligible. While the IR spectrum of **3a** is described in my own master thesis,[2] this spectrum was not matched with a suitable demonstration of purity by combustion analysis. Thus, the measurement was repeated with analytically pure compound **3a** that was synthesized during this work (Figure 22). As no IR-spectroscopic data for the triflate salt of **4** was presented by *Mirica et al.*,[117] the exemplary spectra of the respective tetraphenylborate (**4a**) and hexafluorophosphate (**4b**) salts are presented in this work for future reference of compounds containing **4** (Figure 23).

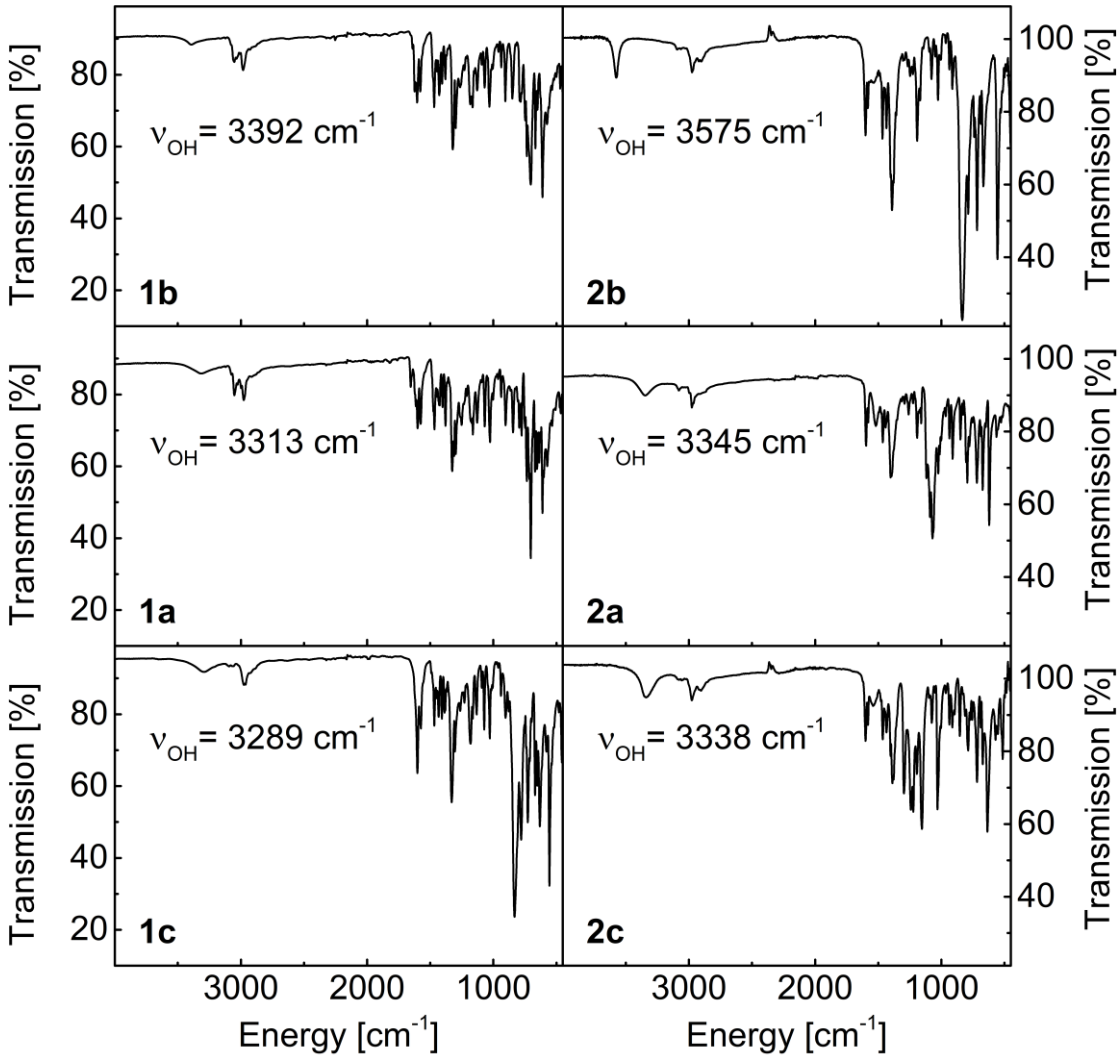

Figure 21. FTIR spectra of solid, crystalline samples of **1a**, **1b** and **1c** (left), and **2a**, **2b**, and **2c** (right) measured with an ATR-accessory under atmospheric conditions (4000 – 450 cm^{-1}). Minor artefacts caused by differences in atmospheric CO_2 content in the background spectrum vs. the sample spectrum can be observed for **2b** and **2c** at approximately 2340 cm^{-1} and 2360 cm^{-1}.

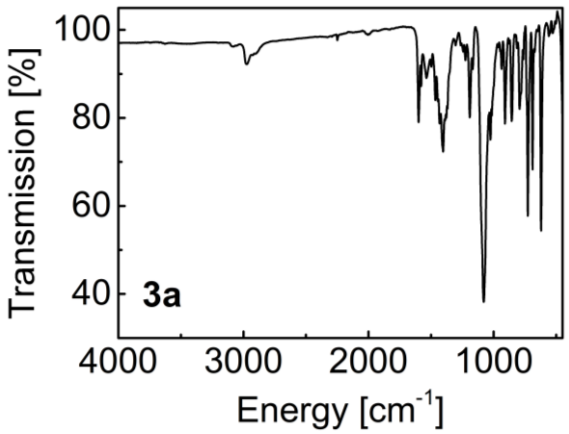

Figure 22. FTIR spectrum of solid, crystalline **3a** measured with an ATR-accessory under atmospheric conditions (4000 – 450 cm^{-1}).

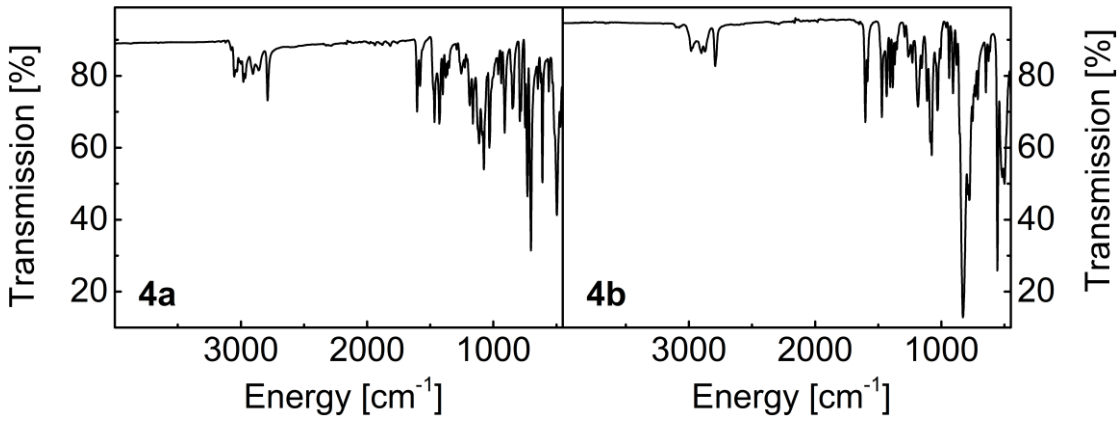

Figure 23. Representative FTIR spectra of solid, crystalline samples containing **4** collected on **4a** (left) and **4b** (right) measured with an ATR-accessory under atmospheric conditions (4000 – 450 cm^{-1}).

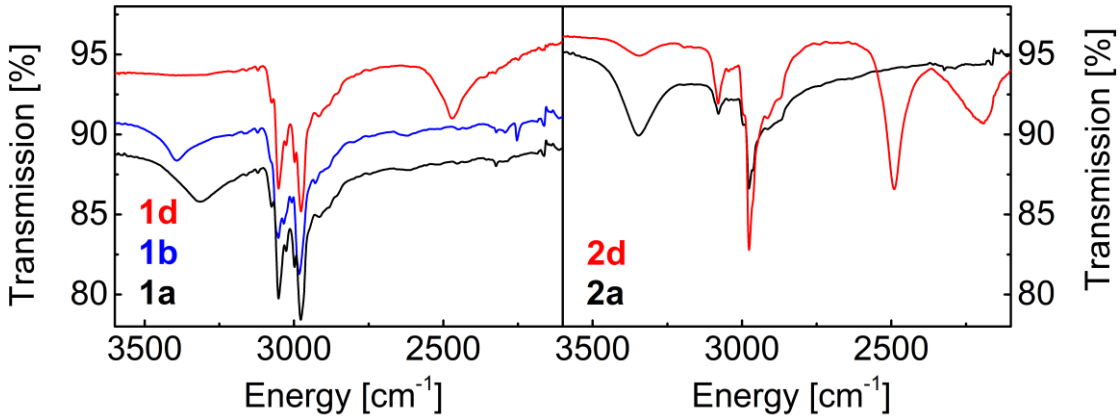

Figure 24. FTIR spectra of solid, crystalline samples of **1a**, **1b** and **1d** (left) and **2a** and **2d** (right) between 3600-2100 cm^{-1} collected with an ATR-accessory under atmospheric conditions. O–H vibrational energies: 3313 cm^{-1} (**1a**), 3392 cm^{-1} (**1b**), 3345 cm^{-1} (**2a**); O–D vibrational energies: 2470 cm^{-1} (**1d**), 2490 cm^{-1} and 2192 cm^{-1} (**2d**). The broad, second O–H vibration in the aqua iron(II) complexes is overlaid by the C–H stretching modes and cannot be unambiguously discerned. The O–H and O–D vibrations with relative higher energies in **2a** (3345 cm^{-1}) and **2d** (2490 cm^{-1}) refer to the O–H / O–D functions that do not engage in intramolecular hydrogen bonding.

The width of the signals observed at energies above 3250 cm^{-1} for **1a**, **1b**, **1c**, **2a**, **2b**, and **2c** are considerably reduced compared to that of free water. Rather narrow vibrational modes are additionally observed for **1d** and **2d** between 2600-2000 cm^{-1}, supporting a coordinated water/hydroxide in **1** and **2**.

Depending on the substance investigated (**1a**, **1b** or **1c**), the ATR-IR spectrum of **1** displays a feature between 3289 and 3392 cm^{-1} (Figure 21). Based on the shift in energy of the vibration to 2470 cm^{-1} upon H/D isotope substitution in the tetraphenylborate salt of **1** (**1a**), the vibration can be unambiguously assigned to the O**–**H stretching vibration (Figure 24). The difference of 79 cm^{-1} for the O**–**H vibrational frequencies between **1a** and **1b** demonstrate that even slight differences in the crystal packing and the co-crystallization of solvent molecules can exert a significant influence on the energy of the O**–**H vibration. The extent of decrease in energy of the O**–**H vibration compared to the value of an unperturbed free hydroxide in gas phase (3700-3570 cm^{-1})[126] is a measure of the binding strength of the hydroxide ligand to the metal ion as well as of the extent of involvement of the hydroxide ligand in hydrogen bonding interactions. Similar O**–**H vibrational energies have been observed for other iron(III) hydroxide complexes.[75,81]

For the aquairon(II) complex **2** two distinct O**–**H stretching vibrations are expected. However, only a single O**–**H stretching vibration between 3575 and 3338 cm^{-1} (**2a**-**c**) is observed (Figure 21). The deuterium substitution experiments of **2a** proved very helpful in identifying the weaker and broader second vibration (Figure 24). Thus, two features at 2490 and 2192 cm^{-1} are detected for the deuterated sample **2d** as compared to one feature at 3345 cm^{-1} in **2a**. The small residual peak at 3345 cm^{-1} in the deuterated sample indicates that the isotope substitution was not quantitative. Using the same ratio for the changes of vibrational energies due to H/D substitution effect ν_{OH}/ν_{OD} = 3345/2490 = 1.343, the second O–H vibrational frequency corresponding to the O**–**D vibration at 2192 cm^{-1} is calculated to occur at 2944 cm^{-1} for the H-substituted complex **2a**. The value 1.343 deviates slightly from the theoretical value as calculated with reduced masses because the mode is coupled to other vibrations. The width of the absorption and the energetic position of this vibration suggests that this absorption is obscured by the more intensive C**–**H vibrations in **2a**. The vibrations at 3345 and 2944 cm^{-1} are assigned to the individual O**–**H bonds involved in *inter*molecular and *intra*molecular hydrogen bonding interactions, respectively.

Because of these different types and strengths of hydrogen bond interactions, the difference in energy between the two expected O**–**H stretching modes of the coordinated water in **2** are anticipated to be larger than that between the symmetric and antisymmetric stretching vibrations of free water. As is observed, the exact energy of the observable O**–**H stretching mode is also highly dependent on the surrounding environment, and thus spans a range with different crystal packings, solvent content, interactions, contacts and counterions.

Because of the stronger H-bonding interaction to the benzoate carbonyl oxygen atom, it is reasoned that the lower energy O**–**H vibration possesses more contribution of the O**–**H bond involved in the intramolecular H-bonding interaction. The energy of 3313 cm^{-1} for **1a** compared to the calculated value of 2944 cm^{-1} for **2a**, agrees with the notion from the structural data analyses that the strength of the intramolecular hydrogen bonding interaction is considerably increased in the ferrous aqua complex as compared to the ferric hydroxide complex.

The most characteristic peak observed in the IR spectra of **4a**, **4b**, and **4c** is the peak at 2770-2800 cm^{-1}(**4a**, 2788 cm^{-1}; **4b**, 2792 cm^{-1}; **4c**, 2774 cm^{-1}; resolution 4 cm^{-1}).

This can be related to the excitation of the C–H stretching mode of the methyl group in the MeO^- ligand. The relatively low excitation energy is a result of the weakening of the C–H bond by the strong electron-withdrawing effects of the electronegative oxygen atom of the methoxide and the enhancement of this effect by its coordination to the iron site.

The absence of an O–H vibration in the spectrum of **3a** underlines the capability of the carboxylate ligand to complete the pseudo-octahedral coordination environment via a chelating coordination mode. For the spectrum of **3a** (and **1b**), it is additionally notable that the characteristic C≡N vibration expected around ~2250 cm^{-1} is barely visible. The reason for this is the experimental ATR-setup which contains a diamond puck that shows strong absorptions in this region and limits the resolution for vibrational modes between ~1900-2300 as evident by the low relative energy transmission in the background spectrum shown in Figure 25.

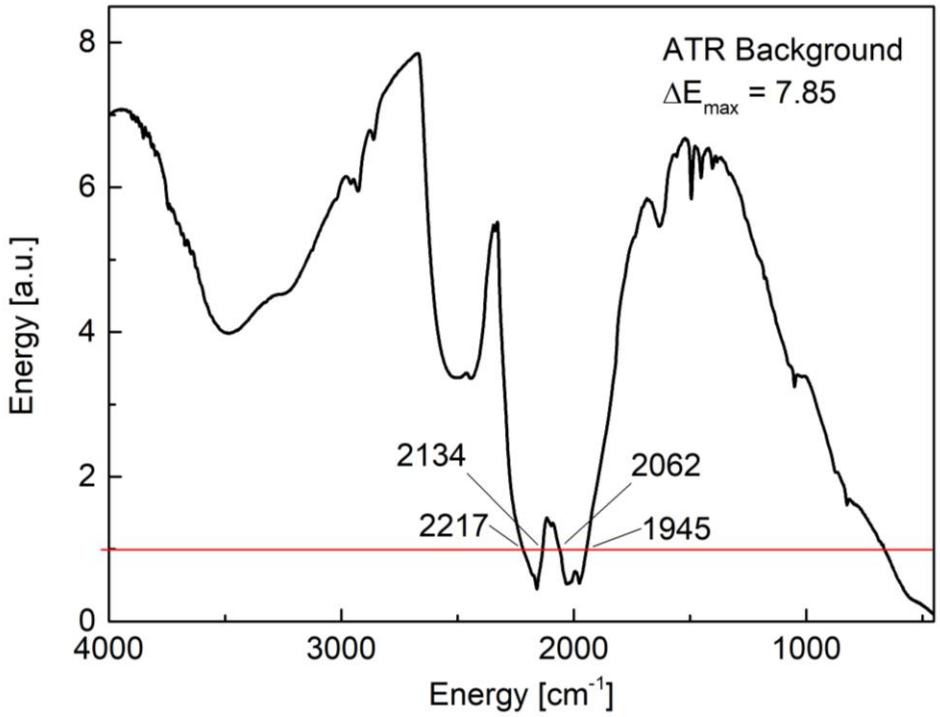

Figure 25. Background spectrum recorded with the *Specac* ATR accessory containing a diamond puck and a ZnS ATR-crystal using a *Spectrum Two* infrared spectrometer by *Perkin Elmer*. The red trace indicates relative transmission energies >1 a.u. with values indicated where the line is crossed.

2.1.6. Solid Electronic Spectroscopic Analysis

UV-vis-NIR spectra of the solid compounds as ground powders were measured for the ferric complex compound **1a** and both ferrous complex compounds **2a** and **3a** (Figure 26). A measurement of ground KBr powder was used to approximate the scattering background component *S* for the calculation of *K*/*S* employing the Kubelka-Munk equation (Equation 4).[127] As electronic spectroscopy on the triflate salt of **4** was reported by *Mirica et al.*,[117] no further investigation was conducted with this method on **4a**, **4b**, or **4c**.

$$(4) \quad \frac{K}{S} = \frac{(1-R_\infty)^2}{2R_\infty}$$

Only very weak absorptions are observed in the vis-NIR spectrum of the solid ferric compound **1** (Figure 26), mostly resulting from the tailing of a strong absorption in the UV-range most probably caused by π-π* absorptions in the diazapyridinophane and the benzoate ligand. The absence of spin-allowed d-d transitions and strong absorptions in the visible spectrum is consistent with the high spin d^5 configuration.

Similarly, only rather weak absorptions are observed in the vis-NIR spectra of the ferrous compounds **2a** and **3a**. Between 300-500 nm, however, the spectra differ noticeably, demonstrating that the different coordination units in **2a** and **3a** affect the charge-transfer (CT), π → π* and n → π* transitions of the iron(II) complexes. Additionally, in contrast to **1**, the spectra of the solid ferrous compounds **2a** and **3a** both display two weak, well separated bands between 700 and 1600 nm which are attributed to spin-allowed d-d transitions and are consistent with a distorted octahedral high-spin iron(II) state (Figure 26). Here, the changes induced by the different coordination environments are even more evident as the d-electron excitations are achieved at vastly different energies (736 and 1370 nm for **2a**, and 891 and 1307 nm for **3a**).

While high-spin iron(II) is already a Jahn-Teller ion and thus splits the $^5E_g \leftarrow ^5T_{2g}$ transition in O_h symmetry into two spin-allowed transitions, the splitting is probably mostly a result of the tetragonal distortions imposed by the coordination of the macrocyclic ligand L-$N_4{}^t Bu_2$. The splitting of the $^5E_g \leftarrow ^5T_{2g}$ transition can be understood as a result of the overall symmetry reduction of O_h to an (idealized) D_4h local symmetry caused by the sum of both effects. The ^5E_g excited state is thus split into two well

separated $^5A_{1g}$ and $^5B_{1g}$ states, yielding two distinct absorptions in the UV-vis-NIR spectra. For solid **2a** an energy difference between the two d-d transitions (at 736 and 1370 nm) of 6300 cm^{-1} is measured. In contrast, the energy separation between the two d-d transitions for **3** (at 891 and 1307 nm) is reduced to 3570 cm^{-1}. The decrease in energetic separation of the two absorptions from 6300 to 3570 cm^{-1} indicates that the difference in ligand field strength between the axial and the equatorial ligands is reduced in **3**.

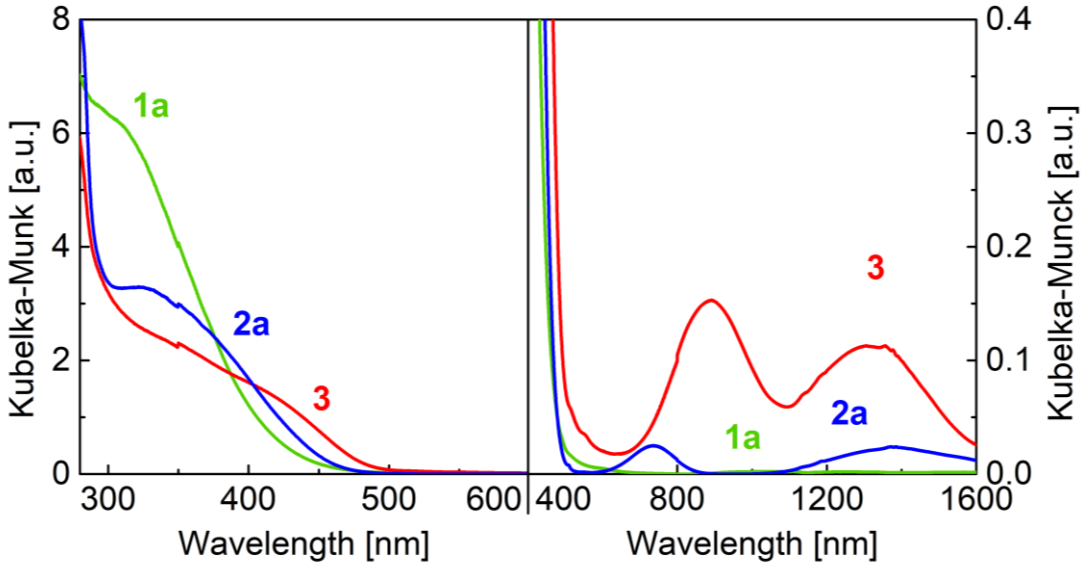

Figure 26. UV-Vis-NIR spectra of **1a**, **2a** and **3** in the solid state. Kubelka-Munk plot for pure, ground powder samples of **1a**, **2a** and **3a** under atmospheric conditions (280-600 nm and 400-1600 nm).

While the relative intensities of the d-electron excitations in **3a** appear to be significantly stronger than those observed for **2a** and may indicate a softened Laporte-rule because of the rather narrow O(1)-Fe-O(2) angle that results from the chelating coordination mode of the carboxylate ligand (section 2.1.2), it must be noted that the solid electronic spectroscopy applied here is only of qualitative nature and such reasoning remains speculative. A more quantitative approach with solution based electronic spectroscopy is described in the following section alongside a more in-depth analysis and interpretation of the solid vs solution-based spectra.

2.1.7. Solution-Based Electronic Spectroscopic Analysis

Electronic absorption spectra of **1b**, **2a** and **3a** in MeCN were recorded (Figure 27). As stated above (section 2.1.6), no further investigation was done for cation **4** as previously published results have already discussed the electronic spectroscopy of the complex cation. The respective energies of the spin-allowed d-d transitions for the iron(II) complexes are compared in Table 9.

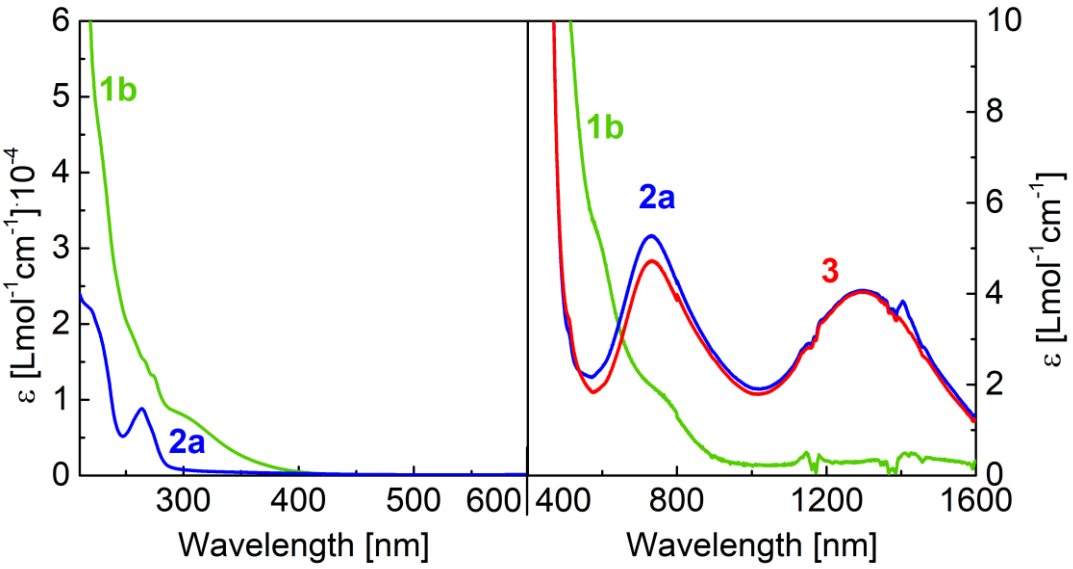

Figure 27. Electronic absorption spectra of **1b** and **2a** in acetonitrile solutions between 210-600 nm with a molar extinction coefficient ranging from 0-60000 $Lmol^{-1}cm^{-1}$ (left) and of **1b**, **2a** and **3a** between 400-1600 nm with a molar extinction coefficient ranging from 0-10 $Lmol^{-1}cm^{-1}$ (right). No differences in the spectra of **3a** and **2a** in MeCN can be resolved in the spectral range between 210 and 600 nm. Therefore, the spectrum of **3a** in this energy range is not shown here.

For **1b**, the spectrum is consistent with a high-spin d^5 metal ion in solution. In the visible range no distinctive absorption pattern is observed. A rather featureless absorption starts around 500 nm, increasing monotonously in intensity until the end of the measurable spectral range. At 300 nm there is a broad CT band, which is observed as a shoulder with a molar extinction coefficient of approximately 8000 $L \cdot mol^{-1} \cdot cm^{-1}$. At the lower-energy flank of this absorption, two very weak absorptions can be discerned as shoulders around 590 and 750 nm. An additional broad feature is recognized between 1000-1600 nm with a molar extinction coefficient below 1 $L \cdot mol^{-1} \cdot cm^{-1}$. These latter three very weak absorptions are tentatively attributed to spin-forbidden d-d transitions. It is noteworthy that no distinctive moderately intense absorption with a molar extinction coefficient of approximately 1000 $L \cdot mol^{-1} \cdot cm^{-1}$ can be noticed between 500-600 nm. Such an absorption would correspond to a CT transition that is characteristic for a linear μ-oxo bridged diferric complex.[114] Therefore, the generation of substantial amounts of such a species due to the occurrence of an equilibrium in acetonitrile solution can be excluded. The ferric hydroxide complex **1** appears to maintain its mononuclearity and its high-spin state in solution.

In contrast to the different spectra for both iron(II) complexes in the solid state, solutions of both ferrous complexes **2** and **3** in MeCN render almost identical electronic absorption spectra with two absorption maxima observed at 732 and 1296 nm (Figure 27, Table 9). The energetic separation of both maxima of 5945 cm^{-1} lies between those observed for the spectra of the solid complexes (section 2.1.6, Figure 26). In addition, the slightly asymmetric appearance of the absorption bands, especially that around 732 nm, points towards a superposition of two spectra most likely arising from cations **2** and **3**, respectively. A superposition of two spectral components with similar transitions as those observed for the solid complexes **2** and **3** can be confirmed by Gaussian curve analysis of the spectra of the dissolved complexes (Figure 28). These results suggest that an equilibrium between complexes **2** and **3** exists in MeCN solutions.

Table 9. Energies of the spin-allowed d,d-transitions of **1a, 2a** and **3a** in the solid state and **1b**, **2a**, and **3a** in MeCN solution. Solid state spectra were recorded on pure, ground samples. Solution spectra were recorded at the following concentrations: 0.008 mol/L (**2a**), 0.0077 mol/L (**3a**), 0.008 mol/L (**1b**) in MeCN.

	2a$_{(solid)}$	**3a**$_{(solid)}$	**1a**$_{(solid)}$	**2a**$_{(MeCN)}$	**3a**$_{(MeCN)}$	**1b**$_{(MeCN)}$
ν [cm^{-1}]	7250, 13550	7650, 11220	-	7715, 13660	7715, 13660	-
$\Delta\nu$ [cm^{-1}]	6300	3570		5945	5945	

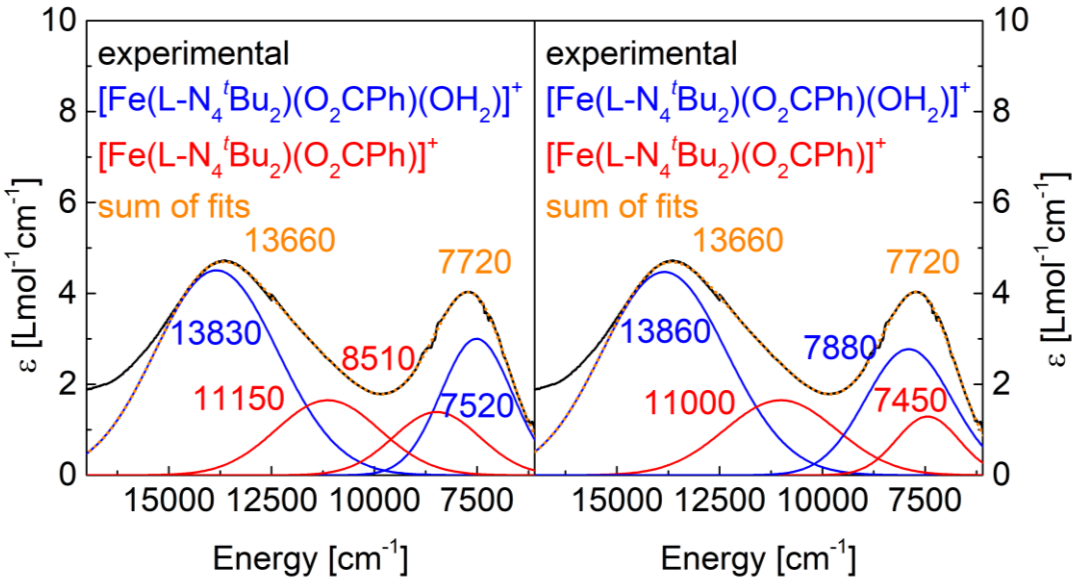

Figure 28. Two possibilities of decomposing the vis-NIR spectrum of **3** in MeCN solution into contributing subspectra using four gaussian curves (Fitting range 6241-14805 cm^{-1}). The spectrum was analyzed using MagicPlotStudent.

Two optimal fits were obtained. Each of these fits is composed of four Gaussian curves that could adequately describe the experimental spectrum. These two fits are depicted in Figure 28. By comparing the energies and the relative intensities of the contributing bands with those displayed in the solid-state spectra, the fit shown on the right hand side appears favorable. Based on this fit, two contributing species which exhibit absorption bands with maxima at 723 and 1330 nm and at 897 and 1175 nm, respectively are concluded to occur in an equilibrium in solution. The assignment of these two species to be complex cations **2** and **3** appears most likely at first, however

alternative assignments to other compositions such as e.g. **2** and $[Fe(L\text{-}N_4{}^tBu_2)(O_2CPh)(NCCH_3)]^+$ cannot be ruled out. The slight differences between the subspectra and the spectra of the solid complexes are tentatively explained by solvatochromic effects. Based on empirical observations during the synthetic efforts indicating hygroscopic properties for **3a**, a high sensitivity of the complex cation **3** towards minute amounts of water impurities in solution is assumed. The contamination of previously dried acetonitrile by trace amounts of water could not be totally excluded during the preparation of the samples in a glovebox.

2.1.8. EPR-spectroscopic Analysis on Frozen Solutions

The electronic absorption spectroscopy investigation shows that the spin states and coordination environments of the iron(III) complexes **1** and **4** are preserved in solution. Thus, a further investigation of the magnetic properties with EPR spectroscopy seems worthwhile. Spectra were recorded for frozen solutions of **1a** and **4a** between 10-40 K in dimethylformamide (DMF) containing 0.2 mol·L^{-1} tetrabutylammonium perchlorate (TBAP) as an additive to obtain a frozen glass (Figure 29). Even though frozen MeCN solutions of these samples show near identical spectra, DMF was chosen because of its established use for such investigations and because it produces a better glass and, thus, better resolved spectra.

While the EPR spectrum of the ferric complex **1** with effective *g*-values at 8.12, 3.55 and 1.69 (attributed to the M_S = ±1/2 Kramer doublet) and at 5.65 and 2.27 (attributed to the M_S = ±3/2 Kramer doublet) is characteristic for a high-spin S = 5/2 ion with substantial rhombicity, the more symmetric complex **4** renders an almost axial signal with effective *g*-values at 6.63, 5.35 and 1.98 (attributed to the M_S = ±1/2 Kramer doublet) and at 5.98 (attributed to the M_S = ±3/2 Kramer doublet). Some very small paramagnetic impurities were found to be present at *g* = 4.84 and *g* = 4.28. The signal at 4.28 is commonly observed for ferric samples.[61,128,129]

Using EasySpin (Version 5.2.28) and equation 5 (with μ_B = Bohr magneton),[130] the EPR spectra of **1a** recorded at various temperatures were fitted to an *S* = 5/2 species characterized by *g*-values of 1.999, 1.997 and 1.995, a zero-field splitting constant *D* = +2.75 cm^{-1} and a rhombicity *E/D* = 0.107 (Figure 30). In contrast, the spectra of **4a** agree with a *S* = 5/2 species corresponding to *g*-values of 1.965, 2.035 and 1.998, a zero-field splitting constant *D* = +3.62 cm^{-1} and a rhombicity *E/D* = 0.024 (Figure 31). The differences in rhombicity match the symmetry reduction between **4** and **1** that originates in the difference in coligands that complete the coordination of the iron site in the Fe(L-N$_4$^{t}Bu$_2$)-fragment.

$$(5)\quad \widehat{H} = \mu_B \boldsymbol{B}^T \cdot \boldsymbol{g} \cdot \widehat{\boldsymbol{S}} + D\left[\hat{S}_z^2 - \frac{S(S+1)}{3}\right] + E\left[\hat{S}_x^2 - \hat{S}_y^2\right]$$

A zero-field splitting constant *D* of similar size is obtained by fitting the magnetization data of solid **1** assuming an isotropic *g*-value (g_{iso} = 2.008, *D* = +3.23 cm^{-1}) (section 2.1.3). A stronger deviation is observed for **4**, where the fitting of the magnetization data yielded a *D*-value of 0.90 cm^{-1} with an assumed isotropic *g*-value (g_{iso} = 2.073). This larger error in *D*, that is however still acceptable, can be explained by larger deviations in the g_x, g_y and g_z-values of **4** that result in a more erroneous g_{iso}-value that contributes to the calculation of *D*.

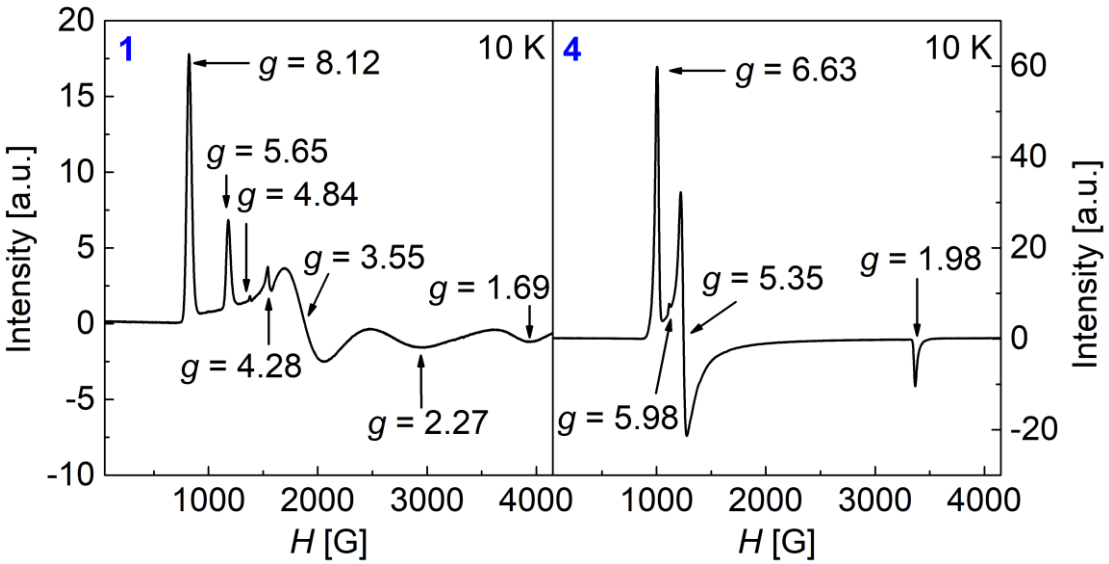

Figure 29. X-band EPR spectra of frozen solutions of **1** (9.3452 GHz) and **4** (9.3439 GHz) in DMF containing 0.2 mol·L^{-1} TBAP at 10 K. Effective *g*-values are indicated. Some very minor paramagnetic contaminants are found at g_{eff} = 4.84 and g_{eff} = 4.28 in the spectrum of **1**. The latter is commonly observed for ferric samples.[61,128,129]

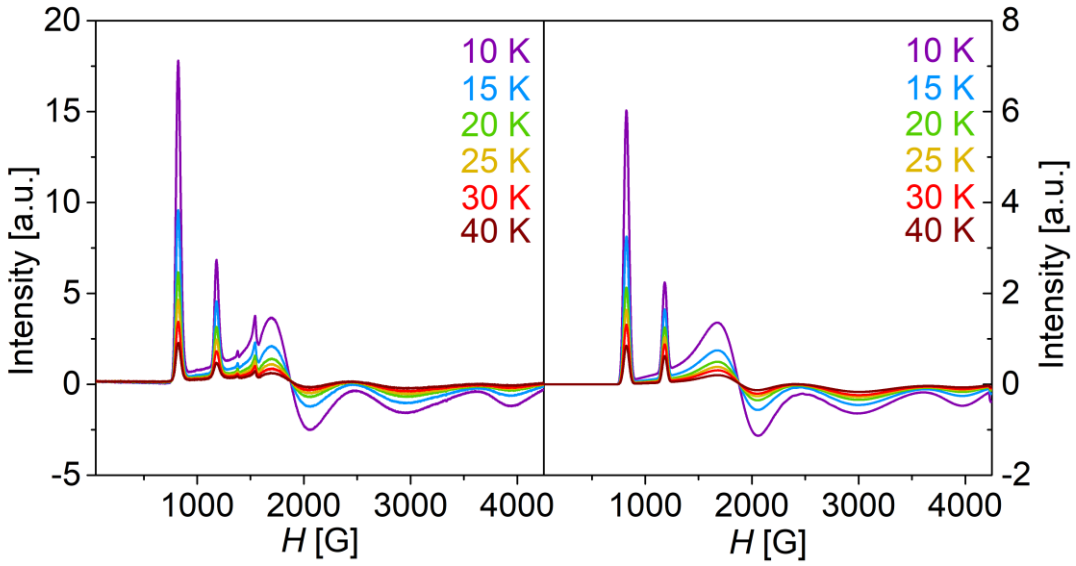

Figure 30. Experimental (left) and fitted (right) X-band EPR spectra of **1a** at variable temperatures between 10-40 K. Optimal fits were obtained using EasySpin 5.2.28.[130] Frequencies in GHz (Temperature): 9.3452 (10 K), 9.3450 (15 K), 9.3449 (20 K), 9.3448 (25 K), 9.3447 (30 K), 9.3444 (40 K).

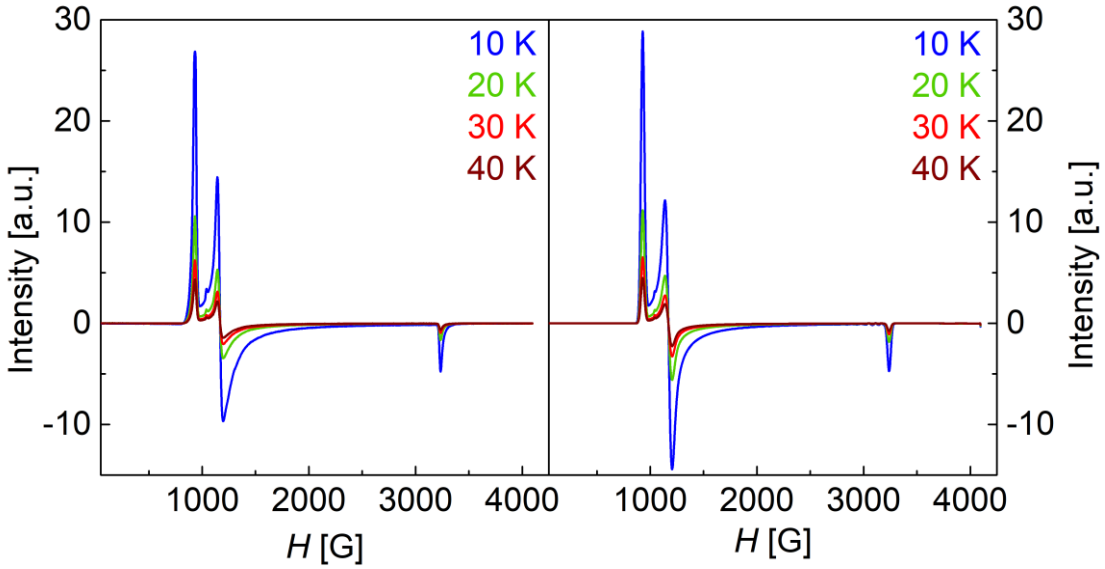

Figure 31. Experimental (left) and fitted (right) X-band EPR spectra of **4a** at variable temperatures between 10-40 K. Optimal fits were obtained using EasySpin 5.2.28.[130] Frequencies in GHz (Temperature): 9.3439 (10 K), 9.3438 (20 K), 9.3436 (30 K), 9.3433 (40 K).

2.1.9. ESI-Mass-Spectrometric Investigation

Electrospray ionization mass spectrometry (ESI-MS) was used to investigate the presence of the complex cations **1**, **2**, **3**, and **4** in acetonitrile solutions of analytically pure samples with different counterions. The spectra obtained for **1a**, **2a** are shown in Figure 32.

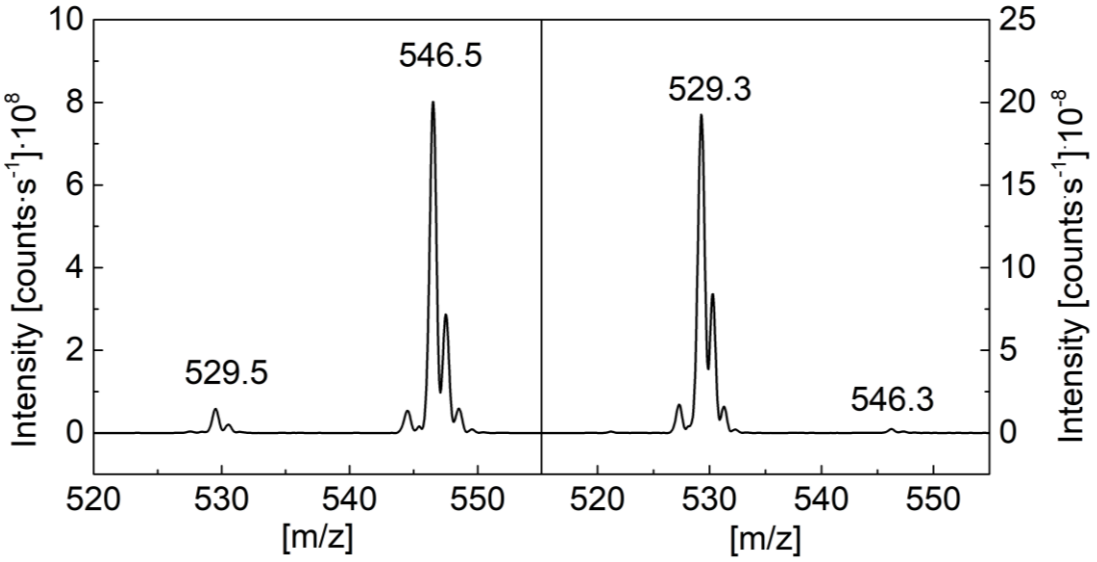

Figure 32. ESI mass spectra of acetonitrile solutions of **1a** (left) and **2a** (right) under a nitrogen atmosphere. The observed species correspond to $[Fe(L\text{-}N_4{}^tBu_2)(O_2CPh)]^+$ (m/z = 529.3) and $[Fe(L\text{-}N_4{}^tBu_2)(O_2CPh)(OH)]^+$ (m/z = 546.3). No further significant signals were observed in these spectra using the Advion mass express preset “soft ionization” (see methods). The measurement of **3a** rendered identical spectra to measurements of complex **2**, thus only the spectrum of **2a** is shown.

ESI-mass spectra of solutions of **1** in MeCN show a dominant signal at a *m/z* value of 546.3 which, based on the *m/z* value and its isotope pattern, corresponds to the monocationic complex **1** (Figure 33). There is no mass spectrometric evidence that a partial condensation reaction of two molecules of **1** yielding the μ–oxo-bridged diferric complex $[\{Fe(L\text{-}N_4{}^tBu_2)(O_2Ph)\}_2(\mu\text{–}O)]^{2+}$ occurs in solution. This result supports the notion that the ferric hydroxide species **1** exhibits considerable stability in solution. However, a far less intense second signal at *m/z* = 529.3 is observed, which is attributed to the monocationic ferrous complex **3**. The strength of this signal varies substantially with the experimental conditions employed in the mass spectrometric

investigation (Figure 34). Since the mass spectrometric experiments were only performed with verified analytically and spectroscopically pure compounds **1a** and **1c** (see also section 2.1.4), the observation of **3** is attributed to the partial loss of a hydroxyl radical from **1** under the rather harsh ESI-MS experimental conditions.

Application of anaerobic solutions of **2a** and **3a** to the mass spectrometer render essentially the same mass spectra (Figure 32). The main signal in these spectra is found at m/z = 529.3, which corresponds to the monocationic complex **3** as demonstrated by a comparison of the isotope pattern of this signal with that calculated for **3** (Figure 33). No signal corresponding to the presence of complex cation **2** is observed at m/z = 547.3 upon injection of anaerobic acetonitrile solutions of **2a**. It is concluded that during the transfer of the dissolved cation **2** into the gas phase of the ESI mass spectrometer, the coordinated water molecule is quantitatively lost rendering only complex cation **3** in the gas phase. Therefore, the detection of a signal at m/z = 529.3 in mass spectrometric experiments can be interpreted as an indication of the presence of the complex cations **2** and/or **3** in solutions, in line with the electronic spectroscopic investigations (section 2.1.7). In addition, in the mass spectra of anaerobic solutions of **2a** and **3a**, a very small signal is found at m/z = 546.3 which, based on its isotope pattern, is identified as the oxidized complex cation **1**. In the experimental setup of the mass spectrometer available to our research group, the strict exclusion of oxygen during the entire transfer process of the ions from the solution into the gas phase cannot be completely guaranteed. Thus, in the investigation of dissolved samples of the oxygen-sensitive ferrous complexes by ESI mass spectrometry, the oxidation of **2** to **1** cannot be completely prevented, but at least it can be kept to such a minimum that it does not entirely prohibit any interpretation of the mass spectrometric results obtained in reactivity studies (see below). The generation of the ferric hydroxide complex **1** provides indirect evidence that the aqua-complex **2** is indeed present in solution.

To elucidate the influence of the experimental conditions on the observation of this partial fragmentation and to minimize the generation of **3** a further investigation was undertaken in which the parameter settings were varied (Figure 34). Thereby, it was found that a significantly stronger fragmentation of the ferric complex occurs when higher source voltages are applied and that high capillary voltages lead to an increase in the relative signal strength of m/z = 529.3. This effect can be minimized when

capillary voltages of 160 V or lower are employed. Variation of the temperature between 200 and 250 K does not show any significant influence on the generation of **3** at low source voltage settings. Therefore, the soft ionization conditions preset by the manufacturer (T = 250 °C, U_{Cap} = 160 V, source voltage offset = 20 V, source voltage span = 0 V, see methods for more information) was found to be best suited to measure ESI mass spectra of **1** and to minimize fragmentation/artefacts. But, even under these ESI-MS conditions, the formation of the ferrous complex cannot fully be avoided. The relative amount of the formed ferrous complex with respect to the ferric complex under the soft ionization setting was determined to be ~10 % based on integration of the signals as well as relative peak heights.

The ESI mass spectra of compounds containing **4** are well behaved and show a single signal at m/z = 470.3 corresponding to the monocationic $[Fe(L\text{-}N_4{}^tBu_2)(OMe)_2]^+$ complex. Although this finding is expected and not particularly noteworthy, it is important to track the spectral region where this signal occurs to probe for any conversion issues during the synthesis of ferric hydroxide complexes and, thus, for impurities in the bulk material. This has shown to be particularly important for derivatives of **1**, as is discussed in section 3.1.8 of chapter 3 in more detail.

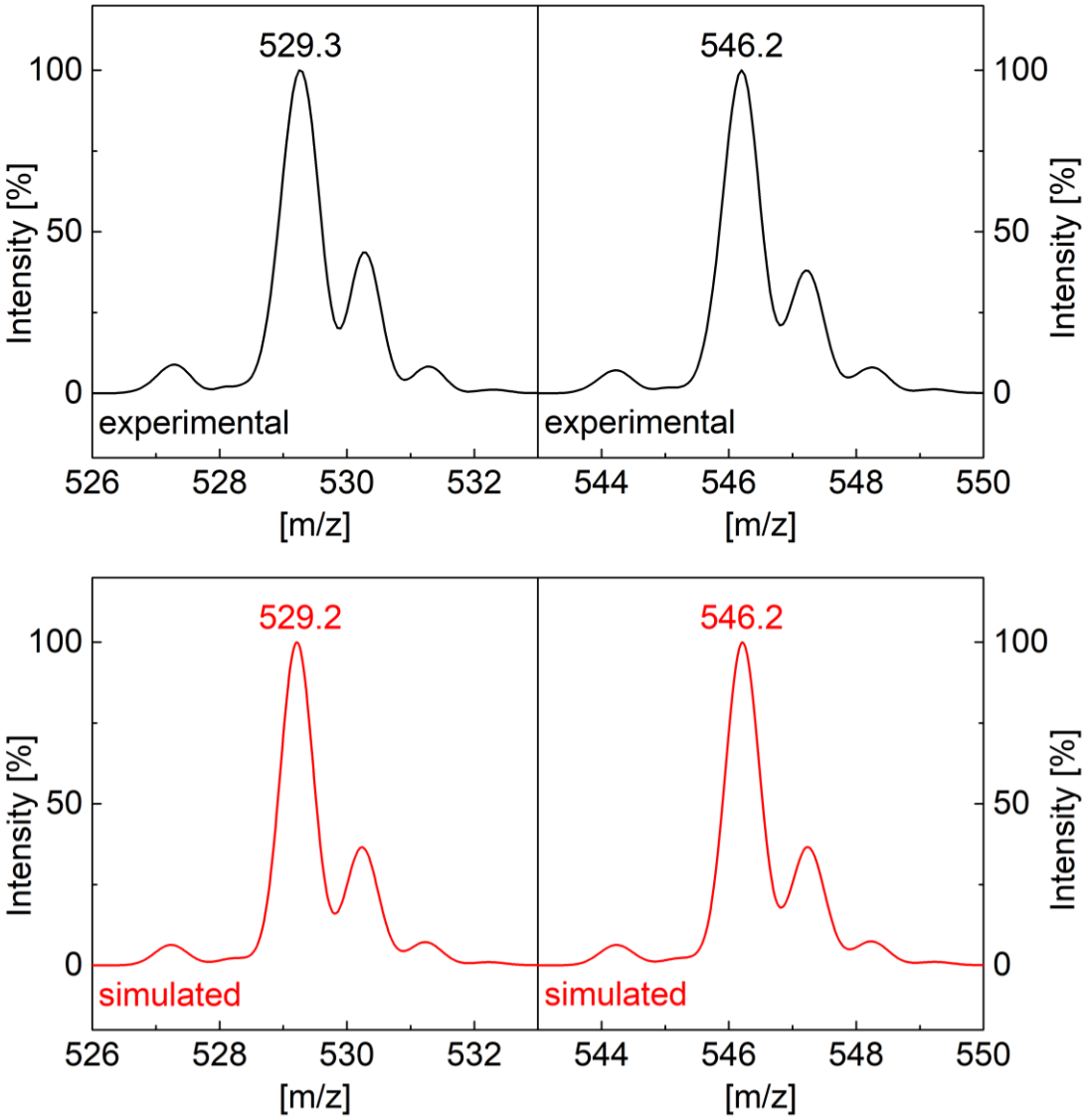

Figure 33. Comparison of the experimental spectra (top, black trace) of **2** (left) and **1** (right) with the simulated spectra (bottom, red trace) of **3** (calculated for $C_{29}H_{37}N_4O_2Fe_1^+$), and **1** (calculated for $C_{29}H_{38}N_4O_3Fe_1^+$). Both simulations were performed using IsoPro 3.1. A loss of the coordinated water ligand in **2** is assumed to occur during the transition of the complex cation into the gas phase.

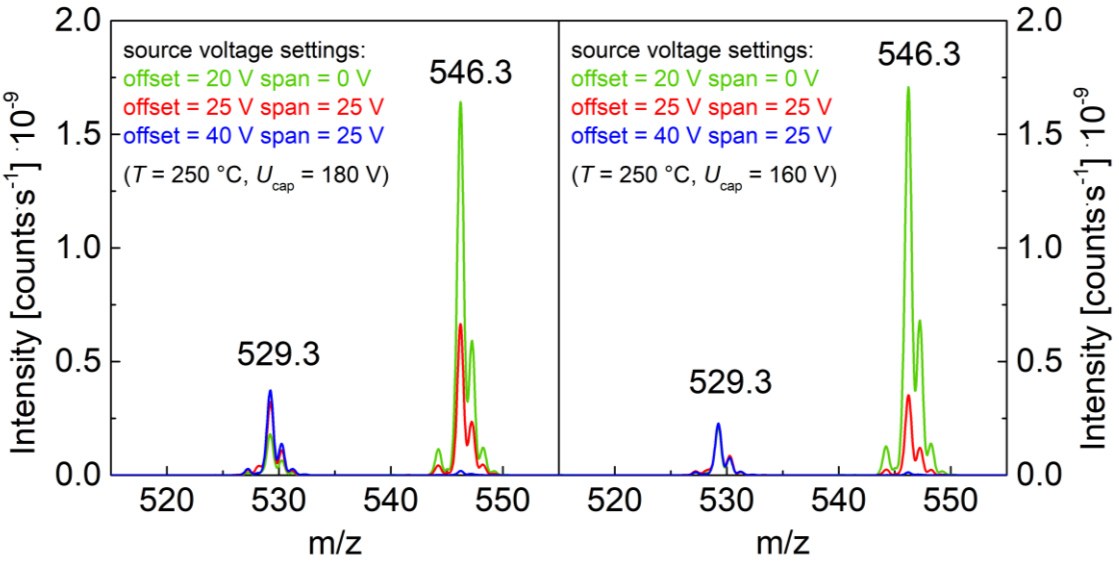

Figure 34. ESI mass spectra of an acetonitrile solution of **1a** obtained at different instrumental ionization presets with varying voltages. Variation of the source voltage settings was done in three increments according to the manufacturer's presets with capillary voltages of U_{Cap} = 180 V (left) and U_{Cap} = 160 V (right). Each measurement was done using 20 µL of the same solution of **1a** (loop 5 µL) to ensure quantitative comparability. The solution was prepared and stored under aerobic conditions throughout the measurement cycle.

In summary, the application of ESI mass spectrometry does not only verify solution stability of **1** but also proves to be very useful for a qualitative determination of products in reactivity studies of **1** with reducing substrates (section 2.3), as the ferric and the ferrous signals are found to occur as well separated peaks because of the loss of the neutral aqua ligand in **2** under ESI-MS conditions. The quantification of the peaks, however, must be taken with caution, as the ESI-MS conditions can lead to the partial loss of a hydroxide radical from **1**. Nevertheless, if these methodological limitations are heeded, the results by ESI mass spectrometric measurement can still render valuable information.

2.1.10. Electrochemical Investigation

Cyclic voltammetry (CV) measurements were performed on the ferric complex solutions of **1c** and **4b** and on the ferrous complex solutions of **2a** and **3a** under a nitrogen atmosphere in 0.2 $mol \cdot L^{-1}$ TBAP/MeCN (Figure 35 and Figure 36, respectively). The complexes display only irreversible electrochemical behavior as would be expected for redox processes coupled to protonation/deprotonation.[97]

At a scan rate of 100 mV/s, the cyclic voltammogram of complex **1**, recorded on an acetonitrile solution of **1c** that contained 0.2 $mol \cdot L^{-1}$ TBAP, displays an irreversible reduction process at a peak potential $E_{p,red}$ of -0.37 V vs SCE with a considerably less intensive first reoxidative current peak at $E_{p,ox}$ of -0.26 V vs SCE (with $E_{1/2}(Fc/Fc^+)$ = 0.48 V vs SCE, Figure 35). Attributing both current peaks to the redox pair $[Fe^{III}(L\text{-}N_4{}^tBu_2)(OBz)(OH)]^+/[Fe^{II}(L\text{-}N_4{}^tBu_2)(OBz)(OH)]^0$ (**1**/**1**$^-$), a half-wave redox potential $E_{1/2}$ = -0.31 V vs. SCE (-0.79 V vs Fc/Fc^+) is calculated. The irreversibility of the process is maintained even at high scan rates and the presence of further redox responses provides evidence that other species are present in solution which cannot be unambiguously identified without considerably more extensive investigations that were not conducted during this work. A comparison of the redox potential of **1/1**$^-$ to that of other (hydroxo)iron(III) complexes in acetonitrile solution is provided in section 2.3.6 (Table 13).

The reduction process of **4** appears to be even more irreversible, as no corresponding reoxidation response can be observed on the reverse sweep to more positive potentials. Moreover, the peak reduction potential (-1.44 V vs Fc/Fc^+) is strikingly more negative as compared to **1** (E_p(**4**) -0.85 vs Fc/Fc^+, ΔE = 0.59 V) despite their very similar N_4O_2-ligand environment. One reason for this may be the rather short bond lengths of both methoxide ligands and their localized charge character as well as the +I effect of the methyl groups which stabilize the ferric state very well despite the overall cationic charge. Generally, the -I effect of the distal oxygen of a singly coordinated carboxylate leads to a weaker sigma donor strength which destabilizes the ferric state. Here, this effect is even increased by the intramolecular hydrogen bond interaction of this distal oxygen with the aqua/hydroxo ligand.

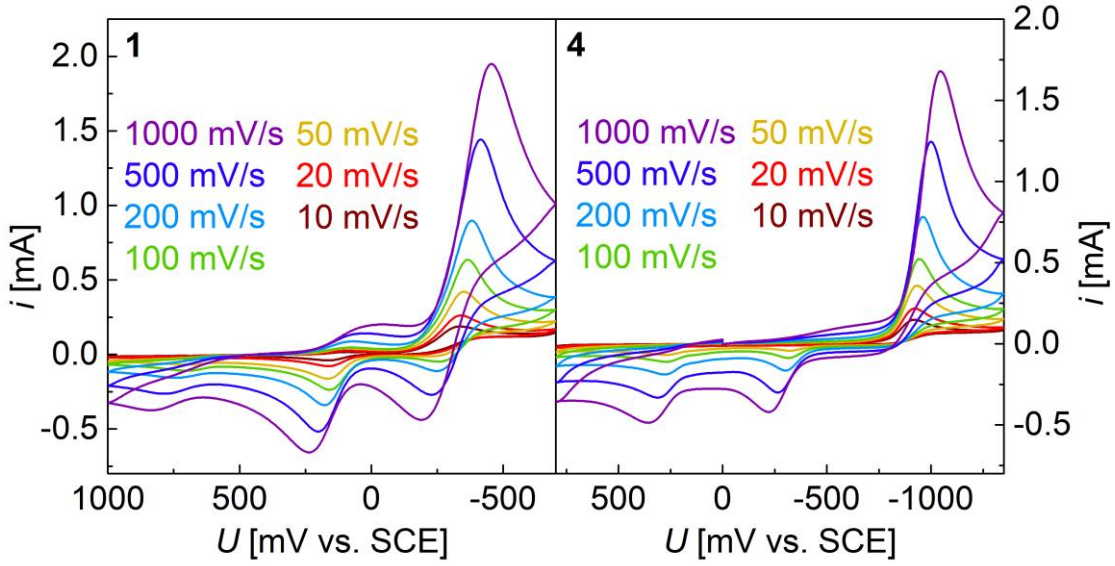

Figure 35. Cyclic voltammograms at variable scan rates of the ferric complexes **1** and **4** in 0.2 mol L^{-1} TBAP/MeCN solution at room temperature under a nitrogen atmosphere. Sweeps: (**1**) 500 mV → -700 mV → 1000 mV → 500 mV (Fc/Fc^+ = 0.48 V vs SCE); (**4**) 0 mV → -1350 mV → 800 mV → 0 mV (Fc/Fc^+ = 0.49 V vs SCE). **Peak potentials** (100 mV/s, all vs SCE): (**1**) $E_{p(red)}$ = -366 mV, $E_{p(ox1)}$ = -262, $E_{p(ox2)}$ = 158 mV, $i_{p(ox3)}$ = 694 mV. (Fc/Fc^+ = 0.48 V vs SCE); (**4**) $E_{p(red)}$ = -946 mV, $E_{p(ox1)}$ = -316, $E_{p(ox2)}$ = 270 mV. (Fc/Fc^+ = 0.49 V vs SCE).

The oxidation of solutions of **3a** and **2a** in acetonitrile, respectively, occur irreversibly at oxidative peak potentials $E_{p,ox}$(**3**) = 734 mV vs SCE and $E_{p,ox}$ (**2**) = 678 mV vs SCE at 100 mV/s (with $E_{1/2}(Fc/Fc^+)$ = 0.45 V vs SCE, Figure 36). The observation of the rather intense oxidative current is tentatively assigned to an irreversible oxidation process of the cationic ferrous aqua complex **2**, probably also present in **3** as derived from electronic absorption spectroscopy results (section 2.1.7). Although the CV results for **3** and **2** appear similar, they are distinct in some features, which is attributed to the differences in water content in the respective solutions. Excluding even the slightest amount of water is a challenge to be met under the conditions present in our glovebox, which contains aqueous potassium chloride solutions to store the standard calomel reference electrode. An electrochemical study in solvents containing defined amounts of water also proves to be complicated due to solubility problems, the occurrence of further equilibrium reactions involving water, and the undefined water residue in the glove box atmosphere. The assignments of the other electrochemical

responses observed for **2** and **3** in these rather complicated cyclic voltammograms require more detailed investigations.

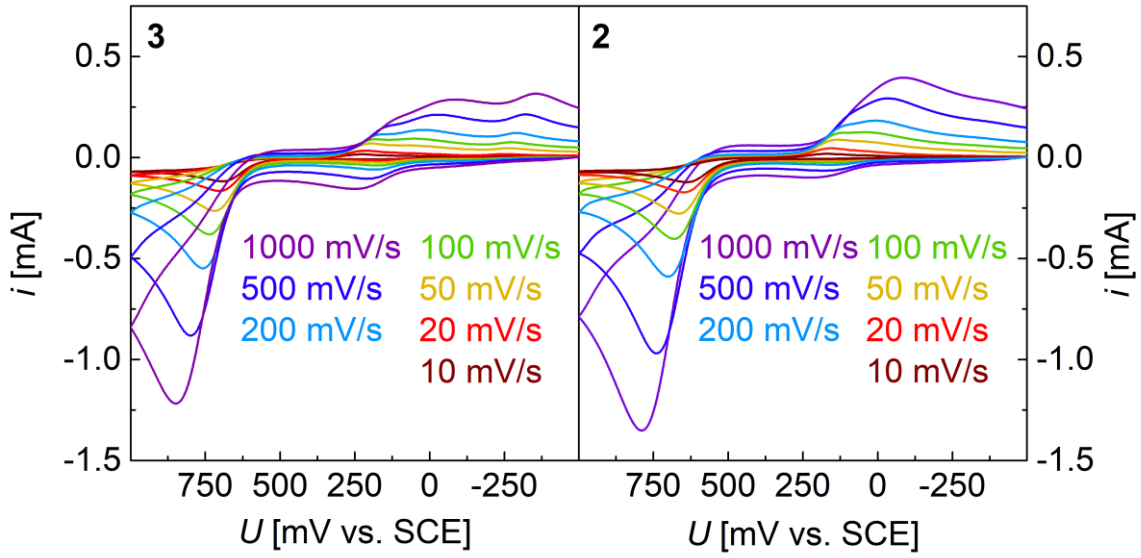

Figure 36. Cyclic voltammograms at variable scan rates of the ferrous complexes **3** and **2** in 0.2 mol L^{-1} TBAP/MeCN solution at room temperature under a nitrogen atmosphere. Sweeps: -500 mV → 1000 mV → -500 mV (Fc/Fc^+ = 0.45 V vs SCE). **Peak potentials** (100 mV/s, all vs SCE): (**3**) $E_{p(ox1)}$ = 168 mV, $E_{p(ox2)}$ = 734 mV, $E_{p(red1)}$ = 178, $E_{p(red2)}$ = 94 mV, $E_{p(red3)}$ = -274 mV. (Fc/Fc^+ = 0.45 V vs SCE)); (**2**) $E_{p(ox1)}$ = 168 mV, $E_{p(ox2)}$ = 678 mV, $E_{p(red1)}$ = 118 mV, $E_{p(red2)}$ = 125 mV. (Fc/Fc^+ = 0.45 V vs SCE)).

*Note: The SCE reference electrode in our setup showed a Fc/Fc^+ oxidative process at 0.48 V vs SCE at the time the described measurement on **1c** was done. In the original publication, a standard potential of 0.45 V vs SCE for Fc/Fc^+ was assumed. However, it was later reiterated from a logbook that this was not the case for the measurement of **1** but only for that of **2** and **3** as the reference electrode was manipulated in between these measurements.*

2.1.11. NMR-Spectroscopic Analysis

^{1}H-NMR and ^{2}H-NMR spectroscopic analysis was performed for **1c** and **2a** and their analogues with pentadeuterated benzoate ligands **1^{D}c** and **2^{D}a**, respectively.

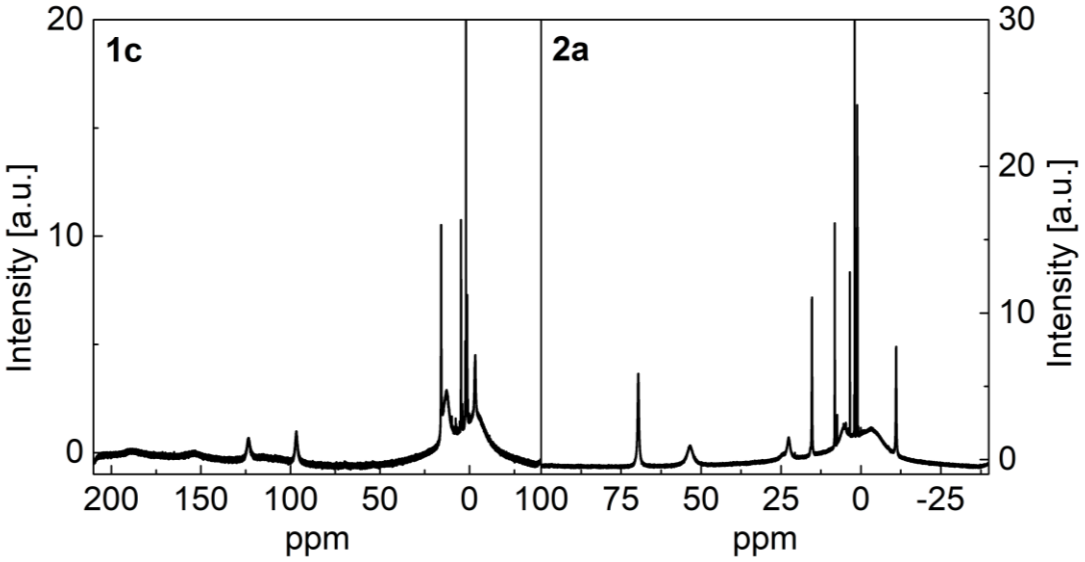

Figure 37. ^{1}H-NMR spectra of **1** and **2** obtained with 0.02 mol·L^{-1} solutions of **1c** and **2a**, respectively, in CD_3CN at room temperature. ^{1}H-NMR(600 MHz, CD_3CN, **1**) δ(ppm) = 188.99 (br), 154.15 (br), 123.46 (br), 96.6 (br), 15.83 (s), 12.80 (br), 4.73 (s), 2.31 (s), -2.90 (sh), -3.27 (s). ^{1}H-NMR (600 MHz, CD_3CN, **2**) δ(ppm) = 69.61 (br), 53.44 (br), 24.43 (sh), 22.55 (br), 15.31 (s), 8.18 (s), 5.43 (br), 1.05 (s), -3.28 (br), -11.04 (s). br = broad, s = singlet, sh = shoulder. Impurities at 3.42 and 1.12 correspond to diethylether residues.[131] Some relevant relative integer integrals are given below in the caption of Figure 38.

The ^{1}H-NMR measurement of the S = 5/2 complex of **1c** in CD_3CN reveals a paramagnetic spectrum with signals between 200 and -25 ppm (Figure 37, left). Expectedly, the less paramagnetic S = 2 species of **2a** shows signals in a more narrow range between 75 and -25 ppm (Figure 37, right). The interpretation of the broad, highly shifted signals was pursued but not achieved. However, at least the signals corresponding to the benzoate ligand are thought to be unambiguously identifiable by supplementary ^{2}H-NMR spectra of isotope-labled derivatives (see below).

Thus, **1c** and **2a** were synthesized with pentadeuterated benzoate $C_6D_5CO_2^-$ (d5-$PhCO_2$; **1^{D}c**, **2^{D}a**, see experimental section for synthesis) and comparative

^{2}H-NMR spectra were recorded (Figure 38). Despite best efforts and the use of rather concentrated (0.02-0.08 mol·L^{-1}) solutions of **1^{D}c** and **2^{D}a**, respectively, the obtained spectra remained rather noisy and some artefacts are observed (poor baseline, splitting of a signal in the ^{2}H-NMR spectrum of **2^{D}a**) even with 1024 scans and the FID set to 128k. The challenge with ^{2}H-NMR spectroscopy is to introduce an internal reference for shimming by addition of a ^{2}H-NMR active species (CD_3CN) while also keeping the reference signal small enough to allow for a good resolution of the species of interest. Here, this was problematic and ultimately made locking and shimming of the signal partially unattainable (0.2 mol·L^{-1} CD_3CN in CH_3CN). Because of the poor signal strength produced by the samples for ^{2}H-NMR spectra, the samples were ultimately measured with the shim of a blank 0.2 mol·L^{-1} solution of CD_3CN in CH_3CN. Despite some artefacts and a poor spectrum quality, the signals of the benzoate ligand could be unambiguously assigned in for both **1^{D}** and **2^{D}** in the range between 24 and 3 ppm and agree with the respective signals observed in the ^{1}H-NMR of **1c** and **2a**. The observation of only three distinct signals for the benzoate ligand in the NMR spectra of **2^{D}a** and **2a** is evidence of either a rapid equilibrium between the cations of **2** and **3** or the existence of one dominant species in solution. Paired with the results from UV-vis-NIR spectroscopic investigations (section 2.1.7), the dominance of **2** is considered to be more likely. The assignment of the signals can be done based on the magnitude of the shift, and the broadening of the signals. A close proximity to the paramagnetic center leads to a larger shift and an increased broadening, and vice versa. For **1**, the signals at 15.8 ppm and 14.5 ppm are assigned to the *meta*- and the *ortho*-proton resonances of the benzoate ligand, respectively. This is done based on the signal broadening that is related to the interaction strength with the paramagnetic core because differences in chemical shift are not meaningful enough. The signal at 4.7 ppm is assigned to the *p*-proton resonance of the benzoate ligand, because the chemical shift is much closer to the expected value for aromatic ring protons in a diamagnetic environment and the relatively sharp appearance of the signal indicates weaker interaction with the paramagnetic iron site and, thus, a larger distance of this proton to the iron. For **2**, the signals are assigned as 22.55 (*o*-proton), 15.31 (*m*-proton), 8.18 (*p*-proton) with similar reasoning. As can be deduced from this assignment, the interaction of the paramagnetic iron core appears to be stronger in the ferrous complex, despite a smaller spin multiplicity and a weaker metal-ligand interaction as derived from the extended Fe-O_{OOCPh} bond length in **2** compared to **1**. It

can be assumed that more spin density is localized at the benzoate ligand in the ferrous complex, however accompanying density field theory (DFT) spin-density calculations of geometrically optimized structures (see 9.1 for method details) were inconclusive (see attachment). No further interpretation of this observation was attempted as paramagnetic NMR shifts are challenging to predict accurately.

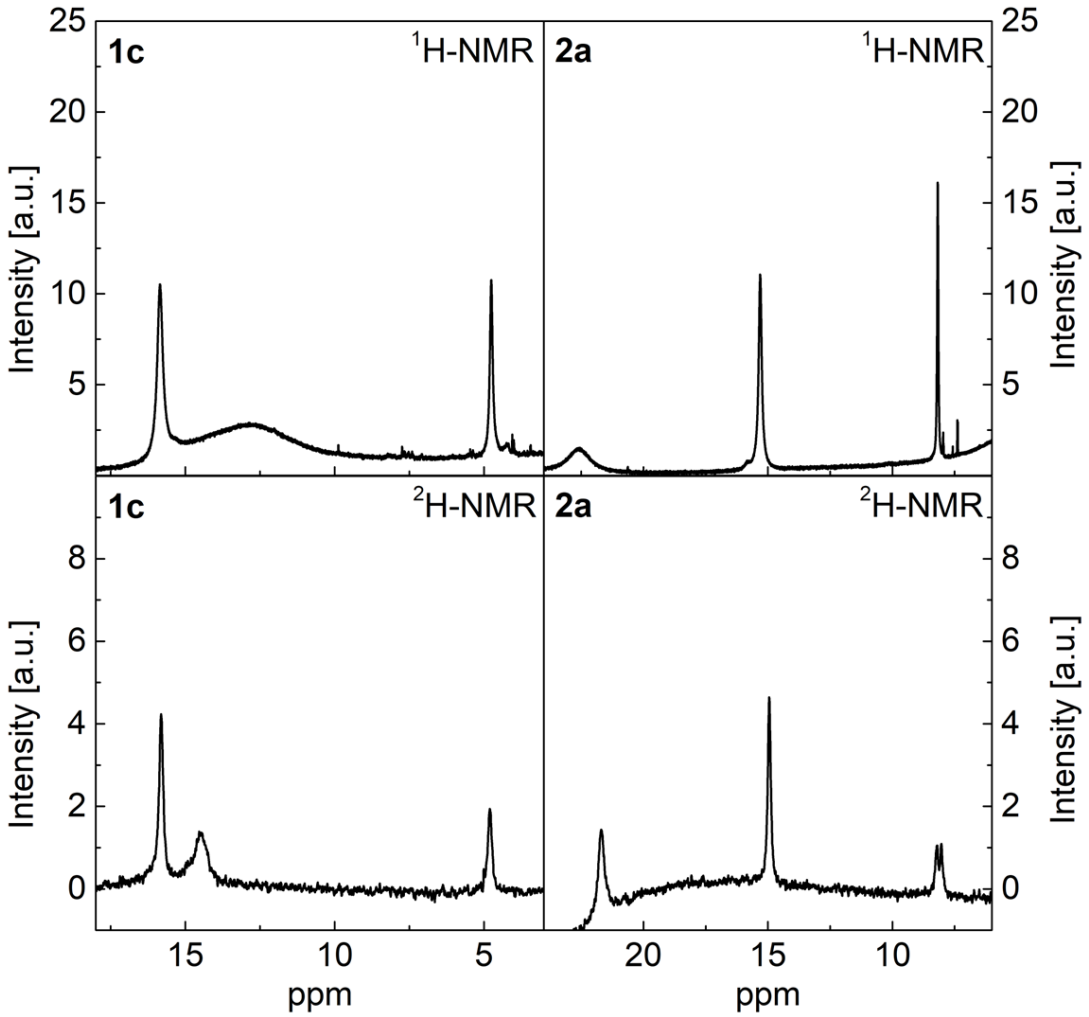

Figure 38. ^{1}H-NMR spectra of **1c** and **2a** (0.02 mol·L^{-1}) in CD_3CN (top) and ^{2}H-NMR spectra of their respective $C_6D_5CO_2$-analogues **1^{D}c** and **2^{D}a** (0.02 mol·L^{-1}) in a 0.2 mol·L^{-1} CD_3CN in CH_3CN solution (bottom) between 24 and 3 ppm at room temperature. ^{1}H-NMR (400 MHz, CD_3CN, **1**) = 15.83 (s), 12.80 (br), 4.73 (s); ^{2}H-NMR (400 MHz, 0.2 mol·L^{-1} CD_3CN in CH_3CN, **1**) = 15.81 (s, 2H), 14.49 (s, 2H), 4.81 (s, 1H); ^{1}H-NMR(400 MHz, CD_3CN, **2**) = 22.55 (br), 15.31 (s), 8.18 (s); ^{2}H-NMR(400 MHz, 0.2 mol·L^{-1} CD_3CN in CH_3CN, **2**) = 21.70 (s, 2H), 14.95 (s, 2H), 8.12 (m, 1H). Deviations between ^{1}H- and ^{2}H-NMR shifts may be a result of shimming or phase correction differences. Artefacts in the ^{2}H-NMR spectra result from a poor shim and resolution.

In addition to the ^{1}H- and ^{2}H-NMR spectra, the relaxation times t_1 were determined for **1** and **2** by a sequential 180° pulse and a 90° pulse with differing times between the pulses. The results of this analysis, performed on 20 mmol·L^{-1} acetonitrile solutions of **1c** and **2a**, are listed in Table 10 and supplemented with the half-widths of the individual signals. It should also be noted that a cross checking of the above presented interpretation for the benzoate protons with the relative integrals spectra further supports the assignment (see caption of Figure 38, *ortho*:*meta*:*para*, 2:2:1).

Table 10. Relaxation times t_1 and half-widths $\Delta_{1/2}$ for selected signals obtained from solutions of **1c** and **2a** for the cations of **1** and **2**.

Fragment	**1**		**2**	
	ppm	t_1 [ms] ($\Delta_{1/2}$)	ppm	t_1 [ms] ($\Delta_{1/2}$)
L-N$_4$*t*Bu$_2$				
n.d.	188.99	n.d.[b] (>2400 Hz)	69.61	0.8 ms (165 Hz)
n.d.	154.15	n.d.[b] (>2400 Hz)	53.44	0.6 ms (860 Hz)
n.d.	123.46	n.d.[b] (1000 Hz)	24.43	0.7 ms (840 Hz)
n.d.	96.6	n.d.[b] (570 Hz)	5.43	0.3 ms (1300 Hz)
n.d.	12.80	n.d.[b] (1300 Hz)	-3.28	<1 ms (>2400 Hz)
n.d.[a]	-2.90, -3.27	1.4 ms (330 Hz)	-11.04	4.3 ms (85 Hz)
O$_2$C-C$_6$H$_5$				
o-proton	14.49	n.d.	22.55	1.2 ms (480 Hz)
m-proton	15.84	4.3 ms (85 Hz)	15.31	11.5 ms (55 Hz)
p-proton	4.73	7 ms (45 Hz)	8.18	26.0 ms (20 Hz)

o = ortho, *m* = meta, *p* = para, n.d. = not determined. t_0 was experimentally determined, t_1 values are calculated and given as $t_1 = t_0/\ln(2)$. [a] Based on the relaxation time for the supposed L-N$_4$*t*Bu$_2$ signals, this peak may be speculated to correspond to the pyridine proton in 4-position because it is furthest apart from the paramagnetic centrum and shows the longest relaxation time t_1 for the macrocycle. The shoulder at 2.90 ppm in **1** maybe a result of a stronger asymmetry lifting the chemical equivalence of the two

protons in 4-position of the two pyridines, respectively. [b] t_1 values were not determined as all are expected to be below 1 ms (as derived from their signal half-widths) and the resolution was not sufficient to accurately resolve the signals in the t_1 measurement series.

In the case of **2**, the relaxation times obtained for the benzoate protons agree well with the assignment deduced from the magnitude of the shifts of the signals above. As a closer proximity or stronger interaction with the paramagnetic metal site yields shorter relaxation times, the sequence of decreasing relaxation times as t_1(*p*-proton) > t_1(*m*-proton) > t_1(*o*-proton) is also reasonable. In an additional H,H-COSY experiment, cross peaks can be observed only for the signals at 15.3 and 8.2 ppm, further verifying the assignment. The absence of any other cross peaks in the 2-dimensional COSY-spectra even at long measurement times, extensive amounts of scans, and higher temperatures to decrease the paramagnetism (line broadening) according to the Curie law demonstrate the challenge to gain further information about the signals with large half-widths (>60 MHz) and/or extremely short relaxation times (<5 ms). An assignment of the signals corresponding to the macrocyclic ligand was thus not achieved. It is, however, speculated, that the extremely broad baseline deviations between 40 and -20 ppm are caused by the protons of the ^{t}Bu-groups of the macrocyle. These may experience dynamic line broadening (rotation of the ^{t}Bu-groups) as well as paramagnetic broadening and would typically not be positioned at very high or very low fields. Thus, the remaining, only moderately broadened signals should correspond to the 8 methylene protons, the 4 pyridine protons in 3- and 5-position of both pyridine residues, respectively, and the 2 pyridine protons in 4-position. As the pyridine protons in 4-position are furthest away from the paramagnetic center and should, thus, show the longest relaxation time, it is reasoned that the signal situated at -11.0 ppm with a relaxation time of 4.3 ms corresponds to these protons. Such an interpretation is supported by the calculated spin density map that shows a spin density with opposite sign at this proton as opposed to the other pyridine ring protons.

For **1**, the relaxation times of the *meta*- and the *para*-proton at the benzoate could be determined, as the *ortho*-proton signal is obscured, and the expected extremely short relaxation times render the signal practically unobservable under the given conditions. Generally, the relaxation times are shorter than those observed for **2**, which is attributed to the increased paramagnetism of the ferric iron site. Because of these

shorter relaxation times and broader half-widths, a H,H-COSY experiment failed to return any cross-peaks (see attachment). The protons of the macrocylic ligand can, again, also not be assigned because of their extremely short relaxation times and broad signals. However, in analogy to **2**, the negative signal in **1** at -3.27 ppm, which includes a shoulder at -2.90 ppm, is suspected to correspond to the protons in 4-position of the pyridine donors, as the relative relaxation time t_1 is yet again longer than that of all the other suspected L-$N_4{}^t Bu_2$ signals and the DFT spin-density calculations return a similar result as for **2**. The shoulder could indicate an increased asymmetry in the Fe-O distances, which would cause the lifting of the chemical equivalence of the pyridine donors because of the *trans*-influence.

2.2. Summary of the Structural, Spectroscopic, Spectrometric, Magnetic, and Electrochemical Investigations

To summarize the results presented up to this point, a thorough investigation reveals two high spin iron(III) and two high spin iron(II) pseudooctahedral complexes with an N_4O_2 ligand environment that can be isolated with a variety of counterions. The ferric *cis*-$[Fe^{III}(L\text{-}N_4{}^tBu_2)(OMe)_2]^+$ (**4**) and *cis*-$[Fe^{III}(L\text{-}N_4{}^tBu_2)(O_2CR)(OH)]^+$ (**1**) complexes have been shown to maintain their coordination environment in solution. For the ferrous *cis*-$[Fe^{II}(L\text{-}N_4{}^tBu_2)(O_2CR)(OH_2)]^+$ (**2**) and *cis*-$[Fe^{II}(L\text{-}N_4{}^tBu_2)(O_2CR)]^+$ (**3**) complexes, an equilibrium is suggested in MeCN solution which strongly favours **2**. All complexes show a high spin state even at very low temperatures in the solid state; for the ferric complexes this could also be verified with EPR-spectroscopic methods for frozen solutions. No evidence for the formation of dinuclear iron(III)-μ-oxo complexes was found, underlining the (kinetic) stability of the ferric hydroxide species in solution. In the cases of **1** and **2**, a significant intramolecular hydrogen bonding between the two *cis*-coordinated oxygen donor ligands is observed. This interaction is thought to be the basis of the stability of **1** along the steric shielding of the *tert*-butyl groups of the macrocyclic ligand and the reason for the favouring of **2** over **3**, also evident by empirical observations of hygroscopic properties of **3**. Furthermore, the intramolecular interactions inhibit rotations of the carboxylate ligand and pre-organize a channel for a potential substrate to interact with the lone pair of the hydroxide ligand in **1**, suggesting the capability to perform hydrogen atom abstraction (HAT) reactions. Such a preorganization cannot be observed for **4**, as no intermolecular interactions are present. Thus, **4** could also prove valuable as a reference in understanding the potential reactivity of **1**.

In particular, the investigation shows that the structural aspects of the active site in rabbit Lipoxygenase (rLOX), namely the FeN_4O_2 immediate coordination environment and, particularly, the intramolecular hydrogen bonded *cis*-$[Fe^{III}(O_2CR)(OH)]^+$ and *cis*-$[Fe^{II}(O_2CR)(OH_2)]^+$ coordination units, are well reproduced in the ferric complex **1** and the ferrous complex **2**, respectively. In addition to the structural model qualities, the complexes display the same electronic properties as the enzyme. One could speculate that even complex **3** could prove itself to be an adequate model for an enzymatic state

of lipoxygenase, which has not yet been explicitly demonstrated to exist for rLOX. However, in soybean LOX (sLOX), spectroscopic studies and EXAFS investigations reveal the existence of an equilibrium between a 5-coordinate and a 6-coordinate species in solution (40/60%), thus implying a dynamic coordination environment at the active iron(II) site when no substrate is present.[66,120,132] This observation is in line with the generally accepted role of carboxylate ligands in metalloproteins of providing easy access to a further open coordination site at a metal ion by switching from the bidentate chelating to the monodentate coordination mode.[133] Such an equilibrium also exists between complexes **2** and **3**.

Although the structural and electronic properties of the enzyme site are well reproduced by the presented complexes, the model complexes do not seem to match the redox properties of the enzyme. A considerably higher redox potential has been reported for the enzyme (+0.6 ±0.1 V vs. SHE for pH = 7-9 in H_2O).[134] The reason behind this discrepancy could be the slightly longer Fe–N and Fe–O bonds in rLOX and the extensive hydrogen bonding donor network provided by the protein environment around the active site of the enzyme.[64,67,68] However, further investigations are needed to identify the origin of this discrepancy.

As the model complexes **1** and **2** show unprecedently close electronic and structural similarities to the properties of the active site of the enzyme in both biologically relevant oxidation states, a further investigation of the reactivity of **1** appears promising. Such investigations are described in the following subsections of 2.3.

2.3. H-Atom Abstraction Reactivity Studies

After the structural and electronic model properties of **1** and **2** were established, the capability of **1** to perform H-atom abstraction reactivities was investigated. For this, the complex was reacted with 2,2,6,6-tetramethylpiperidin-*N*-hydroxid, TEMPOH (**I**) and 2,4,6-tri(*tert*-butyl)phenol, TTBP (**II**) which contain weak O–H bonds, and cyclohexadiene, CHD (**III**) and dihydroanthracene, DHA (**IV**) which contain weak C–H bonds, under anaerobic conditions (Scheme 6). The reactions with TTBP and DHA were also probed under aerobic conditions.

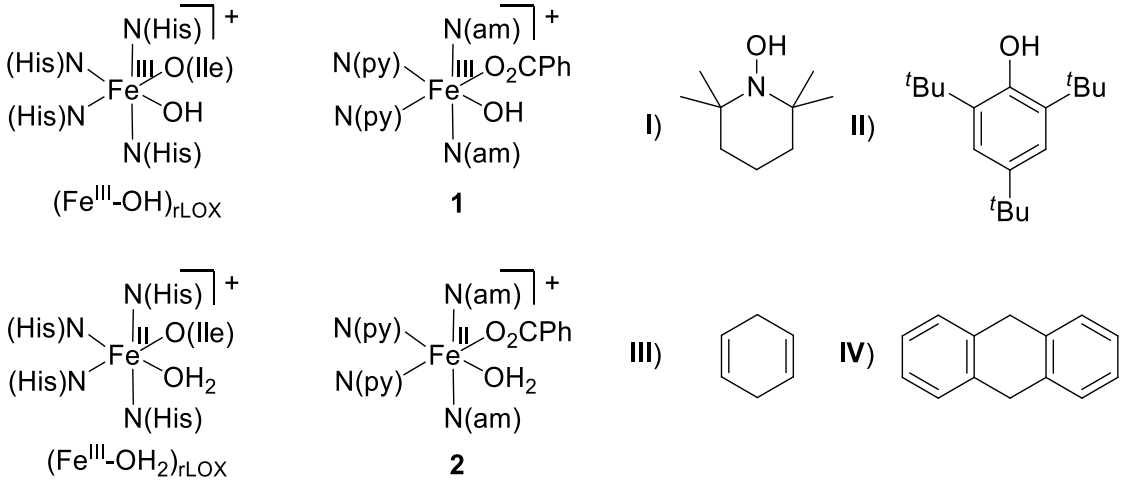

Scheme 6. Iron sites of the enzymatic states in rLOX, schematic depictions of the complex cations in **1** and **2**, and substrates with weak O–H (**I**, **II**) and C–H bonds (**III**, **IV**) that were probed for reactivity with **1** in the following.

Overall, the investigations pertained radical initiation, stoichiometric and catalytic reaction properties as well as studies regarding reaction thermodynamics and kinetics. In this, it is assumed that **2** is always the main ferrous species in the reaction solutions and that the equilibrium between **2** and **3** does not affect the studies significantly. This is justified by the results described in section 2.1. To further elucidate the mechanism, the relevance and cooperativity of the special ligand environment in **1** and **2** as well as in rabbit Lipoxygenase (rLOX), and to rule out a simple base assisted oxidation reaction of **1** especially with TEMPOH and TTBP, also the reactivity of **4** was probed for comparison. As no reactivity was observed for **4** under the same conditions, this is not further discussed below. Studies that relate to the mechanism of the X-H bond activation by **1** are accompanied by theoretical calculations in section 2.4.

2.3.1. H-Atom abstraction from TEMPOH

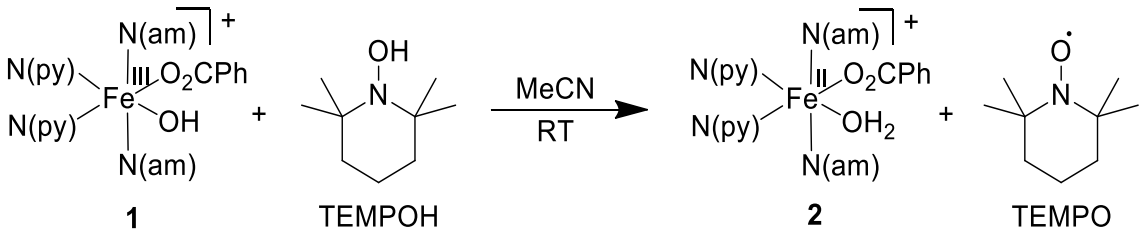

Scheme 7. Proposed reaction of **1** with TEMPOH yielding **2** and TEMPO via H-atom transfer in MeCN at room temperature (RT).

The capability of **1** to abstract a H-atom from TEMPOH was demonstrated by the reaction of **1a** with the substrate in acetonitrile under anaerobic conditions (Scheme 7). The resulting ferrous product was identified by ESI-mass spectrometry (Figure 39) and the organic radical product was identified by EPR spectroscopy (Figure 40).

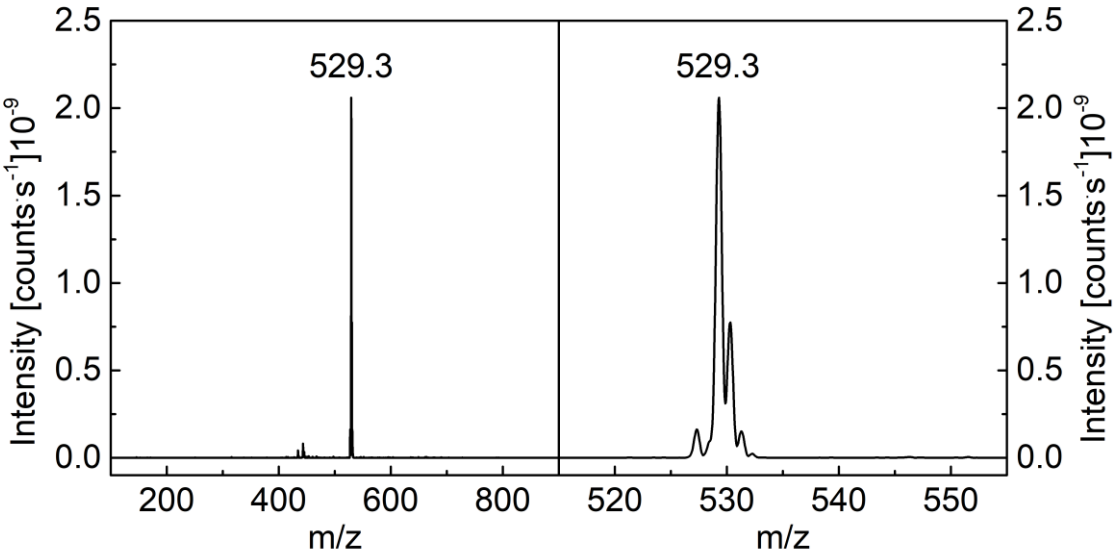

Figure 39. ESI mass spectrum of a reaction solution of TEMPOH and **1a** prepared with a tenfold excess of TEMPOH under nitrogen atmosphere. Depicted ranges: 100-900 m/z (left) and, 515-555 m/z (right).

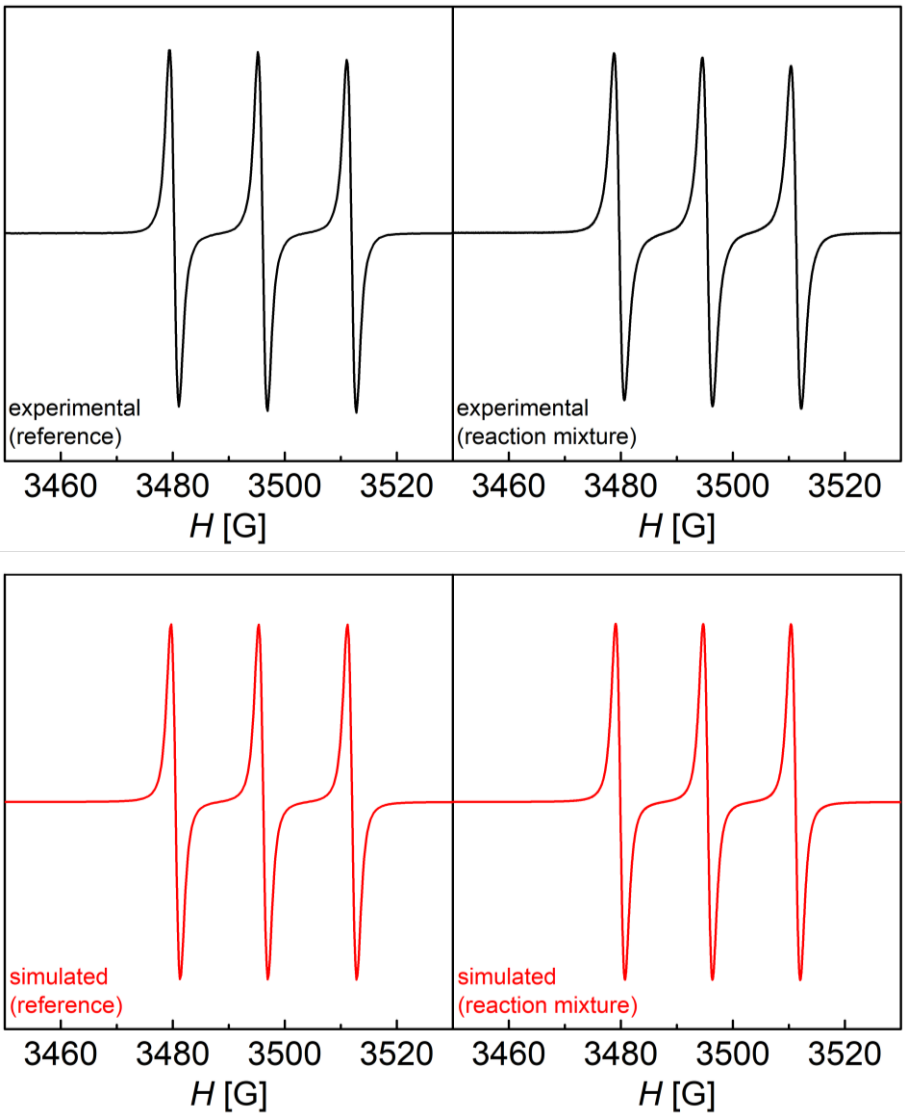

Figure 40. EPR spectra of an authentic sample of TEMPO in MeCN (top left, black trace) and of TEMPO produced in the reaction of **1a** with TEMPOH (top right, black trace) in MeCN under a nitrogen atmosphere (both recorded with a modulation amplitude of 1 G). The EPR spectra were fitted using the EasySpin software rendering: g = 2.0075, A_N = 44 MHz (bottom left, red trace) and g = 2.0076, A_N = 44.4 MHz (bottom right, red trace), respectively.

The ESI-MS spectrum of a reaction mixture of **1a** with a tenfold excess of TEMPOH reveals only a single signal which corresponds to **3** (Figure 39) and probably results from the transfer of **2** into the gas phase under ESI-MS conditions as described in section 2.1.9. This result implies the quantitative conversion of **1** to **2** with TEMPOH.

The room temperature EPR spectrum of the reaction mixture of TEMPOH with **1a** consists of a triplet signal with a hyperfine coupling constant to the nitrogen atom A_N =

44 MHz, which agrees with the EPR spectrum of an authentic sample of the TEMPO radical in acetonitrile solution. The slight broadening of the signal in the reaction mixture sample is attributed to the presence of the paramagnetic iron complex. The stoichiometric reaction with TEMPOH appears to be almost complete as judged by quantitative EPR studies with a flat cell (Figure 41), indicating a significantly higher bond dissociation free energy for **2** than present in the O–H bond of TEMPOH ($BDFE_{MeCN}$ = 66 kcal·mol^{-1}).[97]

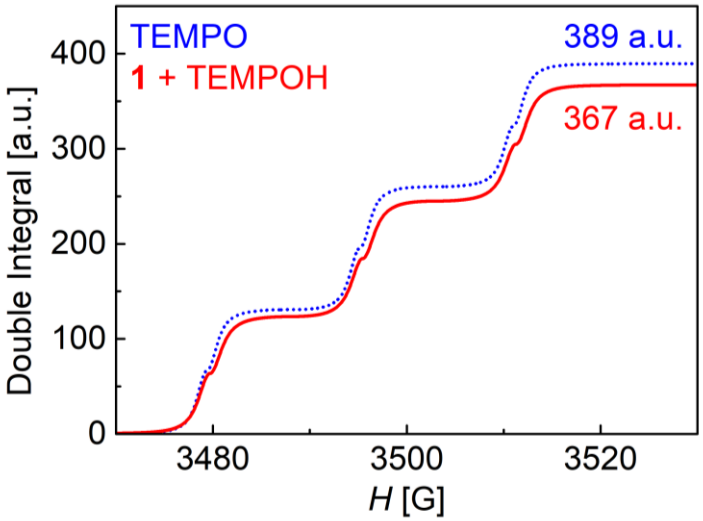

Figure 41. Double integrals of EPR spectra similar to those depicted in Figure 40. Blue trace: c_{TEMPO} = 5 mmol L^{-1}, integral 389 a.u.; red trace: reaction mixture of **1a** with TEMPOH (each 5 mmol·L^{-1}, integral 367 a.u.).

These results strongly suggest the capability of the ferric complex **1** to perform an overall hydrogen atom abstraction reaction from TEMPOH yielding the TEMPO radical and a ferrous product, implying a functional model character of both **1** and **2**. As this reaction is quantitative and the BDFE of **2** appears to be higher than that of TEMPOH, a substrate with a higher BDFE could prove useful to gain more information about the driving force and the BDFE of **2**.

2.3.2. H-Atom abstraction from TTBP

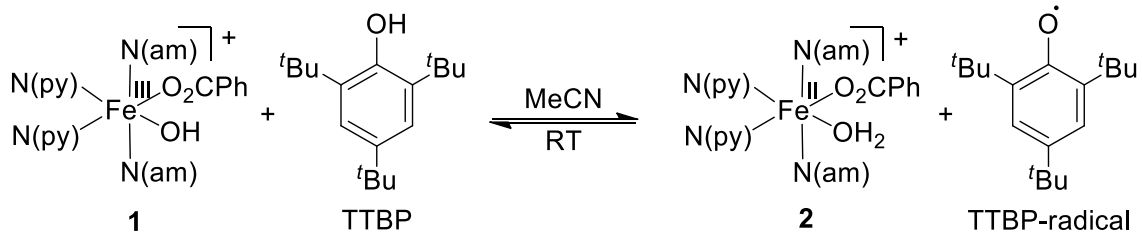

1 TTBP **2** TTBP-radical

Scheme 8. Proposed dynamic H-atom transfer equilibrium between **1** + TTBP and **2** + TTBP-radical in MeCN at room temperature (RT).

The reaction of **1** with TTBP (Scheme 8) was investigated by EPR-spectroscopy, ESI-MS and time dependent UV-vis-spectroscopy in MeCN at room temperature. In contrast to the reaction of **1** with TEMPOH ($BDFE_{MeCN}$(TEMPOH) = 66 kcal·mol^{-1}), the reaction of **1** with TTBP ($BDFE_{MeCN}$(TTBP) = 74.8 kcal·mol^{-1}) only showed a partial rather than a quantitative conversion under anaerobic conditions, suggesting the attainment of an equilibrium.[97]

In the EPR spectrum of the reaction solution after 20 minutes of reaction time, a triplet signal is observed (Figure 42) which corresponds to the phenoxyl radical. In this, the triplet arises from the coupling of the electron spin of the radical to the nuclear spins of the two magnetically equivalent hydrogen atoms at the 3- and 5-positions of the aryl ring with A_H = 4.6 MHz. The broadening of the signal is thought to originate from the presence of the high-spin iron(II) and iron(III) species and/or from dynamic effects.

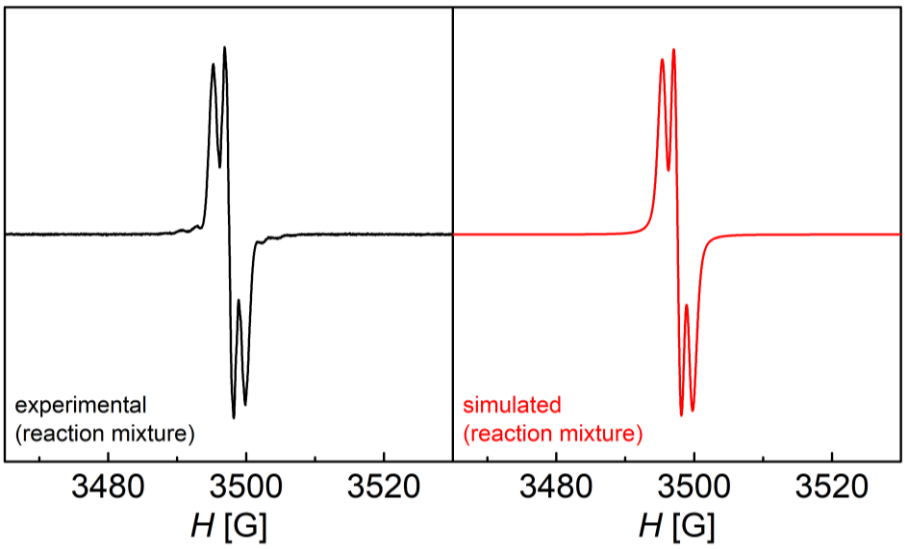

Figure 42. EPR spectrum of the 2,4,6-tri(*tert*-butyl)phenoxyl radical produced in the reaction of **1** with TTBP in MeCN under a nitrogen atmosphere (left, black trace) and the simulated spectrum (right, red trace). Experimental conditions: **J** as described in Table 11 of section 2.3.5. Experimental parameters: Modulation amplitude = 1 G, Attenuation = 25 dB (Power = 0.6377 mW), Frequency = 9.8215 MHz. Values obtained from the simulation: g = 2.0063, A_H = 4.63 MHz.

As is the case for the reaction of **1** with TEMPOH, the formation of the ferrous complex is also observed in the reaction of **1** with TTBP by ESI-mass spectrometry. However, the conversion appears to be only partial with equimolar amounts (Figure 43).

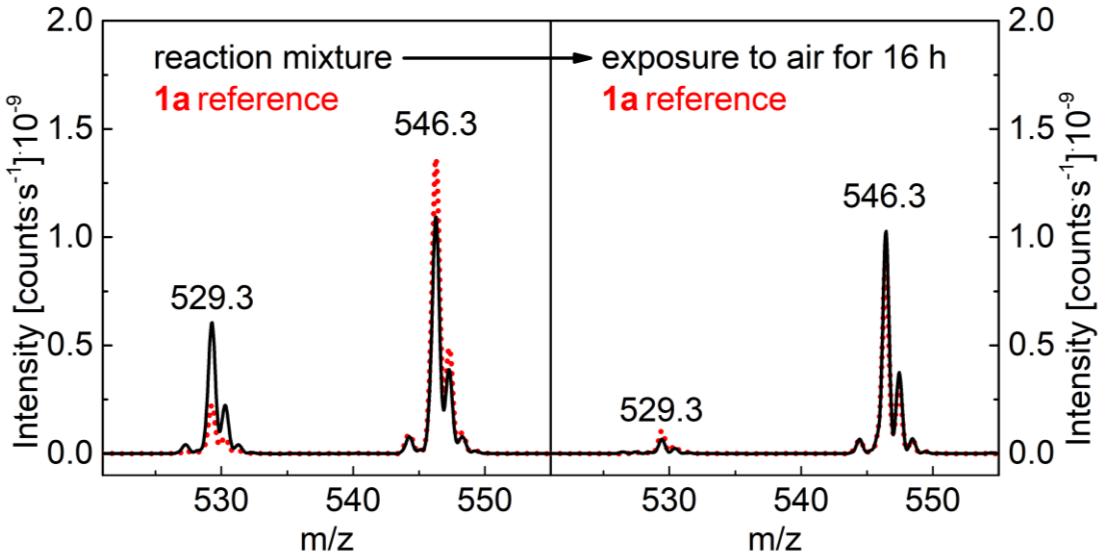

Figure 43. ESI mass spectra of reaction solutions of **1a** with TTBP. Left: Comparison of the ESI mass spectrum of a reaction solution of **1a** with TTBP in MeCN (each 0.2 mmol·L^{-1}) at room temperature after 20 min of reaction time under an atmosphere of nitrogen (black trace) with that of a 0.2 mmol·L^{-1} solution of **1a** in the absence of TTBP (red, dotted trace). Right: The same reaction solution after exposure to air at room temperature for 16 hours (black trace) compared to an authentic 0.2 mmol·L^{-1} solution of **1a** in the absence of TTBP recorded shortly prior to the measurement of the reaction solution (red, dotted trace).

As previously shown in section 2.1.9, the formation of minor amounts of the iron(II) species at m/z = 529.3 is always observed for pure samples of **1a** in acetonitrile even if soft ionization conditions are used in the mass spectrometric experiment (Figure 43, red dotted trace). However, after 20 minutes of reaction of **1a** with equimolar amounts of TTBP under a nitrogen atmosphere, the signal at m/z = 529.3 is significantly enhanced, while the signal at m/z = 546.3 is clearly decreased (Figure 43, black trace) compared to a reference solution of **1a** in acetonitrile. As a signal at m/z = 529.3 corresponding to complex cation **3** is also observed in the mass spectrum of the ferrous aqua complex **2** due to loss of the coordinated water ligand upon transfer of the complex from solution into the gas phase under ESI-MS conditions (see section 2.1.9); this result is regarded as evidence for the occurrence of a hydrogen atom abstraction from TTBP by the ferric hydroxide complex **1** affording complex **2** as the direct product. The relative intensities of the signals at m/z = 529.3 and m/z = 546.3 do not change

after 20 minutes, indicating the achievement of equilibrium conditions after this (arbitrary) reaction time.

Upon exposure of the reaction solution to air for some time (16 h, arbitrarily chosen interval), the resulting mass spectrum of this reaction solution was identical to that of pure solution of **1** in acetonitrile without TTBP. This demonstrates the regeneration of the ferric complex cation **1** (Figure 43) from **2** by oxidation under aerobic conditions, and, thus, further strengthens the argument that the enhanced signal at m/z = 529.3 is a result of a H-atom abstraction reaction of **1** from TTBP.

The above-mentioned reaction times of 20 min prior to the ESI-MS and the EPR measurements are a necessity for the time spent between start of the sample preparation in the glove box and the actual measurement but do not necessarily represent the actual reaction time until the equilibrium is reached. The 20 minutes were timed with minute accuracy to ensure reproducibility and equal conditions for all experiments, but it is expected that the equilibrium is reached earlier. To elucidate this, a qualitative time-dependent UV-vis measurement was done.

In this, the generation of the phenoxyl radical of TTBP could also be established (Figure 44) and the formation of the phenoxyl radical can be followed by the appearance of an absorption band with a maximum at 626 nm (reported ε_{626} = 400±10 $mol \cdot L^{-1} \cdot cm^{-1}$).[135] The reaction between **1** and TTBP under aerobic conditions is close to the equilibrium state after ~50 seconds when assuming pseudo-first order kinetics (approximately 6 half conversion times as derived from the linear regression shown in the Figure), further changes to the spectrum are attributed to following reactions of the phenoxyl radical with molecular oxygen.

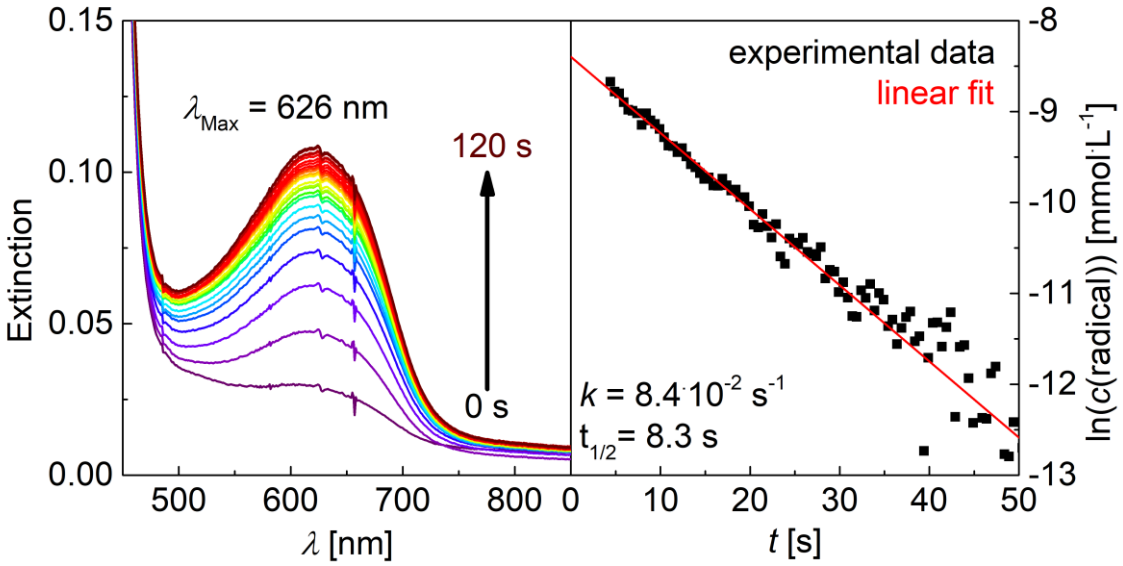

Figure 44. Time-dependent electronic absorption spectra of the reaction of **1a** (0.5 mL, 10.0 mmol·L^{-1}) with TTBP (1 mL, 2.0 mmol·L^{-1}) in MeCN under aerobic conditions. The spectra were recorded every 0.5 s and are depicted for every 5 s (first trace depicted at 3.5 s after starting the experiment) in the image on the left. All data points obtained for the reaction in the first 50 seconds are displayed in a logarithmic fashion on the right. Kinetic parameters are preliminary as they are only obtained from a single measurement with the above-mentioned concentrations and with the assumption of 1st order kinetics. The values were calculated using the reported molar extinction coefficient of the phenoxyl radical (see above) and the linear fit of the data obtained during the first 20 seconds. It is assumed that the reaction of **2** with oxygen from air is significantly slower than the reaction of **1** with TTBP (see below), thus the influence of reoxidation on the equilibrium can be neglected.

2.3.3. Oxidation of 2 under aerobic conditions

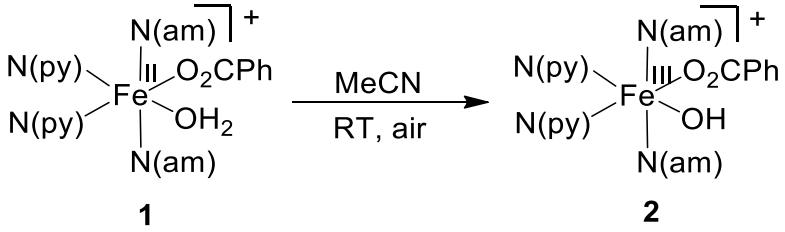

1 **2**

Scheme 9. Oxidation of **1** to **2** with oxygen from air in MeCN at room temperature.

As was also found in previous works for the analogue *cis*-(HOR)(O_2CPh)-complexes (HOR = HOMe, HOEt, HOBz),[2,112,113] also **2** can be oxidized by oxygen from air to produce **1** (Scheme 9). The reaction progresses rather slow as observed with ESI-MS over 24 hours. Nonetheless, this indicates the possibility of catalytic transformations under aerobic conditions (Figure 45). It should be noted that longer times of exposure of solutions of **1** to air lead to minor decomposition products such as a free protonated ligand at m/z = 353.5 (0.05 counts·s^{-1}·10^{-9} after 24 hours), thus probably limiting the long-term persistence of the complexes under air and high catalytic turnovers, respectively.

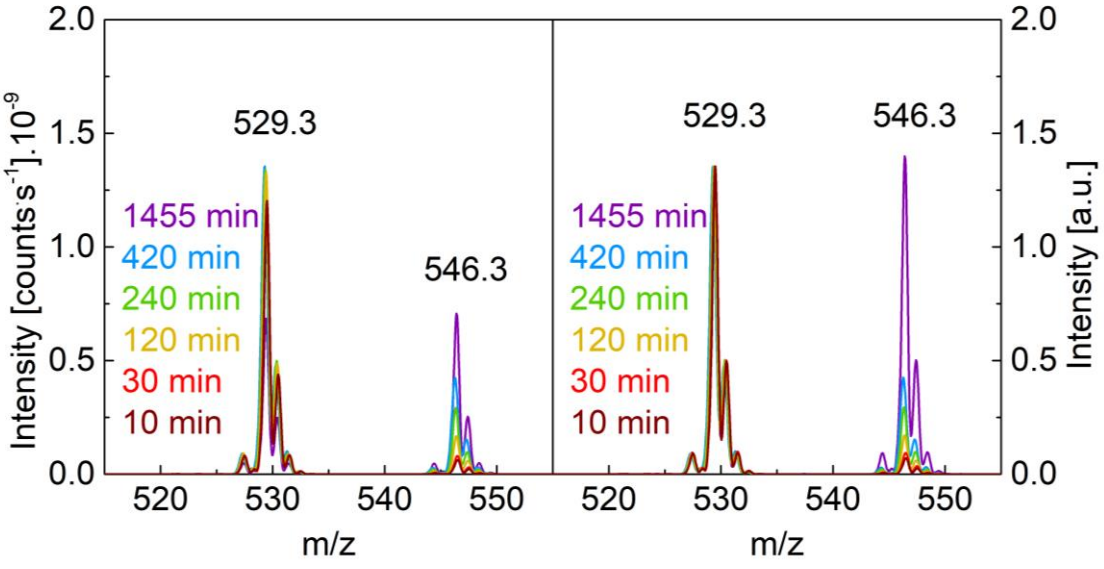

Figure 45. ESI mass spectra of the oxidation of **2a** by air in MeCN monitored over 24 h (left). For better visibility of the relative increase of the signal at m/z = 546.3 with time all signals at m/z = 529.3 of the mass spectra were normalized to the height of the signal after a reaction time of 7 h (right).

2.3.4. Catalytic peroxidation of TTBP

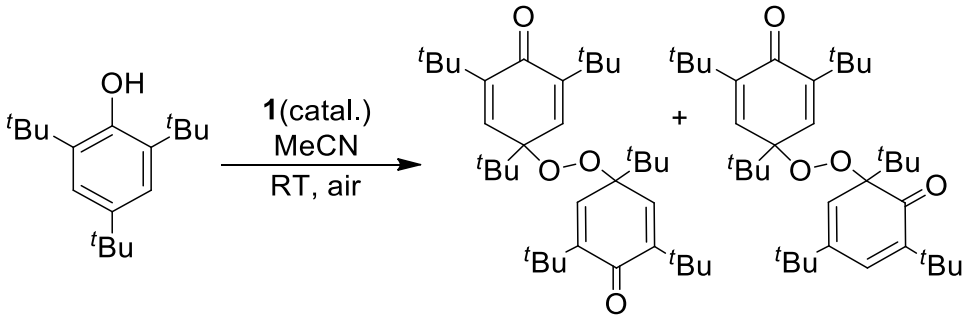

Scheme 10. Peroxidation of TTBP with oxygen from air in MeCN with catalytic amounts of **1**. Isolated reaction products: 4,4'-peroxybis[2,4,6-tri-(*tert*-butyl)-2,5-cyclohexadienone] and 2,4,6-tri(*tert*-butyl)-6-((1,3,5-tri(*tert*-butyl)-4-oxocyclohexa-2,5-dien-1-yl)peroxy)cyclohexa-2,4-dienone.

Under aerobic conditions, complex **1** was found to function as a catalyst for the peroxidation of TTBP, rendering a mixture of 4,4'-peroxybis(2,4,6-tri(*tert*-butyl)-2,5-cyclohexadien-1-one) and its 2,4-isomer (Scheme 10) as shown by NMR- and IR-spectroscopic as well as X-ray structure analytical investigations of the crystalline material formed.[136] The peroxidation of TTBP is assumed to proceed via a radical recombination step between two phenoxyl radicals and a triplet oxygen molecule from air. The catalyst **1** is regenerated under air because the ferrous complex **2** reacts readily with molecular oxygen to produce **1** as described above (section 2.3.3).

While the oxidation of TTBP with ferric complexes such as $K_3[Fe(CN)_6]$ as oxidants is commonly known to occur under strong basic conditions,[137] **1** functions as a catalyst under aerobic conditions in an acetonitrile solution without the addition of a base. In a reaction of **1c** with a tenfold excess of TTBP, the solution instantly turned green and afterwards a dark blue color persisted for several hours. After one day, the formation of yellow crystals was observed. The empirically observed colour changes paired with the time-dependent UV-vis study mentioned above (Figure 44, section 2.3.2) are evident of the formation of the phenoxyl radical as an intermediate.[135] The yellow crystals likely represent a secondary product from the reaction of molecular oxygen from air with the phenoxyl radical. Notably, no such observations were made when attempting the same reaction with **4**, providing evidence that the reactivity does likely not originate from a simple base-assisted mechanism because of dissociation of one of the basic ligands prior to a redox reaction with the ferric metal site.

The NMR-spectroscopic analysis of the crystalline product produced in the reaction of **1** with TTBP under air revealed a 1:1 mixture of the two isomers (Figure 46). All doublet signals in the region between 6.0 ppm and 7.0 ppm are attributed to ring protons in the 2,4-isomer with the signals at 6.87 ppm and 6.64 ppm localized at the 4'-fragment and the signals at 6.81 ppm and 6.08 ppm localized at the 2-fragment. The signal at 6.69 ppm corresponds to the four ring proton resonances of the more symmetric 4,4'-isomer. The impurity at 6.51 ppm is attributed to 2,6-di(*tert*-butyl)-p-benzoquinone (4 % with respect to the main components).[138]

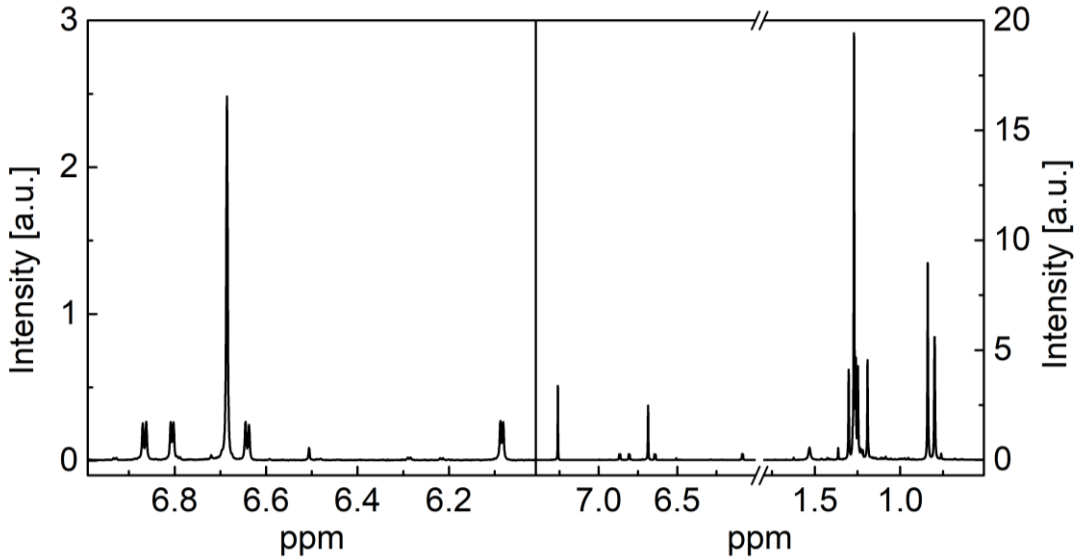

Figure 46. ^{1}H-NMR spectra of the reaction products from **1c** with a tenfold excess of TTBP in MeCN under aerobic conditions. Products were identified as 4,4'-peroxybis(2,4,6-tri(*tert*-butyl)-cyclohexa-2,5-dienone) (**A**) and 2,4,6-tri(*tert*-butyl)-6-((1,3,5-tri(*tert*-butyl)-4-oxocyclohexa-2,5-dien-1-yl)peroxy)cyclohexa-2,4-dienone (**B**). ^{1}H-NMR (400 MHz, $CDCl_3$) δ = 6.87 (d, J = 3.0 Hz, 1 H, ring proton of **B**), 6.81 (d, J = 2.4 Hz, 1 H, ring proton of **B**), 6.69 (s, 4 H, ring protons of **A**), 6.64 (d, J = 3.0 Hz, 1 H, ring proton of **B**), 6.08 (d, J = 2.4 Hz, 1 H, ring proton of **B**), 1.30 (s, 9 H, protons of ^{t}Bu-groups of **B**), 1.27 (s, 36 H, protons of ^{t}Bu-groups of **A**), 1.26 (s, 9 H, protons of ^{t}Bu-groups of **B**), 1.25 (s, 9 H protons of ^{t}Bu-groups of **B**), 1.19 (s, 9 H protons of ^{t}Bu-groups of **B**), 0.84 (s, 18 H protons of ^{t}Bu-groups of **A** or **B**), 0.80 (s, 18 H, protons of ^{t}Bu-groups **A** or **B**). Traces of 2,6-di(*tert*-butyl)-p-benzoquinone are observed at 6.51 ppm.

It must be noted that the oxidation of TTBP in the presence of oxygen can yield a manifold of reaction products as has been previously reported by *Knaudt* et al.,[138] however, the 2,4,6-tri(*tert*-butyl)-6-((1,3,5-tri(*tert*-butyl)-4-oxocyclohexa-2,5-dien-1-yl)peroxy)cyclohexa-2,4-dienone product is rarely mentioned and no NMR or IR data could be found for comparison.[139] The interpretation of the NMR study leans, besides the IR spectrum being in close agreement with reported spectra for the 4,4'-isomer (see below), on the interpretation of X-ray diffraction data. Although the characterization by X-ray structure analysis was limited to the determination of the bond connectivity in addition to the cell parameters (*a* = 12.2355, *b* = 10.2174, *c* = 15.1733, α = 90°, β = 104.060°, γ = 90°) due to the rather poor quality of the crystals and the high extent of disorder found in these crystals, the peroxidized products could be unambiguously identified. The electron density map supports the interpretation of an isomeric mixture of 4,4'-peroxybis(2,4,6-tri(*tert*-butyl)2,5-cyclohexadien-1-one) and the 2,4-isomer contained in a single crystal. However, the high disordering of the isomers does not allow any discussions of bond lengths or angles. Further details about the structural characterization can be found in the attachment and the experimental section (8.2.2.4).

The IR spectroscopic analysis revealed a spectrum almost identical to the reported spectrum for the 4,4'-peroxybis(2,4,6-tri(*tert*-butyl)-2,5-cyclohexadien-1-one) (Figure 47).[136] It is speculated that the spectra of the two isomers are either very similar, or that the reference spectrum shows a spectrum of the mixture where the occurrence of the 2,4-isomer in the sample went unnoticed.

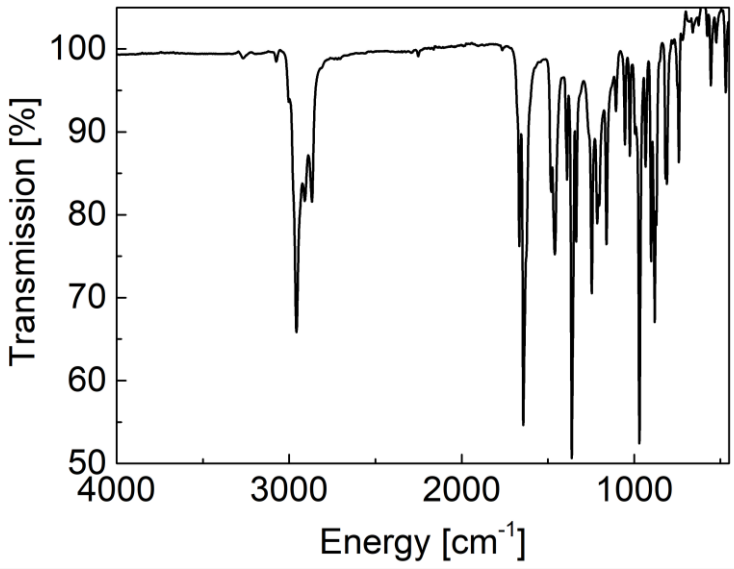

Figure 47. Infrared spectrum of the isolated, crystalline product from the reaction of **1c** with a tenfold excess of TTBP in MeCN under aerobic conditions. IR (ATR, cm^{-1}): 2958, 2909, 2866, 1666, 1643, 1483, 1460, 1389, 1362, 1336, 1246, 1214, 1202, 1161, 1106, 1054, 1025, 995, 970, 934, 902, 881, 871, 819, 810, 741, 555, 460.

The combined yields of these products in a reaction of **1c** with a tenfold excess of TTBP were determined to be 35 % with respect to TTBP. No formation of these products was observed in the absence of **1c** or when employing a compound containing **4** rather than **1**. Since both products derive from the reactions of the phenoxyl radical with oxygen molecules, the catalytic role of **1c** is established with a turnover number (TON) of at least 3.5 as the yield refers only to isolated products. No investigation of the products in the reaction mixture was done and there was no attempt to improve the reaction conditions, as this work focuses on the fundamental mechanistic aspects rather than high catalytic turnovers. Studies with *in situ* generated **1** by oxidation of a *cis*-(HOR)(O_2CPh)iron(II) (HOR = HOEt, HOBz) precursor under pure O_2 that yield other oxidation products such as 2,6-di(*tert*-butyl)benzoquinone can be found in the previous work of *Rauber*.[112]

Note: Parts of the results described in this section had been obtained and previously reported in my master thesis but were included in this work for completeness.[2] The reaction of 1 with TTBP was, however, reproduced. The IR spectrum was recorded anew and the XRD and NMR results were verified.

2.3.5. Determination of the BDFE of 2 via equilibrium studies with 1

As stated above (section 2.3.2), the immutability of the ratio of intensities of the signals corresponding to **3** and **1** detected by ESI-MS indicates that the reaction of TTBP and **1** under nitrogen atmosphere is not quantitative but instead leads to the constitution of an equilibrium. To determine the associated equilibrium constant *K* and the driving force Δ*G*, an adapted method that has previously been used for the determination of the bond dissociation free energy (BDFE) of organic compounds was applied.[140]

For this, a series of nine quantitative EPR experiments was carried out with varying initial concentrations of the reactants **1** and TTBP under nitrogen atmosphere (Table 11, Figure 48). The attainment of equilibrium conditions and thermal stability at 20 °C was ensured. The double integration of the EPR signal intensities obtained in this quantitative study allowed the determination of the equilibrium concentrations of the phenoxyl radical produced in each of the nine reactions. This was achieved by utilizing a TEMPO-radical solution with a defined concentration for calibration, as had also successfully been done for the experiments described in section 2.3.1. Using the obtained phenoxyl radical concentrations, the concentration of **2** can also be calculated when assuming an A + B ⇌ C + D type reaction. With the knowledge of the employed initial concentrations of complex **1** and TTBP, the equilibrium constant K_{eq} and the free reaction energy ΔG_{MeCN} can be calculated. The results for the individual reactions are summarized in Table 11. The mean values of these results are calculated to be $K_{eq} = 1.77 \cdot 10^{-2}$ and $\Delta G = 2.35$ kcal·mol^{-1} (estimated method error ±0.2 kcal·mol^{-1}), respectively, at 20°C. Using the literature value of $BDFE_{MeCN}$(TTBP) = 74.8 ± 1 kcal/mol,[97] the $BDFE_{MeCN}$(**2**) can thus be calculated to be 72.4 ± 1.2 kcal/mol. The error margins of this approach are discussed below and a comparison to previously reported values for iron(II) complexes is presented in section 2.3.6 Table 12.

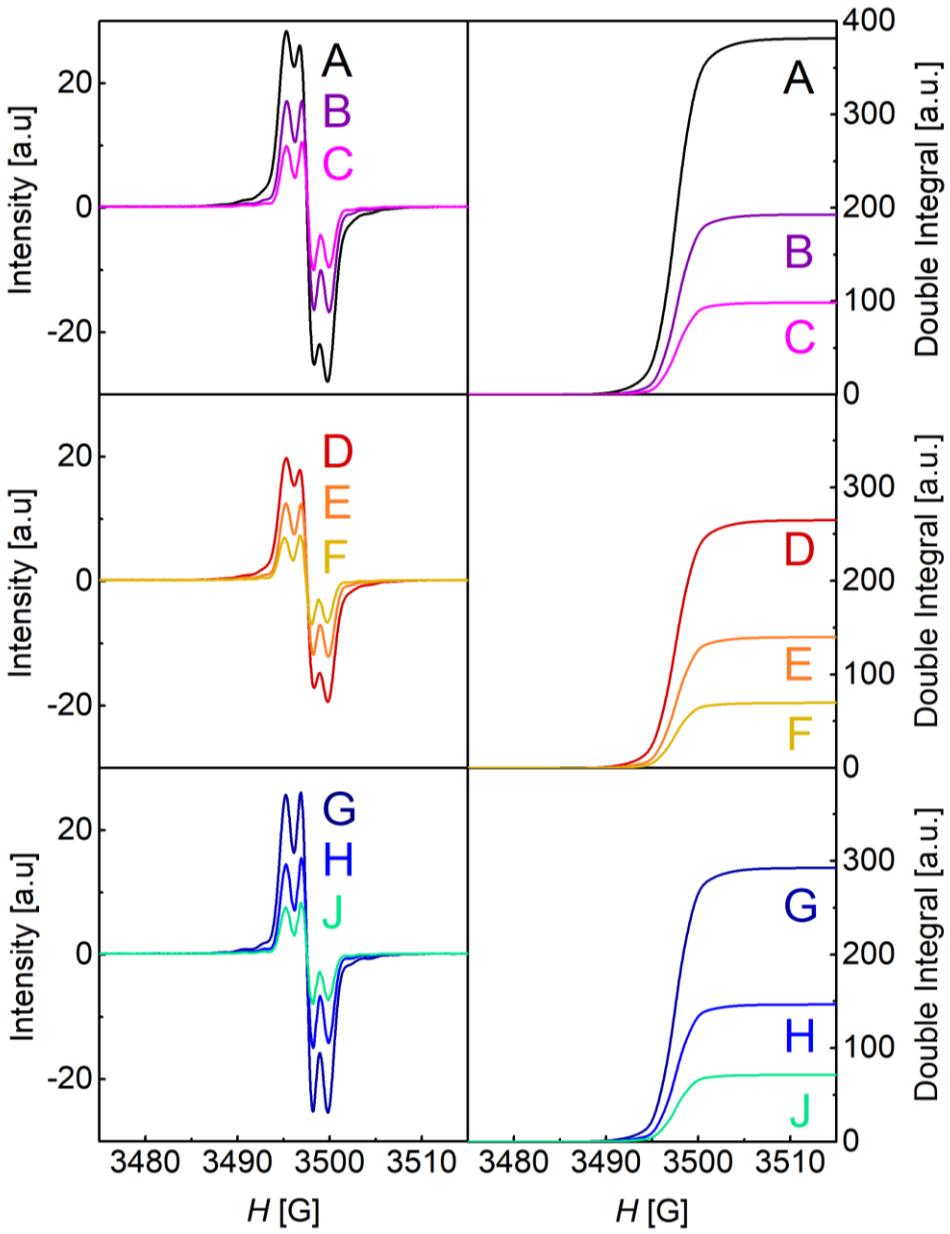

Figure 48. EPR spectra obtained from reaction mixtures of **1** and TTBP at various initial concentrations (left) and double integrals of the EPR signals used for calculating K_{eq} and ΔG_{MeCN}, respectively (right). The letters **A**-**J** reference the experimental conditions listed in Table 11. Integration of the signals was performed using the double integration tool of the Bruker Xepr software. A narrow integration range was applied to minimize baseline errors. Therefore, while the EPR spectra were recorded in the range between 3430 and 3520 G, the integration of the signals was performed within the magnetic field range from 3475-3515 G.

Table 11. Results of the quantitative EPR spectroscopic study of the reactions of **1a** with TTBP in MeCN (abs.) under a nitrogen atmosphere.

Exp.	c_0(**1a**) [mmol·L^{-1}]	c_0(TTBP) [mmol·L^{-1}]	Double integral[a] [a.u.]	c(PhO·) [mmol·L^{-1}]	K_{eq}	ΔG_{MeCN}[b],[c] [kcal·mol^{-1}]
A	2.00	2.00	389	$2.30 \cdot 10^{-1}$	$1.69 \cdot 10^{-2}$	2.38 ± 0.14
B	1.00	1.00	193	$1.14 \cdot 10^{-1}$	$1.66 \cdot 10^{-2}$	2.39 ± 0.14
C	0.50	0.50	98	$5.80 \cdot 10^{-2}$	$1.72 \cdot 10^{-2}$	2.36 ± 0.14
D	2.00	1.00	265	$1.57 \cdot 10^{-1}$	$1.59 \cdot 10^{-2}$	2.41 ± 0.14
E	1.00	0.50	137	$8.11 \cdot 10^{-2}$	$1.70 \cdot 10^{-2}$	2.34 ± 0.14
F	0.50	0.25	70	$4.14 \cdot 10^{-2}$	$1.75 \cdot 10^{-2}$	2.35 ± 0.14
G	1.00	2.00	293	$1.73 \cdot 10^{-1}$	$1.98 \cdot 10^{-2}$	2.28 ± 0.14
H	0.50	1.00	146	$8.64 \cdot 10^{-2}$	$1.95 \cdot 10^{-2}$	2.29 ± 0.14
J	0.25	0.50	71	$4.20 \cdot 10^{-1}$	$1.85 \cdot 10^{-2}$	2.32 ± 0.14

[a] Double integration of the EPR signals of the respective reaction mixtures in the magnetic field ranging from 3475-3515 G. The calibrating solution of 0.2 mmol·L^{-1} TEMPO radical solution in MeCN (abs., N_2 atmosphere) resulted in an integral of 338 a.u. (averaged value of two samples with a standard deviation smaller than the methodic error). The larger width of the triplet signal of TEMPO (generated in the reaction solutions) was considered by integrating the signal in the magnetic field range between 3465-3520 G. The magnitude of the integral signal is not to be compared with the magnitude described in Figure 40 as other parameter settings were used here. [b] Calculated for 293 K. [c] Methodic error margin of ±5% was estimated in the integration of the EPR signals of the reaction mixtures. This error was applied to calculate the error of ΔG_{MeCN}. The total error is composed of ±0.07 kcal mol^{-1} derived from the integrals of the reference and an additive error of ±0.07 kcal mol^{-1} derived from the integrals of the reaction mixtures (see also Figure 49). The methodic error includes all errors attributed to parameter fluctuations, spectrometer accuracy and sample preparation.[141]

In this study, the variation in initial concentrations ranged from 0.25-2.00 mmol·L^{-1} for each reactant (Table 11). For the determination of the K_{eq}, Δ*G* and the BDFE of **2**, only initial concentrations of 2 mmol·L^{-1} or less were used for each reagent, as additional experiments at higher initial concentrations of **1** and/or TTBP resulted in somewhat lower relative intensities of the radical signal. It is assumed that this observation might be related to the increased occurrences of further equilibrium reactions at higher initial concentrations of the species present in solution (e.g. the forming of associates) that reduce the activity of **1**. This aspect is further discussed below and in chapters 3 and 4. The intensity of the organic radical signal did not change (within the margin of error) within 30 minutes after the measurement at 20 minutes reaction time.

Quantitative EPR spectroscopy is generally described as a challenging method in literature. Therefore, under optimal conditions, accuracies of 3 % are described to be possible with modern spectrometers.[141] We estimate our methodic error to be about 5 % for the double integral values of the EPR signals. With this uncertainty in mind the mean value of ΔG_{MeCN} was determined via a linear fit using *OriginPro 9 64 bit* (instrumental weight) with a fixed slope of zero and an error of 0.14 kcal·mol^{-1} was found, which is generously rounded to 0.2 kcal·mol^{-1}. This relatively small error of ΔG is a result of the logarithmic relation of the desired value to the measured quantity. As demonstrated in Figure 49, the resulting values for the BDFE lie very close to each other within the series of measurements and all experimental values are scattered within the expected error margin of the applied method. In the literature, error margins for BDFEs are often much larger. Thus, this result appears to produce more accurate results which is an important finding. However, the much larger experimental error reported for BDFE($TTBP_{MeCN}$) of ± 1 kcal/mol eventually provides a large contribution to the estimated error of BDFE($\mathbf{2}_{MeCN}$), which can be termed to be overall ± 1.2 kcal·mol^{-1}.[97]

Note: A somewhat larger error margin for the quantitative EPR approach was deduced from additional experiments that are described in chapter 3 (section). Thus, although the intrinsic error of this experiment appears smaller, it should be considered that the true error may well be slightly higher than described in this study. However, for consistency with the original publication, this is not discussed in this section.

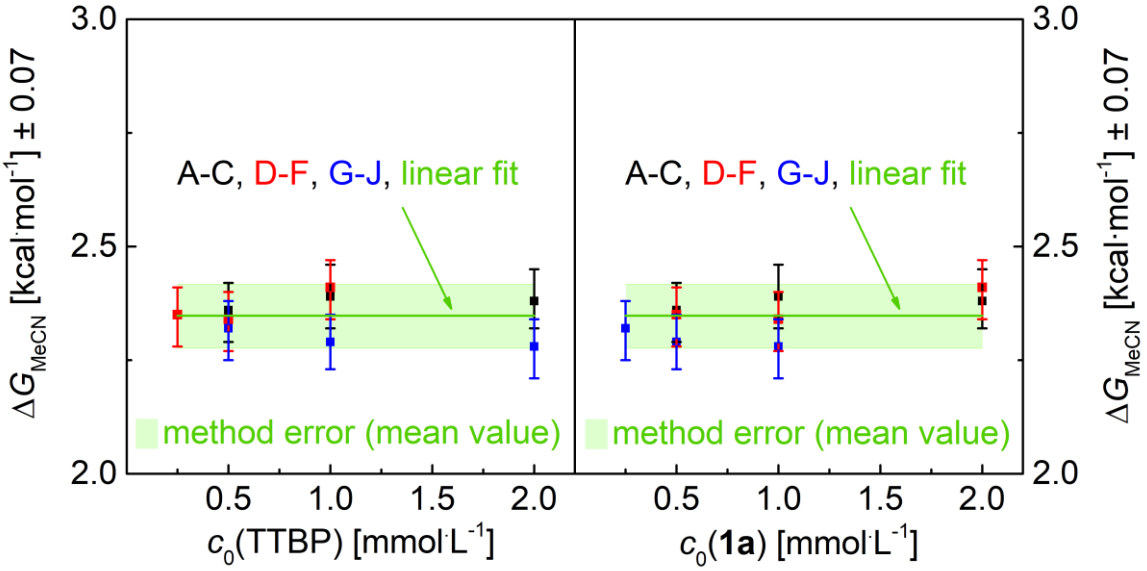

Figure 49. Graphic presentation of the dependence of the experimentally determined values of ΔG_{MeCN} on the initial concentrations of the reactants in the reaction of **1a** and TTBP (referring to entries **A**-**J** in Table 11). Left: ΔG_{MeCN} vs c_0(TTBP), right: ΔG_{MeCN} vs c_0(**1a**). The expected scattering is verified to lie around the mean value (linear fit with a slope of zero, green trace) within the maximum error of the integrals of ±5% (±0.07 kcal·mol^{-1}). Since the calculation is based on a reference measurement of a TEMPO radical solution that exhibits the same error of ±5%, the y-axis is displayed as having an error of equal size. These errors are additive, the total error sum is, thus, $\Delta\Delta G_{MeCN}$ = ±0.14 kcal mol^{-1}.

With the results presented in this work, the equilibrium approach with quantitative EPR (first reported by *Lucarini* and *Pedulli*) could be established as a viable method for the investigation of the reactivity of metal complexes and for quantifying the driving force ΔG.[140] Notably, even a preliminary electronic absorption spectroscopic investigation (compare section 2.3.2, Figure 44) resulted in concurring values and magnitudes with $K_{eq} \approx 10^{-2}$, further supporting the suitability of the approach for these types of investigations.

2.3.6. Literature Comparison of the Thermodynamic Values Determined for 2

In general, a comparison with values reported in the literature turns out to be difficult because the respective BDFE values of the complexes depend decisively on the method used for their determinations. In addition, a limited understanding of the thermodynamics that govern these processes or the neglect of a critical review of previously published work can lead to several pitfalls as has also happened in literature.[96,97] Firstly, it is important to understand that the comparison of BDFE values obtained in different solvents, especially when the solvents differ substantially in hydrogen bonding properties, is accompanied by a high degree of inaccuracy. Secondly, one must be aware that, in the past, errors in deriving certain solvent constants used for the BDFE determination (C_G-values) have led to wrong calculations of BDFEs by authors that built on these erroneous constants and that the affected values need to be recalculated for accurate comparison.[96,97,109] Similarly, one should always consider if a reference substance was used to determine the reported BDFE-values of a new compound and how accurate this reference value is. Lastly, another challenge that complicates the comparison of the BDFE values is the apparent confusion concerning the usage of BDFE versus BDE. In some cases, but not all, BDE is used as a synonym for BDFE, although only the latter considers an entropy contribution. Thus, a critical review of how these values were obtained, where errors may have occurred, and which reference values were used is a prerequisite for a meaningful comparison.

In terms of different methods, the one that is most frequently used is the “Bordwell” analysis based on measuring the redox potentials and p*K*a values of species involved in the proton-coupled electron transfer reaction of a metal complex (equation 3 yields BDFE in kcal/mol, more details on the input values are given in 1.2.8).[59] Here however, experimental problems such as the frequent observation of irreversible electrochemical responses in cyclic voltammograms lead to less reliable data which needs to be considered. The recently reported method of open-circuit potential measurement by J. M. Mayer seems to avoid some of these kinetic problems,[97] rendering thermodynamically more accurate data.

$$(3)\quad BDFE_{HA} = 1.37pK_{HA} + 23.06E_{ox}(A^-) + C_G$$

The equilibrium approach described in section 2.3.5 to determine the BDFE of a substance via quantitative EPR is another suitable method, although it appears that it has not been previously used to study metal-organic complexes. Nonetheless, it has proven successful with organic compounds and reported to display a relatively small error when an appropriate reference substance (such as TTBP) is used.[140] Here, the small error margin for the free reaction energy Δ*G* is because of the logarithmic dependency of Δ*G* on the experimentally determined equilibrium concentrations in this method.

Neglecting the intrinsic difficulties in determining BDFEs and the resulting uncertainties in comparisons, the value determined in this study lies within the general range of values (62-84 kcal·mol^{-1}) observed for other iron(III) complexes capable of H-atom abstraction (references are given in Table 12). At the lower end of the range, there is the iron(II) complex $[Fe^{II}(H_2bim)_3]^{2+}$ possessing a N–H bond that participates in H-atom transfer reactions. Generally, iron(II) aqua complexes seem to display O–H bonds with higher BDFE. The BDFE increases with the positive charge of the complex, as it affects the redox potential and the relative stability of the iron(II) and the iron(III) states. This effect can also be easily retraced in the Bordwell equation (equation 3). Thus, the tetracationic low-spin iron(II) complex $[Fe^{II}(PyPz)(OH_2)_2]^{4+}$ with a *trans* FeN_4O_2 coordination environment containing a positively charged planar tetraazamacrocyclic ligand exhibits the highest BDFE with 84 kcal·mol^{-1}. The BDFE is lowered somewhat in $[Fe^{II}(PY5)(OH_2)]^{2+}$ with a FeN_5O coordination environment arising from neutral ligands. Both monocationic complexes **2** and $[Fe^{II}(O^{Me2}N_4(tren))(OH_2)]^{+}$ possess a high-spin *cis*-$Fe^{II}N_4O_2$ coordination environment, but only in **2** is the aqua ligand involved in an intramolecular hydrogen bonding interaction. The presence of a hydrogen bonding interaction involving one of the O–H bonds of the coordinated water ligand and the carbonyl oxygen atom stabilizes the second O–H bond of the water ligand resulting in an increase of its BDFE and is, therefore, considered as an essential feature for the reactivity of the active site in the enzyme.

Table 12. Comparison of O**–**H (and N**–**H) bond dissociation free energies (BDFE) of various iron(II) complexes and organic substrates.

Compound	solvent	BDFE [kcal·mol^{-1}]	Reference
TTBP	MeCN	74.8	[97]
TEMPOH	MeCN	66	[97]
$[Fe^{II}(PyPz)(OH_2)_2]^{4+}$	H_2O	84	[92]
$[Fe^{II}(PY5)(OH_2)]^{2+}$	DMSO	80	[75]
$[Fe^{II}(L\text{-}N_4{}^tBu_2)(O_2CPh)(OH_2)]^{+}$	MeCN	72.4	[1]
$[Fe^{II}(^{OMe2}N_4(tren))(OH_2)]^{+}$	MeCN	62.4[a]	[79]
$[Fe^{II}(H_2bim)_3]^{2+}$	MeCN	68.4	[97]

[a] The value in the original publication was determined to be 64.7 kcal·mol^{-1} using $C_{G,MeCN}$ = 54.9 kcal·mol^{-1}.[79,96] The value for $C_{G,MeCN}$ has later been revised to be 52.6 kcal·mol^{-1}.[96,97,109] Employing the new value of $C_{G,MeCN}$ the BDFE(MeCN) for $[Fe^{II}(O^{Me2N4}(tren))(OH_2)]^{+}$ was recalculated. The structures of all referenced complexes are depicted in Scheme 11. [b] PyPz = tetramethyl-2,3-pyridinoporphyrazine, PY5 = 2,6-bis-(bis(2-pyridyl)methoxymethyl)pyridine, H_2bim = 2,2′-bis-imidazoline, ($O^{Me2}N_4(tren)$ = 3-((2-(bis(2-aminoethyl)amino)ethyl)imino)2-methylbutan-2-olate).

Based on the value for the BDFE of **2**, the reaction of **1** with 2,2,6,6-tetramethylpiperidin-1-ol (TEMPOH) is expected to be almost quantitative, which agrees with the results of the experiment (section 2.3.1). It is noteworthy that, in contrast to **2**, the complex $[Fe^{II}(O^{Me2}N_4(tren))(OH_2)]^{+}$ reacts as a H-atom donor with the TEMPO radical to form TEMPOH and a diferric μ-oxo complex. This is attributed to the lack of the stabilizing hydrogen bond interaction in this complex.

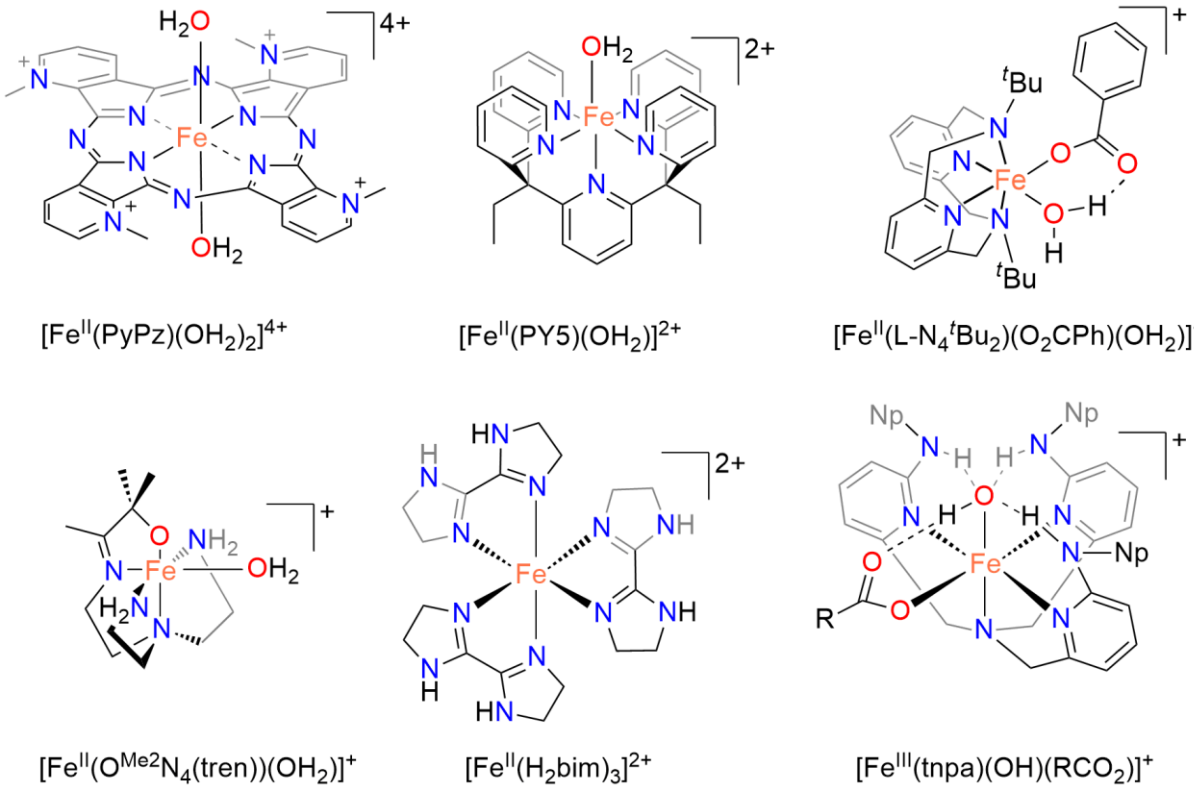

Scheme 11. Depictions of the structural formulae of all complexes discussed in Table **12** and the structural model complex $[Fe^{III}(tnpa)(OH)(RCO_2)]^+$ bei Watanabe *et al*.[81]

A further literature comparison can be done using the determined BDFE value for **2** and the electrochemical potential of the Fe^{3+}/Fe^{2+} reduction. Although the reduction is not electrochemically reversible as found in cyclic voltammetry experiments (section 2.1.10), a half-wave potential can be estimated from the incomplete Fe^{2+}/Fe^{3+} reoxidation process which supposedly relates to the oxidation of a respective hydroxoiron(II) intermediate. This half-wave potential value (-0.79 V vs Fc/Fc^+) can then be used alongside the BDFE of **2** (72.4 kcal mol^{-1}) and the solvent constant $C_{G,MeCN}$ = 52.6 kcal·mol^{-1} to estimate a pKa$_{MeCN}$(**2**) ≈ 27.8 by employing the Bordwell equation (equation 3).[1,59,97] For comparison, the redox potentials and pKa values for selected non-heme hydroxoiron(III) complexes are given in Table 13 and Table 14, respectively.

Table 13. Redox potentials of some selected non-heme hydroxo iron(III) complexes.

Compound	$E^0(Fe^{III}/Fe^{II})$ in CH_3CN			Ref.
	vs. SCE	**vs. NHE**	**vs. Fc/Fc$^+$**	
$[Fe^{III}(BNPA^{Ph2}O)(solv)(OH)]^{+[a]}$	-0.24	0	**-0.69**	[89]
$[Fe^{III}(tnpa)(CH_3CO_2)(OH)]^{+[b]}$	**-0.20**	+0.04	-0.65	[81]
$[Fe^{III}(tnpa)(HCO_2)(OH)]^{+[b]}$	**-0.10**	+0.14	-0.55	[81]
$[Fe^{III}(tnpa)(PhCO_2)(OH)]^{+[b]}$	**-0.09**	+0.15	-0.54	[81]
$[Fe^{III}(Py_2Py(afa^{Cy})(pi^{Cy})(OH)]^{+[d]}$	-0.14	+0.10	**-0.59**	[86]
$[Fe^{III}(L\text{-}N_4{}^tBu_2)(PhCO_2)(OH)]^+$ (**1**)	**-0.31**	-0.07	**-0.79***	[1]
$[Fe^{III}(^{OMe2}N_4(tren))(OH)]^{+[c]}$	-0.50 (in H_2O)	**-0.25 (in H_2O)**		[79]
$[Fe^{III}(N4Py^{2Np})(OH)]^{2+[d]}$	+0.45	+0.69	**0**	[87]
$[Fe^{III}(N4Py^{2Ph})(OH)]^{2+[d]}$	+0.24	+0.48	**-0.21**	[87]

NHE = normal hydrogen electrode, SCE = standard calomel electrode, Fc = ferrocene Fc$^+$ = ferrocenium. All values rounded to two decimals. Values in bold are those reported in the original publications. SCE-values are converted to NHE as NHE = SCE + 0.244 V. For conversion of the literature values vs. a Fc/Fc$^+$ reference, a potential of E^0(Fc/Fc$^+$) = 0.45 V vs SCE is assumed. [a] This value was reported for $[Fe^{III}(BNPA^{Ph2}O)(OTf)(OH)]$, however it is noted in the main text that the observation of free OTf$^-$ in the ^{19}F-NMR spectrum of the compound points towards displacement of the anionic ligand in CD_3CN. Thus, the reported electrochemical potential in CH_3CN is likely that of the monocationic species where a solvent molecule replaces the OTf$^-$-ligand. [b] values reported for the perchlorate salt. [c] This compound was not isolated, the value was determined by Bordwell analysis of the respective $[Fe^{II}(^{OMe2}N_4(tren))(OH_2)]$ complex (derived from pKa and BDFE values) in the original publication. [d] values reported for the OTf$^-$-salt. **Note: In the original publication,[1] the potential was stated as -0.76 V vs. Fc/Fc$^+$ because of an erroneous SCE reference potential, which was later revised. For more details see chapter 2.1.10*.

Table 14. pKa-values of some reported Fe(II)-complexes with H-atom transfer reactivity and some selected reference substances.

Compound	p*K*a MeCN	p*K*a H_2O	BDFE MeCN	BDFE H_2O	Ref.
$[Fe^{II}(L\text{-}N_4{}^tBu_2)(O_2CPh)(OH_2)]^+$ (**2**)	~27.8* [a]		72.4		[1]
$[Fe^{II}(^{OMe2}N_4(tren))(OH_2)]^+$		12.3	62.4[c]	68.6	[79]
$[Fe^{II}(Py_2Py(afa^{Cy})(OH)]^+$	~18.8-22[b]		69[c]		[86]
$[Fe^{II}(H_2bim)_3]^{2+}$	~26		68.4		[97,98]
$[Fe^{II}(H_2O)_6]^{2+}$		9.5		79.5	[96]
$[Fe^{II}(PyPz)(OH_2)_2]^{4+}$		8.0		84	[92]
H_2O		14		122.7	[96,97,142,143]
TTBP	28	13	74.8	80.3	[96,97,143]
Phenol	27.2- 29.2	9.9		89.5	[96,142–144]
HOOCPh	20.7- 21.5	4.2			[142,143]
NEt_3[d]	18.7	10.7			[144]

BDFE values in kcal·mol^{-1}. [a] Estimated by applying equation 3 using $C_{G,MeCN}$ = 52.6 kcal·mol^{-1} and the experimentally obtained E^0 vs. Fc/Fc$^+$ and BDFE values in MeCN. [b] The original value is given as pKa > 18.8, the upper limit is derived from the BDFE value estimated in the publication by employing the Bordwell equation with $C_{G,MeCN}$ = 52.6 kcal·mol^{-1}. [c] The values in the original publication were estimated using $C_{G,MeCN}$ = 54.9 kcal·mol^{-1}. The value for $C_{G,MeCN}$ has later been revised to be 52.6 kcal·mol^{-1}, thus the difference is subtracted for this table.[96,97,109] [d] pKa value refers to corresponding acid $HNEt_3^+$. **Note: In the original publication, the pKa was stated as ~27 because of an erroneous SCE reference potential that led to a miscalculation of the pKa using the Bordwell equation. For more details see chapter 2.1.10.*

Experimental verification of the calculated p*K*a value proved to be challenging. While pH-dependent cyclic voltammetry is impractical because of the likelihood of ligand exchange reactions with buffer components and the known existence of a potential equilibrium between **2** and **3** in solution. Moreover, experiments using reference bases are not always effective because suitable reference bases with known p*K*a-values in

acetonitrile in the correct range need to be found, which in addition will not react with the complex in a ligand exchange reaction or lead to counterion metathesis reaction. For the current study tetraethylammonium-2,4,6-tri-(*tert*-butyl)phenolate (p*K*a$_{MeCN}$(corresponding acid) = 28)[96,97] and triethylamine (NEt_3, pKa$_{MeCN}$(corresponding acid) = 18.7)[144] were identified as potential reference substances. However, experiments of **2** with equimolar amounts of tetraethylammonium-2,4,6-tri-(*tert*-butyl)phenolate were ambiguous because some immediate precipitation occurred. This could not clearly be attributed to a specific reaction and the broad signals in the NMR spectrum of the mixture could not be assigned and identified. Because the addition of NEt_3 to a solution of **2** in acetonitrile did not result in a change of the NMR spectrum, it was concluded that the value of pKa$_{MeCN}$ (**2**) must be higher than 18.7.

Although an experimental determination of the p*K*a of **2** was limited to describing a lower limit, a comparison of the calculated value (using equation 3) with those determined for other (aqua)iron(II) complexes reveals that the calculated value lies in a reasonable range (Table 14).

2.3.7. H-Atom Abstractions from C–H Bonds Under Anaerobic Conditions

To demonstrate the capability of a H-atom abstraction from weak C–H bonds, anaerobic reactions of **1** with an excess of 1,4-cyclohexadiene or 9,10-dihydroanthracene (DHA) were investigated at room temperature (Scheme 12).

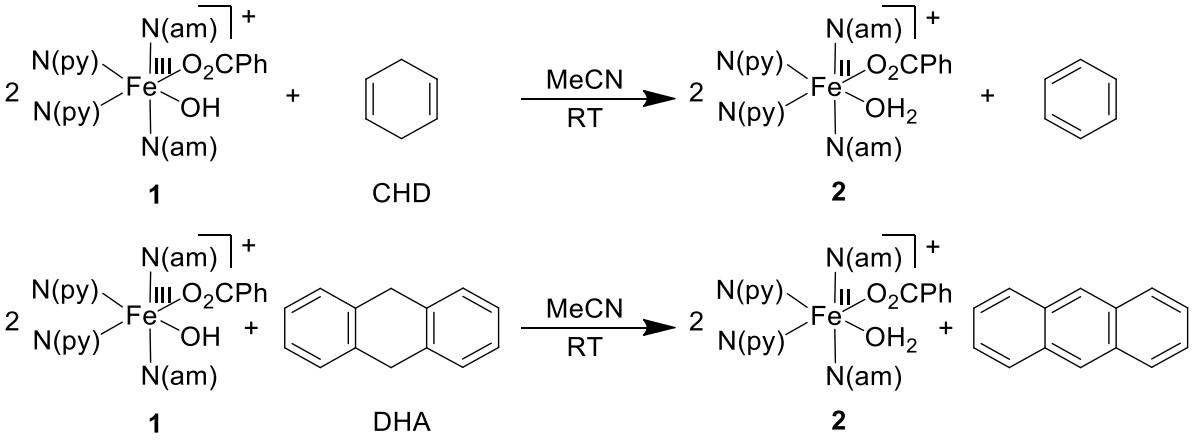

Scheme 12. Stoichiometric oxidation reaction of CHD and DHA with **1** to benzene and anthracene, respectively.

Both CHD and DHA are frequently used substitute substrates for the 1,4-pentadiene-unit of the fatty acid derivatives, which are the physiological substrates of the enzyme. As their BDFEs are reported low (ΔG = ~76 kcal·mol^{-1}),[145] a H-atom abstraction from these substrates should be thermodynamically accessible for **1**, despite this being a slightly more endergonic reaction as that with the tri-(*tert*-butyl)phenol substrate (ΔG = 74.8 kcal·mol^{-1}). The reaction is expected to be much slower than the O–H abstraction from the phenol, as H-atom abstractions from C–H bonds by metal complexes with similar BDFE are known to occur at an approximately 10^4 times lower rate than that of O–H bonds.[94]

To follow the reaction at the metalorganic site, a solution of **1** and CHD was investigated via ESI-MS. Figure 50 displays the respective mass spectra of the reaction solution (c_0(**1**) = 2.10^{-4} mmol L^{-1}, c_0(CHD) = 2·10^{-3} mmol L^{-1} in MeCN under an atmosphere of nitrogen) at the beginning of the reaction (20 min after preparation of the reaction solution) and after a reaction time of 23 days. The progress of the reaction at room temperature was monitored by measuring the ESI mass spectra of the reaction

solution on a daily routine during almost the entire investigation. The results of the time-dependent study are presented in Figure 51. To follow the oxidation of the organic reactants, reaction solutions were investigated via NMR-spectroscopy. Figure 52 and Figure 53 display the respective time-dependent NMR spectra of the two reaction solutions of **1c** with CHD and **1c** with DHA (c_0(**1c**) = $4 \cdot 10^{-2}$ mmol·L^{-1}, c_0(CHD) = $2 \cdot 10^{-2}$ mmol·L^{-1} in CD_3CN; c_0(**1c**) = $2 \cdot 10^{-2}$ mmol·L^{-1}, c_0(DHA) = $1 \cdot 10^{-2}$ mmol·L^{-1} in CD_3CN).

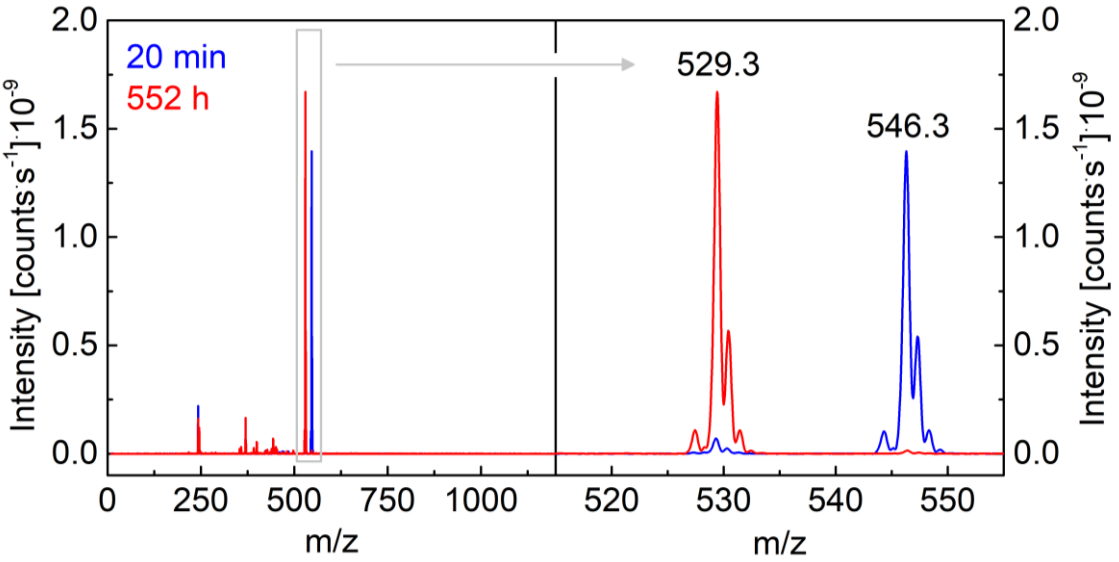

Figure 50. ESI mass spectra of a reaction solution of **1c** with a tenfold excess of CHD in MeCN under a nitrogen atmosphere. Left: Complete range of the mass spectra (m/z = 0-1200) obtained from reaction solutions after 20 min (blue trace) and after 552 h (23 d, red trace). Right: Selected range with a focus on the maximum signals. Relevant peaks after 20 min: m/z = 546.3 (100 %). Relevant peaks after 23 d: m/z = 529.3 (100 %), m/z = 369.4 (10 %), m/z = 245.3 (7 %), m/z = 399.4 (3 %), m/z = 357.4 (2 %). Other signals (>2 %): 242.3 (10 %) (tetrabutylammonium $N(Bu)_4^+$ residues present in the injection chamber), m/z = 443.3 (4 %) and 445.3 (1.5 %) (minor $[Fe(L\text{-}N_4{}^tBu_2)(Cl)_2]^+$ impurities present in or generated with Cl^- residues the injection capillary chamber).

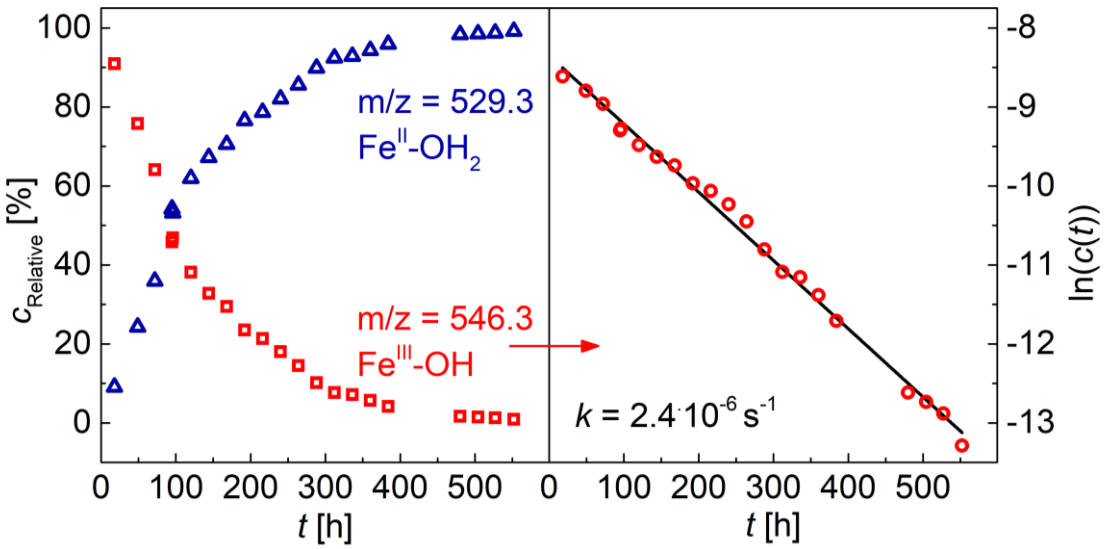

Figure 51. Reaction monitoring via ESI-MS by sampling the reaction solution of **1** with CHD on an almost daily basis. Left: Plot of the peak intensity *I* of the ESI mass signal representing the concentrations of **1** (m/z = 546.3) and **2** (m/z = 529.3) versus the reaction time *t* for the reaction (initial concentrations c_0(**1c**) = $2 \cdot 10^{-4}$ mol·L^{-1} and c_0(CHD) = $2 \cdot 10^{-3}$ mol·L^{-1}) under a nitrogen atmosphere. Right: Logarithmic plot of the calculated concentration *c*(**1**) versus reaction time *t* demonstrating pseudo first order kinetic properties.

The initial mass spectrum is dominated by a signal at m/z = 546.3 corresponding to the cation **1** (Figure 50). The intensity of this signal decreases over the course of the reaction. After 23 days of reaction of **1** with a tenfold excess of CHD, the hydroxo iron(III) complex is almost completely consumed (by more than >99%). At the same time, the appearance of a signal at m/z = 529.3 attributed to the cation **3** is observed. As the mass spectrum of the *cis*-(aqua)(benzoate)iron(II) complex **2** renders only a signal at m/z = 529.3 because of the loss of the coordinated water ligand (section 2.1.9) during the transfer of the cation from solutions into the gas phase under ESI experimental conditions, and based on the observation of the same rates for the decrease in the signal arising from **1** and the increase in the signal originating from **3**, it is concluded that a stoichiometric conversion of **1** into **2** occurs. With respect to other iron products, the reaction of **1** and CHD seems to be rather well-behaved. Some decomposition products can be observed to increase somewhat in concentration over the course of the reaction, however, the species of interest at m/z = 546.3 and m/z = 529.3, respectively, clearly remain the major components of the reaction mixture. The signal at m/z = 242.3 arises from some persistent contamination in the ESI mass

spectrometer chamber by tetrabutylammonium cation. The investigation of the reaction of **1** with tenfold excess of DHA shows qualitatively similar results with respect to the iron-containing product.

Conveniently, the loss of the water ligand in **2** results in well-separated signals that simplify the monitoring of the reaction progression and further analysis. With the assumption of similar flight properties of **1** and **2** (**3**) in the instrument, time-dependent concentrations can be derived which reveal a pseudo-first order reaction (Figure 51) and allow the calculation of a second order rate constant. Importantly, the kinetics of this rather slow reaction under anaerobic conditions match the expectations for a C–H abstraction by **1** very well. From transition state theory, one expects a 10^4 slower reaction for C–H abstractions as opposed to O–H abstractions, as these lie on different Evans-Polanyi lines.[94] Here, the second order rate constant derived for this experiment (k_{CHD} = $2.4 \cdot 10^{-6}$ s^{-1}) is indeed smaller by a factor of approximately 10^4 as opposed to the second order rate constant derived from a reaction of **1** with TTBP (k_{TTBP} = $8.4 \cdot 10^{-2}$ s^{-1}, Figure 44), which has a similar thermodynamic driving force (BDFE). Despite this good accordance in the first instance, this result must be taken with a grain of salt. A study to determine the kinetic substrate dependency by changing the CHD substrate concentrations failed and gave conflicting results, implying a possibly more intricate mechanism at higher substrate concentrations. Thus, the second order rate constant determined for the experiment with a tenfold excess of CHD should not be taken as absolute but rather as an example for these exact experimental conditions. Analogous studies with DHA yield a similarly slow reaction under the same conditions, as is expected from the similarity of their BDFEs and their steric properties. The steric properties are regarded similar in this case, as their structures do not extend out of the plane and their differences in interaction with the *tert*-butyl groups of the macrocyclic ligand scaffold above and below this plane can be neglected. Observing approximately the same kinetics for CHD and DHA despite their expected differences in p*K*a points towards a concerted proton-coupled electron transfer (cPCET) mechanism which is further investigated in section 2.4.[146]

The second products in these oxidative hydrogen atom abstraction reactions of **1** with CHD and DHA are benzene and anthracene, respectively. The identification of these products was carried out by means of NMR spectroscopy.[131] In order to avoid considerable broadenings and signal overlay by the paramagnetic iron complexes, the

reaction was only performed in stoichiometric ratios of the reactants (with CHD: c_0(**1c**) = $4 \cdot 10^{-2}$ mol·L^{-1} and c_0(CHD) = $2 \cdot 10^{-2}$ mol·L^{-1}, in CD_3CN; with DHA: c_0(**1c**) = $2 \cdot 10^{-2}$ mol·L^{-1} and c_0(DHA) = $1 \cdot 10^{-2}$ mol·L^{-1} in CD_3CN). The resulting reaction was, therefore, slow and led only to a partial formation of the products. Nevertheless, after 18 and 4.9 days of reaction time, respectively, the formation of the organic products (benzene, anthracene) can be unambiguously confirmed with yields of 27 % and 5 %, respectively (Figure 52 and Figure 53). In control experiments under the same conditions in the absence of complex **1c**, no formation of benzene and anthracene was observed by NMR spectroscopy.

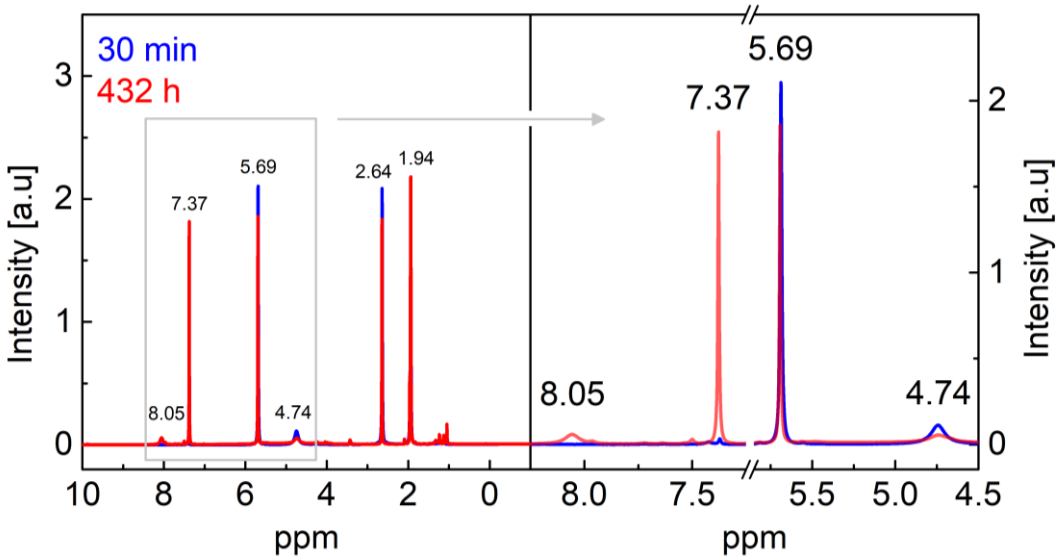

Figure 52. ^{1}H-NMR spectra of a reaction solution containing stoichiometric amounts of **1c** and 1,4-cyclohexadiene (CHD) in MeCN-d3 under a nitrogen atmosphere after reaction times of 0.5 and 432 h. Left: in the range between -1-10 ppm and right: in the range between 8.25-4.5 ppm. Most peaks are assigned based on the spectrum recorded after 432 h. Slight shifts of the signals may be attributed to the change in composition of the paramagnetic species due to the consumption of the ferric high-spin complex (S = 5/2) and the formation of the ferrous high spin complex (S = 2). Peak assignment: (^{1}H-NMR, 600 MHz) δ = 1.94 ppm (MeCN-d3), 2.64 ppm (s, 4 H, aliphatic protons of CHD), 4.74 (proton in *para*-position of the benzoate ligand in **1**), 5.69 (s, 4 H, olefinic protons of CHD), 7.37 ppm (s, 6 H, aromatic protons of benzene), 8.05 (proton in *para*-position of the benzoate ligand in **2**). The content of benzene contamination in the pure, freshly distilled CHD used for this experiment was determined to be less than 1 %. After a reaction time of 432 h, a yield of formed benzene was ascertained to be 27 %.

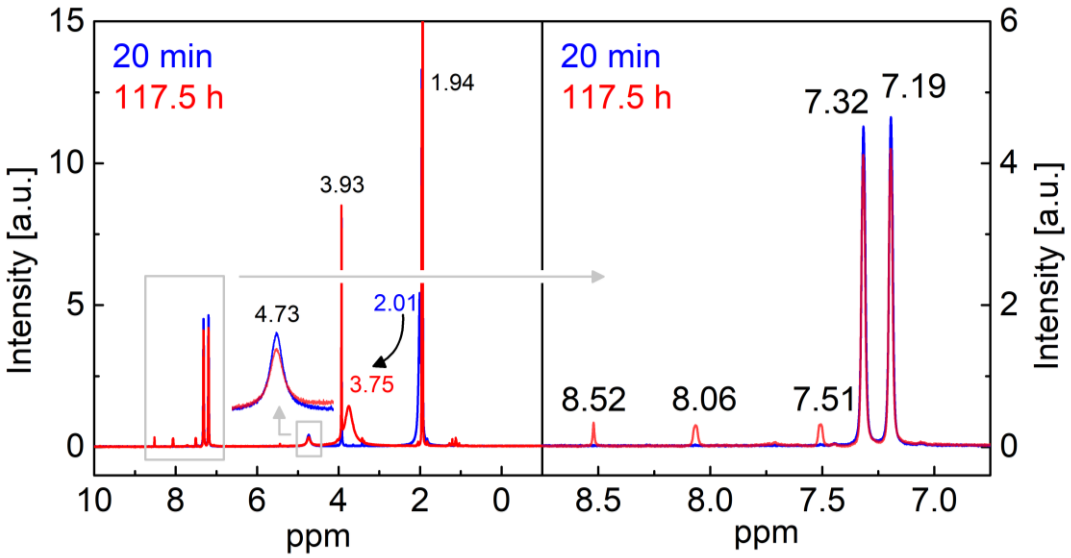

Figure 53. ^{1}H-NMR spectra of a reaction solution containing stoichiometric amounts of **1c** and 9,10-dihydroanthracene (DHA) in MeCN-d3 under a nitrogen atmosphere after reaction times of 0.33 and 117.5 h. Left: In the range between -1-10 ppm and right: in the range between 6.75-8.75 ppm. Most peaks are assigned based on the spectrum recorded after 117.5 h. The applied labelling of the hydrogen atoms for DHA and anthracene used in the peak assignment is shown in Scheme 13. Peak assignment: (^{1}H-NMR, 600 MHz) δ = 1.94 ppm (MeCN-d3), 3.75 (H_2O residue), 3.93 ppm (4 H, $H^{(A)}$), 4.73 (proton in *para*-position of the benzoate ligand in **1**), 7.19 ppm (4 H, $H^{(B)}$), 7.32 ppm (4 H, $H^{(C)}$), 7.51 ppm (4 H, $H^{(F)}$), 8.06 ppm (4 H, $H^{(E)}$), 8.52 ppm (2 H, $H^{(D)}$). The displacement of the broad water signal from 2.01 ppm to 3.75 ppm over the course of the reaction may be attributed to the formation of the ferrous aqua complex and the associated change in composition of paramagnetic species in solution. After 117.5 h the conversion of DHA to anthracene was measured to be 5%.

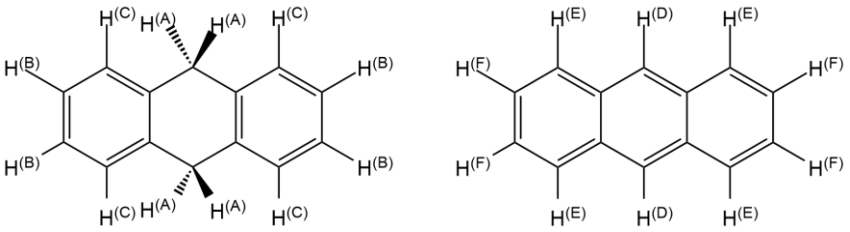

Scheme 13. Labelling of protons in DHA (left) and Anthracene (right) for the proton assignment in the NMR spectra of the reaction mixture of **1c** and DHA.

Importantly, not only does the NMR spectrum of the reaction of **1c** with CHD (Figure 52) clearly reveal formation of benzene (7.37 ppm) and partial consumption of CHD (2.64 and 5.69 ppm) after 18 days, but it also shows a decrease of a signal

corresponding to the proton in *para*-position of the benzoate ligand in **1** (4.7 ppm) and the appearance of a signal corresponding to the proton in *para*-position of the benzoate ligand in **2** (8.1 ppm, see also section 2.1.11). While the resolution is rather poor for these signals because of the relative signal intensities of the paramagnetic metal complexes and the organic compounds, the assignment can be done unambiguously. Since the decrease of signals of both educts and the formation of both products in the reaction can be observed by this method, this NMR-spectroscopic reactivity study provides strong evidence for the interpretation of a C–H abstraction by **1** from CHD to form **2** and benzene.

As for the reactivity study with DHA, the formation of Anthracene (8.52, 8.06, and 7.51 ppm) and the decrease of the aromatic signals corresponding to DHA (7.32 and 7.91 ppm) is also clearly observable (Figure 53). The decrease of the aliphatic proton signal in DHA (3.94 ppm) cannot be followed sufficiently, as a broad signal at 3.75 obscures the signal of interest. Nonetheless, the evidence for the oxidation of DHA to Anthracene is unambiguous. The broad signal at 3.75 ppm is observed to originate from a displacement and broadening of the signal at 2.01 ppm already present in the initial spectrum. An explanation for this may be that both signals arise from a water residue in the NMR solvent that is affected by the changing conditions in solution, mainly because of the varying rations of **1** and **2**. Differences in ratios over the course of the reaction may affect the shift because of the varying pH, paramagnetism, and equilibria in solution. Signals corresponding to the iron-complexes cannot be observed as clearly as is the case for the study with CHD, supposedly because overall lower concentrations were used and the reaction was followed for a shorter time, only to probe for the conversion of DHA to anthracene with stoichiometric amounts of **1** in general. While a slight decrease of a signal at 4.73 can be observed, the formation of a signal at 8.1 is not visible in the spectrum after 117.5 h. Interpretations regarding the metal complexes in this NMR study do appear likely when comparing them to the results obtained from the study with a mixture of **1** and CHD, however, they remain more speculative for this experiment. As CHD was the main focus of this study and already established the proof of principle, another experiment with longer reaction times was renounced.

In summary, the reactivity studies with CHD and DHA under anaerobic conditions unambiguously demonstrate the capability of **1** to abstract Hydrogen atoms from weak

C–H bonds. Regarding the kinetics, the reactivity of **1** appears to be slower than that observed for other literature examples such as $[Fe^{III}(PyPz)(OH)(OH_2)_2]^{4+}$ (in H_2O), $[Fe^{III}(Py5)(OH)]^{2+}$ (in MeCN), and $[Fe^{III}(H_2bim)_2(Hbim)]^{2+}$ (in MeCN).[75,92,98] This could be explained either by thermodynamic or with steric arguments for the individual complexes, however an interpretation of this remains speculative, especially since no kinetic substrate dependency could be found for this example (see section 2.3.6 for information on driving forces and structures). The kinetics in the NMR investigation are significantly slower than those derived from the ESI-MS investigation, which may originate from the differing concentrations. The kinetics of the NMR study are further explored in chapter 3 and, thus, not further discussed in this chapter.

2.3.8. H-Atom Abstractions from C–H Bonds Under Aerobic Conditions

After establishing the capability of **1** to oxidize organic substrates containing 1,4-pentadiene units with weak C–H bonds under anaerobic conditions, the reaction of **1c** with DHA was further investigated under aerobic conditions to probe for indirect evidence of intermediate radical formation and to demonstrate the ability of the ferric hydroxide complex **1** to act as a radical initiator via a hydrogen atom abstraction reaction.

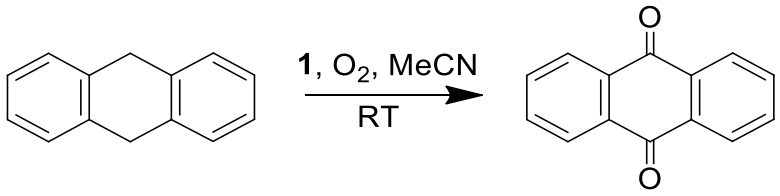

DHA Anthraquinone

Scheme 14. Oxidation of 9,10-dihydroanthracene (DHA) under aerobic conditions with **1** as radical initiator.

The reaction with DHA is especially suited for this purpose because it is well known that, with a radical initiator, DHA reacts readily with molecular oxygen to form anthraquinone.[147] Additionally, in contrast to CHD, both the educt and the expected product are solids with low vapor pressure which simplifies the study. Possible mechanistic pathways involve the addition reaction of triplet O_2 to the doublet organic radical that is formed via C–H abstraction of one of the H-atoms at one of the two 1,4-pentadiene units contained in DHA. A stoichiometric oxygen rebound oxidation with **1** can be ruled out as no anthraquinone formation was observed under a nitrogen atmosphere. Thus, a formation of anthraquinone is only expected if the C–H oxidation of DHA by **1** progresses via initial H-atom abstraction. The reaction can, thus, be used to probe for evidence of such a reactivity. While one could expect similar reactivity patterns for CHD as a substrate, the volatilities of the organic educt and product significantly complicate such an investigation and product isolation/characterization. Thus, the study was only carried out with DHA as an example.

Preliminary experiments conducted by T. Bonck had already revealed that under a pure oxygen atmosphere in the presence of 1 % of **1**, yields of 53 % of anthraquinone can be achieved over night, seemingly demonstrating that **1** acts as a radical initiator

via H-atom abstraction. However, the absolute purity of the metal complex used for this experiment cannot be verified retrospectively as described at the beginning of this chapter.[113] In this work, the reaction was only investigated under aerobic conditions in the presence of 20% of **1** anthraquinone. The mixture was kept in a vial at room temperature for 7 days, and was covered with slightly pierced Parafilm©. Pale, yellow crystals formed within 1 day. The total yield of the reaction was determined to be 17 % with respect to DHA and 87% with respect to one equivalent of **1c**. There was no attempt to optimize the reaction conditions for higher yields as this work deals mainly with the investigation of fundamental reactivity and mechanisms. The product could be crystallized from the reaction mixtures and confirmed by NMR (Figure 54) and IR (Figure 55) spectroscopy, as well as by single crystal X-ray structural analysis.

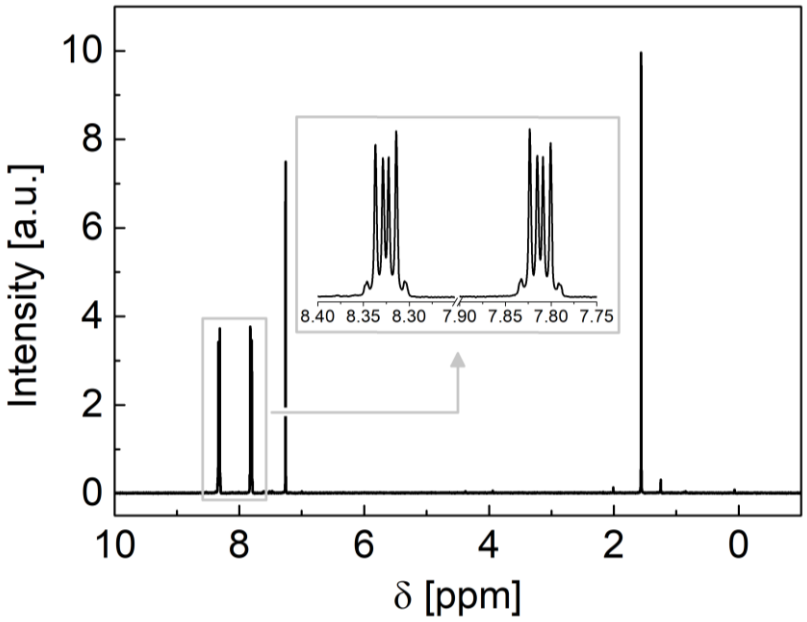

Figure 54. ^{1}H-NMR spectrum of the isolated product from the reaction of **1c** with a fivefold excess of 9,10-dihydroanthracene (DHA) in MeCN under aerobic conditions displayed between 10 and -1 ppm. The region of interest is enhanced and presented in the inset. ^{1}H-NMR (400 MHz, $CDCl_3$) δ = 8.33 (m, AA'BB', 4 H), 7.81 (m, AA'BB', 4 H). The product can be identified as anthraquinone.[148] The signal at 1.56 ppm is attributed to water contaminations in the deuterated solvent.[131]

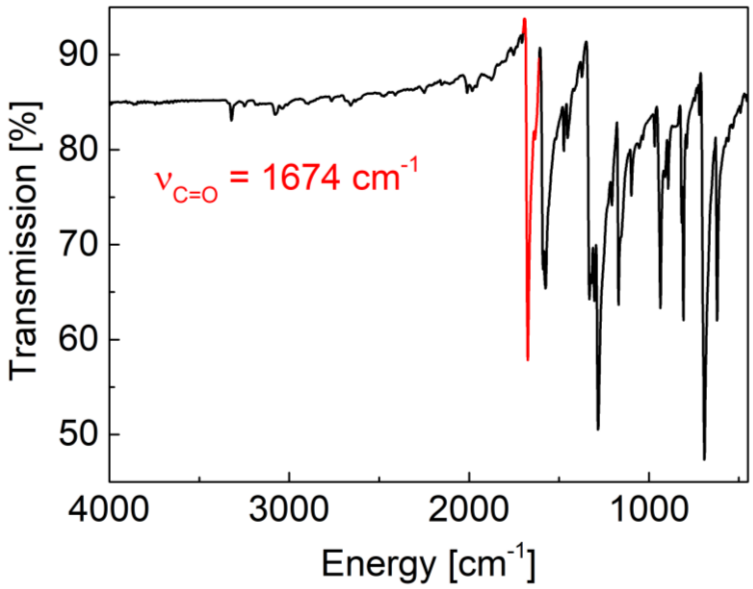

Figure 55. Infrared spectrum of the isolated, crystalline product from the reaction of **1c** with a fivefold excess of 9,10-dihydroanthracene (DHA) in MeCN under aerobic conditions. IR (ATR, cm^{-1}): 3321, 3074, 1674 (C=O), 1575, 1473, 1452, 1331, 1303, 1283, 1206, 1169, 1098, 968, 936, 893, 818, 808, 720, 691, 620. Baseline distortions appeared to be reoccurring/reproducible with the used setup, thus, the spectrum is depicted as recorded.

The spectral properties of the isolated, crystalline compound (Figure 54 and Figure 55) are sufficient evidence to clearly identify the bulk reaction product as anthraquinone. Additional X-Ray diffraction analysis of single crystals obtained directly from the reaction mixture revealed a unit cell that matches a known crystal structure for anthraquinone, strongly supporting this interpretation: (data of the know structure in brackets, CCDC accession code: 1031904)[149] T = 150 K, (T = 200 K), a = 15.7165 Å(15.713(6) Å), b = 3.8960 Å (3.921(1) Å), c = 15.7196 Å (15.722(6) Å), α = γ = 90° (α = γ = 90°) β = 102,476° (β = 102,670(<1)°).

The conclusive evidence obtained by the characterization of this product from a reaction of DHA with **1c** under aerobic conditions exemplifies the radical initiation capability of **1c** and, thus, further underlines the capability of **1** to abstract H-atoms from weak C–H bonds.

2.4. Theoretical Calculations

Experimental results up to this point have shown that the synthesized complexes **1** and **2** are excellent structural, electronic, and functional models. Notably, the capability of **1** to perform H-atom abstraction reactions is unprecedented for structural model complexes. Thus, it is of high interest to further investigate if the mechanisms of these reactions also match the mechanism that is proposed for the enzymatic reaction. The initial step in the enzymatic oxidation of unsaturated fatty acids containing 1,4-pentadiene units has been described as a concerted proton-coupled electron transfer (cPCET) mechanism. Here, the proton and the electron are transferred simultaneously (concerted) but – distinct from H-atom transfer (HAT) as a discrete entity as known e.g. for organic HAT-reactions – to different sites: While the proton is accepted by the hydroxide ligand, the electron is transferred to the ferric metal site. To probe if such a mechanistic scenario is viable also for **1**, the initial C-H bond cleaving step was studied computationally.

Note: All theoretical calculations and interpretations were done by collaborators, Prof. Dr. Johannes E. M. N. Klein and Matina E. de Waal Malefijt of Stratingh Institute for Chemistry at University of Groningen. The results of these studies are only reported in this thesis for completeness. The following paragraphs in this section are reproduced with permission from the previously published article and the respective supporting information this chapter is based on.[1] Figures, tables, and references have been adapted. All figures were provided by the collaborators and adjusted for this thesis.

As a computational methodology (PW6B95-D3(BJ)/def2-TZVPP/SMD(MeCN)//M06-L/def2-SVP/PCM(MeCN)) was selected.[150] Subsequently, the transition states for C–H bond cleavage for the model substrates CHD and DHA were computed. The choice of the methodology is motivated by previous reports using the M06-L functional for obtaining geometries in the study of X–H bond activation with iron complexes.[151] The PW6B95-D3(BJ) functional was selected for obtaining electronic energies at the stationary points as it is broadly applicable for obtaining thermodynamic/kinetic parameters. In representative benchmark studies, including transition metals, this functional is commonly among the better performing candidates[152] and has shown particularly good performance for obtaining correct spin ground states for iron complexes.[153]

For both complexes **1** and **2**, high-spin ground states are found computationally (Table 15 and Table 16). In addition, the reaction of **1** with TTBP turns out to be essentially energy neutral within a couple of kcal·mol^{-1} (Table 17). These findings are in line with the experimental observations for the spin states and an equilibrium for the reaction of **1** with TTBP, providing further evidence for the suitability of the empirical choice of methodology for these types of calculations. Nevertheless, as the prediction of these properties can be very sensitive to the chosen method, a variety of functionals were probed to demonstrate this sensitivity. It was found that M06-L largely overstabilizes **1**/TTBP over **2**/TTBP-H, which is not consistent with experimental observations. Energetically, the use of B3LYP and PW6B95 positions these values much more closely. Therefore, PW6B95 was selected for the computation of electronic energies for the analysis of the hydrogen atom abstraction reactions by **1** from CHD and DHA. Because the choice of the solvation had some influence, both the PCM and SMD solvation models were tested. The barriers ($\Delta G^{\ddagger}_{298K}$) for the C–H bond cleavage for the model substrates were calculated to be 24.9 (CHD) and 25.0 (DHA) kcal·mol^{-1}, respectively, consistent with a reaction that occurs slowly at RT (Table 18).

Table 15. Computed spin state splitting energies for **2**.

Spin State	M06-L		B3LYP-D3(BJ)		PW6B95-D3(BJ)		PW6B95-D3(BJ)-SMD	
	ΔE	***ΔG$_{298}$***	***ΔE***	***ΔG$_{298}$***	***ΔE***	***ΔG$_{298}$***	***ΔE***	***ΔG$_{298}$***
S = 2	0.0	0.0	0.0	0.0	0.0	0.0	0.0	0.0
S = 1	15.8	18.6	9.6	12.3	12.8	15.5	12.9	15.7
S = 0	6.3	12.0	12.5	18.1	12.9	18.5	12.5	18.1

All values are given in kcal·mol^{-1}. Electronic energies are computed with the indicated functional using the def2-TZVPP basis set and PCM solvation model (MeCN) unless stated otherwise at M06-L/def2-SVP/PCM geometries.

Table 16. Computed spin state splitting energies for **1**.

Spin State	M06-L		B3LYP-D3(BJ)		PW6B95-D3(BJ)		PW6B95-D3(BJ)-SMD	
	ΔE	***ΔG*$_{298}$**	***ΔE***	***ΔG*$_{298}$**	***ΔE***	***ΔG*$_{298}$**	***ΔE***	***ΔG*$_{298}$**
S = 5/2	0.0	0.0	0.0	0.0	0.0	0.0	0.0	0.0
S = 3/2	10.3	12.5	0.6	2.8	3.5	5.7	3.6	5.7
S = 1/2	13.6	18.4	9.2	14.0	9.8	14.6	9.4	14.2

All values are given in kcal·mol^{-1}. Electronic energies are computed with the indicated functional using the def2-TZVPP basis set and PCM solvation model (MeCN) unless stated otherwise at M06-L/def2-SVP/PCM geometries.

Table 17. Computed energetics (ΔE and ΔG_{298}) for the reaction between **1** and TTBP for the spin ground state of **1**.

Functional[a]	*ΔE*	*ΔG*$_{298}$
M06-L	13.0	10.4
B3LYP-D3(BJ)	1.2	-1.5
PW6B95-D3(BJ)	1.0	-1.6
PW6B95-D3(BJ)-SMD	2.3	-0.3

All values are given in kcal·mol^{-1}. [a] Electronic energies are computed with the indicated functional using the def2-TZVPP basis set and PCM solvation model (MeCN) unless stated otherwise at M06-L/def2-SVP/PCM geometries.

Table 18. Computation of hydrogen atom abstraction from CHD and DHA by **1**.

Functional	Substrate	1 + Substrate	RC	TS	IC	2 + Substrate-H
PW6B95-D3(BJ)-PCM	CHD	0.0	2.0	22.7	-4.0	-6.7
	DHA	0.0	3.0	22.0	0.7	-3.2
PW6B95-D3(BJ)-SMD	CHD	0.0	3.6	24.9	-2.2	-6.1
	DHA	0.0	5.3	25.0	3.2	-2.5

All values are given in kcal·mol^{-1}. Gibbs free energies (ΔG_{298}) are computed at the PW6B95-D3(BJ)/def2-TZVPP/*Solvation Model*//M06-L/def2-SVP/PCM level of theory.

With the computed reaction paths, not only was an overall H-atom abstraction step confirmed to be mechanistically reasonable, but, even more interestingly, the exact

nature of the C–H bond cleaving step could also be determined. For reactions that follow a concerted proton-coupled-electron-transfer-type (cPCET, alternative acronyms are EPT, CPET) mechanism,[95,96,154] two possible pathways can be differentiated: a H-atom transfer (HAT), which is characterized by the transfer of a genuine H-atom (electron and proton are transferred as a discrete entity) and, alternatively, a cPCET where the proton and electron are transferred separately.[99] For LOXs a cPCET scenario has been well established.[54,64,76,77] Therefore, the electron flow along the intrinsic reaction coordinates (IRCs) of these reactions was studied using intrinsic bond orbitals (IBOs),[155,156] a methodology which has previously been shown to be capable of differentiating these scenarios.[103] In Figure 56 and Figure 57 the changes of the individual IBOs associated with the α (i) and β (ii) spin manifold of the C–H bonds in CHD and DHA, respectively, are shown. As the C–H bond is cleaved homolytically, the β IBO transforms into an iron d-orbital, and the α IBO remains with the derived organic radical in a continuous fashion. This finding is based on plotting the root square deviation of the partial charge changes of the studied IBOs (Figure 58). This establishes the fate of the C–H bond and indicates that the electron transfer is decoupled from the proton transfer. If the lone pairs on the oxygen of the Fe^{III}-OH unit are inspected in an analogous way, the β-spin manifold reveals how a lone pair is transformed into an O–H bond simultaneously, which corresponds to the proton transfer (Figure 56, Figure 57, (iii)). Thus, it is concluded that both electron and proton transfers are indeed very much concerted.

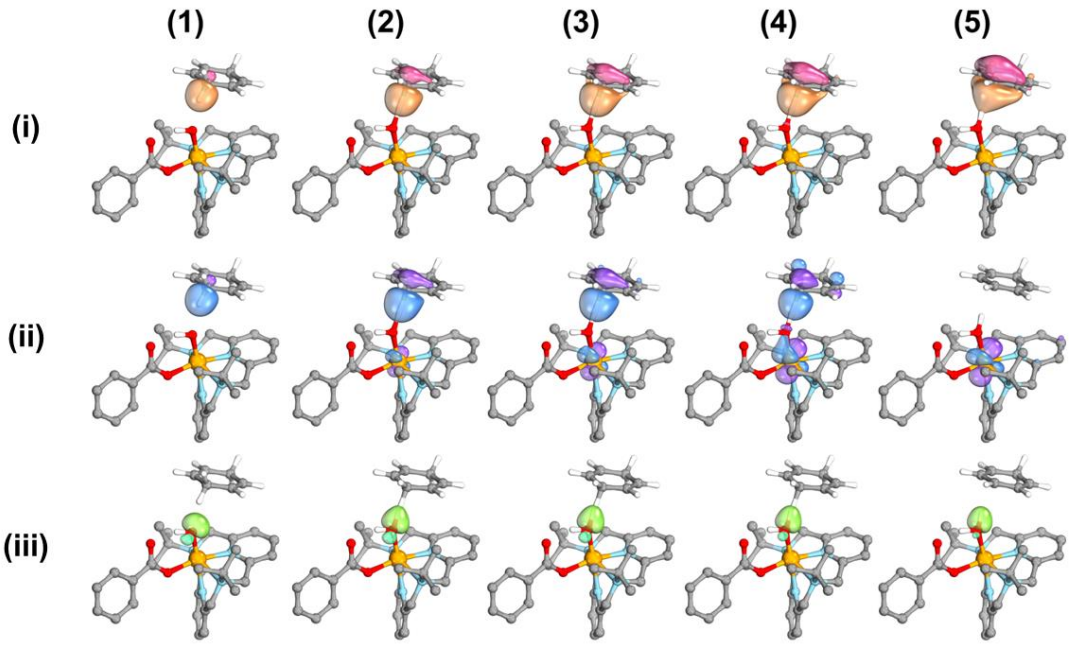

Figure 56. Depiction of changes to IBOs relevant to C**–**H cleavage of CHD by **1** along the IRC. Localized orbitals are depicted separately for the α (i) and β (ii) spin manifolds of the C**–**H bonds and the α IBO corresponding to the lone pair on O resulting in the newly formed O**–**H bond (iii). IBOs are obtained at the M06-L/def2-SVP/CPCM level of theory.

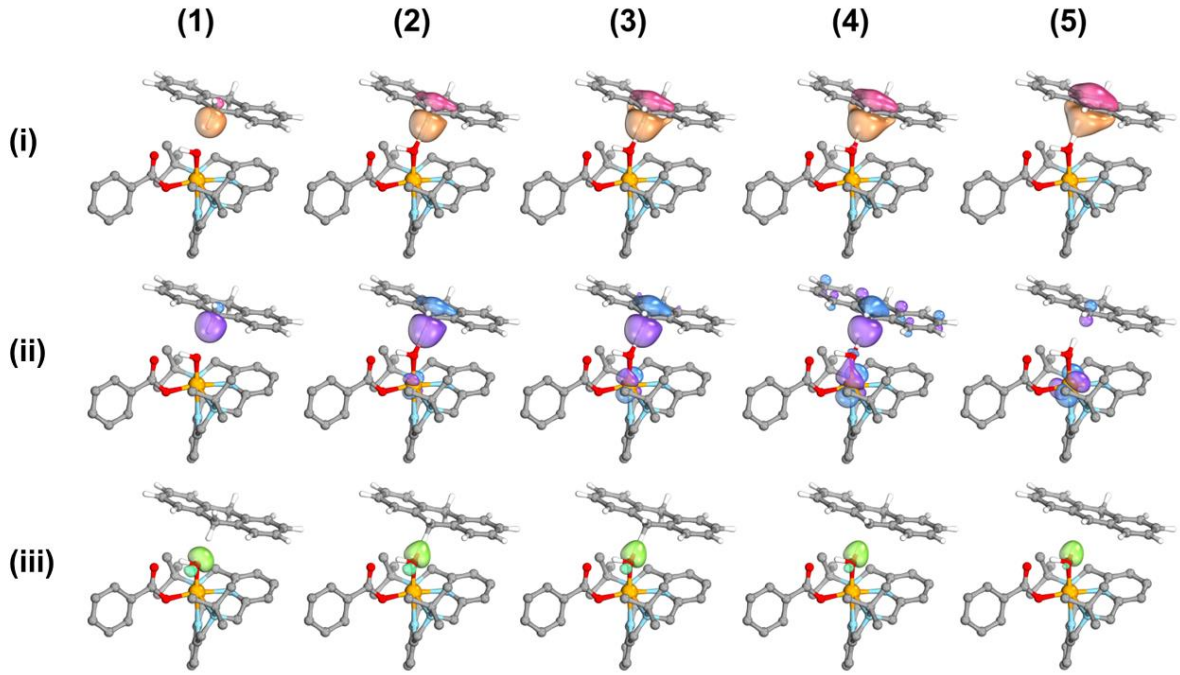

Figure 57. Depiction of changes to IBOs relevant to C**–**H cleavage of DHA by **1** along the IRC. Localized orbitals are depicted separately for the α (i) and β (ii) spin manifolds of the C**–**H bonds and the α IBO corresponding to the lone pair on O resulting in the newly formed O**–**H bond (iii). IBOs are obtained at the M06-L/def2-SVP/CPCM level of theory.

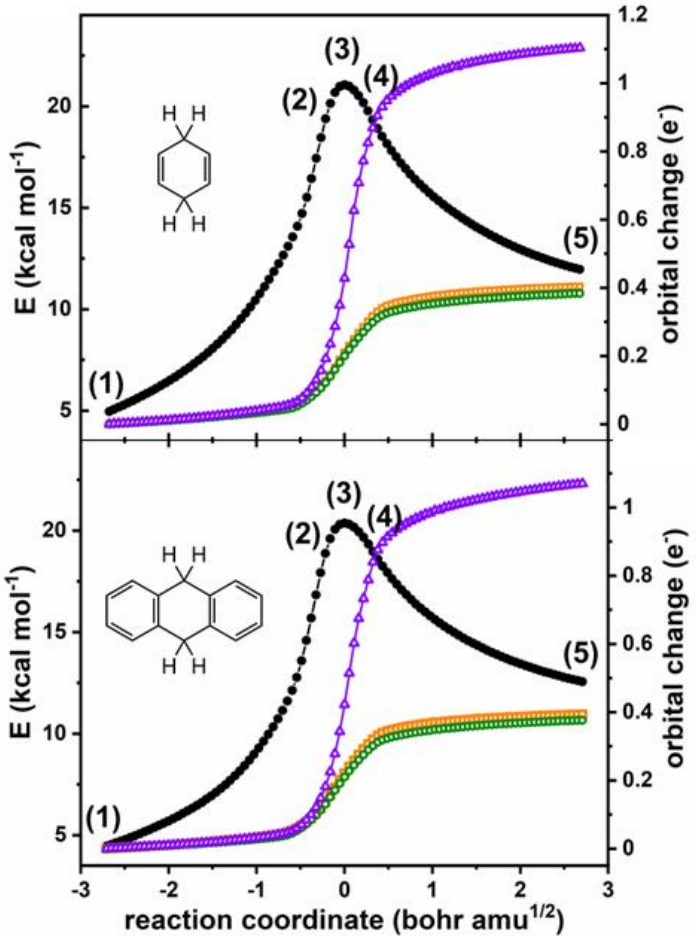

Figure 58. Plots of the orbital changes (e^-) along the IRCs for the C**–**H cleavage of CHD (top) and DHA (bottom) by **1** along the IRCs. Relative changes to the electronic energies are plotted in black circles and changes to IBOs plotted separately for the α (orange squares) and β (purple triangles) spin manifolds of the C**–**H bonds and the α IBO corresponding to the lone pair on O resulting in the newly formed O**–**H bond (green circles). All data obtained at the M06-L/def2-SVP/CPCM level of theory.

In summary, the theoretical calculations establish that the model complex **1** is not only a structural and functional model of LOX, but also mimics the event of C–H bond cleavage in the same fashion as LOX at an electronic structure level, which makes complex **1** a complete model.

2.5. Summary of the Reactivity Studies and Theoretical Investigation

The presented reactivity studies show, that the (hydroxo)iron(III) complex **1** indeed engages in the H-atom abstraction from weak O–H and C–H bonds to form the (aqua)iron(II) complex **2** and, accordingly, oxidized organic products, as had been proposed in previous works by *Rauber*, *Bonck* and *Dobbelaar*.[2,112,113] This is in contrast to the absence of such reactivity when exposing **4** to the same reaction conditions, which rules out a simple base-assisted mechanism.

In all reactivity studies with **1** under anaerobic conditions, direct evidence for the formation of a ferrous complex could be found, that could be retraced to the formation of **2** upon hydrogen atom abstraction by **1** from the organic substrates. The bond energy of the O–H bond formed in **2** upon hydrogen atom transfer (HAT) to **1**, which is derived from quantitative EPR equilibrium studies with 2,4,6-tri(*tert*-butyl)phenol (TTBP) as $BDFE_{MeCN}$(**2**) = 72.4 $kcal \cdot mol^{-1}$,[97,140] is found to be one of the highest reported for monocationic iron(II) complexes that engage in such reactions.[79,97] Preliminary kinetic results for the reactions with both X–H bond types show good agreement with expectations from transition-state and electron-transfer theory,[94,107] and hint at a concerted proton-coupled electron transfer (cPCET) mechanism because the kinetics of the reaction with 1,4-cyclohexadiene and 9,10-dihydroanthracene (both $BDFE_{MeCN} \approx 76$ $kcalmol^{-1}$)[145] appear to be very similar despite expected significant differences in their pKa values.[59,146,157] This interpretation is supported by a theoretical investigation which indeed identifies a cPCET mechanism for such reactions analogous the enzyme.[54,64,76,77] However, indications for a concentration-dependent activity of 1 were found, the potential origin of which is further discussed in chapter 4.

In addition to the establishment of the fundamental reactivity of the ferric complex, it is observed that **1** can be regenerated by oxidation of **2** under atmospheric conditions at room temperature, which establishes the basis for the catalytic activity of the model system and, thus, the functional model character of both species. Such a catalytic activity is demonstrated for the aerobic peroxidation of TTBP with **1**. Because both **1** and **2** have also been established as structural and electronic models in section 2.1, this concludes the successful synthetic analogue approach.

The successful structural-functional modelling establishes that the fundamental H-atom abstraction reactivity of rabbit lipoxygenase (rLOX) is achieved by the *cis*-(carboxylato)(hydroxo)iron(III) coordination unit in an FeN_4O_2 ligand donor environment and precedents the feasibility of small molecule analogues. Though the observation of a significantly slower reaction hints towards further protein matrix effects not captured by these simplified model complexes, a closer look at this system offers a unique and advantageous opportunity to elucidate structural and electronic features that govern the functionality of the enzymatic active site. Further studies appear worthwhile; specifically, how well-defined changes of structural and electronic factors at this coordination unit will influence its reactivity – a study that is hardly possible only with the enzyme. Thus, electronic derivatives of the complexes presented in this chapter were synthesized, characterized, and studied in the following, the results of which are described in chapter 3.

3. Study of Electronic Influences by Derivatization

After establishing the first functional as well as structural model complexes for rabbit lipoxygenase (rLOX) in the previous chapter, it was of interest to further investigate how differing electronic influences in derivatives affect the properties of similar complexes to gain a deeper understanding of what governs the reactivity of the enzyme. For this, an electron donating (–OMe, +M effect) and an electron withdrawing ($–NO_2$, –M effect) substituent (Table 19), respectively, were introduced in *para*-position of the aromatic ring of the benzoate ligand of **1** and **2** (**3**), respectively (Scheme 15).

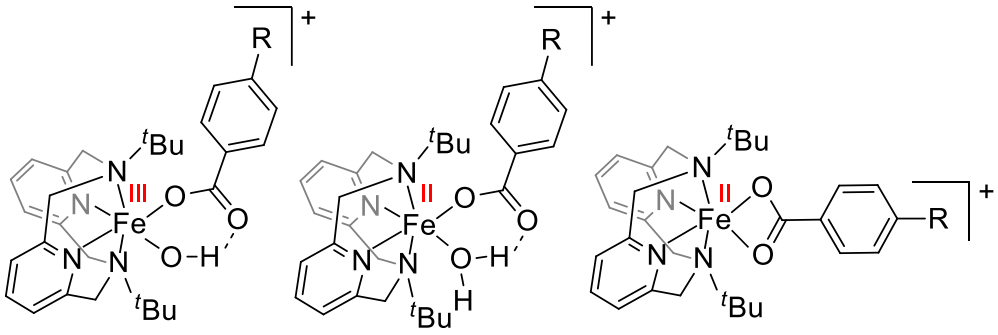

1 R = H
7 R = NO_2
10 R = OMe

2 R = H
8 R = NO_2
11 R = OMe

3 R = H
9 R = NO_2
12 R = OMe

Scheme 15. Schematic depiction of the derivatives (**7**-**12**) of complex cations **1**-**3** with different electronic properties.

The introduction of such substituents in the carboxylate ligand affects the electronic situation of these complexes mainly in two ways which are relevant for this work: Firstly, the acidity of the corresponding carboxylic acid (Table 19) and, thus, the basicity of the carboxylate ligand will differ for the functionalized compounds as opposed to the benzoate ligand contained in **1**. Secondly, the the σ- and π- donor properties of the ligand will differ for all three ligands, benzoate ($^{-}O_2CPh$), *p*-nitrobenzoate ($^{-}O_2CPh^{pNO2}$), *p*-methoxybenzoate ($^{-}O_2CPh^{pOMe}$), and affect the stabilization of the two iron oxidation states (iron(II) and iron(III)). Both influence the strength of the secondary intramolecular hydrogen bonding, the bond strength of the hydroxide or aqua ligand to the iron core, respectively, and thus, the BDFE of the reactive O–H bond.

Table 19. Relative substituent effects (M-effect, I-effect) for and acidities (p*Ka*) of the corresponding acids of the carboxylate ligands employed in **1**–**3** and **7**–**12**.[143]

	p*Ka*	Substituent M-Effect	Substituent I-Effect
HO_2CPh^{pNO2}	3.43	–M	–I
HO_2CPh	4.20	-	-
HO_2CPh^{pOMe}	4.50	+M	–I

When estimating the effect of the substituent on this BDFE of the reactive O–H bond, multiple competing effects to be considered:

Firstly, a less basic carboxylate ($pK_B(O_2CPh^{pOMe}) < pK_B(O_2CPh) < pK_B(O_2CPh^{pNO2})$) could exert a weaker pull on the non-reactive O–H bond even when coordinated to a metal site (η^1) and, thus, prime the reactive O–H bond for easier bond cleavage and a lower BDFE. Consequently, a more basic carboxylate ligand would increase the bond strength of the second, reactive O–H bond at the aqua ligand and lead to a higher BDFE of such a *cis*-(carboxylato)(aqua)iron(II) complex. When regarding only this effect, the highest BDFE in this series would be expected for the $[Fe(L\text{-}N_4{}^tBu_2)(O_2CPh^{pOMe})(OH)]^+$ complex cation.

Secondly, a stronger (σ- and π-)donor ($O_2CPh^{pOMe} > O_2CPh > O_2CPh^{pNO2}$) is expected to better stabilize the ferric state, meaning that the reduction potential for a complex with such a ligand will be more negative. A more negative reduction potential can be translated to a lesser tendency for the complex to be reduced, decreasing the driving force for a (proton-coupled) one-electron reduction and, thus, the BDFE of the reactive bond. In analogy, a weaker donor should destabilize the ferric state and lead to a more positive potential and a larger driving force. When regarding only this effect, the highest BDFE in this series is expected for the $[Fe(L\text{-}N_4{}^tBu_2)(O_2CPh^{pNO2})(OH)]^+$ complex cation.

As a third effect, the change in donor strength of one ligand will affect the donor/acceptor interactions for all other ligands. In this case, it would be expected that especially the oxygen-metal bonding of the aqua ligand in an $[Fe(L\text{-}N_4{}^tBu_2)(O_2C^R)(OH_2)]^+$ complex cation would be affected, as it is not inhibited by

any rigidity as is the case for the macrocyclic ligand. In the case of a weaker carboxylate donor, the Fe-OH_2 bond strength would increase, O–H bond strength of the aqua ligands would decrease, and the acidity of the complex would increase. This would reduce the BDFE of the reactive O–H bond. In the case of a stronger carboxylate donor, the Fe-OH_2 bond strength would decrease, the O–H bond strength of the aqua ligand would increase, and the acidity of the complex would decrease. This would increase the BDFE of the reactive O–H bond. When regarding only this effect, the highest BDFE in this series would be expected for the $[Fe(L\text{-}N_4{}^tBu_2)(O_2CPh^{pOMe})(OH)]^+$ complex cation.

It is apparent that all above mentioned effects are directly linked to the Bordwell-equation, which describes the proportionality of the BDFE of a reactive X–H bond to the electrochemical potential and the p*Ka* of the respective compounds (equation 3).

$$(3) \quad BDFE_{HA} = 1.37pK_{HA} + 23.06E_{ox}(A^-) + C_G$$

However, the magnitude of the competing effects cannot be satisfyingly reasoned by chemical intuition or pure theoretical considerations which highlights the complexity of the different influences of derivatization on the BDFE of the reactive O–H bond. This makes the experimental approach even more intriguing.

3.1. Synthesis and Characterization

3.1.1. Synthesis

The synthesis of the derivatives containing benzoate ligands with different substituents in *para*-position to the carboxylate group was approached in an analogous way as done for complex cations **1**-**3** (Scheme 16, adapted from section 2.1.1).[1] However, unexpected challenges arose which required some synthetic modifications that will be elaborated on in the following.

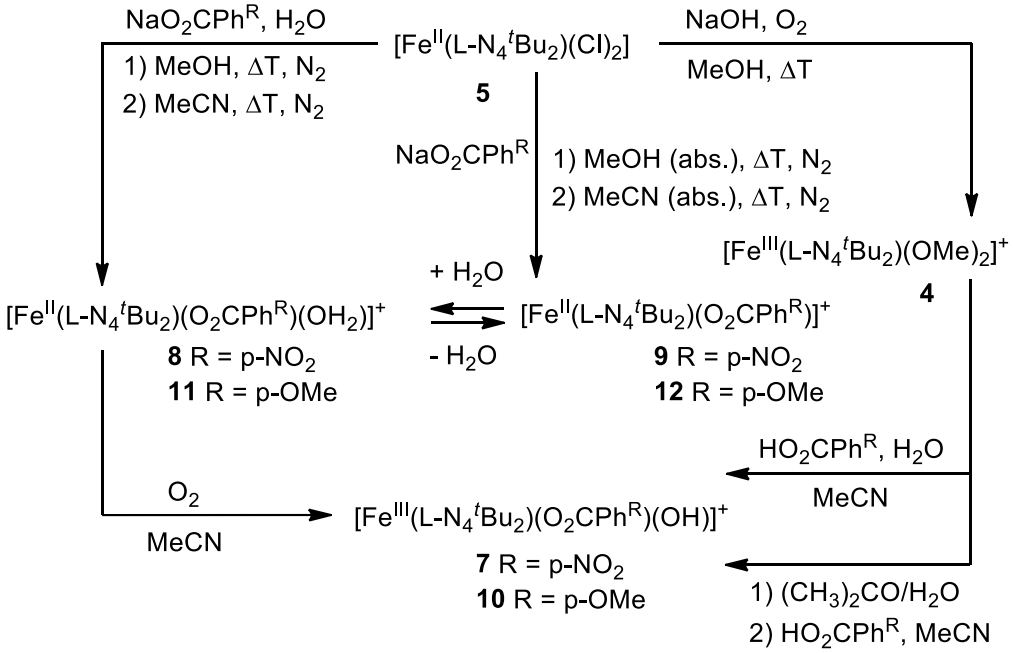

Scheme 16. Synthetic reactions. The cationic complexes were crystallized and isolated as [**4**](BPh$_4$) (**4a**), [**4**](PF$_6$) (**4b**), [**4**](ClO$_4$) (**4c**), [**7**](BPh$_4$) (**7a**), [**7**](ClO$_4$) (**7b**), [**9**](ClO$_4$)•MeCN (**9a**), [**10**](BPh$_4$) (**10a**), [**10**](ClO$_4$)•1H$_2$O (**10b**) (isolated only as powder), [**10**](PF$_6$)•Et$_2$O (**10c**), [**11**](CF$_3$SO$_3$) (**11a**), [**12**](ClO$_4$)•MeCN (**12a**). Complex **8** could not be successfully isolated.

Generally, the hydroxo iron(III) complexes **7** and **10** could be crystallized and isolated rather well with a suitable counterion under the right conditions. However, the conversion of **4** with the functionalized benzoic acids was often not quantitative when approached in the same way as for the synthesis of **1**, leaving iron-species still containing methoxide ligands as impurities in the bulk product as can be identified by

ESI-MS and IR-spectroscopy. Eventually, two suitable modified synthetic approaches could be identified.

The most straightforward modified approach is to first prepare the reaction solutions for **7** and **10** analogous to the synthetic procedure of **1** and then evaporate all solvent molecules under reduced pressure. The residue can then be taken up in MeCN for crystallization via fractional addition or diffusion of freshly distilled diethylether at 4 °C in the dark to yield analytically pure products. The crucial extra step of intermediately evaporating the solvent is thought to quantitatively remove the methanol solvent, driving the reaction to the desired hydroxo iron(III) product according to the principles of Le Chatelier. Importantly, the mixture should not be heated to remove the solvent, as the hydroxo iron(III) complexes reported in this dissertation are all rather sensitive to even moderate warming (40 °C) and tend to show increased decomposition when kept above room temperature in acetonitrile solution for an extended period of time.

The second approach to exchange any residual bound methoxide ligands during the synthesis of **7** or **10** from **4** follows a similar principle. Here, **4** is first treated with a mixture of acetone/water (50/20 vol/vol) and the solvent is completely evaporated under atmospheric conditions. It was found that the treatment of **4** with the acetone/water mixture exchanges the methoxide ligands with hydroxide ligands and yields a dihydroxo iron(III) complex as intermediate species suitable for further conversion after solvent evaporation. The synthesis and characterization of this unusual dihydroxo iron(III) complex is further described in chapter 5. The treatment of the dried residue with HO_2CPh^{pNO2} or HO_2CPh^{pOMe} in MeCN allows for the formation of the respective products **7** and **10** and their analytically pure isolation via fractional addition or diffusion of freshly distilled diethylether at 4 °C. Notably, this approach does not work with **4a** but only with **4b** or **4c**, as significant decomposition of **4a** is observed in the acetone/water mixture. The reason for the decomposition of the tetraphenylborate salt is not clear and was not further investigated. It is suspected, that the BPh_4^- anion is somehow oxidized under the conditions present in the mixture and triggers unspecific following (radical chain) reactions.

Because of the limitations of the second approach related to the tetraphenylborate anion, the first approach was used to obtain **7a** and **10a**, while the second approach was used to synthesize **7b**. In the case of **10**, a perchlorate salt [**10**]ClO_4•H_2O (**10b**) and a hexafluorophosphate salt [**10**]PF_6•Et_2O (**10c**) could also be synthesized via the

second method. However, **10b** was isolated as a powder and the proposition of exactly one crystal water molecule per cation is only derived from elemental analysis and a qualitative IR spectrum rather than a crystal structure (Table 20 and Figure 67 shown in section 3.1.5). For **10c**, some crystals of poor quality could be used to determine at least the structural motif and verify the content of exactly one Et_2O molecule per cation. However, the elemental analyses of the bulk materials for batches of **10c** did not match this finding. Thus, because of the uncertainties about the exact composition of the isolated products **10b** and **10c**, **10a** was favoured for slightly more reliable analytical investigations and characterizations of **10** in the solid state whenever possible.

The isolation of the iron(II) complexes **8**, **9**, **11**, and **12** was more challenging than in the case of **2** and **3**, as they were much less prone to crystallization despite best efforts of counterion variation. While complexes **9**, **11** and **12** could eventually be crystallized and isolated in a pure form, a structure could not be obtained for all (see section 3.1.2) because of the size and quality of these crystals and the limitations of the departmental X-ray diffraction instrument (see methods). The isolation of **8** was not achieved at all, synthetic efforts only resulted in the formation of red oils and/or amorphous, inhomogeneous substances. Compounds containing complex **9** or **12** appeared to be hygroscopic, analogous to the observations for **3** in **3a**. The isolated compound **11a** appeared to contain solvent molecule(s) in the crystal (**11a***) that seemingly evaporate fully under atmospheric conditions to yield an analytically pure powder (see Table 20 and Figure 68 shown in section 3.1.5). Compound **12a** showed a rapid change of colour from yellow to a more reddish colour in the solid state immediately after isolation. Nonetheless, the elemental composition according to combustion analysis appeared to fit the theory when measured within the first hours after isolation.

The oxidation of the ferrous complexes (**8**-**9**,**11**-**12**) to the ferric species with oxygen from air was found to be possible yet not further investigated as a synthetic pathway, as similar problems as with the oxidation of **2** to **1** are expected.

Table 20. Exemplary elemental analysis results and maximal deviations in % for the compounds relevant to this chapter. Data is given in the format “calculated (found)”.

	C [%]	**H** [%]	**N** [%]	**S** [%]	max. dev. [%]
7a	69.90 (69.64)	6.31 (6.22)	7.69 (7.66)	-	0.26
7b	50.41 (50.19)	5.40 (5.38)	10.14 (9.99)	-	0.22
9a	50.80 (50.62)	5.64 (5.62)	11.47 (11.25)	-	0.22
10a	72.41 (72.16)	6.75 (6.82)	6.25 (6.21)	-	0.25
10b	51.92 (51.90)	6.10 (5.91)	8.07 (8.22)	-	0.19
10c[a]	51.33 (49.13)	6.33 (5.68)	7.04 (7.68)	-	2.20
11a[b]	51.24 (51.45)	5.69 (5.87)	7.71 (7.81)	4.41 (4.31)	0.21
12a[c]	55.14 (54.52)	5.64 (5.93)	10.05 (8.47)		1.58

max. dev. = maximal deviation. Method error ≤0.30 %. [a] Calculations as [**10**](PF_6) (C, 49.94; H, 5.59; N, 7.77) or [**10**](PF_6)•1H_2O (C, 48.73; H, 5.72; N, 7.58) show smaller maximal deviations of 0.81% and 0.40%, respectively, but are not supported by a crystal structure. [b] The listed data was obtained after storage under atmospheric conditions for one month to allow for complete solvent evaporation from the crystal packing. An elemental analysis obtained two days after isolation of the compound (**11a***) still gave values consistent with residual water content in the crystal lattice (C, 50.71; H, 6.07; N, 7.34; S, 4.09) as supported by IR spectroscopic analysis (section 3.1.5, Figure 68). [c] The sample was measured after prolonged storage in a vial under air. Calculations as [**12**](ClO_4) (C, 54.93; H, 5.53; N, 8.54), [**12**](ClO_4)•H_2O (C, 53.47; H, 5.68; N, 8.31) or [**12**](ClO_4)•0.5H_2O (C, 54.19; H, 5.61; N, 8.43) show smaller maximal deviations of 0.41%, 1.05%, and 0.33%, respectively. Because the bulk combustion analysis results do not match the structural analysis results within the instrumental error of 0.30 %, it is considered likely that the MeCN molecule evaporated, and the hygroscopic compound possibly attracted water from air. Additional compound specific tables with calculated vs experimental results can be found in the experimental section.

3.1.2. Structural Analysis

Complexes **7, 10**, **11**, and **12** were crystallized directly from synthetic procedures and structurally characterized by single crystal X-ray structure analyses. Perspective views of the complex cations **7**, **10**, and **12** derived from the structures **7a**, **7b**, **10a**, and **12a** are given in Figures 59-61, respectively. Structural parameters, a full list of bond lengths, angles, and hydrogen bonds for the structures derived from **7a**, **7b**, **10a**, and **12a** can be found in the attachment. For **11a** and **10c**, only a determination of the structural motif was achieved because of the size and quality of the crystals and (also compare methods and instruments for contextualization). The structural motif allows for the identification and assignment of the target product cations, further information on these two structures can be provided upon request by Dr. Harald Kelm (internal reference numbers 21248ocb, **11a**, and 210660o, **10c**).

General aspects of the structures of $[Fe^{III}(L\text{-}N_4{}^tBu_2)(O_2CPh^R)(OH)]$, $[Fe^{II}(L\text{-}N_4{}^tBu_2)(O_2CPh^R)(OH_2)]$, and $[Fe^{II}(L\text{-}N_4{}^tBu_2)(\eta^2\text{-}O_2CPh^R)]$ cations, the stabilization of the ferric hydroxide species, the achievement of high spin states even for the ferric complexes, and the coordination mode of the macrocyclic ligand $L\text{-}N_4{}^tBu_2$ have been extensively described exemplary for **1**, **2**, and **3** in chapter 2. All arguments also apply to the derivatives and, thus, they are not further discussed in this chapter. Instead, the differences in the bond lengths, interatomar distances, angles, and notable structural features of complex **1** and its derivatives (**7** and **10**), and **3** and its derivative (**12**), respectively, are highlighted and compared in the following Tables and discussion.

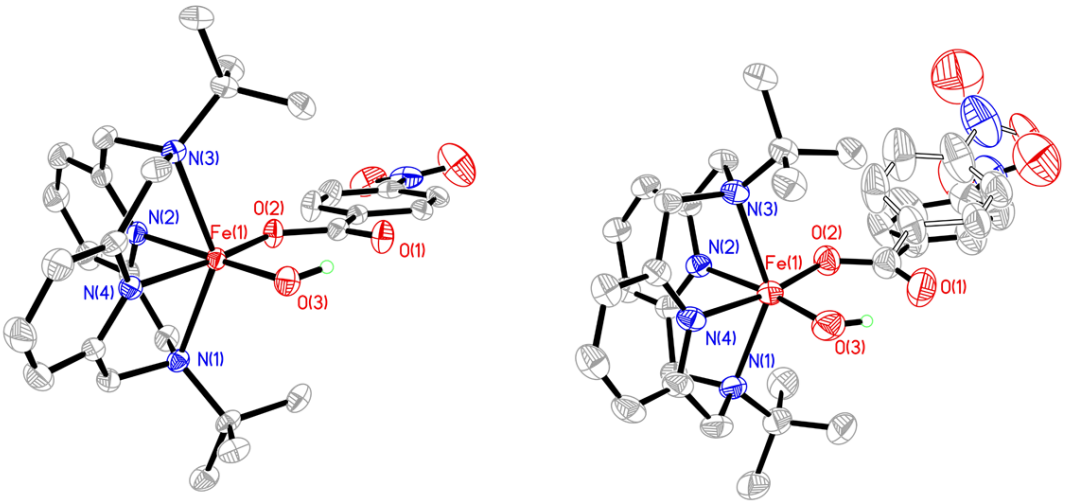

Figure 59. Perspective views of the complex cations in the ferric compounds **7a** (left) and **7b** (right) with thermal ellipsoids displaying a probability level of 50%. Hydrogen atoms are omitted for clarity with the exception of the hydroxide proton at O(3). The derivatized aromatic residue of the carboxylate ligand in **7b** is disordered.

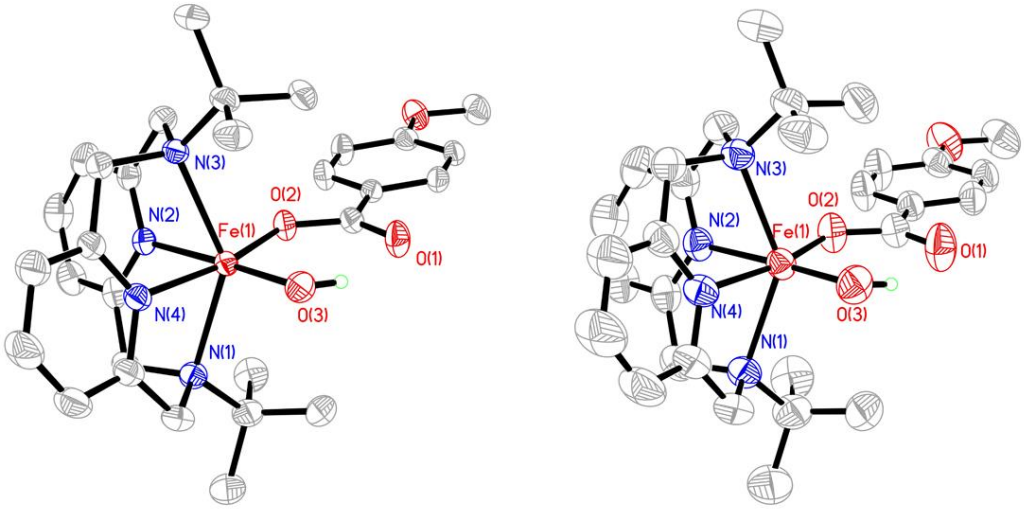

Figure 60. Perspective views of the complex cation in the ferric compound **10a** at 150 K (left) and 293 K (right) with thermal ellipsoids displaying a probability level of 50%. Hydrogen atoms are omitted for clarity with the exception of the hydroxide proton at O(3). See attachment for more details on minor temperature influences on the structural parameters.

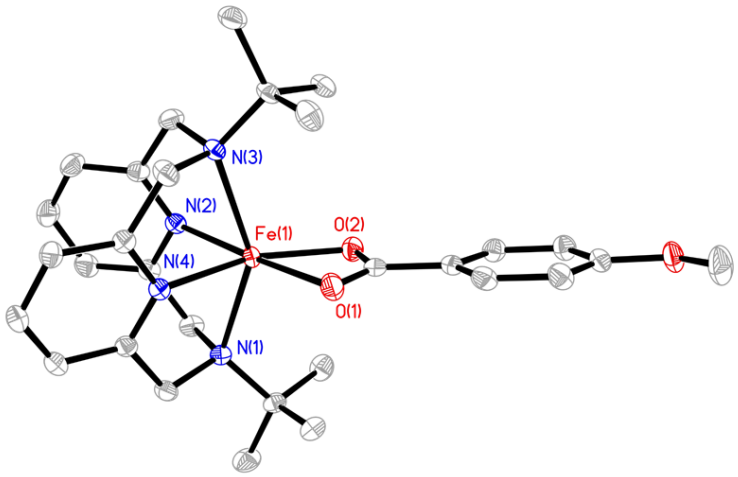

Figure 61. Perspective view of the complex cation in the ferrous compound **12a** at 150 K with thermal ellipsoids displaying a probability level of 50%. Hydrogen atoms are omitted for clarity.

Table 21. Selected bond lengths and interatomar distances (in Å) in the ferric complex cations of the structurally similar compounds **10a**, **7a**, and **1a** at 150 K and averaged bond lengths for the structures measured at 150 K that contain **7** (**7a**, **7b**) and **1** (**1a**, **1b,** adapted from chapter 2 and previously published results).[1]

distance	10a	7a	1a	7a, 7b	1a, 1b
Fe-O(2)	1.969(1)	1.980(1)	1.955(1)	1.97 – 1.98	1.95 – 1.96
Fe-O(3)	1.838(1)	1.833(1)	1.835(1)	1.83 – 1.85	1.84 – 1.85
Fe-N(1), Fe-N(3)	2.302(2), 2.309(1)	2.296(1), 2.304(1)	2.323(2), 2.290(1)	2.30 – 2.32	2.29 – 2.34
Fe-N(2)	2.104(1)	2.102(1)	2.107(1)	2.10 – 2.11	2.10 – 2.11
Fe-N(4)	2.089(2)	2.080(2)	2.097(2)	2.08	2.08 – 2.10
Fe•••O(1)	3.324(2)	3.340(1)	3.322(1)	3.25 – 3.34	3.30 – 3.36
O(1)•••O(3)	2.821(2)	2.870(2)	2.955(2)	2.81 – 2.87	2.87 – 2.96
C(23)-O(2)	1.305(2)	1.301(2)	1.305(2)	1.30	1.30
C(23)-(O1)	1.234(2)	1.228(2)	1.224(2)	1.23	1.22-1.23
C(23)-C(ring)	1.489(3)	1.508(2)	1.499(3)	n.d.[a]	1.50
Σ (hexagon)[b]	9.25(3)	9.31(3)	9.32(3)	9.25[c] – 9.32(3)	9.31(5) – 9.35(4)

[a] The value for **7b** is subject to major inaccuracies because of the disorder, no mean distance was determined. [b] Sum of the distances contained in the hexagon spanned by Fe-O(1)-C(23)-O(2)-H(3A)-(O3)-Fe. [c] No ESD could be calculated because the O–H distance was geometrically localized and fixed; a high uncertainty is expected for this value. Despite the higher experimental accuracy, averaged bond lengths are rounded to a hundredth of an Å for clarity. N(1) and N(3) are the axial amine donors, N(2) is the pyridine nitrogen atom *trans* to the hydroxide oxygen donor O(3), N(4) is the pyridine nitrogen atom *trans* to the carboxylate oxygen donor O(2). O(1) refers to the carbonyl oxygen atom of the carboxylate ligand. C(23) is the carboxylate carbon atom and C(ring) is the adjacent carbon atom. For more details see attachment.

Table 22. Structural parameters of the structurally similar compounds **1a** (adapted from chapter 2 and previously published results),[1] **7a**, and **10a**.

	1a	**7a**	**10a**
Spacegroup	$P\bar{1}$ (triclinic)	$P\bar{1}$ (triclinic)	$P\bar{1}$ (triclinic)
T	150 K	150 K	150 K
Z	2	2	2
a [Å]	11.3035(5)	12.1533(5)	11.8410(4)
b [Å]	13.9434(8)	13.9213(5)	14.0597(6)
c [Å]	15.4818(8)	14.5995(5)	14.9777(6)
α	91.780(4)°	75.910(3)°	105.415(4)°
β	109.394(5)°	83.422(3)°	97.843(3)°
γ	102.135(4)°	89.341(3)°	90.114(3)
V [Å^3]	2236.7(2)	2379.66(16)	2379.40(17)

Overall, only subtle differences in the interatomar distances of **7** and **10** as opposed to **1** can be observed (Table 21), no significant differences are found for the relevant bond angles (see attachment). To minimize the contributions of differing packing effects and intermolecular interactions, the analysis is focused on the data obtained from the structurally similar tetraphenylborate salts **1a**, **7a**, **10a** (Table 22). Still, different steric properties, electronic interactions, and strains may have non-negligible contributions that need to be considered. The significance of such solid-state effects on e.g., bond lengths/interatomar distances can also be seen by the ranges of distances obtained from structures with differing environments at the same temperature (Table 21). Although the subtle changes paired with the potentially non-negligible solid-state effects make accurate interpretations challenging, it is attempted to interpret the interatomar distance changes with the toolbox of valence and ligand field theory.

Generally, the electronic situation of the carboxylate ligands appears to be reflected in the C–C bond lengths between the carboxylate carbon atom C(23) and the adjacent

ring carbon atom C(ring) (Table 21). Here, the C–C distance is increased for **7** (1.508(2) Å) and decreased for **10** (1.489(3) Å) as compared to **1** (1.499(3) Å). This matches theoretical considerations that a higher electron density in the π-system is linked to a higher bond order with increased π-interactions that are sensitive to the mesomeric effects of substituents. However, it appears that this is the only reliable trend that can be derived from the structural data. Although multiple influences and their expected trends that should be reflected in the interatomar distances were considered, no reliable trend can be identified from the presented data sets. For reference, an exhaustive discussion that attempts to identify any trend but comes to this conclusion is provided in the following paragraphs. However, this is only for readers that are interested in the trains of thought that lead to this conclusion.

From a simple ligand field theory approach, one could expect that the Fe–O bond lengths of the coordinating carboxylate oxygen (Fe-O_{RCOO}) decrease with increasing electron density and ligand field strength, respectively. Here however, there are two interactions that compete for this electron density: The coordination to the metal site and the proton accepting role of the carbonyl oxygen atom in the intramolecular hydrogen bond interaction. These interactions at two different sites, that are different in nature, are affected differently by variations in basicity, charge density, ligand field strength, σ-, and π-interactions. Additionally, all relevant bonds and interactions are contained in the almost planar hexagon formed by the iron ion, the coordinated carboxylate group, the hydroxide ligand, and the hydrogen bonding interaction between carboxylate and hydroxide moieties (Table 24, Table 25) and mutually affect each other. Noticeably, the sum of all distances in the hexagon remains almost the same for **1**, **7**, and **10** within the margin of error, indicating cooperative distance adjustments within this hexagon upon perturbations such as the introduction of substituents in the backbone of the benzoate. This makes the electronic situation complex and the interpretation of bond length changes within the hexagon even more challenging and not straightforward, but at the same time, all the more intriguing.

For **7**, the elongation of the Fe-O_{RCOO} bond as compared to **1** (1.955(1) Å → 1.980(1) Å) does agree with the expected reduction of the ligand strength by the introduction of an electron withdrawing –NO_2 (-M, -I) substituent. Accordingly, the Fe-N_{py} length in *trans* position is affected by the differing carboxylate ligand strength and is reduced (2.097(2) Å → 2.080(2) Å). The accompanied observation of a reduction in the Fe-O_{OH} distance

may also be expected as a stronger coordination of the negatively charged hydroxide ligand could equally compensate for the reduced electron density at the coordinating carboxylate oxygen donor. However, this effect appears to be negligibly small (1.835(1) Å → 1.833(1) Å). While the interaction with the metal site weakens as compared to **1**, the intramolecular hydrogen bond interaction appears to grow stronger despite the reduced basicity of a free $–NO_2$ substituted benzoate compared to a free benzoate (Table 19). This can be deduced from a decrease in the D…A distance (2.9552(18) Å → 2.8698(17) Å) and a decrease in the H…A distance (2.184(13) Å → 2.132(13) Å) in Table 23. Accordingly, a very minor elongation is also found for the carbonyl C–O bond (1.228(2) Å → 1.224(2) Å), albeit at the resolution limit. Because of this uncertainty, the slightly shorter D…A and H…A distances do not necessarily indicate a stronger H-bonding interaction. However, they do hint at an intricate cooperativity of the coordinative and intramolecular H-bonding interactions in these metal complexes.

In the case of **10**, the Fe-O_{RCOO} bond length would, in the first instance, be expected to follow the opposite trend (as for **7**) because the ligand strength should be increased by the electron donating –OMe substituent (-I, +M). However, this is not observed, as the Fe-O_{RCOO} bond is also slightly elongated rather than shortened as compared to **1** (1.955(1) Å → 1.969(1) Å). However, the hydrogen bond interaction apparently grows stronger as is deduced from a meaningful elongation of the carbonyl C-O bond (1.224(2) Å → 1.234(2) Å), a decrease in the D…A distance (2.9552(18) Å → 2.8209(19) Å), and a significant decrease in the H…A distance (2.184(13) Å → 2.065(15) Å) (Table 21 and Table 23). Consequently, in this case, the increased basicity of the –OMe substituted benzoate may be the dominant effect and ultimately lead to a cooperative reduction in ligand field strength of the coordinating carboxylate oxygen as compared to benzoate. This may be understood to originate from a partial delocalization of the negative charge that is induced by the H-bond-acceptor interaction of the carbonyl oxygen which reduces the electron density at the coordinating carboxyl oxygen donor.

Table 23. Selected hydrogen bond lengths and angles found in **7a**, **7b**, **10a**, **1a, 1b** and **1c.** Data for compounds containing **1** are adapted from chapter 2 and previously published results.[1]

	7a	**7b**	**10a** (150 K)	**10a** (293 K)
O(3)-H(3A)…O(1)				
d(D-H) [Å]	0.835(5)	0.840[a]	0.838(10)	0.820[a]
d(H…A) [Å]	2.132(13)	2.064[a]	2.065(15)	2.091[a]
d(D…A) [Å]	2.8698(17)	2.808(3)	2.8209(19)	2.820(3)
<(D-H-A)	147(2)°	147.3° [a]	150(2)°	147.9° [a]
	1a	**1b (a)**	**1b (b)**	**1c**[b]
O(3)-H(3A)…O(1)				
d(D-H) [Å]	0.823(10)	0.848(10)	0.839(10)	0.814(10)
d(H…A) [Å]	2.184(13)	2.11(2)	2.18(2)	2.034(17)
d(D…A) [Å]	2.9552(18)	2.874(3)	2.924(3)	2.785(2)
<(D-H-A)	156(2)°	149(3)°	147(3)°	153(3)°

D = donor, A = acceptor. [a] Here, no ESD is given because the H-atom was geometrically localized with fixed distances. [b] This structure was measured at 293 K. If not stated otherwise, the structural data is presented for measurements at 150 K.

In brief, in the case of **7**, the dominant electronic effect is suspected to be the weakening of the ligand field strength that leads to an elongation of the coordinative bond. The shortening of the O(1)…H(3A) distance can be regarded as a result of the cooperativity mediated by the hexagonal feature. In the case of **10**, the dominant electronic effect is suspected to be the increased basicity of the carboxylate that leads to the shortening of the O(1)…H(3A) distance. Here, the elongation of the coordinative bond can be regarded as the result of the cooperativity mediated by the hexagonal feature. In both cases, the cooperativity leads to a retainment of a stable configuration of the hexagon where the sum of all distances remains almost the same.

Other than for the comparison of **1** and **2**, the magnitude of the differences in H-bond strength between **1**, **7**, and **10** are so minor that the O(3)-H(3A)…(O1) angle is not a suitable measure to compare the intramolecular bond strengths because of its large uncertainty (angle highlighted in grey in Table 23). Similarly, the charge density differences at the iron sites are too minor to significantly influence the Fe-N_{amine} bond lengths (Table 21). Additionally, both structural aspects are also highly sensitive to structural strains and packing effects and, thus, poor measures for this analysis.

Table 24. Angles within the hexagon formed by the hydrogen bonding in the (carboxylato)(hydroxo)iron(III) unit in **7a**, **7b**, **10a** (150 K and 293 K) and in **1a**, **1b** and **1c**. Data for compounds containing **1** are adapted from chapter 2 and previously published results.[1]

<(L-M-L)	**7a**	**7b**	**10a** (150 K)	**10a** (293 K)
O(1)-C(23)-O(2)	125.8(2)°	125.1(3)°	124.5(2)°	124.8(2)°
C(23)-O(2)-Fe(1)	130.3(1)°	127.5(2)°	130.8(1)°	130.6(2)°
O(2)-Fe(1)-O(3)	99.81(5)°	101.88(9)°	99.01(6)°	99.23(8)°
Fe(1)-O(3)-H(3A)	110(1)°	109.5° [a]	109(2)°	109.5° [a]
O(3)-H(3A)…O(1)	147(2)°	147.3° [a]	150(2)°	147.9° [a]
H(3A)-O(1)-C(23)	104.9(5)°	108.5° [a]	105.5(6)°	105.1° [a]
Σ [°]	718(3)°	719.8° [a]	719(3)°	717.1° [a]

<(L-M-L)	**1a**	**1b (a)**	**1b (b)**	**1c**[b]
O(1)-C(23)-O(2)	124.68(15)°	123.9(2)°	124.8(2)°	124.7(2)°
C(23)-O(2)-Fe(1)	131.20(11)°	130.62(17)°	132.94(17)°	130.5(2)°
O(2)-Fe(1)-O(3)	102.93(6)°	100.33(8)°	100.13(8)°	98.16(7)°
Fe(1)-O(3)-H(3A)	101.7(17)°	107(2)°	110(2)°	108(2)°
O(3)-H(3A)…O(1)	156(2)°	149(3)°	147(3)°	153(3)°
H(3A)-O(1)-C(23)	103.0(6)°	105.2(9)°	104.6(8)°	104.5(8)°
Σ [°]	720(3)°	716(4)°	719(4)°	719(4)°

[a] No ESD is given because the H-atom was geometrically localized with fixed distances. [b] This structure was measured at 293 K. The sum of all angles is given as a measure for planarity. Ideal planarity for a six membered ring would be observed with a sum of all internal angles Σ = 720°. The estimated standard deviation (ESD) for the sum was calculated as the root sum of the squares of each individual angle. The summarized values and ESDs were subsequently rounded to integer numbers. If not stated otherwise, the structural data is presented for measurements at 150 K.

Table 25. Deviation (in Å) of the position of the atoms from the least-squares planes calculated to pass through the atoms Fe(1), O(3), H(3A), O(1), C(23), and O(2) of the (carboxylato)(hydroxo)iron(III) units in **7a**, **7b**, **10a** (150 K and 293 K), **1a**, **1b** and **1c**. Data for compounds containing **1** are adapted from chapter 2 and previously published results.[1]

	7a	**7b**	**10a** (150 K)	**10a** (293 K)
Fe(1)	0.0370 (0.0012)	0.0263 (0.0019)	0.0214 (0.0013)	0.0224 (0.0019)
O(3)	-0.0713 (0.0094)	-0.0220 (0.0180)	-0.0532 (0.0106)	-0.0695 (0.0155)
H(3A)	0.0469 (0.0129)	-0.0017 (0.0252)	0.0469 (0.0149)	0.0665 (0.0213)
O(1)	0.0278 (0.0055)	0.0286 (0.0110)	0.0003 (0.0063)	-0.0063 (0.0090)
C(23)	-0.0370 (0.0011)	-0.0188 (0.0023)	-0.0077 (0.0012)	-0.0073 (0.0018)
O(2)	-0.0035 (0.0029)	-0.0124 (0.0056)	-0.0076 (0.0032)	-0.0057 (0.0046)
rmsd[a]	0.0424	0.0204	0.0306	0.0406

	1a	**1b (a)**	**1b (b)**	**1c**[b]
Fe(1)	-0.0366 (0.0013)	0.0070 (0.0014)	-0.0093 (0.0015)	0.0440 (0.0017)
O(3)	0.0285 (0.0101)	-0.0684 (0.0147)	0.0109 (0.0147)	-0.0382 (0.0138)
H(3A)	0.0029 (0.0142)	0.0582 (0.0210)	-0.0077 (0.0200)	0.0122 (0.0195)
O(1)	-0.0379 (0.0058)	0.0367 (0.0089)	0.0020 (0.0086)	0.0131 (0.0082)
C(23)	0.0256 (0.0011)	-0.0860 (0.0018)	-0.0073 (0.0019)	0.0146 (0.0015)
O(2)	0.0176 (0.0028)	0.0525 (0.0046)	0.0113 (0.0044)	-0.0456 (0.0039)
rmsd[a]	0.0276	0.0572	0.0087	0.0316

[a] root mean square deviation. [b] This structure was measured at 293 K. If not stated otherwise, the structural data is presented for measurements at 150 K.

Concerning the derivative **12a** of compound **3a**, there is much less information to gain from the comparative structural analysis (Table 26). The only noteworthy difference is that the –OMe functionalized benzoate ligand in **12** displays a more localized character at the proximal oxygen donor as its non-functionalized counterpart. However, because

these compounds crystallize in different space groups, different strains apply that may also lead to this difference. Thus, it cannot be related directly to a ligand field effect.

Table 26. Selected bond lengths and interatomar distances (in Å) in the ferrous complex cations **12** and **3** as obtained from the structural analysis of the compounds **12a** and **3a** at 150 K. Data for **3** are adapted from chapter 2 and previously published results.[1]

	12	**3**
Fe-O(2)	2.040(2)	2.079(2)
Fe-N(1), Fe-N(3)	2.384(2), 2.394(2)	2.380(2), 2.395(1)
Fe-N(2)	2.139(1)	2.137(2)
Fe-N(4)	2.105(2)	2.107(2)
Fe-O(1)	2.305(1)	2.238(1)
C(23)-O(2)	1.273(2)	1.266(2)
C(23)-O(1)	1.261(3)	1.252(3)
C(23)-C(ring)	1.484(3)	1.496(3)

Selected distances for **12** and **3**. Despite the higher experimental accuracy, all bond lengths are rounded to a hundredth of an Å for clarity. N(1) and N(3) are the axial amine donors, N(2) is the pyridine donor *trans* to O(1) and N(4) is the pyridine donor *trans* to O(2). For more details see attachment.

In summary, it appears that an intricate cooperative interplay between the basicity and ligand field strength of the substituted benzoate ligands leads to complex interactions with the metal site and the O–H bond of the coordinated hydroxide in **1**, **7**, and **10**. All relevant bonds and interactions affected by this are contained in the almost planar hexagon formed by the iron ion, the coordinated carboxylate group, the hydroxide ligand and the hydrogen bonding interaction between carboxylate and hydroxide moieties. This hexagonal feature might mediate the cooperativity as it allows for flexible one-dimensional length adjustments in the plane to accommodate electronic changes that affect the basicity and ligand field strength differently to maintain an energetically favourable configuration of this stabilizing arrangement.

The magnitudes of the individual effects are poorly understood and difficult to derive from solid-state structures, as other effects (packing, strains, …) may also be at play and the differences between the similar structures of the three ferric complexes **1**, **7**, and **10** are small. Thus, many interpretations remain rather speculative. Despite revealing potential cooperative effects, the structural analysis alone does not allow for any prediction about the influences of these variations on the BDFE of the corresponding ferrous aqua complexes because no reasonable estimates of relative electrochemical potentials or pK_a-values can be made. The poor crystallization properties of the derivatives of **2** (**8**, **9**) and **3** (**11**, **12**) prohibit a detailed comparative analysis, as only a single derivative of **3** (**12**) and no derivative of **2** could be structurally characterized sufficiently.

3.1.3. SQUID Magnetometric Analysis

Temperature-dependent measurements of the magnetic susceptibility and magnetization at low temperatures in the solid state were done for **7b** (Figure 62) and **10a** (Figure 63) to compare the results with those obtained for **1b** (Table 27, also see section 2.1.3). A magnetic field sweep of 0-7 T at 100 K was also done to rule out significant paramagnetic impurities, proven by a linear correlation of *M* vs. *H*. Measurements on **12a** were disregarded for the same reasons as for **3a** (see section 2.1.3). However, analogous to **3a**, the magnetic ground state between 150 K and room temperature is expected to be high spin as deduced from structural bond length analysis and ligand field theory considerations (3.1.2).

Analogous to the results obtained for **1**, the derivatized hydroxo iron(III) complexes **7** and **10** display a high spin (HS) state across a temperature range between 2 K and 300 K. Deviations from the spin-only (SO) value $\chi_M T_{SO}$ = 4.38 cm^3Kmol^{-1} for an S = 5/2 HS state are well in line with previous observations[123] and are attributed to mixing of the wavefunctions of excited states and their orbital contributions into the ground state wavefunctions.

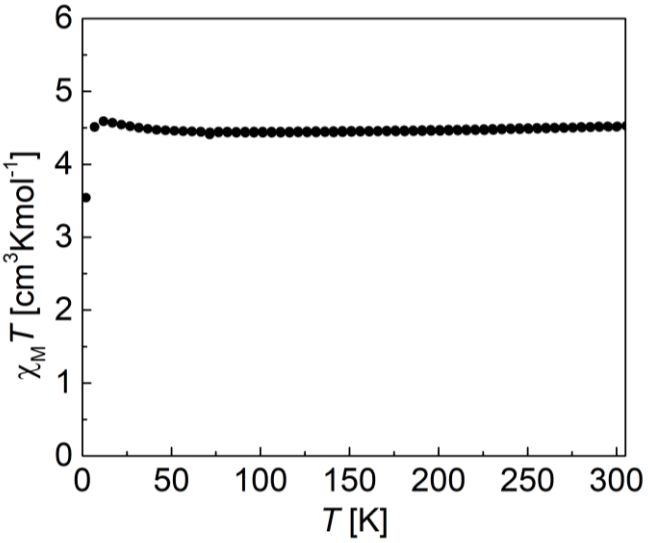

Figure 62. Temperature dependence of $\chi_M T$ for **7b** between 2 and 300 K measured at 0.5 T with a sweep rate of 2 K/min. Data points of cooling mode (300 K → 2 K) and heating mode (2 K → 300 K) are layered on top of each other.

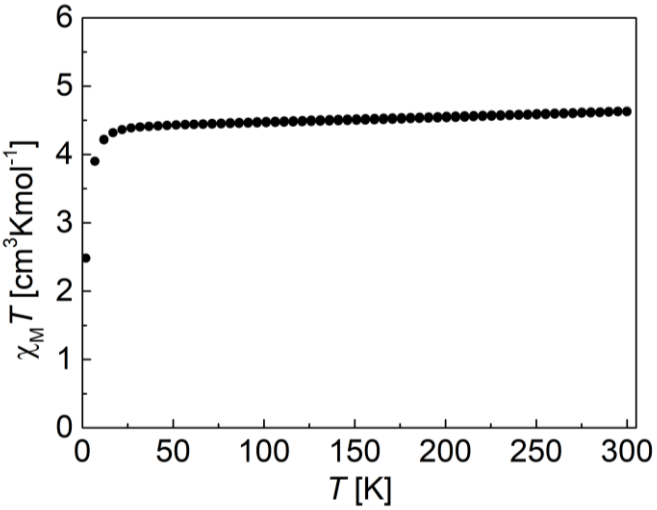

Figure 63. Temperature dependence of $\chi_M T$ for **10a** between 2 and 300 K measured at 0.5 T with a sweep rate of 2 K/min. Data points of cooling mode (300 K → 2 K) and heating mode (2 K → 300 K) are layered on top of each other.

Table 27. Magnetic data (χT) for **1**, **7** and **10** as obtained by SQUID-magnetometric measurements on **1b**, **7b**, and **10a** at 298 K, 50 K, and 2 K. Data presented for **1b** are adapted from chapter 2 and previously published results.[1]

T [K]	**1b** [cm^{3}Kmol^{-1}]	**7b** [cm^{3}Kmol^{-1}]	**10a** [cm^{3}Kmol^{-1}]
298	4.61 (HS)	4.51 (HS)	4.62 (HS)
50	4.44 (HS)	4.46 (HS)	4.43 (HS)
2	2.64	3.54	2.48

HS = high spin. Data is given at 50 K to represent the low temperature magnetic moment and spin-state without the influence of zero-field splitting effects.

Magnetization was also measured for **7b** and **10a** at temperatures between 2 K and 10 K in 1 K increments with magnetization sweeps from 0 – 7 T to obtain information about the magnitude of zero-field splitting by fitting of the temperature-dependent data. As was also the case for **1b** (section 2.1.3), satisfactory fits could be achieved for **7b** (Figure 64) and **10a** (Figure 65) despite the simplified assumption of an isotropic *g*-value.[124] However, because of such simplifications for fitting (and the differing environments in the solid state), it has to be noted that a comparative study of the magnetization properties of **1**, **7** and **10** with this method is limited to highlighting similarities and may not yield meaningful trends.

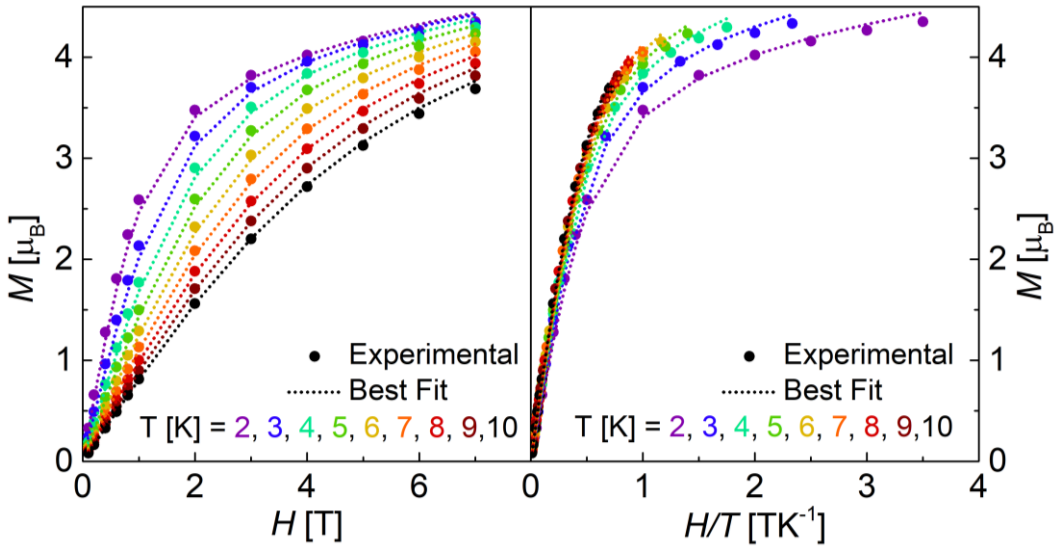

Figure 64. Variable temperature magnetization (left) and reduced magnetization plots (right) for the data (solid circles) and fits (dotted lines) obtained for **7b** between 2 and 10 K in 1 K increments. The fits were done with the PHI software by the Chilton group, assuming an isotropic *g*-value for a powdered sample.[124] Deviations of the fit vs. the experimental data at higher fields and lower temperatures are attributed to the approximation of an isotropic *g*-value. Fitting results (simplex): **7b** *g*-value = 2.028 ± 0.001, zero-field-splitting = 2.19 ± 0.02 cm^{-1} (weak parameter correlation), residual = 0.31.

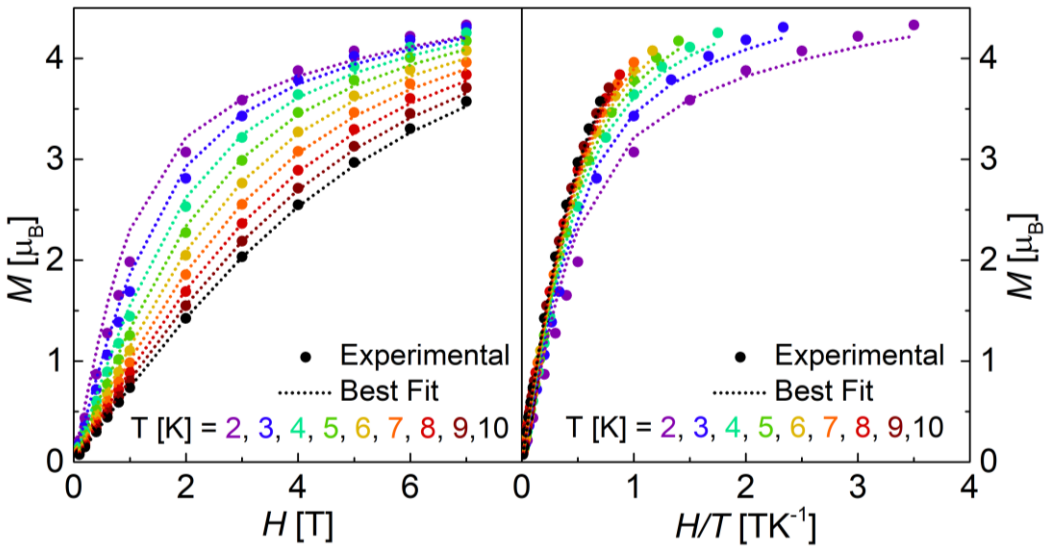

Figure 65. Variable temperature magnetization (left) and reduced magnetization plots (right) for the data (solid circles) and fits (dotted lines) obtained for **10a** between 2 and 10 K in 1 K increments. The fits were done with the PHI software by the Chilton group, assuming an isotropic *g*-value for a powdered sample.[124] Deviations of the fit vs. the experimental data at higher fields and lower temperatures are attributed to the approximation of an isotropic *g*-value. Fitting results (simplex): **10a** *g*-value = 2.014 ± 0.010, zero-field-splitting = 3.35 ± 0.17 cm^{-1} (strong parameter correlation), residual = 0.70.

For all hydroxo iron(III) complexes, a positive zero field splitting of similar magnitude ($D \approx$ 2-3 cm^{-1}) and a *g*-value of $g_{iso} = 2.0$ were found when assuming an isotropic *g*-value (Table 28). A re-examination of the of the anisotropic real *g*-values for the individual complex cations **1**, **7**, and **10** can be found in section 3.1.7, where the results of the EPR-spectroscopic analysis on frozen solutions of the hydroxo iron(III) complexes are discussed.

Table 28. Fitting results for the magnetization measurements on **1b**, **7b** and **10a** between 2 K and 10 K in 1 K increments. Data presented for **1b** are adapted from chapter 2 and previously published results.[1]

	1b	**7b**	**10a**
D	3.23 ± 0.18	2.19 ± 0.02	3.35 ± 0.17
g_{iso}	2.008 ± 0.011	2.028 ± 0.001	2.014 ± 0.010
residual	0.91	0.31	0.70
parameter correlation	0.9 (strong)	0.4 (weak)	1.0 (strong)

An isotropic *g*-value was assumed as a simplification. D = zero field splitting parameter in cm^{-1}, g_{iso} = isotropic g-value. The parameter correlation is considered strong if the magnitude is > 0.8.

In summary, the magnetic properties of **7** and **10** are very much alike those found for **1**. No significant differences are apparent within the margin of error when comparing the derivatives.

3.1.4. Mößbauer Spectroscopic Analysis

To further compare the electronic situation at the iron sites in the structurally similar compounds **1a**, **7a**, and **10a**, and to probe for any ferrous impurities (also see section 2.1.4 and chapter 4), the Mößbauer spectra of **1a**, **7a** and **10a** were measured at room temperature (Figure 66).

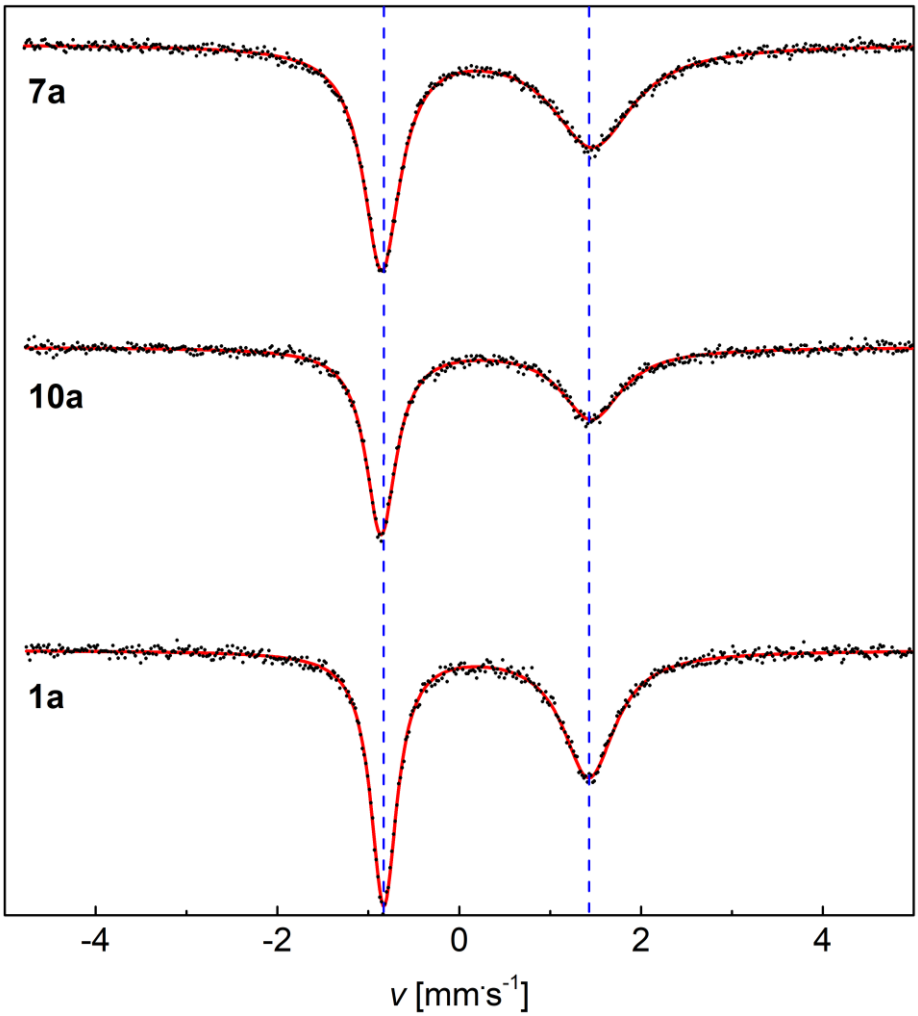

Figure 66. Stacked plots of velocities ($mm \cdot s^{-1}$) vs. relative transmissions for the experimental Mößbauer spectra (black dots) obtained on **7a**, **10a**, and **1a** at room temperature after 3 days and their respective fits (red trace). Blue dashed lines indicate deviations of the signal positions in **7a** and **10a** relative to the minima determined for the doublet in **1a** as guides for the eye. The characteristic Mößbauer parameters can be found in Table 29.

Table 29. Mößbauer parameters and selected bond lengths obtained for **1a**, **7a**, and **10a** at room temperature.

	1a	**7a**	**10a**
δ_{IS}	0.30 mms^{-1}	0.31 mms^{-1}	0.30 mms^{-1}
ΔE_Q	2.26 mms^{-1}	2.32 mms^{-1}	2.31 mms^{-1}
χ^2	1.00	1.27	1.03
Fe-O(2)	1.955(1) Å	1.980(1) Å	1.969(1) Å
Fe-O(3)	1.835(1) Å	1.833(1) Å	1.838(1) Å
Δd	0.120 Å	0.147 Å	0.131 Å

δ_{IS} = isomeric shift relative to α-Fe foil (δ_{IS}(α-Fe vs source) = 0.107 $mm \cdot s^{-1}$). ΔE_Q = quadrupole splitting. χ^2 = measure of fitting quality. Δd describes the difference in length between the two Fe–O bonds in the metal complexes with O(2) as the carboxylic donor and O(3) as the hydroxide donor as a measure for differences in anisotropy. All measurements were conducted over multiple days, the room temperature was approximately constant at 295 K during this time.

Although the Mößbauer effect in **1a**, **7a**, and **10a** was weak and the spectral resolution is rather poor at room temperature, extended data collection periods of approximately 3 days clearly allowed for the identification of a broad, asymmetric doublet with similar Mößbauer parameters in all three spectra (Figure 66, Table 29). The isomeric shift of $\delta_{IS} \approx 0.3$ mms^{-1} at room temperature as observed for **1**, **7**, and **10** is characteristic for an iron(III) site, while the rather large quadrupole splitting $\Delta E_Q \approx 2.3$ indicates a high anisotropy induced by the ligand environment. Although the quadrupole splitting is unusually high for typical ferric high spin complex, the magnitudes of the quadrupole splitting, and the isomeric shifts, are consistent with such a species containing the diazapyridinophane ligand L-$N_4{}^t Bu_2$. As explained in chapter 2 this anisotropy is characteristically caused by the strong axial distortion induced by this macrocyclic ligand and complemented by the unequal distribution of negatively charged ligands in the *cis*-(carboxylato-hydroxo)iron(III) moiety. The broad, asymmetric signal form that is observed in the spectra of **1**, **7**, and **10** when no external magnetic field is applied

and can be understood as a relaxation effect that results from a high internal magnetic field, further supporting the interpretation of an S = 5/2 high spin state.

A comparison of the spectrum of **1a** with the structurally similar derivatives **7a** and **10a** does not reveal any meaningful trends. A noticeable nuance is that in both **7a** and **10a**, the quadrupole splitting is slightly increased compared to **1a**, hinting at a more anisotropic environment around the iron(III) core. This could be a result of the increased differences in the structurally determined Fe-O distances for the negatively charged hydroxide and carboxylate donors (section 3.1.2) that may cause a more anisotropic electric field gradient. However, the minor quadrupole splitting differences only leave room for speculation rather than a resilient discussion. For the isomeric shift, all compounds effectively show the same value within the margin of error.

In summary, the data analysis confirms the spin and oxidation states in **1**, **7** and **10** to be high spin d^5 at room temperature, as expected from the results presented up to this point. Moreover, no evidence of ferrous impurities is found for any of the hydroxo iron(III) compounds. A decrease of the isomeric shift of **1a** at room temperature as compared to the previous results obtained at 90 K (0.42 → 0.30 mms^{-1}, also see section 2.1.4)[1] is attributed to temperature effects (mainly second order doppler shift).[125]

3.1.5. Infrared Spectroscopic Analysis

Infrared spectra were measured for the ferric compounds **7a**, **7b**, **10a**, **10b**, **10c** (Figure 67), and for the ferrous compounds **11a** (Figure 68), **9a** and **12a** (Figure 69). The target of the analysis, and the focus of the discussion, lies in the comparison of the O–H bond energies of the hydroxide ligands contained in the structurally similar ferric compounds **1a**, **7a**, and **10a**. The spectra of the ferrous complexes **3a**, **9a**, and **12a**, containing (derivatized) benzoate ligands that are coordinated in a chelating fashion, are also provided. A pure ferrous aqua compound containing the nitro-substituted benzoate ligand (**8**) could not be obtained. Thus, only the results obtained for **11a** which contains the methoxy-substituted benzoate ligand, are presented. All O–H bond energies obtained for the hydroxo iron(III) and the aqua iron(II) containing compounds are listed in Table 30. The spectra are depicted below, accordingly.

Table 30. O–H vibration energies obtained for all compounds containing ferric hydroxide or ferrous aqua complexes. Data presented for compounds containing **1** are adapted from chapter 2 and previously published results.[1]

	1a	**1b**	**1c**	**7a**	**7b**	**10a**	**10b**	**10c**
ν_{OH} [cm^{-1}]	3313	3392	3289	3391	3372	3308	3401[a]	3450, 3550[b]
	2a	**2b**	**2c**	**11a**[c]	**11a***[c]			
ν_{OH} [cm^{-1}]	3345	3575	3338	3368	3486			

[a] This peak was determined as the minimum of a broad signal which contains the hydroxide ligand O–H vibration but is obscured by O–H vibrations of water contained in the sample. [b] The spectrum contains two O–H vibrations, which may be attributed to a non-uniform bulk material produced by the partial loss of Et_2O, contained in the crystal, under atmospheric conditions. [c] Compound **11a*** contains solvent molecules in the crystal packing, as deduced from elemental analysis (3.1.1) and preliminary X-ray diffraction (XRD) results, which are lost under atmospheric conditions (XRD details can be provided by Dr. Harald Kelm upon request, internal reference number: 21248ocb). **11a*** represents the sample with apparent water content and **11a** represents the sample after all water has evaporated.

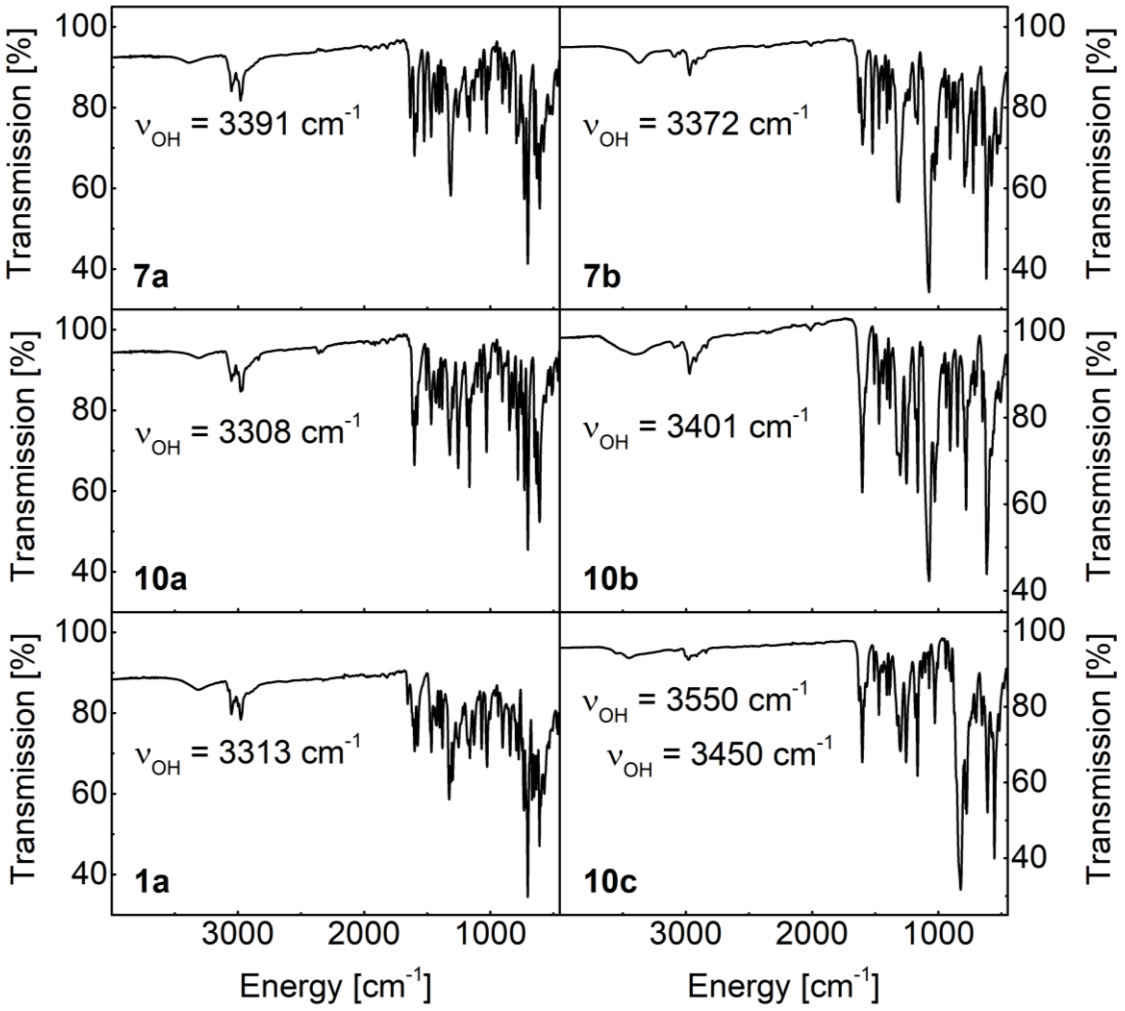

Figure 67. FTIR spectra of solid samples of **1a**, **7a**, and **10a** (left), and **7b**, **10b**, and **10c** (right) measured with an ATR-accessory under atmospheric conditions (4000 – 450 cm^{-1}). Spectra presented for compounds containing **1** are adapted from chapter 2 and previously published results.[1]

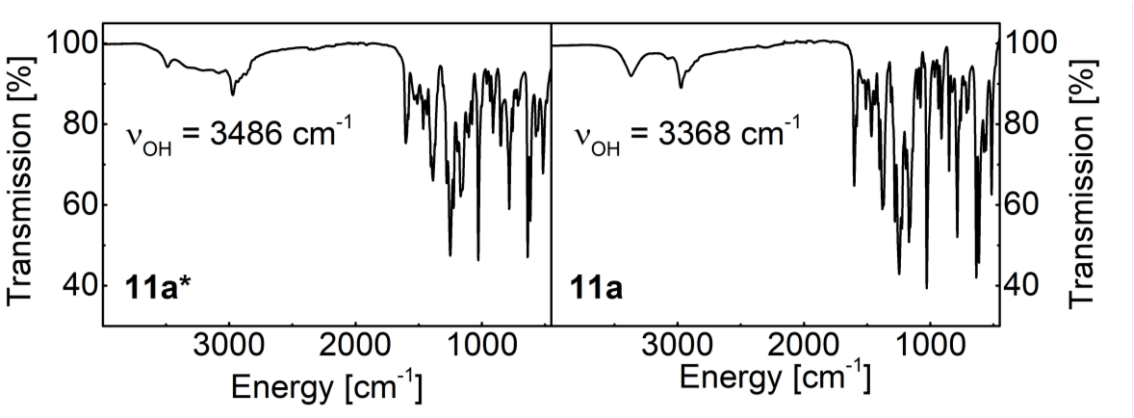

Figure 68. FTIR spectra of a solid sample of **11a**, measured directly after isolation (left) and **11a**, measured after one month of storage under aerobic conditions, with an ATR-accessory under atmospheric conditions (4000 – 450 cm^{-1}). The asterisk indicates crystal water content present in the freshly isolated sample.

As described in section 3.1.1, **10b** and **10c** may not produce reliable, representative product characterization results because of the uncertainties of solvent content in the crystals. Because of the uncertainties about the compositions of the bulk materials of **10b** and **10c**, these spectra and O–H bond energies should be treated as preliminary. Similarly, because **11a** contains solvent molecules in the crystal upon isolation (**11a***) that only evaporate completely after one month storage under atmospheric conditions, the results presented for **11a*** are only a snapshot of a bulk material with an uncertain amount of solvent residue (seemingly water) contained in the sample. Thus, only the results for the solvent free sample **11a**, obtained by allowing the crystal solvent contained in **11a*** to evaporate over one month, are reliable and reproducible.

The results for the compounds with similar compositions **1a**, **7a**, and **10a** containing different carboxylate ligands are highlighted in grey in Table 30. These compounds were chosen for comparison as no additional contacts and interactions which could influence the results were found in the structures. When comparing these compounds containing $[Fe(L\text{-}N_4{}^tBu_2)(O_2CPh^R)(OH)]^+$ cations, a slight decrease in the hydroxide O–H bond energy for R = *p*-OMe (**10**), and an increase in the hydroxide O–H bond energy for R = *p*-NO_2 (**7**) can be observed. This indicates a weakening of the O–H bond in $[Fe(L\text{-}N_4{}^tBu_2)(O_2CPh^{pOMe})(OH)]^+$ and a strengthening of the O–H bond in $[Fe(L\text{-}N_4{}^tBu_2)(O_2CPh^{pNO2})(OH)]^+$ when compared to $[Fe(L\text{-}N_4{}^tBu_2)(O_2CPh)(OH)]^+$. Such a trend would agree with a strengthening of the intramolecular H-bond between the hydroxide ligand and the carbonyl oxygen of the carboxylate ligand and can be

explained by the different basicity of these benzoate ligands. The stronger basicity of the methoxy-substituted benzoate in **10** leads to a stronger pull on the proton of the hydroxide and decreases the O–H bond energy even more than the unsubstituted benzoate in **1** (3313 cm^{-1} → 3308 cm^{-1}). The weaker basicity of the nitro-substituted benzoate leads to a weaker pull on the proton of the hydroxide and decreases the O–H bond energy less than the unsubstituted benzoate ligand in **1** (3313 cm^{-1} → 3391 cm^{-1}). The magnitude of this effect, however, is also dependent on the coordination strength of the benzoate ligands which also influences their acid/base-properties in a cooperative manner. This complex cooperativity has been explored in section 3.1.2. Additionally, as is evident by the ranges of the O–H bond energies listed in Table 30, it must be noted that the O–H bond energies are highly sensitive to structural differences. Thus, even for the structurally similar compounds, the results should be treated with caution and the above interpretations remain speculative.

As no derivative with an environment that is reliably comparable to that of **2a**, **2b(1)**, **2b(2)** or **2c**, respectively, was obtained, a comparison of the O–H bond energies with **11a** is not expected to be meaningful beyond placing it in a similar range. Thus, the O–H bond energy for **11a** is only presented in Table 30 but not further discussed.

In **3a**, **9a**, and **12a**, the C-O and C=O vibrations of the benzoate ligands are obscured by several other modes such as aromatic ring vibrations in the fingerprint of the spectrum (Figure 69). A comparison of the complex spectra with the free acids and their respective sodium salts to reliably identify the C-O and C=O vibrations was not successful and, thus, the identification of the vibrations of interest could not be achieved. Thus, although there may be some information to gain from the relative C=O and C-O bond strength that could be related to the structural analysis and be of relevance for an interpretation of the ligand field strength and H-bond strength in the ferric complexes, and the localized character of the negative charge in the ferrous complexes, it was decided to refrain from any speculative interpretations because of the high degree of uncertainty in correct peak assignment in the fingerprint of the spectra (1800 – 400 cm^{-1}). Consequently, the spectra of **3a**, **9a**, and **12a** are presented but not further discussed. Nonetheless, it should be mentioned that, although all these compounds contain one equivalent of MeCN as determined by either structural analysis and/or elemental analysis, the characteristic C≡N vibration is barely

observable because of the poor resolution because of the experimental ATR setup (see also 2.1.5).

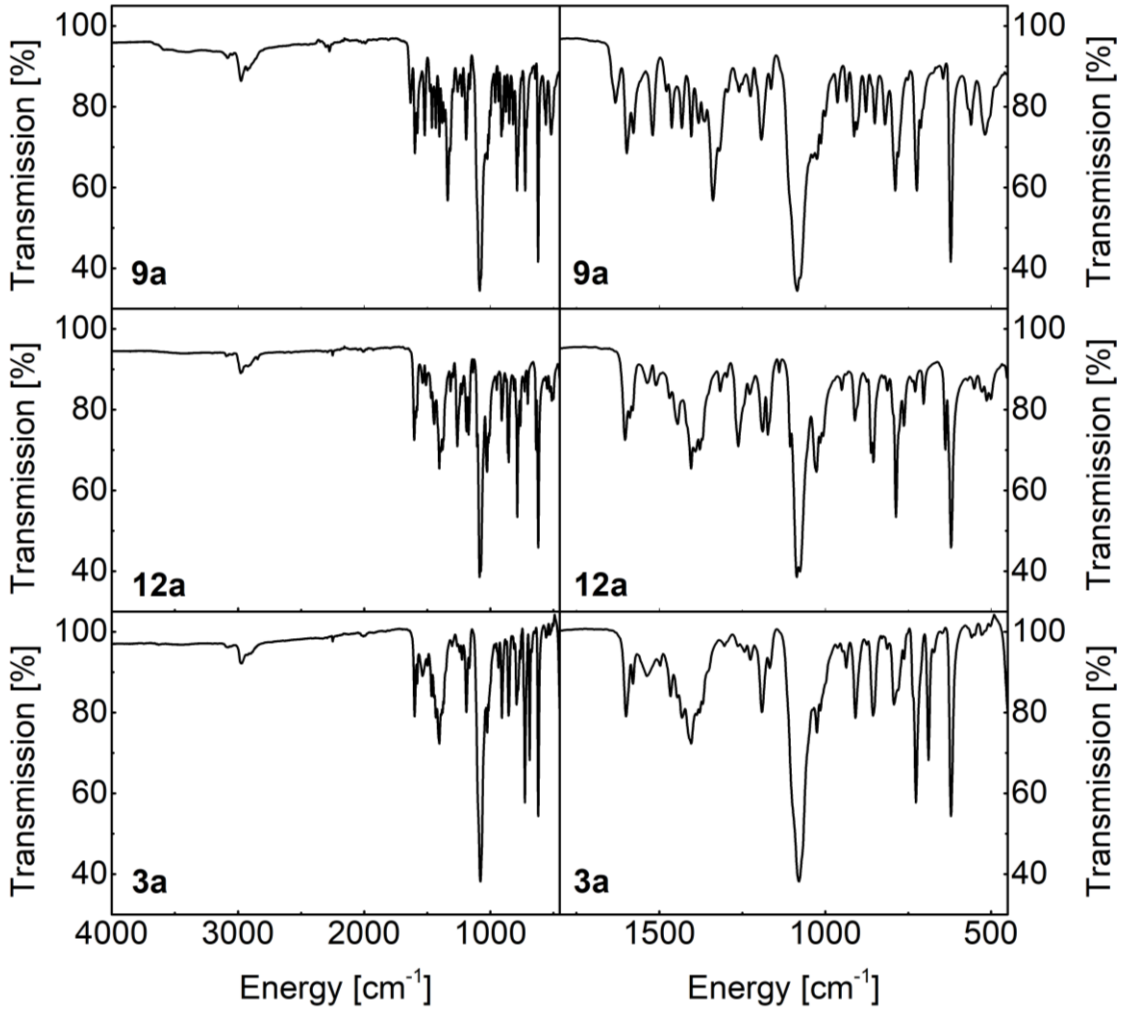

Figure 69. FTIR spectra of solid samples of **9a**, **12a**, and **3a** measured with an ATR-accessory under atmospheric conditions (4000 – 450 cm^{-1}, left; 1800 – 450 cm^{-1}, right) after isolation. Spectra presented for **3a** are adapted from chapter 2 and previously published results.[1]

3.1.6. Electronic Spectroscopic Analysis

UV-vis-NIR absorption spectra were recorded for solid samples and acetonitrile solutions of the ferric compounds **7b** and **10a** and compared with the previously described spectra for **1a** (solid, section 2.1.6), and **1b** (solution, section 2.1.7). For the spectra in solution (Figure 70), concentrations between 0.32 mmol·L^{-1} and 8 mmol·L^{-1} were used to obtain accurate molar extinction coefficients for the strong charge-transfer bands in the UV-vis region and to check for any d-d-absorptions in the vis-NIR region. For the solid spectra (Figure 71), a measurement of ground KBr powder was used to represent the scattering component *S* in equation 4 of the Kubelka-Munk approach (section 2.1.6).[127] While the absorption component *K* was obtained from a mixture of ground KBr and the respective sample **7b**, or **10a** for the UV-vis spectra, a pure ground powder without the addition of KBr was measured in the vis-NIR region to assure the absence of transitions with small molar extinction coefficients.

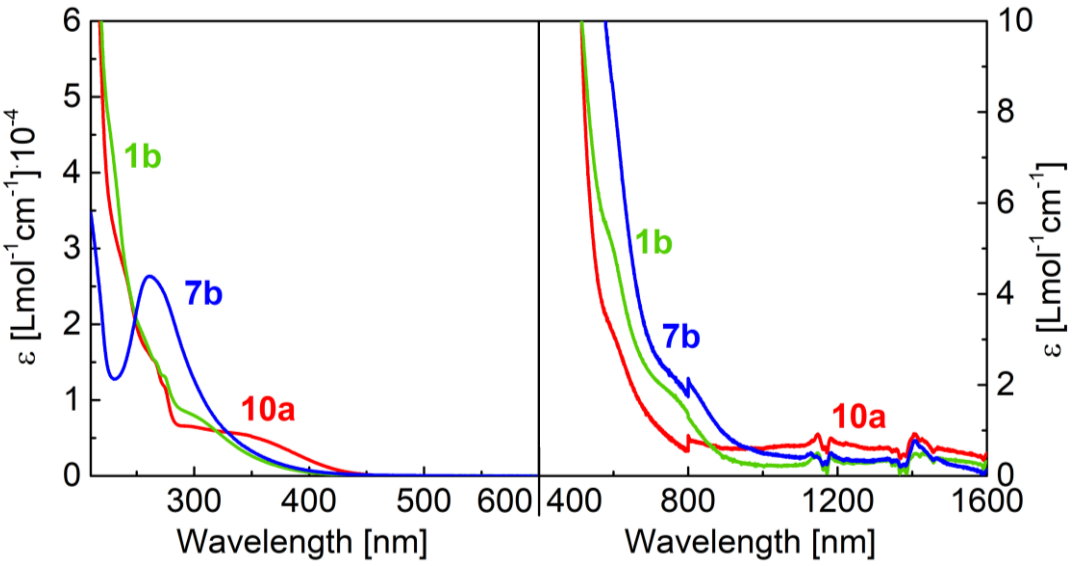

Figure 70. Electronic absorption spectra of **1b**, **7b**, and **10a** in acetonitrile solutions between 210 and 600 nm with a molar extinction coefficient ranging from 0 to 60000 Lmol^{-1}cm^{-1} (left) and of **1b**, **7b** and **10a** between 400 and 1600 nm with a molar extinction coefficient ranging from 0 to 10 Lmol^{-1}cm^{-1} (right). Spectra presented for **1b** are adapted from chapter 2 and previously published results.[1]

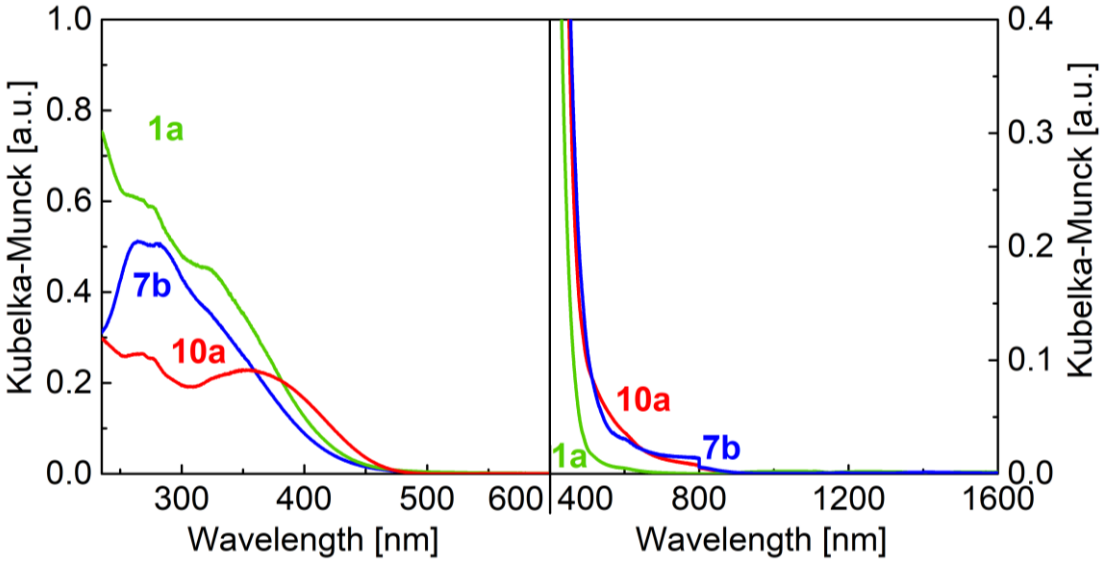

Figure 71. UV-Vis-NIR spectra of **1a**, **7b**, and **10a** in the solid state. Kubelka-Munk plot for mixtures of KBr with **1a**, **7b** and **10a**, respectively, depicted between 235-600 nm (left), and pure ground powders of **1a**, **7b**, and **10a**, depicted between 400-1600 nm (right). Spectra presented for **1a** are adapted from chapter 2 and previously published results.[1] All samples were prepared and measured under atmospheric conditions. Relative intensities for the spectra in the left image are arbitrary, as the mixtures of KBr and the respective samples were prepared qualitatively. Reflectance values for the absorption component spectra dropped below ~10 % at wavelengths lower than 235 nm. Source changeover offsets that appeared at 350 nm were corrected, detector changeover offsets that appear at 800 nm were not corrected for.

In all spectra, no spin-allowed d-d transitions in the vis-NIR spectra are observed, in agreement with d^5 high spin states for **7** and **10** analogous to **1**. Only minor absorptions are observed in the vis-region, mostly resulting from the tailing of ligand π-π^* transitions and, in the spectra of **1a** and **10a**, likely also from the vibronic excitations of the aromatic phenyl rings in the BPh_4^- counterion. To better compare the differences in the spectra of **1a**, **7b**, and **10a**, the solution-based spectra were deconvoluted into gaussian curves using MagicPlotStudent 2.8.2. The deconvoluted spectra are depicted in Figure 72. For the solid-state spectra, such a curve analysis was not done, as the relative intensities obtained from the Kubelka-Munck transformation are qualitative and generally not reliable, especially because the source change of the instrument caused an offset at 350 nm that was corrected for and would falsify any curve analysis.

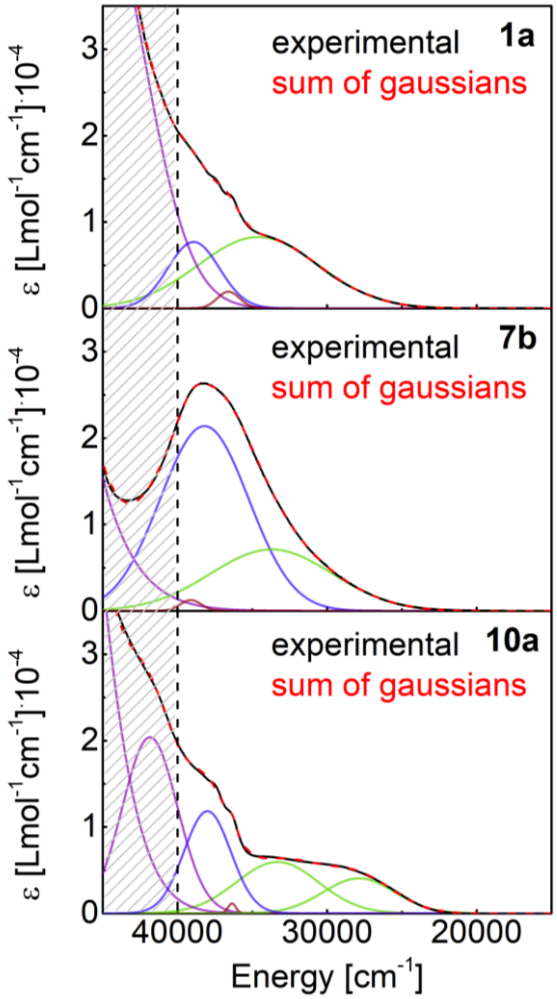

Figure 72. Deconvoluted spectra of **1a** (top), **7b** (middle), and **10a** (bottom) in acetonitrile solution fitted with gaussians depicted between 45000 – 15000 cm^{-1}. The grey hatched section above 40000 cm^{-1} is disregarded in the analysis because the absorbance of the features above 40000 cm^{-1} (250 nm) in the recorded spectra exceeded a value of 1 and, thus, the obtained fits and molar extinction coefficients for this region may not be representative. The individual curves are color-coded for a more facile comparison in Table 31. The envelope curve (sum of all gaussians) is given as red dashed line, the experimental data is given as black line. Fitting region: 45000 – 10000 cm^{-1}.

While the spectra of **1a** and **10a** are partly obscured by additional transitions of the BPh_4^- counterion, all three spectra contain somewhat similar absorptions at energies below 40000 cm^{-1} that can be attributed to the complex cation. The fitting of the spectra resulted in the identification of three distinct features, the energies and molar extinction coefficients of which are listed in Table 31.

Table 31. Results of gaussian curve analysis (Figure 72). Energies and molar extinction coefficients for the absorptions determined below 40000 cm^{-1} (250 nm).

	1a		**7b**		**10a**	
curves	cm^{-1}	$Lmol^{-1}cm^{-1}$	cm^{-1}	$Lmol^{-1}cm^{-1}$	cm^{-1}	$Lmol^{-1}cm^{-1}$
green	34608	8255	33722	7100	27869, 33318[a]	5950, 4955[a]
brown	36595	1933	39110	1247	36357	1138
blue	38921	7684	38200	21281	38003	11822

[a] The broad absorption in the lower UV energy range around 30000 cm^{-1} was fitted with two gaussians (green curves) to attain a satisfactory fit. Data presented for **1a** are adapted from chapter 2 and previously published results.[1]

A rather minor feature is situated at an energy of 36595 cm^{-1} in **1a** and 36357 cm^{-1} in **10a**, respectively. Despite this not being apparent at first glance for the solution spectrum of **7b** in acetonitrile, the solid-state spectrum clearly shows that such a feature is also observed for this sample. A gaussian with a similar molar extinction coefficient of 1000 – 2000 $Lmol^{-1}cm^{-1}$ at a slightly shifted energy of 39110 cm^{-1} is, in fact, required to obtain a reasonable fit for the spectrum of **7b** in acetonitrile solution.

The most prominent feature in the solution spectrum of **7b** is a strong absorption at 38200 cm^{-1} (~21281 $Lmol^{-1}cm^{-1}$). Although weaker and slightly shifted, a similar absorption is also present in the solution spectra of **1a** (38921 cm^{-1}, 7684 $Lmol^{-1}cm^{-1}$), and **10a** (38003 cm^{-1}, 11822 $Lmol^{-1}cm^{-1}$). It is assumed, that this absorption is a π-π^* transition of the benzoate ligand.[158] Notably, the excitation is shifted to lower energies (batochromic shift) as the substituents compliment the delocalization of the π-electron system by inductive and, most importantly, mesomeric effects. The differences in intensities may be explained by an increased transition probability in the enhanced π-electron systems, especially in the case of the $-NO_2$ substituent that contributes with a delocalization over two N–O bonds rather than just one C–O bond as is the case for the -OMe substituent.

At the border of the vis-region, the tailing of the strong signal at 38200 cm^{-1} in **7b** cannot be fitted by a single gaussian but requires the overlaying of a second gaussian situated

at 33722 cm^{-1} (7100 $Lmol^{-1}cm^{-1}$) according to the fitting model. This interpretation is supported by a similar absorption determined for **1a** (34608 cm^{-1}, 8255 $Lmol^{-1}cm^{-1}$). In **10a**, it appears that the feature is also present, however it requires two gaussians for appropriate fitting (27869 cm^{-1}, 4955 $Lmol^{-1}cm^{-1}$; 33318 cm^{-1}, ~5950 $Lmol^{-1}cm^{-1}$). Nevertheless, the sum of these two gaussians yield the same magnitude for the molar extinction coefficient as observed for the absorptions in **1a** and **7b** situated at similar energies, supporting the interpretation that these two gaussians represent the splitting of a single feature present in the other spectra. Generally, a batochromic shift can also be observed for this absorption in the derivatized complexes **7** and **10** as compared to **1**. As this is also suspected to be a π-π^* transition of the benzoic acid ligand, the batochromic shift matches the expectations.

Although the deconvolution of the solid-state spectra is not feasible and although **1a** and **10a** are distinct from **7b** because of the differences in counterions, the most prominent features attributed to the cations are clearly present at similar energies. Some additional observations are that the low energy absorption extends furthest into the vis-region for **10a** and that the strongest absorption in **7b** remains at ~260 nm (~38500 cm^{-1}). The minor feature at ~275 nm (~36500 cm^{-1}) is visible in all spectra. The similarities of **7** and **10** with **1** in the UV-vis region and the absence of absorptions in the lower energy vis-NIR region indicate that the mononuclear high spin hydroxo iron(III) species **7** and **10** are also retained in solution (also see chapter 2 for arguments of stabilization of **1** in solution).

Finally, as has been reported for **1** (section 2.1.7),[1] also **7** and **10** do not appear to exhibit a significant absorption between 500 – 600 nm with a molar extinction coefficient of approximately 1000 $Lmol^{-1}cm^{-1}$ even in solution, excluding the formation of diferric μ-oxo bridged complexes.

3.1.7. EPR-Spectroscopic Analysis on Frozen Solutions

The electronic spectroscopic analysis described above highlights the stability of the cations **7** and **10** in solution. Thus, an EPR-spectroscopic analysis on frozen solutions in dimethylformamide (DMF) containing 0.2 mol·L^{-1} tetrabutylammonium perchlorate (TBAP) was conducted with **7b** and **10a** to further investigate their magnetic properties. The effective *g*-values were determined for the spectra recorded at 10 K and the real *g*-values as well as the rhombicity were determined by fitting of these spectra using EasySpin (Figure 73).[130] The results are compared to those obtained for **1** in Table 32. Spectra at varying temperatures were used to probe for any significant differences in the *T*-dependent populations of the M_S levels (zero-field splitting, ZFS) compared to **1**, for which the ZFS parameters were explicitly determined by correlated fitting of all *T*-dependent spectra (see section 2.1.8).

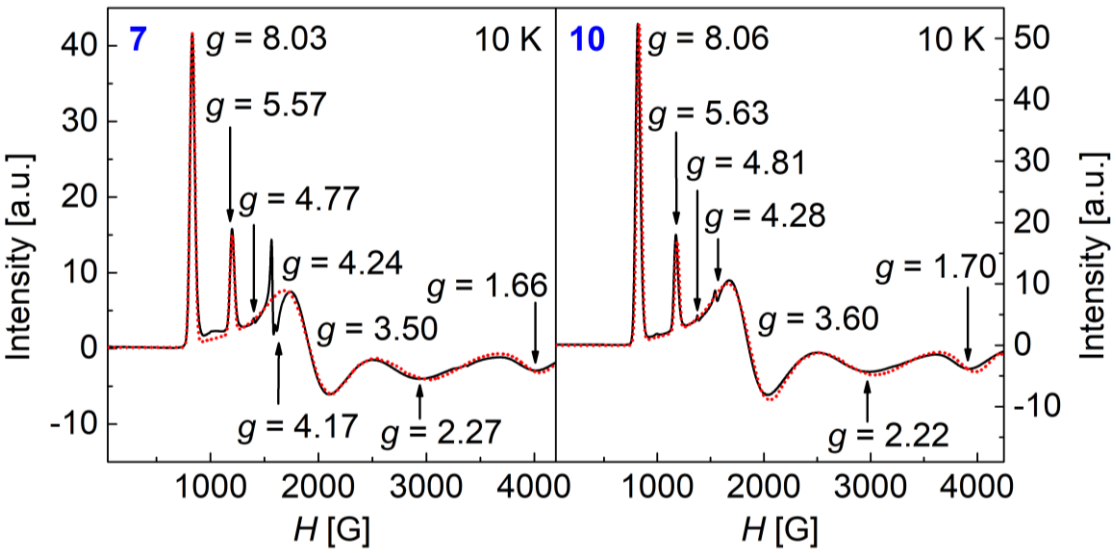

Figure 73. Experimental X-band EPR spectra (50 – 4200 G) of frozen solutions of **7** (9.3527 GHz) and **10** (9.3481 GHz) in DMF containing 0.2 mol·L^{-1} TBAP at 10 K (black trace) and simulated spectra (red dotted trace).[130] Effective *g*-values obtained from the experimental spectrum are indicated. Very minor paramagnetic contaminants are found at g = 4.77, g = 4.24, and g = 4.17 for **7**, and g = 4.81 and g = 4.24 for **10**, respectively.

Table 32. Experimental and fitted parameters obtained for the EPR-spectra of frozen solutions of **1a**, **7b**, and **10a** at 10 K and the respective simulations.

	1[a]	**7**[c]	**10**[c]
M_S = ±1/2 Kramer Doublet	g_x = 3.55	g_x = 3.50	g_x = 3.60
	g_y = 8.12	g_y = 8.02	g_y = 8.06
	g_z = 1.69	g_z = 1.66	g_z = 1.70
M_S = ±3/2 Kramer Doublet	g_x, g_y = 2.27	g_x, g_y = 2.27	g_x, g_y = 2.22
	g_z = 5.65	g_z = 5.57	g_z = 5.63
E/D	0.107	0.108	0.106
real g_x, g_y, g_z	1.999, 1.997, 1.995	1.982, 1.963, 1.970	2.003, 1.982, 1.991

[a] Measured at 9.3452 GHz, impurities found at *g* = 4.84 and *g* = 4.28. [b] Measured at 9.3527 GHz, impurities found at *g* = 4.77, *g* = 4.24, and *g* =4.17. [c] Measured at 9.3481 GHz, impurities found at *g* = 4.81 and *g* = 4.28. Data presented for **1** are adapted from chapter 2 and previously published results.[1]

The experimental spectra obtained for **7** and **10** closely resemble the spectrum obtained for **1**. Only negligible differences are found for the effective *g*-values of the complex cations. Likewise, the fitting of the spectra to an S = 5/2 species with equation 5 using EasySpin resulted in similar rhombicities, and real *g*-values, with an increased rhombicity and *g*-anisotropy for **7**, and a decreased rhombicity and *g*-anisotropy for **10**, compared to **1**.[130] The *g*-values of the minor impurities at $g \approx 4.8$ and $g \approx 4.3$ in the spectra of **7** and **10** have also been found in **1**, the latter is commonly observed for ferric samples.[61,128,129] Minor systemic offsets of the *g*-values between **1**, and **7** and **10** especially at lower fields may occur because of minor calibration differences, as the spectra of **7** and **10** were recorded with a different spectrometer than **1** (see methods).

$$\widehat{H} = \mu_B \boldsymbol{B}^T \cdot \boldsymbol{g} \cdot \widehat{\boldsymbol{S}} + D\left[\hat{S}_z^2 - \frac{S(S+1)}{3}\right] + E\left[\hat{S}_x^2 - \hat{S}_y^2\right] \quad (5)$$

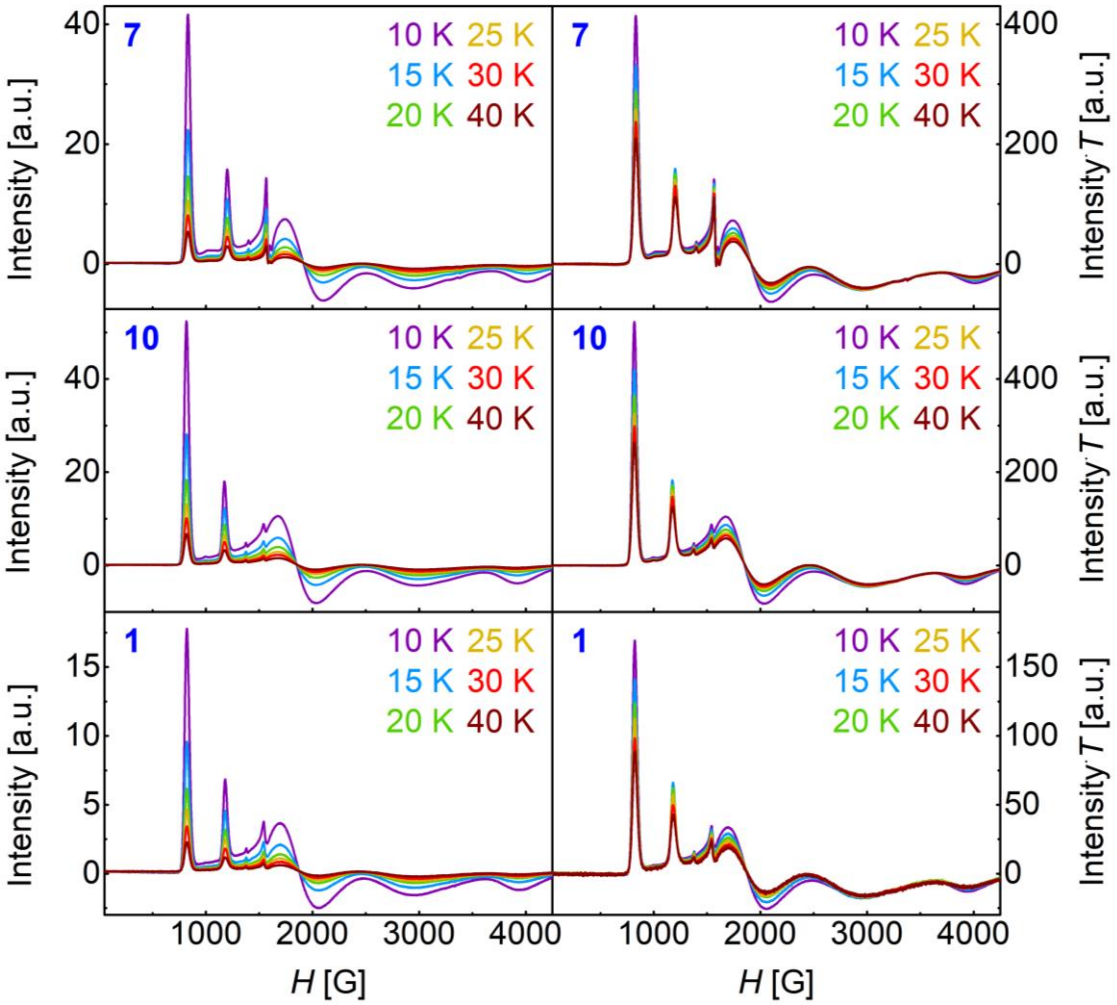

Figure 74. X-Band EPR spectra at variable temperatures (left) and X-Band EPR spectra at variable temperatures multiplied by temperature (right) between 50-4200 G for **7**, **10** and **1**. Spectra presented for **1a** are adapted from chapter 2 and previously published results.[1] Frequencies in GHz for **7** (*T*): 9.3427 (10 K), 9.4010 (15 K), 9.3483 (20 K), 9.3482 (25 K), 9.3480 (30 K), 9.3476 (40 K); **10** (*T*): 9.3481 (10 K), 9.3479 (15 K), 9.3478 (20 K), 9.3475 (25 K), 9.3474 (30 K), 9.3472 (40 K); **1** (*T*): 9.3452 (10 K), 9.3450 (15 K), 9.3449 (20 K), 9.3448 (25 K), 9.3447 (30 K), 9.3444 (40 K).

The temperature dependent population of the Kramer doublets M_S = ±1/2, ±3/2, ±5/2 and their transition probabilities appear almost identical for all three compounds in the respective set of spectra (Figure 74). This is especially clear, when the temperature effect on the magnetic susceptibility and, thus, on the relative intensities, is mostly subtracted by multiplying the spectra with the measurement temperatures. Here, in all spectra, a positive ZFS of similarly small magnitude can be deduced as M_S = ±3/2

transitions increase in relative intensity compared to $M_S = \pm 1/2$ transitions at higher temperatures. Transitions for $M_S = \pm 5/2$ cannot be observed in any of the spectra. The close similarity of the magnitudes for the zero-field splitting is in good agreement with the results obtained from magnetization experiments described in sections 2.1.3 and 3.1.3 and leads to the conclusion, that the zero-field splitting parameter for all hydroxo iron(III) complexes **1**, **7** and **10** presented up to this point is $D \approx +3$ cm^{-1}.

3.1.8. ESI-Mass Spectrometric Investigation

ESI-mass spectrometry was measured for acetonitrile solutions of the ferric compounds **7b**, **10b**, and the ferrous compounds **9a**, **11a**, and **12a**.

Because the synthesis of the derivatives of **1** (**7** and **10**) was more challenging regarding the full conversion of the precursor complex $[Fe(L\text{-}N_4{}^tBu_2)(OMe)_2]^+$ to the desired products as for **1** (see section 3.1.1), the ESI mass spectra proved to be a useful tool to probe for purity and to optimize the synthesis to yield analytically pure bulk samples, as precursor contaminants could be clearly discerned at m/z = 470.2, if present (Figure 75).

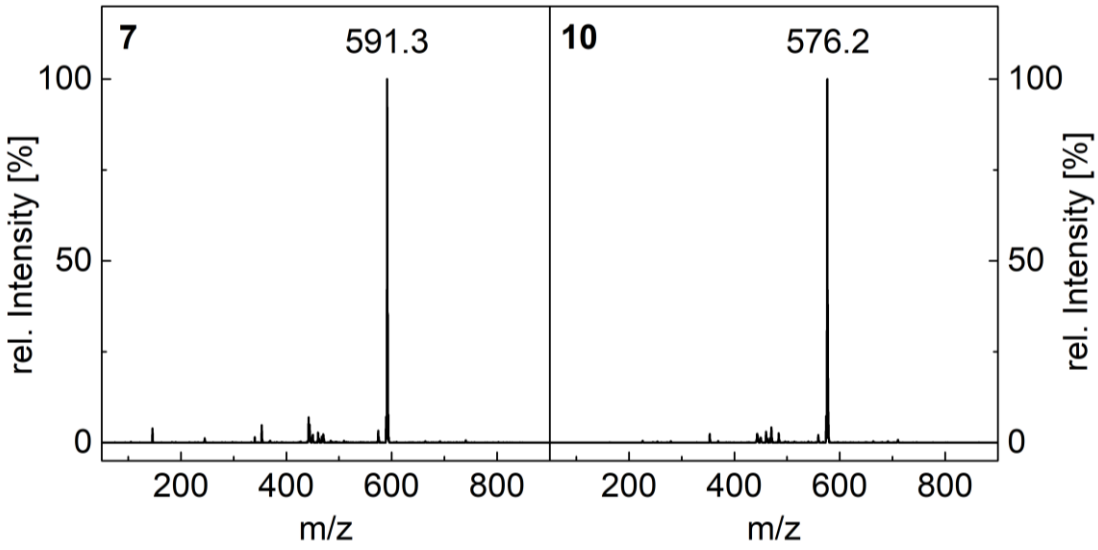

Figure 75. ESI-mass spectra of **7** and **10**, each obtained from acetonitrile solutions of **7b** and **10b** with the soft ionization preset of the instrument between m/z = 50-900. Minor background signals and fragmentation products are observed, no significant signal was found at m/z = 470.2.

As has been described for **1**,[1] also **7** and **10** are sensitive to the ionizing conditions of the ESI mass spectrometric method even under ideal soft ionization parameter settings (see section 2.1.9) and produce minor signals at 574.3, and 559.2, respectively (Figure 76), corresponding to the loss of a hydroxide radical and the formation of **9** and **12** (see below).

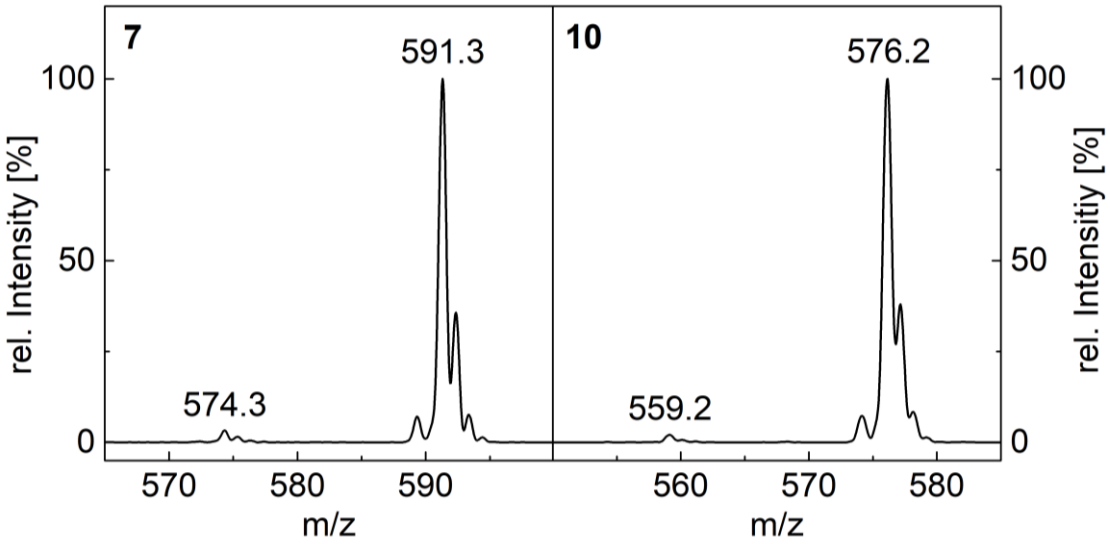

Figure 76. Enhanced region of interest for the ESI-mass spectra of **7** and **10**, each obtained from acetonitrile solutions of **7b** and **10b** with the soft ionization preset of the instrument (see methods).

When comparing the experimental spectra with the simulated spectra, the isotope pattern and the m/z-values match well (Figure 77). Minor deviations are attributed to calibration errors (tolerated methodic error ±0.3, here much smaller). Measurements of acetonitrile solutions of compounds containing **7** or **10** with other counterions render essentially identical cationic spectra and are, thus, not depicted explicitly.

Generally, it can be deduced that the derivatives (**7** and **10**) of **1** show similar behaviour with respect to the ionization and mass-spectrometric flight properties, as would be expected for the rather subtle change of a substituent in the carboxylate ligand backbone. Although these properties are well understood in analogy to investigations with **1**, and no relevant trends related to the derivatization can be deduced, mass spectrometric analysis proved to be a valuable tool in the development of a suitable synthesis to obtain pure samples and remains important to probe for possible educt impurities of **4** present in individual batches.

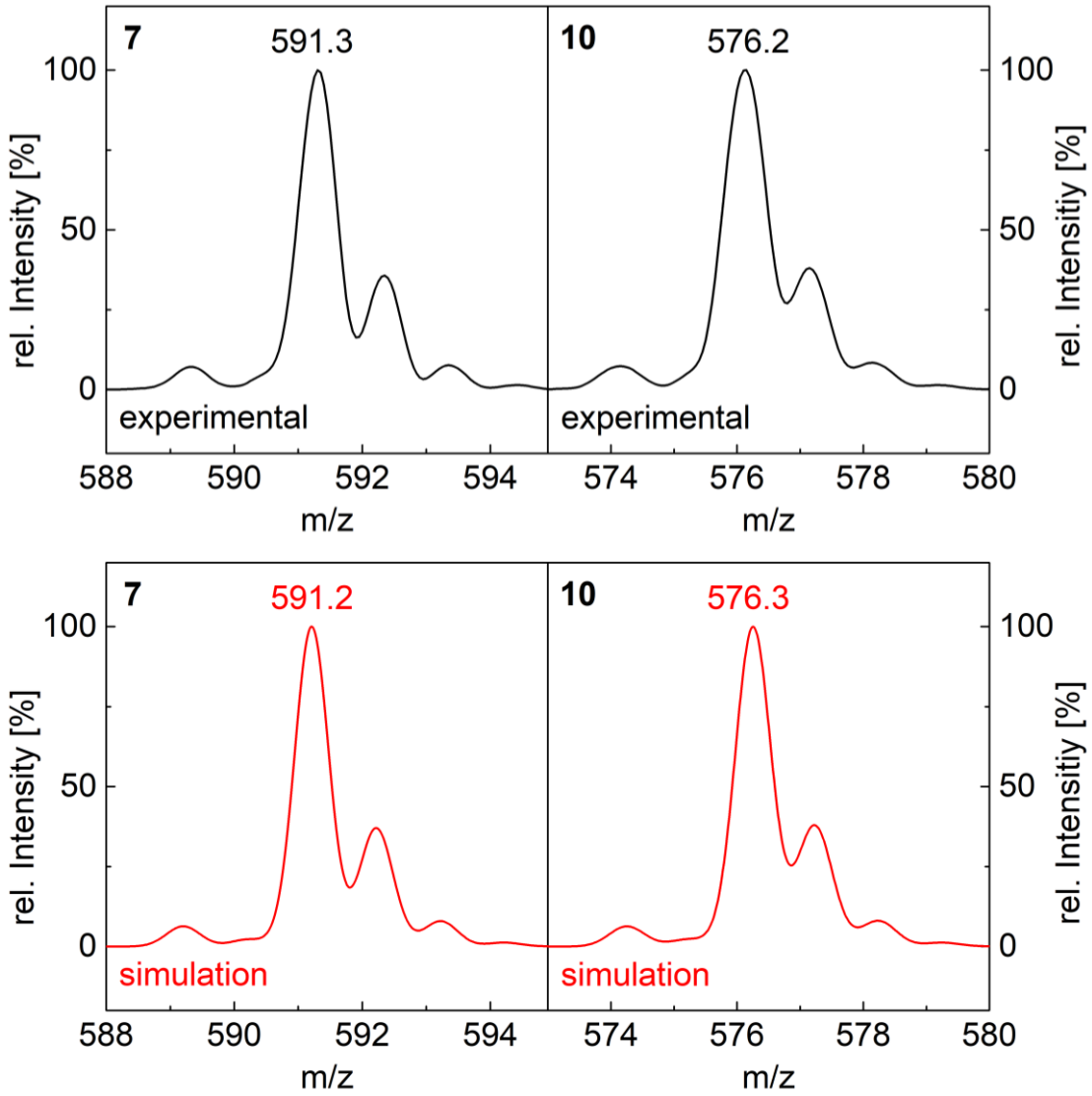

Figure 77. Experimental ESI mass spectra of **7** and **10** (top), each obtained from acetonitrile solutions of **7b** and **10a** with the soft ionization preset of the instrument, and respective simulations (bottom) for $Fe[L\text{-}N_4{}^tBu_2](O_2CPh^{pNO2})(OH)]^+$ (**7**, m/z = 591.2), and $[Fe(L\text{-}N_4{}^tBu_2)(O_2CPh^{pOMe})(OH)]^+$ (**10**, m/z = 576.3).

As is the case for the ferric complexes, also the derivative of **2** (**11**) and the derivatives of **3** (**9** and **12**) show similar behaviour under ESI mass spectrometric conditions (Figure 78, see also Figure 32, section 2.1.9). On the one hand, under ionizing conditions, the water ligand in **11** is lost and a spectrum that is essentially identical to the cationic spectrum of an acetonitrile solution of **12a** with a major signal at m/z = 559.5 is observed for **11a**. On the other hand, the spectrum of a solution of **9a** is well-behaved and shows a signal at m/z = 574.3 corresponding to **9**. The identification of the observed signals at m/z = 559.5 and m/z = 574.3 as cations **12** and **9**, respectively, matches well with accompanying simulations (Figure 79).

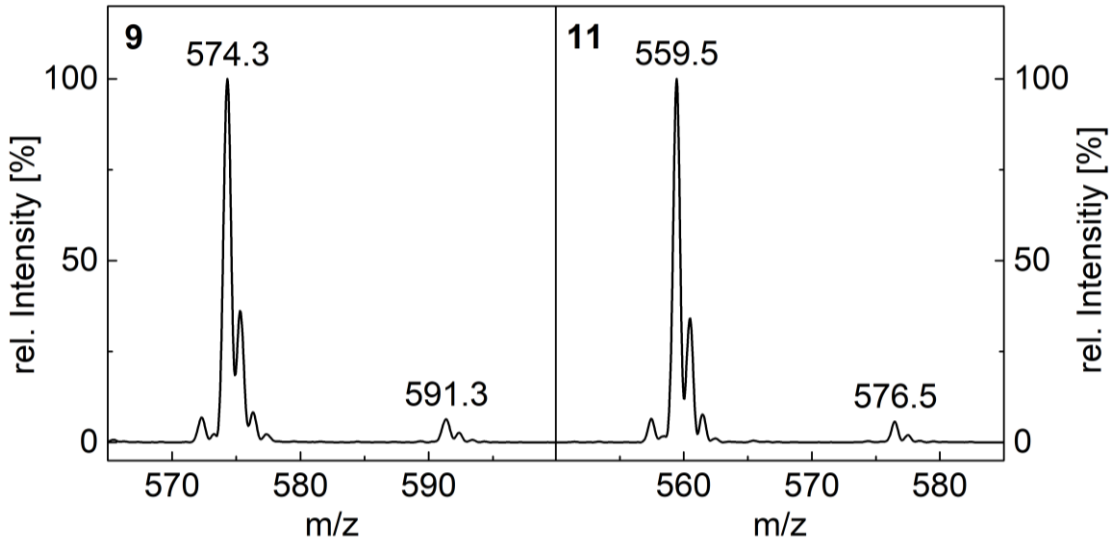

Figure 78. Enhanced region of interest for the ESI-mass spectra obtained from acetonitrile solutions of **9a** and **11a** with the soft ionization preset of the instrument. The spectrum of **11a** is essentially identical to the spectrum obtained with an acetonitrile solution of **12a**.

It should also be mentioned that, in analogy to the equilibrium observed for **2** and **3** in solution (section 2.1.7), similar equilibria are expected to be present in acetonitrile solutions for **8** and **9**, and **11** and **12**, respectively, which may further contribute to the observance of cation **12** in the ESI-mass spectrum recorded for the solution of a compound containing **11**.

These results demonstrate that the loss of a water ligand under ESI-MS ionizing conditions, and most likely also the above-mentioned equilibria, are intrinsic properties of the ferrous carboxylate complexes described in this work. However, also for the ferrous compounds, the ESI-mass spectrometric analysis purely serves as a characterization method, since no trends linked to the derivatization of **2** or **3**, respectively, can be deduced from the spectra.

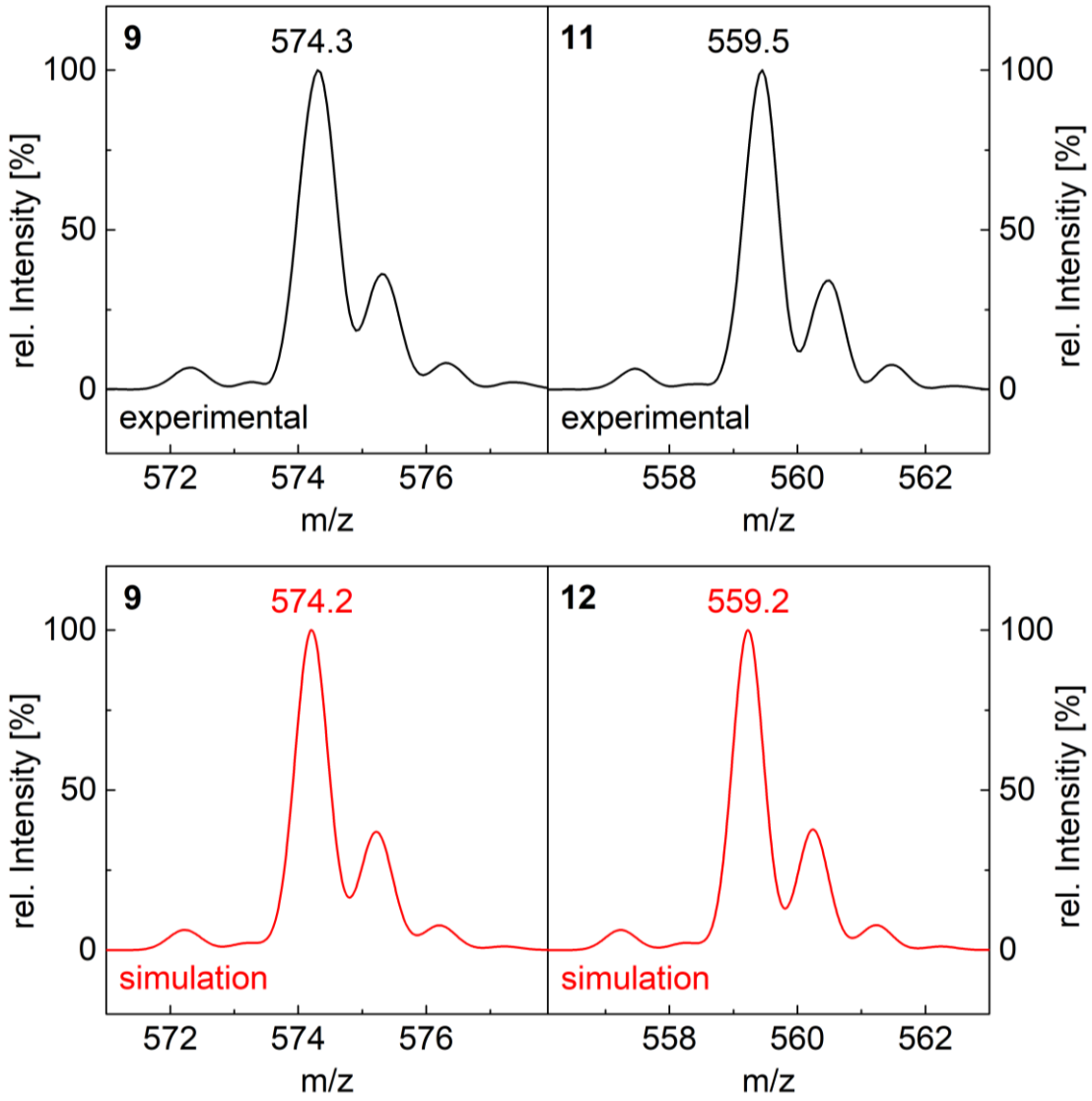

Figure 79. Experimental ESI mass spectra of acetonitrile solutions of **9a** and **11a** with the soft ionization preset of the instrument, and respective simulations (bottom) for Fe[L-N$_4$*t*Bu$_2$](O$_2$CPh^{pNO2})]$^+$ (**9**, m/z = 574.2), and [Fe(L-N$_4$*t*Bu$_2$)(O$_2$CPh^{pOMe})(OH)]$^+$ (**12**, m/z = 559.2). In the case of **11a**, the neutral aqua ligand is lost under ionizing ESI mass spectrometric conditions, leading to the observation of cation **12**. Spectra of **12a** render essentially the same spectrum as **11a**.

3.1.9. Electrochemical Investigation

To study the reduction potentials of **1**, **7** and **10**, cyclic voltammetry (CV) was measured at varying scan rates for acetonitrile solutions of **1a**, **7b**, and **10a** containing 0.2 $molL^{-1}$ tetrabutylammonium perchlorate (TBAP) as electrolyte under a nitrogen atmosphere in a glove box (Figure 80). Although **1** had already been measured on a solution of **1c** (section 2.1.10), a remeasurement of this cation was done to ensure the same conditions within the series. This was considered necessary as the appearance of the obtained CV curves for all the ferric hydroxide compounds seemed to be sensitive to water impurities in the glovebox and consequently in the acetonitrile solvent that was used to prepare the solutions because of its protic properties. This sensitivity is expressed as broadening of the features and a decrease in the intensity of the $[Fe^{II}(L\text{-}N_4{}^tBu_2)(O_2CPh^R)(OH)]/[Fe^{III}(L\text{-}N_4{}^tBu_2)(O_2CPh^R)(OH)]^+$ reoxidation process, supposedly caused by the protonation of the electrochemically generated neutral ferrous hydroxide complex by water residues. The water content in the glovebox atmosphere could not be controlled because the storing of the calomel electrode and the required saturated KCl solution was necessary for electrochemical measurements and no sensor was available for external monitoring. Thus, a sequential measurement of the series under the same conditions is expected to exhibit the most reliable results concerning the trends in relative electrochemical potentials.

Although two of the three compounds (**1a** and **10a**) contain the rather unfavorable BPh_4^- anion that is often avoided in electrochemical studies because it limits the study of oxidation processes at half-wave potentials of above about +700 mV, there is good reasoning for this choice.[159] The arguably most interesting potential for the Fe^{3+}/Fe^{2+} redox pairs in these complexes is expected to lie at redox potential that is more than 1 V more negative, which is thus not influenced by the limitations imposed by the counterion. Moreover, the study of the redox potentials is most relevant to the investigation of relative reactivities and bond dissociation free energies (BDFEs). As these require highly pure and well-defined compounds, and this was best achieved with **7b** and **10a**, the named compounds were chosen for the electrochemical investigation. To maintain good comparability, the compound used in the reactivity studies for the determination of the BDFE, **1a**, was chosen as a reference point. As the calomel reference electrode was under maintenance multiple times over the course of

this work and it showed deviations in the relative potentials for the ferrocene/ferrocenium redox pair (see section 2.1.10), the comparison of all potentials was done relative to the half-wave potential of this redox pair $E_{1/2}$(Fc/Fc$^+$) to ensure consistency and accurate ΔE determinations (Table 33).

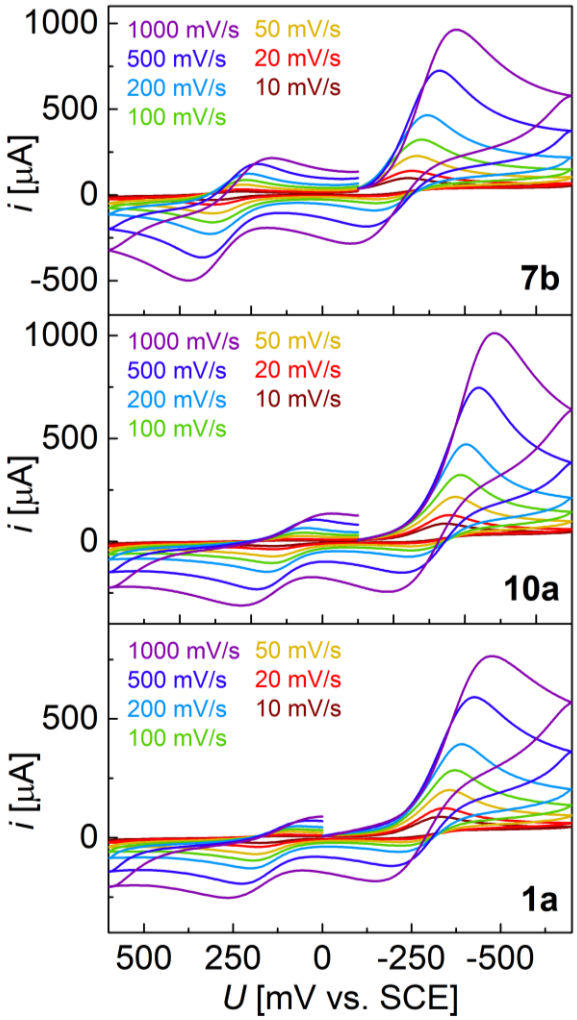

Figure 80. Scan-rate dependent cyclic voltammetry results for **7**, **10**, and **1** measured on acetonitrile solutions of **7b**, **10a**, and **1a** under nitrogen atmosphere in a glove box vs a saturated calomel electrode (SCE). Under the given experimental conditions for this series of measurements, the half-wave potential of the ferrocene/ferrocenium redox pair was determined to be $E_{1/2}$(**Fc/Fc$^+$**) = 495 mV vs SCE. Only one cycle is depicted. The difference in current at 0 mV is an artefact created by the choice of initial voltage, with multiple cycles or different initial voltages the curves would represent closed loops like those shown for **1** in section 2.1.10.

Table 33. Redox potentials and error margins obtained at sweep rates of 100 mV/s for the CV measurements with acetonitrile solution of **7b**, **10a**, and **1a**. Previous results obtained for **1c** are given for comparison (all listed values referenced against Fc/Fc^+).[1]

	7b[a]	**10a**[a]	**1a**[a]	**1c**[b]
$E_p(red)_1$ [mV]	-775 ± 2	-883 ± 5	-867 ± 3	-846 ± 2
$E_p(ox)_1$ [mV]	-647 ± 7	-744 ± 8	-714 ± 14	-734 ± 10
$\Delta E_p(red\text{-}ox)_1$ [mV][c]	128 ± 5	139 ± 7	153 ± 10	112 ± 7
$E_{1/2}(redox)_1$ [mV][c]	-711 ± 3	-814 ± 4	-791 ± 5	-790 ± 4
$E_p(ox)_2$ [mV]	-187 ± 8	-362 ± 5	-302 ± 7	-321 ± 6
$E_p(ox)_2$ [mV]	-282 ± 2	-444 ± 16	-422 ±20	-404 ± 8
$\Delta E_p(red\text{-}ox)_2$ [mV][c]	95 ± 6	82 ± 12	120 ± 15	83 ± 7
$E_{1/2}(redox)_2$ [mV][c]	-235 ± 3	-403 ± 6	-362 ± 7	-362 ± 4

E_p = peak potential, red = reduction, ox = oxidation, $E_{1/2}$ = half-wave potential. The potentials for Fe^{3+}/Fe^{2+} pair of interest are indicated with the number 1, the second process is indicated with number 2. [a] $E_{1/2}(Fc/Fc^+)$ = 495 mV vs SCE. [b] Adapted and revised previously published values to display error margins,[1] $E_{1/2}(Fc/Fc^+)$ = 480 mV vs SCE. [c] rounded standard deviations given. [d] half rounded standard deviations given. Error margins are mostly a result of broad features and limited resolution (scan increment 1 mV).

For all measurements, the determination of a half-wave potential for the Fe^{3+}/Fe^{2+} redox pair of the hydroxide complexes **1**, **7**, and **10** exhibits a rather large uncertainty. Two main factors contribute to this uncertainty. Firstly, as stated above, the water content in the glovebox setup leads to the broadening of features and a decrease in intensity of the Fe^{2+}/Fe^{3+} reoxidation oxidation process. The broadening additionally causes the peak potentials of the reduction and oxidation process for one redox pair to be increasingly separated (ΔE_p) around the half-wave potential, prominently visible when comparing the results obtained with **1a** and **1c** under differing conditions (see Figure 80, and Figure 35, section 2.1.10). Secondly, because of the resolution limits of the setup (scan increment 1 mV) at the given sweep range, broad features lead to

indifferent currents in an applied voltage range around the peak potential. The values in Table 33 indicate the mean current and variance for the relevant signal maxima and minima. Another contributing factor is the intensity of the signals, which additionally influences the resolution. Thus, similar concentrations were used to maintain a similar current response and to equalize this effect within the series.

Despite the described uncertainties, the half-wave potentials for **1a** and **1c** are in good agreement, demonstrating that the influences of water content mainly affect the positioning of the peak potentials and the resolution by broadening effects, rather than the characteristic half-wave potential. Moreover, the half-wave potentials of **1**, **7**, and **10** are separated enough to identify a clear trend.

In solution, the electron withdrawing effect of the nitro-substituent in **7** results in a decrease of the donor strength for the carboxylate ligand and a decrease in basicity. Overall, this leads to a destabilization of the ferric oxidation state, as less electron density is donated by the carboxylate. Additionally, the weakening of the intramolecular hydrogen bond interaction (because of the weaker basicity of the carboxylate) leads to a lesser “partial oxo-character” of the hydroxide donor that is induced by the intramolecular hydrogen bonding in the *cis*-hydroxo(carboxylato)iron(III) moiety. The increased positive charge density at the metal site leads to the expectation of a more positive reduction potential than that of **1** which is verified by the experimental results of $E_{1/2}(\text{redox})_1$ for **7** compared to **1** (Table 33). Accordingly, the exact opposite is expected for **10**, as the electron donating methoxy substituent increases the carboxylate donor strength as well as its basicity. This expected trend can likewise be verified by the experimental results for $E_{1/2}(\text{redox})_1$ for **10** compared to **1**.

It remains unclear to what the feature at $E_{1/2}(\text{redox})_2 \approx$ -300 mV vs Fc/Fc^+ corresponds, although it is likely linked to a product formed upon reduction of the ferric hydroxide complex, as it is absent when no prior reduction at $E_{1/2}(\text{redox})_1$ has taken place. A clear trend can again be seen with the potential becoming increasingly more positive in the series of **10**, **1** and **7** in this order, further substantiating the suspicion that it corresponds to a benzoato-iron complex. It has been established, that this process does not correspond to the redox processes of the Fe^{2+}/Fe^{3+} pairs of the aqua **2**, **8**, **11**, or the η^2-carboxylato complexes **3**, **9**, **12**, as these processes are expected to occur at much more positive potentials. Additionally, the rather negative oxidation potential of $E_p(\text{ox})_1$ indicates that the species is likely not monocationic, further ruling out this

possibility. Thus, based on the results presented in chapter 4 (see below), it is speculated that the electrochemically generated species corresponds to a hydrogen bridged iron(II)-iron(III) complex associate.

3.1.10. NMR-Spectroscopic Investigation

^{1}H-NMR and ^{2}H-NMR spectroscopic analysis was performed for **7b** and **10c** (Figure 81, Figure 82). The results are compared to those obtained for **1c** (Table 34, also see section 2.1.11 for the reasoning behind the assignment of the aromatic ring protons of the carboxylate ligand).

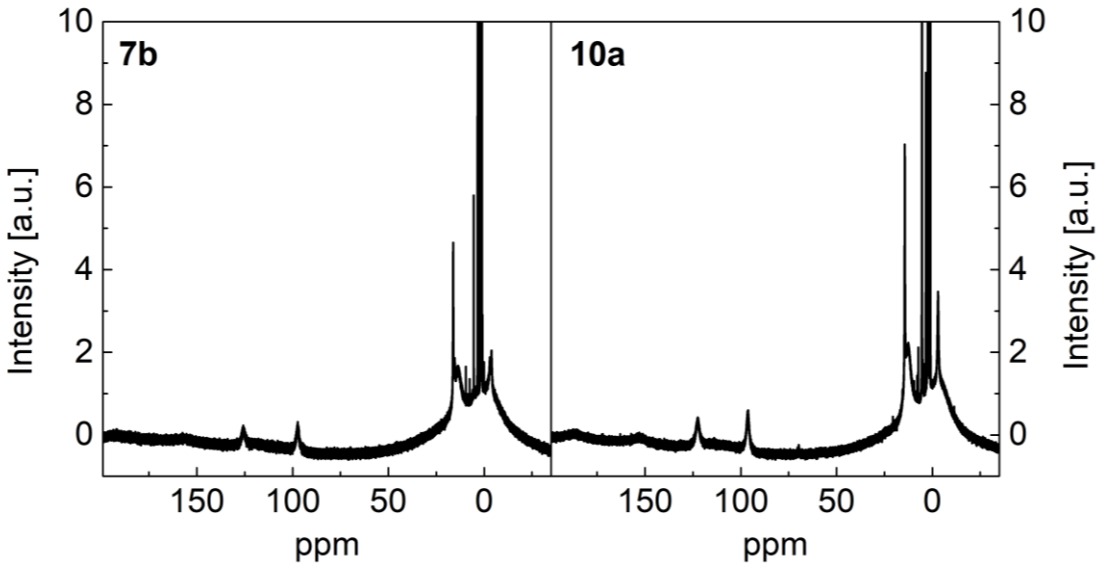

Figure 81. ^{1}H-NMR spectra of **7** and **10** between -35-200 ppm obtained with 0.02 mol·L^{-1} solutions of **7b** and **10a**, respectively, in CD_3CN. ^{1}H-NMR(400 MHz, CD_3CN, **7**) δ(ppm) = 192.36 (br), 156.40 (br), 125.75 (br), 97.34 (br), 16.19 (s), 15.40 (s), 13.65 (br), 2.15 (s), -2.99 (br), -3.84 (br). ^{1}H-NMR(400 MHz, CD_3CN, **10**) δ(ppm) = 188.99 (br), 154.15 (br), 123.46 (br), 96.60 (br), 14.40 (s), 12.55 (br), 5.43 (s), -3.0 (br). br = broad, s = singlet. Impurities at 3.42 and 1.12 correspond to diethylether residues.[131]

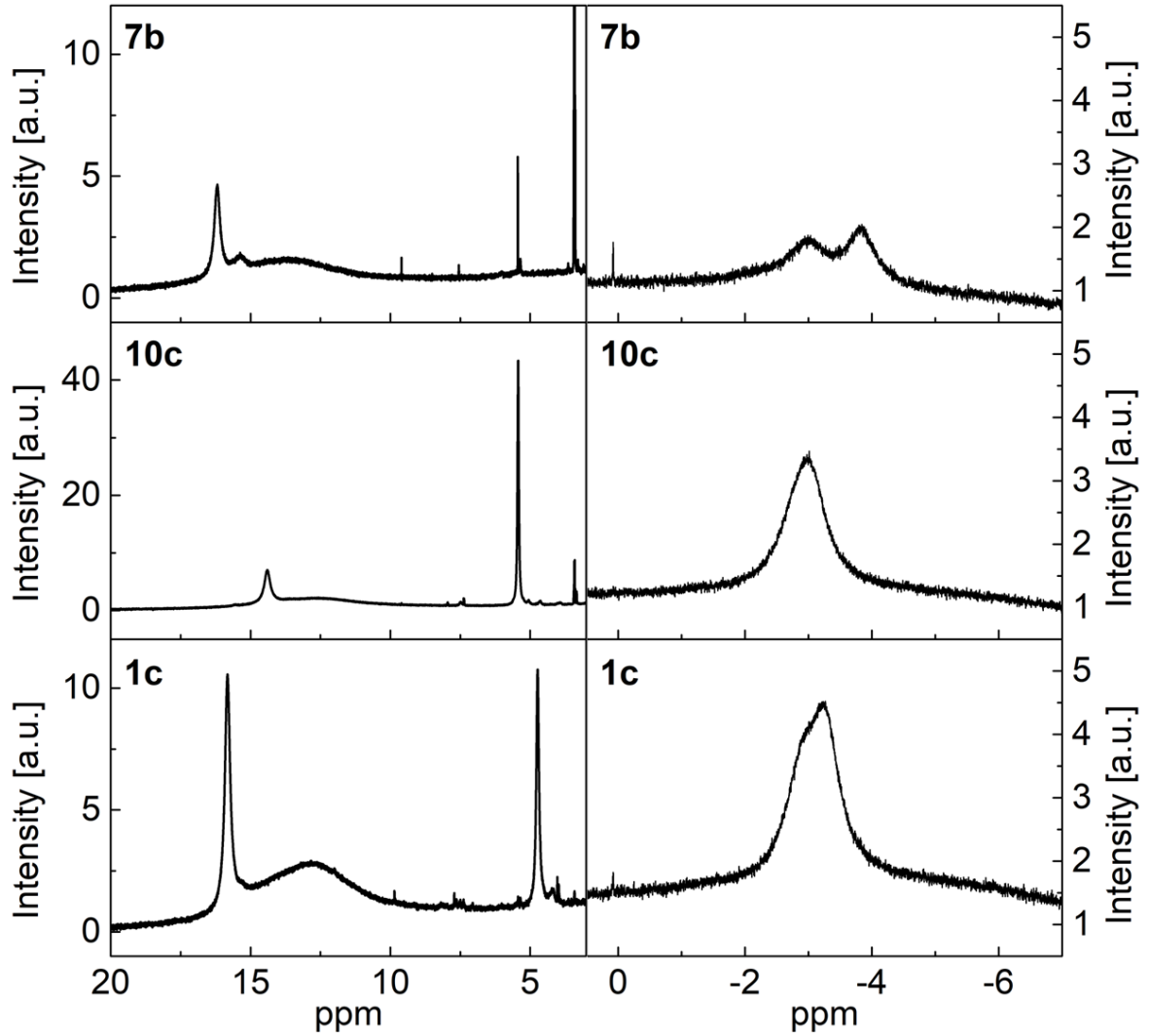

Figure 82. ^{1}H-NMR spectra of **7**, **10**, and **1** between 3-20 ppm (left) and -7-1 ppm (right), obtained with 0.02 mol·L^{-1} solutions of **7b** and **10a**, and **1a**, respectively, in CD_3CN. ^{1}H-NMR(400 MHz, CD_3CN, **7**) *d*(ppm) = 16.19 (s, *m*-proton of O_2CPh^{NO2}), 15.40 (br, *o*-proton of O_2CPh^{pNO2}), 13.65 (br). ^{1}H-NMR(400 MHz, CD_3CN, **10**) *d*(ppm) = 14.40 (s, *m*-proton of O_2CPh^{pOMe}), 12.55 (br), 5.43(s, –OCH_3 residue). ^{1}H-NMR(400 MHz, CD_3CN, **1**) *d*(ppm) = 15.83 (s, *m*-proton of O_2CPh), 12.80 (br), 4.73 (s, *p*-proton of O_2CPh). Impurities at 3.42 and 1.12 correspond to diethylether residues.[131]

Table 34. Comparison of the NMR signals (in ppm) in **7**, **10**, and **1** obtained from solutions of **7b**, **10c**, and **1c**, respectively (each 20 mmolL^{-1} in CD_3CN).

Fragment	**7**	**10**	**1**
$O_2C\text{-}C_6H_5^R$	R = NO_2	R = OCH_3	R = H
o-proton	15.40	13.6[a]	15.3[a]
m-proton	16.17	14.40	15.8
p-proton	-	-	4.73
-OCH_3 residue	-	5.43	-
Other			
n.d.	192.36[b]	185.98[b]	188.99[b]
n.d.	156.40[b]	152.99[b]	154.15[b]
n.d.	125.75	122.52	123.46
n.d.	97.34	96.24	96.60
n.d.	13.65	12.55	12.80
n.d.[c]	2.15	2.45	2.31
n.d.[d]	-3.84 | -2.99	-3.0	-3.27 (sh) | -2.90

o = ortho, *m* = meta, *p* = para, n.d. = not determined. Values measured at 400 MHz. All signals appear as broad singlets. [a] *o*-proton signals are obscured and weak. Thus, the accuracy of the peak picking is limited and the assignment ambiguous. [b] very broad, noisy signals with poor resolution. [c] opposite trend in relative shifts between **1**, **7**, and **10** highlighted in grey. [d] Based on relaxation time t_1 measurements (see section 2.1.11) on **1** it is speculated that these signals correspond to the pyridine proton in 4-position.

Generally, the NMR-spectra obtained for **7** and **10** (Figure 81) mostly resemble the spectrum of **1** (Figure 37, section 2.1.11), which allows some comparative peak assignment based on the findings for this complex cation because of seemingly synchronous peak shifting to higher fields (**10**) or lower fields (**7**), respectively.

However, especially the signals between 20 and -3 ppm differ notably, because of the differing carboxylate co-ligands (Figure 82). In both **7** and **10**, a signal corresponding to the proton in *para*-position to the carboxylate group is absent, as this position is functionalized by a nitro-, or methoxy group, respectively. Consequently, in **10**, a signal corresponding to the methyl protons of the methoxy substituent appears at 5.43 ppm that is assigned via the determination of the relative signal integrals. The positioning of this signal indicates barely any interaction with the paramagnetic metal core, as it lies at only slightly lower fields than would be expected for the free carboxylic acid / carboxylate from theoretical considerations. This can be explained by the large distance between these protons and the paramagnetic iron site.

In all three spectra, the signal assigned to the proton in *ortho*-position to the carboxylate is very weak, broad, and obscured (Figure 11, Figure 82), probably because of the expected extremely short relaxation times. Although peak picking was possible for **7**, the picking accuracy for **10** and **1** is very limited because the signal appears only as a minor deviation in the baseline at the tailing of the relatively strong signal corresponding to the proton in *meta*-position. Thus, the picked positions are unreliable but given as an estimate in Table 34.

Interestingly, despite the challenge of predicting and interpreting paramagnetic NMR shifts, a clear trend can be observed both for the benzoate signals and the remaining signals that are thought to correspond mostly to the L-$N_4{}^t Bu_2$ and the hydroxide ligand (Table 34). For the benzoate signals, the *ortho*- and the *meta*-proton are shifted downfield in **10**, whereas they are shifted upfield for **7**, as compared to **1**. Similarly, nearly all remaining signals follow this trend, apart from the signal around 2 ppm, which follows the opposite trend (highlighted in grey in Table 34). An explanation for this could be, in the first instance, that the σ- and π-donor properties of the benzoate ligands become stronger in the series O_2CPh^{pNO2} < O_2CPh < O_2CPh^{pOMe}. The increased compensation of the positive charge at the metal site may allow for slightly weaker metal-ligand interactions, reducing the spin-density at the ligands and, thus, the magnitude of shifting. Such an interpretation, although rather speculative, would agree with the results of the electrochemical investigation (section 3.1.9). Since the assignment of several signals remains unclear, a meaningful interpretation of the opposite trend in shifting for the signal around 2 ppm is not possible. However, because it is the only peak that shows this opposite trend, one could argue that it corresponds

to neither the benzoate nor the L-$N_4{}^tBu_2$ ligand, but to the coordinated hydroxide. The downfield shift could, in this case, be explained by a deshielding of the proton because of an increased hydrogen bond interaction with the most basic benzoate ligand (O_2CPh^{pOMe}), and a decreased hydrogen bond interaction with the weakest coordinated base (O_2CPh^{pNO2}).

One of the more notable differences in the spectra is the behaviour of the signal(s) around -3 ppm (Figure 82). While only a single signal is observed in the spectrum of **10**, a shoulder arises in **1**, and a second peak is observed in **7**. Previous reasoning suggested that this feature could correspond to the proton in 4-position of the pyridine donors contained in the macrocyclic ligand (section 2.1.11). This assignment would allow a reasonable interpretation of the peak splitting from **10** → **1** → **7** based on the *trans* influence of the carboxylate donor. As the *trans* influence is related to the relative donor strength, differences in this property for the carboxylate ligand could cause increased anisotropy and asymmetry in the complex cation. This concept is supported by the EPR results (section 3.1.7) that indicate a slight increase in the rhombicity and *g*-anisotropy from **10** → **1** → **7**. Thus, the pyridine protons in 4-position could become increasingly chemically different depending on the donor strength of the carboxylate ligand and the resulting *trans* influence differences, which would ultimately cause a splitting of the NMR signals for these two protons with increased asymmetry/anisotropy in the molecule. However, although feasible, the presented data is not strong enough to convincingly evidence this claim.

In summary, the interpretation of paramagnetic ^{1}H-NMR spectra remains a challenge, that only allows for limited interpretations and some speculative arguments based on the results obtained from different analytical investigations. While clear trends could be observed for the comparative study of **1**, **7**, and **10**, the spectra remain poorly understood apart from the assignments of the protons pertaining the benzoate ligands. However, this assignment alone will be extremely helpful in studying relative reactivities, self-exchange reactions of **1** and **2** as well as hydrogen atom transfer reaction equilibria between **7** and **2**, and **10** and **2**, respectively, to determine the relative bond dissociation free energies (BDFE) for **8** and **11** based on the previously reported BDFE obtained for **2** (chapter 2, section 2.3.5). The results of such reactivity studies are presented in the following (3.3 and chapter 4).

3.2. Summary of the Structural, Spectroscopic, Spectrometric, Magnetic, and Electrochemical Investigation

The results presented so far describe the successful synthesis and characterization of derivatives of *cis*-$[Fe^{III}(L\text{-}N_4{}^tBu_2)(O_2CPh)(OH)]^+$ **1** with an electron donating (–OMe, **10**) and an electron withdrawing substituent ($–NO_2$, **7**) in *para*-position of the benzoate ligand. Both derivatives exhibit similar structural and electronic properties as **1** (see also chapter 2) and are retained in solution; notable differences and observed trends as compared to **1** are summarized below. Although the synthesis and crystallization of the corresponding *cis*-$[Fe^{II}(L\text{-}N_4{}^tBu_2)(O_2CPh^R)(OH_2)]^+$ (**8** and **11**) and $[Fe^{II}(L\text{-}N_4{}^tBu_2)(\eta^2\text{-}O_2CPh^R)]^+$ (**9** and **12**) provided some challenges, the spectroscopic investigation of analytically pure samples of **9**, **11**, and **12** ascertained similar properties and behavior for the derivatives as observed for the (benzoato)iron(II) complexes *cis*-$[Fe^{II}(L\text{-}N_4{}^tBu_2)(O_2CPh)(OH_2)]^+$ **2** and $[Fe^{II}(L\text{-}N_4{}^tBu_2)(\eta^2\text{-}O_2CPh)]^+$ **3**. This concludes the successful synthesis of additional structural model complexes for rabbit lipoxygenase (rLOX), the study of which further highlights important features and interactions that may also exist and be at play at the active site of the enzyme, respectively.

Overall, the differences in the electronic and structural properties of **1**, **7**, and **10** are minor. This is attributed to the counteracting effects of adjusted basicity and donor strength in the carboxylate ligands that are mediated in a hexagonal feature that connects the iron core, the three heavy atoms of the carboxylate, and the hydroxide ligand through an intramolecular hydrogen bridging interaction in the individual cations. While the electron donating methoxy group can be considered a stronger donor, its increased basicity creates a stronger hydrogen bond interaction, directing some electron density to the distal oxygen of the coordinated carboxylate which, in turn, somewhat weakens the electron donating capability again. In contrast to this, the electron withdrawing nitro substituent weakens the donor capability of the benzoate ligand but, at the same time, the decreased basicity also weakens the hydrogen bridge and, therefore, allows for a somewhat better direction of the electron density to the proximal, coordinated oxygen.

This effective negation of competing influences introduced by the electronic variations can be observed in the structural analysis, as no apparent changes of the interatomar distances are found. Also, only minor differences in hydroxide O–H bond strengths with strengthening as **10** < **1** < **7** can be observed in structurally similar compounds in an IR-spectroscopic investigation. Although a minor anisotropy increase is found for **10** > **1** > **7** in Mößbauer (solid), EPR (solution) and suggested in NMR (solution), even these results may be ambiguous. Nonetheless, because the anisotropy may link to different charge distributions at the coordinating oxygen ligands because of the cooperative interactions mediated by the hexagonal feature, these indicative results are considered to show relevant trends. Differences in charge distribution and, thus, stabilization of the positive charge at the iron site, can also be observed by cyclic voltammetry. Here, weaker electron donating effects are observed in the series **10** > **1** > **7** leading to more positive potentials as **7** > **1** > **10**. This agrees well with an overall electron withdrawing effect in **7**, and electron donating effect in **10** – a general trend that is untouched by the hexagonal hydrogen bridging interaction.

Because of the intricate interactions at the *cis*-(carboxylato)(hydroxo)iron(III) units that affect both the Fe^{III}-OH/Fe^{II}-OH reduction potential and the pK_a of the reactive O–H bonds in the corresponding *cis*-(carboxylato)(aqua)iron(II) units in opposing ways, theoretical considerations, chemical intuition, and in-depth characterization do not suffice to estimate the effects of the electronic derivatization on the BDFE of the O–H bonds in the ferrous complexes, and the reactivity of the ferric complexes, respectively. Thus, reactivity studies were conducted and are described in 3.3 in an attempt to further shed light on the influences of electronic derivatization.

3.3. Reactivity studies

To demonstrate how the electronic variations introduced in the benzoate ligand influence the reactivity of the model complexes **1**, **7**, and **10**, reactivity studies that probe for their relative capability to abstract hydrogen atoms from weak O–H (section 3.3.1) and weak C–H bonds are described (section 3.3.2). In this, 2,4,6-tri-*tert*-butylphenol and 1,4-cyclohexadiene, respectively, are employed as substrates to allow for good comparability to the results previously obtained for **1** (section 2.3). The main goal of these studies is to illuminate any differences in the thermodynamic parameters and kinetics between **1** and its derivatives **7** and **10** that can be linked to the electronic derivatization and to better understand the fundamental reactivity of these types of complexes. To further strengthen the results, the hydrogen atom transfer reactivity of **2** towards **1**, **7**, and **10**, respectively, is also probed as an additional reference point that removes any substrate-specific influences (section 3.3.3).

3.3.1. Reactivity with weak O–H bonds

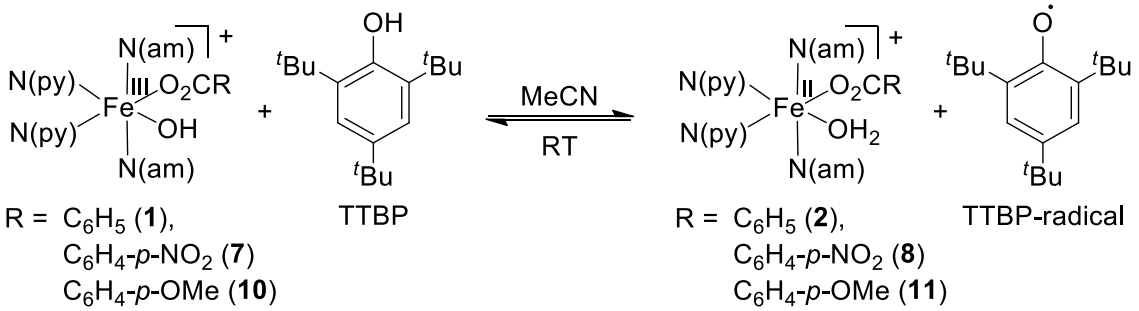

R = C_6H_5 (**1**), C_6H_4-*p*-NO_2 (**7**) C_6H_4-*p*-OMe (**10**)

TTBP

R = C_6H_5 (**2**), C_6H_4-*p*-NO_2 (**8**) C_6H_4-*p*-OMe (**11**)

TTBP-radical

Scheme 17. Proposed dynamic H-atom transfer equilibria between **1**, **7**, and **10** with 2,4,6-tri-(*tert*-butyl)phenol (TTBP), respectively and **2**, **8**, and **11** with the 2,4,6-tri-(*tert*-butyl)phenoxyl radical (TTBP-radical) in MeCN at room temperature (RT).

*Note: This section solely focusses on the comparative reactivity of **1** and **7** as studied by quantitative EPR-spectroscopy. No further product analysis is provided or discussed. This approach is justified by the previously described results. For more detailed information on the reactivity of [Fe(L-N-^{t}Bu$_2$)(OH)(O$_2$C^R)]$^+$ complexes with phenols, see chapter 2.3. Because of a defective instrument for several months, the reactivity of **10** could not be quantitatively studied with this method. However, other methods were employed to allow for comparison and are described in sections 3.3.2 and 3.3.3.*

The reaction of TTBP with **1** has proven to be a useful model reaction to obtain accurate thermodynamic values for the O–H bond strength of these types of [Fe(LN$_4$-^{t}Bu$_2$)(OH)(O$_2$C^R)]$^+$ ferric hydroxide complexes (see sections 2.3.2 and 2.3.5). Thus, it was also attempted to investigate the reactions of TTBP with **7** and **10**, respectively, (Scheme 17) in MeCN at room temperature. As observed for the reaction of **1** with TTBP, the reaction mixtures of TTBP with the derivatives **7** and **10**, respectively, quickly turn from yellow to green indicating the formation of a phenoxyl radical (compare to the time resolved UV-vis spectrum of a mixture of **1a** and TTBP in Figure 44). For **7**, a moderately intense phenoxyl radical signal in EPR analysis (Figure 83) was found. A further quantification reveals a partial conversion. The observation of a constant intensity within the margin of error for 30 minutes concludes the attainment of an equilibrium (first measurement at 20 minutes reaction time). Consequently, similar thermodynamic preconditions for the reactions of TTBP with **1** and **7** are assumed. Although such spectra could not be obtained for **10** because the instrument

was defective for several months, the qualitative analysis indicates that the thermodynamics of the reaction of **10** and TTBP must be within a similar range. Because of time constraints, alternative methods were employed to study the relative reactivities of **1** and **7** as compared to **10** in more detail (see following sections).

For the reaction of **7** with TTBP, a detailed concentration-dependent quantification of the respective equilibrium constant K_{eq} is done to calculate the $BDFE_{MeCN}$(O–H) of **8**. The results are then compared to the equilibrium constant K_{eq} for the reaction of **1** with TTBP, $BDFE_{MeCN}$(O–H) of **2**, and the method error derived from this previous study (section 2.3.5).

To determine the equilibrium constant K_{eq} and the driving force ΔG for the reaction **7** + TTBP ⇌ **8** + TTBP-radical, the same method as described in chapter 2.3 was applied: A series of nine quantitative EPR experiments was carried out with varying initial concentrations of the reactants under nitrogen atmosphere and thermal stability at 20 °C (Figure 83, Table 35). In exact analogy to the study described for **1**, the variation in initial concentrations ranged from 0.25 to 2.00 $mmol \cdot L^{-1}$ for each reactant. Equilibrium concentrations of the phenoxyl radical were calculated from the double integration of the EPR signal intensities referenced against a standard TEMPO-radical solution with a defined concentration (0.2 $mmol \cdot L^{-1}$). Equilibrium concentrations of **8** were derived assuming an A + B ⇌ C + D type reaction which allowed the calculation of the equilibrium constant K_{eq} and the free reaction energy ΔG_{MeCN} (Table 35).

The mean values of the results for this reaction (**7** + TTBP ⇌ **8** + TTBP-radical) are calculated to be $K_{eq} = 1.32 \cdot 10^{-2}$ and ΔG = 2.52 $kcal \cdot mol^{-1}$, respectively, at 20°C. Using the literature value of $BDFE_{MeCN}$(TTBP) = 74.8 ± 1 kcal/mol,[97] the $BDFE_{MeCN}$(**8**) can thus be calculated to be 72.3 kcal/mol. The equilibrium constant K_{eq} and the free energy difference between the cleaved and formed O–H bonds ΔG are similar but distinct from those found for the reaction of **1** with TTBP ($K_{eq} = 1.77 \cdot 10^{-2}$, ΔG = 2.35 $kcal \cdot mol^{-1}$) and, consequently, the derived BDFE for **8** appears to be slightly lower than that obtained for **2** ($BDFE_{MeCN}$(**2**) = 72.4 kcal/mol). Although the error margins for the BDFE-values overlap, the obtained results do indicate a clear trend caused by the introduction of a NO_2-group in the benzoate backbone for the reactivity of the complexes (see below).

Note: Figure 83 shows fields (in G) for the TTBP-radical signal that differ from those reported in chapter 2.3, (Figure 42, Figure 48). This is due to differences in calibration and measurement frequencies, as the spectra were recorded on different instruments. Because even slight differences in parameter settings can influence the absolute signal intensities, the double integrals are not to be compared to other measurement series but should always be contextualized with a reference measurement of a solution with a defined radical concentration, as is also done for all calculations in Table 35.

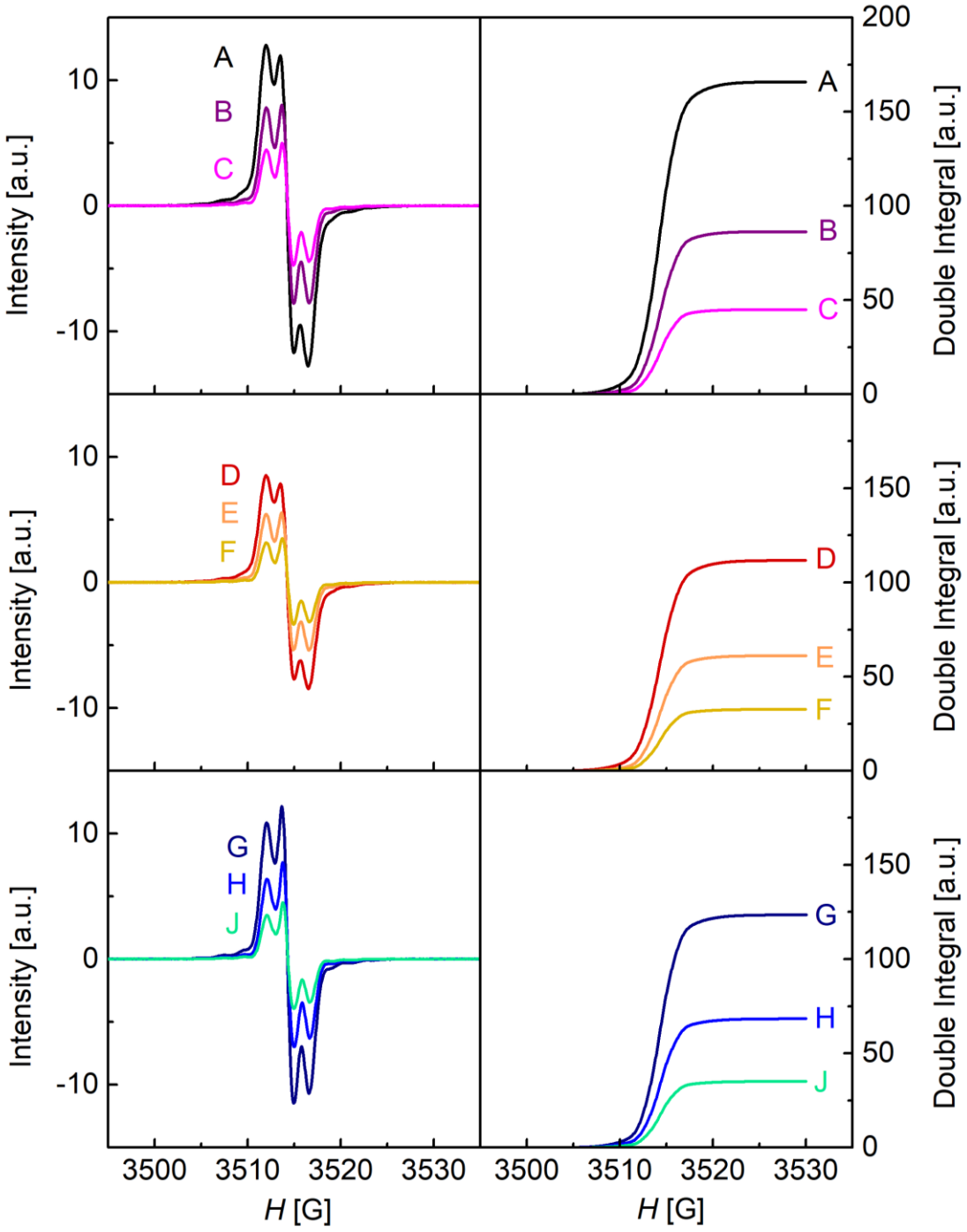

Figure 83. EPR spectra obtained from reaction mixtures of **7b** and TTBP in MeCN (abs.) at various initial concentrations (left) and double integrals of the EPR signals used for calculating K_{eq} and ΔG_{MeCN}, respectively (right). The letters **A**-**J** reference the experimental conditions listed in Table 35. Double integration of the signals was performed using the integration tool of the Origin Pro 9 software. A narrow integration range was applied to minimize baseline errors. Therefore, while the EPR spectra were recorded in the range between 3425 and 3625 G, the integration of the signals was performed within the magnetic field range from 3500 to 3530 G.

Table 35. Results of the quantitative EPR spectroscopic study of the reactions of **7b** with TTBP in MeCN (abs.) under a nitrogen atmosphere.

Exp.	c_0(**7b**) [mmol·L^{-1}]	c_0(TTBP) [mmol·L^{-1}]	Double integral[a] [a.u.]	c(PhO·) [mmol·L^{-1}]	K_{eq}	ΔG_{MeCN}[b],[c] [kcal·mol^{-1}]
A	2.00	2.00	165.9	$1.92 \cdot 10^{-4}$	$1.13 \cdot 10^{-2}$	2.61
B	1.00	1.00	85.55	$9.88 \cdot 10^{-5}$	$1.20 \cdot 10^{-2}$	2.57
C	0.50	0.50	44.75	$5.17 \cdot 10^{-5}$	$1.33 \cdot 10^{-2}$	2.52
D	2.00	1.00	111.7	$1.29 \cdot 10^{-4}$	$1.02 \cdot 10^{-2}$	2.67
E	1.00	0.50	61.1	$7.06 \cdot 10^{-5}$	$1.25 \cdot 10^{-2}$	2.55
F	0.50	0.25	31.75	$3.67 \cdot 10^{-5}$	$1.36 \cdot 10^{-2}$	2.50
G	1.00	2.00	123.5	$1.43 \cdot 10^{-4}$	$1.28 \cdot 10^{-2}$	2.54
H	0.50	1.00	68.4	$7.90 \cdot 10^{-5}$	$1.61 \cdot 10^{-2}$	2.40
J	0.25	0.50	35.2	$4.06 \cdot 10^{-5}$	$1.71 \cdot 10^{-2}$	2.37

[a] Double integration of the EPR signals of the respective reaction mixtures in the magnetic field ranging from 3425 and 3625 G. The calibrating solution of 0.2 mmol·L^{-1} TEMPO radical solution in MeCN (abs., N_2 atmosphere) resulted in an integral of 173 a.u. (averaged value of three samples with a standard deviation smaller than the methodic error). The absolute magnitude of the integrals is not to be compared with previous measurements, as a different instrument was used (also see note above). [b] Calculated for 293.15 K. [c] No error is given; a detailed discussion is given below.

The error margins of the quantitative EPR spectroscopy approach have previously been discussed and the overall error was estimated to be ±0.14 kcal·mol^{-1} (section 2.3.5). However, it was found that the above discussed experiment with **7b** exhibits a larger error than previously assumed (Figure 84). Consequently, it is suggested that the rather small error margin of ±0.14 kcal·mol^{-1} should be reconsidered. To avoid misinterpretations, the estimated maximum error margin is generously increased to ±0.5 kcal·mol^{-1} (composed of two additive errors of ±0.25 kcal·mol^{-1} for each the reference and the sample measurement), although the actual error is thought to be

smaller. Such an error is still comparatively small (the literature error of the reference substance TTBP is ±1 kcal·mol^{-1})[97] but should ensure that no trends regarding the reactivities and relative bond strengths of derivatized [Fe(L-N$_4$^{t}Bu$_2$)(OH)(O$_2$C^R)]$^+$ complexes are put out of context.

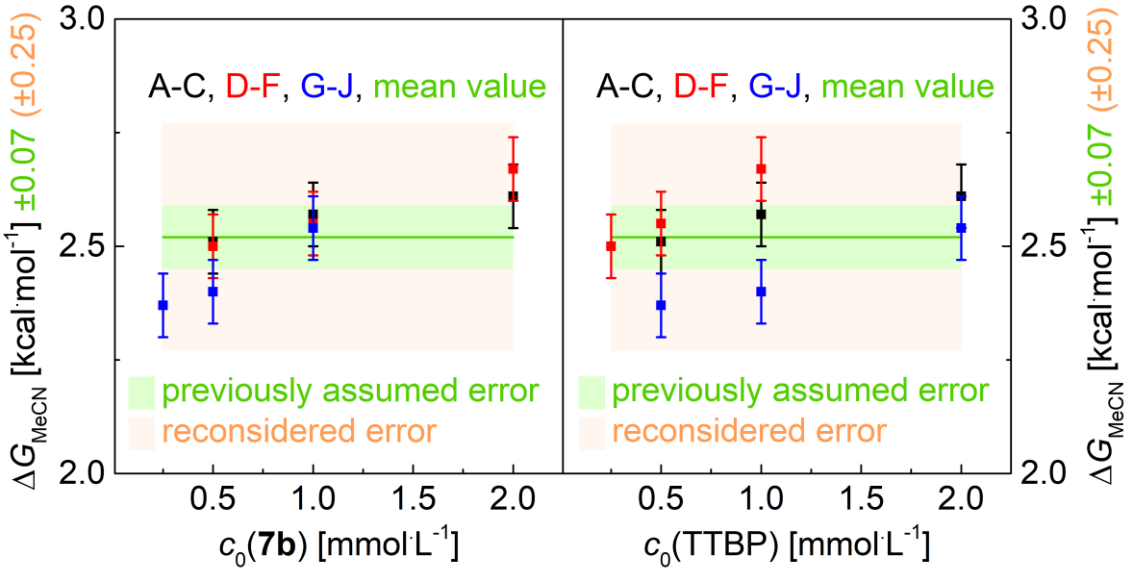

Figure 84. Graphic presentation of the dependence of the experimentally determined values of ΔG_{MeCN} on the initial concentrations of the reactants in the reaction of **7b** and TTBP (referring to entries **A**-**J** in Table 35). Left: ΔG_{MeCN} vs c_0(**7b**), right: ΔG_{MeCN} vs c_0(TTBP). The experimental values are placed in expected scattering error margins for an error of ±0.07 kcal·mol^{-1} (green area) and ±0.25 kcal·mol^{-1} (green and orange area) around the mean value (linear fit with a slope of zero, green trace). Since the calculation is based on a reference measurement of a TEMPO radical solution, an additive error for the y-axis with equal size (±0.07 and ±0.25, respectively) needs to be considered. As the experimental values only lie within the larger, generously chosen error margin, the total error is considered $\Delta\Delta G_{MeCN}$ = ±0.5 kcal mol^{-1} (sum of additive errors).

Although the adjustment of the error margin is necessary in this case, it must be stated, that Figure 84 reveals a potentially relevant dependency of the **7** + TTBP ⇌ **8** + TTBP-radical equilibrium on c_0(**7b**) that may be interpreted as an inhibition/partial deactivation of the reaction at higher complex concentrations. Such concentration dependent inhibitions have also been noted for **1** (although less pronounced in the concentration regime of 0.25 – 2.00 mmol·L^{-1}) but were not further studied in chapter 2.3. A possible explanation could be concentration-dependent formations of, e.g.

{[Fe(L-N$_4$*t*Bu$_2$)(OH)(O2C^{pNO2})][Fe(L-N$_4$*t*Bu$_2$)(OH$_2$)(O2C^{pNO2})]}$^{2+}$ associates of **7** and **8** via hydrogen bonding interactions between the hydroxide and the aqua ligand, respectively, as this could block the reaction pathway for a substrate with **7** and reduce the overall molar activity of the complex. Although this self- or product-inhibition appears highly speculative at this point, further evidence for such interactions and concentration-dependent inhibitions are provided in chapter 4.

A comparison of **2** to previously reported values for iron(II) complexes is presented in section 2.3.6 Table 12. Because the BDFE of **8** differs from that of **2** by less than 0.5 kcal·mol^{-1} and literature values often have errors of ±1 kcal·mol^{-1}, no further comparison is provided in this section.

3.3.2. Reactivity with weak C–H bonds

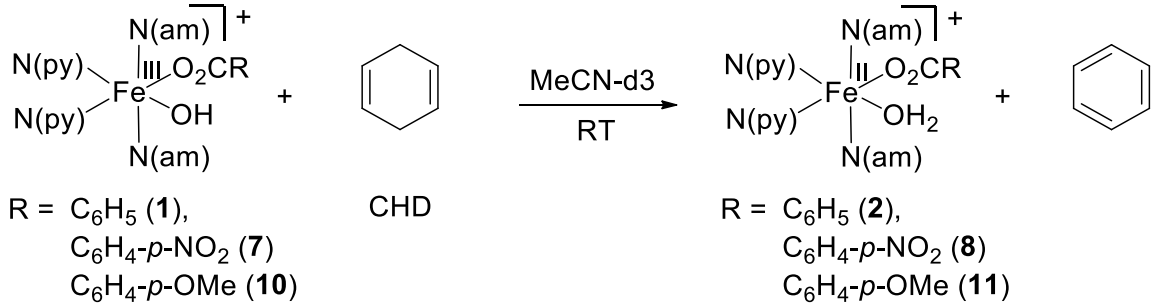

R = C_6H_5 (**1**), C_6H_4-*p*-NO_2 (**7**) C_6H_4-*p*-OMe (**10**)

CHD

R = C_6H_5 (**2**), C_6H_4-*p*-NO_2 (**8**) C_6H_4-*p*-OMe (**11**)

Scheme 18. Proposed H-atom transfer reactivity of Cyclohexadiene (CHD) with **1**, **7**, and **10**, respectively, in MeCN-d3 at room temperature (RT).

*Note: This section solely focusses on the comparative reactivity of **1**, **7**, and **10** as studied by time-resolved NMR spectroscopic sampling. No further product analysis e.g., via ESI-MS is provided or discussed. This approach is justified by the previously described results and the similarity of the studied iron complexes. For additional information on the reactivity of $[Fe(LN_4\text{-}^tBu_2)(OH)(O_2C^R)]^+$ complexes with weak C-H bonds, see chapter 2.3.*

As the results obtained from the reactivity study of **1**, **7**, and **10** with weak O–H bonds demonstrated rather similar thermodynamic preconditions, this is also expected for the reactions of all ferric hydroxide complexes with CHD. Thus, a hydrogen abstraction from weak C–H bonds with **7** and **10** appears feasible.

To verify such a reactivity, NMR spectra of stoichiometric reactions of CHD with **1**, **7**, and **10**, respectively, were recorded after 14 days of reaction time in a Young tube and investigated regarding product formation, both for the organic product (C_6H_6) and the complex products (**2**, **8**, and **11**). Because the assignment of the proton resonances of the benzoate ligands in **1**, **2**, **7**, and **10** has been achieved (see section 2.1.11 and section 3.1.10), the qualitative progression of the reaction can be tracked, as has been preliminary demonstrated in section 2.3.7. With a reaction time of 14 days, very clear evidence can be found for the formation of benzene and a (relative) decrease of the signals corresponding to the protons at the benzoate ligands of the ferric hydroxide complexes. Moreover, additional signals appear that can be assigned to the formation of the respective ferrous aqua complexes **2**, **8** and **11** (Figures 85-87).

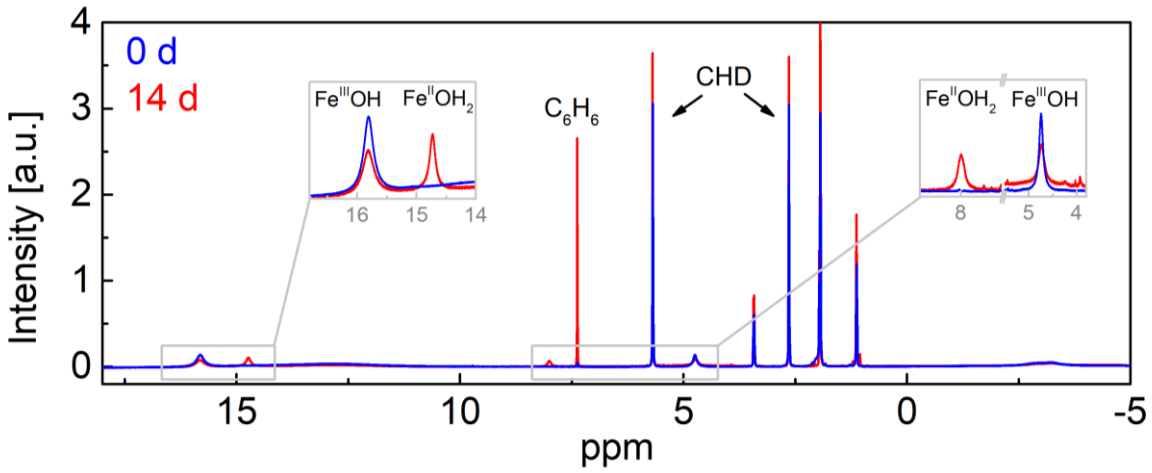

Figure 85. Initial NMR-spectrum (blue trace) and a spectrum recorded after 14 days (red trace) of a reaction mixture of **1** with CHD. Absolute intensities of CHD only appear larger after 14 d because of narrower signal half-widths. The signals at 15.8 and 4.7 ppm correspond to the *meta*- and *para*-protons in the benzoate ligand of **1**, respectively. The signals at 14.7 and 8.0 ppm correspond to the *meta*- and *para*-protons in the benzoate ligand of **2**, respectively. Impurities at 3.46 and 1.31 are attributed to Et_2O residues.[131]

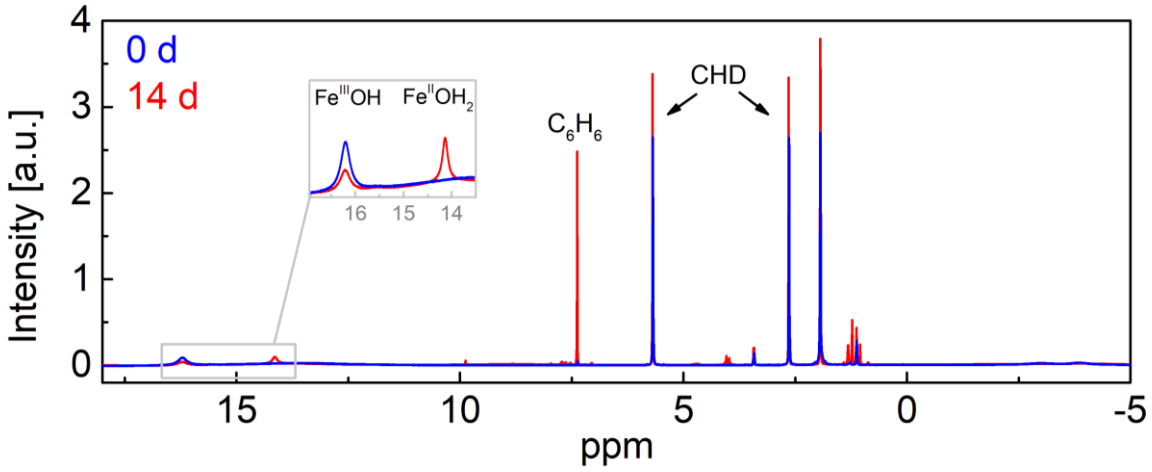

Figure 86. Initial NMR-spectrum (blue trace) and a spectrum recorded after 14 days (red trace) of a reaction mixture of **7** with CHD. Absolute intensities of CHD only appear larger after 14 d because of narrower signal half-widths. The signal at 16.2 ppm corresponds to the *meta*-proton in the *para*-nitrobenzoate ligand of **7**. The signal that occurs at 14.1 ppm after 14 d is accordingly assigned to the *meta*-proton in the *para*-nitrobenzoate ligand of **8**. Signals at 3.46 and 1.31 correspond to Et_2O residues.[131] The minor additional diamagnetic signals that occur after 14d remain unassigned.

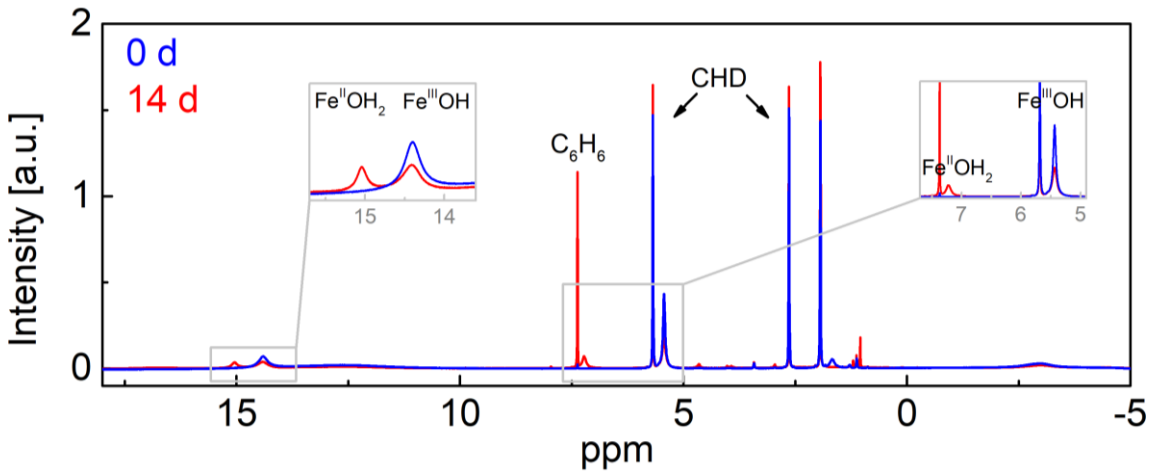

Figure 87. Initial NMR-spectrum (blue trace) and a spectrum recorded after 14 days (red trace) of a reaction mixture of **10** with CHD. Absolute intensities of CHD only appear larger after 14 d because of narrower signal half-widths. The signal at 14.4 ppm corresponds to the *meta*-proton and the signal at 5.4 corresponds to the CH_3-group of the *para*-methoxybenzoate ligand of **10**, respectively. The signals that occur at 15.0 ppm and 7.2 after 14 d are accordingly assigned to the *meta*-proton and the CH_3-group of the *para*-methoxybenzoate ligand of **11**, respectively. Signals at 3.46 and 1.31 correspond to Et_2O residues.[131] The minor additional signals that occur after 14d remain unassigned.

Importantly, these results not only provide strong evidence that all three $[Fe^{III}(L\text{-}N_4{}^tBu_2)(OH)(O_2C^R)]^+$-type complexes, **1**, **7**, and **10**, engage in a hydrogen atom abstraction from 1,4-cyclohexadiene to yield benzene and the corresponding $[Fe^{II}(L\text{-}N_4{}^tBu_2)(OH_2)(O_2C^R)]^+$ complexes **2**, **8**, and **11**, but also provide valuable information about the position of the benzoate signals in the ferrous aqua complexes **8** and **11** that were challenging to isolate and had thus not been satisfyingly characterized via NMR spectroscopy before.

Since all reactions do occur and a relative quantification of the diamagnetic organic educt and product is feasible, the kinetics of all three reactions are also studied via NMR reaction monitoring. This allows for a further elucidation of the thermodynamic preconditions of the reactions (and complexes) and may conclude further evidence for similar activation barriers and O–H bond dissociation free energies (BDFE) of the ferrous aqua complexes **2**, **8**, and **10** as suggested by the quantitative EPR spectroscopic results and qualitative visible light absorption observations presented

above (sections 2.3 and 3.3.1). For this, the reaction progression of a stoichiometric reaction of the ferric hydroxide complexes **1**, **7**, and **10** with CHD was followed. Although generally not favored for kinetic studies, in the NMR approach, stoichiometric reactions exhibit the best resolution for relative product/educt quantification. Initial concentrations of 40 $mmol \cdot L^{-1}$ of the respective ferric hydroxide complex (**1**, **7**, or **10**) and 20 $mmol \cdot L^{-1}$ of distilled, degassed CHD were employed to match the initial substrate CHD concentration used in the kinetic study with ESI mass spectrometry for a reaction of **1** with CHD (section 2.3.7) for better comparability. Although the reaction progression is extremely slow, the second order rate constant can be calculated when fitting the relative concentration changes of CHD and Benzene after 14 days of reaction time, albeit with limited accuracy. A H/D exchange between CHD and MeCN-d3 is not expected, a H/D exchange between the hydroxide complex and MeCN-d3 is considered unlikely and should not influence the rate determining step (the H-atom abstraction) in the oxidation of the substrate. All reactions were done diffusion controlled in a sealed NMR tube under nitrogen atmosphere. The results of the kinetic investigation for all three reactions in the initial linear regime are described in Figure 88 and discussed below.

The rate constants are derived as k(**1** + CHD) = $8.2 \cdot 10^{-6}\ Lmol^{-1}s^{-1}$, k(**7** + CHD) = $8.8 \cdot 10^{-6}\ Lmol^{-1}s^{-1}$, k(**10** + CHD) = $8.6 \cdot 10^{-6}\ Lmol^{-1}s^{-1}$. Thus, it appears that all three reactions contain the same activation barrier within the margin of error. Notably, although the comparison is somewhat unreliable because of the comparatively large error in the calculation of kinetic constants in this study, these rates are significantly slower than that derived from the ESI-MS study of the reaction of **1** (2 $mmol \cdot L^{-1}$) with CHD (20 $mmol \cdot L^{-1}$) in MeCN but match the previous results derived from the NMR study of the reaction of **1** (40 $mmol \cdot L^{-1}$) with CHD (20 $mmol \cdot L^{-1}$) in MeCN-d3 (section 2.3.7). Because concentration dependent activity of the ferric hydroxide complexes is also suggested in the reactivity studies with weak O–H bonds (section 3.3.1), the case for an activity reduction at higher concentrations as an intrinsic property is strengthened. More specifically, because of the strong activity reduction even in the initial period of the reaction it is suggested that both, pairs of educt complexes $\{[Fe(L\text{-}N_4{}^tBu_2)(OH)(O_2C^R)][Fe(L\text{-}N_4{}^tBu_2)(OH)(O_2C^R)]\}^{2+}$ and product-educt pairs $\{[Fe(L\text{-}N_4{}^tBu_2)(OH)(O_2C^R)][Fe(L\text{-}N_4{}^tBu_2)(OH)(O_2C^R)]\}^{2+}$, can associate via hydrogen bridging interactions in a concentration-dependent manner. Evidence for the possibility

of such associations is provided in chapter 4 alongside a more elaborate discussion. Therefore, the reliability of the determined absolute values for the second order rate constants is limited and should not be taken out of context, because their calculation precludes a concentration dependency.

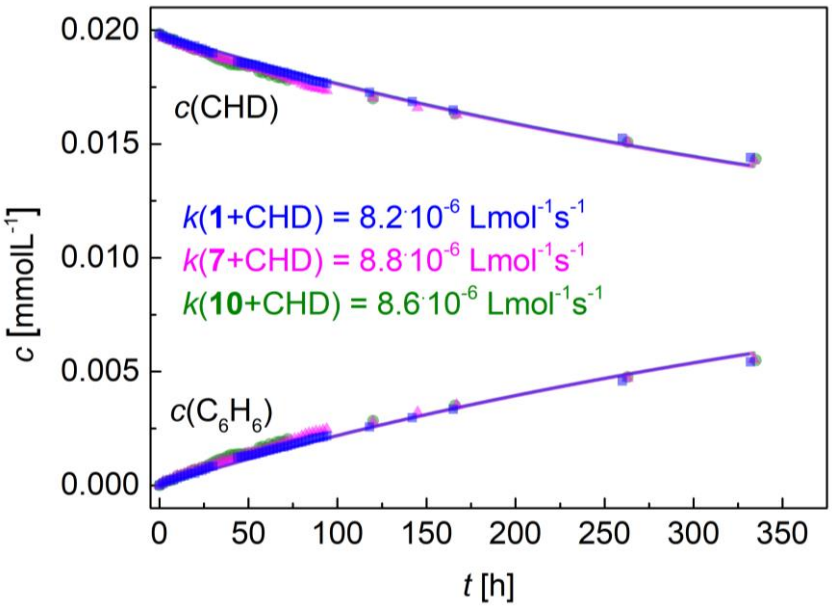

Figure 88. Kinetic study of the diffusion-controlled reactions of **1** (blue), **7** (magenta), and **10** (green) with CHD in 1 mL MeCN-d3 under nitrogen atmosphere in a Young NMR tube. The kinetic constants were calculated from the fits obtained with MatLab R2020a. Errors in the experimental data may result from integration errors and limited accuracy of the initial CHD concentrations that were added with a 2 μL Hamilton syringe to the solution. Errors of the fit are due to limited data availability for longer reaction times.

In summary, it can be concluded that all reported $[Fe^{III}(L\text{-}N_4{}^tBu_2)(OH)(O_2C^R)]^+$ complexes (**1**, **7**, and **10**) perform hydrogen atom abstraction (HAT) from weak C–H bonds. The kinetics found for the reactions under the same conditions point towards similar activation barriers for the reactions of CHD with **1**, **7**, and **10**, respectively. However, the differences cannot be reliably discerned because of the rather large error of this study that results from the slow reaction kinetics and limited rate-constant determination reliability. Thus, it only supports the notion that the $BDFE_{MeCN}$ of the corresponding ferrous aqua product complexes of the HAT reaction (**2**, **8**, and **11**) are similar ($BDFE_{MeCN} \approx 72.4$ kcal·mol^{-1}) but does not allow further interpretation of any trends caused by the introduction of the substituents. The observed concentration-dependent inhibition of the activity of the ferric complexes appears to be an intrinsic

property of $[Fe(L\text{-}N_4{}^tBu_2)(OH)(O_2C^R)]^+$ complexes that is further discussed in chapter 4.

3.3.3. Hydrogen atom exchange reactions between *cis*-(carboxylato)(hydroxo/aqua) iron complexes with diazapyridinophane ligands

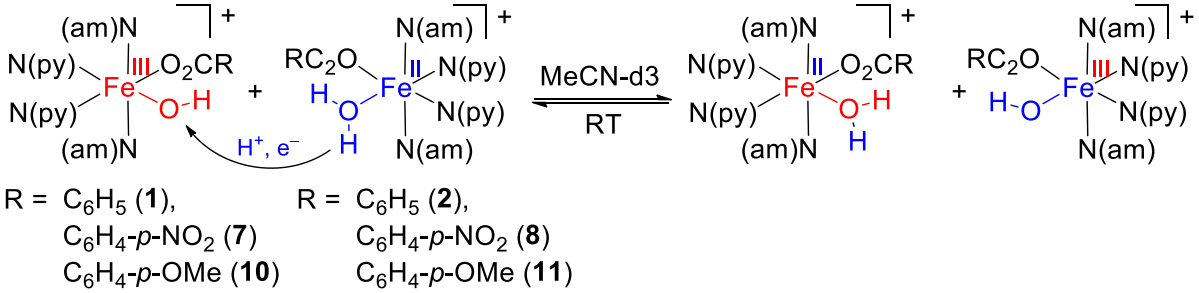

R = C_6H_5 (**1**), C_6H_4-*p*-NO_2 (**7**) C_6H_4-*p*-OMe (**10**) R = C_6H_5 (**2**), C_6H_4-*p*-NO_2 (**8**) C_6H_4-*p*-OMe (**11**)

Scheme 19. Schematic representation of possible H-atom exchange equilibria between the *cis*-(carboxylato)(hydroxo/aqua)iron complexes **1**, **7**, and **10**, and **2**, **8**, and **11**.

From the results presented up to here, it is deduced that the similar reactivities of the derivatives **1**, **7**, and **10** are a result of similar thermodynamic preconditions and O–H bond strengths in the corresponding ferrous aqua complexes **2**, **8**, and **11**. To further probe for a substituent influence and trend while excluding any substrate effects, the hydrogen atom self-exchange reaction between **2** and **1** is studied and used as a reference point to compare the exchange equilibria between **2** and **7**, and **2** and **10** via NMR-spectroscopy.

At first, the principle self-exchange reaction between **1** and **2** needs to be established and its time scale needs to be estimated to ensure that the approach is feasible, and the NMR method is suitable. For this, an isotope-labeled (deuterated) sample of **1** [Fe(L-N$_4$^{t}Bu$_2$)($C_6D_5CO_2$)(OH)](PF$_6$) (**1^D** 20 mmol·L^{-1}) was added to a stoichiometric amount of **2a** in MeCN-d3 and a ^{1}H-NMR spectrum was recorded swiftly. Already the initial spectrum of the mixture contained discrete proton resonances for the $C_6H_5CO_2^-$ ligands of **1** and **2** in an approximate 1:1 ratio (Figure 89). Because the employed sample of **1^D** does not contain $C_6H_5CO_2^-$ but an ^{1}H-NMR-inactive $C_6D_5CO_2^-$ ligand, this result is evidence of a H-atom transfer from **2** to **1^D** yielding **1** and **2^D**. A ligand exchange of the negatively charged benzoate is considered unlikely.

The time between the preparation of the sample in a Young NMR tube in a glovebox and the initial measurement was about 8 minutes. When recording the spectrum and comparing it to a sequence of spectra after longer reaction times, no changes were

observed. Thus, it can be concluded that an equilibrium is reached in under 8 minutes at room temperature.

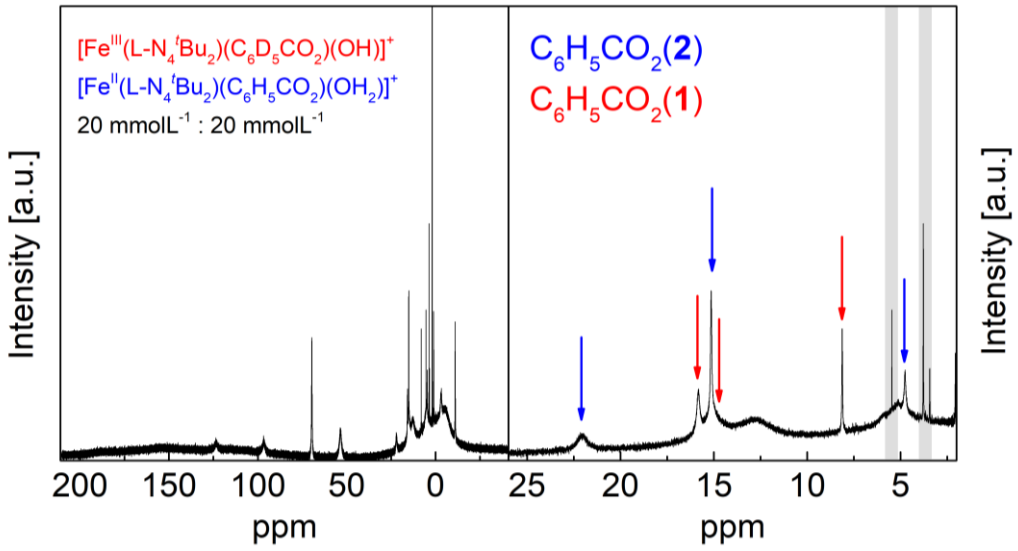

Figure 89. ^{1}H-NMR spectra of a mixture of isotope labeled (deuterated) **1c** [Fe^{III}(L-N$_4$)(^{t}Bu$_2$)(C$_6$D$_5$CO$_2$)OH](PF$_6$) (**1^{D}c**, 20 mmolL^{-1}) and **2a** [Fe^{II}(L-N$_4$)(^{t}Bu$_2$)(C$_6$H$_5$CO$_2$)(OH$_2$)](ClO$_4$) (20 mmolL^{-1}) between -40-210 ppm (left) and 2-26 ppm (right) obtained after 8 minutes in MeCN-d3. Discrete signals for C$_6$H$_5$CO$_2$ in both **1** and **2** are found as evidence for a H-atom exchange reaction between the employed complexes. For detailed assignment of the proton resonances, see section 2.1.11.

In a further study of the above-mentioned reaction mixture at variable temperatures between 233-348 K, it is found that the discrete signals corresponding to **1** and **2** do not show any indication of coalescence in this temperature range (Figure 90). This concludes a self-exchange reaction rate that is slower than the ^{1}H-NMR experiment even at high temperatures because of the separation of the signals and the measurement frequencies of the employed instruments. Likewise, no coalescence is observed in a stoichiometric mixture of isotope labeled **1^D** and **2^D** (both with ring-deuterated benzoate ligands), in a ^{2}H-NMR experiment between 233-348 K (see attachment). The changes in shifts and broadening effects found in the temperature-resolved spectra are attributed to temperature-dependent relaxation behavior of the sample according to the Curie law.[160]

*Note: The kinetic window of the self-exchange reaction between **2** and **1** under the above-described conditions allows for a closer investigation via two-dimensional EXSY-NMR spectroscopy. However, because the exact kinetics are not relevant to the thermodynamic objective studied in this section, this more in-depth kinetic study is described in section 4.3 in a more relevant context.*

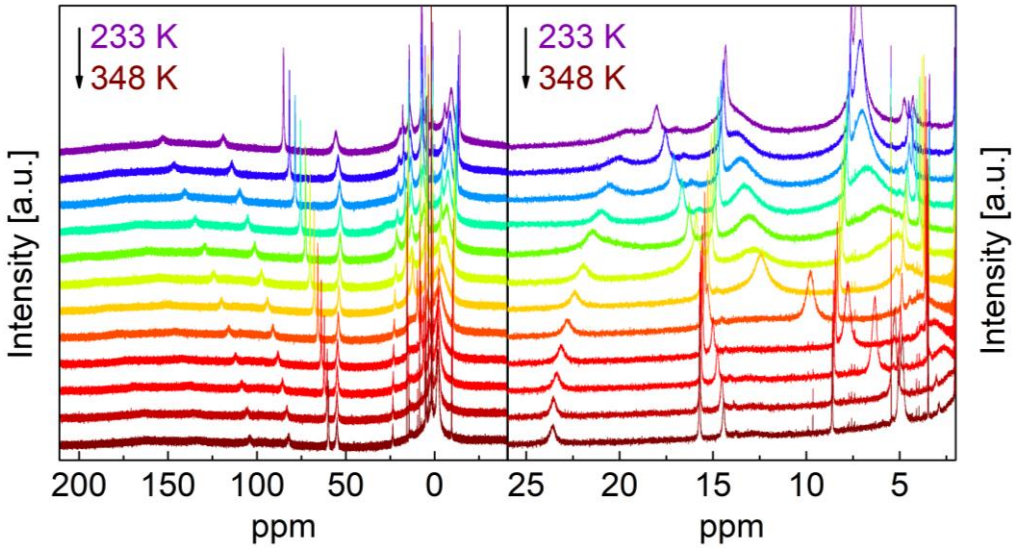

Figure 90. ^{1}H-NMR spectra of a mixture of isotope labeled (deuterated) **1c** [Fe^{III}(L-N_4)(^{t}Bu_2)($C_6D_5CO_2$)OH](PF_6) (**1^{D}c**, 20 mmolL^{-1}) and **2a** [Fe^{II}(L-N_4)(^{t}Bu_2)($C_6H_5CO_2$)(OH_2)](ClO_4) (20 mmolL^{-1}) between -40-210 ppm (left) and 2-26 ppm (right) obtained at temperatures between 233-348 K in MeCN-d3. Spectra are shown in 10 K steps from 233 K → 343 K (purple trace → light brown trace) and a 5 K step from 343 K → 348 K (light brown trace → dark brown trace). Discrete signals for both **1** and **2** and no evidence for signal coalescence are found in the studied temperature range.

In summary, the NMR method is found to be suitable to investigate the H-atom exchange equilibria of **2** with **1**, **7** and **10** and, therefore, contribute to the study of substituent effects on the thermodynamic parameters of the lipoxygenase model complexes. The kinetic preconditions for the self-exchange reaction between **2** and **1** suggest that the observation of discrete signals for all complexes involved in the H-atom exchange equilibrium reaction is possible, if the thermodynamic driving force places the reaction in an equilibrium regime as would be expected from the previous results. This assumption is justified by the similarity in structure and reactivity of the complexes **1**, **7**, and **10**, and **2**, **8**, and **11** (see above). The presented results further suggest that the equilibria are attained in under 8 minutes at room temperature and

that the educts and products in the **A** + **2** ⇌ **B** + **1** equilibria (A = **1**, **7**, **10**; B = **2**, **8**, **11**) should be individually quantifiable at room temperature ($T_{experiment} << T_{coalescence}$) via the assignable benzoate protons (given that they are not obscured). This would allow the calculation of the equilibrium constant K_{eq} and the driving force ΔG for all three exchange reactions and yield a direct comparison of the relative O–H bond strengths (BDFEs) of the aqua ligands in the ferrous complexes **2**, **8** and **11**.

As a proof of concept, the equilibrium constant K_{eq} for the self-exchange reaction **2** + **1** ⇌ **1** + **2** is determined via the integration of the signals with the longest relaxation times (*para*-protons of the benzoate ligands). For this, broad underlying responses were removed via a baseline correction to obtain more representative values for the signals of interest. A quantification was done for both the above-mentioned experiment with isotope labelled **1^{D}c** + **2a** (Figure 91), and for a mixture of **1c** + **2a** (Figure 92) as additional reference point.

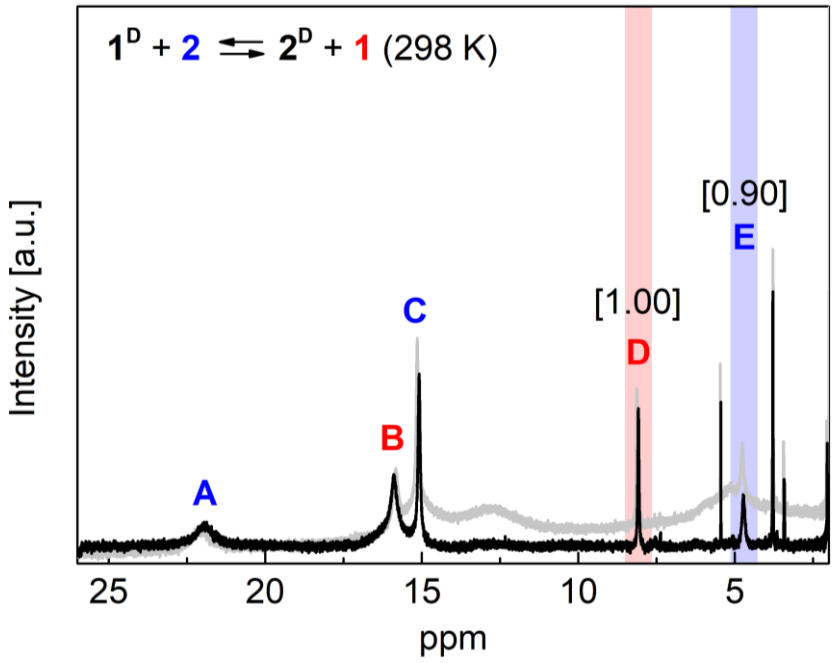

Figure 91. ^{1}H-NMR spectrum (2-26 ppm) of a stoichiometric mixture of **1^{D}c** and **2a** (each 20 mmol·L^{-1}) in MeCN-d3 at 298 K. The raw spectrum is given in grey, a spectrum with adjusted baseline for better integration is given in black. A, C, and E correspond to the *ortho*-, *meta*-, and *para*-protons of **2**, respectively. B and D correspond to the *meta*- and *para*-protons of **1**, respectively; the *ortho*-proton is obscured. The relative integrals for D and E are given in brackets. Some diamagnetic impurities occur at 5.46 and 3.43 ppm, the latter of which is assigned to Et_2O.[131]

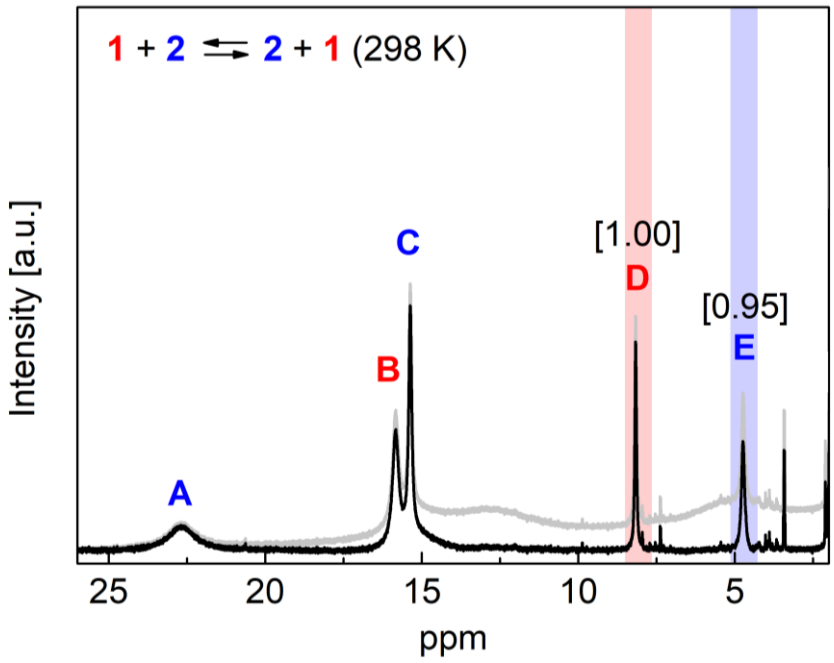

Figure 92. ^{1}H-NMR spectrum (2-26 ppm) of a stoichiometric mixture of **1c** and **2a** (each 20 mmol·L^{-1}) in MeCN-d3 at 298 K. The raw spectrum is given in grey, a spectrum with adjusted baseline for better integration is given in black. A, C, and E correspond to the *ortho*-, *meta*-, and *para*-protons of **2**, respectively. B and D correspond to the *meta*- and *para*-protons of **1**, respectively; the *ortho*-proton is obscured. The relative integrals for D and E are given in brackets. Minor impurities are observed at 7.38 and 3.43 ppm, the latter of which is assigned to Et_2O.[131]

In both experiments, an approximate 1:1 ratio for the complexes **1** and **2** in solution was found, resulting in an equilibrium constant of K_{eq} = 1 and a free reaction energy of ΔG = ±0, as would be expected for a self-exchange reaction.

After establishing the self-exchange reaction itself and the feasibility of the approach, **7** and **10** were each reacted with **2**, respectively. Based on the results obtained in 3.3.1 and 3.3.2, a H-atom exchange reactivity and equilibrium should be observable. With the knowledge of the ^{1}H-NMR chemical shifts of the benzoate protons in **1**, **7**, **10**, **2**, **8**, and **11**, the quantification of the rather sharp signals is expected to also yield the thermodynamic parameters K_{eq} and ΔG. The respective spectra and relative integrations are described in Figure 93, for the reaction of **7** with **2**, and in Figure 94, for the reaction of **10** with **2**.

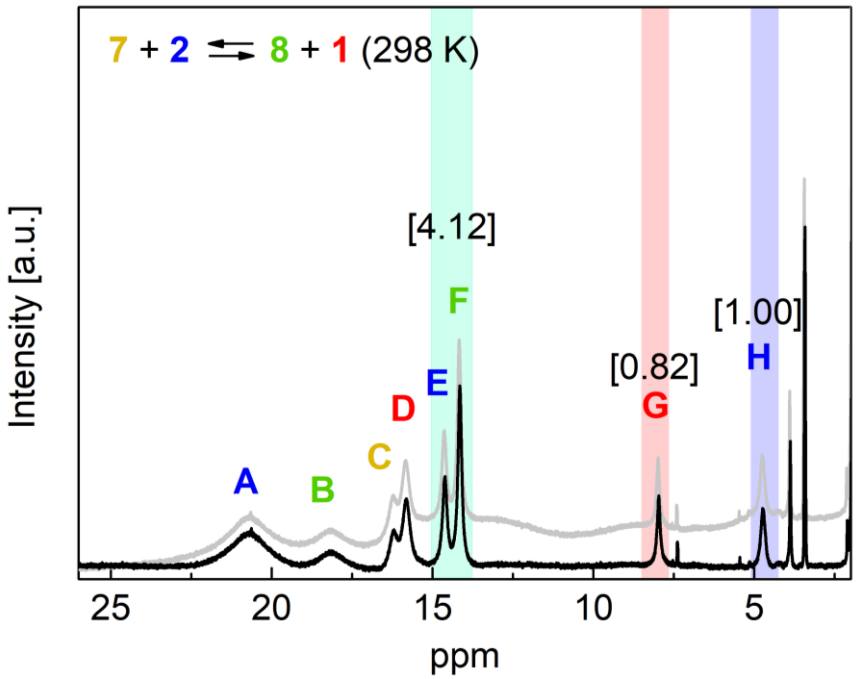

Figure 93. ^{1}H-NMR spectrum (2-26 ppm) of a stoichiometric mixture of **7b** and **2a** (each 20 mmol·L^{-1}) in MeCN-d3 at 298 K. The raw spectrum is given in grey, a spectrum with adjusted baseline for better integration is given in black. A, E, and H correspond to the *ortho*-, *meta*-, and *para*-protons of **2**, respectively. B and F correspond to the *ortho*- and *meta*-protons of **8**, respectively. D and G correspond to the *meta*- and *para*-protons of **1**, respectively; the *ortho*-proton is obscured. C corresponds to the *meta*-proton of **7**; the *ortho*-proton is obscured. The relative integrals for G, H and the sum of E+F are given in brackets. The sum for E+F is given, as a good separation of the integrals is challenging because of tailing. A preliminary attempt returned integrals of 1.55 for E and 2.57 for F. Some impurities are observed at 7.41, 5.46, 3.89, and 3.43 ppm, the latter of which is assigned to Et_2O.[131]

For the reaction of **7** with **2**, eight signals can be assigned to belong to the four complexes **7**, **2**, **8**, and **1** based on previous studies (see above). This provides clear evidence for the occurrence of a H-atom exchange reaction between **2** and **7** and the attainment of an equilibrium. In the spectral range between 2-26 ppm, the only well-separated, rather sharp and somewhat reliably integratable signals are those that represent the *para*-protons of the unsubstituted benzoate in **1** and **2**. However, to calculate the equilibrium constant for the reaction, an integral value for **7** and/or **8** is also required to determine the relative concentrations. Thus, two approaches to attain relative integral values for **8** from the overlapping meta-proton signals of **2** and **8**, respectively, were taken:

As a first attempt, the theoretical integral of 2.00 *meta*-protons from **2** (as justified by the reference value of 1.00 for the *para*-proton of **2**) was subtracted from the sum of the integrals of the two meta-proton signals (integral value = 4.12, see integral of E and F in Figure 93). This yiels a remaining integral of 2.12 and, thus, 1.06 per *meta*-proton of **8**, which represents the relative concentration c_{rel}(**8**) of this species. When assuming exact 1:1 initial concentrations of **7** and **2**, the sum of the relative concentrations of all iron(II) complexes must be identical to the sum of the relative concentrations of all iron(III) complexes. Consequently, the relative concentration of **7** can be calculated as c_{rel}(**7**) = c_{rel}(**2**) + c_{rel}(**8**) - c_{rel}(**1**). As the relative concentrations of **1** and **2** are obtained as the integral values from the *para*-protons, c_{rel}(**7**) = 1.24. By employing these concentrations to calculate the equilibrium constant and the free reaction energy, values of K_{eq} = 0.70 and ΔG = +0.21 kcal·mol^{-1} are obtained.

As a second attempt, c_{rel}(**8**) was obtained via the attempt to integrate only the signal F (Figure 93), ignoring any overlap and tailing by the signal E (c_{rel}(**8**) = 1.31). The relative concentration c_{rel}(**7**) was calculated analogous to the first approach (c_{rel}(**7**) = 1.49). By employing these concentrations to calculate the equilibrium constant and the free reaction energy, values of K_{eq} = 0.72 and ΔG = +0.19 kcal·mol^{-1} are obtained.

Although an experimental error for the integration must be considered (~10% as estimated from the self-exchange reactions above), the above-mentioned result agree very well with those obtained from the quantitative EPR approach presented in section 3.3.1, where the reaction of **7** with TTBP was found to be 0.17 kcal·mol^{-1} more endergonic than the reaction of **2** with TTBP under the same conditions.

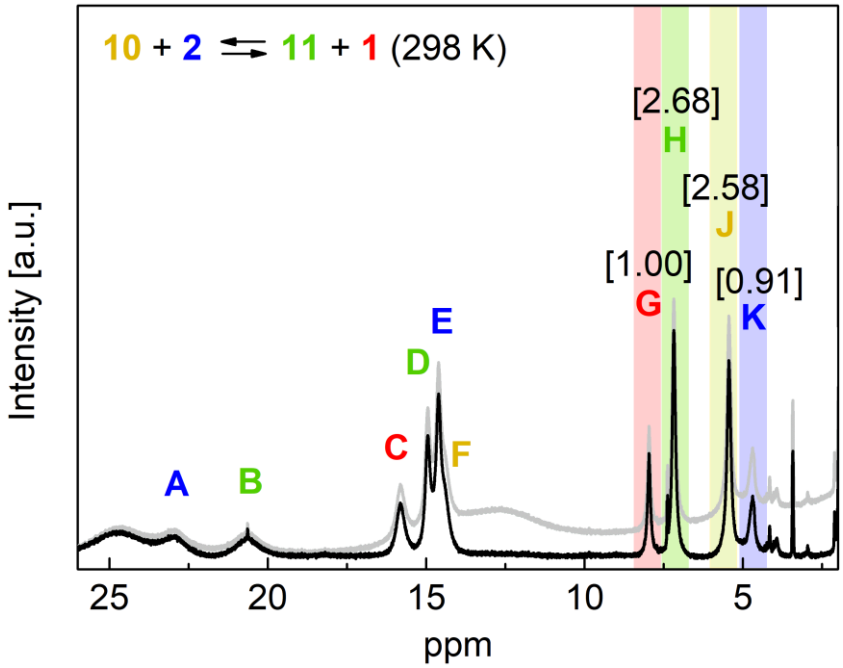

Figure 94. ^{1}H-NMR spectrum (2-26 ppm) of a stoichiometric mixture of **10b** and **2a** (each 20 mmol·L^{-1}) in MeCN-d3 at 298 K. The raw spectrum is given in grey, a spectrum with adjusted baseline for better integration is given in black. A, E, and K correspond to the *ortho*-, *meta*-, and *para*-protons of **2**, respectively. B and D correspond to the *ortho*- and *meta*-protons of **11**, respectively. C and G correspond to the *meta*- and *para*-protons of **1**, respectively; the *ortho*-proton is obscured. F (shoulder) corresponds to the *meta*-proton of **10**; the *ortho*-proton is obscured. H and J correspond to the protons of the –OCH$_3$ substituent in para-position of the benzoate in **11** and **10**, respectively. The broad signal that occurs at 24.7 ppm remains unassigned. The relative integrals for G, H, J, and K are given in brackets. Some impurities are observed at 4.16, 3.93, 2.96, and 3.43 ppm, the latter of which is assigned to Et_2O.[131]

For the reaction of **10** with **2**, ten signals can be assigned to belong to the four complexes **10**, **2**, **11**, and **1** based on previous studies (see above). This provides clear evidence for the occurrence of a H-atom exchange reaction between **2** and **7** and the attainment of an equilibrium. In the spectral range between 2-26 ppm, the signals that represent the *para*-protons of the unsubstituted benzoate in **1** and **2** and the signals that represent the CH$_3$ protons of the methoxy substituted benzoate are rather well-separated, sharp, and good measures to obtain relative concentrations of all four species from their integrals. The integration and normalization to each 1 H yields the relative concentrations as c_{rel}(**1**) = 1.00, c_{rel}(**2**) = 0.91, c_{rel}(**10**) = 2.58/3, c_{rel}(**11**) = 2.68/3. Conveniently, the sum of the concentrations of the ferric species and that of the ferrous

species is near identical. Although, this may be somewhat serendipitous as integration errors are still possible, it is a good control measure to probe if these relative concentrations are realistic. By employing these concentrations to calculate the equilibrium constant and the free reaction energy, values of K_{eq} = 1.14 and ΔG = -0.08 kcal·mol^{-1} are obtained. This result agrees very well with the notion, that the electronic influences of a nitro substituent and a methoxy substituent are opposite, as the reaction of **10** and **2** appears to be exergonic rather than endergonic as was found for the reaction of **7** and **2** (see above). For an even further comparison, a correlation with the substituent influences (Hammett parameters) is done in section 3.3.4.

Table 36. Results of the NMR equilibrium study of H-atom exchange reactions in MeCN-d3 under a nitrogen atmosphere.

Exp.[a]	c_{rel}(Fe^{III})		c_{rel}(Fe^{II})		K_{eq}	ΔrG[c]
1^{D} + **2**	[**1**] = 1.00		[**2**] = 0.90		1	0
1 + **2**	[**1**] = 1.00		[**2**] = 0.95		1	0
7 + **2**[d]	[**1**] = 0.82	[**7**] = 1.24	[**2**] = 1.00	[**8**] = 1.06	0.70	+0.21
7 + **2**[d]	[**1**] = 0.82	[**7**] = 1.49	[**2**] = 1.00	[**8**] = 1.31	0.72	+0.19
10 + **2**	[**1**] = 1.00	[**10**] = 0.86	[**2**] = 0.91	[**11**] = 0.89	1.14	-0.08

K_{eq} and ΔrG for the self-exchange (**1** + **2**) and pseudo self-exchange reactions (**1^{D}** + **2**) are not calculated but taken as a given from theoretical considerations. [a] Educts employed in the [Fe^{III}(L-N$_4$*t*Bu$_2$)(L^1)(OH)] + [Fe^{II}(L-N$_4$*t*Bu$_2$)(L^2)(OH$_2$)] ⇌ [Fe^{II}(L-N$_4$*t*Bu$_2$)(L^1)(OH$_2$)] + [Fe^{III}(L-N$_4$*t*Bu$_2$)(L^2)(OH)] type H-atom exchange reaction. [b] Relative concentrations as derived from the representative integrals. [c] Free reaction energy in kcal·mol^{-1} at 293 K. [d] Two different approaches were used to calculate the relative concentrations/equilibrium constants, see discussion above for more details.

In summary, the thermodynamic driving force for the H-atom exchange reactions of **2** with the complexes with derivatized benzoate ligands **7** and **10** appears to be similar to that of the self-exchange reaction of **2** with **1**. However, distinct energetic differences are found that represent a trend for the electronic derivatization study. Consequently, it can be concluded that the relative O–H bond strengths in the aqua ligands of **2**, **8**, and **11**, which are broken and formed in the equilibrium, follow the following trend:

$BDFE_{MeCN}$(**8**) < $BDFE_{MeCN}$(**2**) < $BDFE_{MeCN}$(**11**). These findings agree with those described in the sections 3.3.1 and 3.3.2 above and will be put into context with established substituent parameters for electronic influences in the following section.

3.3.4. Correlation between the Relative Reactivities and the Hammett Parameters

Because the studied complexes contain substituted benzoate ligands, a comparison to the Hammett parameters that theoretically describe linear electronic substituent influences in derivatives can serve to critically review the obtained trends and gain deeper insights.[161,162] This is especially true because the results obtained have overlapping error margins that somewhat weaken the argument for a reliable trend.

When plotting the bond dissociation free energies obtained from the studies mentioned above against the σ-values for the *para*-substituents of the benzoate ligand (σ(OMe) = -0.27, σ(H) = 0, σ(NO_2) = 0.78),[162] a very good linear correlation is obtained (Figure 95). The obtained equation for the linear fit is $\Delta G = -0.264\sigma + 72.40$ kcal·mol^{-1} (intercept error = 0.004 kcalmol^{-1}, slope error = 0.008).

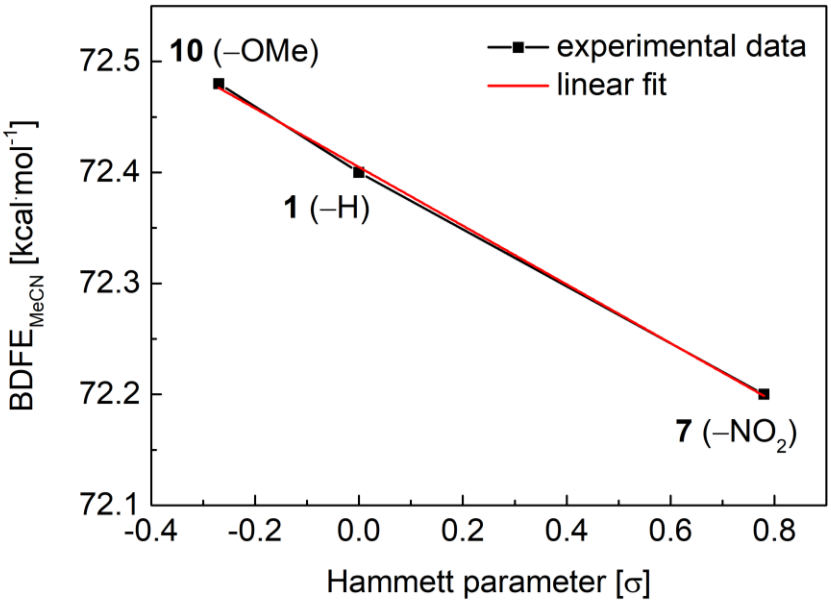

Figure 95. Linear fit of a plot of the Hammett parameters (σ) versus the O–H bond dissociation energies of the aqua iron(II) complexes **2**, **8**, and **11** with $BDFE(2)_{MeCN}$ = 72.40 kcal·mol^{-1} as a reference point for the calculation of the absolute BDFE values for 8 and 11 with the energy differences obtained from the above-mentioned studies (72.20 and 72.48 kcalmol^{-1}, respectively). The fit was obtained with OriginPro 9; residual sum of squares: $3.96 \cdot 10^{-5}$, Pearson's r = -0.999, adjacent r^2 = 0.998.

When plotting the electrochemical potentials of the Fe^{3+}/Fe^{2+} reduction of **1**, **7**, and **10** obtained from the electrochemical investigation against the σ-values for the *para*-substituents of the benzoate ligand, again a very good linear correlation is obtained (Figure 96). The obtained equation for the linear fit is $\Delta E_{1/2} = 98.8\sigma - 788$ mV (intercept error = 1.21 mV, slope error = 2.53).

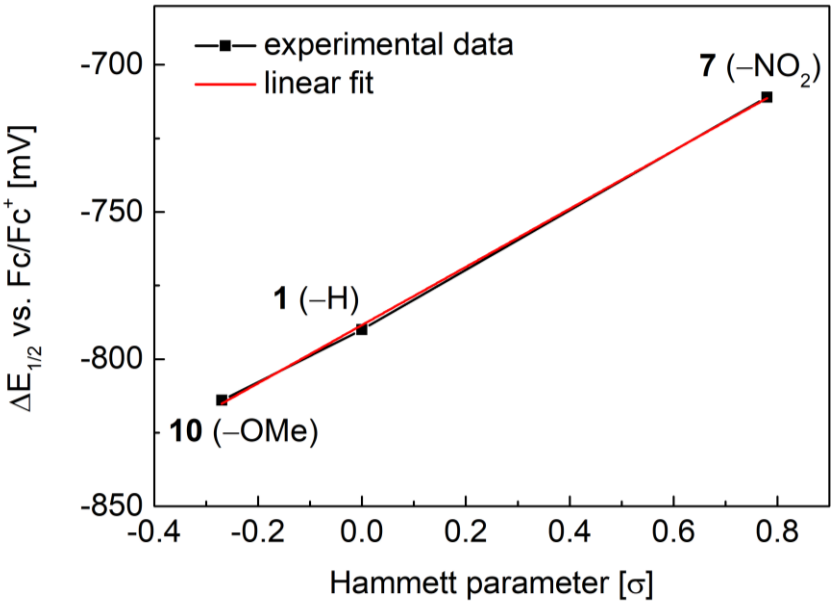

Figure 96. Linear fit of a plot of the Hammett parameters (σ) versus the reduction potentials of the hydroxo iron(III) complexes **1**, **7**, and **10** as obtained directly from the electrochemical study. The fit was obtained with OriginPro 9; residual sum of squares: 3.82, Pearson's r = 1.00, adjacent r^2 = 1.00.

With the Bordwell equation (equation 3),[96,97,109,157] the pK_a values for the individual complexes can be derived and also plotted against the Hammett parameters (Figure 97). The approach yields pK_a values for the aqua iron(II) complexes in acetonitrile as pK_a(**2**) = 27.75, pK_a(**8**) = 26.27, and pK_a(**11**) = 28.21. The obtained equation for the linear fit is $\Delta pK_a = -1.859\sigma - 27.73$ mV (intercept error = 0.019 mV, slope error = 0.040).

$$(3)\quad BDFE_{HA} = 1.37pK_{HA} + 23.06E_{ox}(A^-) + C_G$$

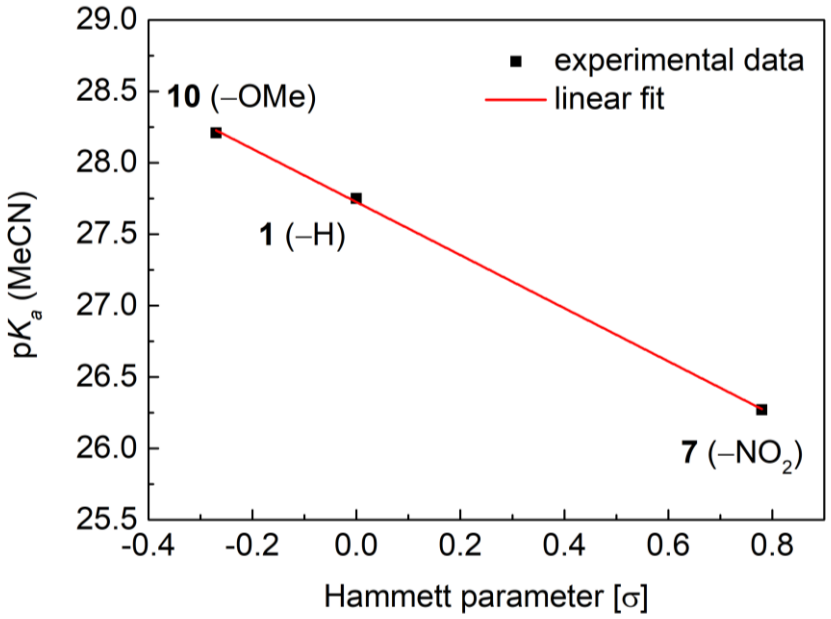

Figure 97. Linear fit of a plot of the Hammett parameters (σ) versus the pK_a values of the hydroxo iron(III) complexes **1**, **7**, and **10** as obtained from the experimental data and equation 3. The fit was obtained with OriginPro 9; residual sum of squares < 0.00, Pearson's r = -1.00, adjacent r^2 = 1.00.

Not only do the excellent correlations validate the derived trends from this extensive derivatization study but they, furthermore, allow an interpretation of the strengths of the competing influences of the pK_a value and the electrochemical potential on the BDFEs in the model complexes, and lastly also in the enzymatic active site that served as a model. When employing $\Delta G(\mathbf{A}) = -n \cdot F \cdot \Delta E_{1/2}(\mathbf{A})$ with n = 1, F = 96485 C·mol^{-1}, and A = **1**, **7**, or **10**, the energetic differences contributed by the electron transfer can be determined as -0.55 kcalmol^{-1} for **10** and +1.82 kcalmol^{-1} for **7**. However, the results from the reactivity studies point toward a higher BDFE in complex **10** by +0.08 kcalmol^{-1} and a lower BDFE in complex **7** by -0.20 kcalmol^{-1} referenced to **1**. This means that the contribution of the pK_a value counteracts the effect of the electrochemical potential by +0.63 kcalmol^{-1} in the case of **10** and by -2.02 kcalmol^{-1} in **7** and is, thus, dominant for the manipulation of the O–H bond strength. The findings for the different energy contributions by pK_a and $\Delta E_{1/2}$ are presented in Table 37 for direct comparison.

Table 37. Energetic contributions of the electrochemical potential $\Delta E_{1/2}$ and the pK_a to the strength of the reactive O–H bond in the aqua ligands of **2**, **8**, and **11**.

–R[a]	BDFE[b] [kcal·mol^{-1}]	$\Delta E_{1/2}$[c] vs Fc^0/Fc^+ [V]	$\Delta E_{1/2}$ [kcal·mol^{-1}]	pK_a[d]	pK_a [kcal·mol^{-1}]	C_G(MeCN) [kcal·mol^{-1}]
–H	72.40	-0.790	-18.22	27.75	+38.02	+52.6
–NO_2	72.20	-0.711	-16.40	26.27	+35.99	+52.6
–OMe	72.48	-0.814	-18.77	28.21	+38.65	+52.6

[a] Substituents in the *para*-position of the benzoate ligand in the studied aqua iron(II) and hydroxo iron(III) complexes. [b] BDFE values in MeCN for the aqua iron(II) complexes referenced against the rounded value of $BDFE_{MeCN}$(**2**). [c] Reduction potential of the hydroxo iron(III) complexes. [d] pK_a values of the aqua iron(II) complexes. The energy values of $\Delta E_{1/2}$ and pK_a represent their contributions to the BDFE of the ferrous aqua complexes.

3.4. Summary of the Reactivity Studies

In summary, the comparative reactivity studies of electronic derivatives of $[Fe(LN_4{}^tBu_2)(O_2CPh)(OH)]^+$ (**1**) containing *para*-substituted benzoate ligands ($–NO_2$, **7** and –OMe, **10**, section 3.1) conclude additional successful synthetic analogue approaches and expand the library of previously unprecedented structural-functional models for rabbit lipoxygenase (rLOX). The activity of **7** and **10** towards hydrogen atom abstraction from weak O–H and C–H bonds and the interpretation of the concerted production of the corresponding ferrous complexes **8** and **11**, respectively, is demonstrated via quantitative EPR spectroscopy and NMR spectroscopy. In terms of EPR spectroscopy, the same approach as in chapter 2 was used to obtain the equilibrium constant and the free reaction energy for a reaction of **7** with TTBP. In terms of NMR spectroscopy, kinetic studies were employed to compare the activation barriers for the hydrogen atom abstraction from weak C–H bonds by **1**, **7**, and **10**, and pseudo-self-exchange equilibria between **7** + **2** ⇌ **8** + **1** and **10** + **2** ⇌ **11** + **1** were followed to derive the equilibrium constants, free reaction energies, and consequently the relative bond strengths and reactivities of the complexes. The thermodynamic and kinetic results obtained for **7** and **10** are at first glance similar to those obtained for **1**. A closer investigation of the thermodynamic results allowed for the distinction of small bond energy differences and a trend that shows a linear correlation when plotted against the Hammett parameters. From the Hammett plots for the BDFEs, for the electrochemical potentials, and by employing the Bordwell equation, the pK_a values of the aqua iron(II) complexes **2**, **8**, and **11** could also be determined and the influences of the relative competing effects on the bond strengths by the electrochemical potential modulation and the complex pK_a modulation could be exemplified. In this, the pK_a modulation appeared to be slightly more dominant. This reveals important aspects of the hexagonal feature spanned by the intramolecular interaction in the *cis*-(carboxylato)(hydroxo)iron(III) unit also contained in the enzyme which likely mediates the counteracting effects in a way that they almost cancel each other out.

It is noteworthy, that the unexpectedly low activity of the ferric hydroxide complex **1** toward C–H abstraction from CHD at higher concentrations, a kinetic irregularity found during the studies described in chapter 2, is reproduced by the derivatives **7** and **10**. At the same time, their relative thermodynamic parameters appear to be concentration

independent as derived from similar results at differing concentration regimes in the EPR and NMR experiments, respectively. This points toward a systemic cause of inhibition/loss of activity as an intrinsic property of these types of complexes when reacting with organic substrates. An attempt to explain the reduced activity via concentration-dependent association of complex cations in solution (self- and/or product-inhibition) is provided in the following chapter.

4. Hydrogen-bridged Associates of Monocationic *cis*-(carboxylato)(hydroxo)iron(III) and Monocationic *cis*-(carboxylato)(aqua)iron(II) Complexes

This work has described synthetic pathways, characterizations, and reactivity studies of multiple *cis*-(carboxylato)(hydroxo)iron(III) and *cis*-(carboxylato)(aqua)iron(II) complexes (chapters 2 and 3). Although the studies were extensive and highly elusive, especially the kinetics of the H-atom abstraction reactions from organic substrates (all done in MeCN) have been puzzling. The previous discussions have concluded an inhibition of the activity of the H-atom abstraction reactivity of the ferric complexes at increasing complex concentrations. It has been hinted at a potential association of two complex units via intermolecular hydrogen bonding, particularly between the hydroxide/aqua ligands (Scheme 20). Although such associates describe key intermediates in the "outer-sphere-type" H-atom exchange reactions between ferric hydroxide and ferrous aqua complexes that have been exemplified in this work, their persistence in solution and influence on (re-)activities of the individual complexes with other substrates remains speculative to this point. The association of two ferric complexes via hydroxide-hydroxide hydrogen bridging is even more speculative to this point, although not implausible.

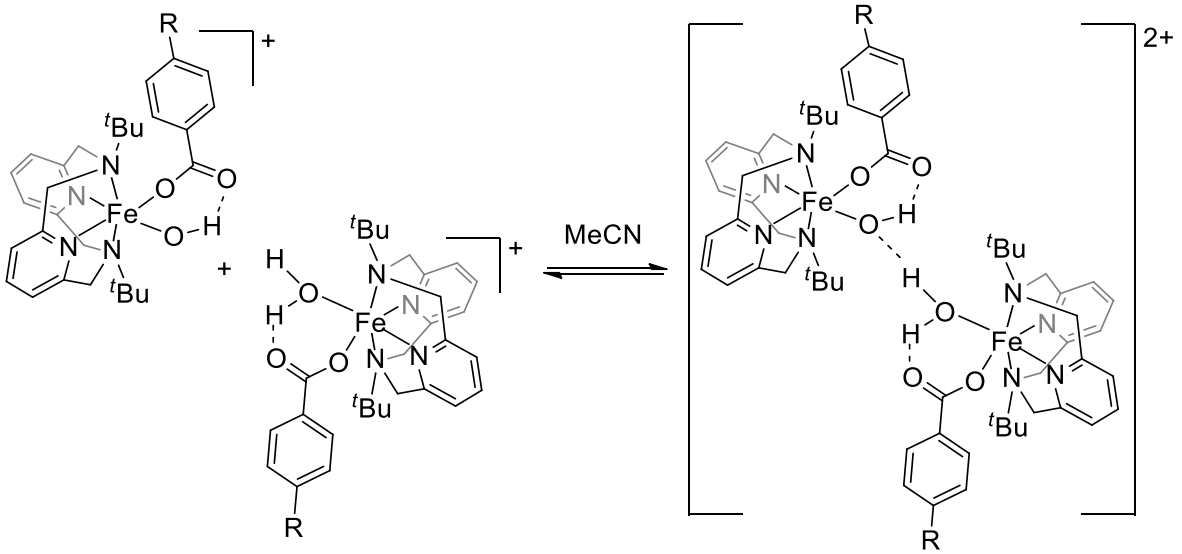

Scheme 20. Schematic depiction of the formation of hydrogen-bridged $\{[Fe^{III}(L\text{-}N_4{}^tBu_2)(O_2CPh^R)(OH)][Fe^{II}(L\text{-}N_4{}^tBu_2)(O_2CPh^R)(OH_2)]\}^{2+}$ associates from $[Fe^{III}(L\text{-}N_4{}^tBu_2)(O_2CPh^R)(OH)]^+$ and $[Fe^{II}(L\text{-}N_4{}^tBu_2)(O_2CPh^R)(OH_2)]^+$ in MeCN solution.

In this chapter, evidence for the formation of such associates is provided to support the hypothesis of a concentration dependency of the activity of the *cis*-(carboxylato)(hydroxo)iron(III) complex originating from self-inhibition. At the same time, this evidence provides a reasonable explanation for the observation that a synthetic approach via direct oxidation of *cis*-(carboxylato)(aqua/alcohol)iron(II) precursors is impractical to obtain analytically pure *cis*-(carboxylato)(hydroxo)iron(III) complexes, albeit the synthetic pathway chosen in all previous works, because the partial association of **1** and **2** via hydrogen bridging may inhibit or at least slow down the quantitative oxidation of **2** with oxygen. [2,112,113]

For this, **1** and **2** were co-crystallized with two BPh_4 counterions as {[**1**][**2**]}$(BPh_4)_2$ in an exemplary attempt to prove that hydrogen-bridged associates are feasible and thermodynamically well-accessible despite the cationic charges of both complexes. The following sections describe the synthesis and characterization of {[**1**][**2**]}$(BPh_4)_2$ to illuminate the nature of the associate and potential electronic interactions between the iron sites. Moreover, the kinetics of the self-exchange reaction between **1** and **2** are studied in more detail via EXSY-NMR spectroscopy in an attempt to elucidate irregularities in concentration dependency which are to be expected if pre-organized associates are stabilized and persistent at least in part in solution.

4.1. Synthesis and Characterization

4.1.1. Synthesis

The first synthetic achievement of a co-crystallization of $[Fe^{III}(L\text{-}N_4{}^tBu_2)(O_2CPh^R)(OH)]^+$ (**1**) and $[Fe^{II}(L\text{-}N_4{}^tBu_2)(O_2CPh^R)(OH_2)]^+$ (**2**) in a 1:1 ratio was serendipitous: After a crystallization attempt of $[Fe(L\text{-}N_4{}^tBu_2)(O_2CPh)(OH_2)][BPh_4]$ in MeCN/Et_2O under N_2 atmosphere failed (synthetic procedure closely related to those described for **2a**-**c** in section 2.1.1), the mixture was kept in the freezer at -35 °C for two weeks. Likely because the employed sealing grease is not suitable for such low temperatures (Tribuflon III, temperature range given on the tube: -30-300°), some air diffused into the mixture and partially oxidized the ferrous complex in solution. Two well-separable crystals formed under these conditions: The bulk amount of crystals (brown-yellow needles) could be identified as {[**1**][**2**]}$(BPh_4)_2$ (Scheme 21, pathway 1) and a few small lemon-yellow crystals could be identified as $[Fe(L\text{-}N_4{}^tBu_2)(O_2CPh)(OH_2)]_2(BPh_4)_2{\cdot}2H_2O{\cdot}2Et_2O{\cdot}MeCN$ (**2e**). This event became important in understanding that a co-crystallization of **1** and **2** is possible, and ultimately led to the revelation, that all attempts to synthesize **1** via oxidation of **2** or *cis*-(benzoato)(alcohol)iron(II) precursors resulted in crystallizations of **1** containing some content of **2** because the oxidation was never quantitative. The remaining iron(II) contents in bulk samples prepared in this way can be identified via Mößbauer spectroscopy (see also section 4.1.4) and somewhat followed via single crystal X-ray structural analysis, if the iron(II) impurities are very significant (section 4.1.2).

When the interest in a further study of the {[**1**][**2**]}$(BPh_4)_2$ sample rose, a reproducible synthetic pathway was developed. It was found that a stoichiometric solution of **2a** and **1a** with one equivalent of $NaBPh_4$ under nitrogen atmosphere in MeCN affords the {[**1**][**2**]} associate that crystallizes well with the two BPh_4^- anions upon addition/diffusion of distilled Et_2O. Because the solubility of $NaClO_4$ in MeCN with increasing Et_2O content is higher than that of {[**1**][**2**]}$(BPh_4)_2$, a fractional crystallization yields analytically pure (Table 38) crystalline bulk material (Scheme 21, pathway 2).

Generally, the tendency of **1** and **2** to form associates with good crystallization properties may well be the reason why the oxidation of **2** to **1** was found to not be

quantitative. It demonstrates that the $\{[\mathbf{1}][\mathbf{2}]\}^{2+}$ association is thermodynamically favorable despite the positive charges of the individual cations and likely also occurs in solution prior to the long-range ordering of many $\{[\mathbf{1}][\mathbf{2}]\}^{2+}$ pairs in a crystal lattice.

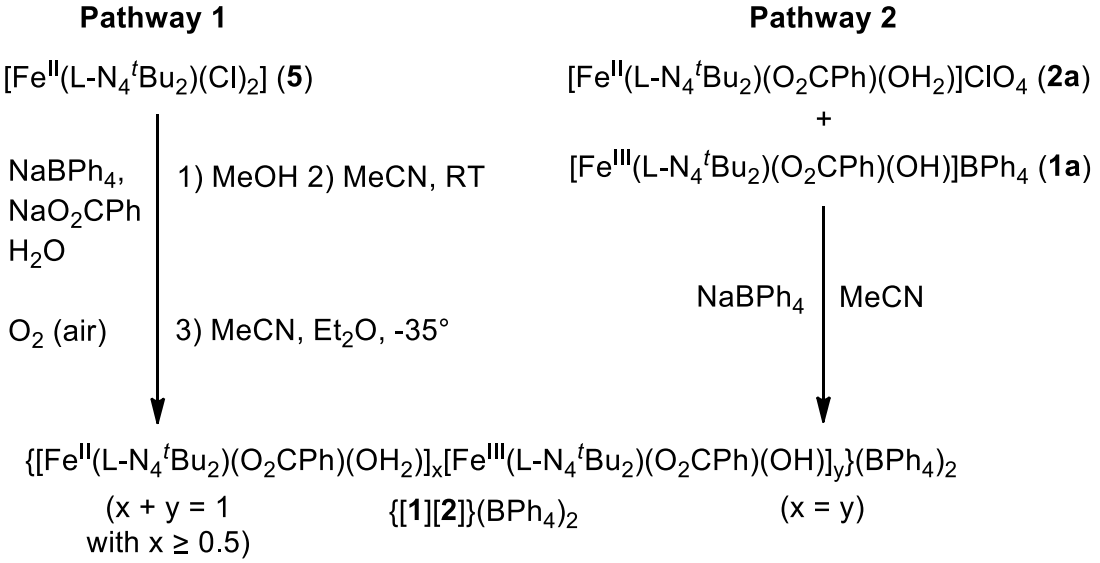

Scheme 21. Two possible synthetic pathways to afford $\{[\mathbf{1}][\mathbf{2}]\}(BPh_4)_2$. Pathway 1 affords mixtures of **1** and **2** $\{[\mathbf{1}]_x[\mathbf{2}]_y\}(BPh_4)_2$ with $x \geq 0.5$ and is unreliable as a targeted synthesis of the 1:1 complex (x = y). Pathway 2 describes a reliable, reproducible way to synthesize $\{[\mathbf{1}][\mathbf{2}]\}(BPh_4)_2$. Pathway 1 also yielded small amounts of $[Fe(L\text{-}N_4{}^tBu_2)(O_2CPh)(OH_2)]_2(BPh_4)_2{\cdot}2H_2O{\cdot}2Et_2O{\cdot}MeCN$ (**2e**).

Table 38. Exemplary elemental analysis results and maximal deviations in % for $\{[\mathbf{1}][\mathbf{2}]\}(BPh_4)_2$ synthesized via pathway 2. Data is given in the format “calculated (found)”.

	C [%]	**H** [%]	**N** [%]	max. dev. [%]
$\{[\mathbf{1}][\mathbf{2}]\}(BPh_4)_2$	73.49 (73.28)	6.81 (6.72)	6.47 (6.51)	0.21

4.1.2. Structural Analysis

Compound {[**1**][**2**]}$(BPh_4)_2$ was crystallized directly from the synthetic pathways 1 and 2 (see above) and characterized by single crystal X-ray structure analysis at 150 K and 293 K, respectively. A perspective view of the structure obtained at 293 K is given in Figure 98. Notably, The structural parameters of {[**1**][**2**]}$(BPh_4)_2$ are very similar to those of **1a** (Table 40). When expanding the structure of **1a** (see also section 2.1.2) by one symmetry generated cation, it is observed that a {[**1**][**1**]}$(BPh_4)_2$ unit is present (Figure 99). Because the purity of **1a** is verified via Mößbauer spectroscopy (section 2.1.4), a contamination of **2** in **1a** is ruled out. Although the hydrogen atom at the hydroxide was freely refined, it is reasoned that partial hydrogen bonding occurs via rotation of the O–H bond around the Fe–O axis to stabilize the $\{[\mathbf{1}][\mathbf{1}]\}^{2+}$ unit. This shows that the association/hydrogen bonding interaction of these complexes is not limited to $\{[\mathbf{1}][\mathbf{2}]\}^{2+}$ but may also occur in intermediate ratios of $\{[\mathbf{1}]_x[\mathbf{2}]_y\}^{2+}$. However, the ratios in such a motif must be limited by $0.5 \leq x \leq 1$ with $x + y = 1$ to ensure that at least one lone pair acceptor function is present. This is demonstrated by the additional crystallization of minor amounts of the purely ferrous [Fe(L-$N_4{}^t Bu_2$)$(O_2CPh)(OH_2)]_2(BPh_4)_2 \cdot 2H_2O \cdot 2Et_2O \cdot MeCN$ (**2e**) compound in the crystallization attempt following synthetic pathway 1 (Figure 100).

Interestingly, however, the structure of **2e** demonstrates that at least a partial association of $\{[\mathbf{2}][\mathbf{2}]\}^{2+}$ units is also achieved. Here, hydrogen bond interactions between the aqua ligand protons and the carboxylate ligand of a second molecule stabilize the association of two $[\mathbf{2}]^+$ cations via an extensive secondary hydrogen bond network (Figure 100, Table 41). Although a controlled synthesis of **2e** was not achieved and only single-crystal X-ray structural analysis was performed on the few crystals obtained serendipitously, the structure reveals the importance of hydrogen bond interactions in stabilizing $[\mathbf{1}]_x[\mathbf{2}]_y(BPh_4)_2$ compounds and provides an insight into the strong tendency of association of the monocationic *cis*-(carboxylato)(hydroxo/aqua)iron(II/III) complexes with *tert*-butyl substituted diazapyridinophane macrocyclic ligands.

The structural parameters, selected distances and angles, and short distance interactions for {[**1**][**2**]}$(BPh_4)_2$ and **2e** are given in Tables 38-40 and compared to those obtained for **1a** (Tables 38, 39, and 41). Because general aspects of the structures of the $[Fe^{III}(L\text{-}N_4tBu_2)(O_2CPh)OH]^+$ (**1**) and $[Fe^{II}(L\text{-}N_4tBu_2)(O_2CPh^R)OH_2]^+$ (**2**) cations have been extensively described in section 2.1.2, only supplementary aspects related to the $\{[\mathbf{1}]_x[\mathbf{2}]_y\}^{2+}$ associations are discussed in this section. Structural parameters, a full list of bond lengths, angles, and hydrogen bonds for the structures derived from {[**1**][**2**]}$(BPh_4)_2$, **1a**, and **2e** can be found in the attachment.

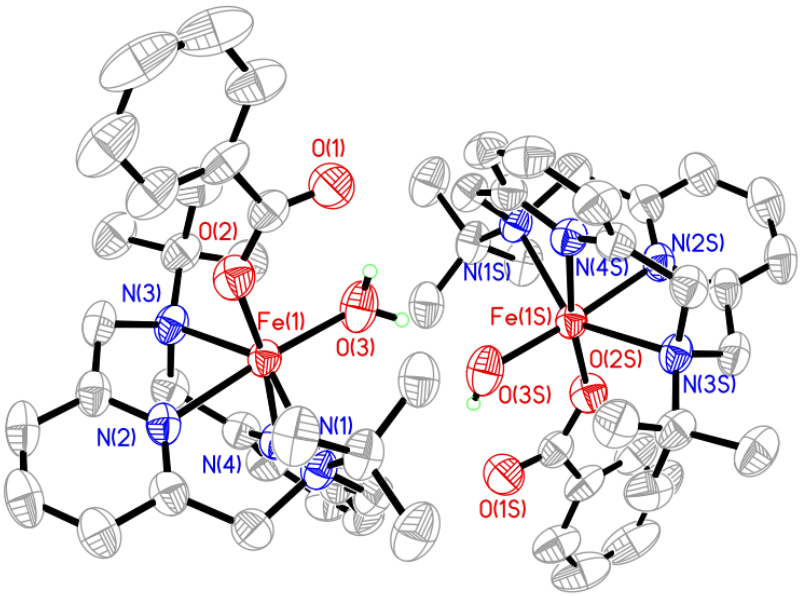

Figure 98. Perspective view of the complex cation (298 K, averaged bond lengths) and a symmetry generated counterpart in the structure of {[**1**][**2**]}$(BPh_4)_2$ with thermal ellipsoids displaying a probability level of 50%. The atoms of the symmetry generated molecule are labelled with an S. Hydrogen atoms are omitted for clarity with the exception of the protons bound to the water and hydroxide ligands O(3) and O(3S), respectively. Because the associates only differ in one hydrogen atom, the localization of **2** and **1** cannot be refined and intermediate bond distances for a single site with an inversion center between the two cations are found. The bridging hydrogen at O(3) is refined with 50% occupation at the averaged single site. Thus, for clarity, the hydrogen is only shown at one of the two O(3) sites to afford the theoretical water and hydroxide ligands at O(3) and O(3S), respectively. The hydrogen atoms at O3 (O(3S)) were geometrically localized.

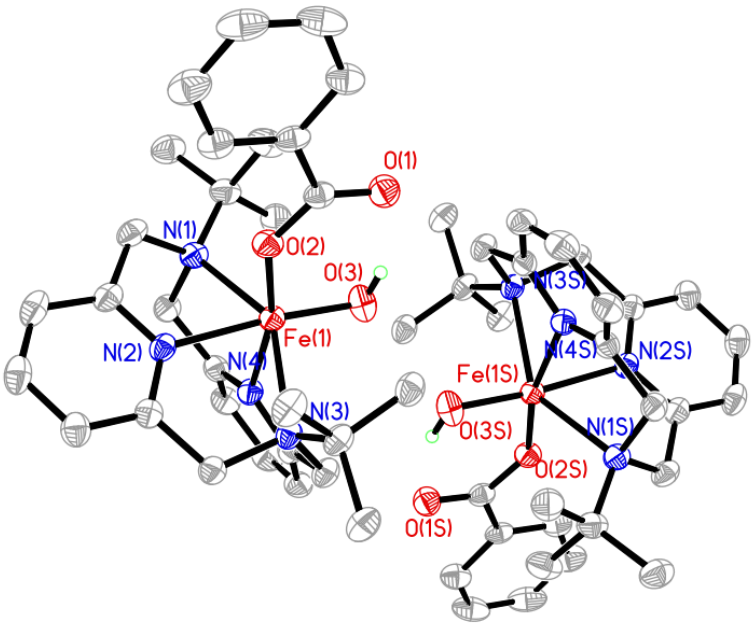

Figure 99. Perspective view of the ferric complex cation (150 K) and a symmetry generated counterpart in the structure of **1a** with thermal ellipsoids displaying a probability level of 50%. The atoms of the symmetry generated molecule are labelled with an S. Hydrogen atoms are omitted for clarity with the exception of the protons bound to the hydroxide ligands O(3) (O(3S)). The hydrogen at O3 (O(3S)) was freely refined.

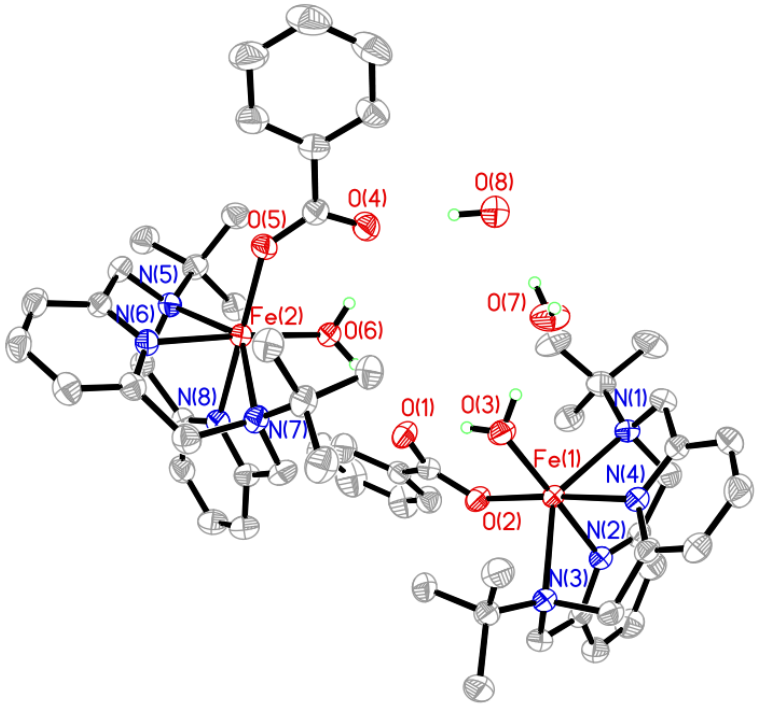

Figure 100. Perspective views of the ferrous complex cations (150 K) and water molecules in the structure of **2e** with thermal ellipsoids displaying a probability level of 50%. Hydrogen bond interactions are indicated in grey. Hydrogen atoms are omitted for clarity with the exception of the protons bound to O(3), O(6), O(7), and O(8) which were freely refined (one H is obscured by O(8)).

Table 39. Selected bond lengths and interatomar distances (in Å) rounded to the third decimal in the complex cations of {[**1**][**2**]}$(BPh_4)_2$, **2e**, and **1a** at 150 K, and {[**1**][**2**]}$(BPh_4)_2$ from a different batch at 293 K (**1a** adapted from chapter 2 and previously published results).[1] For **2e**, values are given for the two individual cations (Fe(1), Fe(2)). The nature of the packing in {[**1**][**2**]}$(BPh_4)_2$ (inversion center between **1** and **2**) only allows the determination of averaged bond distances.

distance	**1a** (150 K)	{[**1**][**2**]}$(BPh_4)_2$ (150 K)	{[**1**][**2**]}$(BPh_4)_2$ (293 K)	**2e**[a] (150 K)
Fe-O(2)	1.955(1)	1.969(1)	1.964(2)	2.058(2), 2.035(2)
Fe-O(3)	1.835(1)	2.005(1)	1.988(2)	2.091(2), 2.129(2)
Fe-N(1)	2.323(2)	2.306(1)	2.319(2)	2.369(2), 2.361(2)
Fe-N(3)	2.290(1)	2.356(1)	2.370(2)	2.371(2), 2.375(2)

Fe-N(2)	2.107(1)	2.086(1)	2.096(2)	2.090(2), 2.093(2)
Fe-N(4)	2.097(2)	2.086(1)	2.093(2)	2.090(2), 2.098(2)
Fe•••O(1)	3.322(1)	3.344(1)	3.343(2)	3.454(2), 3.441(2)
O(1)•••O(3)	2.955(2)	2.794(2)	2.813(3)	2.675(2), 2.661(2)
C(23)-O(2)	1.305(2)	1.286(2)	1.292(3)	1.266(3), 1.268(3)
C(23)-(O1)	1.224(2)	1.241(2)	1.230(3)	1.258(3), 1.256(3)
C(23)-C(ring)	1.499(3)	1.499(3)	1.494(3)	1.502(4), 1.505(3)
O(3)•••O(3S)	3.017(2)	2.777(2)	2.795(3)	4.372(2)
Fe(1)•••Fe(1S)	6.0000(5)	6.1242(5)	6.1350(5)	7.3966(9)
Σ (hexagon)[b]	9.32(3)	9.35(4)	9.37(5)	9.38(4), 9.39(3)

[a] The numbering for the second cation was adjusted to match that of the first cation for better comparability. [b] Sum of the distances contained in the hexagon spanned by Fe-O(1)-C(23)-O(2)-H(3A)-(O3)-Fe. N(1) and N(3) are the axial amine donors, N(2) is the pyridine nitrogen atom *trans* to the hydroxide/aqua oxygen donor O(3), N(4) is the pyridine nitrogen atom *trans* to the carboxylate oxygen donor O(2). O(1) refers to the carbonyl oxygen atom of the carboxylate ligand. C(23) is the carboxylate carbon atom and C(ring) is the adjacent carbon atom. For more details see attachment.

Table 40. Structural parameters for {[**1**][**2**]}$(BPh_4)_2$, **2e**, and **1a** (**1a** adapted from chapter 2 and previously published results).[1]

	1a	{[**1**][**2**]}$(BPh_4)_2$	{[**1**][**2**]}$(BPh_4)_2$	**2e**
Spacegroup	$P\bar{1}$ (triclinic)	$P\bar{1}$ (triclinic)	$P\bar{1}$ (triclinic)	$P2_1/c$ (monoclinic)
T	150 K	150 K	293 K	150 K
Z	2	1	1	4
a [Å]	11.3035(5)	11.3453(5)	11.4553(5)	30.5776(9)
b [Å]	13.9434(8)	13.7682(5)	13.8985(5)	13.9734(4)
c [Å]	15.4818(8)	15.3513(8)	15.4938(5)	25.6180(6)
α	91.780(4)°	90.366(4)	90.956(3)	90.0
β	109.394(5)°	107.897(4)	108.081(3)	98.633(3)
γ	102.135(4)°	99.365(4)	99.791(3)	90.0
V [$Å^3$]	2236.7(2)	2247.43(18)	2304.46(16)	10821.9(5)

[a] Z differs between **1a** and {[**1**][**2**]}$(BPh_4)_2$ because the {[**1**][**2**]}$^{2+}$ unit is considered as one formula unit whereas a single [**1**]$^+$ cation is considered for **1a** despite the presence of {[**1**][**1**]}$^{2+}$ units with short distance interactions. The volume, however, relates to the asymmetric unit which only considers a single cation for all three structures containing ferric cations because of the inversion center found between the cations in the {[**1**][**2**]}$^{2+}$ and {[**1**][**1**]}$^{2+}$ units.

The differences found for the structural parameters of **1a** and {[**1**][**2**]}$(BPh_4)_2$ (Table 40) are extremely minor, meaning that the structures are very closely related and likely any intermediate composition between {[**1**][**2**]}$(BPh_4)_2$ and **1a** (≙ {[**1**][**1**]}$(BPh_4)_2$) with variable amounts of [**2**]$^+$ is also feasible. The close resemblance of the structural parameters is despite the significant differences in the bond distances of the complex cations: {[**1**][**2**]}$(BPh_4)_2$ displays intermediate bond lengths between the two valence-pure reference compounds **1a** and **2e**. Thus, significant co-crystallized amounts of [**2**]$^+$ in the structure of **1a** should be detectable via bond length analysis.

Notably, the distance between the di- or triatomic oxygen donor ligands is shortest for {[**1**][**2**]}$(BPh_4)_2$, suggesting that the Fe^{II}/Fe^{III}-pair has the strongest intermolecular interaction. Although the bond distances are averaged between the two valences of **1** and **2** and the short O···O distance of 2.777(2) leaves room for speculation that a H-atom self-exchange reaction could take place in the solid state, the X-ray structural analysis is not a suitable method to identify such events. Even though the hydrogen atom belonging to the aqua ligand in **2** that is oriented towards the theoretical lone pair of **1** could be localized and freely refined the intermediate bond lengths could equally originate from statistical distributions of **1** and **2** as well as hydrogen atom self-exchange reactions at a timescale faster than the XRD experiment. No preferred occupation of either of the two positions is expected in either case because the $\{[\mathbf{1}][\mathbf{2}]\}^{2+}$ units are isolated in the structure by an encompassing “cloud” of negatively charged BPh_4^- anions (Figure 101).

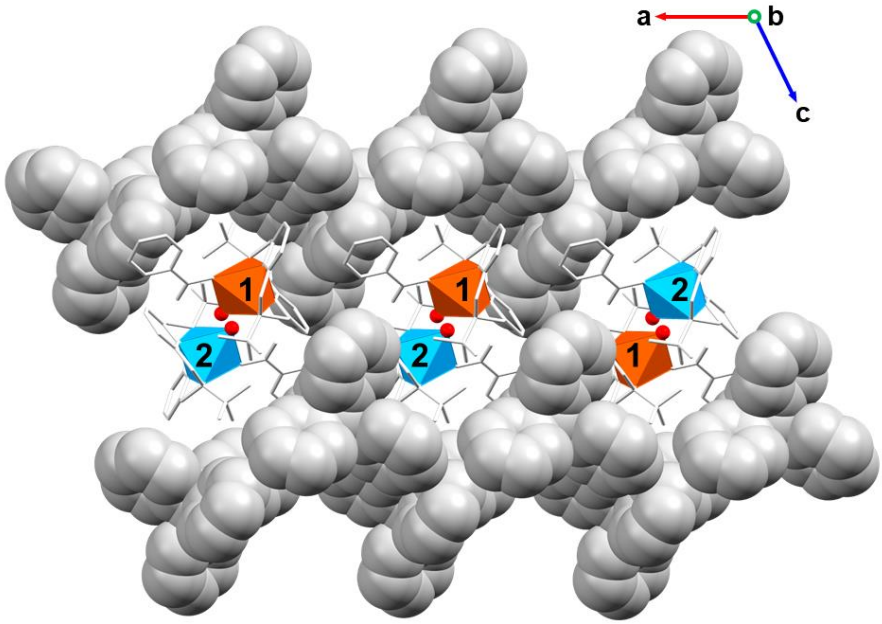

Figure 101. Perspective view of the packing in the crystal structure {[**1**][**2**]}$(BPh_4)_2$ at 293 K as viewed through the *b*-axis. The first coordination spheres are depicted as polyhedra, the ligand backbone as capped sticks, and the BPh_4^- counter anion as grey space-fill model. The hydroxide/aqua ligands are depicted as red balls. The polyhedra are labelled arbitrarilly as **1** and **2** for illustration purposes only, no correct assignment is possible, and no ordering was found. H-atoms are omitted for clarity.

Because of the apparent necessity of an extensive hydrogen bond network and additional solvent molecules (Figure 100, Table 41), [**2**](BPh_4) could only be crystallized once and only in the form of **2e** over the course of this work. In contrast, [**2**]$^+$ could be well-crystallized as [**2**](ClO_4^-) (**2a**), [**2**](PF_6) (**2b(1)** and **2b(2)**), and [**2**](CF_3SO_3) (**2c**) salts without the necessity of auxillary solvent molecules, because they all act as hydrogen bond acceptors in the respective structures (see chapter 2). In the case of [**2**](BPh_4) and, a second cation of **2** is required to satisfy the apparently strong tendency to form hydrogen bridging interactions, as is found in the structure of **2e**. It is surprising, that interactions with another monocationic complex are favored over a simpler interaction with only a solvent molecule. This may imply that there is also a non-negligible tendency for homo-association of [**2**]$^+$ cations as hydrogen bonded {[**2**][**2**]}$^{2+}$ pairs where the aqua ligand of one molecule forms an interaction to the benzoate ligand of another.

Table 41. Hydrogen bond lengths and angles found in **2e** at 150 K.

	d(D-H) [Å]	d(H…A) [Å]	d(D…A) [Å]	<(D-H-A)
O(3)-H(3A)...O(1)	0.828(17)	1.88(2)	2.676(2)	161(3)
O(3)-H(3)...O(7)	0.857(17)	1.809(18)	2.665(3)	176(3)
O(6)-(6B)...O(1)	0.847(17)	1.861(18)	2.705(2)	174(3)
O(6)-(6A)...O(4)	0.833(17)	1.87(2)	2.661(2)	158(3)
O(7)-(7A)...O(8)	0.834(18)	1.991(19)	2.820(3)	173(4)
O(7)-H(7B)...O(9)#1	0.841(18)	1.971(19)	2.803(3)	171(3)
O(8)-H(8B)...O(4)	0.857(18)	1.872(19)	2.726(3)	174(3)

D = donor, A = acceptor, symmetry transformation: #1 x,-y-1/2,z-1/2. O(9) is the oxygen atom of one of two Et_2O solvent molecules contained in the crystal packing.

The results for the hydrogen bond interaction analysis of {[**1**][**2**]}(BPh_4)$_2$ are less surprising: As would be expected, the averaged intramolecular hydrogen bond distance between the hydroxide/aqua ligand and the benzoate in the {[**1**][**2**]}$^{2+}$ associate (Table 42) lies between those observed for valence-pure examples of [**1**]$^+$ and [**2**]$^+$ (see also section 2.1.2). However, it is peculiar that the O(1)…O(3)…O(3)#1 angle is almost identical for {[**1**][**2**]}(BPh_4)$_2$ and **1a** (representing {[**1**][**1**]}(BPh_4)$_2$).

Although this is likely a necessity for the structures to be so similar, it is intriguing and points toward an intermolecular hydrogen bond interaction between the {[**1**][**1**]}$^{2+}$ unit in **1a** that had not been considered before but is explicitly found in {[**1**][**2**]}$^{2+}$. This underlines that not only a tendency for hetero-association as {[**1**][**2**]}$^{2+}$ exists, but also for homo-association as {[**1**][**1**]}$^{2+}$.

Table 42. Selected hydrogen bond lengths and angles found in **1a** and {[**1**][**2**]}$(BPh_4)_2$. Data for **1a** are partially adapted from chapter 2 and previously published results.[1]

	1a (150 K)	{[**1**][**2**]}$(BPh_4)_2$ (150 K)	{[**1**][**2**]}$(BPh_4)_2$ (293 K)
O(3)-H(3A)…O(1)			
d(D-H) [Å]	0.823(10)	0.824(10)	0.808(19)
d(H…A) [Å]	2.184(13)	2.031(15)	2.02(3)
d(D…A) [Å]	2.9552(18)	2.794(2)	2.795(3)
<(D-H-A)	156(2)°	154(3)°	161(6)°
O(3)-H(3B)…O(3)#1	[a]		[b]
d(D-H) [Å]	-	0.833(10)	0.81
d(H…A) [Å]	-	1.976(19)	2.09
d(D…A) [Å]	3.017(2)	2.777(3)	2.813(3)
<(D-H-A)	-	161(5)	148.4
O(3)…O(1)…O(3)#1			
<(O-O-O)	137.44(6)	135.52(7)	135.01(9)

D = donor, A = acceptor, #1: -x+1,-y,-z. [a] Here, a H-bond is assumed to partially occur via rotation of the hydroxide ligand around the Fe–O(3) bond. This is justified by the short O(3)···O(3)#1 distance but cannot be identified because the electron density is mainly located at the freely refined H(3A) position oriented towards O(1). [b] Here, no ESD is given because the H-atom was geometrically localized and fixed. Thus, the reported accuracy of the results appears higher than it actually is. It should be noted that, similar to the related compounds containing **1** and **2** discussed in section 2.1.2, the hexagons spanned by the atoms Fe(1), O(3), H(3A), O(1), C(23), and O(2) are also planar in {[**1**][**2**]}$(BPh_4)_2$ and **2e**. Because the cations **1** and **2** have already shown to exhibit this characteristic feature, a discussion is renounced here.

In summary, the structural analysis highlights that **1** and **2** show a tendency to form associated pairs as {[**1**][**2**]}$^{2+}$, {[**1**][**1**]}$^{2+}$, and even as {[**2**][**2**]}$^{2+}$ to some degree. The hetero-association is demonstrated by the structure of {[**1**][**2**]}$(BPh_4)_2$ which contains Fe^{II}–OH_2 and Fe^{III}–OH complex pairs that are associated via a hydrogen bridging interaction between the aqua and the hydroxide ligand, respectively. Moreover, it is found that the structural parameters and packings of {[**1**][**2**]}$(BPh_4)_2$ and **1a** are extremely similar and a homo-association of **1** with a symmetry generated neighboring molecule is found as {[**1**][**1**]}$(BPh_4)_2$ in close analogy to {[**1**][**2**]}$(BPh_4)_2$. This supports the theory that co-crystallizations of **2** in the lattice of **1a** can also likely happen for any intermediate content of **2**. The observation of a second crystallization of **2e** beside the crystals of {[**1**][**2**]}$(BPh_4)_2$ in the synthetic approach according to pathway 1 underlines that the content of **2** in the structure of **1a** cannot exceed 50 %. The complicated arrangement in the {[**2**][**2**]}$^{2+}$ homo-associate requires many auxiliary crystal solvent molecules and is, thus, a statistically rather unlikely arrangement. This is considered strong evidence, that Fe^{2+} impurities of **2** found in bulk samples of **1a** are because of {[**1**]$_x$[**2**]$_y$}$(BPh_4)_2$ co-crystallization rather than side-by-side crystallizations of [**1**](BPh_4) and [**2**](BPh_4) in variable ratios.

Aside from the proof, that associations via hydrogen bridging between **1**+**1**, **2**+**1**, and **2**+**2** occur despite the positive charge of the individual cations, a key finding is that **1a** and {[**1**][**2**]}$(BPh_4)_2$ are effectively identically packed. Consequently, any intermediate {[**1**]$_x$[**2**]$_y$}$(BPh_4)_2$ structures containing only a few percent of **2** can be easily mistaken for a valence-pure sample of **1a**. A revision of previous works shows such a misinterpretation has likely happened e.g. in the thesis of *C. Rauber*:[112] Here, the Fe–O(3) distance in the **1**[BPh_4] structure is reported as 1.873(13) Å, whereas the verified valence-pure sample in this work shows an Fe–O(3) distance of 1.835(1) Å. Although such a distance analysis is rather qualitative and dependent on the quality of the refinement, the deviation is large enough to assume that the structure of *Rauber* contained significant impurities of co-crystallized **2**. Because none of the previous works accounted for co-crystallization of **1** and **2** or provided evidence (Mößbauer spectroscopy) for valence-purity of the structures containing **1** all previous reports and characterizations must be viewed as preliminary and unreliable. This is also true for the works of *Bonck* and *Dobbelaar*. Even though the Fe-O(3) distances (*Bonck*: 1.8381(15), *Dobbelaar*: 1.8306(12)) appear to describe a valence-pure structure of

[**1**](BPh$_4$), these works applied synthetic approaches where impurities of **2** cannot be ruled out.

Finally, it should be noted that, although the association and co-crystallization is demonstrated for the BPh$_4$-salts in this section, even **1c** shows similar packing and 1···1 interactions to those found in **1a**. Despite weaker interactions in **1c** (<O(1)…O(3)-H(3)…O(3S) = 118°, d(O(3)…O(3S)) = 4.026(3) Å), it is an important finding that a {[**1**][**1**]}$^{2+}$ association also occurs in an environment where other, anionic hydrogen bond acceptors (PF_6^-) are present. With this in mind, and the fact that all crystallizations were done in the presence of MeCN, it can be reasoned that associations of such cationic pairs do also occur in MeCN solution, where other hydrogen bond acceptors compete for the interaction. Moreover, it can be assumed that such a competition exhibits concentration dependency, a further investigation of which appears worthwhile (see section 4.3).

4.1.3. SQUID-Magnetometric Analysis

To probe for magnetic interactions between the high-spin iron sites in the {[**1**][**2**]} and {[**1**][**1**]} units, a temperature-dependent measurement of the magnetic susceptibility in the solid state was done for {[**1**][**2**]}$(BPh_4)_2$ (Figure 102) and **1a** (Figure 103). Selected values at different temperatures are further compared in Table 43.

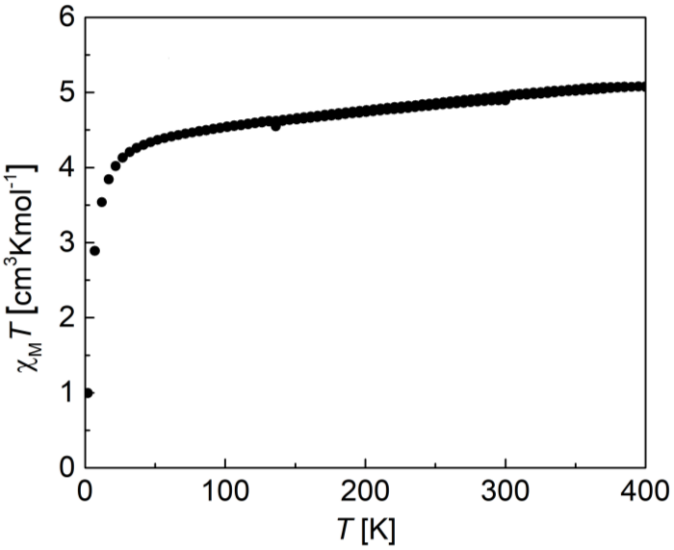

Figure 102. Temperature dependence of the average $\chi_M T$ per cation for {[**1**][**2**]}$(BPh_4)_2$ between 2 and 400 K measured at 0.5 T with a sweep rate of 2 K/min. Data points of cooling mode (300 K → 2 K) and heating mode (2 K → 400 K) are layered on top of each other.

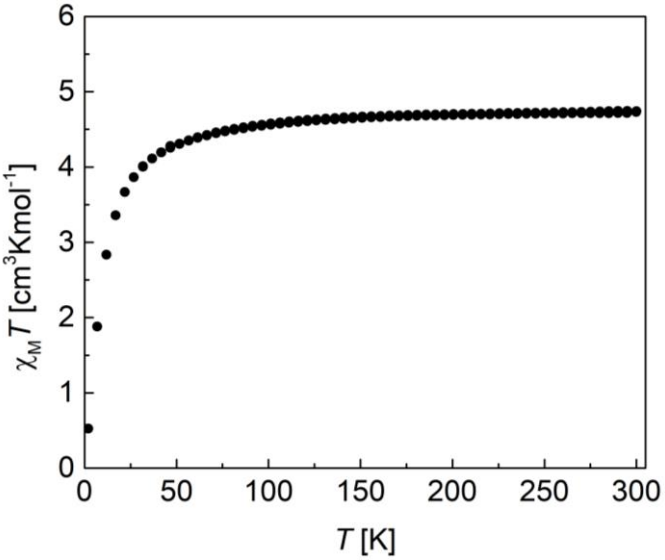

Figure 103. Temperature dependence of $\chi_M T$ for {[**1**][**1**]}$(BPh_4)_2$ (**1a**) between 2 and 300 K measured at 0.5 T with a sweep rate of 2 K/min. Data points of cooling mode (300 K → 2 K) and heating mode (2 K → 300 K) are layered on top of each other.

Table 43. Magnetic data (χT) for {[**1**][**2**]}$(BPh_4)_2$ and **1a** as obtained by SQUID-magnetometric measurements at 400 K, 298 K, 50 K, and 2 K.

T [K]	{[**1**][**2**]}$(BPh_4)_2$ [cm^{3}Kmol^{-1}]	{[**1**][**1**]}$(BPh_4)_2$ (**1a**) [cm^{3}Kmol^{-1}]
400	5.08	-
298	4.89 – 4.96[a]	4.74
50	4.37	4.31
2	1.00	0.55

[a] lower value was obtained initially; the higher value was obtained in heating mode and after cooling down from 400 K → 300 K. Data is given at 50 K to represent the low temperature magnetic moment and spin-state without the influence of zero-field splitting effects.

Generally, the values obtained for the magnetic susceptibility are very similar and it can be stated that the iron complexes in both samples are all in the high-spin state which concurs with the structural data (section 4.1.2). Because of the similarities, it is stressed that the valence distribution in both samples and the absence of significant amounts of paramagnetic iron impurities were ensured via Mößbauer spectroscopy (see sections 4.1.4 ({[**1**][**2**]}$(BPh_4)_2$) and 2.1.4 (**1a**)).

In both cases, no strong magnetic coupling is apparent at low temperatures. Because no indications for ferromagnetic coupling are found, a weak antiferromagnetic coupling is assumed to be present because of the short iron-iron distances of about 6 Å (see section 4.1.2). In {[**1**][**2**]}$(BPh_4)_2$, the positive slope towards higher temperatures, that is larger than that observed for the temperature independent paramagnetism in samples containing only **2** (see section 2.1.3), is observed, reaching a value of χT = 5.08 cm^3Kmol^{-1} at 400 K. The slope is not entirely linear and the high temperature value is significantly higher than the expected intermediate value of $\chi T \approx 4.1$ cm^3Kmol^{-1} between **2** and **1** in a fully decoupled system (considering a 1:1 mixture of χT(**2**) = 3.61 cm^3Kmol^{-1} and χT(**1**) = 4.61 cm^3Kmol^{-1} according to previous results described in section 2.1.3). Because the slope is non-linear and larger than for the pure iron(II) compound, it is considered not to be a pure temperature independent paramagentism effect. Interpretations for the origin of additional contributions remain speculative, however a (slow) hydrogen atom self-exchange at high temperatures in the solid state between **2** and **1** may explain the occurrence of a very weak ferrimagnetic coupling of the associated iron sites which would result in an increased magnetic moment.

With consideration of the structural data, the thermal energy could induce an increasing probability for a H-atom self-exchange in the solid state at higher temperatures. However, with consideration of the magnetic data, this reactivity can neither be verified nor falsified. In any case, the absence of a significant ferromagnetic interaction excludes the possibility of a rapid H-atom exchange and the presence of a fully delocalized Robin-Day class III type system. However, the increased magnetic moment at higher temperatures in the data obtained for [{**1**}{**2**}]$(BPh_4)_2$ leave room for speculation that the associate represents a Robin-Day class II type system with a high activation barrier for the hydrogen atom self-exchange reaction. The high activation barrier is understood to be linked to the magnetic properties and despite the preorganized reaction coordinate provided by the relatively short O(3S)···O(3) distance of the hydroxide/aqua ligands in the hydrogen bridged $\{[\mathbf{1}][\mathbf{2}]\}^{2+}$ unit (see section 4.1.2).

Because a H-atom self-exchange reactivity in the solid state can neither be denied nor verified by this magnetic analysis, more data are required to support such a hypothesis, especially because such an interaction is unprecedented.

4.1.4. Mößbauer-Spectroscopic Analysis

To gather further information about the localization/delocalization of the valences in the {[**1**][**2**]}$^{2+}$ pairs in {[**1**][**2**]}$(BPh_4)_2$ at room temperature, to probe for iron impurities, and to determine the ratio of [**1**]$^+$:[**2**]$^+$ in a bulk sample and compare it to the results of the single-crystal structural analysis, Mößbauer spectroscopy was measured for {[**1**][**2**]}$(BPh_4)_2$. To study the reproducibility of the ratio, this was done for both samples obtained via pathway 1 and pathway 2, respectively. The spectrum obtained with the sample synthesized via pathway 2 is given exemplary in Figure 104. The results for both measurements are given in Table 44 and compared to pure samples containing **1** and **2**, respectively ([**1**]BPh_4 (**1a**) and [**2**]ClO_4 (**2a**)).

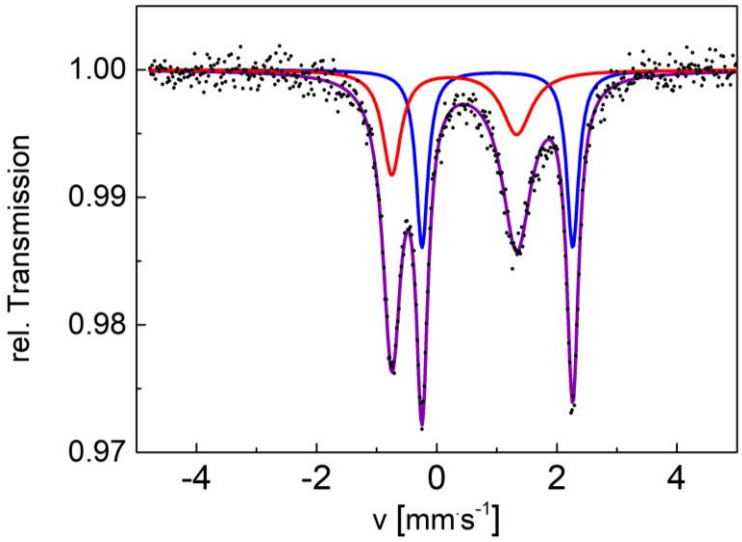

Figure 104. Experimental Mößbauer spectrum (black dots) of {[**1**][**2**]}$(BPh_4)_2$ at room temperature (RT) and fits (red trace, **1**; blue trace, **2**; purple trace, sum of fits). Mößbauer parameters are given in Table 44. The isomeric shift δ_{IS} is depicted relative to α-Fe foil (δ_{IS}(α-Fe vs source) = 0.107 mm·s^{-1}

For the spectrum of {[**1**][**2**]}$(BPh_4)_2$, two distinct doublets can be identified that are assigned to each a subspectrum of **1** and a subspectrum of **2**. The observance of reproducible approximate 1:1 ratios of [**1**]$^+$:[**2**]$^+$ further supports the notion of a co-crystallized mixture of **1** and **2** in one compound rather than the occurrence of two separate compounds in the bulk sample. The clear identification of two subspectra is thus viewed as strong evidence that no relevant valence delocalization / (proton-

coupled) electron transfer occurs in the {[**1**][**2**]}$^{2+}$ units at room temperature on the timescale of the Mößbauer experiment (~10^{-6} s).[125]

Table 44. Mößbauer parameters obtained for {[**1**][**2**]}$(BPh_4)_2$, **1a**, and **2a** at room temperature.

	{[**1**][**2**]}$(BPh_4)_2$[a]		{[**1**][**2**]}$(BPh_4)_2$[b]		**1a**	**2a**
subspectrum	**1**	**2**	**1**	**2**	-	-
δ_{IS} [mms^{-1}]	0.29	1.02	0.29	1.01	0.30	1.04
ΔE_q [mms^{-1}]	2.03	2.53	2.08	2.51	2.26	2.63
χ^2	1.01		0.98		1.01	1.11
relative area	55%	45%	58%	42%	100%	100%

δ_{IS} = isomeric shift relative to α-Fe foil (δ_{IS}(α-Fe vs source) = 0.107 mm·s^{-1}). ΔE_q = Quadrupole splitting. χ^2 = measure of fitting quality. [a] Obtained via pathway 1. [b] Obtained via pathway 2. Average room temperatures may have differed between the measurements. The relative area is not an accurate measure for the true distribution but serves merely as rough indication. Changes in the isomeric shift may be attributed to second order doppler effects.

When comparing the Mößbauer parameters, it is found that the magnitude of quadrupole splitting in {[**1**][**2**]}$(BPh_4)_2$ differs somewhat from that found in samples containing only **1** or **2**, respectively. In {[**1**][**2**]}$(BPh_4)_2$, the quadrupole splitting of **1** is smaller by $\Delta\Delta E_q$ = 0.25 – 0.27 mms^{-1} and that of **2** is smaller by $\Delta\Delta E_q$ = 0.10 – 0.12 mms^{-1}. Although the parameters obtained with **2a** provide a somewhat limited reference, because the structures differ in their crystallographic environments, **1a** provides a good reference as it represents a valence-pure {[**1**][**1**]}$(BPh_4)_2$ analogue of {[**1**][**2**]}$(BPh_4)_2$ with a near identical crystallographic environment (see section 4.1.2). Thus, it is especially intriguing that the quadrupole splitting differs so significantly in {[**1**][**2**]}$(BPh_4)_2$. It is likely, that the differences are a result of the hydrogen bridge between **1** and **2** in {[**1**][**2**]}$(BPh_4)_2$ as this interaction distinguishes the cations most from those present in the valence-pure structures. Thus, one may conclude that the H-bond interaction contributes to an equilibrating reduction of cation anisotropy in **1** and

2 in some way, the nature of which is not further described to avoid speculative interpretations.

4.1.5. Infrared Spectroscopic Analysis

Infrared (IR) spectroscopy was measured for {[**1**][**2**]}$(BPh_4)_2$ for characterization purposes and compared with spectra obtained for **1a**. The spectrum of {[**1**][**2**]}$(BPh_4)_2$ was recorded in a wider range to include the near infrared (NIR) region (4000 – 7800 cm^{-1}, 2500 – 1282 nm) and probe for potential inter-valence charge transfer (IVCT) bands which can be expected for Robin-Day class II and class III mixed-valence systems. The results are presented in Figure 105.

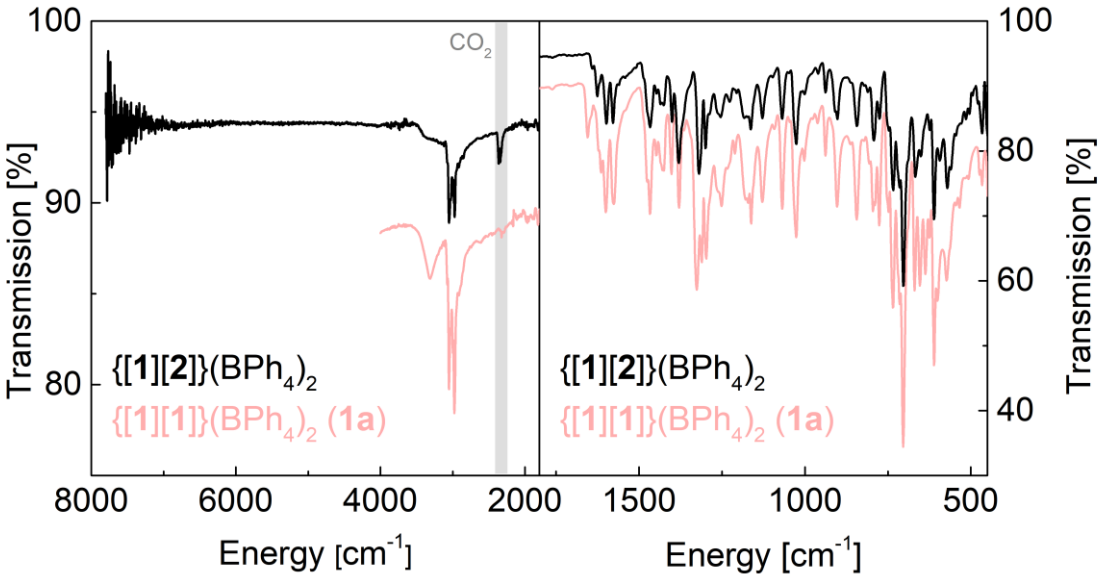

Figure 105. FTIR spectra of solid crystalline samples of {[**1**][**2**]}$(BPh_4)_2$ and {[**1**][**1**]}$(BPh_4)_2$ (**1a**) between 8000 – 2000 cm^{-1} (left) and between 2000 – 450 cm^{-1} (right) measured with an ATR-accessory under atmospheric conditions. Signals between 2392 – 2286 cm^{-1} occurred because of fluctuations in the atmospheric CO_2 content during the measurement. Data for **1a** are adapted from chapter 2 and previously published work.[1]

The spectra of {[**1**][**2**]}$(BPh_4)_2$ and **1a** only differ significantly in the O–H vibrations above 3100 cm^{-1}. Despite the presence of **2** in the structure, apparently no additional bands in {[**1**][**2**]}$(BPh_4)_2$ as compared to {[**1**][**1**]}$(BPh_4)_2$ (**1a**) can be identified in the finger print region (2000 – 450 cm^{-1}). The rather sharp O–H vibration corresponding to **1** in **1a** at 3313 cm^{-1} cannot be discerned in {[**1**][**2**]}$(BPh_4)_2$. Instead, a broad feature is observed between 3100 – 3500 cm^{-1} which likely superimposes with other signals with energies below but in proximity of 3100 cm^{-1} in the spectrum. Although broad, this

feature is in the range expected for both **1** and **2**. The broadening is considered to result from the intra- and intermolecular hydrogen bond network ($PhCO_2$···H-O-H···O-H···O_2CPh) which softens the vibrational modes of all involved O–H bonds.

The NIR spectral range is found to be devoid of any IVCT signal, which points toward a localized $\{[\mathbf{1}][\mathbf{2}]\}^{2+}$ pair at room temperature. Because no evidence for valence-delocalization is found in Mößbauer spectroscopy, the absence of an IVCT band is somewhat expected for the faster IR method and concurs with the results described above.

*Note: Because the interesting spectral range for this compound is the NIR region and cations **1** and **2** have already been well-characterized individually in section 2.1 by electronic spectroscopy, no additional UV-vis-NIR investigation was done for* $\{[\mathbf{1}][\mathbf{2}]\}(BPh_4)_2$ *in the solid state.*

4.1.6. NMR-Spectroscopic Analysis

Because most solution-based spectra of {[**1**][**2**]}$(BPh_4)_2$ are expected to merely represent a sum of the spectra of the individual cations **1** and **2** which have been well-characterized in section 2.1, only ^{1}H-NMR spectroscopy was conducted as it represents a rather quantitative method. To quantify the relative concentrations of **1** and **2** in a MeCN-d3 solution via the benzoate signals with relatively long relaxation times (see section 2.1.11 for detailed assignment), broad underlying responses were removed via a baseline correction (Figure 106).

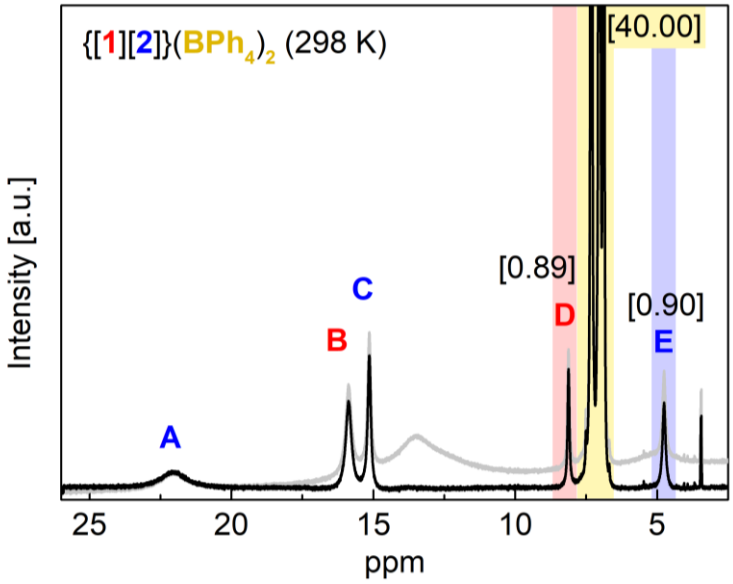

Figure 106. ^{1}H-NMR spectrum (2.2-26 ppm) of {[**1**][**2**]}$(BPh_4)_2$ (20 mmol·L^{-1}) in MeCN-d3 at 298 K. The raw spectrum is given in grey, a spectrum with adjusted baseline to facilitate signal integration is given in black. Assignment: A, C, and E correspond to the *ortho*-, *meta*-, and *para*-protons of **2**, respectively. B and D correspond to the *meta*- and *para*-protons of **1**, respectively; the *ortho*-proton is obscured. The multiplet between 6.5-7.7 ppm is assigned to the aromatic ring protons of the BPh_4 counterions. The relative integrals for D, E and the BPh_4 protons are given in brackets. The diamagnetic signal at 3.43 ppm is assigned to Et_2O residues in the solvent.[131]

The spectrum of {[**1**][**2**]}$(BPh_4)_2$ shows a ratio of 1:1 between **1** and **2** in a bulk sample, which concurs with previous results. As would be expected, the spectrum is near identical to that obtained for a solution of [**1**]PF_6 (**1c**) and [**2**]ClO_4 (**2a**) (see section 3.3.3) apart from the signals corresponding to the BPh_4^- counterions, which serve as an internal reference in the spectrum of {[**1**][**2**]}$(BPh_4)_2$. Minor integral errors for the *para*-protons of the benzoate ligands (integral < 1 H referenced against 40 H of 2 equiv. BPh_4^-) are attributed to signal broadening and errors introduced by the baseline correction.

In summary, the 1:1 ratio of **1** and **2** in {[**1**][**2**]}$(BPh_4)_2$ is demonstrated via NMR spectroscopy. Although the ^{1}H-NMR spectrum is not able to distinguish if {[**1**][**2**]}$^{2+}$ associates are present in solution, it has been discussed that self-exchange reactions between **1** and **2** require such a species at least as an intermediate. The separation of the signals at the given concentration and temperature gives some indication about the timescale of such self-exchange reactions. A more elaborate study of the kinetics is provided in the section 4.3.1.

4.2. Summary of the Structural, Spectroscopic, and Magnetic Investigation

In summary, compelling evidence for the tendency of close hetero-association of *cis*-(carboxylato)(hydroxo)iron(III) (**1**) and *cis*-(carboxylato)(aqua)iron(II) (**2**) complexes as **1**+**2** via intermolecular hydrogen bonding between their respective hydroxide/aqua ligands is provided via solid-state characterization methods. Additionally, the homo-associates **1**+**1** and **2**+**2** are demonstrated, although the interactions in the latter are somewhat limited and the nature of the hydrogen bonding interaction differs in the acceptor function (carboxylate) because no hydroxide lone pair is available. With synthetic and structural reasoning, it is concluded that a co-crystallization of varying contents of Fe^{2+}–OH_2 in the structures of seemingly pure Fe^{3+}–OH complexes as $\{[\mathbf{1}]_x[\mathbf{2}]_y\}^{2+}$ (with $y \leq 0.5$ and $x+y = 1$) can occur which limits the reliable accessibility of pure samples in the synthesis via direct oxidation of *cis*-(carboxylato)(aqua/alcohol)iron(II) precursors as done in the past.[2,112,113] Indications for such co-crystallizations that went unnoticed in previous studies are found (especially in the thesis of *Rauber*),[112] rendering all previous works that did not reconfirm valence-purity via Mößbauer spectroscopy unreliable and preliminary. Magnetic studies of $\{[\mathbf{1}][\mathbf{2}]\}(BPh_4)_2$ hint at a weak magnetic interaction between the iron sites that may be mediated by a hydrogen-atom self-exchange reaction in the solid state over the short distance between the donor and acceptor functions of the hydrogen bridging interaction (O···O distance <2.8 Å). However, no such scenario could be concluded from the IR/NIR- and Mößbauer-spectroscopic studies at room temperature.

Although this study only pertained complex cations **1** and **2**, the derivatives of the ferric complex **7** and **10** also show a tendency towards homo-association in the crystal packings with BPh_4^- counterions; although in a different environment than found for **1** and with longer O···O distances (3.7 – 3.8 Å). Because all were crystallized from a $MeCN/Et_2O/H_2O$ mixture, it appears likely that homo- (and hetero-) associates are also present in MeCN solution. The following chapter attempts to further illuminate if this assumption is feasible and describes the effort to explain the kinetic irregularities in the reactions of CHD with **1**, **7**, and **10**, respectively (sections 2.3.7 and 3.3.2), with a concentration-dependent $[\mathbf{A}]^+ + [\mathbf{A}]^+ \rightleftharpoons \{[\mathbf{A}][\mathbf{A}]\}^{2+}$ self-association equilibrium (A = **1**, **7**, or **10** for the respective reaction solutions).

4.3. Kinetic Investigation of Self-Exchange Reactions

4.3.1. EXSY-NMR Spectroscopic Study

As has been established via 1D-NMR characterization (see 3.3.3 and 4.1.6), in solution, the dissolved associate [{**1**}{**2**}]$^{2+}$ is identical to a mixture of [**1**]$^{+}$ and [**2**]$^{+}$ with equal concentration. Thus, for simplicity and product economy, the exchange correlated nuclear magnetic resonance spectroscopy (EXSY-NMR) study was done with a mixture of **1** and **2** rather than dissolved {[**1**][**2**]}$(BPh_4)_2$. This also avoids large cross peaks produced by the correlated spectra of the phenyl protons that could obscure relevant exchange correlated cross-peaks of the benzoate protons.

For the study, EXSY-NMR was measured for two different solutions containing equimolar amounts of **1** and **2** with mixing times of 5 – 20 ms in 1 ms steps, as the resolution became poor at longer relaxation times and no cross peaks were observed at very short relaxation times. This was done for a solution containing 20 mmolL^{-1} of each iron complex and for a solution containing 10 mmolL^{-1} of each iron complex, both on a 400 MHz instrument. For the solution with higher concentration, measurements were done with and without a gradient method to ensure that the method does not influence the results at shorter mixing times. Also, it was verified that the results were not influenced by the chosen instrument/measurement frequency by sampling some data points with a 200 MHz instrument. For all measurements, a H,H-COSY experiment was done to ensure that the observed crosspeaks via EXSY-NMR-spectroscopy result from exchange correlated signals rather than more simple intramolecular nuclear magnetic interactions. For all obtained spectra, data workup and rate constant calculations were done for both the *para*- and the *meta*-protons of the iron complexes to better demonstrate the uncertainty and scattering of the method. The rate constant was calculated for different mixing times (t_m) from the relative integrals of the cross- (I_{AB}, I_{BA}) and diagonal (I_{AA}, I_{BB}) responses as follows (also see Figure 107):[163]

$$(6) \qquad k = \frac{1}{t_m} ln \frac{r+1}{r-1} \quad \text{with} \quad r = \frac{I_{AA} + I_{BB}}{I_{AB} + I_{BA}}$$

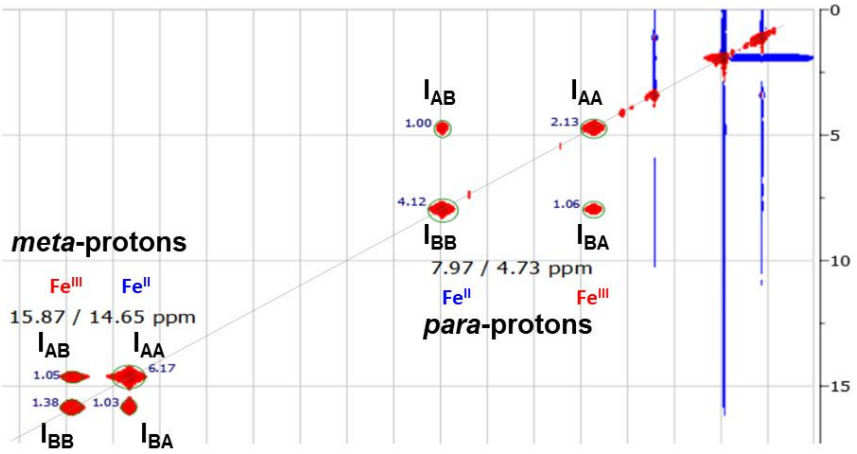

Figure 107. Exemplary integration of the *meta*- and *para*-proton signals of **1** (Fe^{III}) and **2** (Fe^{II}) (Screenshot from MestReNova NMR software) obtained via a gradient pulse EXSY-NMR method on a solution of **1** (20 mmolL^{-1}) and **2** (20 mmolL^{-1}) in MeCN-d3 with a mixing time of 5 ms. The chemical shifts of the respective signals are indicated (15.87, 14.65, 7.97, and 4.73 ppm), the relative integral values are given in blue. Additionally, the assignment of the variables I_{AA}, I_{AB}, I_{BA}, and I_{BB} representing the relative integral values is provided as relevant for equation 6.

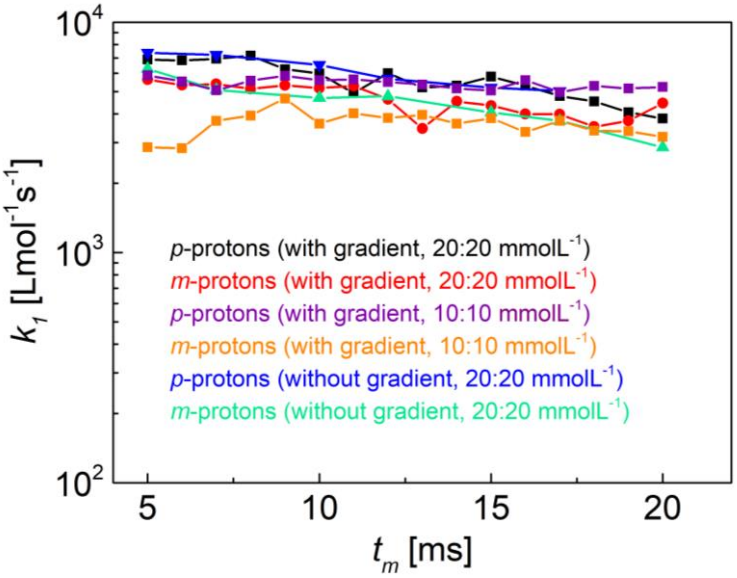

Figure 108. Concentration-independent self-exchange reaction rate constants k_1 as obtained from EXSY-NMR spectroscopy for mixing times between 5-20 ms in 1 ms increments with a 400 MHz instrument on solutions containing **1** (20 mmolL^{-1}) and **2** (20 mmolL^{-1}), and **1** (10 mmolL^{-1}) and **2** (10 mmolL^{-1}), respectively. Methods with and without a gradient yielded essentially the same results. Connection lines between the data points are guides for the eyes.

In the studied concentration regime, no concentration dependency of the self-exchange reaction rate was apparent within the margin of error. Attempts to investigate a more diluted mixture with concentrations of 2 mmolL^{-1} of each cation failed, as the signal strength was too weak, and no well-resolved cross peaks could be observed. From these results, it can be reasoned that the number of associates in solution is almost identical in a 10 mmolL^{-1} and a 20 mmolL^{-1} solution of [{**1**}{**2**}]$^{2+}$ (10:10 mmolL^{-1} solution of [**1**]$^{+}$ + [**2**]$^{+}$ and a 20:20 mmolL^{-1} solution of [**1**]$^{+}$ + [**2**]$^{+}$). However, it cannot be derived how many (or if any) associates are present in solution. To probe for consistency of equal kinetics at even lower concentrations, the result of this study is compared with that obtained from the preliminary kinetic study of a reaction of **1** with TTBP that was performed at lower reagent concentrations (see section 2.3.2). For this, the Marcus theory is exploited as its validity for hydrogen atom exchange reactions was shown by James Mayer.[94] The Marcus theory states, that a rate constant k_{12} of a cross reaction of two reagents can be calculated from their equilibrium constant K_{12} and the self-exchange rate constants k_{11} and k_{22} of these reagents (equation 1).

$$(1) \quad k_{12} = \sqrt{k_{11} k_{22} K_{12} f} \quad \text{with} \quad f = 1$$

For the reaction of **1** with TTBP (TTBP = (^{t}Bu)$_3$Ph-OH), the equilibrium constant was determined as $K_{12} = 1.76 \cdot 10^{-2}$ (for each c(**1**) and c(TTBP) < 2 mmolL^{-1}) and the concentration-independent rate constant was preliminary determined as $k_{12} \approx 30$ Lmol^{-1}s^{-1} (for c(**1**) = 3.3 mmolL^{-1} and c(TTBP) = 1.3 mmolL^{-1}) under the assumption of pseudo-first order kinetics which is somewhat flawed. Nonetheless, with knowledge of the self-exchange rate constant k_{22} of TTBP and its phenoxyl radical counterpart, k_{11} for the self-exchange rate of **1** + **2** ⇌ **2** + **1** can be calculated to compare it with the results presented above. In literature, an experimental value for the self-exchange rate of TTBP and its phenoxyl radical in MeCN solution was found as $k_{22} = 20$ Lmol^{-1}s^{-1}.[164] Consequently, the self-exchange reaction rate constant for **1** + **2** ⇌ **2** + **1** is calculated as follows:

$$k_{11} = \frac{{k_{12}}^2}{k_{22} K_{12}} = \frac{30^2}{20 \cdot 1.76 \cdot 10^{-2}} Lmol^{-1}s^{-1} = 2.6 \cdot 10^3 \, Lmol^{-1}s^{-1}$$

The calculated rate constant of $2.6 \cdot 10^3$ Lmol^{-1}s^{-1} via Marcus theory (calculated from experimental data obtained with c(Fe^{III}) = 3.3 mmolL^{-1} and c(TTBP) = 3.3 mmolL^{-1}) is

in good agreement with the results obtained via EXSY-NMR spectroscopy (calculated from experimental data obtained with $c(Fe^{III})$ = 10-20 mmolL^{-1} and $c(Fe^{II})$ = 10-20 mmolL^{-1}), which are in the range of $6{\cdot}10^{3}$ Lmol^{-1}s^{-1}. Additionally, the magnitude is similar to previously reported examples for hydrogen atom self-exchange reactions and to the value that was obtained by Mayer for an iron complex system (Fe(Hbim), $5.8{\cdot}10^{3}$).[94,165] The consistent results validate both the EXSY and the self-exchange approach. The slightly slower rate obtained for the lower concentration regime could support the overall claim of preorganized complex associates in solution at higher concentrations, although one must consider uncertainties in the input values of the Marcus-theory approach, especially for the preliminary cross-reaction rate constant, which somewhat weaken the argument.

As the order of magnitude for the self-exchange reaction rate has reliably been determined, it can also be used to estimate the rate constants for the cross reaction of **1** with 9,10-dihydroanthracene (DHA), for which a self-exchange rate constant of $5{\cdot}10^{-11}$ Lmol^{-1}s^{-1} is reported in DMSO,[164] and the thermodynamically similar reaction of **1** with 1,4-Cyclohexadiene (CHD), by assuming that the BDFEs of CHD and DHA are similar to that of TTBP and, thus, the same K_{eq} can be used for the equation. However, this is only a rough estimate, as the comparison between different solvents does generally not produce accurate results because of different environmental influences (e.g. polarity and C_G value) and no experimental equilibrium constant could be determined to verify the similarity assumption.[96,109] Nonetheless, such an estimate produces a cross reaction rate constant for the reaction of **1** with DHA as k_{12} = 4.6 – 7.3.10^{-5} for the underlying concentration regimes. This is in the order of magnitude as preliminary estimated from the NMR studies in the same concentration regime ($k_{12} \approx 8.5{\cdot}10^{-6}$ s^{-1} Lmol^{-1}s^{-1}, see section 3.3.2) and slower than observed in the ESI-MS studies in a lower concentration regime ($6{\cdot}10^{-3}$ Lmol^{-1}s^{-1}, see chapter 2, Figure 50). This, again, adds to the suspicion that some association occurs at higher concentrations which reduces the activity of the complex (and the rate of the cross-reaction) and, in turn, increases the observed self-exchange rate through the formation of precursor complexes as [{**1**}{**2**}]$^{2+}$.

5. An Unprecedented Example for a Mononuclear *cis*-di(hydroxo)iron(III) Complex with Solution-Stability

Over the course of this work, speculations quickly arose about the existence of a special kind of mononuclear hydroxo iron(III) complex: A mononuclear *cis*-di(hydroxo)iron(III) complex.

Such a species had only once been reported in 2006 by *Bénisvy et al.*,[78] however as a seemingly serendipitous result (Scheme 22). A mononuclear, five-coordinated hydroxoiron(II) complex had been oxidized under aerobic conditions in methanol and, after one month, it was found that crystals containing a six-coordinate di(hydroxo)iron(III) complex had formed. This di(hydroxo)iron(III) complex is stabilized by intermolecular hydrogen bonding to neighbouring complexes in the crystal lattice. However, despite the crystallization of this complex from a methanolic solution, the presence of the species in solution was not further investigated but simply claimed. Although it was proposed that intermolecular interactions with methanol could stabilize the complex in solution, it is likely, that the hydroxide ligands will be at least partially exchanged by methoxide ligands, driven by the excess of methanol in such a solution, especially because the stabilizing hydrogen bond interactions to neighbouring complexes cannot prevail in solution. Thus, the current literature still lacks a systematic study on the solution stability of non-heme di(hydroxo)iron(III) complexes.

In this work, and even during my own research for my master thesis,[2] it had been observed, that ESI-MS investigations of *cis*-(carboxylato)(hydroxo)iron(III) complexes showed signals at m/z = 442 that were dependent on the water content of the solvent. When adding a substantial amount of water to the acetonitrile solutions used for ESI-MS investigations, this signal could even become the maximum signal in the spectrum, completely vanishing the signals corresponding to the originally investigated complexes. Theoretical considerations resulted in the assumption, that this could be explained by the formation of an $[Fe^{III}(L\text{-}N_4{}^tBu_2)(OH)_2]^+$ cation via ligand exchange with excess amounts of water after the principle of Le Chatelier. However, the attainment of the isolated product to prove the feasibility of such an assumption remained a significant challenge for the most part of this work.

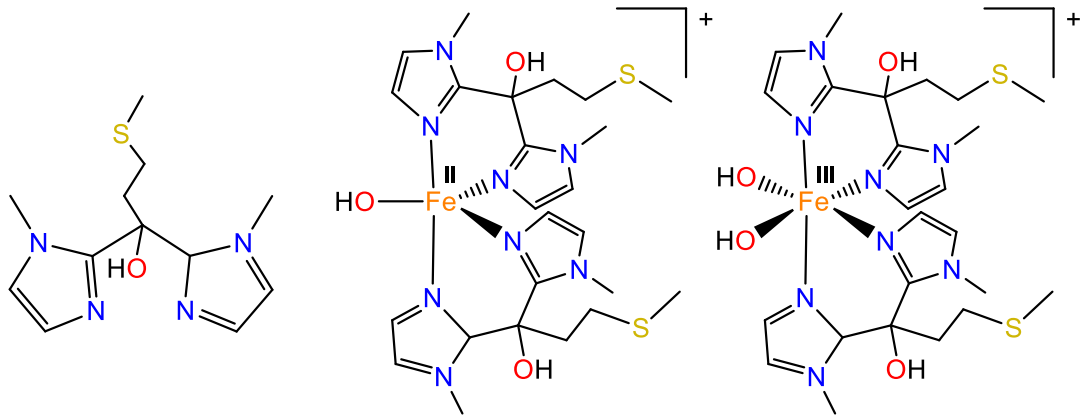

L = bis(N-methylimidazol-2-yl)-3-methylthiopropanol

$[Fe^{II}(\mathbf{L})_2](OH)]^+$

$[Fe^{III}(\mathbf{L})_2](OH)_2]^+$

Scheme 22. Schematic depictions of the Ligand (**L**), the hydroxo iron(II) ($[Fe^{II}(\mathbf{L})_2(OH)]^+$), and the *cis*-di(hydroxo)iron(III) complex ($[Fe^{III}(\mathbf{L})_2(OH)_2]^+$) described by Bénisvy *et al*.

In the meantime, a serendipitous crystallization by Pascal Peter showed the achievement of a dicationic *cis*-di(aqua)iron(II) complex $[Fe^{II}(L\text{-}N_4{}^tBu_2)(OH_2)_2]^{2+}$ (**13**).[3] Although the properties of the complex were not of further interest for his work, this sparked the investigation of the complex for this work, and the hunt for an extremely rare oxidized, deprotonated *cis*-di(hydroxo)iron(III) analogue.

Although countless efforts to synthesize and isolate such a complex solely resulted in red-orange, insoluble precipitation products that were assigned to the formation of ill-defined iron oxide/hydroxide substances (rust) after loss of the iron ion from the ligand scaffold, the desired $[Fe^{II}(L\text{-}N_4{}^tBu_2)(OH)_2]^+$ (**14**) species (Scheme 23) could, ultimately, be synthesized in a facile way and be fully characterized. The synthetic procedure, characterization, and analytical investigations are described in the following alongside the results for the corresponding reduced and protonated $[Fe^{II}(L\text{-}N_4{}^tBu_2)(OH_2)_2]^{2+}$ complex (Scheme 23).

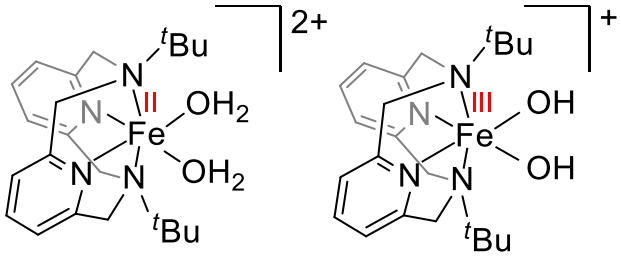

13 **14**

Scheme 23. Schematic depictions of the *cis*-di(aqua)iron(III) complex $[Fe^{II}(L\text{-}N_4{}^tBu_2)(OH_2)_2]^{2+}$ (**13**) and the *cis*-di(hydroxo)iron(III) complex $[Fe^{III}(L\text{-}N_4{}^tBu_2)(OH)_2]^{+}$ (**14**).

5.1. Synthesis and Characterization

5.1.1. Synthesis

The synthesis of $[Fe^{II}(L\text{-}N_4{}^tBu_2)(OH_2)_2]^{2+}$ (**13**) is rather straightforward and follows similar conditions to those employed in the synthesis of $[Fe^{II}(L\text{-}N_4{}^tBu_2)(OH_2)_2]^{2+}$ (**5**, section 2.1.1) with a $[Fe^{II}(H_2O)_6](OTs)_2$ complex as the iron precursor rather than $FeCl_2$. The crystalline product could be isolated by diffusion of Et_2O into the concentrated (wet) acetonitrile solution after filtration of the reaction mixture and solvent volume reduction under reduced pressure. Pascal Peter developed an additional synthetic pathway to obtain $[Fe^{II}(L\text{-}N_4{}^tBu_2)(OH_2)_2](CF_3SO_3)_2$ (**13b**) by salt metathesis of $[Fe^{II}(L\text{-}N_4{}^tBu_2)(Cl)_2]$ with two equivalents of $Ag(CF_3SO_3)$ in parallel to this work.[3] Although this approach was not used, and **13b** was not synthesized during this work, the pathway is also described in Scheme 24 and the structural data are presented with permission in the following chapter (5.1.2) for future reference.

In contrast to the straightforward synthesis of **13**, the development of an adequate synthesis of $[Fe^{II}(L\text{-}N_4{}^tBu_2)(OH)_2]^{+}$ (**14**) poses major challenges to overcome. Firstly, the weak hydroxide ligands are often a poor competition compared to stronger donors from precursor complexes or coordinating solvents. Thus, a suitable precursor complex and solvent mixture is required. Secondly, the species is expected to be very sensitive to protonation and ligand exchange in the presence of protic solvents such as alcohols. Thus, again, the careful selection of a suitable solvent or solvent mixture is crucial. The final challenge is, of course, the nature of a mononuclear ferric hydroxide complex itself. Although the $L\text{-}N_4{}^tBu_2$ ligand has already impressively shown to suppress the formation of μ-oxo or μ-hydroxo dinuclear complexes to achieve mononuclear ferric hydroxide complexes (chapters 2 and 3),[1] it has yet to be shown that the ligand is also capable of suppressing undesired reactions of an iron(III) complex core with not only one but two hydroxide ligands to highly insoluable and thermodynamically favored iron oxide/hydroxide mixtures (rust). If not controlled, even minor side reactions would eventually lead to the complete decomposition of the targeted complex driven by the removal of the iron oxide products from the equilibrium upon precipitation, following the principle of Le Chatelier.

A multitude of precursors, synthetic pathways, procedures, solvents, and solvent mixtures were tested, failing in all but one case. In the end, a 5:2 mixture of acetone and water was found to successfully dissolve and convert the $[Fe(L\text{-}N_4{}^tBu)_2(OMe)_2]^+$ (**4**) complex cation to the desired product at ambient conditions, inhibit decomposition, allow for its crystallization with suitable counterions upon slow solvent evaporation and, finally, afford an analytically pure product. In this, no additional reactant or reagent is needed. The strategy behind this procedure is to use acetone as an only very weakly coordinating, polar, aprotic solvent capable of dissolving **4**. The dilution of the acetone solvent with water allows for a still reasonable solubility of **4** at an (arbitrarily chosen) 5:2 ratio (volumes acetone:water) while at the same time providing a large excess of water. The excess water can protonate the methoxide ligands in an equilibrium, now favoring ligand exchange of a methoxide with a hydroxide ligand. At the same time, the lower vapor pressure of methanol as compared to the solvent mixture results in the consecutive removal of methanol from the equilibrium by evaporation, further driving the desired conversion. While the required energetics are delicate, it is found that, at room temperature and normal pressure, the energy supply for the reaction is, on the one hand, high enough to allow for the transformation and solvent evaporation and on the other hand, too low to overcome the activation barrier for the conversion of the formed $[Fe(L\text{-}N_4{}^tBu_2)(OH)_2]^+$ to undesired, thermodynamically favored iron oxide products.

It must be noted that, while the synthetic approach for **14** is successful with precursors **4b** (PF_6) and apparently also with **4c** (ClO_4) at least as an intermediate raw product during the synthetic pathway of **7b** (see section 3.1.1), synthetic efforts with **4a** (tetraphenyl borate salt) fail.

In this work, crystals could be obtained with PF_6^- in two different modifications, containing different amounts of crystal water. Additionally, the product could be obtained as a solvent free powder [**14**]PF_6 (**14c**) when attempting to recrystallize **14b** and accompanying amorphous precipitates from MeCN as demonstrated by elemental analysis (Table 45) and IR spectroscopy (Figure 122, section 5.1.5). In some cases, well defined pale yellow blocks of $[Fe(L\text{-}N_4{}^tBu_2)(OH)_2]PF_6{\cdot}H_2O$ (**14a**) could be isolated, in other cases, less aesthetic pale yellow plates with the composition $[Fe(L\text{-}N_4{}^tBu_2)(OH)_2]_3(PF_6)_3{\cdot}5H_2O$ (**14b**) were found in an inhomogeneous mixture with additional powder. The parameters that allow for the targeted crystallization of either

modification could not be found. However, the morphology of the modifications allowed for easy visible distinction and the elemental analysis allowed for clear assignment of the water content in the bulk material. To achieve a homogeneous sample for further analysis, only a few well-defined single crystals of **14b** could be separated from the bulk sample. The initial formation of **14** upon oxidation of **13** under aerobic conditions in acetonitrile is likely, however, this does not provide a suitable synthetic pathway as the counterions contained in **13a** and **13b** are expected to compete with the hydroxide ligands.

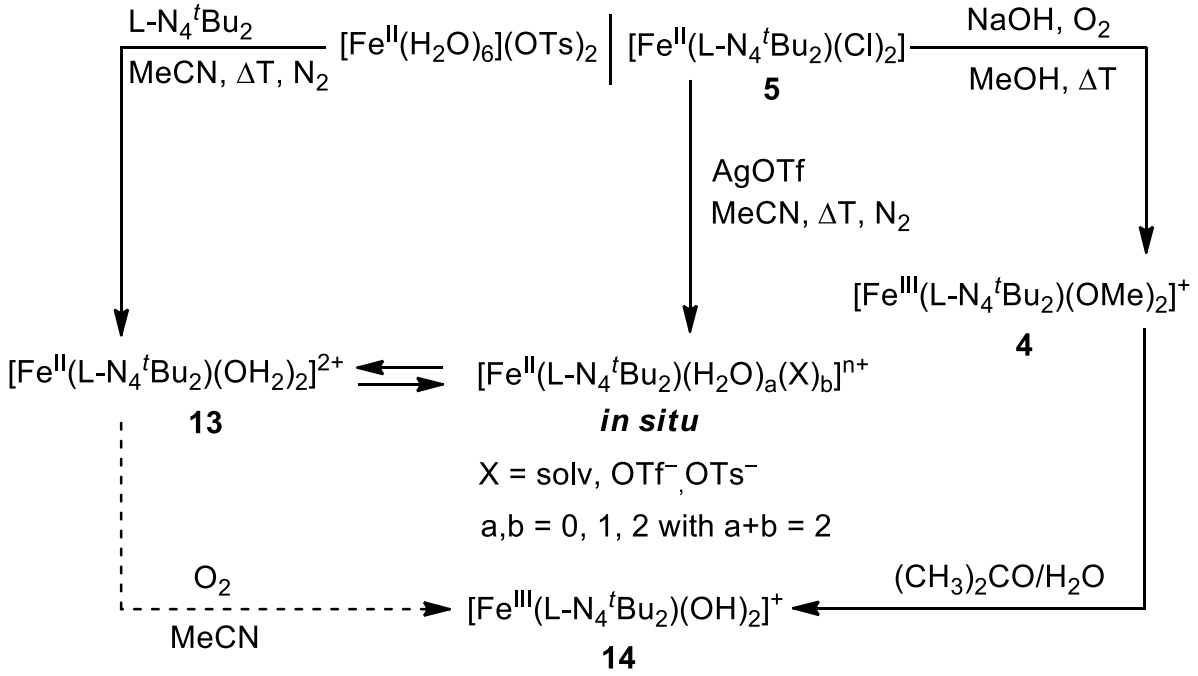

Scheme 24. Synthetic reactions. The cationic complexes were crystallized and isolated as [**4**](BPh$_4$) (**4a**), [**4**](PF$_6$) (**4b**), [**4**](ClO$_4$) (**4c**), [**13**](OTs)$_2$ (**13a**), [**14**](PF$_6$)•H$_2$O (**14a**), [**14**]$_3$(PF$_6$)$_3$•5H$_2$O (**14b**). A solvent free compound [**14**](PF$_6$) (**14c**) could be isolated as powder when attempting to recrystallize **14b** from MeCN. The pathway for the synthesis of **13** with AgOTf was not used in this thesis but has been shown to be feasible to obtain [**13**](OTf)$_2$ (**13b**) in parallel to this work by P. Peter.[3] Ligand exchange reactions of **13** with the counterion and/or solvent are observed *in situ* in solution (see below). The oxidation of **13** to **14** under aerobic conditions in MeCN is expected in analogy to the previously described aqua/hydroxide iron complexes but was not explicitly investigated.

Table 45. Exemplary elemental analysis results and maximal deviations in % for the compounds relevant to this chapter. Data is given in the format “calculated (found)”.

	C [%]	**H** [%]	**N** [%]	**S** [%]	max. dev. [%]
13a	54.82 (54.95)	6.29 (6.41)	7.10 (7.12)	-	0.13
14a	43.65 (43.57)	5.99 (5.97)	9.26 (9.29)	-	0.08
14c	44.99 (44.85)	5.83 (5.70)	9.54 (9.61)	-	0.14

Max. dev. = maximal deviation. Instrumental error margin <0.3 %. Only very few well-defined single crystals of **14b** could be obtained, thus they were not analyzed via combustion analysis but employed in other analytical investigations (see below).

It should be noted that efforts towards an intermediate *cis*-(hydroxo)(aqua)iron(II) complex species were made but failed. Such efforts are described in section 5.1.11 along the analytical methods (NMR) employed to study the possible *in situ* formation of the complex. Additionally, some comments about the feasibility (and presence) of such a species are given alongside the solution-based studies of **13** and **14** (sections 5.1.7 and following).

5.1.2. Structural Analysis

Complexes **13** and **14** were crystallized directly from synthetic procedures and structurally characterized by single crystal X-ray structural analysis. Although crystals of **13a** were obtained in this thesis, it must be stated that the structures of **13a** and **13b** were first obtained by Peter.[3] Nonetheless, for future reference, the workup of the structural data was done for this work, the results of which are described below. Perspective views of the complex cations **13** and **14** derived from the structures **13a**, **13b**, and **14a** are given in Figure 109 and Figure 110, respectively. Because the obtained structure of **14b** showed large thermal ellipsoids for some cations contained in the asymmetric unit (see below), the structural analysis was limited to a poor quality of the refinement model, insufficient for bond length analysis. Nonetheless, supplementary discussions highlighting the intermolecular hydrogen bond interactions in the two structurally distinct modifications of **14a** (Figure 111) and **14b** (Figure 112) are attempted. Such a discussion is also provided for **13a** (Figure 113) and **13b** (Figure 114) further down. Structural parameters, a full list of bond lengths, angles, and hydrogen bonds of the structures derived from **13a**, **13b**, and **14a** can be found in the attachment. Some structural parameters, selected bond lengths, angles, and hydrogen bonds relevant to the discussion are given in Tables 45-48, respectively.

*General note: For the labelling of the fully solved and refined structures (**13a**, **13b**, **14a**) described in the following, an adjunct "A" labels protons pointing inward and included in the ring-forming intramolecular hydrogen bond network, "B" labels those pointing outward. O(1) always represents a hydroxide/aqua oxygen donor ligand that acts as a H-donor, O(2) represents the remaining hydroxide/aqua oxygen donor ligand. In **14a**, O(3) represents the oxygen atom of the co-crystallized water molecule. In **13a** and **13b**, O(3) represents the accepting oxygen for H(1A) in the $–SO_3$ groups of the counter anion, and O(4) is the accepting oxygen for H(2A), respectively.*

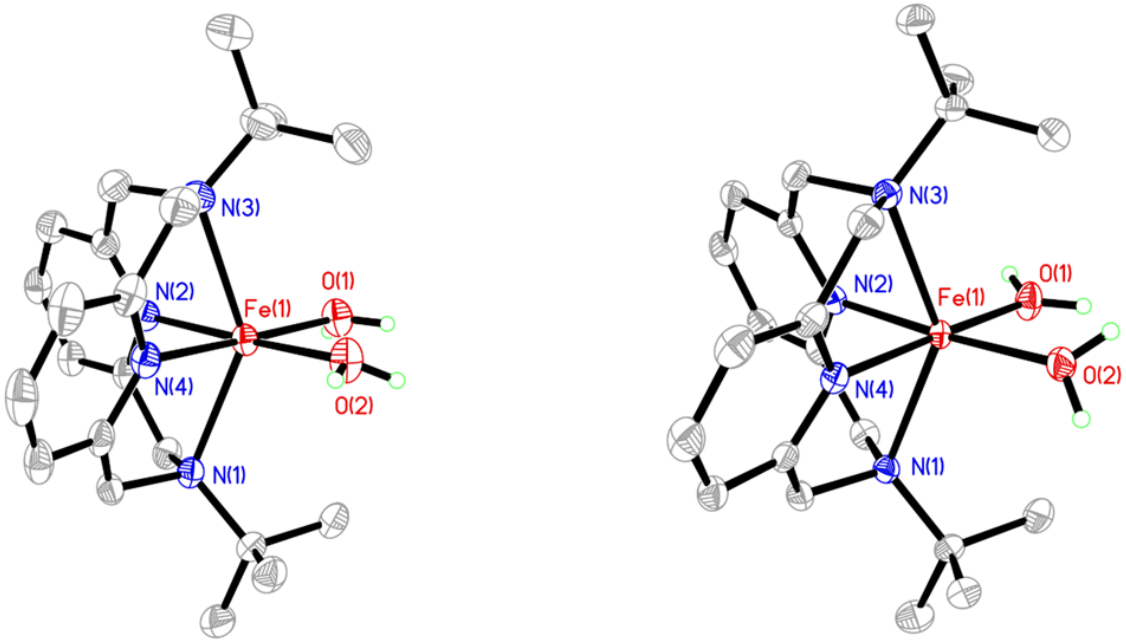

Figure 109. Perspective views of the complex cations in the ferrous compounds **13a** (left) and **13b** (right) with thermal ellipsoids displaying a probability level of 50% (150 K). Hydrogen atoms are omitted for clarity with the exception of the protons bound to the water ligands O(1) and O(2).

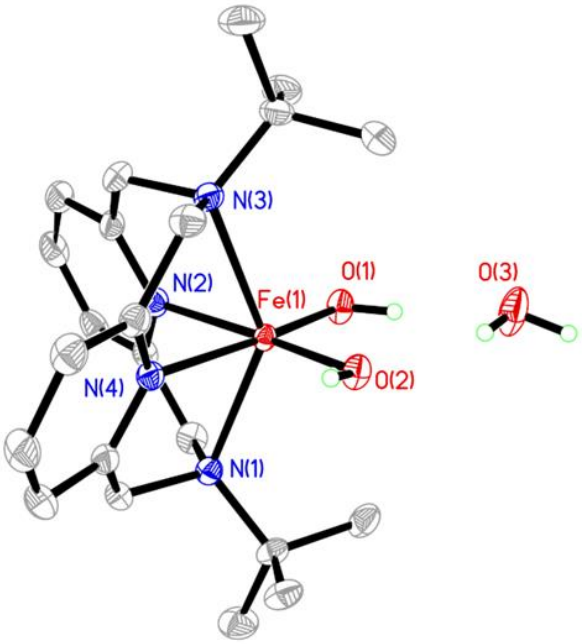

Figure 110. Perspective view of the complex cation and the crystal water contained in the ferric compound **14a** with thermal ellipsoids displaying a probability level of 50% (150 K). Hydrogen atoms are omitted for clarity with the exception of the protons bound to the hydroxide ligands O(1) and O(2) and the crystal water O(3).

Table 46. Structural parameters of **13a**, **13b**, **14a**, and **14b**.

	13a	**13b**	**14a**	**14b**
Spacegroup	$P2_1/c$ (monoclinic)	$P2_1/c$ (monoclinic)	$P2_1/c$ (monoclinic)	$P\bar{1}$ (triclinic)
T	150 K	150 K	150 K	150 K
Z	4	4	4	2
a [Å]	15.8735(4)	11.8398(2)	13.7151(3)	15.2660(8)
b [Å]	12.8732(3)	13.3692(2)	9.6662(2)	17.5849(13)
c [Å]	18.9253(4)	19.7266(3)	20.7391(5)	19.1074(10)
α	90°	90°	90°	114.146(6)
β	103.245(3)°	90.608(1)°	104.686(2)°	103.123(5)
γ	90°	90°	90°	103.837(5)
V [Å^3]	3764.38(16)	3122.32(8)	2659.62(11)	4228.25

Table 47. First coordination sphere bond lengths for complex cations **13** and **14** as obtained from the structural analysis of **13a**, **13b**, and **14a**, and the sum of selected distances in the hexagonal (**14**) or octagonal ring (**13**) formed by hydrogen bonds engaging with the aqua/hydroxide ligands at 150 K.

distance	**13a**	**13b**	**14a**
Fe-O(1)	2.08	2.07	1.86
Fe-O(2)	2.08	2.09	1.88
Fe-N(1)	2.36	2.35	2.32
Fe-N(3)	2.40	2.38	2.33
Fe-N(2)	2.10	2.10	2.12
Fe-N(4)	2.11	2.13	2.13
Σ (polygon)[a]	12.47[b]	12.62[b]	9.47[b]

All values given in Å. [a] Sum of the distances contained in the hexagon spanned by Fe-O(1)-H(1)-O(3)-H(3A)-(O2)-Fe in **14**, or the octagon spanned by Fe-O(1)-H(1A)-O(3)-S(1)-O(4)-H(2A)-O(2)-Fe in **13**, respectively. [b] No ESD could be calculated because the O-H distances were corrected with DFIX; a high uncertainty in the second decimal is expected. Despite the higher experimental accuracy bond lengths are rounded to a hundredth of an Å for clarity. N(1) and N(3) are the axial amine donors, N(2) and N(4) are the pyridine donors of the macrocyclic ligand, O(1) and O(2) are the aqua/hydroxide donors.

The bond lengths of **13** in **13a** and **13b** (Table 47) agree well with a high spin state for the octahedral, dicationic iron(II) complex coordinated by the L-N$_4$*t*Bu$_2$ macrocyclic ligand. Moreover, the Fe–O bond distances support the interpretation of two aqua ligands and are overall expectedly similar for the two structures.[121] However, there are some minor but notable differences: In **13a**, the hydrogen bond donor interactions of the aqua ligands are approximately equally strong, as can be derived from the distances to the acceptor atoms (Table 49). Thus, their polarization and partial charge can be regarded as similar and effectively no differences are observed in the Fe–O distances, or the Fe–N$_{Py}$ distances in *trans*-position, respectively. In **13b**, however, a stronger interaction of H(1B), bound to O(1), with one of the OTf$^-$ counterions leads to

a relative higher partial charge and slight hydroxo character at O(1) as opposed to O(2), observable by the relative shortening of the Fe-O(1) distance compared to the Fe-O(2) distance (Δ = 0.02 Å). Naturally, the *trans*-influence then leads to the elongation of the Fe-N(4) bond compared to the Fe-N(2) bond. It is interesting that, despite the dicationic character of **13**, both structures show rather long Fe-N_{amine} as well as Fe-N_{Py} distances similar to those observed for the monocationic N_4O_2 complexes with this ligand described in previous chapters. It is reasoned that the rigidity and already strong distortion of the macrocyclic ligand is partially responsible for these similarities. However, the slightly shorter Fe–O distances than typically observed for neutral oxygen donors indicate that the stronger polarization and partial hydroxide character of the aqua ligands induced by the H-bond interactions may also play a part in this.

When comparing the distances of **13** to **14**, it is immediately apparent that the Fe–O distances are significantly reduced to values typical for hydroxide ligands at iron(III) sites and close to those observed for the methoxide analogue **4** (see chapter 2 section 2.1.2). In addition, the Fe-N_{amine} distances are drastically reduced while the Fe–N_{Py} distances are slightly elongated. The shortening of the already quite elongated Fe–N_{amine} distances is a result of the oxidation state change and the depopulation of the degenerate d_{xz} and d_{yz} orbitals that may interact unusually strong with the amine donors because of the distortion out of the z-axis observed in the N_{amine}–Fe–N_{amine} angle (~140°, Table 48). The extent of the shortening is hereby also attributed to the rather soft vibration modes. The slight increase in bond length despite the oxidation state is a result of the strong *trans*-influence of the hydroxide ligands. Both effects have already been observed and discussed for a previous example (see chapter 2 section 2.1.2). In **14**, an asymmetry in the Fe-O bond lengths is caused by their differing secondary hydrogen bonding interactions. While both engage in H-bonding interactions as both an acceptor and a donor, the hydrogen atom H(2B) at O(2) engages in a weaker O–H···F bond with the PF_6^- counterion as opposed to the hydrogen atom H(1A) at O(1), which engages in a stronger O–H···O interaction with the crystal water. Thus, O(1) is slightly more polarized and has more oxo-character than O(2), leading to a relatively shortened Fe–O bond and a relatively extended Fe–N_{Py} bond in *trans*-position.

In addition to these aspects, another notable difference between **13** and **14** lies in the the polygon formed by the intramolecular interactions of the hydroxide/aqua ligands with a second molecule above the *cis*-di(aqua)/di(hydroxo)iron(II/III)-pocket (Σ(poygon), Table 47). This aspect will be discussed further down after the more general analysis of the hydrogen bond interactions in the structures of **13a**, **13b**, **14a**, and **14b**.

Table 48. Selected angles for the first coordination sphere of **13** and **14**, respectively, in **13a**, **13b**, and **14a**.

angle	13a	13b	14a
O(1)-Fe-O(2)	86.92(6)	86.56(6)	99.57(5)
O(1)-Fe-N(4)	177.71(6)	175.10(6)	169.48(5)
O(2)-Fe-N(4)	91.69(6)	97.05(6)	90.68(5)
O(1)-Fe-N(2)	96.56(6)	91.32(6)	88.24(5)
O(2)-Fe-N(2)	175.42(6)	176.32(6)	172.04(5)
N(4)-Fe-N(2)	84.75(6)	85.24(6)	81.60(5)
O(1)-Fe-N(1)	104.72(6)	98.67(6)	98.08(5)
O(2)-Fe-N(1)	107.50(6)	109.39(5)	106.99(5)
N(4)-Fe-N(1)	77.43(6)	77.03(6)	76.43(5)
N(2)-Fe-N(1)	74.56(6)	73.90(5)	73.16(5)
O(1)-Fe-N(3)	104.36(6)	108.06(8)	107.31(5)
O(2)-Fe-N(3)	99.73(6)	99.70(5)	99.42(5)
N(4)-Fe-N(3)	74.07(6)	74.67(6)	73.03(5)
N(2)-Fe-N(3)	76.55(6)	78.08(6)	76.56(5)
N(1)-Fe-N(3)	140.82(6)	141.41(5)	139.48(5)

All structures show interesting H-bond interactions, chains, or even networks that are described and discussed in more detail below. This includes the preliminary structure of **14b**, which shows intrinsically large ellipsoids for some, but not all, of the contained cations in the asymmetric unit. A list of all relevant hydrogen bonds of the fully solved and refined structures is given in Table 49 on the next two pages.

Table 49. Selected hydrogen bond lengths and angles found in **13a**, **13b** and **14a.**

	13a	**13b**	**14a**
O(1)-H(1A)…O(3)			[a]
d(D-H) [Å]	0.828(10)	0.835(17)	0.84*
d(H…A) [Å]	1.874(10)	1.900(18)	2.00*
d(D…A) [Å]	2.701(2)	2.735(2)	2.8101(19)
<(D-H-A)	176(3)	179(3)	163.1*
O(1)-H(1B)…O(6)	[b]		
d(D-H) [Å]	0.835(10)	0.837(17)	
d(H…A) [Å]	1.847(11)	1.810(18)	
d(D…A) [Å]	2.6777(19)	2.6398(19)	
<(D-H-A)	173(3)	171(3)	
O(2)-H(2A)…O(4)			
d(D-H) [Å]	0.834(10)	0.835(17)	
d(H…A) [Å]	1.855(11)	1.962(19)	
d(D…A) [Å]	2.683(2)	2.7788(19)	
<(D-H-A)	172(3)	166(3)	
O(2)-H(2B)…O(8)			
d(D-H) [Å]	0.834(10)		
d(H…A) [Å]	1.858(11)		
d(D…A) [Å]	2.6853(19)		
<(D-H-A)	171(3)		

	13a	13b	14a
O(2)-H(2B)…O(5)		[c]	
d(D-H) [Å]		0.835(17)	
d(H…A) [Å]		1.937(19)	
d(D…A) [Å]		2.7377(18)	
<(D-H-A)		160(3)	
O(2)-H(2B)…F(2)			[d]
d(D-H) [Å]			0.84*
d(H…A) [Å]			2.32*
d(D…A) [Å]			3.0744(18)
<(D-H-A)			150.2*
O(3)-H(3A)…O(2)			[e]
d(D-H) [Å]			0.840(17)
d(H…A) [Å]			2.06(2)
d(D…A) [Å]			2.8102(17)
<(D-H-A)			149(3)
O(3)-H(3B)…O(1)			
d(D-H) [Å]			0.854(17)
d(H…A) [Å]			1.825(18)
d(D…A) [Å]			2.6711(18)
<(D-H-A)			170(3)

D = donor, A = acceptor. Symmetry transformations: [a] -x+1,y-1/2,-z+3/2, [b] x,-y+1/2,z+1/2, [c] -x+1,-y+1,-z+2, [d] -x,y-1/2,-z+3/2, [e] -x+1,y+1/2,-z+3/2. ESDs for D–H distances of freely refine H-atoms with distance corrections (DFIX) in **13a** and **13b** are presumptive. *No ESDs given for large positional uncertainties of H-atoms.

As can already be seen in Figure 110, complex **14** is stabilized by intramolecular interactions to a co-crystallized water molecule in **14a**. The water molecules in the structure bridge adjacent cations, forming chains (Figure 111). Here, one hydroxide ligand functions as a H-bridge donor to a free electron pair of the water molecule, while the other functions as a H-bridge acceptor in an interaction with one of the H-atoms of the water molecule, forming a distorted hexagonal motif in the Fe(1)-O(1)-H(1)···O(3)-H(3A)···O(2)-Fe(1) plane. Additionally, the accepting hydroxide engages in a H-bridge donor interaction to the PF_6^- counterion while the second proton of the water molecule engages in a donor interaction to the hydroxide ligand of a neighboring cation that is already functioning as a H-bridge donor to the next water molecule. Thus, all hydrogens of the crystal water and the hydroxide ligands are saturated with H-bridging interactions. The hexagonal motif formed by H-bond interactions with the hydroxide ligands is suspected to be a key feature for a sufficient stabilization of the complex, as similar features have been observed for all other mononuclear ferric hydroxide complexes reported in this work and their stabilizing properties have already been discussed (chapters 2 and 3).[1]

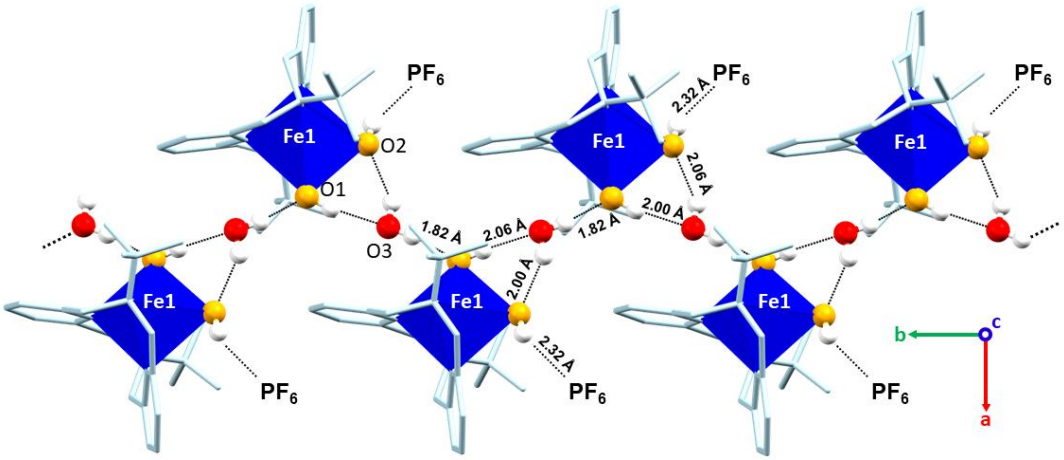

Figure 111. Perspective view of the packing and intermolecular interactions in the crystal structure of **14a** as viewed along the *c*-axis. The first coordination sphere is depicted as polyhedron, the ligand backbone as capped sticks, and the hydroxide ligands and the water molecule in a ball and stick style. The relative positions of the counterions are indicated. H-atoms except for those engaging in H-bonding are omitted for clarity. Red balls represent crystal water oxygen atoms, golden balls represent coordinated hydroxide ligands. Black dotted lines show short O–H···X (X = O, F) distances with the respective values rounded to two decimals. Oxygen atom labels are given for reference.

As opposed to a single cation and one crystal water molecule in the asymmetric unit of **14a**, the structure of **14b** shows three distinct cations connected by a manifold of intermolecular hydrogen bonds to residues assigned as formally five distinct crystal water molecules (and neighboring complex cations) that form channels along the *b*-axis. Interestingly, here the PF_6^- counterion is not involved in this complex hydrogen bond network but appears to be in domains between these channels alongside the lipophilic residues of the macrocyclic ligand. Increasingly distorted and large thermal ellipsoids from cations 1 over 2 to 3 (referring to the Fe1, Fe2, Fe3 sites depicted in Figure 112) and increasing disorders for the respective counterions do not allow for a satisfactory refinement that would make reliable bond length analysis or assignment of hydrogen positions feasible. However, the structural motif and the connectivity could be modeled with sufficiently small residual electron density upon assignment of the heavy atoms and C–H hydrogens (Highest difference peak: 2.405, deepest hole: -1.531, 1-sigma level: 0.137, R_1 = 13.08% (14.69% all data), GooF = 1.026). The

reproducibly large ellipsoids obtained for multiple single crystals point towards an intrinsic property, supposedly derived from the elasticity of the intermolecular hydrogen bond interactions. The disorder of the PF_6^- counterion may be a result of the lack of orientation preference because it is not engaged in the hydrogen bond network of this structure. The connectivity and intramolecular interactions for **14b** are schematically depicted in Figure 112. It is apparent that, again, all hydroxide complex units containing the macrocyclic ligand L-$N_4{}^tBu_2$ seemingly show a hexagonal, or even an octagonal hydrogen bond stabilized ring system, each of which appears to be almost planar within the limited positional certainty of the heavy atoms, to accommodate the *cis*-di(hydroxo)iron(III) complex. This structure of **14b** demonstrates three different possible interactions with water molecule neighbours at the three crystallographically distinct iron sites. At the Fe1 site, one water molecule hovers over the *cis*-di(hydroxo)iron(III) moiety forming an (almost isosceles) triangle of oxygen atoms and probably a heaxagonal hydrogen bond network Fe1–O···H···O_w···H···O–Fe1 (O_w = oxygen atom of the water molecule). At the Fe2 site, two water molecules are positioned above the moiety where the oxygen atoms form a square and probably an octagonal hydrogen bond network Fe2–O···H···O_w···H···O_w···H···O–Fe2. For Fe3, the interaction with the water molecules is mostly sideways, with one water molecule positioned next to the hydroxide ligands rather than above the *cis*-di(hydroxo)iron(III) moiety, connecting the cations in chains as ···O_w···H···O–Fe3–O···H···O_w···. Because the hydrogen atoms at the oxygen atoms could not be assigned in this structure, it cannot be determined which of the water molecules or hydroxide ligands engage as hydrogen bond donors, and which as acceptors, respectively. However, the diverse interactions with guest molecules (as well as neighboring cations) in **14b** showcase the diversity of stabilizing opportunities for this *cis*-di(hydroxo)iron(III) complex with e.g., solvents, especially water. Thus, the complex cation is a promising candidate for stabilization of such a unique species in solution as had been speculated from serendipitous ESI-MS observations,[2] and will be further investigated and discussed in following chapters.

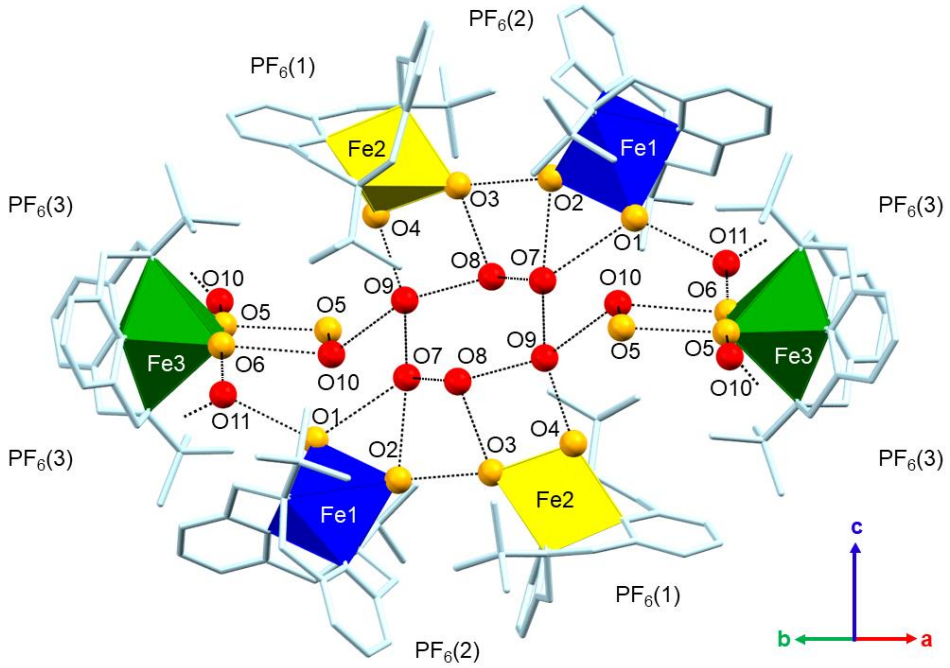

Figure 112. Perspective view of the packing and intermolecular interactions in the crystal structure of **14b** as viewed along the bisector of the γ-angle between the cell lengths *a*, and *b*. The first coordination sphere is depicted as polyhedron, the ligand backbone as capped sticks, and the hydroxide ligands and the water molecule in a ball and stick style. The relative positions of some PF_6^- counterions and their symmetry equivalents are indicated. H-atoms were not refined for the oxygen atoms because of positional uncertainties. All other H-atoms are omitted for clarity. Red balls represent crystal water oxygen atoms, golden balls represent coordinated hydroxide ligands, and their symmetry equivalents, respectively. Labels are given for reference. Black dotted lines show short O···O distances (longest: ~3.20 Å, shortest ~2.55 Å) where H-bond interactions are likely. Most O···O distances shown are in the range of 2.60-2.90 Å. No accurate distance determination can be achieved because of the uncertainties in the atomic positions.

Like **14**, also **13** engages in rich hydrogen bonding interactions. In both structures, **13a** and **13b**, the aqua ligands engage in similar hydrogen bond interactions: Two hydrogen atoms (H1A, H2A) face an R–SO_3^- group to form an octagonal ring with the first coordination sphere oxygen donors and the iron ion while the remaining two hydrogen atoms (H1B, H2B) of the water ligands face neighboring counterion R–SO_3^- groups that form a bridge to the next complex cation. In **13a**, these bridging interactions form long chains along the *c*-axis (Figure 113). In **13b**, however, the bridging is limited to the formation of two complex cations and four counterions (Figure 114). This is because, in **13a**, the bridging counterions and the ones forming the octagonal hydrogen bond feature are two distinct anions participating in only one of the two interactions. In **13b**, however, one of the bridging counterions engages in the hydrogen bond network of the octagonal feature of the neighboring, symmetry generated cation, thus limiting the H-bond chain length in this structure.

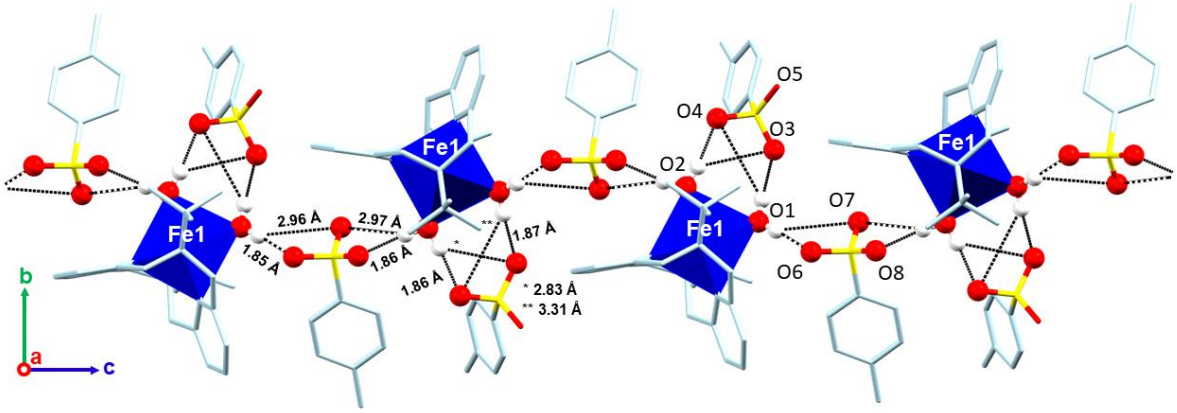

Figure 113. Perspective view of the packing and intermolecular interactions in the crystal structure of **13a** as viewed along the *a*-axis. The first coordination sphere is depicted as polyhedron, the ligand backbone as capped sticks, and the aqua ligands and the oxygen atoms engaging in H-bonding in a ball and stick style. H-atoms except for those engaging in H-bonding are omitted for clarity. Red balls represent oxygen atoms. Black dotted lines show short O–H···O distances with the respective values rounded to two decimals. Oxygen atom labels are given for reference.

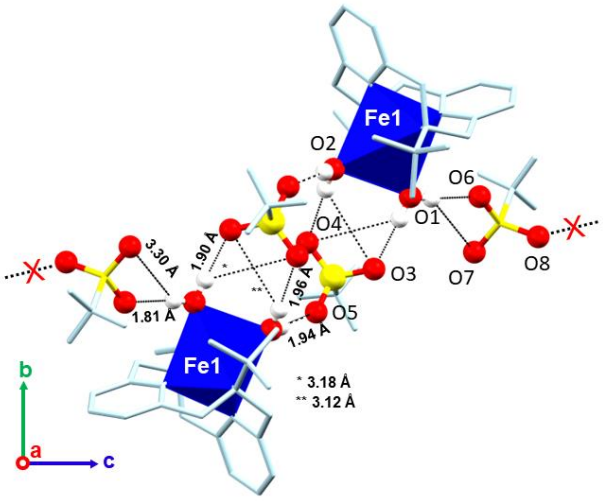

Figure 114. Perspective view of the packing and intermolecular interactions in the crystal structure of **13b** as viewed along the *a*-axis. The first coordination sphere is depicted as polyhedron, the ligand backbone as capped sticks, and the aqua ligands and the oxygen atoms engaging in H-bonding in a ball and stick style. H-atoms except for those engaging in H-bonding are omitted for clarity. Red balls represent oxygen atoms. Black dotted lines show short O–H···O distances with the respective values rounded to two decimals, the red X crossing a black dotted line indicates that no further relevant interactions are observed beyond this point. Oxygen atom labels are given for reference.

The most noticeable feature in all complexes is the ring formed by the hydrogen bond network of the *cis*-di(hydroxo)iron(III) or the *cis*-di(aqua)iron(II) units, respectively, with a secondary molecule. A similar hydrogen bond ring feature is also observed in the *cis*-(carboxylato)(hydroxo)iron(III) and *cis*-(carboxylato)(aqua)iron(II) complexes with the tetradentate macrocyclic ligand L-N$_4$^{t}Bu$_2$ as discussed in previous chapters of this thesis (chapters 2 and 3). It appears that such a ring-forming interaction is highly favored and acts as a stabilizing feature for the aqua/hydroxo iron-complexes with this macrocyclic ligand. In the case of **14a**, the hexagonal ring is yet again almost planar, with an angle sum of 720° within the margin of error (716°, Table 50) and only very minor deviations from the constructed plane through the atoms in question (Table 51). Interestingly, even the sum of all distances in this *inter*molecular hydrogen bond network (9.47 Å, Table 47) is rather close to the individual sums observed for the *intra*molecular hydrogen bond networks that form the hexagons in the other mononuclear hydroxo-iron(III) complexes **1** (9.31 – 9.35 Å), **7** (9.25 – 9.32), and **10**

(9.25 Å) (section 3.1.2, Table 21). Although this does, again, hint at an energetic minimum for the reoccurring geometry, it can ultimately not be verified experimentally.

In the case of **13a** and **13b**, the larger octagonal ring appears to allow for a somewhat larger torsion, as the atoms show larger deviations from ideal constructed planes and the angle sum lies slightly below the ideal 1080° expected for an octagon (**13a**, 1041°; **13b**, 1043°, Table 50). The sum of distances within the octagon appears to be similar (**13a**, 12.47 Å; **13b** 12.62 Å, Table 47), which is expected as the octagon is spanned by the same atoms with the same connectivity. An analysis of the different polygons for the structure of **14b** was extremely limited because of the large positional uncertainties (ellipsoids) of the atoms involved. However, subjectively the planes spanned by the heavy atoms appear to be rather planar and very rough estimates suggest a similar magnitude in the sums of distances for both the hexagonal (9.5 Å) as well as the octagonal (12.5 Å) geometry for the individual sites in **14b**.

Table 50. Angles within the rings formed by the hydrogen bonding between the *cis*-di(aqua)iron(II) unit and the R-SO_3^- group of the counterion in **13a** and **13b**, and the *cis*-di(hydroxo)iron(III) unit and the water molecule in **14a**.

<(L-M-L)	**13a**	**13b**	**14a**
Fe(1)-O(1)-H(1A)	120(2)	129(2)	
O(1)-H(1A)…O(3)	176(2)	179(2)	
H(1A)…O(3)-S(1)	134.9(7)	123.8(7)	
O(3)-S(1)-O(4)	111.2(1)	114.51(8)	
S(1)-O(4)…H(2A)	115.2(7)	122.7(7)	
O(4)…H(2A)-O(2)	172(2)	165(2)	
H(2A)-O(2)-Fe(1)	127(2)	121(2)	
O(2)-Fe(1)-O(1)	86.91(6)	86.56(5)	
Fe(1)-O(1)-H(1A)			109.5[a]
O(1)-H(1A)…O(3)			163.10[a]
H(1A)…O(3)-H(3A)			87[a]
O(3)-H(3A)…O(2)			149(2)
H(3A)…O(2)-Fe(1)			107.9(7)
O(2)-Fe(1)-O(1)			99.57(5)
Σ [°]	1043(5)	1041(5)	716[b]

[a] No ESD is given because of the positional uncertainty of H(1A). Thus, the reported accuracy of angles involving H(1A) appears higher than it actually is. [b] ESD for the sum of angles is expected to be within a similar magnitude as in similar examples (~4°, see previous sections). The sum of all angles is given as a measure for planarity. Ideal planarity would give Σ = 720° for a six membered ring, and Σ = 1080° for an eight membered ring, respectively. The estimated standard deviation (ESD) for the sum was calculated as the root sum of the squares of each individual angle. The summarized values and ESDs were subsequently rounded to integer numbers.

Table 51. Deviation (in Å) of the position of the atoms from the least-squares planes calculated to pass through the atoms Fe(1), O(1), H(1A), O(3), S(1), O(4), H(2A), O(2) of the *cis*-di(aqua)iron(II) unit and the R-SO_3^- group of the counterion in **13a** and **13b**, and the atoms Fe(1), O(1), H(1A), O(3), H(3A), and O(2) of the *cis*-di(hydroxo)iron(III) unit and the water molecule in **14a** respectively.

	13a	**13b**	**14a**
Fe(1)	0.1560 (0.0062)	-0.1008 (0.0060)	
O(1)	0.1034 (0.0095)	-0.2144 (0.0093)	
H(1A)	-0.0026 (0.0188)	-0.0259 (0.0187)	
O(3)	-0.2050 (0.0069)	0.3917 (0.0072)	
S(1)	-0.0025 (0.0072)	-0.0680 (0.0032)	
O(4)	0.3224 (0.0072)	-0.3514 (0.0068)	
H(2A)	-0.0784 (0.198)	0.0089 (0.0178)	
O(2)	-0.2934 (0.0088)	0.3600 (0.0089)	
Fe(1)			0.0014 (0.0059)
O(1)			-0.0301 (0.0073)
H(1A)			-0.0059 (0.0109)
O(3)			-0.0108 (0.0116)
H(3A)			0.0265 (0.0150)
O(2)			0.0190 (0.0080)
rmsd[a]	0.1848	0.2419	0.0188

[a] root mean square deviation.

In summary, the structures allow for the unambiguous identification of high-spin $[Fe^{II}(L\text{-}N_4{}^tBu_2)(OH_2)_2]^{2+}$ (**13**) and high-spin $[Fe^{III}(L\text{-}N_4{}^tBu_2)(OH)_2]^{+}$ (**14**) complexes. In the respective structures, the cations are stabilized by rich intermolecular hydrogen bonding interactions which likely contribute to the stabilizing of the cations in the solid state by spanning polygonal geometries. For **13**, the counterion plays a major role as hydrogen bond acceptor for the aqua ligands while the counterion is much more passive in **14**. Here, mainly co-crystallized water molecules in **14a** and **14b** act as both hydrogen bond donors and acceptors for the coordinated hydroxide ligands. The direct hydrogen bonding between the two hydroxide ligands is not observed. The diverse interactions stabilizing **14** through crystal water molecule interactions rather than interactions with neighboring cations (as was observed in the example of Bénisvy)[78] holds promise for the possible stabilization of the mononuclear *cis*-di(hydroxo)iron(III) complex in solution that is further studied in solution-based studies below.

5.1.3. SQUID-Magnetometric Analysis

Temperature-dependent measurements of the magnetic susceptibility and magnetization at low temperatures in the solid state were done for **13a** and **14a**. Magnetic field sweeps of 0-7 T at 100 K were done to rule out significant paramagnetic impurities, proven by a linear correlation of *M* vs. *H*. Some results for the magnetic susceptibility are displayed in Figure 115, Figure 116 and Table 52, the results of the magnetization are given further down.

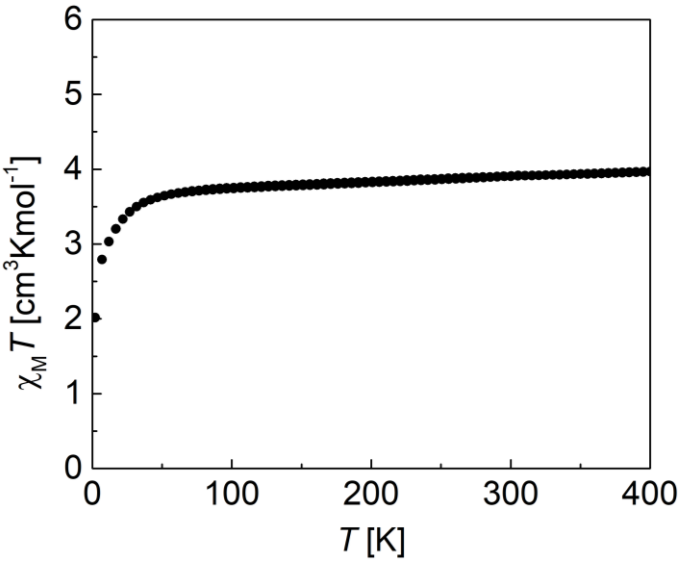

Figure 115. Temperature dependence of $\chi_M T$ for **13a** between 2-400 K measured at 0.5 T with a sweep rate of 2 K/min. Data points of cooling mode (300 K → 2 K) and heating mode (2 K → 400 K) are layered on top of each other.

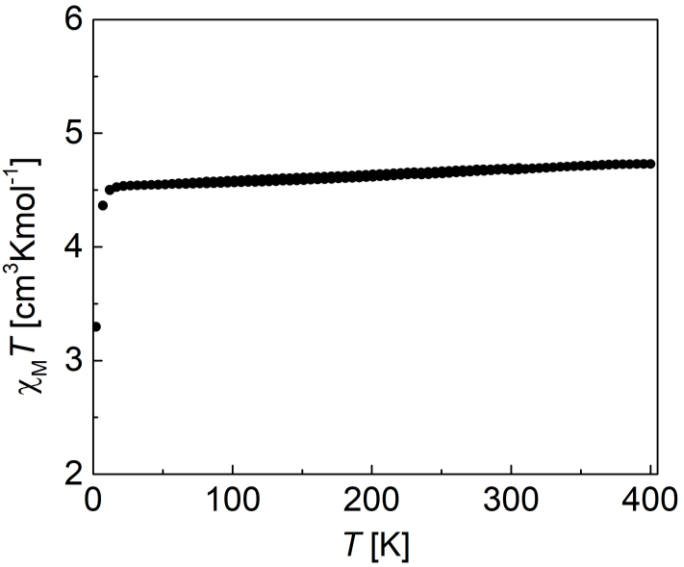

Figure 116. Temperature dependence of $\chi_M T$ for **14a** between 2-400 K measured at 0.5 T with a sweep rate of 2 K/min. Data points of cooling mode (300 K → 2 K) and heating mode (2 K → 400 K) are layered on top of each other.

Table 52. Magnetic data (χT) for **13** and **14** as obtained by SQUID-magnetometric measurements on **13a** and **14a** at 400 K, 298 K, 50 K, and 2 K.

T [K]	**13a** [cm^{3}Kmol^{-1}]	**14a** [cm^{3}Kmol^{-1}]
400	3.97 (HS)	4.73 (HS)
298	3.91 (HS)	4.68 (HS)
50	3.65 (HS)	4.55 (HS)
2	2.02	3.30

HS = high spin. Data is given at 50 K to represent the low temperature magnetic moment and spin-state without the influence of zero-field splitting effects.

The magnetic susceptibility measurements reveal that both complexes are in the high spin state at temperatures between 2-400 K. This concurs with the spin states expected from the bond length analysis (section 5.1.2) and ligand field theoretical considerations. Compound **13a** shows a minor upward slope that can be attributed to temperature independent paramagnetism (TIP), the increased magnetic moment as compared to the theoretical spin-only (SO) value (S = 2, $\chi_M T_{SO}$ = 3.00 cm^{3}Kmol^{-1}) is attributed mostly to orbital contributions. Deviations from the SO-value in **14a** (S = 5/2,

$\chi_M T_{SO}$ = 4.38 cm^3Kmol^{-1}) are within the range of previously reported high-spin d^5 complexes with similar environments (sections 2.1.3 and 3.1.3).

It is noteworthy that the susceptibility measurement of **14a** shows an unperturbed trend even at temperatures as high as 400 K. This suggests that the crystal water molecule is well-bound within the crystal packing and not lost by evaporation at these high temperatures, supporting the argument for strong intermolecular interactions.

Magnetization was measured with 0-7 T magnetic field sweeps at variable temperatures between 2-10 K in 1 K increments for **13a** and **14a** to investigate the zero-field splitting (ZFS) magnitude and *g*-value anisotropy by fitting of the temperature-dependent data. Satisfactory fits for **13** and **14** were achieved with the assumption of an isotropic *g*-value and are represented in Figure 117 and Figure 118.[124] The fact that such satisfactory fits could be obtained for **13a**, even though this was not achieved for [Fe(L-$N_4{}^tBu_2$)(O_2CPh)(OH_2)]ClO_4 (**2a**) (see section 2.1.3), provides evidence of a smaller *g*-anisotropy in **13** as opposed to **2**. This agrees with the expectations for this more symmetric dicationic aqua iron(II) complex. For **14**, the data can be fitted very well with a *g*-value very close to 2.00, thus suggesting only very minor anisotropy for the real *g*-values, similar to what is observed for the other ferric hydroxide complexes reported in this work (see sections 3.1.3 and 3.1.7). The resulting ZFS magnitude for both complexes is also well matched with the range obtained for the iron(III) complexes described in previous chapters, where fitting was successful (Table 53). Especially the zero-field splitting parameters of **14** and **4** are similar, likely because they only differ in a methyl group at the two oxygen ligands.

More detailed information about the *g*-anisotropy and the real g_x, g_y, and g_z-values was obtained for **14** via temperature dependent X-band EPR spectroscopy on frozen solutions, as described in section 5.1.8. This was not possible for **13**, as the transitions between the integer Kramer doublets of the S = 2 cation cannot be observed at X-band frequencies, thus the description of these parameters remains limited to the results of the magnetization experiments.

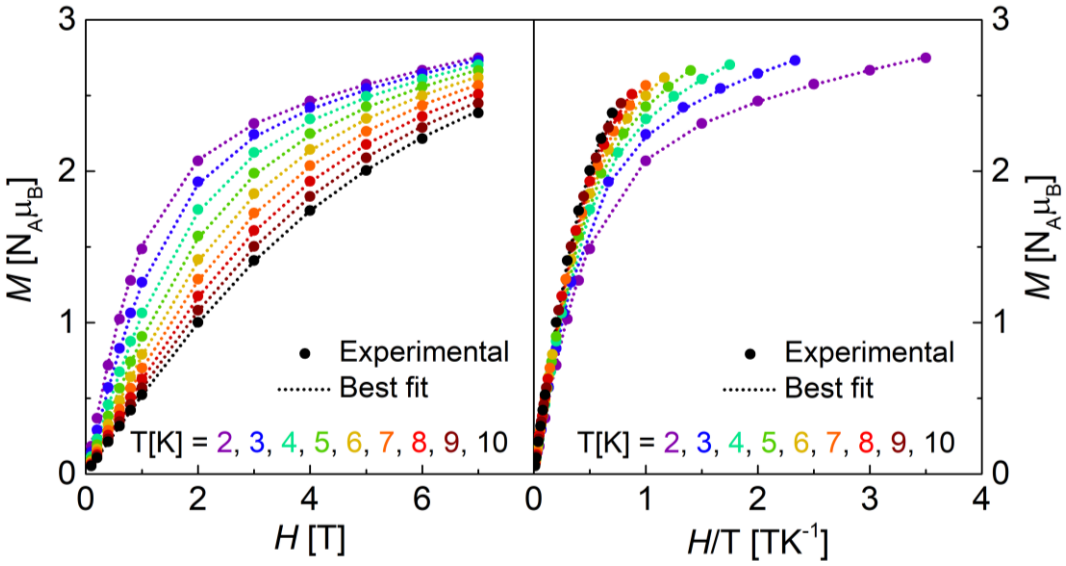

Figure 117. Variable temperature magnetization (left) and reduced magnetization (right) for the data (solid circles) and fits (dotted lines) obtained for **13a** between 2-10 K in 1 K increments. The fits were done with PHI assuming isotropic *g*-values.[124] Best fits were achieved by correlated magnetization and susceptibility fitting of the experimental data. Fitting results (simplex): **13a** *g*-value = 2.2567 ± 0.013, zero-field-splitting D = 3.33 ± 0.17 cm^{-1}, residual = 0.0017.

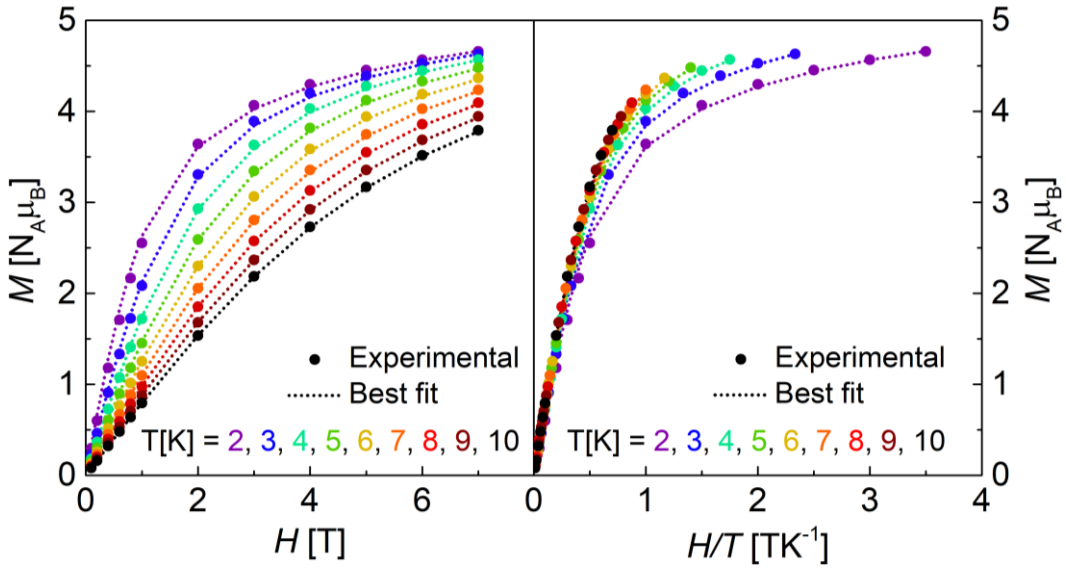

Figure 118. Variable temperature magnetization (left) and reduced magnetization (right) for the data (solid circles) and fits (dotted lines) obtained for **14a** between 2-10 K in 1 K increments. The fits were done with PHI assuming isotropic *g*-values.[124] Best fits were achieved by correlated magnetization and susceptibility fitting of the experimental data. Fitting results (simplex): **14a** *g*-value = 2.0504 ± 0.0008, zero-field-splitting D = 1.06 ± 0.01 cm^{-1}, residual = 0.0244.

Table 53. Fitting results for the magnetization measurements on **1b**, **7b**, and **10b**, and **4a**, **14a**, an **13a** between 2-10 K in 1 K increments. Results for **1b** are adapted from previously published results.[1]

	1b, 7b, 10a	**4a**	**14a**	**13a**
D	2.19 – 3.23 ± 0.18[a]	0.90 ± 0.02	1.06 ± 0.01	3.33 ± 0.17
g_{iso}	2.008 – 2.028 ± 0.011[a]	2.073 ± 0.000	2.050 ± 0.001	2.257 ± 0.013
res.	0.31 – 0.91[a]	0.37	0.02	<0.01

res. = residual, *D* = zero field splitting parameter in cm^{-1}, g_{iso} = isotropic *g*-value. [a] Maximum error given for the grouped values. An isotropic *g*-value was assumed as simplification.

5.1.4. Mößbauer-Spectroscopic Analysis

Mößbauer spectra of **13a** and **14c** confirm both the spin state and the oxidation state in complexes **13** and **14** to be high-spin d^6 and high-spin d^5, respectively (Figure 119).

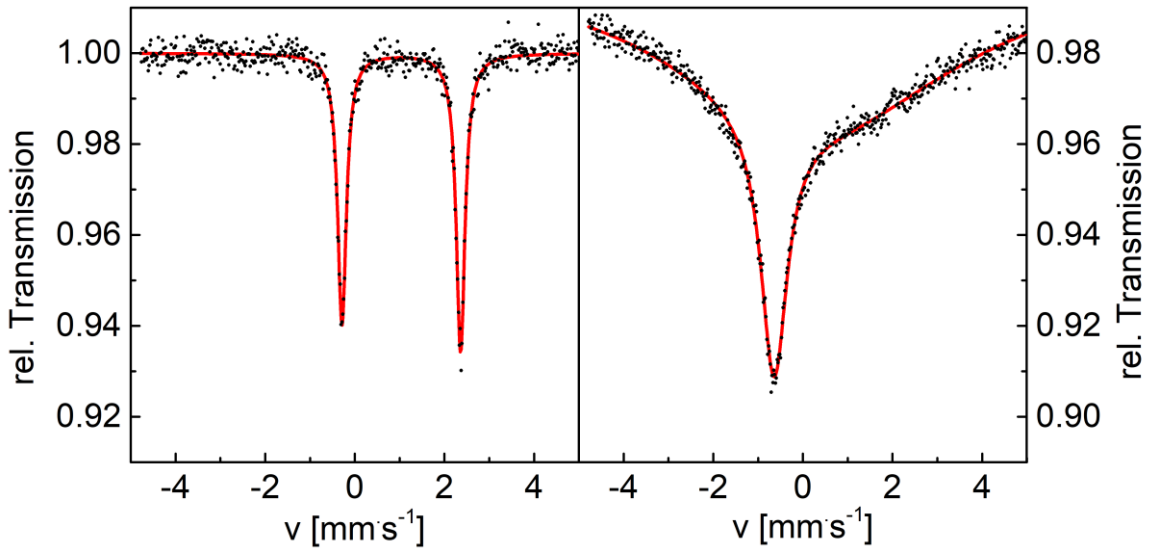

Figure 119. Experimental Mößbauer spectra (black dots) and fits (red trace) of **13a** (left) at room temperature (RT) and **14c** (right) at 70 K. Mößbauer parameters for **13** (RT): δ_{IS} = 1.04 mms^{-1}, ΔE = 2.65 mms^{-1}; Fitting quality χ^2 = 0.96. Mößbauer parameters for **14** could not be determined, the peak of the broad singlet is situated at -0.64 mms^{-1}. The isomeric shift δ_{IS} is given relative to α-Fe foil (δ_{IS}(α-Fe vs source) = 0.107 mm·s^{-1}).

For **13a**, a narrow doublet with δ_{IS} = 1.04 mms^{-1} and a large quadrupole splitting ΔE = 2.65 mms^{-1}, typical for high-spin iron(II) ions with the macrocyclic ligand L-N$_4$^{t}Bu$_2$, is observed at room temperature. While **13a** produces a well-behaved spectrum, **14c** produces an extremely broad asymmetric signal as is often observed for Mößbauer spectra of high-spin iron(III) complexes without applied external fields.[125] This can occur because of the high internal magnetic field produced by the S = 5/2 iron site which can cause intermediate relaxation times for the magnetic interaction. As a result, the spectrum could not be fitted. However, as it resembles the almost equally poorly resolved spectrum of **4a** and a preliminary fit was achieved for this spectrum, the spectrum of **14c** can be compared to both the experimental results of **4a** and this fit to at least place it in context (Figure 120).

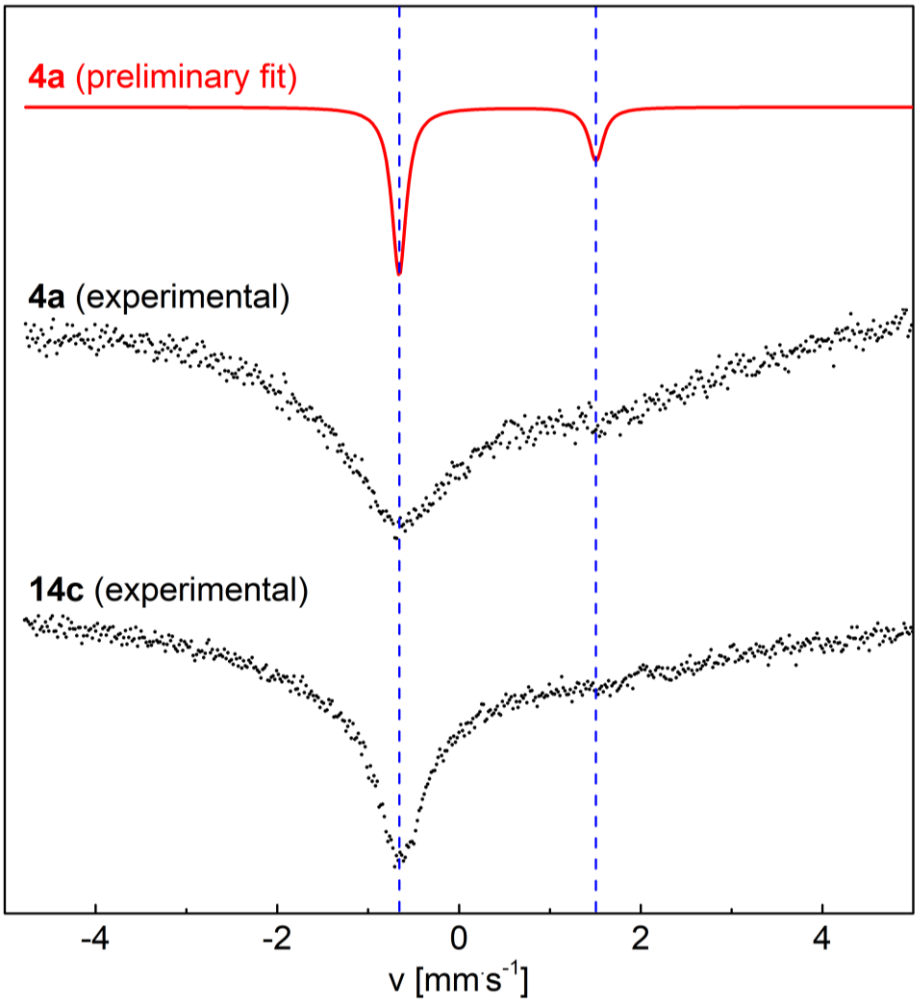

Figure 120. Stacked plots of velocities ($mm \cdot s^{-1}$) vs relative transmissions for the experimental Mößbauer spectra (black dots) obtained for **4a** (10 K) and **14c** (70 K) and the estimated, preliminary fit of **4a** as described in chapter 2 section 2.1.4 (red trace). The blue dashed lines are guides for the eyes that pass through the peaks of the simulated doublet. Indicated temperatures are those observed at the thermometer, sample temperatures are probably much higher especially at very low set temperatures. The isomeric shift δ_{IS} is given relative to α-Fe foil (δ_{IS}(α-Fe vs. source) = 0.107 $mm \cdot s^{-1}$).

For **14c**, an isomeric shift at velocities lower than that observed for **13a** can be expected from the positioning of the resolved signal at negative velocities (-0.64 mms^{-1}). The quadrupole splitting should be reduced in the $^6A_1$ high-spin iron(III) ion in **14** compared to the anisotropic $^5T_2$ high-spin iron(II) ion in **13**. In contrast, an isomeric shift similar to that of **4** can be expected for **14**, as the two iron(III) samples only differ in a methyl group at the oxygen ligand and both produce a signal at the same negative velocity (-0.64 mms^{-1}), albeit at different set temperatures. Although the

second signal of the expected asymmetric, broadened doublet is not resolved in either case, a preliminary fit for **4a** was done to estimate the Mößbauer parameters. Some baseline deviations that are present in **14c** as well as in **4a** at positive velocities do allow for the speculation of a similar, probably slightly larger quadrupole splitting in **14c** as compared to **4a**. A comparison of all Mößbauer parameters obtained for the high-spin iron(III) and high-spin iron(II) complexes containing the macrocyclic ligand L-$N_4{}^tBu_2$ and a pseudo-octahedral N_4O_2 environment with the oxygen donors in *cis*-position is given in Table 54. A more detailed discussion about the differences between high-spin iron(II) and high-spin iron(III) complexes containing this macrocyclic ligand is provided in sections 2.1.4 and 3.1.4.

Table 54. Mößbauer parameters obtained for **1a**, **7a**, and **10a**, and **2a** and **13a** at room temperature, and preliminary Mößbauer parameters estimated for **4a** and **14c** at low temperatures.

	1a, 7a, 10a	**2a**	**13a**	**4a**	**14c**
δ_{IS} [mms^{-1}]	0.30 – 0.31	1.04	1.04	0.42	~0.4[a]
ΔE_q [mms^{-1}]	2.26 – 2.32	2.63	2.65	2.16	>2.2[a]
χ^2	1.00 – 1.27	1.11	0.96	30.13	-

δ_{IS} = isometic shift relative to α-Fe foil (δ_{IS}(α-Fe vs source) = 0.107 mm·s^{-1}). ΔE_q = Quadrupole splitting. χ^2 = measure of fitting quality. [a] Estimate based on visual comparison with the preliminary fit of **4a**.

Surprisingly, despite the difference in charge at the metal site and the ligands, as well as the overall symmetry of the complexes, the Mößbauer parameters of **2a** and **13a** are strikingly similar. It appears that the dicationic charge at the metal site in **13** is well-compensated by the partially negative water ligands because of their hydrogen bonding interaction, ultimately leading to the same isomeric shift as observed for the monocationic complex **2**. This concurs with the interpretation of Fe–O bond shortening because of hydrogen bond induced partial polarization as described in section 5.1.2. Additionally, the charge asymmetry in the oxygen ligands in **2** do not seem to majorly affect the magnitude of the electric field gradient, as an almost identical value for the quadrupole splitting is found for **13** which contains two formally neutral aqua ligands. This suggests that the distortion of the macrocyclic ligand is the main contributor to the

quadrupole splitting, as is in agreement with the untypically large splitting for the high-spin iron(III) complexes.

5.1.5. Infrared-Spectroscopic Analysis

Infrared (IR) spectra were measured for **13a**, **14a**, **14b**, and **14c**. For reference, the IR spectrum of **13b** is also presented and compared to that of **13a** (Figure 121). To identify the relevant vibrations of the hydroxide ligands in **14**, rather than the O–H vibrational excitations of the crystal water molecules, the water-free compound **14c** was compared with **14a** and **14b** (Figure 122). Moreover, deuterated analogues of **13a** (**13d**) and **14b** (**14d**) were specifically synthesized and measured to unambiguously identify the O–H/O–D vibrations of the compounds (Figure 123). In all cases, polycrystalline samples (if available) were investigated using an ATR accessory to ensure that the bands assigned to O–H vibrations represent the respective compound spectra rather than atmospheric moisture or adventitious water in a KBr pellet.

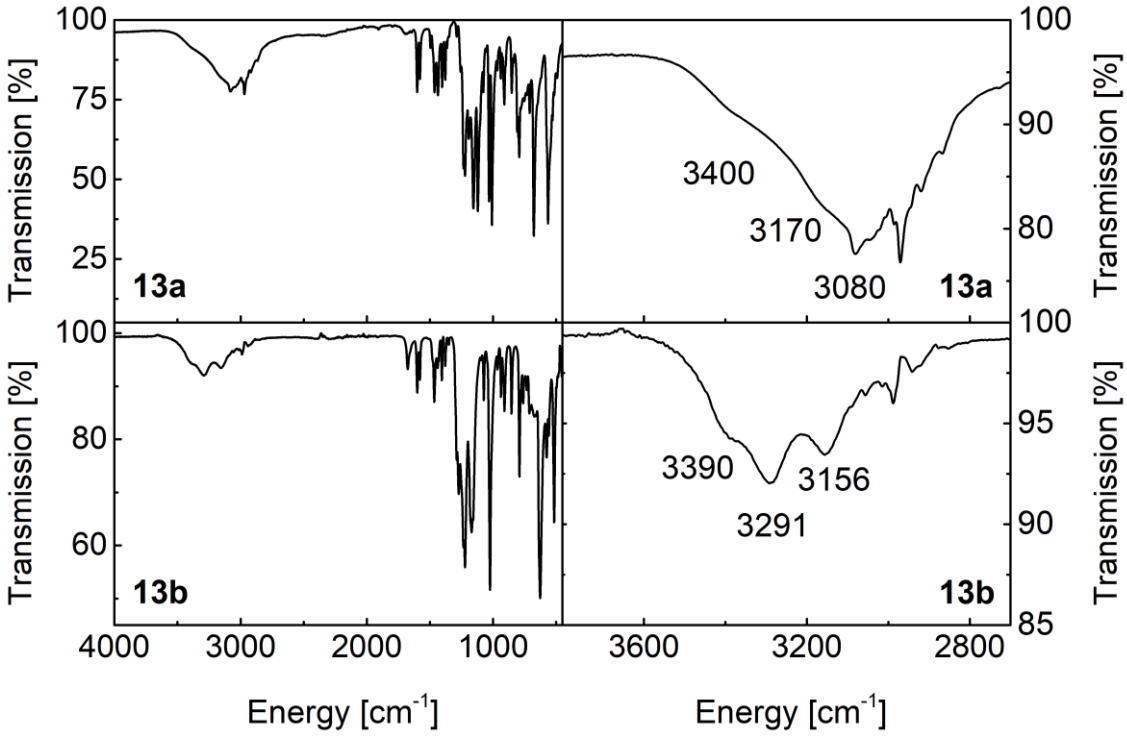

Figure 121. FTIR spectra of solid, crystalline samples of **13a** and **13b** between 4000-450 cm^{-1} (left) and between 3800-2700 cm^{-1} (region of interest, ROI) measured with an ATR-accessory under atmospheric conditions. Energies of relevant peaks and shoulders are provided in units of cm^{-1} in the ROI spectra. Data for the spectrum of **13b** were provided by *Pascal Peter* and used for this work with permission.[3]

Although the high-energy absorptions appear slightly more narrow in **13b**, the spectra of **13a** and **13b** both display rather broad vibrations between 2800-3600 cm^{-1} which

are overlayed by typical C–H vibrations around 3080 cm^{-1} and 2970 cm^{-1} (Figure 121). These broad bands can be attributed to the symmetric and anti-symmetric O–H stretching vibrations of the aqua ligands. The more narrow bands in **13b** allow for the discerning of three bands, all of which exhibit energies within or below the region expected for symmetric and antisymmetric O–H stretching vibrations of crystal water (3550 – 3200 cm^{-1}).[166] A more exact assignment of these bands was not achieved. The reduced energies are because the O–H bond is weakened upon coordination to the metal site and engaging in hydrogen bonding interactions with neighboring molecules. The rich intermolecular interactions observed in the crystal structures lead to broad absorptions, as they create a spectrum of energetically similar O–H bond lengths with differing excitation energies. This is especially true for somewhat elastic superstructures formed by the bridging of cations via long hydrogen bonded chains formed by sequential cation-anion interactions in **13a**. It stands in contrast to the observation of more narrow bands for the more isolated *intra*molecular hydrogen bonds in the *cis*-carboxylato(aqua)iron(II) units of compounds containing e.g. **2** (section 2.1.5).

In contrast to **13**, **14a** and **14b**, both crystallized with crystal water molecules. This makes the assignment of the O–H stretching vibrations pertaining the cation somewhat ambiguous. To accurately identify the O–H stretching vibrations corresponding to the hydroxide ligands, compound **14c**, although not crystalline, proved to be valuable. The IR-spectrum of **14c** does indeed present a suitable reference to adequately assign the extremely narrow band at ~3650 cm^{-1}, also contained in both **14a** and **14b**, to the O–H stretching vibrations of the hydroxide ligands (Figure 122). The broader bands in **14a** and **14b** are, thus, assigned to O–H vibrations of the crystal water molecules which become more diffuse with increased water content as can be exemplified by the vibration centered at 3450 cm^{-1}.

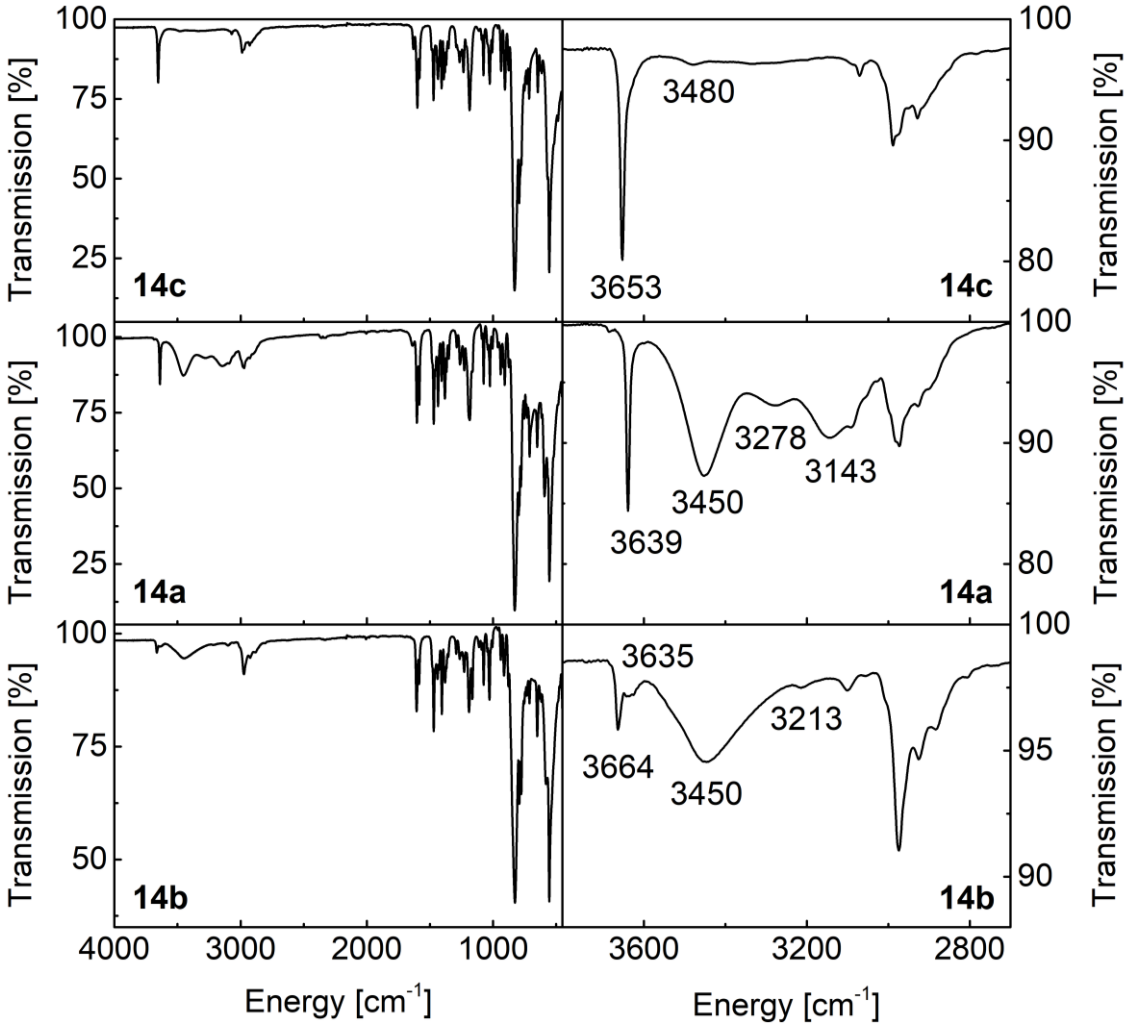

Figure 122. FTIR spectra of solid crystalline samples of **14a** and **14b**, and a powder sample of **14c**, between 4000-450 cm^{-1} (left) and between 3800-2700 cm^{-1} (region of interest, ROI) measured with an ATR-accessory under atmospheric conditions. Energies of relevant peaks are provided in units of cm^{-1} in in the ROI spectra. The weak signal at 3480 cm^{-1} and a sluggish baseline between 3600-3200 cm^{-1} in **14c** suggest that some minor water residues are still present in the bulk material.

The rather high energy of the O–H stretching vibration at 3639-3664 cm^{-1} for the hydroxide ligands is surprising, as it is well-within the range of O–H bond vibrational energies of free hydroxides in the gas phase (3700-3570 cm^{-1}).[126] Because of the coordination to the metal site as well as the hydrogen bond interactions within the crystal packing, the O–H bond strength would be expected to be reduced. Such a bond strength reduction is in fact observed for the previously discussed mononuclear *cis*-(carboxylato)(hydroxo)iron(III) complexes **1**, **7**, and **10** which exhibit O–H bond stretching vibrations mostly in the range between 3300-3400 cm^{-1} (sections 2.1.5 and

3.1.5). Even more surprising is the fact that the signal is extremely narrow, and that the excitation energy barely changes despite the differing environments and H-bond interactions in **14a**, **14b**, and **14c**. This suggests that the differing hydrogen bond interactions and environments do not strongly influence the O–H bond energy of the hydroxide ligands. This is interesting because it opposes the previous observations with mononuclear iron(III) complexes with a single hydroxide. For example, in the case of $[Fe(L\text{-}N_4{}^tBu_2)(O_2CPh)(OH)]^+$ (**1**), the O-H stretching vibration is broader and spans a range of 3289-3392 cm^{-1} even in spite of strong interactions with the environment as the hydroxide mostly engages in an intramolecular hydrogen bond with structural preorganization. A possible explanation for these discrepancies is that the O–H bond in the $[Fe(L\text{-}N_4{}^tBu_2)(OH)_2]^+$ cation is less polarized and/or less partially deprotonated than the O–H bond in the $[Fe(L\text{-}N_4{}^tBu_2)(O_2CPh^R)(OH)]^+$ cations. A reason for this could be the intramolecular interaction with a moderate base in the *cis*-carboxylato(hydroxo)iron(III) moiety in **1**, **7**, and **10** as opposed to the intermolecular interactions with water, a weaker base, in the *cis*-di(hydroxo)iron(III) moiety of **14**. This leaves the conclusion that the coordination of the hydroxide does not influence the O–H bond energy significantly but that the hydrogen bond interactions are the main contributors to the weakening of the bond, supposedly because of the weak ligand strength of hydroxide anions.

To unambiguously identify the O–H stretching vibrations especially at lower energies, and to better resolve any of these bands obscured by C–H stretching vibrations, **13a** was synthesized with D_2O and **14c** was recrystallized from an acetonitrile solution containing D_2O to yield the (partially) deuterated compounds **13d** and **14d**. Because **14** can by crystallized in different modifications with varying water content, it is at first glance ambiguous which structural packing and (heavy) crystal water content is achieved in **14d**. However, as can be seen in Figure 122, the IR spectra are well-suited to differentiate between the differing compositions. Thus, **14d** is assigned to be an analogue of **14b** and the respective spectra are compared in Figure 123.

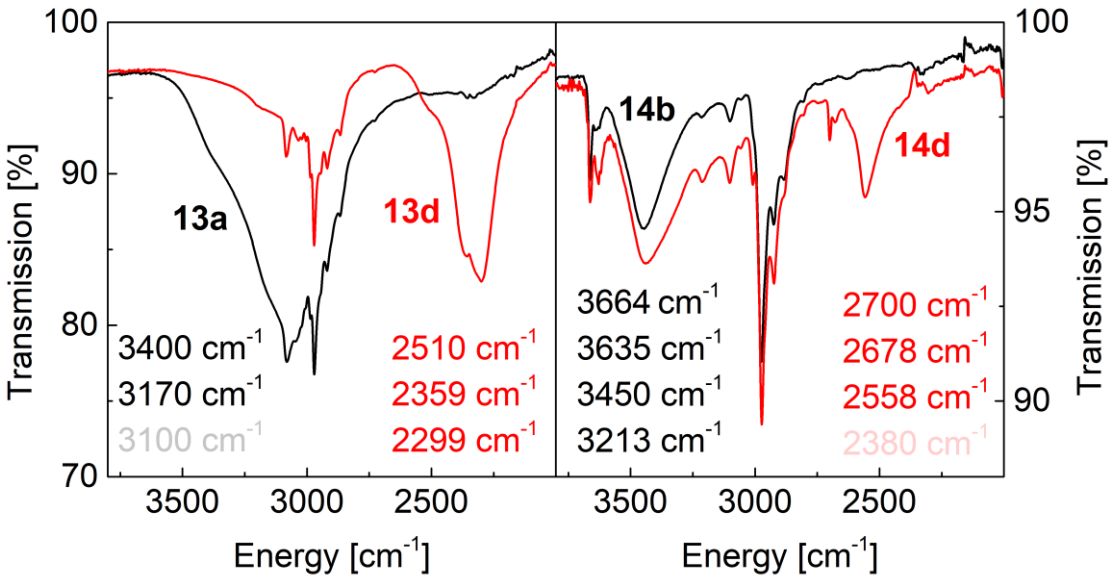

Figure 123. FTIR spectra of solid, crystalline samples of **13a** and **13d** (left), and **14a** and **14d** (right) between 3800-2000 cm^{-1} collected with an ATR-accessory under atmospheric conditions. O–H vibrational energies are given in red for the deuterated compounds and in black for the protonated compounds. Pale grey and pale red energy values are calculated using a factor of 1.35 for the isotope effect as the bands could not be discerned. The calculated band in **13a** at 3100 cm^{-1} is obscured by C–H vibrations centered at 3080 cm^{-1}, the calculated weak band in **14d** at 2380 cm^{-1} is obscured by artefacts of carbon dioxide content fluctuations in the atmospheric background. Complexes **13d** and **14d** are only partially deuterated, thus the O–H frequencies are still observable in the respective spectra.

The spectra of **13d** and **14d** (Figure 123) reveal a factor of approximately 1.35 for the isotope effect for all O–H bands which is in good agreement with theoretical considerations and a reported magnitude of 1.35 – 1.41 for H–D substitution isotope effects in vibrational spectroscopy.[167]

The spectrum of the deuterated compound **13d** exhibits three bands contained in a broad feature with two shoulders and one peak. While the shoulders are clearly visible in **13a**, the peak is obscured by an aliphatic a C–H vibration at 3080 cm^{-1} although it is expected because of the structural similarity to **13b**, which does show broad, but better-defined bands. By applying the factor of 1.35 that represents the isotope effect to the vibration at 2299 cm^{-1} in **13d**, the previously obscured band can be identified at 3100 cm^{-1}. As all O–H bonds of the aqua ligands in **13** engage in hydrogen bonding, it

cannot be discerned with certainty which vibration corresponds to which O–H bond. Thus, no further interpretation was attempted.

Similar to **13**, the factor of 1.35 was used to discover that the weak band situated at 3213 cm^{-1} in the spectrum of **14a** is probably obscured by baseline deviations caused by fluctuations of atmospheric CO_2 content in **14d**, as it can be expected at 2380 cm^{-1}. The narrow O–D vibration at 2700 cm^{-1} can clearly be identified to correspond to the deuteroxide ligands while the interpretation of the vibration at 2678 cm^{-1}, and 3635 cm^{-1} in **14b**, respectively, remains ambiguous. Although this could be a vibration caused by crystal water, it could also be a signal corresponding to the hydroxide/deuteroxide ligands of one of the three distinct cations in the asymmetric unit of the structure with differing environments.

Overall, the IR-spectroscopic analysis reveals new and interesting insights into the influences of coordination and hydrogen bonding interactions on the O–H bond strengths of aqua/hydroxide ligands in mononuclear aqua iron(II) and mononuclear hydroxo iron(III) complexes.

5.1.6. Solid Electronic Spectroscopic Analysis

UV-vis NIR spectra were measured for solid samples of **13a** and **14a** (Figure 124). For **13a**, pure ground powder was measured to resolve the d,d-bands and a ground powder containing small amounts of **13a** in KBr was measured to resolve the charge transfer bands in the UV region. For **14a**, a ground powder mixture of the sample with KBr was used for both measurements. In all cases, a ground KBr powder was measured as reference prior to the sample measurement to approximate the scattering component *S* for the calculation of *K/S* when employing the Kubelka-Munk equation (equation 4).[127]

$$\frac{K}{S} = \frac{(1-R_\infty)^2}{2R_\infty} \quad (4)$$

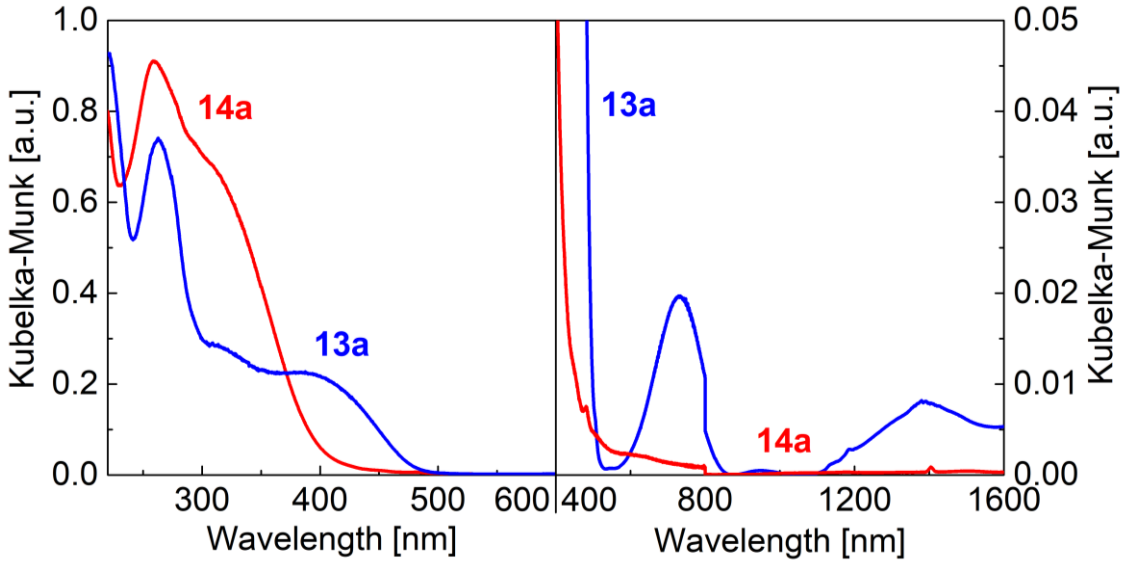

Figure 124. UV-Vis-NIR spectra of **13a** and **14a** in the solid state. Kubelka-Munck plot for ground powder mixtures of KBr with **13a** and **14a**, respectively, depicted between 220-600 nm (left), and pure ground powder of **13a** and a ground powder mixture of KBr with **14a** depicted between 400-1600 nm (right). All samples were prepared and measured under atmospheric conditions. Relative intensities for the spectra in the left image are arbitrary, as the mixtures of KBr and the respective samples were prepared qualitatively. Reflectance values for the absorption component spectra dropped below ~10 % at wavelengths lower than 220 nm. Source changeover offsets that appeared at 350 nm were corrected by subtraction of a constant for all values below 350 nm. Detector-change artefacts at 800 nm are not corrected for.

For **13a** only weak absorptions are present in the vis-NIR spectrum. This includes the tailing of stronger charge-transfer absorptions in UV-region, probably caused by π-π^* excitations in aromatic rings contained in the compound, and two d,d-absorptions at 731 nm and 1385 nm with an energetic separation of 6460 cm^{-1}. The positioning of the d,d-bands and the absence of strong charge-transfer bands in the vis-region resembles the observations for previously reported pseudo-octahedral high-spin iron(II) complexes containing the macrocyclic ligand L-$N_4{}^t Bu_2$ and two oxygen donor co-ligands (see prior chapters). For further arguments about the interpretation of the spin-state of ferrous complexes with similar environments, positioning of the d,d-bands, absence of charge transfer bands in the vis-region, and the rather large energetic separation, see the analysis of the spectra of **2a** in chapter 2 (sections 2.1.6 and 2.1.7).

For **14a**, no absorptions in the vis-NIR region are observed and tailing effects from the strong absorption in the UV-region are even weaker as these bands are localized at higher energies. This is consistent with a high spin d^5 configuration and a $^6A_{1g}$ ground state, respectively, as would be expected with the weak hydroxide co-ligands in *cis*-position that complete the distorted, pseudo-octahedral coordination environment of the $Fe^{III}(LN_4{}^t Bu_2)$-fragment.

Although the solid-state spectra provide a good reference of the compound spectra with correlation to the solid-state structures obtained from single-crystal x-ray diffraction, the Kubelka-Munk method is only qualitative. A more quantitative analysis and the investigation of solution stability of the cations **13** and **14** is provided in the following.

5.1.7. Solution-Based Electronic Spectroscopic Analysis

UV-vis-NIR spectra of acetonitrile solutions of **13a** and **14c** and an aqueous solution of **13a** were recorded to investigate solution-based electronic absorptions for complexes **13** and **14** (Figure 125). The respective energies of the spin-allowed d,d transitions for the iron(II) complex measured in water and acetonitrile are compared with those obtained from the solid state measurement (section 5.1.6) in Table 55.

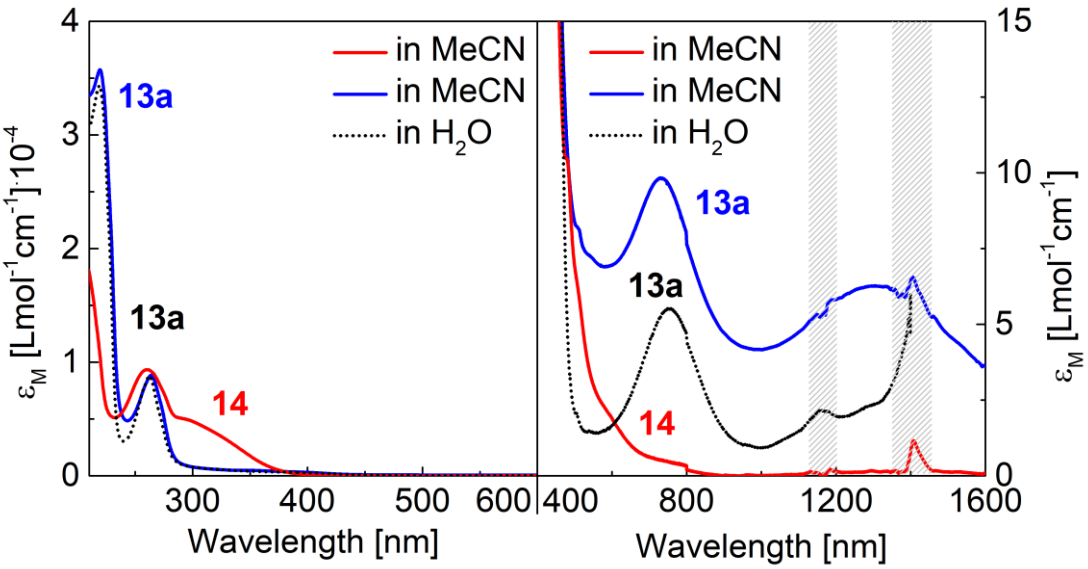

Figure 125. Electronic absorption spectra for solutions of **13a** in acetonitrile and water and **14c** in acetonitrile displayed between 210-600 nm with a molar extinction coefficient ranging from 0-40000 $Lmol^{-1}cm^{-1}$ (left) and between 400-1600 nm with a molar extinction coefficient ranging from 0-15 $Lmol^{-1}cm^{-1}$ (right). Water bands, and the strong absorption that causes a resolution limit of water as a solvent above wavelengths of 1310 nm, are hatched in grey. In all spectra, a weak but discrete feature is observed between 480-510 nm that is attributed to a spin-flip transition.

Table 55. Experimentally determined energies of the spin-allowed d,d-transitions produced by samples of **13a** in the solid state and solution. Solid state spectra were recorded on a pure, ground powder. Solution spectra were recorded at concentrations of $8 \cdot 10^{-3}$ molL^{-1} in MeCN and water, respectively.

	13a$_{(solid)}$	**13a**$_{(MeCN)}$	**13a**$_{(water)}$
Energy [cm^{-1}]	7220, 13680	7670, 13660	n.d. [a], 13260
Δ [cm^{-1}]	6460	5990	n.d. (>5640)

[a] A band can be seen to increasingly grow until the resolution limit of water obscures the complex spectrum above 1312 nm (<7620 cm^{-1}). The absorption maximum cannot be discerned.

The solution spectra obtained for **13a** in water and in acetonitrile are, at first glance, similar in the UV-region: Both exhibit a band centred at 218 nm (in H_2O) and 219 nm (in MeCN) with molar extinction coefficients of ε_M = 34000-36000 L·mol·cm^{-1}, and a band at 262 nm (H_2O) and 264 nm (in MeCN) with molar extinction coefficients of ε_M = 8750-8850 L·mol·cm^{-1}, respectively. However, the aqueous solution of **13a** shows an additional weak charge transfer band at 381 nm with a molar extinction coefficient of ε_M = 362. In contrast, only a very weak shoulder is found at this wavelength in the spectrum of the acetonitrile solution of **13a** (Figure 126).

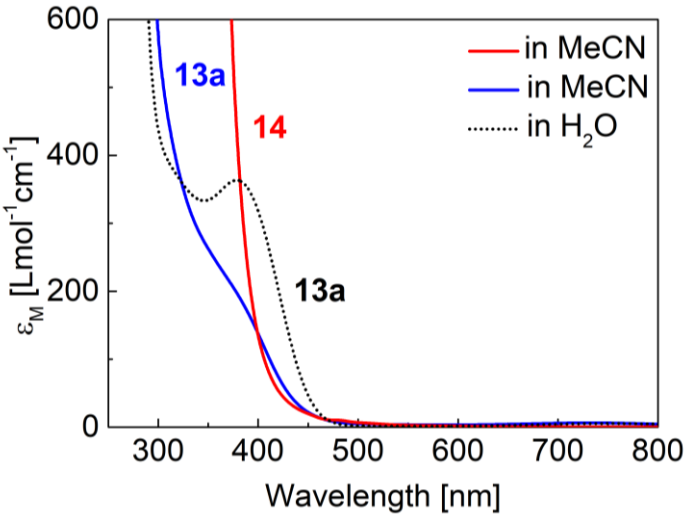

Figure 126. Electronic absorption spectra for solutions of **13a** in acetonitrile and water and **14**, obtained from a solution of **14c** in acetonitrile, displayed between 250-800 nm with a molar extinction coefficient ranging from 0-600 Lmol^{-1}cm^{-1}.

In the solid-state spectrum of a ground powder mixture of **13a** and KBr, the band at 262 nm can also be discerned and, although the resolution is not sufficient below 220 nm, a second band at these short wavelengths can be anticipated from the spectrum. While this agrees with the bands of the solution based-spectra as they likely result from π-π* transitions of the conjugated π-electron systems contained in the compound, it is noteworthy, that the solid-state spectrum also shows a prominent broad band at 385 nm. The appearance of this band in both the aqueous solution and the solid-state spectra, yet not in the spectrum of the acetonitrile solution of **13a**, leads to the conclusion that **13** is not the main species in acetonitrile solution but well-present in the aqueous solution.

Efforts to fit the vis-NIR spectrum of **13a** in water were ambiguous and allowed for multiple different combinations of gaussians that resulted in enveloping curves that matched the spectrum. However, all fits required at least two gaussians to satisfyingly match the slightly asymmetric absorption centred at 13680 cm^{-1} in the experimental spectrum, hinting at the existence of at least one other high-spin iron(II) species in solution. One example of a fitted spectrum is provided in Figure 127. It is likely that the second species corresponds to either a deprotonated *cis*-(aqua)(hydroxo)iron(II) complex $[Fe(L\text{-}N_4{}^tBu_2)(OH_2)(OH)]^+$ because of the expected acidity of the dicationic *cis*-di(aqua)iron(II) complex $[Fe(L\text{-}N_4{}^tBu_2)(OH_2)_2]^{2+}$ (**13**) or a monocationic $[Fe(L\text{-}N_4{}^tBu_2)(OTs)(OH_2)]^+$ species formed *in situ* by the exchange of one water ligand with the counterion. It can, however, not be ultimately discerned which other species are present in aqueous solution.

The deconvolution of the vis-NIR spectrum of **13a** in MeCN revealed that, after the subtraction of a broad additional absorption, the use of only two gaussians is sufficient to fit both observed bands (Figure 127). The broad absorption that overlays the vis-NIR spectrum is speculated to be a tailing of a broad charge transfer band of small amounts of a ferrous species $[Fe(LN_4{}^tBu_2)(MeCN)_2]^{2+}$ that is expected to be at least partially in the low-spin state from ligand field theory considerations and may be produced in small amounts by ligand exchange reactions with the solvent. The two identifiable, rather symmetric d,d-absorptions and the absence of strong charge transfer absorptions in the vis-NIR region suggest that the dominant species present in solution is a single ferrous high-spin complex, although the interpretation of additional species that exhibit very similar ligand field stabilizing energies cannot be

ruled out by this rudimentary analysis. However, because of the absence of the charge transfer band at 380 nm, it is not expected that the dominant species in solution is the dicationic complex cation **13**, but rather that the negatively charged counterions will substitute at least one of the neutral, weakly electron donating aqua ligands to form a monocationic $[Fe(LN_4{}^tBu_2)(OTs)(solv)]^+$ complex (solv = MeCN or water). This assumption is based on experience with 3d metal diazapyridinophane complexes which generally have a preference to be monocationic, and ESI-MS and NMR results that will be presented further down (sections 5.1.9 and 5.1.11).

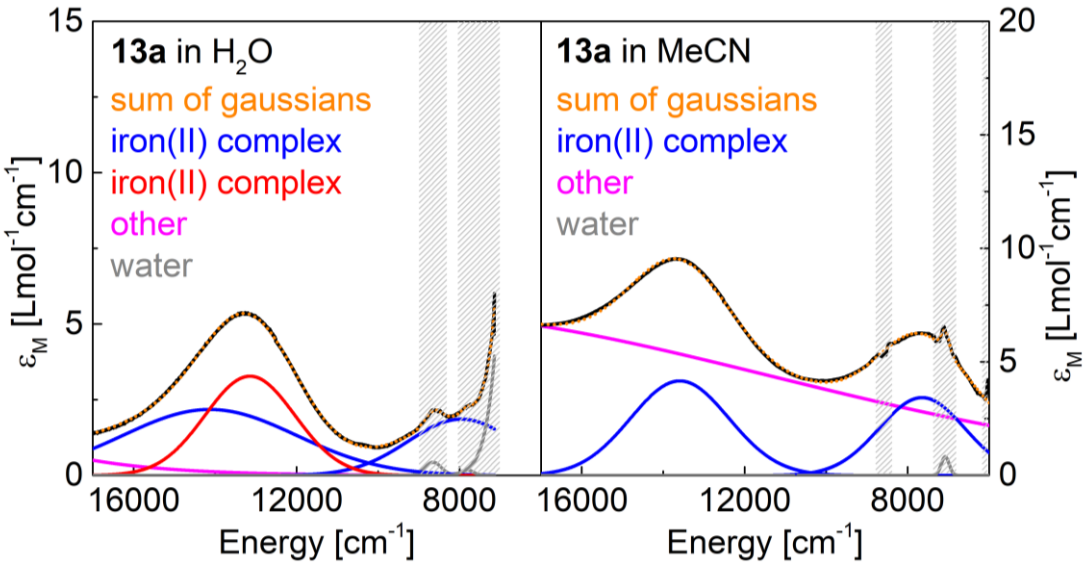

Figure 127. One of multiple possibilities of decomposing the vis-NIR spectrum of **13a** in aqueous solution (left, fitting range 7100-20000 cm^{-1}) and a deconvolution of the vis-NIR spectrum of **13a** in MeCN solution into contributing subspectra using gaussian curve analysis (right, fitting range 6000-20000 cm^{-1}). The spectra and fits were analyzed using MagicPlotStudent and are depicted between 7000-17000 cm^{-1}. Water absorptions are hatched and shown in grey, fits for tailing of other absorptions overlaying the region of interest are shown in pink. For **13a** in MeCN (right), the broad baseline deviation is speculatively attributed to the tailing of a charge transfer band of a ferrous low spin component (supposedly $[Fe(LN_4{}^tBu_2)(MeCN)_2]^{2+}$).

The spectra of the acetonitrile solution of **14c** and a solid ground powder sample of **14a** with KBr are remarkably similar. Not only are both spectra devoid of vis-NIR transitions (apart from minor water impurity artefacts) but they also both show two distinct charge transfer absorptions in the UV-region: The spectrum of solid **14a** in a KBr matrix exhibits a band centred at 260 nm and a broad shoulder at around 310 nm, while the spectrum of **14c** in MeCN solution shows a band at 261 nm and a broad

shoulder around 310 nm. Importantly, like the previous spectra reported for mononuclear hydroxo iron(III) complexes in this work, the spectrum of the solution of **14c** in MeCN does not show any indication for a formation of a dinuclear μ-oxo iron(III) species which would give rise to a moderately intense absorption between 500-600 nm (~1000 $L \cdot mol \cdot cm^{-1}$, Figure 126).[114] This is also in agreement with the results from the ESI-mass spectrometric investigation presented further down (section 5.1.9), where no such species could be detected either.

The electronic absorption spectroscopy results allow the conclusion that the *cis*-di(hydroxo)iron(III) complex cation **14** is indeed stabilized in solution and maintains its coordination environment and spin-state. The cation **13**, however, is found to not be contained as the main species in an acetonitrile solution. It is suspected that the good crystallization properties because of the intermolecular interactions between **13** and the counterions are the driving force for **13** to be the main product from the synthetic efforts described in section 5.1.1. A further investigation of which other species may be contained in acetonitrile solutions of **13a** is done further down.

5.1.8. EPR-Spectroscopic Analysis

From electronic absorption spectroscopy in solid state and solution, it is deduced that the spin state and coordination environment of the *cis*-di(hydroxo)iron(III) complex **14** is preserved in solution (sections 5.1.6 and 5.1.7). However, the evidence is limited and, thus, a further investigation of the magnetic properties with EPR spectroscopy was carried out. Spectra were recorded for frozen solutions of **14a** between 10-40 K in dimethylformamide (DMF) and Acetonitrile (MeCN), both containing 0.2 $mol \cdot L^{-1}$ tetrabutylammonium perchlorate (TBAP) as an additive to obtain a frozen glass (Figure 128 and Figure 129), and for a solid, ground powder sample of **14a** (Figure 130). Even though the previously described hydroxoiron(III) complexes **1**, **7**, and **10** show analogous spectra in both MeCN and DMF solutions, the spectra obtained with these two solvents differ for **14**. It is believed that DMF can engage as a reaction partner with **14**, either producing side products or performing ligand exchange reactions to form additional rhombic iron(III) species in solution. Thus, in contrast to previous analyses with other iron(III) complexes described in this thesis, MeCN was chosen for the investigation, not least also because this solvent was used for other solution-based studies with **14**. Nonetheless, an exemplary spectrum of **14** in frozen DMF containing 0.2 $mol \cdot L^{-1}$ TBAP is provided in Figure 128.

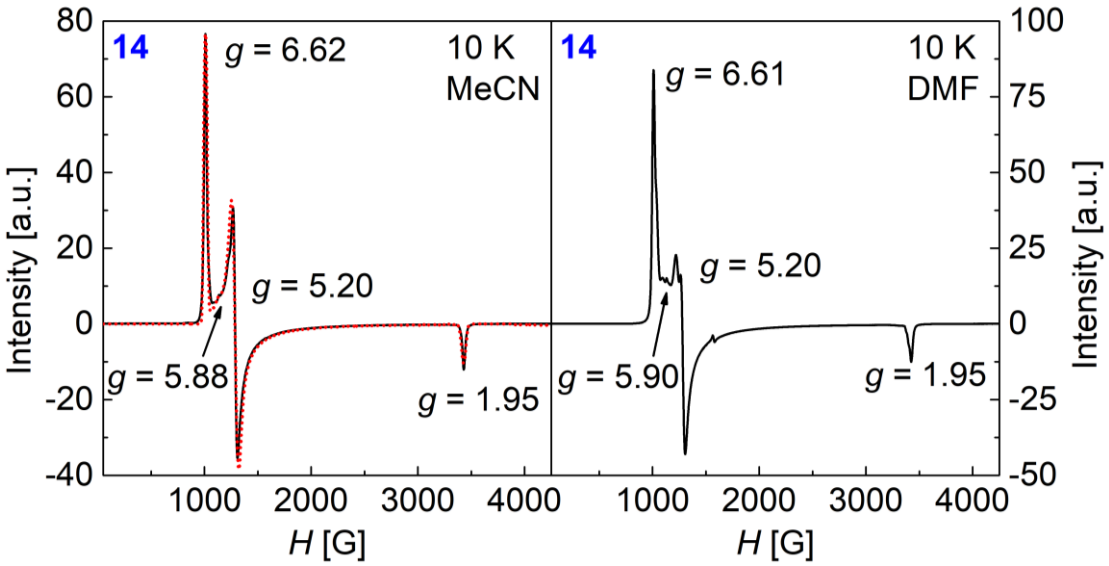

Figure 128. Experimental X-band EPR spectra (50 – 4250 G) of frozen solutions of **14a** in MeCN (left, 9.3527 GHz) and in DMF (right, 9.3430 GHz), respectively, at 10 K (black trace). Both solvents contained 0.2 mol·L^{-1} TBAP. A simulated spectrum is provided for the experimental spectrum of **14** in MeCN as red dotted trace.[130] Effective *g*-values obtained from the experimental spectra are indicated. Additional signals are found in DMF solution at g = 6.43 (sh), g = 6.10 (p), and g = 5.48 (p) and g = 4.24 (ic). sh = shoulder, p = peak, ic = inversion center.

The effective *g*-values of **14** were determined for the spectrum recorded at 10 K in frozen acetonitrile containing 0.2 mol·L^{-1} TBAP and the real *g*-values as well as the rhombicity were derived by fitting of this spectrum using EasySpin (Figure 128).[130] The results are compared to those obtained under different conditions and to those obtained for the structurally similar [Fe(L-N$_4$^{t}Bu$_2$)(OMe)]$^+$ cation (**4**) further down in Table 56. Spectra at varying temperatures were measured to probe for any significant differences in the *T*-dependent populations of the M_S levels (zero-field splitting) compared to **4**, for which the zero-field splitting parameters were explicitly determined by correlated fitting of all *T*-dependent spectra (section 2.1.8).

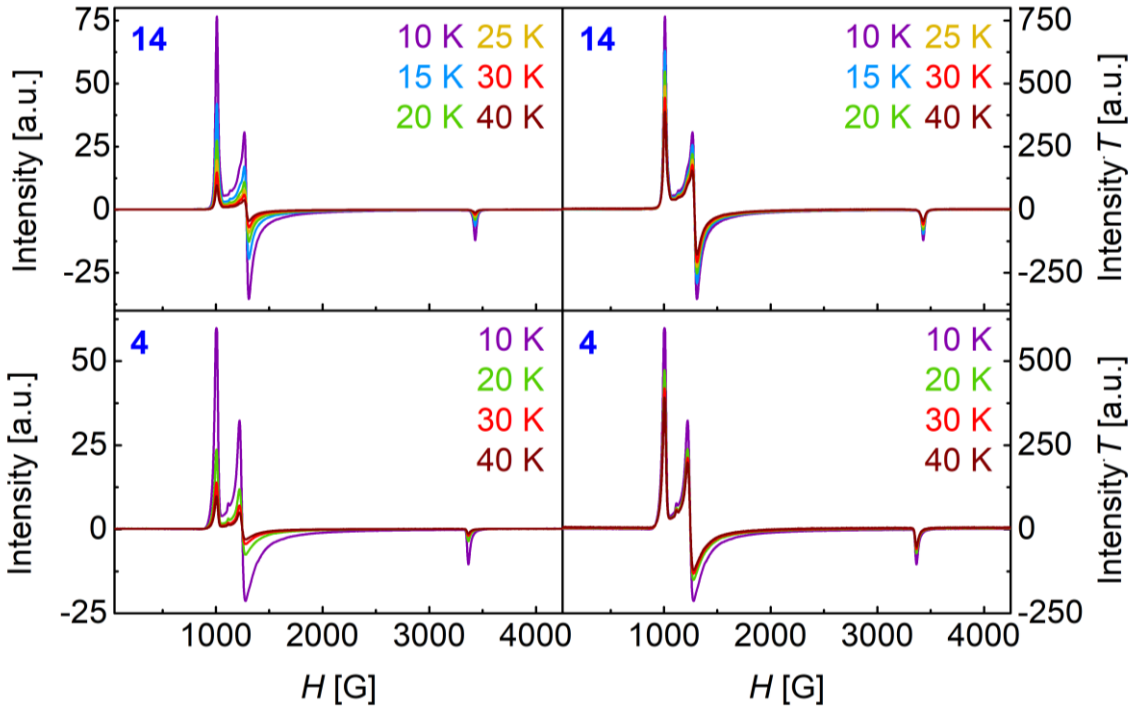

Figure 129. X-Band EPR spectra at variable temperatures (left) and X-Band EPR spectra at variable temperatures multiplied by temperature (right) between 50 – 4250 G for **14** and **4**. Frequencies in GHz for **14** (*T*): 9.3527 (10 K), 9.3527 (15 K), 9.3527 (20 K), 9.3526 (25 K), 9.3526 (30 K), 9.3525 (40 K); **4** (*T*): 9.3439 (10 K), 9.3438 (20 K), 9.3436 (30 K), 9.3433 (40 K). Results presented for **4** are adapted from previously published results.[1]

The experimental spectra obtained for **14** closely resemble the spectra obtained for the structurally similar complex cation **4** which differs from **14** only in a methyl substituent at the oxide ligands instead of a proton. Likewise, the fitting of the spectra to an S = 5/2 species with equation 5 using EasySpin resulted in similar rhombicities, and real *g*-values (Table 56).[130] The striking similarities provide strong evidence that the $[Fe(L\text{-}N_4{}^tBu_2)(OH)_2]^+$ cation is retained in solution. Importantly, the absence of higher-spin species or even amorphous rhombic *S* = 5/2 signals at *g* = 4.3 additionally rules out the formation of dinuclear μ-oxo or iron oxide clusters in acetonitrile solution.

$$(5) \quad \hat{H} = \mu_B \boldsymbol{B}^T \cdot \boldsymbol{g} \cdot \hat{\boldsymbol{S}} + D\left[\hat{S}_z^2 - \frac{S(S+1)}{3}\right] + E\left[\hat{S}_x^2 - \hat{S}_y^2\right]$$

The temperature dependent population of the Kramer doublets M_S = ±1/2, ±3/2, ±5/2 and their transition probabilities are challenging to compare. Although the differences in population can be made more visible when the spectra are multiplied with the measurement temperatures to omit the temperature effects on the magnetic susceptibility of the samples, the contribution of the ±3/2 state to the spectrum is too minor to discern significant effects. Transitions for the M_S = ±5/2 are not observed in either case. Nonetheless, a positive zero-field splitting (ZFS) can be derived as M_S = ±1/2 is found to be the ground state. Both frozen solutions appear to behave similarly, thus, a similar ZFS is also expected for **14** and **4**, which would agree with the results obtained from fitting of magnetization experiments in the solid state (section 5.1.3). Here, the ZFS of **14** is determined to be D = 1.06 cm^{-1}, while for **4** the zero-field splitting was found to be D = 0.90 cm^{-1} from fitting of solid-state magnetization experiments (section 2.1.3).

As these results suggest that cation **14** is indeed present and stabilized in solution, a further investigation was done by measuring a solid-state EPR spectrum of **14a** to compare the results with those obtained from the frozen solution studies. A solid-state spectrum was recorded by measuring a ground powder of **14a** fixed with glass wool in a quartz tube at 10 K in a closed cycle helium cryostat to ensure that the powder does not contaminate the instrument. However, the glass wool was found to contain EPR active impurities at g = 4.25 (inversion signal) and g = 2.0. (multiplet) which contaminate the spectrum. Nonetheless, the g-values of the solid sample could be discerned and determined (Figure 130).

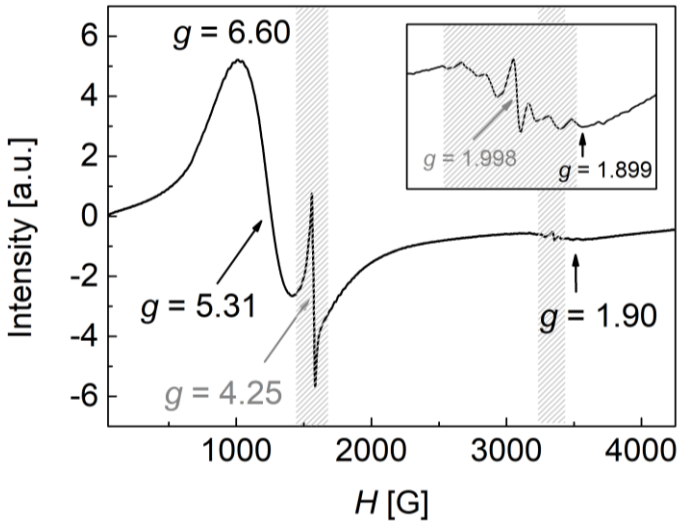

Figure 130. Experimental X-band EPR spectrum (50-4250 G) of a solid ground powder sample of **14a** fixed with glass wool (9.3661 GHz) at 10 K (black trace). Effective *g*-values obtained from the experimental spectrum are indicated. The signals at *g* = 4.25 (ic) and *g* = 1.998 (m) are hatched in grey as they are produced by EPR-active impurities contained in the glass wool (also see methods section). ic = inversion center, m = multiplet.

Although the solid-state spectrum of **14a** is significantly broadened because of the proximity of paramagnetic iron sites that influence the relaxation properties, and although the signals are partially obscured by EPR-active impurities contained in the glass wool that was used to fix the powder in the quartz tube, the *g*-values could be determined with sufficient accuracy. The *g*-values resemble those obtained from the solution spectra well; slight deviations may be explained by differing environments and packing effects that could somewhat distort the geometry and magnetic anisotropy/rhombicity of the cation in the solid-state. Nonetheless, the resemblance of the solid-state and solution-based spectra is in good agreement with the proposition that the mononuclear $[Fe(L\text{-}N_4{}^tBu_2)(OH)_2]^+$ cation **14** is stabilized and present in solution.

Table 56. Effective *g*-values, rhombicities, and real g-values of **14** and **4** obtained from frozen solution spectra of **14a** and **4a**, and solid-state spectra of **14a**. Results presented for **4** are adapted from previously published results.[1]

	14 (MeCN)[a]	**14** (DMF) [b]	**14** (solid) [c]	**4** (DMF) [d]
M_S = ±1/2 Kramer Doublet	g_x = 5.20	g_x = 5.20	g_x = 5.31	g_x = 5.35
	g_y = 6.62	g_y = 6.61	g_y = 6.60	g_y = 6.63
	g_z = 1.95	g_z = 1.95	g_z = 1.90	g_z = 1.98
M_S = ±3/2 Kramer Doublet	g_x, g_y = n.d.	g_x, g_y = n.d.	g_x, g_y = n.d.	g_x, g_y = n.d.
	g_z = 5.88	g_z = 5.90	g_z = n.d.	g_z = 5.98
E/D	0.034	-	-	0.024
real g_x, g_y, g_z	2.010, 1.956, 1.987	-	-	1.965, 2.035, 1.998

[a] Measured at 9.3527 GHz, [b] Measured at 9.3430 GHz, [c] Measured at 9.3661 GHz, [d] Measured at 9.3439 GHz. The assignment of g_x, g_y, and g_z was done with the help of VisualRhombo.[129] The E/D- and real *g*-values were obtained from the simulated spectra.

Overall, the EPR-spectroscopic analysis of **14** provides strong evidence for the achievement of a stabilized *cis*-di(hydroxo)iron(III) complex in solution.

5.1.9. ESI-Mass Spectrometric Analysis

ESI-mass spectrometry was measured for acetonitrile solutions of **13a** and **14c**. The recorded spectra are shown in Figure 131 and Figure 132, the respective simulations for signal assignments are given in Figure 132 and Figure 133. While the cation of **14** was found to be the main species in the ESI-mass spectrum of an acetonitrile solution of **14c**, cation **13** could not be observed. It was found that the neutral aqua ligands in **13** are lost/exchanged in solution and/or under ESI-MS conditions.

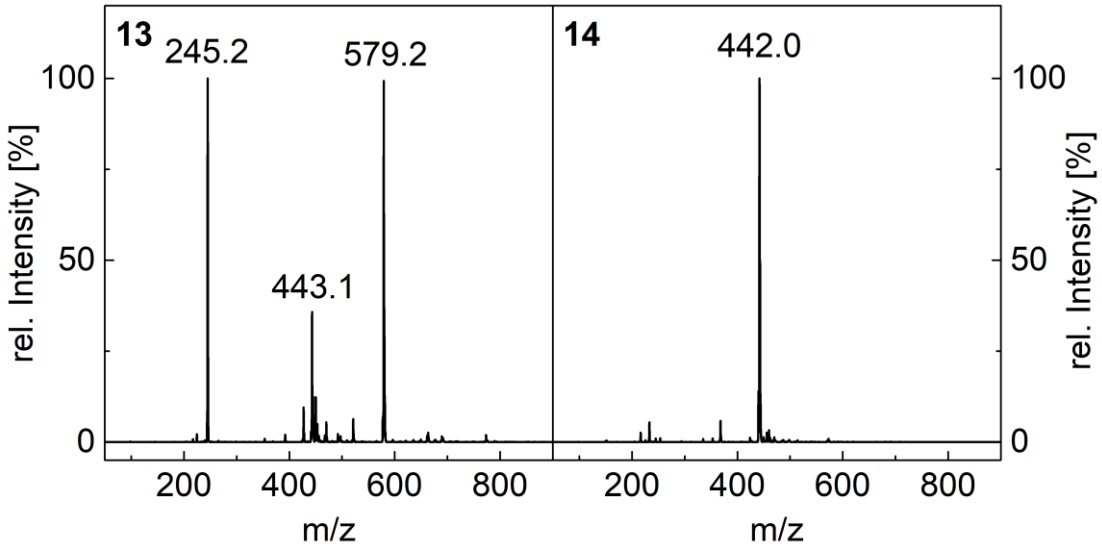

Figure 131. ESI-mass spectra of acetonitrile solutions of **13a** and **14c** obtained with the soft ionization preset of the instrument between m/z = 50-900. Multiple major species are observed for **13a** at m/z = 245.2 (100 %), m/z = 443.1 (36 %), and m/z = 579.2 (99 %) besides other background signals and/or fragmentation products at m/z = 521.2 (6 %), m/z = 470.3 (5 %), m/z = 450.2 (12 %), and m/z = 427.1 (9%). One major species is observed for **14c** at m/z = 442.0 (100 %), minor background signals and/or fragmentation products are observed for **14** at m/z = 368.0 (6%) and m/z = 233.0 (5%).

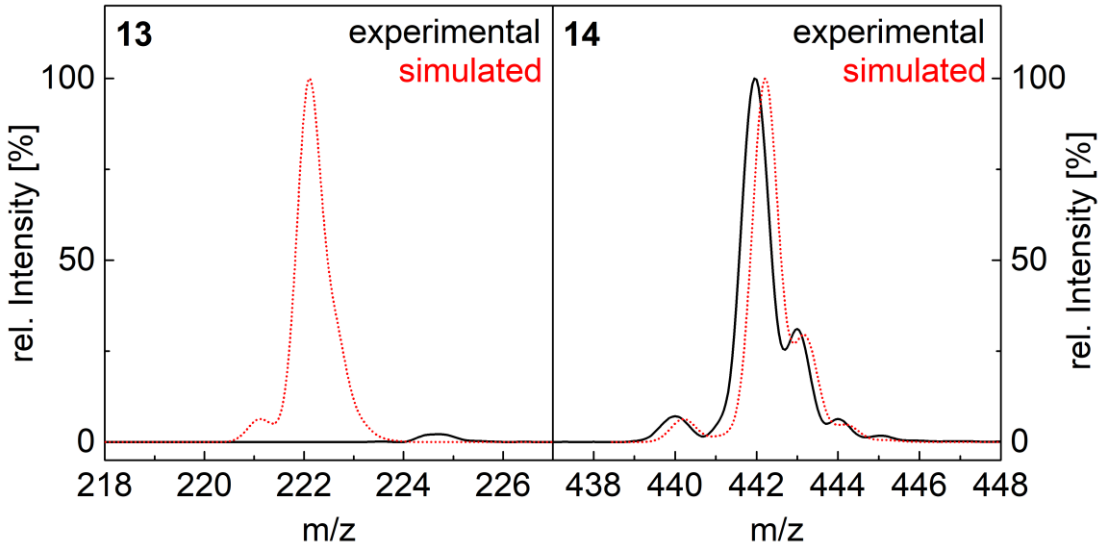

Figure 132. Enhanced regions of interest for the ESI-mass spectra of **13** and **14**, each obtained from acetonitrile solutions of **13a** and **14c** with the soft ionization preset of the instrument, respectively (black traces), and simulations for the cations $[Fe^{II}(L\text{-}N_4{}^tBu_2)(OH_2)_2]^{2+}$ (**13**, m/z = 222.0) and $[Fe^{III}(L\text{-}N_4{}^tBu_2)(OH)_2]^{+}$ (**14**, m/z = 442.2) (red dotted lines). Minor offsets between the experimental spectrum of **14** (m/z = 442.0) and the simulation are attributed to calibration errors. No experimental signal for **13** is observed under ESI-MS conditions.

An ESI-MS analysis of **14c** produces only one major signal that can be attributed to **14**, clearly underlining the stability of the *cis*-di(hydroxo)iron(III) complex in solution. No significant signals pointing towards the formation of bridged μ-oxo dinuclear species are observed.[168] Furthermore, it is important to note that the cation is found at m/z = 442.0, meaning that it is not detected as an adduct with hydrogen bond acceptors or donors such as H_2O, MeCN, or other complex cations. This indicates the stabilization of **14** in solution without the necessity of intermolecular interactions.

As opposed to the observations for the *cis*-(carboxylato)(hydroxo)iron(III) complexes **1**, **7**, and **10** (see sections 2.1.9 and 3.1.8), the *cis*-dihydroxoiron(III) complex **14** appears less sensitive to the ionizing conditions of the ESI-MS method. Additionally, in contrast to the loss of a hydroxyl radical observed for **1**, **7** and **10** under these conditions, the spectrum of **14** shows a signal that could be explained by the loss of a hydroxide ion (m/z = 233.0, 5 % height of the maximum peak, $[Fe(L\text{-}N_4{}^tBu_2)(OH)(MeCN]^{2+}$) but no identifiable signal that could correspond to the loss of a hydroxyl radical. The loss of a hydroxide from the oxophilic, cationic iron(III) site is

rather unusual but may be explained by the large excess of MeCN which could lead to some ligand exchange equilibria with the solvent and partially displace the weak OH^- ligand despite its negative charge under these ionizing conditions. The only other signal worth mentioning in the cationic spectrum of a MeCN solution of **14c** is found at m/z = 368.0 (6 % height of the maximum peak). This minor signal can be calculated to result from fragmentation and the elimination of ^{t}BuOH from **14** under ESI-MS conditions. However, because there is no further evidence that such a fragmentation is feasible, this is not further discussed.

The ESI-MS analysis of **13a** immediately shows that the solution stability of the dicationic species with two weakly coordinating aqua ligands is not a given in acetonitrile, as three major signals are found (Figure 133). As derived from this analysis, the aqua ligands are probably exchanged by the solvent in solution, because acetonitrile functions as a stronger σ-donor than H_2O. This can be seen by the strong signal at m/z = 245.2 which corresponds to $[Fe(L\text{-}N_4{}^tBu_2)(MeCN)]^{2+}$. Moreover, although the anionic oxygen donors of the tosylates are generally weak donors, their charge advantage over the neutral aqua ligands probably results in some ligand exchange equilibria in solution. This is evident by the strong signal at m/z = 579.2 which corresponds to $[Fe(L\text{-}N_4{}^tBu_2)(OTs)]^+$. In solution, this five-coordinate species is probably still saturated with a neutral aqua co-ligand, however, aqua ligands are often lost under ESI-MS conditions as is also observed in the results described in chapters 2 and 3. In the first instance, one could assume that the signal at m/z = 443.1 corresponds to the respective deprotonated cation $[Fe(L\text{-}N_4{}^tBu_2)(OH)(OH_2)]^+$. However, the isotope pattern clearly does not match such a species, as it contains the characteristic pattern of the natural isotope distribution of chlorine. Here, it is assumed that both neutral aqua ligands are lost under ESI-MS conditions and chloride contaminants from the glassware, environment, or present in the instrument saturate one empty coordination site to yield a $[Fe(L\text{-}N_4{}^tBu_2)(Cl)]^+$ complex with the matching m/z-value and isotope pattern (Figure 133).

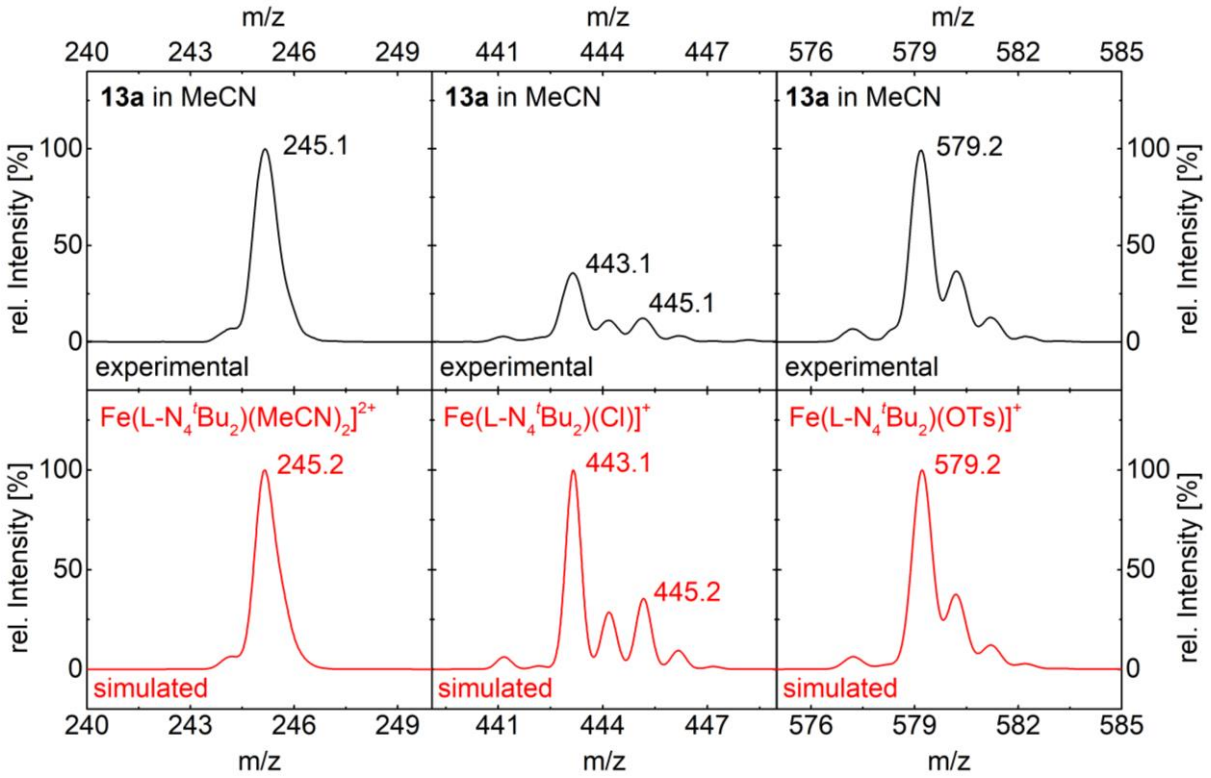

Figure 133. Experimental ESI-mass spectra of an acetonitrile solution of **13a** obtained with the soft ionization preset of the instrument (top), and simulations for suggested cations (bottom) $[FeL\text{-}N_4{}^tBu_2](MeCN_2)]^{2+}$ (m/z = 245.2), $[Fe(L\text{-}N_4{}^tBu_2)(Cl)]^+$ (m/z = 443.1, 445.2), and $[Fe(L\text{-}N_4{}^tBu_2)(OTs)]^+$ (m/z = 579.2) assigned to the three major species observed. $[FeL\text{-}N_4{}^tBu_2](MeCN_2)]^{2+}$ and $[Fe(L\text{-}N_4{}^tBu_2)(OTs)]^+$ are expected to be formed from equilibria in solution, $[Fe(L\text{-}N_4{}^tBu_2)(Cl)]^+$ is suggested to be formed by recombination of $[Fe(L\text{-}N_4{}^tBu_2)]^{2+}$-fragments with anionic Cl^- contaminants after or during the loss of the neutral H_2O ligands from **13** under ESI-MS conditions.

These results demonstrate the unusually high stability of the extremely rare mononuclear *cis*-di(hydroxo)iron(III) species **14** in solution. At the same time, compelling evidence is gathered that complex **13** is not the main species present in acetonitrile solution but could probably only be isolated from such a solution during synthesis because of preferable crystallization properties. This matches the interpretations from the electronic absorption spectroscopy analysis described in section 5.1.7. Thus, solution-based analysis on **13** should be done in water rather than acetonitrile despite poorer solubility and although this impedes comparative investigations of **13** and **14** under the same conditions in solution, as **14** is barely soluble in water.

5.1.10. Electrochemical Analysis

Cyclic voltammetry measurements were done for **14** by employing an acetonitrile solution containing **14c** and 0.2 $molL^{-1}$ tetrabutylammonium perchlorate (TBAP) as conductive salt. As has been established in previous chapters, **13** is not present as main species in acetonitrile and likely also engages in ligand exchange equilibria in other non-aqueous media. However, although our glovebox setup contains some minor water impurities because of the storing of an aqueous saturated KCl solution for the calomel reference electrode (SCE), the use of water as a solvent in the electrochemistry setup would contaminate the glovebox intolerably, limit the measurement range, and compromise the reliability of a qualitative study because of pH-sensitivity. Moreover, as derived from the UV-vis study of an aqueous solution of **13a** (section 5.1.7), the results are still expected to be ambiguous pertaining the nature of the contained complex(es) in solution. Thus, the electrochemical investigation of **13** was found to be impractical and not attempted because of expectedly ambiguous results.

The solution of **14c** in MeCN/TBAP shows an irreversible reduction behavior at a rather negative peak potential $E_{p(red)}$ = -860 mV vs. SCE ($E_{1/2}$(SCE) = +494 mV). The irreversible behavior and the rather negative reduction potential match the results obtained for the dimethoxy analogue [Fe($LN_4{}^tBu_2$)$(OMe)_2$] **4** (Figure 134). In contrast to **4**, however, **14** is found to decompose under the measurement conditions: The scan rate dependent sequence depicted in Figure 134 (100 mVs^{-1}, 50 mVs^{-1}, 20 mVs^{-1}, 10 mVs^{-1}) eventually rendered additional signals that compromised further measurements at higher scan rates. The irreversible behaviour is anticipated to result from a rapid protonation after reduction which could yield a *cis*-(hydroxo)(aqua)iron(II) intermediate that is likely not stable under the given conditions and engages in following reactions or equilibria. Because of this decomposition, no relevant information is expected to be gained from another scan rate dependent electrochemical investigation, thus no additional data at higher scan rates were collected.

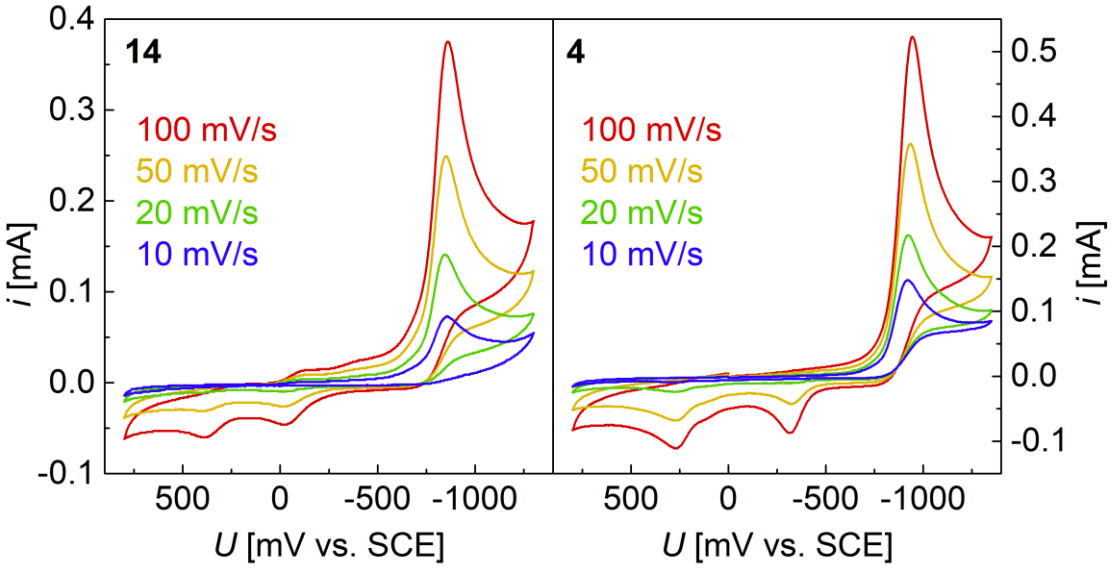

Figure 134. Cyclic voltammograms (800 mV – -1350 mV) at variable scan rates of the ferric complexes **14** (left) and **4** (right) in 0.2 mol L^{-1} TBAP/MeCN solution at room temperature under a nitrogen atmosphere. Sweeps: (**14**) 0 mV → -1300 mV → 800 mV → 0 mV (Fc/Fc^+ = 0.49 V vs SCE); (**4**) 0 mV → -1350 mV → 800 mV → 0 mV (Fc/Fc^+ = 0.49 V vs SCE). Peak potentials: (100 mV/s, all vs SCE): (**14**) $E_{p(red)}$ = -860 mV, $E_{p(ox1)}$ = -20, $E_{p(ox2)}$ = 390 mV. (Fc/Fc^+ = 0.49 V vs SCE); (**4**) $E_{p(red)}$ = -946 mV, $E_{p(ox1)}$ = -316, $E_{p(ox2)}$ = 270 mV. (Fc/Fc^+ = 0.49 V vs SCE). Irreversible oxidation processes that occur at potentials above 800 mV were not studied.

Although the information gained from the investigation is limited because of the irreversible behavior, the similarity of the CV results for **14** and **4** provides further evidence for the persistence of **14** in acetonitrile solution. The slightly more positive peak reduction potential of **14** can be understood by the inductive effect of the methyl groups in **4** which increase the stabilization of the ferric state.

5.1.11. NMR-Spectroscopic Analysis

^{1}H-NMR spectroscopic analysis was performed for **14c** in CD_3CN (Figure 135) and for **13d** in CD_3CN (Figure 136) and D_2O (Figure 137), respectively. The deuterated compound $[Fe(L\text{-}N_4{}^tBu_2)(OD_2)_2](OTs)_2$ (**13d**) was chosen over $[Fe(L\text{-}N_4{}^tBu_2)(OH_2)_2](OTs)_2$ (**13a**) to minimize H_2O signal residues in the NMR spectra and render the coligands ^{1}H-NMR inactive for a more facile investigation of solution stability of the cation by isolating the signals of the coordinated macrocycle and the counterion. This was done because at least partial dissociation of the aqua ligands is expected from previous analysis (sections 5.1.7 and 5.1.9). A spectrum of $[Fe(L\text{-}N_4{}^tBu_2)(OMe)_2]PF_6$ (**4b**) was measured as a reference substance to probe for solution stability of **14** (Figure 135). Additionally, a spectrum of $[Fe(L\text{-}N_4{}^tBu_2)(Cl)_2]$ (**5**) was also recorded, because it contains an $[Fe^{II}(L\text{-}N_4{}^tBu_2)]^{2+}$-fragment with ^{1}H-NMR inactive co-ligands and was found to be suitable as a reference substance to investigate the solution stability of **13** (Figure 136). Furthermore, to estimate the acid-base reactivity of **13** and to investigate if a $[Fe(L\text{-}N_4{}^tBu_2)(OH_2)(OH)]^+$ complex is accessible, deprotonation experiments were also conducted for **13** with NEt_3 (Figure 138).

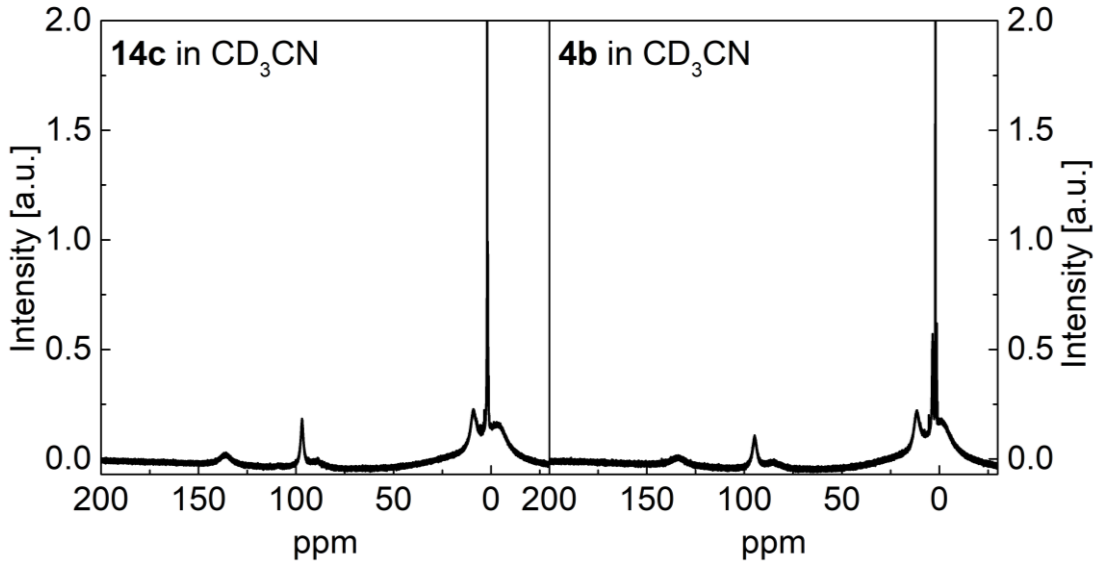

Figure 135. ^{1}H-NMR spectrum (-30-200 ppm) of **14** (left) and **4** (right) each obtained with 0.02 mol·L^{-1} solution of **14c** and **4b**, respectively, in CD_3CN. ^{1}H-NMR(400 MHz, CD_3CN, **14**) δ(ppm) = 135.90 (br), 97.00 (s), 88.88 (br), 9.05 (br), 1.60 (s), -3.89 (br). ^{1}H-NMR(400 MHz, CD_3CN, **4**) δ(ppm) = 133.68 (br), 94.62 (s), 85.41 (br), 11.36 (br), 4.40 – 2.70 (br), -0.45 (br). br = broad, s = singlet. Impurities in the spectrum of **4b** at 3.43 ppm and 1.28 ppm are attributed to Et_2O residues.

The ^{1}H-NMR spectrum obtained for **14** in CD_3CN matches the expectations for a single $[Fe(L\text{-}N_4{}^tBu_2)(OH)_2]^+$ complex cation in solution well. The large chemical shifts agree well with a high spin multiplicity as expected for a high-spin iron complex. The maximum chemical shift of δ = 135.90 ppm is significantly higher than what has been observed for any iron(II) complexes containing this macrocyclic ligand (see 2.1.11 and Figures 133-135) which agrees well with the higher oxidation and spin state of a ferric S = 5/2 species. The spectrum contains five signals with a positive chemical shift (δ = 135.90, 88.88, 97.00, 96.6, 9.05 ppm), and one signal with a negative shift (δ = -3.89) that can be all attributed to the $L\text{-}N_4{}^tBu_2$ ligand in comparison to the previously described complexes, although a reliable assignment of the protons is not achieved (also see sections 2.1.11 and 3.1.10). The remaining proton resonance of the hydroxide ligands can be expected to be either very broad, because of the proximity to the paramagnetic iron site and resulting extremely short relaxation times, or imperceivable with ^{1}H-NMR in CD_3CN because of engagement in H-D exchange reactions with the (although only very weakly acidic)[142] solvent. The clean spectrum representing a single cationic iron(III) complex containing the macrocyclic $L\text{-}N_4{}^tBu_2$

ligand with no observable co-ligands provides strong evidence for unprecedented solution stability of a *cis*-di(hydroxo)iron(III) complex (**14**), as ligand exchange reactions of hydroxide ions from iron(III) complex cations are thermodynamically highly unlikely and the formation of dinuclear μ-oxo complexes in MeCN solution has been ruled out by electronic spectroscopy (section 5.1.7), EPR spectroscopy (5.1.8), and ESI-mass spectrometry (section 5.1.9).

To further establish the solution stability, a spectrum of **4b** was recorded as a reference (Figure 135). The two spectra of **14c** and **4b** are found to be very similar, which is expected because the complexes only differ in a methyl group at the oxide ligands. From the comparison, the moderately broad signal between 4.4 – 2.7 ppm in the spectrum of **4** can be assigned to the proton resonances of the methyl group of the methoxide ligands. The similarity of the spectra strengthens the argument for a very similar complex in the solution of **14c** in CD_3CN that is best explained by the presence of only cation **14** in CD_3CN solution.

The ^{1}H-NMR spectrum of **13d** in acetonitrile shows a multitude of peaks that likely arise from the presence of more than one paramagnetic iron(II) complex containing the macrocyclic ligand L-N$_4$*t*Bu$_2$ in solution (Figure 136). To further establish the suspicion, **5** was measured as a ferrous reference complex containing the L-N$_4$*t*Bu$_2$ ligand with ^{1}H-NMR inactive co-ligands which gave a spectrum containing only six relevant signals (Figure 136) all corresponding to the coordinated macrocycle (see sections 2.1.11 and 3.1.10) that is very different from the spectrum obtained for **13d**. Notably, the absence of diamagnetic signals for the counterions (OTs^-) in the spectrum of **13d** suggests an interaction of the anions with the dicationic iron(II) complex **13** via ligand exchange reactions in solution. Although no further assignment of the ferrous species contained in solution is attempted, the instability of **13** in acetonitrile solution that had been suspected from previous analyses is further evidenced by these results. Thus, another spectrum of **13d** was recorded in D_2O to investigate if the large excess of (heavy) water can limit or even inhibit the ligand exchange reactions with the counterion, a strategy that is also employed in the UV-vis-NIR spectroscopic analysis (5.1.7).

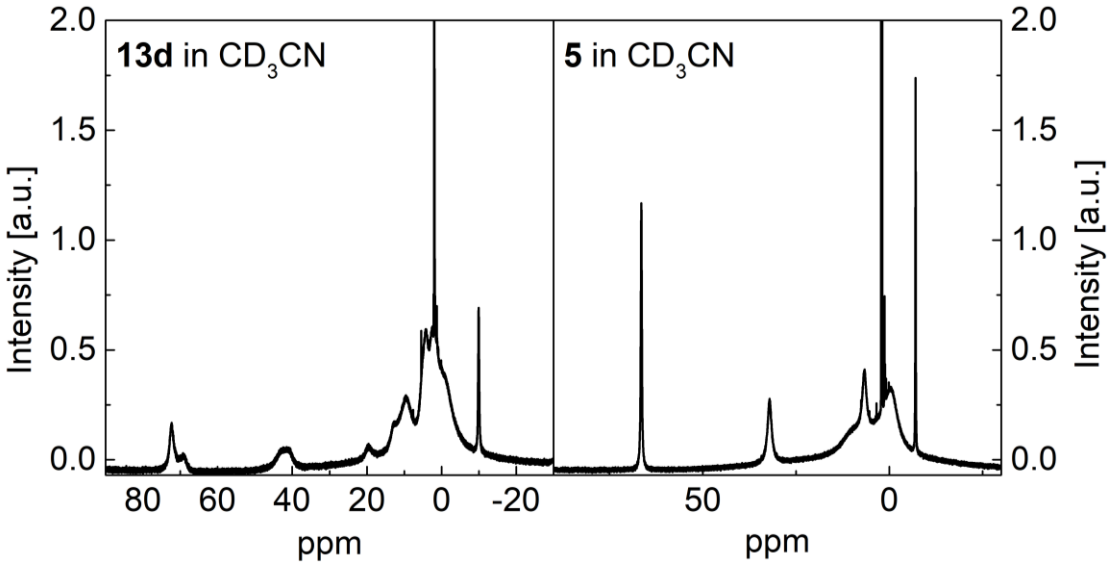

Figure 136. ^{1}H-NMR spectrum (-30-90 ppm) of **13d** and **5**, each obtained with 0.02 mol·L^{-1} solution in CD_3CN, respectively. ^{1}H-NMR(400 MHz, CD_3CN, **13d**) δ(ppm) = 72.39 (s), 69.28 (br), 48.50-36.60 (br), 19.54 (br), 12.77 (sh), 9.59 (br), 7.59 (s), 5.45 (s), 4.19 (br), 2.54 (br), -0.17 (sh), -9.95 (s). ^{1}H-NMR(400 MHz, CD_3CN, **5**) δ(ppm) = 66.46 (s), 32.12 (s), 10.27 (sh), 6.68 (s), -0.31 (br), -7.01 (s). Impurities at 3.46 and 1.31, and 2.20 in the spectrum of **5** are attributed to Et_2O and H_2O residues, respectively.[131] br = broad, s = singlet, sh = shoulder.

The ^{1}H-NMR measurement of a solution of **13d** in D_2O produces a much simpler spectrum than that of the respective CD_3CN-solution (Figure 137). Here, three distinct signals produced by a diamagnetic compound ($\delta(CD_3CN)$ = 7.79 (d, *J* = 7.7 Hz, 4 H), 7.53 (d, *J* = 7.6 Hz, 4 H), 2.54 (s, 6 H)) can be identified to belong to the free tosylate counterions,[169] allowing for the assumption that these anions do not engage in significant ligand exchange reactions in aqueous solution. The rather simple spectrum observed for **13d** in D_2O that suggests a single species is, nonetheless, somewhat surprising: In the electronic spectroscopic analysis of an aqueous solution of **13d**, the d,d-bands could not be fitted under the assumption that only a single iron(II) species is present (section 5.1.7, Figure 127). One explanation for this may be, that a possible ligand exchange reaction or even a simple protonation/deprotonation equilibrium is present where the involved species can only be discerned on the UV-vis-NIR timescale but not on the timescale of the rather slow NMR experiment.

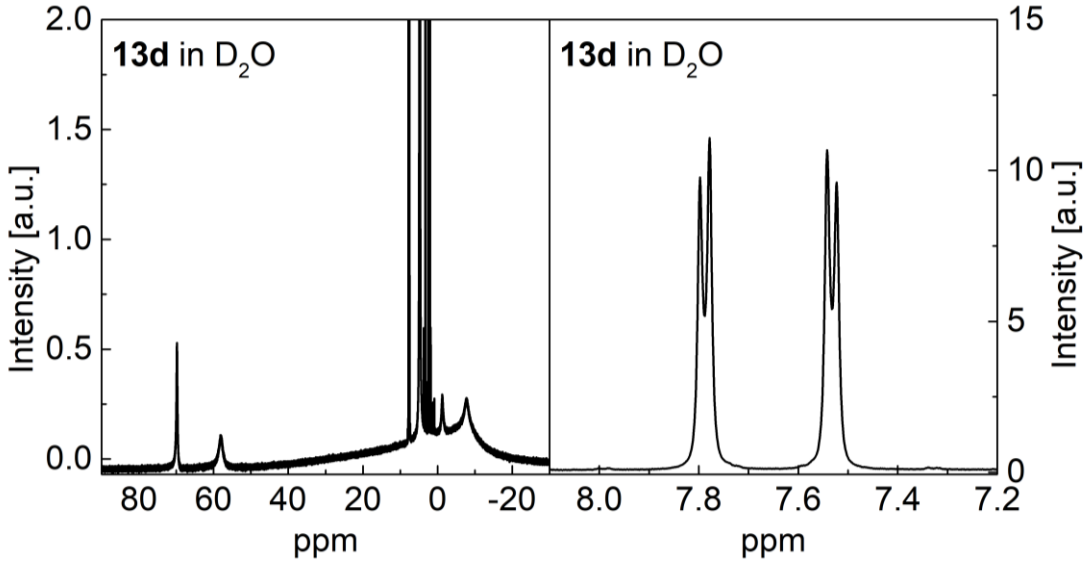

Figure 137. ^{1}H-NMR spectrum of **13d** obtained with a 0.02 mol·L^{-1} solution in D_2O. Left: -30-90 ppm, right: 7.2-8.1 ppm. ^{1}H-NMR(400 MHz, D_2O, **13d**) δ(ppm) = 69.82 (s), 58.10 (s), 7.79 (d, *J* = 7.7 Hz), 7.53 (d, *J* = 7.6 Hz), 3.29 (s), 2.54 (s), 2.01 (s), -1.25 (br), -7.79 (br). br = broad, s = singlet, d = doublet.

The speculation about a rapid protonation/deprotonation equilibrium is intriguing, as it is not unlikely that the dicationic ferrous complex exhibits a reasonable acidity and this would hint at the accessibility of a *cis*-(hydroxo)(aqua)iron(II) complex $[Fe^{II}(L\text{-}N_4{}^tBu_2)(OH)(H_2O)]^+$ – a previously unobserved species. Thus, deprotonation experiments were conducted with a rather bulky, non-coordinating base (NEt_3) and investigated via NMR spectroscopy in both CD_3CN and D_2O (Figure 138). In the case of the acetonitrile solution, the addition of NEt_3 did not result in a change of the spectrum apart from the occurrence of two signals at δ = 0.98 ppm (t, 6 H) and 2.49 ppm (q, 9 H) which closely align with the literature values for NEt_3 residues in CD_3CN (δ(NEt_3, CD_3CN) = 0.96, 2.45 ppm).[131] Thus, it can be assumed that no acid-base reaction took place in this mixture, supposedly because the complex species in solution contain at least one OTs^- ligand and are monocationic, which probably renders their p*K*a higher than that of $HNEt_3$ in acetonitrile (pKa = 18.7) analogous to previously described iron(II) complexes containing an L-$N_4{}^tBu_2$ ligand and one neutral and one anionic oxygen donor in *cis*-position (see section 2.3.6).[1,144] In the aqueous solution, however, some changes in the chemical shifts of the paramagnetic complex are observed and the arising signals at δ = 1.06 and 2.79 ppm from the basic additive are broadened and deviate slightly from the literature values (δ(NEt_3, D_2O) = 0.99, 2.57

ppm). Although at first glance this may indicate some acid-base reactivity in solution, it must be noted that also the signals of the OTs^- counterions are broadened and shifted, thus the moderate and rather systematic changes may also result from the change in polarity of the now protic polar solvent.

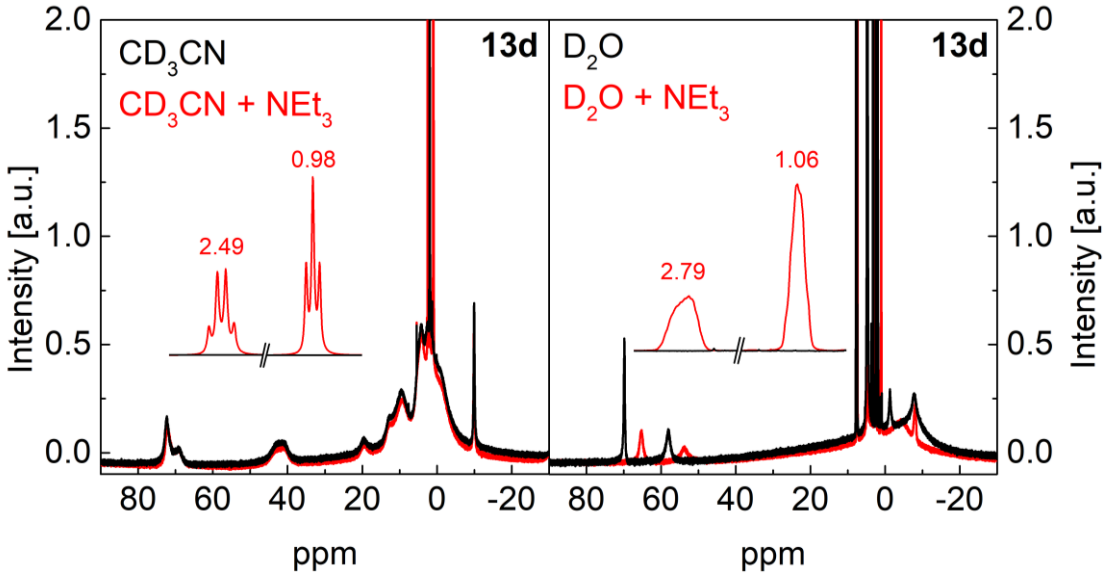

Figure 138. ^{1}H-NMR spectra (-30 – 90 ppm) of **13d** each obtained with 0.02 mol·L^{-1} solution in CD_3CN (left) and H_2O (right), respectively (black traces), and of solutions of **13d** prepared under the same conditions but containing a twofold excess of NEt_3 (red traces). The inset shows the appearance of additional signals and and chemical shift differences that arise in the solutions containing NEt_3. ^{1}H-NMR(400 MHz, CD_3CN, **13d** + NEt_3) δ(ppm) = 72.11 (s), 69.08 (br), 48.50-36.60 (br), 19.48 (br), 12.39 (sh), 9.35 (br), 7.59 (s), 5.45 (s), 4.12 (br), 2.49 (q, *J* = 7.0 Hz), 0.98 (t, *J* = 7.1 Hz), -1.05 (sh), -9.91 (s). ^{1}H-NMR(400 MHz, D_2O, **13d** + NEt_3) δ(ppm) = 65.22 (s), 53.76 (s) 7.61 (d, *J* = 6.6 Hz), 7.31 (d, *J* = 5.1 Hz), 3.18 (s), 2.86-2.62 (br), 2.32 (s), 1.87 (s), 0.98 (br), -4.11 (br), -8.20 (s). Systematic peak offsets of **13d** + NEt_3 in CD_3CN vs. the spectrum of **13d** in CD_3CN are attributed to slightly different phase corrections and peak picking inaccuracies for broad signals. br = broad, s = singlet, t = triplet, q = quartet, sh = shoulder.

Ultimately, as the NMR spectroscopic results were ambiguous, the it was attempted to synthetically achieve and isolate a $[Fe^{II}(L\text{-}N_4{}^tBu_2)(OH)(H_2O)]^+$ species. It was found that the addition of a base to an aqueous solution of **13d** and recrystallization by recondensation of water from the mother liquor under a nitrogen atmosphere only yielded green crystals that could be identified as **13d** (structure of non-deuterated **13a**

as reference) via X-ray diffraction cell parameter analysis of multiple single crystals. Thus, it is likely that the changes observed in the ^{1}H-NMR spectrum of a reaction solution of **13d** and NEt_3 indeed result from a change in polarity of the solvent and possibly some diffuse proton exchange reactions with the protic solvent. Alternatively, it is possible that the crystallization properties of **13a / 13d** are simply better than those of the target complex. However, this theory is highly speculative and currently not supported by any data.

5.2. Summary of the Structural, Spectroscopic, Spectrometric, Magnetic, and Electrochemical Investigation

This chapter describes the successful synthesis, stabilization, crystallization, and extensive characterization of an extremely rare mononuclear *cis*-di(hydroxo)iron(III) complex $[Fe^{III}(L\text{-}N_4{}^tBu_2)(OH)_2]^+$ (**14**) and an analogous *cis*-di(aqua)iron(II) $[Fe^{III}(L\text{-}N_4{}^tBu_2)(OH_2)_2]^{2+}$ (**13**) complex with the macrocyclic ligand L-$N_4{}^tBu_2$. Both **13** and **14** are found to exhibit intricate hydrogen bonding interactions with secondary molecules in the crystal packings that stabilize their structures and relate to those found in other aqua and hydroxide complexes described in this thesis. The solution stability of **14** is established via ESI-MS, UV-vis-NIR-, EPR-, and NMR-spectroscopy which precedents the stabilization of such a mononuclear *cis*-di(hydroxo)iron(III) complex in solution, thus, producing valuable reference spectra for easier spectroscopic identification of such species in e.g. mechanistic studies in the future. Moreover, the characteristic, unusually narrow IR marker band around ~3650 cm^{-1} that appears to be relatively robust against differences in the crystallographic environments of **14a**-**c** and demonstrates the weak donor strength of the hydroxide ligands in the high-spin complex represents an important finding in the solid-state spectra of **14**. For **13**, solution stability could only be found in aqueous solution, however, ligand exchange reactions with the anionic counterions and the solvent were observed in acetonitrile solution. Attempts to detect, synthesize, or even isolate corresponding dicationic ferric, or neutral ferrous *cis*-(aqua)(hydroxo) complexes failed. Preliminary studies indicate decompositions and/or ligand exchange reactions with e.g., counterions in solution which could not be overcome synthetically.

Interestingly, the electrochemical investigation of **14** reveals a reduction peak potential vastly more negative (ΔE_p(red) ≈ 0.5 V) than that observed for the *cis*-(carboxylato)(hydroxo)iron(III) complexes $[Fe^{III}(L\text{-}N_4{}^tBu_2)(O_2CPh^R)(OH)]^+$ **1** (R = H), **7** (R = *p*-NO_2), and **10** (R = *p*-OMe) but similar to the mononuclear *cis*-di(methoxy)iron(III) complex $[Fe^{III}(L\text{-}N_4{}^tBu_2)(OMe)_2]^+$ (**4**) (see chapters 2 and 3). This finding aids in the understanding of structure-function relations in the model complexes **1**, **7**, and **10** and, consequently, the enzyme (rabbit Lipoxygenase) which are further discussed in the conclusion of this thesis.

6. Conclusion and Outlook

This thesis describes the first successful synthetic analogue approaches that rewarded structural-functional models for the active site of rabbit Lipoxygenase (rLOX) including both relevant oxidation states (chapters 2 and 4) and a full concomitant study of electronic derivatives of these synthetic analogues that exhibit excellent linear Hammett correlations (chapter 3). Moreover it reports on the first solution-stable *cis*-di(hydroxo)iron(III) complex and its reduced *cis*-di(aqua)iron(II) counterpart (chapter 5). The results derived from the extensive investigations of the structural, electronic, magnetic, and electrochemical properties of the presented metal complexes as well as relevant reactivity studies provide important new insights into the structure-function relationships present at the active sites of lipoxygenases. Thus, although summaries of the results are given at the end of the individual chapters or sections, this conclusion aims to provide a conclusive interpretation of the most important results and to place them in the context of the overall bioinorganic objective to highlight their relevance. Moreover, the achievement of the primary and secondary objectives listed in 1.3 is evaluated and an outlook for follow-up studies is provided.

6.1. General Conclusions from the Synthetic Analogue Approach

The studies presented in chapter 2 and 3 render functional model complexes $[Fe(L\text{-}N_4{}^tBu_2)(O_2CPh^R)(OH)]^+$ (**1**, R = H; **7**, R = *p*-NO_2; **10**, R = *p*-OMe) which reproduce all the relevant structural and electronic features of the first coordination shell of the active site in the oxidized state of rabbit lipoxygenase (rLOX), namely the high spin *cis*-FeN_4O_2 unit containing a *cis*-(carboxylato)(hydroxo)iron(III) moiety. Particularly noteworthy is that also the corresponding *cis*-(carboxylato)(aqua)iron(II) $[Fe^{II}(L\text{-}N_4{}^tBu_2)(O_2CPh^R)(OH_2)]^+$ (**2**, R = H; **11**, R = *p*-OMe) and η^2-(carboxylato)iron(II) complexes $[Fe^{II}(L\text{-}N_4{}^tBu_2)(\eta^2\text{-}O_2CPh^R)]^+$ (**3**, R = H; **9**, R = *p*-NO_2; **12**, R = *p*-OMe) could be synthesized and characterized to reproduce all relevant electronic and magnetic properties of the resting state of the enzymatic active site. Moreover, the ferrous complexes are found to be oxidized to the corresponding hydroxo iron(III) complexes under air to regenerate the active state which primes each pair of model complexes for

catalytic activity towards substrate oxidation. The reactivity towards hydrogen atom transfer from weak O–H and C–H bonds via a concerted proton-coupled electron transfer (cPCET) mechanism analogous to the enzyme concludes the accurate modelling of the two enzymatic states observed in the catalytic cycle of lipoxygenases (LOX) as complete synthetic analogues. The observation of an equilibrium between $[Fe^{II}(L\text{-}N_4{}^tBu_2)(O_2CPh^R)(OH_2)]^+ \rightleftharpoons [Fe^{II}(L\text{-}N_4{}^tBu_2)(\eta^2\text{-}O_2CPh^R)]^+$ (**3**) + H_2O can be considered as indication for a possible third enzymatic state with a chelating carboxylate that had not been previously considered, although evidence for a dynamic coordination environment in soybean lipoxygenases (sLOX) has been found and such a behaviour is not uncommon for carboxylate ligands in metalloenzymes.[66,120,132,133]

The accomplishment of reactive structural models is significant because previous model studies have only either succeeded in reproducing the structural and electronic aspects of the first coordination sphere of the oxidized active site, however, at the expense of losing its functionality, or were able to provide an adequate functional model with very limited structural resemblance to the active site. From the present study, three strategies are derived to be important to achieve the functionality of a structural model complex for a lipoxygenase:

1) The stabilization of the mononuclear hydroxo iron(III) complex needs to be achieved while maintaining the accessibility of the hydroxide lone pair for proton acceptance.
2) The ligand scaffold should be designed to stabilize both the hydroxo iron(III) and the aqua iron(II) complex in a way that the activation/reorganization energy λ required to accommodate the hydrogen atom transfer as well as entropic changes are minimal.[94,95] This includes maintaining the spin state in the $L\text{-}N_4O_2$ environment both for iron(II) and iron(III) as well as inhibiting large structural rearrangements.
3) The ligand environment should create a rather positive Fe^{3+}/Fe^{2+} reduction potential and reduce the Brønsted acidity of the reactive O–H bond in the reduced state to achieve relatively high BDFE(O–H) values and, thus, a significant thermodynamic driving force towards X–H bond activation of substrates.[59]

In $[Fe(L\text{-}N_4{}^tBu_2)(O_2CPh^R)(OH)]^+$ and $[Fe(L\text{-}N_4{}^tBu_2)(O_2CPh^R)(OH_2)]^+$, the special properties of the tetraazamacrocyclic ligand $L\text{-}N_4{}^tBu_2$ crucially contribute to the fulfilment of the above-mentioned prerequisites: The bulky amine substituents that are oriented above and below the equatorial plane prevent the usually highly favourable formation of μ-oxo-bridged diferric complexes by steric hindrance, ensuring the mononuclearity of the iron(III) site in **1** while maintaining accessibility to the hydroxide lone pair that extends out of the *cis*-(carboxylato)(hydroxo)iron(III) pocket in the equatorial plane. In addition, the rather long axial $Fe–N_{amine}$ distances impair the transfer of electron density from the ligand to the electron-deficient iron(III) ion and, thus, create a weak ligand field that stabilizes the high-spin state for both **1** and **2** in the $L\text{-}N_4O_2$ coordination environment and raise the redox potential of the iron(III) site to some extent. In contrast to this, previously reported examples do not fulfil the above-mentioned strategies, which is the reason why they do not show the same functionality as the enzyme. In the examples presented by Watanabe,[80,81] the stabilization of the hydroxide was achieved via intramolecular hydrogen bridging interactions to the lone-pair of the hydroxide ligand which violates strategy 1 and obstructs proton acceptance from a potential substrate and prevents the formation of a corresponding ferrous aqua complex. Although Kovacs et al. also failed to fulfil strategy 1 and only reported on a structural/electronic model for the ferrous aqua resting state of the active site in rLOX, some HAT reactivity was observed. However, the substitution of the carboxylate ligand by an alcoholate in this example likely compromised strategy 3 yielding a BDFE that is ~10 $kcal{\cdot}mol^{-1}$ lower than that of **2**.[79] This provides further insights into the importance of this ligand and its secondary interactions.

Beyond the effects of the macrocycle and the contributions of the nitrogen donors that prime **1**, **7**, and **10** and **2**, **8**, and **11**, respectively, for their hydrogen atom transfer reactivity, the carboxylate ligand arguably plays an equally important role, as also becomes clear by Kovac's example. Firstly, the secondary hydrogen bonding interaction of the distal carbonyl oxygen with the non-reactive hydrogen at the hydroxide/aqua ligand in all complexes creates a planar hexagonal feature that is maintained in both oxidation states. This not only stabilizes the coordination of the hydroxide ligand in **1**, **7**, and **10** and orients its lone pair towards the accessible cavity in the equatorial plane around the *cis*-(carboxylato)(hydroxo)iron(III) unit for proton-acceptance but also limits structural reorganizations that may occur in hydrogen atom

transfer reactions with these complexes which promotes the hydrogen atom transfer reactivity according to Eyring theory.[170] Moreover, the hydrogen bridging interaction of the carbonyl oxygen partially deprotonates the non-reactive O–H bond in **2**, thus reducing the acidity of the hydrogen atom at the reactive O–H bond. This increases the electron draw (-I effect) of the distal carboxylate oxygen atom which further decreases the sigma donor strength of the carboxylate and increases the reduction potential of the ferric complex **1 –** something an alcohol ligand as in Kovac's example cannot provide. The strong influence of this on the reduction potential becomes especially clear when regarding the complexes $[Fe(L\text{-}N_4{}^tBu_2)(OH)_2]^+$ (**14**) and $[Fe(L\text{-}N_4{}^tBu_2)(OMe)_2]^+$ (**4**) that are expected to exhibit somewhat similar ligand field stabilization energies to **1**, **7**, and **10** but exhibit a reduction potential that is drastically more negative (~0.5 V, see chapter 5). Consequently, the carboxylate ligand, and in particular the secondary hydrogen bridging interaction it creates with the hydroxide/aqua ligands, crucially contributes to the improvement of the reactivity through all three above-mentioned strategies.

6.2. Conclusions from the Electronic Derivatization and (Pseudo-)Self-Exchange Studies

Reactivity studies with the electronically derivatized analogues of **1** (**7** and **10**) conclude very similar thermodynamic parameters ($BDFE_{MeCN}(O–H) \approx 72.4$ kcalmol^{-1}, relates to the O–H bond formed in the ferrous complexes) and kinetic behaviours for the cPCET reaction. It is found, that the relative bond strengths are $BDFE_{MeCN}$(**7**) < $BDFE_{MeCN}$(**1**) < $BDFE_{MeCN}$(**1**) within a range of only 0.3 kcal·mol^{-1}. This is despite the observation of an opposite, more apparent trend pertaining the electrochemical reduction potentials, where that of **7** (*p*-NO_2 substituent, -M effect) is clearly more positive and that of **10** (*p*-OMe substituent, +M effect) is clearly more negative as compared to **1** (no substituent). This may be explained by the influence of the hexagonal feature spanned by the hydrogen bond interaction of the coordinated hydroxide/aqua ligand and the carboxylate ligand, which introduces competing effects: The pK_a changes achieved through the derivatization in the corresponding ferrous aqua complexes **2**, **8**, and **11** counteract the changes in the reduction potential. This is because the BDFE correlates linearly with the pK_a of the ferrous aqua complex *and* the reduction potential of the

ferric hydroxide complex according to the Bordwell equation. Here, the pK_a influence is found to be slightly dominant. Importantly, the fact that the two competing influences almost cancel out in this special arrangement shows that the carboxylate contained in the structure of the enzymatic active site (isoleucinate) is likely not responsible for the large difference in electrochemical potential and reactivity between the studied model complexes and the enzyme itself, especially because its donor strength and basicity are in a similar range as those of the studied benzoate ligands.

What distinguishes the model complexes most from the enzyme, apart from their more negative electrochemical potentials and lower O–H bond strengths, are their rather sluggish kinetics. A possible reason for the unexpectedly slow reaction rates is identified in chapter 4, where the homo- and hetero-association of pairs of the model complexes in solution is suggested from compelling solid-state evidence although concentration dependencies of hydrogen atom self-exchange rates could ultimately not be evidenced because only a limited concentration range was experimentally feasible. With respect to the enzyme, this highlights the role of the protein matrix to avoid intermolecular hydrogen-bridging interactions at the active cavity by guest molecules that could inhibit its reactivity.

6.3. Conclusions from the Synthesis of a *cis*-Di(hydroxo)iron(III) Complex

Although some relevance for the bioinorganic objective and the understanding of the role of the carboxylate ligand is attributed to the synthesis and characterization of the first solution-stable mononuclear *cis*-di(hydroxo)iron(III) complex as stated above, the results of chapter 5 mainly contribute to the precedence of such a species out of fundamental interest. Although a mononuclear di(hydroxo)iron(III) had already been precedented by Bénisvy et al.,[78] the literature was, to date, devoid of an extensive spectroscopic, spectrometric, magnetic, electronic, and electrochemical characterization and any evidence for the persistence of such a species in solution. Thus, the results provided in this chapter may be relevant for the future identification of such species e.g., in enzymatic mechanisms.

6.4. Review of the Objectives

Generally, the objectives described in section 1.3 were all achieved.

The 1st primary objective to synthesize and characterize an analytically pure structural/electronic model complex for the active ferric site of rabbit lipoxygenase was successfully met as a fundamental requirement to achieve the following and based on previous preliminary results of predecessors working on the project, while the achievement of the ferrous aqua complex was a completely new result.

The 2nd primary objective to study the reactivity of the structural model complex was likewise met. Not only could the hydrogen atom abstraction from weak O–H and C–H bonds of suitable substrates with the ferric model complex be strongly evidenced, but also thermodynamic and preliminary kinetic parameters could be obtained as quantitative measures for good comparability to other works. Because of the rather slow kinetics, studies with isotope-marked substrates to study the kinetic isotope effect (KIE) were not feasible. The planned theoretical study to identify the reaction mechanism was successfully conducted via a collaboration with external partners. Although it is worth mentioning that the catalytic activity of the ferric complex under aerobic conditions could also be evidenced, this had already been suggested in previous works in the Krüger group by in-situ generation of the ferric complex and was to be expected.

The 3rd primary objective, which pertained the synthesis, characterization, and analogous study of derivatives of the functional structural model complexes precedented in the first two chapters, was also met. Although the synthesis and characterization of some of the iron(II) complexes was more challenging, the ferric complexes were well-obtainable by adjusted synthetic procedures and could be studied accordingly to derive structure function relations, also by exploiting Hammett parameter correlations.

The 1st secondary objective was also met, as an in-depth characterization of the co-crystallized species **1** and **2** was done and the hydrogen atom self-exchange reaction was evidenced via isotope marked NMR studies. Additionally, the rate constant for the self-exchange reaction could be determined via EXSY NMR spectroscopy and the results could be validated via a complementary Marcus-theory approach.

The 2nd secondary objective was met by the successful synthesis and in-depth characterization of a *cis*-di(hydroxo)iron(III) in both the solid-state and in solution and the evidencing of its solution stability.

6.5. Outlook

This investigation pursued the objectives of the synthetic analogue approach in bioinorganic studies in identifying those intrinsic properties of the enzyme associated with the metal site and its first coordination sphere and those contributed by the protein matrix.[36] very rarely, a synthetic analogue complex is a good model for the structural and/or electronic properties and, at the same time, a good model for the reactivity of an enzyme. Thus, the presented iron-diazapyridinophane scaffold provides a unique platform to further study and illuminate the structure-function relations of the enzyme. While important aspects such as the relevance of the hexagonal feature spanned by the carboxylate ligand, the iron core, and the hydroxide/aqua ligand have been highlighted in this work, the high reactivity of the enzyme as compared to the extremely sluggish activity of the model complexes presented in this work has yet to be explained conclusively. To do this, it is obvious that a derivatization of the macrocyclic ligand may yield interesting results, as it is expected that these electronic influences are not counteracted as strongly by pK_a changes because no secondary hydrogen bonding interactions exist between the macrocycle and the hydroxide/aqua ligand. Because the *tert*-butyl substituents at the axial amine donors are important for the stabilization of the synthetic analogues in the first place and the Fe–N_{amine} distances are already relatively long, electron withdrawing substituents in the backbone of the pyridines appear most worthwhile to increase the reduction potential of the ferric complex without significantly affecting the acidity of the corresponding ferrous complex, thus, achieving a higher reactivity. Although preliminary results for the synthesis and characterization of e.g. *cis*-(acetato)(hydroxo)iron(III) were already obtained, the pursual of additional carboxylate variations appears less promising in light of the results of this work. Beyond these different types of electronic derivatizations, spacers and/or anchor groups could also be introduced in the pyridine backbone to immobilize the reactive model complexes on a surface to study the system as a biomimetic heterogeneous catalyst. This would also supress the inhibition of the reaction via homo- and hetero-association of complexes that is currently suggested to occur in solution and somewhat impairs the reactivity studies.

7. Methods and Instrumentation

7.1. Characterization and Investigation of Electronic, Magnetic and Structural Properties.

7.1.1. Elemental Analysis

Elemental analyses were conducted with a *vario Micro CUBE* by *Elementar Analysetechnik GmbH*. For the calculation of the compositions of deuterated samples the H- and D-atoms were calculated with an effective mass of 1 in the nominator, whereas a mass of 2 was used in the denominator.[171]

7.1.2. Structural Analysis

X-ray diffraction data collections were carried out on a *Gemini S Ultra* by *Rigaku Oxford Diffraction*, equipped with a molybdenum and a copper radiation source and a low-temperature control device. Due to the positioning of the two sources in the device, data collection is somewhat limited to smaller angles, which may result in alerts in some checkcif files. Absorption correction was done with *CrysAlis Pro* 1.171.38.41 and 1.171.40.67a, respectively. All structures were solved using the software programs *SHELXS-2018*, and the positions of all non-hydrogen atoms were refined with *SHELXL-2018*.[172] With the exception of the hydrogen atoms attached to the oxygen atom of the hydroxide and the water ligands, the positions of the hydrogen atoms were calculated and refined using a riding model and isotropic thermal parameters. In contrast, the positions of the hydrogen atoms attached to the oxygen atoms of the coordinated hydroxide or water ligand were determined by Fourier difference maps if possible. More detailed information is given in sections 2.1.2, 3.1.2, 4.1.2, 5.1.2, and the attachment. Perspective views of the complex cations are all drawn with thermal ellipsoids displaying 50 % probability. For clarity most hydrogen atoms are omitted in these depictions.

7.1.3. SQUID Magnetometry

Magnetic susceptibility measurements were carried out with a *Quantum Design MPMS3 Evercool* superconducting quantum interference device (SQUID) magnetometer equipped with a 7 Tesla magnet in the range from 2 to 300 K with a magnetic field of 0.5 T or 0.2 T in DC mode respectively. In selected cases, the measurement was conducted up to 400 K for the heating mode. Magnetization measurements were conducted between 2 and 10 K in 1 K increments, and in selected cases at 100 K, with magnetic field sweeps up to 7 T. The samples were either packed in gelatine capsules and fixed in a non-magnetic sample holder (straw) or the samples were placed in a *Quantum Design* VSM powder capsule and measured with a brass sample holder. Each raw data file for the measured magnetic moment was corrected for the diamagnetic contribution of the sample holder and the gelatine capsule/VSM powder capsule according to $M^{dia} = \chi_g \cdot m \cdot H$. Additionally, the molar susceptibility data were corrected for the diamagnetic contribution of the sample according to χ_M^{dia} (sample) = $-0.5 \cdot M_{rel} \cdot 10^{-6} \cdot cm^3 \cdot mol^{-1}$ (M_{rel} = relative molecular mass).[173] Magnetic data was fitted using the program PHI by the *Chilton* group.[124]

7.1.4. Mößbauer Spectroscopy

Mößbauer spectroscopic measurements were carried out on a Mößbauer Spectrometer purchased from *WissEl GmbH* using the constant acceleration mode of the ^{57}Co-source. Low temperature measurements were achieved by cooling with a closed-cycle-cryostat with an *ARS-4HW* compressor by *Advanced Research Systems*. A *Delrin*® container filled with approximately 50 mg of the polycrystalline sample was placed in a sample holder, which was mounted on the tip of the second stage heat station of the expander unit *DE204SF*. This setup was shielded by a radiation shield and a vacuum shroud, and the expander unit was isolated from vibrations by a *DMX20-41* interface. The temperature was controlled by a *Lakeshore 331S* unit. Spectral analysis was performed by least square fits using a Lorentzian line shape fitting routine of the software *WinNormos-for-Igor* Version 6 by R.A. Brand (*WissEl GmbH*). The isomeric shift is given relative to α-Fe foil ($\delta_{IS(\alpha\text{-Fe vs source})}$= 0.107 mm·s^{-1}). Reported temperatures were recorded at the thermometer in the setup and may not reflect the actual temperature of the sample.

7.1.5. Infrared (IR) Spectroscopy

Infrared spectra were recorded either on a *Jasco FT/IR-6100* Spectrometer or on a *Perkin Elmer Spectrum Two* FT/IR spectrometer equipped with a *Quest Single Reflection* ATR Accessory *P/N GS10800* by *Specac*. For each spectrum the resolution was set to 4 cm^{-1}. For each spectrum the atmospheric background was subtracted. For spectra recorded with the *Perkin Elmer* spectrometer, an additional atmospheric correction for CO_2 and H_2O was applied by the software in some cases after verifying that the absorptions are not significantly altered by the corrections if not stated otherwise. This verification is especially necessary for those compounds exhibiting O–H vibrations pertinent to the discussions. No ATR-correction was applied for the spectra.

7.1.6. UV-vis-NIR Electronic Spectroscopy

Electronic absorption spectra of the iron complexes in MeCN and in H_2O solutions were measured in the UV-vis-NIR range between 200-2000 nm and 200-1400, respectively, using a *Cary 5000* UV-vis-NIR-spectrophotometer by *Varian* in the double beam mode with two QX glass cuvettes, one of which served as a pure solvent reference in the reference beam path. All solutions containing ferrous compounds were prepared in a glove box with dry MeCN under a nitrogen atmosphere. The electronic absorption spectra of the compounds in the solid state were recorded using a *Praying Mantis* accessory by Harrick on the same instrument. The measurements were conducted either on pure, diligently grinded powders of the samples or equally well-grinded powder mixtures of the samples and a KBr matrix. Diligently grinded KBr was used as reflective background material reference and the spectra were processed using the *Kubelka-Munk* theory.[127] All spectra were recorded at room temperature at a scan rate of 180 nm/min. There are minor artefacts in the resulting spectra due to changes in the detector and light source at 800 and 350 nm, respectively, which were not corrected for in the displayed spectra unless stated otherwise. Gaussian curve analysis and fitting of solution-based spectra was done using *MagicPlot* (Student Edition); the fitting parameters are given in the respective figure captions.

7.1.7. Electron paramagnetic resonance (EPR) spectroscopy

EPR spectra reported in the published work (chapter 2)[1] were obtained with an *Elexsys E580* spectrometer and the *Standard Resonator ER 4102ST* by *Bruker*. The low temperature measurements on frozen solutions of the iron(III) complexes in DMF containing 0.2 molL^{-1} TBAP were carried out with the *ER 4122 SHQE* accessory by *Bruker* in combination with an *ESR 900* continuous flow cryostat by *Oxford Diffraction* for providing a flow of cold helium gas as cryogen. Thus, measuring temperatures varied between 10 and 50 K. The temperature was controlled with an *ITC503*-temperature controller by *Oxford Diffraction*.

EPR spectra that have not been published to this date (chapters 3 and 5) were recorded using an *Elexsys E580* spectrometer and the Standard Resonator *ER 4102ST* by *Bruker*. The low temperature measurements on grinded powders and frozen solutions in DMF or MeCN containing 0.2 molL^{-1} TBAP were carried out with a *Bruker ER4112* helium closed cycle cryostate with a *ColdEdge* accessory, an *F-70 Sumimoto Cryogenics* compressor and a *HiCube* turbomolecular vacuum pump. The temperature was controlled with a *Lakeshore Cryotronics Model 336* temperature controller. Solid-state spectra were recorded by measuring of grinded powders fixed with glass wool in a quartz tube to ensure that the powder does not contaminate the instrument. The glass wool was found to contain EPR active impurities at g = 4.25 (inversion signal) and g = 2.0. (multiplet) which may contaminate the spectra.

All room temperature EPR measurements were performed in MeCN solution using a flat quartz cell. Special attention was given to ensure the reproducible perpendicular orientation of the flat cell with respect to the magnetic field when placing the cell in a sample holder accessory.

The EPR spectra were fitted with the program *EasySpin* (*Version 5.2.28*).[130]

7.1.8. Electrospray Ionization Mass Spectroscopy (ESI-MS)

ESI mass spectra were obtained with an *Expression*^{L}*-CMS* spectrometer by *Advion* using the *Advion Mass Express* software suite with different ionization presets at an eluent flow rate of 0.3 mL/min. Acetonitrile was used as eluant and calibrated with the calibration solution software supplied by *Advion.* Analysis of the mass spectra was performed with the *Advion Data Express* software and *IsoPro 3.1* for simulations. The parameters of the presets were as follows: **soft ionization**: Capillary temperature 250 °C, capillary voltage 160 V, source voltage offset: 20 V, source voltage span: 0 V, source gas temperature: 250 °C, ESI voltage: 3500 V; **strong ionization**: Capillary temperature 250 °C, capillary voltage 180 V, source voltage offset: 40 V, source voltage span: 20 V, source gas temperature: 250 °C, ESI voltage: 3500 V; **super soft ionization**: Capillary temperature 200 °C, capillary voltage 150 V, source voltage offset: 25 V, source voltage span: 25 V, source gas temperature: 250 °C, ESI voltage: 3500 V.

7.1.9. Cyclic Voltammetry

Cyclic voltammetric experiments were performed under a nitrogen atmosphere in a glovebox. The cyclic voltammograms were obtained with a Potentiostat/Galvanostat 273 A by *Princeton Applied Research* employing a saturated calomel reference electrode (SCE), a platinum foil electrode by *Metrohm GmbH* as working electrode, and a platinum net as counter electrode. Approximately 10^{-5} moles of sample were dissolved in 10 mL of acetonitrile containing 0.2 molL^{-1} tetrabutylammonium perchlorate (TBAP) as electrolyte. Under these experimental conditions, the potential of the Ferrocene/Ferrocenium Fc/Fc^{+} redox couple was determined versus the standard calomel electrode (SCE) regularly to ensure the accuracy of an internal reference. Generally, there were some fluctuations in the reference SCE over the course of this work, which is why, for every experimentally determined potential vs SCE, the Fc/Fc^{+} potential vs SCE is given as a second reference. Scan rates were varied between 10 mV/s and (up to) 1 V/s. Prior to any scan, the solutions were stirred, and the working electrode was wiped before starting a measurement sequence. Because the setup in the glovebox requires the storing of a KCl solution for the calomel electrode, minor water impurities and, thus, the presence of protons in the studied solutions cannot be fully excluded and may influence the measurements.

7.1.10. Nuclear Magnetic Resonance (NMR) Spectroscopy

NMR spectroscopic characterizations were carried out either on an FT-NMR *Avance III* (400.33 MHz), *Avance I* (400.13 MHz), *Avance I* (600.13 MHz), or an *Avance I* (200.13 MHz) NMR spectrometer by *Bruker*. The signals arising from the residual non-deuterated NMR solvent served as internal reference (^{1}H-NMR: CD_3CN δ = 1.94 ppm, $CDCl_3$ δ = 7.26 ppm, D_2O δ = 4.79 ppm).[131] ^{2}H-NMR experiments were measured by using a 0.2 mol·L^{-1} CD_3CN in CH_3CN solvent mixture. Because of the poor signal strength produced by the samples even at high concentrations (up to 0.16 molL^{-1}), they were measured with the shim of a blank 0.2 mol·L^{-1} solution of CD_3CN in CH_3CN. H,H-COSY experiments were measured with standard settings and a gradient pulse sequence. Relaxation times ($t_1 = t_0/\ln(2)$) were measured via an inversion recovery experiment with a 180° pulse and a second 90° pulse after variable times between 0.1 ms and 20 ms.

The origin of diethylether residues in some spectra may be explained as residues in the degassed solvent. As the solvent was degassed using Schlenk techniques with the same apparatus as used for synthesis, it is possible that the tubing contained diethyl ether that was purged into the deuterated solvent under nitrogen flow during the freeze-pump-thaw procedure and contaminated the CD_3CN. However, these diamagnetic solvent residues did not affect the study of the processes of interest to this work.

7.2. Reactivity Studies

7.2.1. General Considerations

For all reactivity studies, the purities of the employed metal complex compounds were previously verified by elemental analysis as well as by spectroscopic methods. It was found that the ferric complexes decay after prolonged exposure to air at room temperature in the solid state (weeks-months) and after prolonged storage in solution (days). Light exposure appeared to accelerate this decomposition, especially for samples containing tetraphenylborate counterions. Thus, only freshly prepared samples were used for reactivity studies. The substrate 2,4,6-tri-(*tert*-butyl)phenol (TTBP) and the EPR calibration standard 2,2,6,6-tetramethylpiperidin-1-oxyl radical (TEMPO) were either purified by sublimation prior to use or used from freshly opened containers purchased from commercial vendors. 2,2,6,6-Tetramethylpiperidin-1-ol (TEMPOH) was freshly prepared and purified according to a modified literature procedure.[101,174] The substrate 1,4-cyclohexadiene (CHD) was freshly distilled using a Vigreux column and degassed using the freeze-pump-thaw method. The benzene content was determined to be less than 1 % via NMR spectroscopy. No evidence for stabilizing agents as impurities was found. The crystalline substrate 9,10-dihydroanthracene (DHA) was obtained from commercial sources and used without further purification. Deuterated acetonitrile was degassed by the freeze-pump-thaw method, dried over molecular sieve (3 Å) and distilled under a nitrogen atmosphere prior to use. Other anhydrous and degassed solvents were purified prior to use according to standard procedures and Schlenk techniques.[175–178] For the preparation of reaction solutions, solids with minimal masses of at least 10 mg were weighed out using an analytical balance with an accuracy of ±0.1 mg, those with masses below 10 mg using a precision balance with an accuracy of ±0.01 mg. The amount of liquid reactant was measured volumetrically using a 10µL-SGE Hamilton syringe, the amount of solvent was measured with volumetric flasks in any experiment where exact concentrations were relevant.

7.2.2. ESI-MS Reactivity Studies

Acetonitrile was used as an eluent in all experiments. Here, exact temperatures, voltages and injection volume may be subject to some fluctuations. Each spectrum was recorded by injection of 20 µL of an acetonitrile solution at a loop setting of 5 µL with a 100 µL Hamilton syringe. The solution was only injected after the total ion count of the background had stabilized. The spectra were generated by subtracting the averaged stabilized total ion count as background and averaging of the first three scans after injection.

7.2.3. Quantitative EPR Spectroscopy.

Within a series of quantitative EPR measurements of reaction solutions of ferric complexes with 2,4,6-tri-(*tert*-butyl)phenol, the same parameter setting was used; only the necessary tuning procedure during the locking of the signal required some minor adjustments to the bias, iris, and frequency to optimize diode current and lock offset. Great attention was paid to the stability of the lock offset and the diode current during each measurement to ensure a stable baseline and thermal equilibration, which is essential for a meaningful integration of the EPR signals. To minimize errors introduced by slight variations of experimental setups between measurements even further, the quantitative EPR measurements of an entire dilution series were carried out one after the other without interruption within a single session.

A solution of TEMPO in MeCN (0.2 mmol L^{-1}) was used as a calibration standard for determining the concentration of produced radicals by double integration of the EPR signals. The calibration solution was prepared at least twice during each session and measured at the end of the experiment period to warrant the reproducibility and the reliability of the values obtained by integration of the signals.

UV-VIS reactivity studies.

Reaction monitoring was done with an *8453 UV-VIS diode-array* spectrophotometer by *Hewlett Packard* in a thermostated Peltier cell holder that was controlled by a *Hewlett Packard 89090A* Peltier temperature controller. Procedural details and employed concentrations are provided in sections 2.3.2 and 8.2.2.3.

7.2.4. NMR Reactivity Studies

Preparations of reaction solutions of metal complexes with substrates were carried out under a nitrogen atmosphere in a glovebox. Samples were measured using a Young NMR tube equipped with a Teflon valve. The reaction solutions were kept under a nitrogen atmosphere for the duration of the entire experiment. In the kinetic studies, the sample was kept at room temperature over the course of the reaction.

Preparations of mixed reaction solutions of ferric and ferrous metal complexes for self-exchange reactivity investigations were carried out under a nitrogen atmosphere in a glovebox. Defined ratios and reasonable concentrations for the investigations of kinetic and thermodynamic parameters were ensured. Samples were measured using a Young NMR tube equipped with a Teflon valve. The reaction solutions were kept under a nitrogen atmosphere for the duration of the entire experiment.

EXSY experiments were done by measuring a series of NOESY experiments with variable mixing times between 0.1 ms and 1 s both with and without a gradient pulse sequence. All samples were wobbled prior to measurements to ensure optimal resolution and a prior H,H-COSY experiment was measured to ensure that the interpreted cross-signals are not caused by magnetization transfer between neighbouring atoms but relate to the exchange coupled magnetization transfer to be investigated. EXSY measurements were done using an *Avance I* (400.13 MHz) or an *Avance I* (200.13 MHz) NMR spectrometer by *Bruker*.

8. Experimental Procedures

8.1. Synthetic Procedures

8.1.1. General Considerations

Caution! Perchlorate salts are potentially explosive when heated or subjected to friction.

Anhydrous solvents were purified prior to use according to standard procedures.[175–178] Thus, prior to distillation, acetonitrile was dried over CaH_2 and methanol was dried over magnesium methanolate. Diethylether was dried by storage over solid sodium. For the preparation of all *cis*-(carboxylato)(hydroxo)iron(III) complexes it is essential to use freshly distilled diethylether for crystallization in order to remove the antioxidation reagent 2,6-di(*tert*-butyl)hydroxytoluene (BHT) present in commercial diethylether. The exclusion of BHT is necessary because BHT itself can act as a substrate in H-atom abstraction reactions with the *cis*-(carboxylato)(hydroxo)iron(III) complexes,[112] yielding the *cis*-(carboxylato)(aqua)iron(II) complex as contaminant in the isolated product. For preparations under a nitrogen atmosphere, all solvents were evacuated (min. 30 s) and purged with nitrogen gas (several minutes) prior to use to remove oxygen residues (applying at least 3 cycles). In specified cases a freeze-pump-thaw method was used.

All reagents and reactants were purchased from commercial sources, sodium salts of benzoate and its derivatives were synthesized by stoichiometric deprotonation of $^{R}PhCO_2H$ with NaOH in H_2O and dried at 100 °C. The macrocyclic ligand L-$N_4{}^{t}Bu_2$ was synthesized via modified reported methods.[114,179]

8.1.2. Synthesis of 2,6-Di(chloromethyl)pyridine

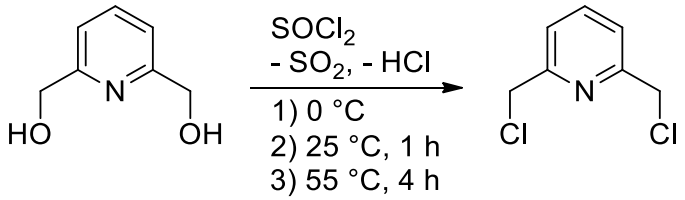

139.06 g/mol 175.00 g/mol

Caution! Thionyl chloride should be handled with care and the forming hazardous SO_2 and HCl fumes should be guided through a sodium hydroxide solution for neutralization.

Approach: 48.92 g (35 mmol) 2,6-di(hydroxymethyl)pyridine
190 mL (0.38 mol) thionyl chloride

The precursor 2,6-di(chloromethyl)pyridine for the synthesis of the macrocyclic ligand L-$N_4{}^t Bu_2$ was synthesized according to a modified literature procedure.[114] Thionyl chloride was added dropwise to 2,6-di(hydroxymethyl)pyridine at 0 °C and the slurry was stirred. The red solution was stirred at room temperature for 1 h and subsequently for 4 h at 55 °C. After cooling to 0 °C, pentane (400 mL) was added to precipitate the hydrochloride raw product. The mixture was filtered, and the filtrate was collected for redistillation. The precipitate was suspended in deionized water (500 mL) and neutralized with NaOH and Na_2CO_3. The colourless solid was filtered, washed with water, and dried under vacuo. Recrystallization from petroleum ether (40/60, 450 mL) yielded colourless crystals. The yield could be increased by slow evaporation of the solvent. The purity of the sample was verified to be suitable for further conversion via NMR spectroscopy.

Yield: 61.5 g, quantitative (Lit. 91 %).[114]

^{1}H-NMR (400 MHz, $CDCl_3$) δ = 7.76 (t, J = 7.8 Hz, 1H, 4-pyH), 7.48 (d, J = 7.8 Hz, 2H, 3,5-pyH), 4.66 (s, 4H, CH_2).

For further analytical data see literature reference.[114]

8.1.3. Synthesis of 2,6-Di(*tert*-butylaminomethyl)pyridine

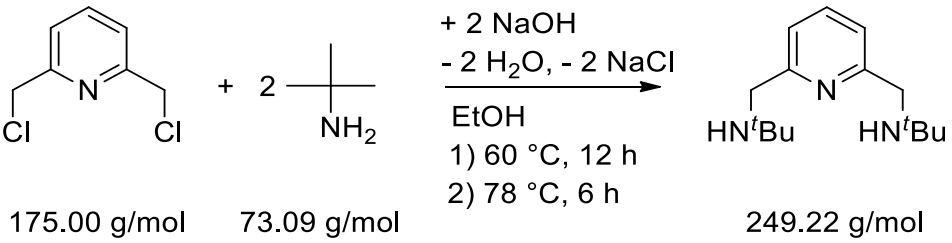

175.00 g/mol 73.09 g/mol 249.22 g/mol

Approach: 22.0 g (0.12 mol) 2,6-di(chloromethyl)pyridine
130 mL (1.24 mol) *tert*-butylamine
11.0 g (0.28 mmol) sodium hydroxide

The precursor 2,6-di(*tert*-butylaminomethyl)pyridine for the synthesis of the macrocyclic ligand L-N$_4$*t*Bu$_2$ was synthesized according to a modified literature procedure.[114] 2,6-di(chloromethyl)pyridine in EtOH (350 mL) was added dropwise to a solution of *tert*-butylamine in EtOH (800 mL) over 4 h at 60 °C and then stirred for 12 h at 60 °C. Subsequently, the mixture was heated until reflux for 6 h. The mixture was cooled to 0 °C and treated with NaOH. The suspension was then filtered, and the solvent was removed under reduced pressure at 40 °C. The yellow oil was taken up in MeCN and filtered again. After removal of the solvent the oil was distilled to yield the pure product as colorless oil. The purity of the sample was verified to be suitable for further conversion via NMR spectroscopy.

Yield: 17.3 g, 55% (Lit. 80%)[114]

^{1}H-NMR (200 MHz, CDCl$_3$) δ = 7.59 (t, *J* = 7.6 Hz, 1H, 4-pyH), 7.21 (d, *J* = 7.6 Hz, 2H, 3,5-pyH), 3.90 (s, 4H, CH$_2$), 1.95 (br, 2H, NH), 1.23 (s, 18H, CH$_3$).

For further analytical data see literature reference.[114]

Note: The described synthesis and characterizations were carried out by Dipl.-Chem. Thomas Frick, a project student I supervised in 2019.

8.1.4. Synthesis of *N*,*N*'-di(*tert*-butyl)-2,11-diaza[3.3](2,6)-pyridinophane (L-$N_4{}^tBu_2$)

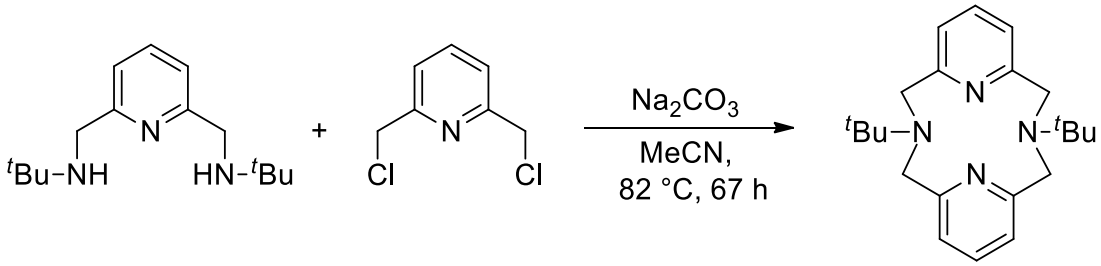

249.22 g/mol 175.00 g/mol 352.26 g/mol

Approach: 4.40 g (25 mmol) 2,6-di(chloromethyl)pyridine
6.23 g (25 mmol) 2,6-di(*tert*-butylaminomethyl)pyridine
5.34 g (50 mmol) sodium carbonate

The macrocyclic ligand L-$N_4{}^tBu_2$ was synthesized according to a modified literature procedure.[114] 2,6-Di(*tert*-butylaminomethyl)pyridine and Na_2CO_3 were suspended in MeCN. The mixture was heated to reflux and a solution of 2,6- di(chloromethyl)pyridine in MeCN (200 mL) was added dropwise over 4 h. The refluxing reaction mixture was stirred for 67 h. The mixture was filtered, and the residue was washed with MeCN twice to obtain a crude product that was extracted with Chloroform (150 mL). The MeCN solvent was stored for redistillation. A colourless solid was obtained as product upon evaporation of the solvent under reduced pressure. The purity of the sample was verified to be suitable for further conversion via NMR spectroscopy.

Yield: 6.62 g, 75 % (Lit. 66 %).[114]

^{1}H-NMR (400 MHz, $CDCl_3$) δ = 7.04 (t, *J* = 7.6 Hz, 2H, 4-pyH), 6.71 (d, *J* = 7.6 Hz, 4H, 3,5-pyH), 3.95 (br s, 8H, CH_2), 1.31 (s, 18H, CH_3).

Note: If the $CDCl_3$ NMR solvent is slightly acidic, a second, smaller set of signals may be observed at δ = 8.00 (t, J = 7.7 Hz, 2H, 4-pyH), 7.48 (d, J = 7.7 Hz, 4H, 3,5-pyH$_2$), 4.64 (br s, 8H, CH_2), 1.06 (s, 18H, CH_3).

For further analytical data see literature reference.[114]

8.1.5. Synthesis of [Fe(L-N$_4$^{t}Bu$_2$)(Cl)$_2$] (5)

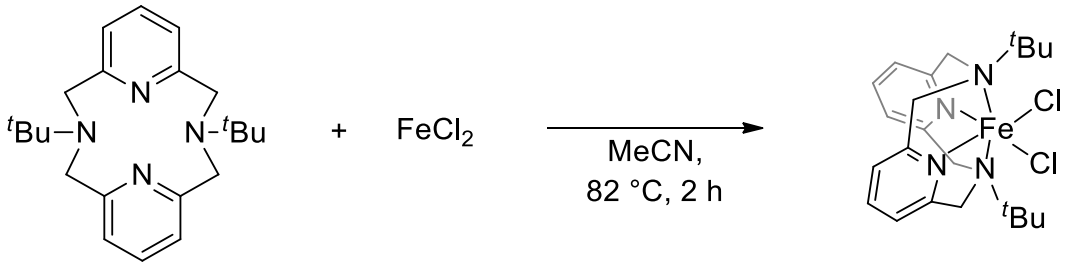

352.26 g/mol 126.75 g/mol 478.14 g/mol

Approach: 360.4 mg (1.02 mmol) L-N$_4$^{t}Bu$_2$
119.7 mg (0.95 mmol) anhydrous iron(II)chloride

The ferrous precursor complex [Fe(L-N$_4$^{t}Bu$_2$)(Cl)$_2$] (**5**) was synthesized according to a modified literature procedure.[114] Under an atmosphere of nitrogen, L-N$_4$^{t}Bu$_2$ and anhydrous FeCl$_2$ were suspended in MeCN (90 mL). The mixture was refluxed for 2 h, then cooled down to room temperature and filtered over celite. The volume of the filtrate was reduced (30 mL). Analytically pure, yellow crystals were obtained by diffusion of Et$_2$O into the concentrated solution.

Yield: 366.0 mg, 81 % (Lit. 47 %).[114]

Elemental Analysis (FeC$_{22}$Cl$_2$H$_{32}$N$_4$):

	C	H	N
calculated	55.13	6.73	11.69
found	54.89	6.96	11.66

IR (ATR, cm^{-1}): 2966, 2902, 1598, 1578, 1462, 1435, 1402, 1378, 1351, 1264, 1249, 1227, 1194, 1154, 1079, 1022, 937, 924, 909, 858, 801, 714, 640.

^{1}H-NMR(400 MHz, CD$_3$CN) δ(ppm) = 66.46 (s), 32.12 (s), 10.27 (sh), 6.68 (s), -0.31 (br), -7.01 (s). Additional signals at 3.46 and 1.31, and 2.20 are attributed to Et$_2$O and H$_2$O residues, respectively.[131]

For further analytical data see literature reference.[114]

8.1.6. Synthesis of [Fe(L-N$_4$*t*Bu$_2$)(O$_2$CPh)(OH$_2$)](ClO$_4$) (2a)

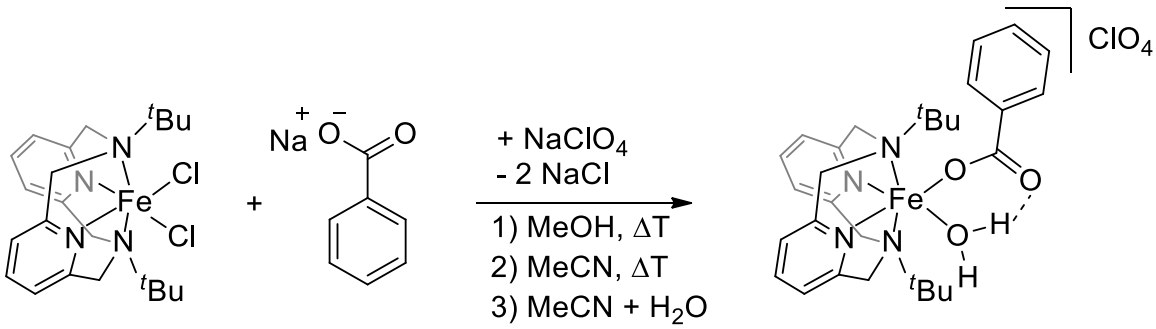

478.14 g/mol 144.02 g/mol 646.19 g/mol

Approach: 240.3 mg (0.50 mmol) [Fe(L-N$_4$*t*Bu$_2$)(Cl)$_2$] (**5**)
72.5 mg (0.50 mmol) sodium benzoate
63.5 mg (0.52 mmol) sodium perchlorate

Under an atmosphere of nitrogen, **5**, PhCO$_2$Na, and NaClO$_4$ were dissolved in MeOH (50 mL). The resulting yellow reaction mixture was heated to reflux twice. After removal of the solvent, the solid residue was treated with MeCN (15 mL). The resulting suspension was heated to reflux before the solvent was once more removed (in order to remove traces of MeOH). The residue was again treated with MeCN (20 mL) and the suspension was filtered through celite. The subsequent addition of a small amount of deionized water (ca. 0.5-1 mL), followed by the slow diffusion of Et$_2$O into the solution afforded analytically pure green crystals.

Yield: 228.8 mg, 71 %.

Elemental Analysis (FeC$_{29}$ClH$_{39}$N$_4$O$_7$):

	C	H	N
calculated	53.84	6.08	8.66
found	53.70	6.01	8.62

IR (ATR, cm^{-1}): 3345, 3079, 2977, 1599, 1579, 1524, 1465, 1442, 1404, 1292, 1260, 1225, 1193, 1160, 1120, 1092, 1074, 1025, 965, 936, 912, 849, 828, 805, 795, 720, 674, 623, 563, 445.

^{1}H-NMR (600 MHz, CD_3CN) δ(ppm) = 69.61 (br), 53.44 (br), 24.43 (sh), 22.55 (br), 15.31 (s), 8.18 (s), 5.43 (br), 1.05 (s), -3.28 (br), -11.04 (s). Additional signals at 3.42 and 1.12 correspond to diethylether residues.[131]

ESI-MS(+): calculated: m/z = 547.2; found m/z = 529.3 (main signal). The H_2O ligand is lost under ESI-MS conditions.

Electronic excitations (ground powder): λ (nm) = 738, 1379 (d,d transitions only).

Electronic excitations (MeCN): λ (nm) = 732, 1296 (d,d transitions only).

Magnetic moment (298 K): μ = 5.37 μ_B (χT = 3.61 cm^3Kmol^{-1}).

Mößbauer parameters (298 K): δ_{IS} = 1.04 mms^{-1} ΔE_q = 2.63 mms^{-1}.

For electrochemical data see 2.1.10. For structural data see 2.1.2 and attachment.

8.1.7. Synthesis of [Fe(L-N$_4$^{t}Bu$_2$)(O$_2$CPh-d5)(OH$_2$)](ClO$_4$) (2^{D}a)

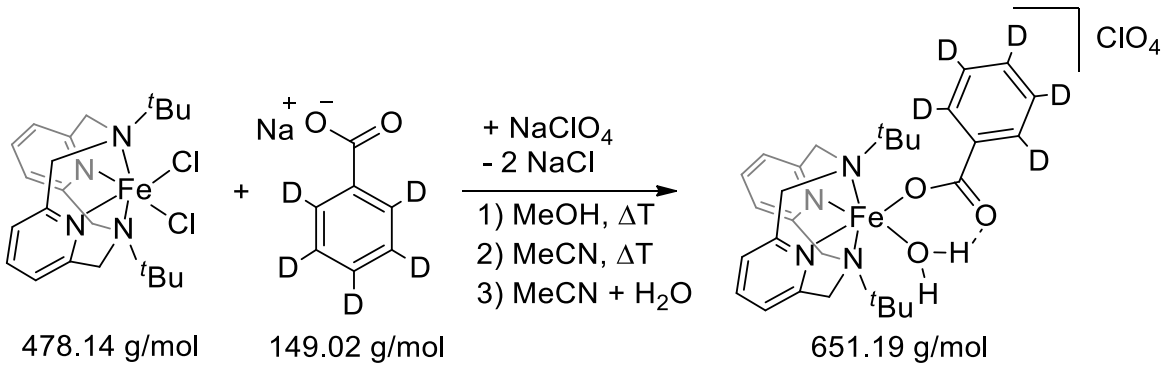

478.14 g/mol 149.02 g/mol 651.19 g/mol

Approach: 238.0 mg (0.50 mmol) [Fe(L-N$_4$^{t}Bu$_2$)(Cl)$_2$] (**5**)
64.1 mg (0.50 mmol) penta ring-deuterated benzoic acid
21.0 mg (0.53 mmol) sodium hydroxide
74.4 mg (0.53 mmol) sodium perchlorate hydrate

Sodium hydroxide and HO$_2$CPh-d5 were dissolved in water and dried under vacuo. Under an atmosphere of nitrogen, **5** and NaClO$_4$ were added and dissolved in MeOH (50 mL). The resulting yellow reaction mixture was heated to reflux twice. After removal of the solvent, the solid residue was treated with MeCN (15 mL). The resulting suspension was heated to reflux before the solvent was once more removed (in order to remove traces of MeOH). The residue was again treated with MeCN (20 mL) and the suspension was filtered through celite. The subsequent addition of a small amount of deionized water (ca. 0.5-1 mL), followed by the slow diffusion of Et$_2$O into the solution afforded analytically pure green crystals.

Yield: 210.5 mg, 65 %.

Elemental Analysis (FeC$_{29}$ClD$_5$H$_{34}$N$_4$O$_7$):

	C	H	N
calculated	53.43	6.08	8.59
found	53.40	5.97	8.61

IR (ATR, cm^{-1}): 3342, 3078, 2995, 2975, 2912, 2285, 2257, 1597, 1578, 1567, 1552, 1505, 1463, 1435, 1418, 1406, 1387, 1375, 1343, 1292, 1259, 1224, 1191, 1168, 1159, 1119, 1090, 1070, 1032, 1023, 1012, 1000, 965, 936, 910, 867, 849, 825, 814, 805, 794, 778, 753, 738, 710, 650, 621, 592, 563, 540, 479. Some vibrational modes may be obscured because of a limited resolution between 2300 – 1900 cm^{-1} and the occurrence of atmospheric CO_2 modes.

^{2}H-NMR (400 MHz, 0.2 mol CD_3CN in CH_3CN, **2a** with O_2CPh-d5) δ(ppm) = 21.70 (s, 2H), 14.95 (s, 2H), 8.12 (m, 1H). Deviations between ^{1}H-NMR shifts of **2a** and the ^{2}H-NMR shifts of the O_2CPh-d5 analogue may result from shimming or phase correction differences.

Structural analysis was not conducted. For representative structural data for the non-deuterated analogue **2a** see 2.1.2 and attachment.

8.1.8. Synthesis of [Fe(L-N$_4$*t*Bu$_2$)(O$_2$CPh)(OD$_2$)](ClO$_4$) (2d)

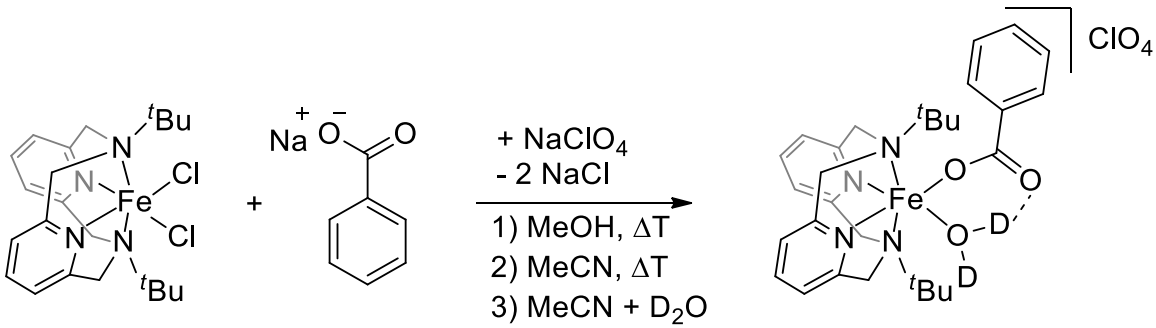

478.14 g/mol 144.02 g/mol 648.19 g/mol

Approach: 241.8 mg (0.51 mmol) [Fe(L-N$_4$*t*Bu$_2$)(Cl)$_2$] (**5**)
72.6 mg (0.50 mmol) sodium benzoate
63.0 mg (0.51 mmol) sodium perchlorate

Under an atmosphere of nitrogen, **5**, PhCO$_2$Na, and NaClO$_4$ were dissolved in MeOH (50 mL). The resulting yellow reaction mixture was heated to reflux twice. After removal of the solvent, the solid residue was treated with dry MeCN (15 mL). The resulting suspension was heated to reflux before the solvent was once more removed (in order to remove traces of MeOH). The residue was again treated with dry MeCN (20 mL) and the suspension was filtered through celite. The subsequent addition of a small amount of D$_2$O (ca. 0.5 mL), followed by the slow diffusion of dry Et$_2$O into the solution afforded analytically pure green crystals.

Yield: 253.2 mg, 78 %.

Elemental Analysis (FeC$_{29}$ClD$_2$H$_{37}$N$_4$O$_7$):

	C	H	N
calculated	53.68	6.06	8.63
found	53.59	5.96	8.74

IR (ATR, cm^{-1}): 3345, 3079, 2976, 2490, 2192, 1597, 1579, 1523, 1464, 1441, 1402, 1292, 1260, 1223, 1191, 1159, 1090, 1069, 1024, 1012, 965, 936, 911, 848, 805, 794, 778, 753, 719, 681, 647, 621, 563, 523.

ESI-MS(+): calculated: m/z = 549.2; found m/z = 529.3 (main signal). The D$_2$O ligand is lost under ESI-MS conditions.

Structural analysis was not conducted. For representative structural data for the non-deuterated analogue **2a** see section 2.1.2 and attachment

8.1.9. Synthesis of [Fe(L-N$_4$^{t}Bu$_2$)(O$_2$CPh)(OH$_2$)](PF$_6$) (2b)

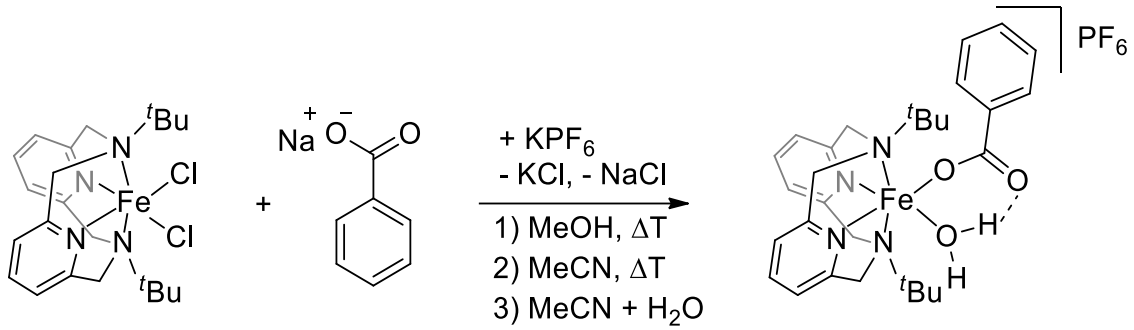

478.14 g/mol 144.02 g/mol 692.46 g/mol

Approach: 241.1 mg (0.50 mmol) [Fe(L-N$_4$^{t}Bu$_2$)(Cl)$_2$] (**5**)
71.9 mg (0.50 mmol) sodium benzoate
92.3 mg (0.50 mmol) potassium hexafluorophosphate

Under an atmosphere of nitrogen, **5**, PhCO$_2$Na, and KP$_6$ were dissolved in MeOH (50 mL). The resulting yellow reaction mixture was heated to reflux twice. After removal of the solvent, the solid residue was treated with MeCN (15 mL). The resulting suspension was heated to reflux before the solvent was once more removed (in order to remove traces of MeOH). The residue was again treated with MeCN (20 mL) and the suspension was filtered through celite. The subsequent addition of a small amount of deionized water (ca. 0.5-1 mL), followed by the slow diffusion of Et$_2$O into the solution afforded analytically pure green crystals.

Yield: 252.0 mg, 73 %.

Elemental Analysis (FeC$_{29}$F$_6$H$_{39}$N$_4$O$_3$P):

	C	H	N
calculated	50.30	5.68	8.09
found	50.20	5.75	8.12

IR (ATR, cm^{-1}): 3575, 2975, 2901, 1601, 1582, 1467, 1435, 1391, 1248, 1225, 1192, 1168, 1078, 1027, 937, 913, 834, 787, 740, 717, 687, 667, 555, 499, 445, 435, 422, 412.

ESI-MS(+): calculated: m/z = 547.2; found m/z = 529.3 (main signal). The H$_2$O ligand is lost under ESI-MS conditions.

For structural data see 2.1.2 and attachment.

8.1.10. Synthesis of [Fe(L-N$_4$*t*Bu$_2$)(O$_2$CPh)(OH$_2$)](CF$_3$SO$_3$) (2c)

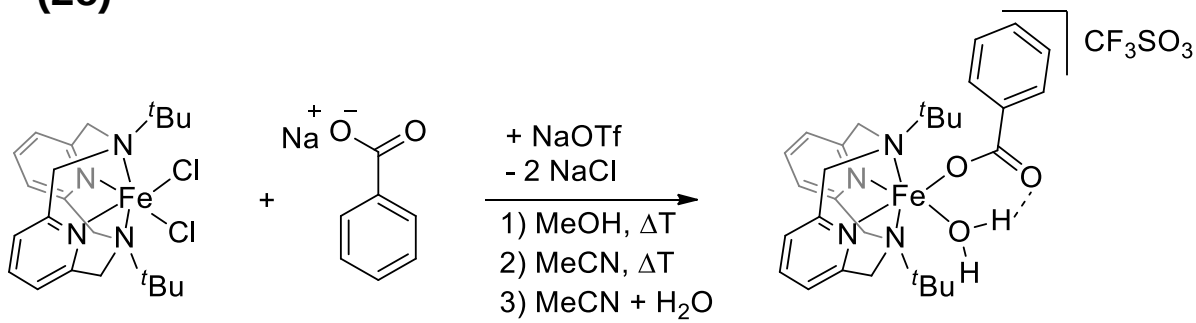

478.14 g/mol 144.02 g/mol 696.56 g/mol

Approach: 242.3 mg (0.51 mmol) [Fe(L-N$_4$*t*Bu$_2$)(Cl)$_2$] (**5**)
72.2 mg (0.50 mmol) sodium benzoate
85.9 mg (0.50 mmol) sodium triflate

Under an atmosphere of nitrogen, **5**, PhCO$_2$Na, and NaOTf were dissolved in MeOH (50 mL). The resulting yellow reaction mixture was heated to reflux twice. After removal of the solvent, the solid residue was treated with MeCN (15 mL). The resulting suspension was heated to reflux before the solvent was once more removed (in order to remove traces of MeOH). The residue was again treated with MeCN (20 mL) and the suspension was filtered through celite. The subsequent addition of a small amount of deionized water (ca. 0.5-1 mL), followed by the slow diffusion of Et$_2$O into the solution afforded analytically pure green crystals.

Yield: 250.9 mg, 71 %.

Elemental Analysis (FeC$_{30}$F$_3$H$_{39}$N$_4$O$_6$S):

	C	H	N	S
calculated	51.73	5.64	8.04	4.60
found	51.70	5.71	8.13	4.71

IR (ATR, cm^{-1}): 3338, 2977, 2904, 1601, 1581, 1541, 1465, 1435, 1403, 1388, 1296, 1241, 1223, 1194, 1153, 1076, 1031, 936, 913, 853, 788, 771, 755, 717, 688, 672, 635, 571, 553, 514, 445, 425, 414, 402.

ESI-MS(+): calculated: m/z = 547.2; found m/z = 529.3 (main signal). The H$_2$O ligand is lost under ESI-MS conditions.

For structural data see 2.1.2 and attachment.

8.1.11. Synthesis of $[Fe(L\text{-}N_4{}^tBu_2)(O_2CPh^{pOMe})(OH_2)](CF_3SO_3)$ (11a)

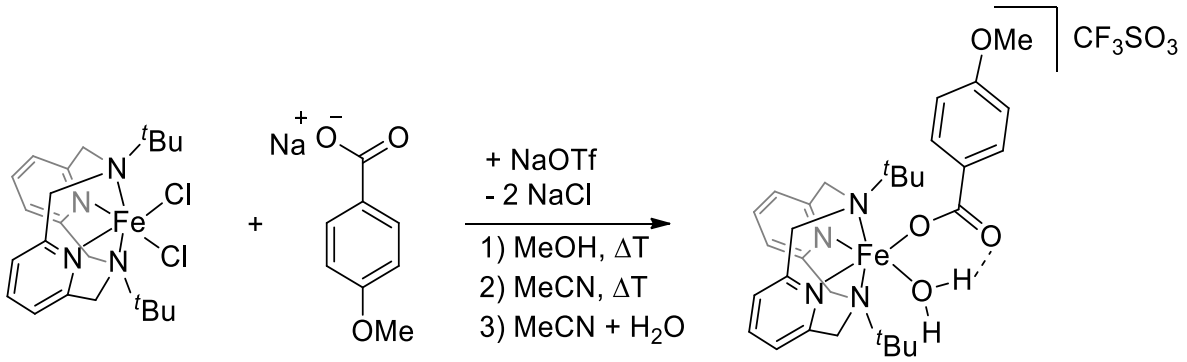

478.14 g/mol 174.05 g/mol 726.59 g/mol

Approach: 119.7 mg (0.25 mmol) $[Fe(L\text{-}N_4{}^tBu_2)(Cl)_2]$ (**5**)
44.1 mg (0.25 mmol) sodium *para*-methoxybenzoate
38.1 mg (0.22 mmol) sodium triflate

Under an atmosphere of nitrogen, **5**, $^{pOMe}PhCO_2Na$, and NaOTf were dissolved in MeOH (30 mL). The resulting yellow reaction mixture was heated to reflux twice. After removal of the solvent, the solid residue was treated with MeCN (10 mL). The resulting suspension was heated to reflux before the solvent was once more removed (in order to remove traces of MeOH). The residue was again treated with MeCN (10 mL) and the suspension was filtered through celite. The subsequent addition of a small amount of deionized water (ca. 0.5 mL), followed by the slow diffusion of Et_2O into the solution afforded analytically pure yellow-green crystals.

Yield: 51.1 mg, 32 %.

Elemental Analysis ($FeC_{31}H_{41}F_3N_4O_7S$):

	C	H	N	S
calculated	51.24	5.69	7.71	4.41
found*	50.71	6.07	7.34	4.09
found**	51.45	5.87	7.81	4.31

* found after storage under air for a few days after isolation. ** found after storage under air for one month after isolation. Differences are explained by evaporation of crystal water contained in the structure of the freshly isolated crystals as identified by IR spectroscopy (see section 3.1.5).

IR (ATR, cm^{-1}): 3336, 3075, 2970, 2920, 1602,1582,1509, 1465, 1439, 1414, 1402, 1379, 1369, 1310, 1280, 1245, 1224, 1193, 1168, 1159, 1138, 1100, 1077, 1048, 1029, 966, 936, 912, 852, 827, 786, 770, 758, 732, 712, 100, 636, 615, 575, 559, 515. (Represents the sample after one month storage under aerobic conditions to allow for evaporation of potential water residues in the crystal packing).

ESI-MS: calculated: m/z = 577.2; found m/z = 559.5 (main signal). The H_2O ligand is lost under ESI-MS conditions.

Preliminary structural data could be obtained to verify the structural motif, determine connectivity, and identify electron density residues that correspond to solvent molecule(s) in the crystal packing upon isolation. Cell parameters (298 K): *a* = 13.2413 Å, *b* = 16.9263 Å, *c* = 19.8044 Å, α = 66.467°, β = 85.844°, γ = 80.116°. More information can be provided upon request by Dr. Harald Kelm (internal reference number: 21248ocb).

8.1.12. Synthesis of [Fe(L-N$_4$*t*Bu$_2$)(O$_2$CPh)](ClO$_4$)·MeCN (3a)

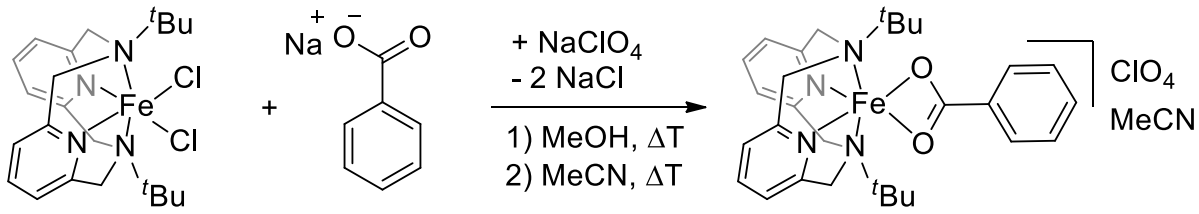

478.14 g/mol 144.02 g/mol 669.98 g/mol

Approach: 240.2 mg (0.50 mmol) [Fe(L-N$_4$*t*Bu$_2$)(Cl)$_2$] (**5**)

72.4 mg (0.50 mmol) sodium benzoate

61.7 mg (0.50 mmol) sodium perchlorate

Under an atmosphere of nitrogen, **5**, PhCO$_2$Na, and NaClO$_4$ were dissolved in MeOH (40 mL, abs.) and heated to reflux three times. After the solvent was removed, the residue was treated with rigorously dried MeCN (20 mL, abs.). The resulting suspension was heated to reflux and then the solvent was removed again. After renewed addition of dry MeCN (20 mL, abs.), the solution was filtered through celite. Yellow crystals were obtained by slow diffusion of Et$_2$O (abs.) into the clear solution.

Yield: 228.8 mg, 71 %.

Elemental Analysis (FeC$_{31}$ClH$_{40}$N$_5$O$_6$):

	C	H	N
calculated	55.57	6.02	10.45
found	55.31	5.92	10.24

IR (ATR, cm^{-1}): 2984, 2902, 2250, 1600, 1579, 1537, 1497, 1467, 1446, 1404, 1226, 1190, 1078, 1023, 1014, 948, 908, 856, 813, 793, 762, 737, 726, 689, 620, 548, 525.

ESI-MS: calculated: m/z = 529.2; found m/z = 529.3 (main signal).

For structural data see 2.1.2 and attachment.

8.1.13. Synthesis of [Fe(L-N$_4$*t*Bu$_2$)(O$_2$CPh^{pNO2})](ClO$_4$)·MeCN (9a)

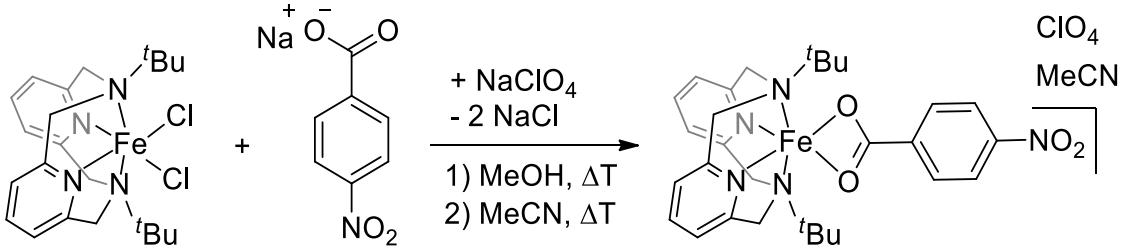

478.14 g/mol 189.02 g/mol 714.98 g/mol

Approach: 120.7 mg (0.25 mmol) [Fe(L-N$_4$*t*Bu$_2$)(Cl)$_2$] (**5**)
47.8 mg (0.25 mmol) sodium *para*-nitrobenzoate
30.8 mg (0.25 mmol) sodium perchlorate

Under an atmosphere of nitrogen, **5**, ^{pNO2}PhCO$_2$Na, and NaClO$_4$ were dissolved in MeOH (40 mL, abs.) and heated to reflux three times. After the solvent was removed, the residue was treated with rigorously dried MeCN (20 mL, abs.). The resulting suspension was heated to reflux and then the solvent was removed again. After renewed addition of dry MeCN (20 mL, abs.), the solution was filtered through celite. A yellow crystalline solid was obtained by slow diffusion of Et$_2$O (abs.) into the clear solution in the dark at 4 °C. The yellow solid rapidly turned orange-red upon isolation and exposure to air.

Yield: 130.5 mg, 73 %

Elemental Analysis (FeC$_{31}$ClH$_{41}$N$_6$O$_9$):

	C	H	N
calculated	11.47	50.80	5.64
found	11.25	50.62	5.62

IR (ATR, cm^{-1}): 3084, 3047, 2976, 2925, 2908, 2275, 1636, 1598, 1578, 1520, 1479, 1463, 1432, 1404, 1381, 1363, 1338, 1319, 1293, 1260, 1226, 1192, 1163, 1085, 1025, 1013, 1000, 963, 936, 913, 904, 877, 851, 819, 789, 780, 751, 724, 712, 645, 622, 561, 518.

ESI-MS(+): calculated: 574.3 m/z =; found m/z = 574.2 (main signal).

No structural data could be obtained.

8.1.14. Synthesis of [Fe(L-N$_4$^{t}Bu$_2$)(O$_2$CPh^{pOMe})](ClO$_4$)·MeCN (12a)

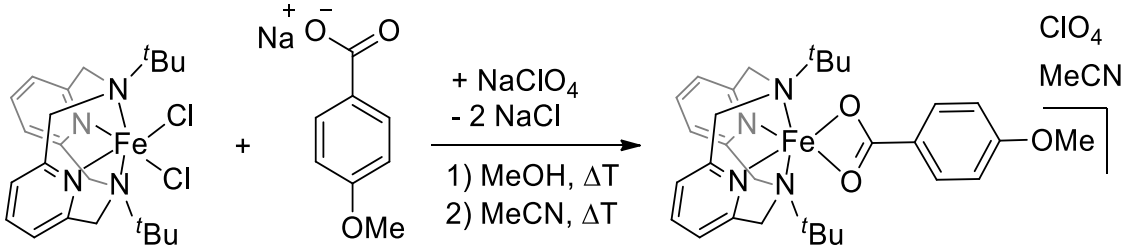

478.14 g/mol 174.05 g/mol 700.01 g/mol

Approach: 240.2 mg (0.50 mmol) [Fe(L-N$_4$^{t}Bu$_2$)(Cl)$_2$] (**5**)
87.1 mg (0.50 mmol) sodium *para*-methoxybenzoate
30.8 mg (0.25 mmol) sodium perchlorate

Under an atmosphere of nitrogen, **5**, ^{pOMe}PhCO$_2$Na, and NaClO$_4$ were dissolved in MeOH (40 mL) and heated to reflux twice. After the solvent was removed, the residue was treated with MeCN (20 mL). The resulting suspension was heated to reflux and then the solvent was removed again. After renewed addition of MeCN (20 mL), the solution was filtered through celite. Yellow crystalline blocks were obtained along other side products by slow diffusion of Et$_2$O (abs.) into the clear solution. *Note: The compound was only obtained once in crystalline form via this method with erroneous stoichiometry but could be well separated via crystal sorting.*

Yield: 35.9 mg, 20 %.

Elemental Analysis (1. FeC$_{32}$ClH$_{39}$N$_5$O$_7$, 2. FeC$_{30}$ClH$_{36}$N$_4$O$_7$, FeC$_{30}$ClH$_{38}$N$_4$O$_8$, FeC$_{30}$ClH$_{39}$N$_4$O$_{7.5}$):

	C	H	N	
calculated (1)	55.14	5.64	10.05	[**12**]ClO$_4$·MeCN
calculated (2)	54.93	5.53	8.54	[**12**]ClO$_4$
calculated (3)	53.47	5.68	8.31	[**12**]ClO$_4$·H$_2$O
calculated (4)	54.19	5.61	8.43	[**12**]ClO$_4$·0.5H$_2$O
found	54.52	5.93	8.47	

The elemental analysis was measured after prolonged storage in a vial under air. The surface of the crystal blocks had visibly turned dull. It is likely that the MeCN molecule was lost and the hygroscopic compound attracted some water from air.

IR (ATR, cm^{-1}): 3093, 3047, 2979, 2967, 2920, 2815, 2250, 1603, 1589, 1580, 1536, 1510, 1469, 1415, 1404, 1391, 1378, 1370, 1317, 1296, 1262, 1227, 1189, 1173, 1139, 1106, 1086, 1076, 1026, 1015, 1006, 950, 911, 875, 862, 855, 813, 787, 763, 737, 729, 704, 638, 621, 571, 551, 527, 513, 501, 452.

ESI-MS(+): calculated: 559.2 m/z =; found m/z = 559.5 (main signal).

For structural data see 3.1.2 and attachment.

8.1.15. Synthesis of [Fe(L-N$_4$*t*Bu$_2$)(OMe)$_2$](BPh$_4$) (4a)

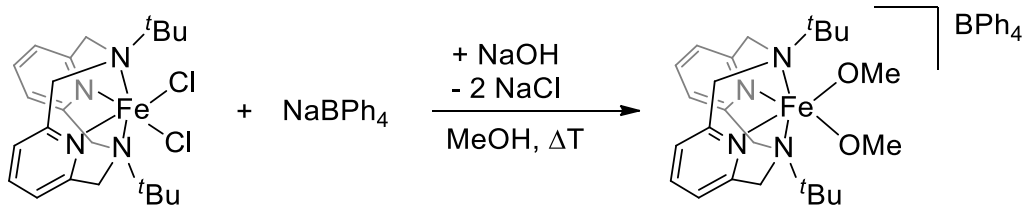

478.14 g/mol 342.22 g/mol 789.64 g/mol

Approach: 282.7 mg (0.59 mmol) [Fe(L-N$_4$*t*Bu$_2$)(Cl)$_2$] (**5**)
201.7 mg (0.59 mmol) sodium tetraphenylborate
106 mg (2.65 mmol) sodium hydroxide

A mixture of **5**, NaBPh$_4$, and an excess of NaOH in MeOH (50 mL) was stirred under air and heated to reflux. Hot MeOH was added until a clear solution was observed. The product crystallised as analytically pure yellow rods upon cooling to 4 °C. The yield could be enhanced by slow evaporation of the solvent. The crystals were washed with freshly distilled Et$_2$O prior to isolation.

Yield: 424.3 mg, 91 %

Note: The product turns dark blue-black when exposed to light, thus the sample should be stored in a brown-glass vial or in the dark. The crystallinity appears to stay intact even after prolonged storage and significant darkening and the cell parameters remain the same. Thus, it is likely that this is a surface effect that was not further studied in this work.

Elemental Analysis (FeBC$_{48}$H$_{58}$N$_4$O$_2$):

	C	H	N
calculated	73.01	7.40	7.09
found	72.83	7.30	7.13

IR (ATR, cm^{-1}): 3053, 2980, 2904, 2855, 2788, 1604, 1580, 1466, 1428, 1400, 1376, 1365, 1254, 1187, 1162, 1113, 1075, 1032, 962, 938, 911, 849, 790, 780, 749, 731, 702, 648, 623, 611, 561, 497.

Magnetic moment (298 K): μ = 6.11 μ_B (χT = 4.66 cm^{3}Kmol^{-1}).

Mößbauer parameters (10 K): δ_{IS} = 0.42 mms^{-1} ΔE_q = 2.16 mms^{-1}. Parameters are preliminary as the signal is very broad and an applied external magnetic field is necessary for a more accurate determination.

EPR (10 K, DMF/TBAP): g_{eff} = 6.63, 5.35, 1.98 (M_s = ±1/2), 5.98 (M_s = ±3/2). g_{real} = 1.965, 2.035, 1.998.

For structural data see 2.1.2 and attachment.

8.1.16. Synthesis of [Fe(L-N$_4$*t*Bu$_2$)(OMe)$_2$](PF$_6$) (4b)

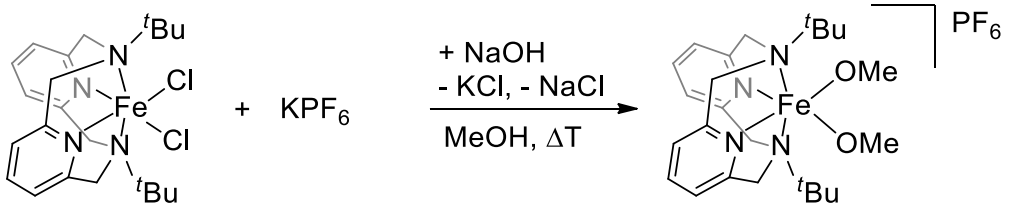

478.14 g/mol 184.06 g/mol 615.40 g/mol

Approach: 240.6 mg (0.50 mmol) [Fe(L-N$_4$*t*Bu$_2$)(Cl)$_2$] (**5**)
99.6 mg (0.54 mmol) potassium hexafluorophosphate
48.3 mg (1.21 mmol) sodium hydroxide

A mixture of **5**, KPF_6, and a slight excess of NaOH in MeOH (50 mL) was stirred under air and heated to reflux. Hot MeOH was added until a clear solution was observed. The product crystallised as analytically pure dark yellow blocks upon cooling to 4 °C. The yield could be enhanced by slow evaporation of the solvent. The crystals were washed with freshly distilled Et_2O prior to isolation.

Yield: 231.7 mg, 75 %.

Elemental Analysis ($FeC_{24}F_6H_{38}N_4O_2P$):

	C	H	N
calculated	46.84	6.22	9.10
found	46.76	6.20	9.19

IR (ATR, cm^{-1}): 2982, 2901, 2873, 2792, 1602, 1585, 1471, 1433, 1406, 1385, 1369, 1291, 1262, 1230, 1185, 1156, 1113, 1088, 1076, 1031, 1006, 938, 907, 879, 829, 791, 779, 752, 730, 711, 647, 626, 556, 517, 500.

^{1}H-NMR(400 MHz, CD_3CN) δ(ppm) = 133.68 (br), 94.62 (s), 85.41 (br), 11.36 (br), 4.40 – 2.70 (br), -0.45 (br). Additional signals found at 3.43 ppm and 1.28 ppm are attributed to Et_2O residues.[131]

For electrochemical data see 2.1.10. For structural data see 2.1.2 and attachment.

8.1.17. Synthesis of [Fe(L-N$_4$^{t}Bu$_2$)(OMe)$_2$](ClO$_4$) (4c)

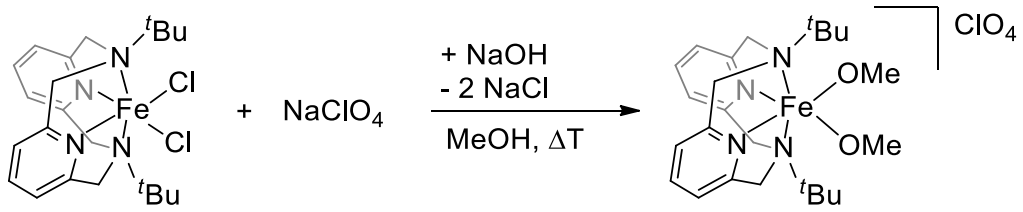

478.14 g/mol 122.44 g/mol 569.89 g/mol

Approach: 241.7 mg (0.51 mmol) [Fe(L-N$_4$^{t}Bu$_2$)(Cl)$_2$] (**5**)
61.3 mg (0.50 mmol) sodium perchlorate
41.5 mg (1.04 mmol) sodium hydroxide

A mixture of **5**, NaClO$_4$, and NaOH in MeOH (50 mL) was stirred under air and heated to reflux. Hot MeOH was added until a clear solution was observed. The product crystallised as analytically pure yellow blocks upon slow cooling to 4 °C. The yield could be enhanced by storing the mixture at -35 °C for 2 weeks or slow evaporation of the solvent at room temperature. The crystals were washed with freshly distilled Et$_2$O prior to isolation.

Yield: 258.7 mg, 91 %.

Elemental Analysis (FeC$_{24}$H$_{38}$N$_4$O$_6$):

	C	H	N
calculated	50.58	6.72	9.83
found	50.32	6.62	9.78

IR (ATR, cm^{-1}): 3091, 3051, 3004, 2970, 2909, 2873, 2839, 2774, 1626, 1604, 1584, 1468, 1443, 1402, 1377, 1350, 1339, 1294, 1265, 1251, 1229, 1191, 1173, 1162, 1155, 1077, 1025, 1004, 962, 939, 910, 852, 802, 792, 781, 752, 732, 713, 647, 620, 560, 531, 504, 481.

For structural data see 2.1.2 and attachment.

8.1.18. Synthesis of [Fe(L-N$_4$*t*Bu$_2$)(O$_2$CPh)(OH)](BPh$_4$) (1a)

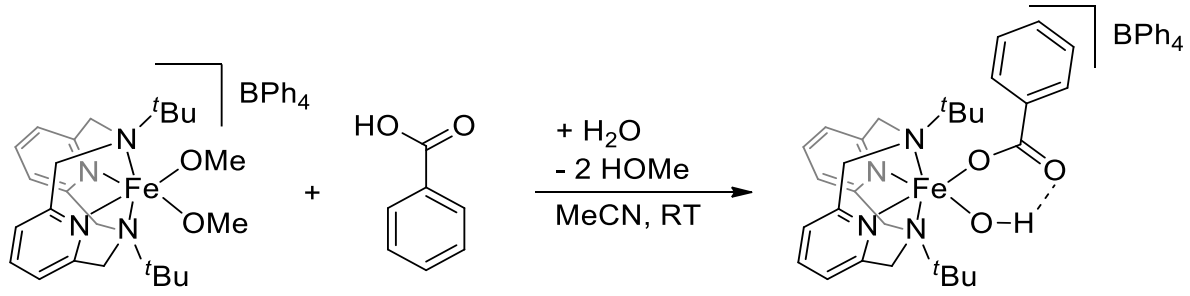

789.64 g/mol 122.12 g/mol 865.69 g/mol

Approach: 157.8 mg (0.20 mmol) [Fe(L-N$_4$*t*Bu$_2$)(OMe)$_2$]BPh$_4$ (**4a**)
24.9 mg (0.20 mmol) benzoic acid

Under air, a mixture of **4a** and benzoic acid was suspended in MeCN (10 mL). The resulting brownish-yellow solution was filtered, and 6 drops of water (deionized) were added. The volume was reduced to 5 mL and the mixture was filtered. Crystallisation was achieved by the fractional addition of freshly distilled Et$_2$O at 4 °C in the dark to the filtrate. The yellow-brown crystals were washed with freshly distilled Et$_2$O prior to isolation.

Yield: 105.2 mg, 61 %.

Elemental Analysis (FeBC$_{53}$H$_{58}$N$_4$O$_3$):

	C	H	N
calculated	73.53	6.75	6.47
found	73.33	6.66	6.56

IR (ATR, cm^{-1}): 3313, 3052, 2977, 1654, 1600, 1578, 1467, 1425, 1402, 1379, 1326, 1311, 1297, 1251, 1162, 1129, 1069, 1026, 938, 903, 844, 795, 776, 748, 734, 704, 670, 670, 654, 637, 625, 611, 601, 573, 466.

ESI-MS(+): calculated: m/z = 546.2; found m/z = 546.3 (main signal).

Magnetic moment (298 K): μ = 6.16 μ_B (χT = 4.74 cm^{3}Kmol^{-1}).

Mößbauer parameters: δ_{IS} = 0.42 mms^{-1} (90 K), 0.30 mms^{-1} (298 K); ΔE_q = 2.25 mms^{-1} (90 K), 2.26 mms^{-1} (298 K).

EPR (10 K, DMF/TBAP): g_{eff} = 8.12, 3.55, 1.69 (M_S = ±1/2), 5.65, 2.27 (M_S = ±3/2). g_{real} = 1.999, 1.997, 1.995.

For electronic spectroscopy data see 2.1.6 (solid). For electrochemical data see 3.1.9. For structural data see 2.1.2 and attachment.

8.1.19. Synthesis of [Fe(L-N$_4$^{t}Bu$_2$)(O$_2$CPh)(OH)](BPh$_4$)·MeCN (1b)

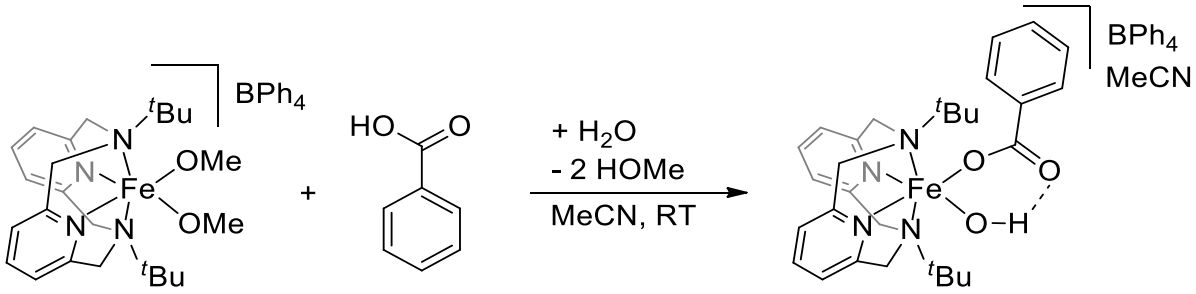

789.64 g/mol 122.12 g/mol 906.74 g/mol

Approach: 281.3 mg (0.36 mmol) [Fe(L-N$_4$^{t}Bu$_2$)(OMe)$_2$]BPh$_4$ (**4a**)
43.7 mg (0.36 mmol) benzoic acid

Under air, a mixture of **4a** and benzoic acid was suspended in MeCN (10 mL). The resulting brownish-yellow solution was filtered, and 4 drops of water (deionized) were added. Crystallisation was achieved by the fractional addition of freshly distilled Et$_2$O at 4 °C in the dark. The brown crystals were washed with freshly distilled Et$_2$O prior to isolation.

Yield: 245.2 mg, 75 %.

Elemental Analysis (FeBC$_{55}$H$_{61}$N$_5$O$_3$):

	C	H	N
calculated	72.85	6.78	7.72
found	72.69	6.95	7.52

IR (ATR, cm^{-1}): 3392, 3052, 2982, 1623, 1603, 1579, 1469, 1447, 1429, 1406, 1380, 1321, 1298, 1264, 1165, 1129, 1092, 1069, 1031, 938, 905, 849, 784, 748, 735, 704, 667, 651, 611, 575, 471.

ESI-MS(+): calculated: m/z = 546.2; found m/z = 546.3 (main signal).

Magnetic moment (298 K): μ = 6.07 μ_B (χT = 4.61 cm^{3}Kmol^{-1}).

For electronic spectroscopy data see 2.1.7 (MeCN). For structural data see 2.1.2 and attachment.

8.1.20. Synthesis of [Fe(L-N$_4$*t*Bu$_2$)(O$_2$CPh)(OH)](PF$_6$) (1c)

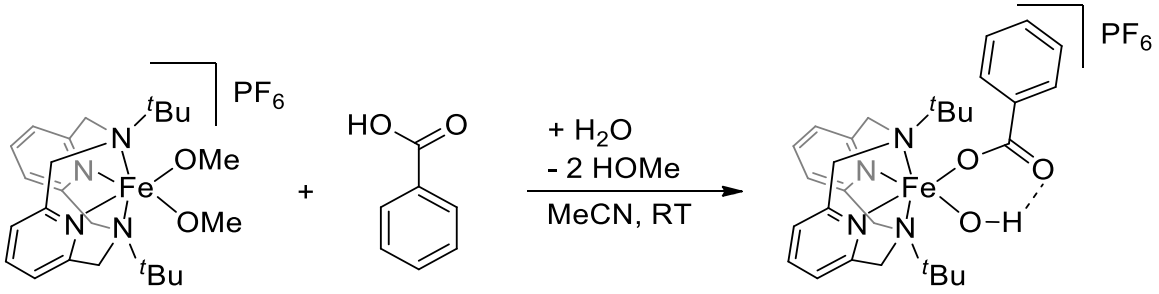

615.40 g/mol 122.12 g/mol 691.45 g/mol

Approach: 228.4 mg (0.33 mmol) [Fe(L-N$_4$*t*Bu$_2$)(OMe)$_2$]PF$_6$ (**4b**)
41.2 mg (0.34 mmol) benzoic acid

Under air, a mixture of **4b** and benzoic acid was suspended in MeCN (10 mL). The resulting brownish-yellow solution was filtered, and 4 drops of water (deionized) were added with a Pasteur pipette. Crystallisation was achieved by the fractional addition of freshly distilled Et$_2$O at 4 °C in the dark. The brown crystals were washed with freshly distilled Et$_2$O prior to isolation.

Yield: 187.2 mg, 82 %.

Elemental Analysis (FeC$_{29}$F$_6$H$_{38}$N$_4$O$_3$P):

	C	H	N
calculated	50.37	5.54	8.10
found	50.08	5.73	8.03

IR (ATR, cm^{-1}): 3289, 2976, 1601, 1574, 1468, 1434, 1408, 1387, 1330, 1304, 1263, 1229, 1180, 1163, 1132, 1092, 1072, 1028, 940, 903, 878, 832, 780, 727, 670, 653, 623, 579, 556, 481, 457.

ESI-MS(+): calculated: m/z = 546.2; found m/z = 546.3 (main signal).

^{1}H-NMR(600 MHz, CD$_3$CN, 1) δ(ppm) = 188.99 (br), 154.15 (br), 123.46 (br), 96.6 (br), 15.83 (s), 12.80 (br), 4.73 (s), 2.31 (s), -2.90 (sh), -3.27 (s). Additional signals found at 3.42 and 1.12 correspond to diethylether residues.[131]

For electrochemical data see 2.1.10. For structural data see 2.1.2 and attachment.

8.1.21. Synthesis of [Fe(L-N$_4$*t*Bu$_2$)(O$_2$CPh-d5)(OH)](PF$_6$) (1^{D}c)

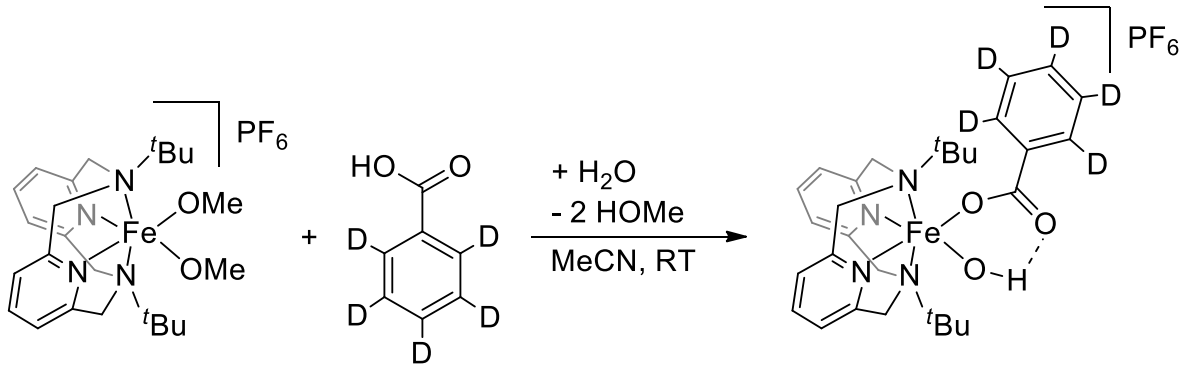

615.40 g/mol 127.12 g/mol 696.45 g/mol

Approach: 138.1 mg (0.22 mmol) [Fe(L-N$_4$*t*Bu$_2$)(OMe)$_2$]PF$_6$ (**4b**)
25.9 mg (0.20 mmol) penta ring-deuterated benzoic acid

Under air, a mixture of **4b** and HO$_2$CPh-d5 was suspended in MeCN (8 mL). The resulting brownish-yellow solution was filtered, and 4 drops of water (deionized) were added with a Pasteur pipette. Crystallisation was achieved by the fractional addition of freshly distilled Et$_2$O at 4 °C in the dark. The brown crystals were washed with freshly distilled Et$_2$O prior to isolation.

Yield: 123.1 mg, 87 %.

Elemental Analysis (FeC$_{29}$H$_{33}$D$_5$F$_6$N$_4$O$_3$P):

	C	H	N
Calculated	50.02	5.71	8.05
found	49.59	5.53	8.00

IR (ATR, cm^{-1}): 3416, 3097, 2976, 2922, 2798, 2280, 1604, 1585, 1568, 1544, 1470, 1438, 1407, 1386, 1331, 1288, 1228, 1184, 1163, 1090, 1073, 1031, 1005, 960, 941, 905, 876, 823, 776, 732, 710, 690, 661, 645, 620, 556, 544, 536. Some vibrational modes may be obscured because of a limited resolution between 2300 – 1900 cm^{-1} and the occurrence of atmospheric CO$_2$ modes.

^{2}H-NMR (400 MHz, 0.2 mol·L^{-1} CD$_3$CN in CH$_3$CN, 1) = 15.81 (s, 2H), 14.49 (s, 2H), 4.81 (s, 1H).

Structural analysis was not conducted. For representative structural data for the non-deuterated analogue **1c** see 2.1.2 and attachment.

8.1.22. Synthesis of [Fe(L-N$_4$^{t}Bu$_2$)(O$_2$CPh)(OD)](BPh$_4$)· xMeCN (1d)

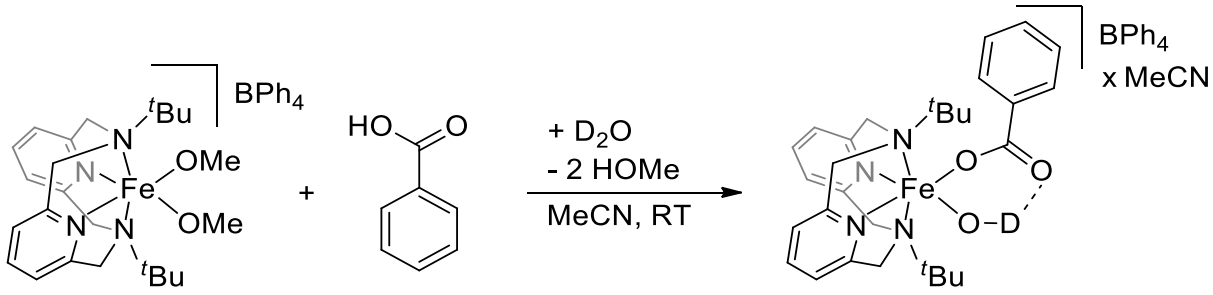

789.64 g/mol 122.12 g/mol 866.69 – 907.74 g/mol

Approach: 197.7 mg (0.25 mmol) [Fe(L-N$_4$^{t}Bu$_2$)(OMe)$_2$]BPh$_4$ (**4a**)
30.6 mg (0.25 mmol) benzoic acid

Benzoic acid (30.6 mg, 0.25 mmol) was dissolved in MeCN/D$_2$O (2 mL/2 mL) for the H/D exchange. After removal of the solvent, **4a** (197.7 mg, 0.25 mmol) was added. The solids were dissolved in MeCN (8 mL). Subsequently D$_2$O was added (0.5 mL). Crystallisation was achieved by fractional additions of freshly distilled, dry Et$_2$O at 4 °C in the dark. All steps were carried out under a nitrogen atmosphere. The brown crystals were washed with freshly distilled Et$_2$O prior to isolation.

Yield: 152.2 mg, 67 – 70 %. Mixtures of both modifications (with MeCN solvent or without) in bulk material possible, thus the percentage yield is given as range.

Elemental Analysis (1. FeBC$_{53}$H$_{57}$DN$_4$O$_3$, 2. FeBC$_{55}$DH$_{60}$N$_5$O$_3$):

	C	H	N
calculated (1)	73.45	6.63	6.46
calculated (2)	72.77	6.66	7.71
found	73.02	6.77	6.53

IR (ATR, cm^{-1}): 3051, 2976, 2470, 1654, 1614, 1600, 1576, 1466, 1425, 1402, 1379, 1326, 1311, 1297, 1250, 1210, 1129, 1069, 1062, 1026, 1001, 938, 904, 844, 795, 776, 735, 704, 653, 636, 625, 611, 595, 571, 534, 506, 466.

ESI-MS(+): calculated: m/z = 547.2; found m/z = 546.3 (main signal). The hydroxide ligand likely participates in H/D exchange with H$_2$O in solution.

Structural analysis was not conducted. For representative structural data for the non-deuterated analogues **1a** and **1b** see 2.1.2 and attachment.

8.1.23. Synthesis of [Fe(L-N$_4$*t*Bu$_2$)(O$_2$CPh^{pNO2})(OH)](BPh$_4$) (7a)

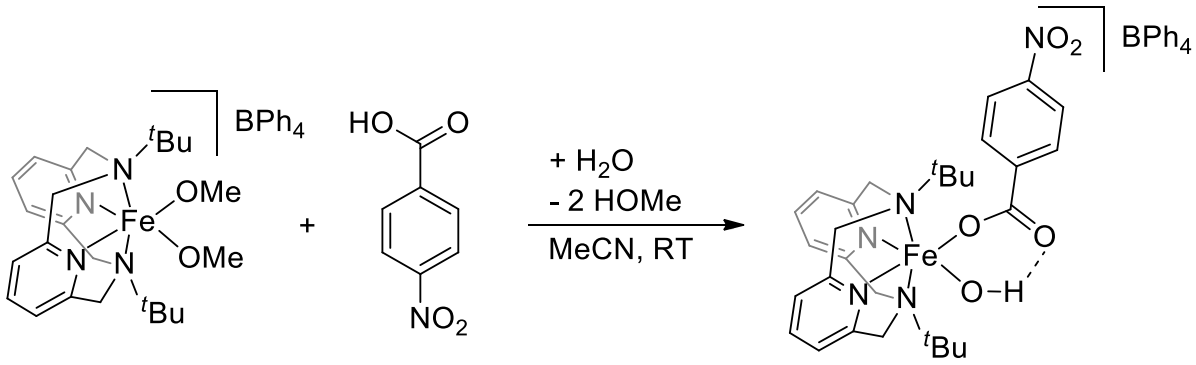

789.64 g/mol 167.12 g/mol 910.71 g/mol

Approach: 151.0 mg (0.19 mmol) [Fe(L-N$_4$*t*Bu$_2$)(OMe)$_2$]BPh$_4$ (**4a**)
34.0 mg (0.20 mmol) *para*-nitrobenzoic acid

Under air, **4a** was dissolved in MeCN (8 mL) and 5 drops of water (deionized) were added with a Pasteur pipette. Neat *para*-nitrobenzoic acid was added to the mixture and the suspension was stirred. The solvent was evaporated under reduced pressure to remove any MeOH residues. The raw product was taken up in MeCN (5 mL) and three drops of water (deionized) were added with a Pasteur pipette. The resulting brownish-orange mixture was filtered, and crystallisation was achieved by the diffusion of freshly distilled Et$_2$O at 4 °C in the dark into the filtrate. The brown crystals were washed with freshly distilled Et$_2$O prior to isolation.

Yield: 122.1 mg, 70 %.

Elemental Analysis (C$_{53}$H$_{57}$BFeN$_5$O$_5$):

	C	H	N
Calculated	69.90	6.31	7.69
found	69.64	6.22	7.66

IR (ATR, cm^{-1}): 3391, 3052, 2980, 1635, 1601, 1580, 1524, 1468, 1430, 1405, 1382, 1366, 1349, 1314, 1258, 1214, 1180, 1165, 1129, 1109, 1099, 1090, 1069, 1030, 1014, 1003, 962, 938, 905, 880, 862, 848, 794, 781, 751, 732, 723, 704, 651, 632, 609, 579, 561, 532, 509, 471, 464.

ESI-MS(+): calculated: m/z = 591.2; found m/z = 591.5 (main signal).

Magnetic moment (298 K): μ = 6.22 μ_B (χT = 4.83 cm^3Kmol^{-1}).

For structural data see 3.1.2 and attachment.

8.1.24. Synthesis of [Fe(L-N$_4$*t*Bu$_2$)(O$_2$CPh^{pNO2})(OH)](ClO$_4$) (7b)

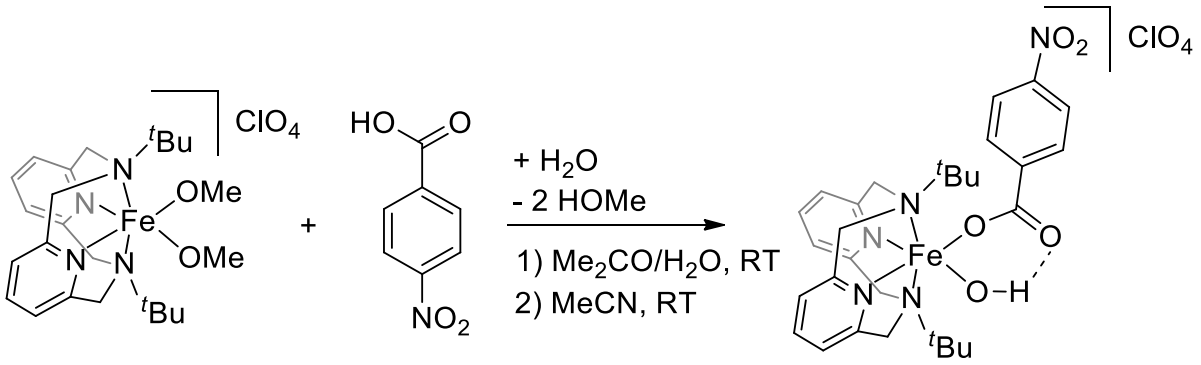

569.89 g/mol 167.12 g/mol 690.94 g/mol

Approach: 148.4 mg (0.26 mmol) [Fe(L-N$_4$*t*Bu$_2$)(OMe)$_2$]ClO$_4$ (**4c**)
38.0 mg (0.23 mmol) *para*-nitrobenzoic acid

4c (148.4 mg, 0.26 mmol) was dissolved in a mixture of Acetone (50 mL) and deionized water (20 mL). The solvent was allowed to evaporate under air and the dry solid was isolated for further conversion (120.6 mg). Under air the crude product was dissolved in MeCN (14 mL) and neat *p*-nitrobenzoic acid (38.0 mg, 0.23 mmol) was added. The mixture was treated with 7 drops of water (deionized) using a Pasteur pipette and the resulting brownish-yellow mixture was filtered over celite. Crystallisation was achieved by diffusion of freshly distilled Et$_2$O at 4 °C in the dark into the filtrate. The ochre-yellow crystals were washed with freshly distilled Et$_2$O prior to isolation.

Yield: 121.1 mg, 77 %.

Elemental Analysis (FeC$_{29}$ClH$_{37}$N$_5$O$_9$):

	C	H	N
calculated	50.41	5.40	10.14
found	50.19	5.38	9.99

IR (ATR, cm^{-1}): 3372, 3096, 3048, 2971, 2923, 2882, 1628, 1600, 1587, 1522, 1470, 1436, 1407, 1383, 1323, 1313, 1267, 1252, 1230, 1182, 1165, 1132, 1073, 1029, 1013, 961, 938, 907, 877, 860, 849, 793, 783, 724, 713, 702, 651, 620, 579, 561, 534, 512.

^{1}H-NMR(400 MHz, CD_3CN) δ(ppm) = 192.36 (br), 156.40 (br), 125.75 (br), 97.34 (br), 16.19 (s), 15.40 (s), 13.65 (br), 2.15 (s), -2.99 (br), -3.84 (br). Additional signals at 3.42 and 1.12 correspond to diethylether residues.[131]

ESI-MS(+): calculated: m/z = 591.2; found m/z = 591.3 (main signal).

Magnetic moment (298 K): μ = 6.01 μ_B (χT = 4.51 cm^3Kmol^{-1}).

Mößbauer parameters (298 K): δ_{IS} = 0.31 mms^{-1}, ΔE_q = 2.32 mms^{-1}.

EPR (10 K, DMF/TBAP): g_{eff} = 8.03, 3.50, 1.66 (M_s = ±1/2), 5.57, 2.27 (M_s = ±3/2). g_{real} = 1.982, 1.963, 1.970. Minor impurities are found at g_{eff} = 4.77, 4.24, 4.17.

For electronic spectroscopy data (solid and MeCN solution) see 3.1.6. For electrochemical data see 3.1.9. For structural data see 3.1.2 and attachment.

8.1.25. Synthesis of [Fe(L-N$_4$*t*Bu$_2$)(O$_2$CPh^{pOMe})(OH)](BPh$_4$) (10a)

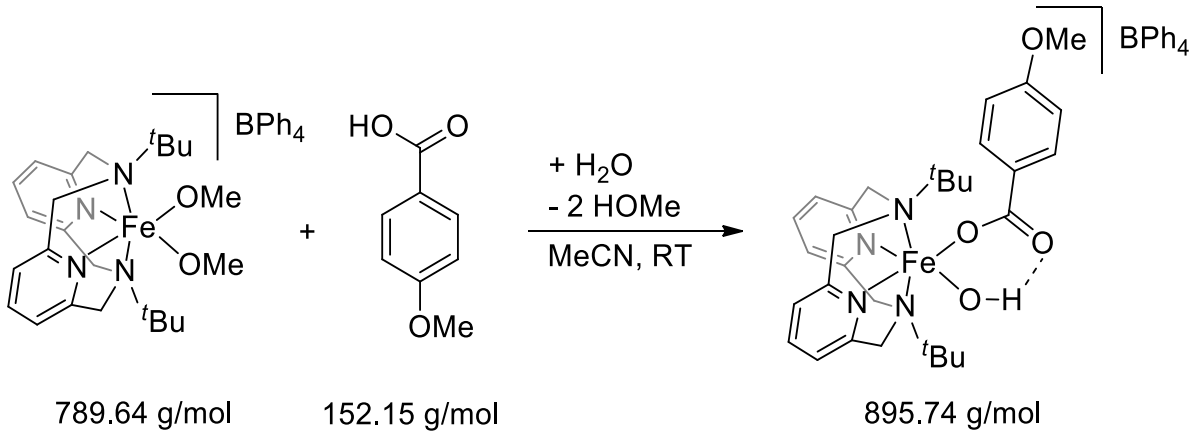

789.64 g/mol 152.15 g/mol 895.74 g/mol

Approach: 112.9 mg (0.14 mmol) [Fe(L-N$_4$*t*Bu$_2$)(OMe)$_2$]BPh$_4$ (**4a**)
22.3 mg (0.15 mmol) *para*-anisic acid

Under air, a mixture of **4a** and *para*-anisic acid was dissolved in MeCN (6 mL). Six drops of deionized water were added using a Pasteur pipette and the resulting brownish-yellow solution was dried under reduced pressure. The residue was again treated with MeCN (6 mL) and 5 drops of water (deionized) were added using a Pasteur pipette. Crystallisation was achieved by diffusion of freshly distilled Et$_2$O at 4 °C in the dark. The ochre-yellow crystals were washed with freshly distilled Et$_2$O prior to isolation.

Yield: 112.7 mg, 88 %.

Elemental Analysis (FeBC$_{54}$H$_{60}$N$_4$O$_4$):

	C	H	N
calculated	72.41	6.75	6.25
found	72.29	6.72	6.27

IR (ATR, cm^{-1}): 3308, 3052, 3033, 3006, 2979, 2965, 2932, 2837, 1616, 1602, 1581, 1507, 1477, 1469, 1429, 1405, 1382, 1367, 1322, 1310, 1295, 1255, 1213, 1185, 1166, 1153, 1133, 1102, 1071, 1031, 1012, 1004, 975, 963, 939, 905, 877, 849, 819, 792, 782, 767, 749, 731, 703, 650, 634, 611, 570, 560, 534, 512, 485, 473, 463.

^{1}H-NMR(400 MHz, CD_3CN, 10) δ(ppm) = 188.99 (br), 154.15 (br), 123.46 (br), 96.60 (br), 14.40 (s), 12.55 (br), 5.43 (s), -3.0 (br). Additional signals at 3.42 and 1.12 correspond to diethylether residues.[131]

Magnetic moment (298 K): μ = 6.08 μ_B (χT = 4.62 cm^3Kmol^{-1}).

Mößbauer parameters (298 K): δ_{IS} = 0.30 mms^{-1}, ΔE_q = 2.31 mms^{-1}.

EPR (10 K, DMF/TBAP): g_{eff} = 8.06, 3.60, 1.70 (M_s = ±1/2), 5.63, 2.22 (M_s = ±3/2). g_{real} = 2.003, 1.982, 1.991. Minor impurities are found at g_{eff} = 4.81, 4.28.

For electronic spectroscopy data (solid and MeCN solution) see 3.1.6. For electrochemical data see 3.1.9. For structural data see 3.1.2 and attachment.

8.1.26. Synthesis of [Fe(L-N$_4$^{t}Bu$_2$)(O$_2$CPh^{pOMe})(OH)](ClO$_4$)·H$_2$O (10b)

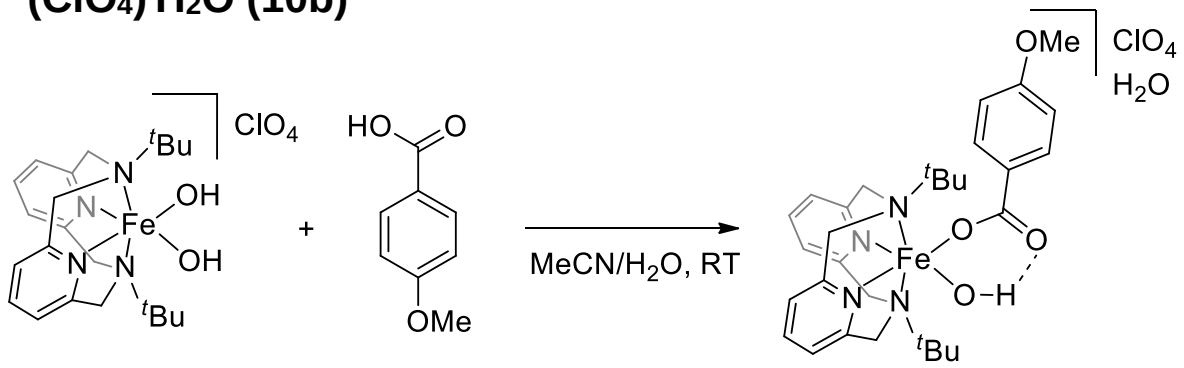

541.82 g/mol 152.15 g/mol 693.97 g/mol

Approach: 135.4 mg (0.25 mmol) [Fe(L-N$_4$^{t}Bu$_2$)(OH)$_2$]ClO$_4$ (*in situ* from **4c**)
31.0 mg (0.20 mmol) *para*-anisic acid

4c was dissolved in a mixture of Acetone (50 mL) and deionized water (20 mL). The solvent was allowed to evaporate under air and the dry solid was isolated for further conversion. Under air, the *in situ* generated [Fe(L-N$_4$^{t}Bu$_2$)(OH)$_2$]ClO$_4$ ([**14**]ClO$_4$) was dissolved in MeCN (12 mL) and neat *p*-anisic acid was added. The mixture was treated with 6 drops of water (deionized) using a Pasteur pipette and the resulting brownish-yellow mixture was filtered over celite. Crystallisation was achieved by diffusion of freshly distilled Et$_2$O at 4 °C in the dark into the filtrate. The yellow microcrystalline solid was washed with freshly distilled Et$_2$O prior to isolation.

Yield: 77.1 mg, 55 %.

Elemental Analysis (FeC$_{30}$ClH$_{40}$N$_4$O$_8$):

	C	H	N
calculated	51.92	6.10	8.07
found	51.90	5.91	8.22

IR (ATR, cm^{-1}): 3401, 3093, 3057, 2972, 2922, 2838, 1602, 1574, 1507, 1470, 1437, 1406, 1383, 1369, 1327, 1317, 1303, 1253, 1230, 1183, 1164, 1134, 1074, 1028, 1006, 961, 938, 907, 848, 802, 791, 781, 761, 752, 731, 712, 698, 650, 635, 617, 578, 561, 534, 507, 486.

ESI-MS(+): calculated: m/z = 576.3; found m/z = 576.2 (main signal).

No structural data could be obtained.

8.1.27. Synthesis of [Fe(L-N$_4$^{t}Bu$_2$)(O$_2$CPh^{pOMe})(OH)](PF$_6$)·Et$_2$O (10c)

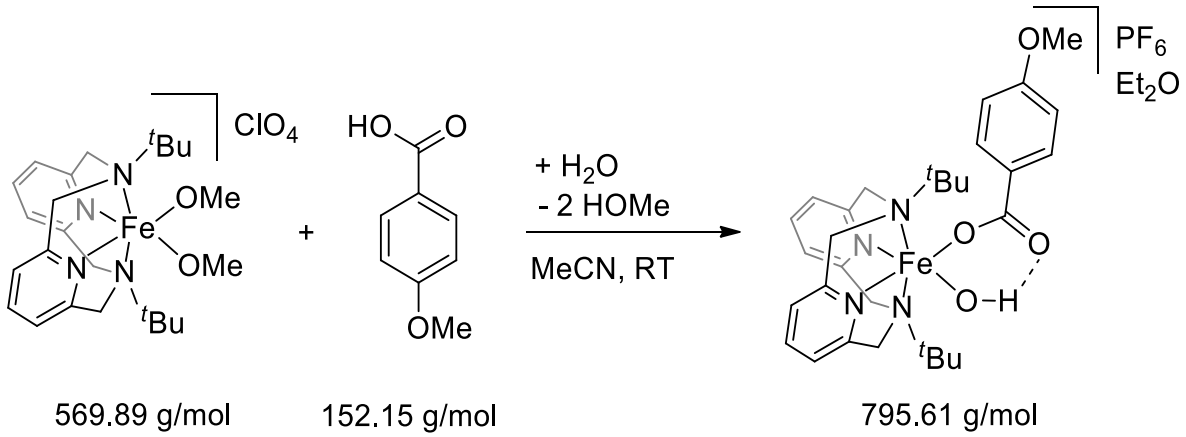

569.89 g/mol 152.15 g/mol 795.61 g/mol

Approach: 130.7 mg (0.23 mmol) [Fe(L-N$_4$^{t}Bu$_2$)(OH)$_2$]ClO$_4$ (**4b**)
36.5 mg (0.24 mmol) *para*-anisic acid

4b was dissolved in MeCN (8 mL) and neat *p*-anisic acid was added. The mixture was treated with 4 drops of water (deionized) using a Pasteur pipette and the resulting brownish-yellow mixture was filtered over celite. Crystallisation was achieved by diffusion of freshly distilled Et$_2$O at 4 °C in the dark into the filtrate. The yellow crystalline solid was washed with freshly distilled Et$_2$O prior to isolation. The crystals rapidly withered after isolation.

Yield: 95.3 mg, 52 % (calculated with respect to [**10**]PF$_6$·Et$_2$O).

Elemental Analysis (1. FeC$_{34}$F$_6$H$_{50}$N$_4$O$_5$P, 2. FeC$_{30}$F$_6$H$_{40}$N$_4$O$_4$P, 3. FeC$_{30}$F$_6$H$_{42}$N$_4$O$_5$P):

	C	H	N
calculated (1)	51.33	6.33	7.04
calculated (2)	49.94	6.33	7.77
calculated (3)	48.73	5.72	7.58
found	49.13	5.68	7.68

IR (ATR, cm^{-1}): 3550, 3450, 3092, 3061, 3001, 2976, 2915, 2840, 1628, 1602, 1586, 1567, 1508, 1471, 1441, 1424, 1408, 1387, 1324, 1300, 1255, 1215, 1181, 1164, 1128, 1103, 1087, 1072, 1028, 1005, 959, 942, 913, 899, 874, 723, 796, 784, 776, 751, 741, 731, 710, 700, 654, 635, 610, 576, 556, 517, 480.

Preliminary structural data could be obtained to verify the structural motif and determine connectivity. Cell parameters (150 K): *a* = 20.2506 Å, *b* = 13.2016 Å, *c* = 14.1732 Å, α = 90.000°, β = 100.544°, γ = 90.000°. More information can be provided upon request by Dr. Harald Kelm (internal reference number: 21066o).

8.1.28. Synthesis of $[Fe^{III}(LN_4{}^tBu_2)(O_2CPh)(OH)]$ $[Fe^{II}(LN_4{}^tBu_2)(O_2CPh)(OH)_2](BPh_4)_2$ ({[1][2]}$(BPh_4)_2$)

Pathway 1

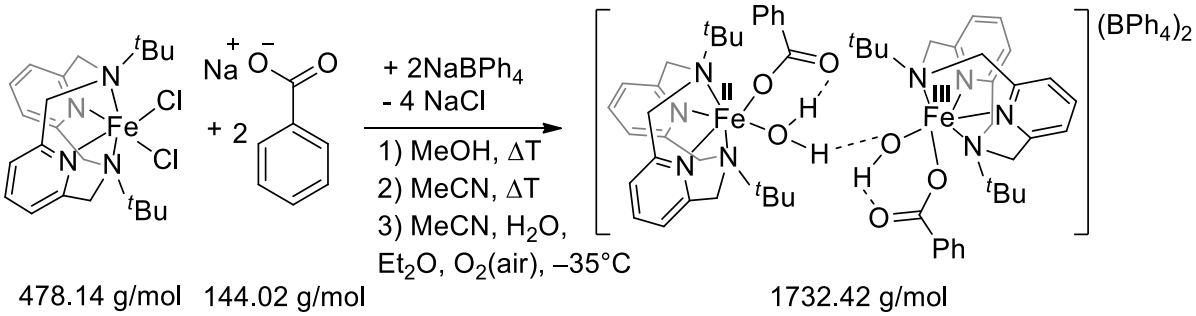

478.14 g/mol 144.02 g/mol 1732.42 g/mol

Approach: 239.5 mg (0.50 mmol) $[Fe(L\text{-}N_4{}^tBu_2)(Cl)_2]$ (**5**)
72.3 mg (0.50 mmol) sodium benzoate
171.0 mg (0.50 mmol) sodium tetraphenylborate

Under an atmosphere of nitrogen, **5**, $PhCO_2Na$, and $NaBPh_4$ were suspended in MeOH (50 mL). The resulting yellow reaction mixture was heated to reflux twice. After removal of the solvent, the solid residue was treated with MeCN (15 mL). The resulting suspension was heated to reflux before the solvent was once more removed (to remove traces of MeOH). The residue was again treated with MeCN (20 mL) and the suspension was filtered through celite. Subsequently, a small amount of deionized water (ca. 0.5-1 mL) was added and Et_2O (~100 mL) was diffused into the solution. Storage of the mixture at -35°C for two weeks afforded yellow-brown crystals (product) and a few lemon-yellow crystals (side product, see below) that were separated.

Yield: 77.7 mg, 18 %.

See below for characterization data ([a] sample obtained via pathway 1, [b] sample obtained via pathway 2)

Pathway 2

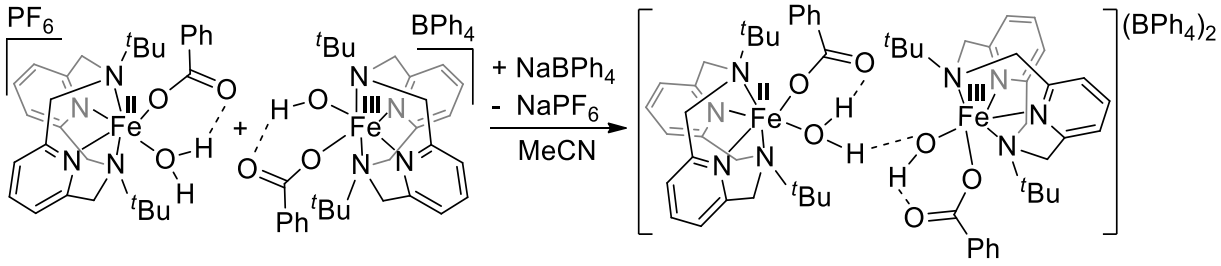

692.42 g/mol 865.69 g/mol 1732.42 g/mol

Approach: 49.6 mg (0.07 mmol) $[Fe(L\text{-}N_4{}^tBu_2)(O_2CPh)_2(OH)_2]PF_6$ (**2c**)
63.7 mg (0.07 mmol) $[Fe(L\text{-}N_4{}^tBu_2)(O_2CPh)_2(OH)]BPh_4$ (**1a**)
26.3 mg (0.08 mmol) sodium tetraphenylborate

Under an atmosphere of nitrogen, **1a**, **2c**, and $NaBPh_4$ were dissolved in MeCN (10 mL). Slow diffusion of Et_2O at 4°C yielded brown crystals.

Yield: 93.2 mg, 75 %.

Elemental Analysis ($Fe_2C_{106}H_{117}N_8O_6$):

	C	H	N
calculated	73.49	6.81	6.47
found[b]	73.28	6.72	6.51

IR (ATR, cm^{-1}):[a] 3500 – 3100 (br), 3051, 3027, 2997, 2983, 2975, 1640, 1625, 1597, 1578, 1467, 1446, 1435, 1425, 1400, 1350, 1319, 1300, 1287, 1253, 1227, 1206, 1183, 1163, 1128, 1097, 1068, 1048, 1025, 1000, 960, 938, 909, 902, 862, 843, 821, 810, 793, 775, 747, 732, 715, 703, 688, 672, 650, 623, 611, 593, 571, 560, 545, 514, 504, 495, 479, 466. br = broad.

Magnetic moment (298 K):[a] μ = 6.25 μ_B (χT = 4.89 cm^3Kmol^{-1}).

Mößbauer parameters (293 K): δ_{IS} = 1.02[a] – 1.01[b] mms^{-1} (Fe^{II}), 0.29[a] – 0.29[b] mms^{-1} (Fe^{III}); ΔE_q = 2.53[a] – 2.51[b] mms^{-1} (Fe^{II}), 2.03[a] – 2.08[b] mms^{-1} (Fe^{III}). Relative areas (Fe^{II}:Fe^{III}): 45:55[a], 42:58[a]. *Note: Average room temperatures may have varied between the two individual measurements.*

For structural data at 150 K[a] and 293 K[b] see 4.1.2 and attachment.

8.1.29. Synthesis of $[Fe^{II}(LN_4{}^tBu_2)(O_2CPh)(OH)_2]_2(BPh_4)_2 \cdot 2H_2O \cdot 2Et_2O \cdot MeCN$ (2e)

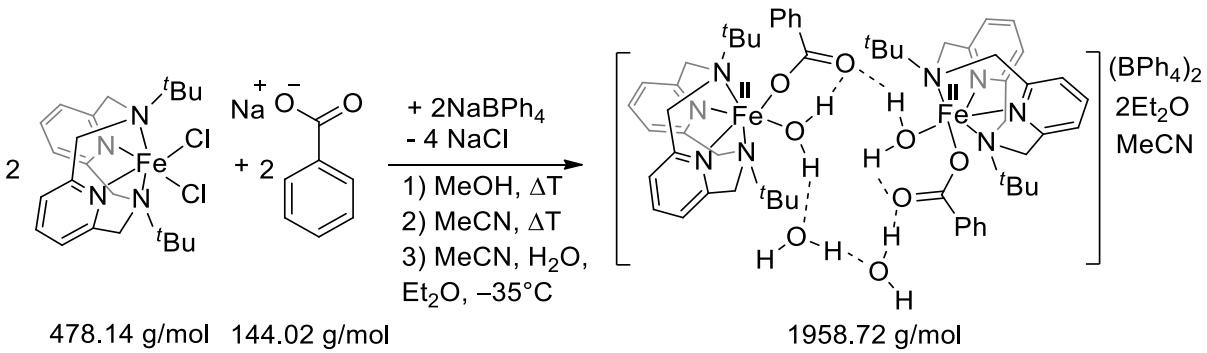

478.14 g/mol 144.02 g/mol 1958.72 g/mol

Approach: See synthesis 8.1.28, pathway 1.

Some lemon-yellow crystals of **2e** were obtained in the synthesis of {[**1**][**2**]}$(BPh_4)_2$ according to pathway 1 as a side product.

Yield: n.d.

For structural data see 4.1.2 and attachment.

8.1.30. Synthesis of [Fe(L-N$_4$*t*Bu$_2$)(OH$_2$)$_2$](OTs)$_2$ (13a)

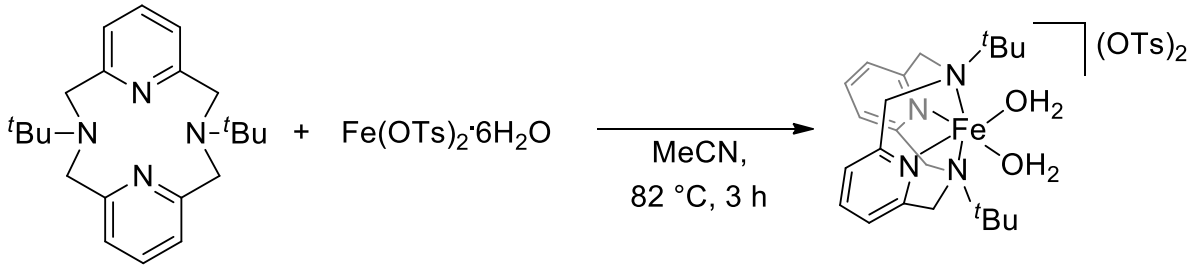

352.26 g/mol 506.32 g/mol 786.15 g/mol

Approach: 359.0 mg (1.02 mmol) L-N$_4$*t*Bu$_2$
506.7 mg (1.00 mmol) iron(II) tosylate hexahydrate

Under an atmosphere of nitrogen, L-N$_4$*t*Bu$_2$ and Fe(OTs)$_2$·6H$_2$O were suspended in MeCN (60 mL). The mixture was refluxed for 3 h, then cooled down to room temperature. After the addition of a few drops of water (deionized) via a steel canula the mixture was again heated to reflux and filtered over celite. Analytically pure, green crystals were obtained by diffusion of Et$_2$O into the solution.

Yield: 611.7 mg, 78 %.

Elemental Analysis (FeC$_{36}$H$_{50}$N$_4$O$_8$S$_2$):

	C	H	N	S
calculated	54.95	6.41	7.12	8.13
found	54.82	6.29	7.10	8.22

IR (ATR, cm^{-1}): 3400 (br. sh), 3170 (br. sh), 3081, 3042, 3022, 3005, 2986, 2970, 2945, 2920, 2866, 1601, 1579, 1496, 1464, 1436, 1403, 1378, 1363, 1347, 1289, 1255, 1234, 1223, 1192, 1156, 1121, 1077, 1054, 1032, 1009, 967, 939, 926, 911, 852, 836, 809, 799, 793, 780, 772, 752, 732, 710, 677, 645, 619, 565, 529, 515, 493. br. sh = broad shoulder.

ESI-MS(+): calculated: m/z = 222.1; found m/z = 245.1, 443.1, 445.1, 579.2 (main signals). The H$_2$O ligands are lost under ESI-MS conditions and exchanged with two MeCN ligands (calc'd m/z = 245.1), one tosylate ligand (calc'd m/z = 579.2), or one chloride ligand (common contaminant in the instrument and glassware, calc'd m/z = 443.1, 445.1).

Electronic excitations (ground powder): λ (nm) = 731, 1385 (d,d transitions only).

Electronic excitations (d,d transitions only): λ (nm) = 732, 1304 (MeCN), 754 (H_2O). Excitation energy for the second d,d-transition in H_2O solution is expected above 1312 nm (beyond the solvent resolution limit).

Magnetic moment: μ = 5.59 μ_B (χT = 3.91 cm^3Kmol^{-1}) (298 K), μ = 5.64 μ_B (χT = 3.97 cm^3Kmol^{-1}) (400 K).

Mößbauer parameters (298 K): δ_S = 1.04 mms^{-1} ΔE_q = 2.65 mms^{-1}.

For structural data see 5.1.2 and attachment.

8.1.31. Synthesis of [Fe(L-N$_4$*t*Bu$_2$)(OD$_2$)$_2$](OTs)$_2$ (13d)

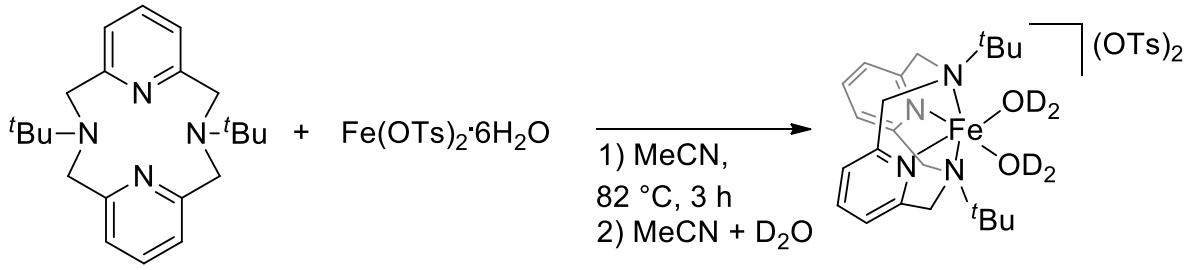

352.26 g/mol 506.32 g/mol 790.15 g/mol

Approach: 177.2 mg (0.50 mmol) L-N$_4$*t*Bu$_2$
253.3 mg (0.50 mmol) iron(II) tosylate hexahydrate

Under an atmosphere of nitrogen, L-N$_4$*t*Bu$_2$ and Fe(OTs)$_2$·6H$_2$O were suspended in MeCN (60 mL). The mixture was refluxed for 2 h, then cooled down to room temperature and filtered over celite. The solvent was removed under vacuo and heat before the residue was dissolved in MeCN (25 mL) containing D$_2$O (ca. 0.5 mL). Green crystals were obtained by diffusion of Et$_2$O into the solution.

Yield: 150.2 mg, 38 %.

Elemental Analysis (FeC$_{36}$H$_{46}$D$_4$N$_4$O$_8$S$_2$):

	C	H	N	S
calculated	54.68	6.37	7.09	8.11
found	54.76	6.40	7.07	8.14

IR (ATR, cm^{-1}): 3083, 3033, 3020, 3004, 2986, 2971, 2944, 2918, 2866, 2523 (br. sh), 2358 (br. sh), 2299, 1601, 1578, 1496, 1463, 1437, 1402, 1378, 1364, 1347, 1288, 1257, 1236, 1223, 1191, 1158, 1122, 1077, 1055, 1032, 1009, 967, 939, 927, 911, 900, 852, 837, 809, 801, 792, 751, 732, 710, 678, 646, 565, 529, 514, 493.

^{1}H-NMR(400 MHz, CD$_3$CN, 13d) δ(ppm) = 72.39 (s), 69.28 (br), 48.50 – 36.60 (br), 19.54 (br), 12.77 (sh), 9.59 (br), 7.59 (s), 5.45 (s), 4.19 (br), 2.54 (br), -0.17 (sh), -9.95 (s).

^{1}H-NMR(400 MHz, D$_2$O, 13a) δ(ppm) = 69.82 (s), 58.10 (s), 7.79 (d, *J* = 7.7 Hz), 7.53 (d, *J* = 7.6 Hz), 3.29 (s), 2.54 (s), 2.01 (s), -1.25 (br), -7.79 (br).

No structural data obtained. For a representative structure see 5.1.2 and attachment.

8.1.32. Synthesis of $[Fe(L\text{-}N_4{}^tBu_2)(OH)_2](PF_6)\cdot H_2O$ (14a)

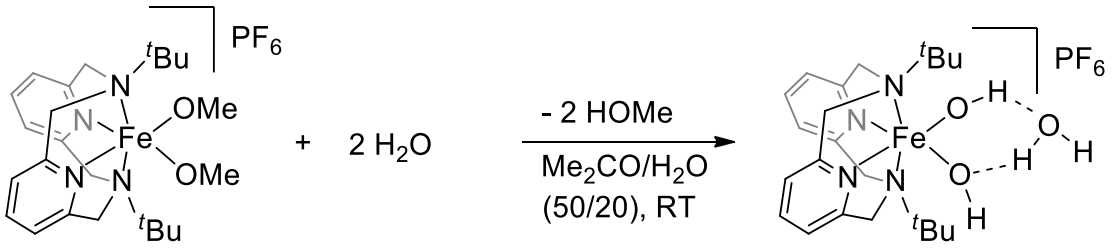

615.40 g/mol 18.02 g/mol 605.36 g/mol

Approach: 151.8 (0.25 mmol) $[Fe(L\text{-}N_4{}^tBu_2)(OMe)_2]PF_6$ (**4b**)

Under air, **4b** was dissolved in Acetone (50 mL) and water (deionized, 20 mL) was added. Among an amorphous precipitate, some crystals formed as pale-yellow blocks upon slow evaporation of the solvent from a 100 mL Erlenmeyer flask. The crystals were separated and washed with freshly distilled Et_2O to obtain an analytically pure product.

Yield: 123.2 mg, 83 %.

*Note: A controlled synthesis of **14a** was not achieved, as the crystallization conditions could not be reproduced. All investigations and characterizations pertaining **14a** were concluded with the product of one batch that was obtained as described above.*

Elemental Analysis ($FeC_{22}H_{36}F_6N_4O_3P$):

	C	H	N
calculated	43.65	5.99	9.26
found	43.52	5.97	9.29

IR (ATR, cm^{-1}): 3639, 3450, 3278, 3143, 3090, 2973, 2926, 2899, 1637, 1603, 1584, 1469, 1456, 1435, 1407, 1381, 1368, 1350, 1288, 1262, 1229, 1185, 1162, 1090, 1075, 1042, 1025, 1005, 963, 940, 918, 908, 874, 829, 797, 780, 752, 739, 730, 711, 650, 615, 592, 554, 519, 482, 454.

Magnetic moment: μ = 6.11 μ_B (χT = 4.68 cm^3Kmol^{-1}) (298 K), μ = 6.15 μ_B (χT = 4.73 cm^3Kmol^{-1}) (400 K).

EPR (10 K, MeCN/TBAP): g_{eff} = 6.623 5.20, 1.95 (M_s = ±1/2), 5.88 (M_s = ±3/2). g_{real} = 2.010, 1.956, 1.987.

EPR (10 K, DMF/TBAP): g_{eff} = 6.61, 5.20, 1.95 (M_S = ±1/2), 5.90 (M_S = ±3/2). Minor impurities at 6.43 (sh), 6.10 (p), 5.48 (p), 4.24 (ip). sh = shoulder, p = peak, ip = inflection point.

EPR (ground powder): g_{eff} = 6.60, 5.31, 1.90 (M_S = ±1/2).

For electronic absorption spectra of solid (KBr) and solution based (MeCN) samples see section 5.1.6 and section 5.1.7, respectively. For electrochemical data see section 5.1.10. For structural data see section 5.1.2 and attachment.

8.1.33. Synthesis of $[Fe(L\text{-}N_4{}^tBu_2)(OH)_2]_3(PF_6)_3{\cdot}5H_2O$ (14b)

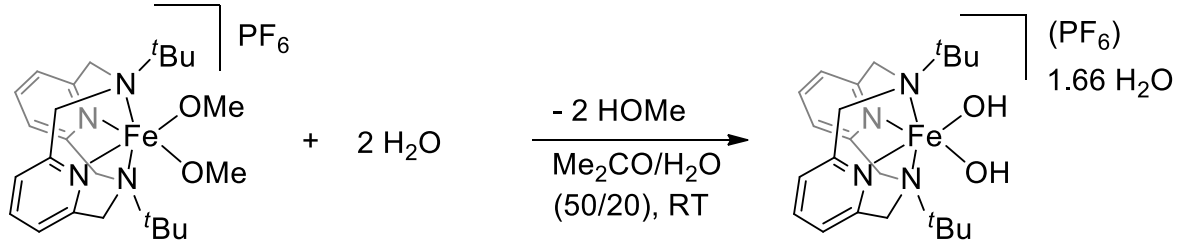

615.40 g/mol 18.02 g/mol 617.37 g/mol

Approach: 151.5 mg (0.25 mmol) $[Fe(L\text{-}N_4{}^tBu_2)(OMe)_2]PF_6$ (**4b**)

Under air, **4b** was dissolved in Acetone (50 mL) and water (deionized, 20 mL) was added. Among an amorphous precipitate, some crystals formed as pale-yellow plates (distinct from the pale-yellow blocks of **14a**) upon slow evaporation of the solvent from a beaker. The crystals were separated and washed with freshly distilled Et_2O to obtain an analytically pure product.

Yield: few single crystals.

*Note: A controlled synthesis of **14b** was not achieved, only a few crystals could be obtained for IR spectroscopic and preliminary X-ray diffraction analysis. In most attempts, most of the residue after slow evaporation was amorphous (also see synthesis of **14c**, 8.1.35).*

IR (ATR, cm^{-1}): 3664, 3635, 3450, 3213, 3099, 2974, 2925, 2881, 2805, 1605, 1585, 1470, 1439, 1427, 1405, 1380, 1369, 1354, 1292, 1262, 1253, 1229, 1214, 1191, 1164, 1110, 1091, 1075, 1045, 1028, 1005, 962, 939, 913, 879, 826, 792, 7760, 752, 742, 732, 712, 650, 627, 617, 581, 555, 470.

Preliminary structural data could be obtained to verify the structural motif and determine connectivity (also see section 5.1.2). Cell parameters (150 K): a = 15.2660 Å, b = 17.5849 Å, c = 19.1074 Å, α = 114.146°, β = 103.123°, γ = 103.837°. More information can be provided upon request by Dr. Harald Kelm (internal reference number: 21039occ12).

8.1.34. Synthesis of $[Fe(L\text{-}N_4{}^tBu_2)(OD)_2](PF_6)\cdot xD_2O$ (14d)

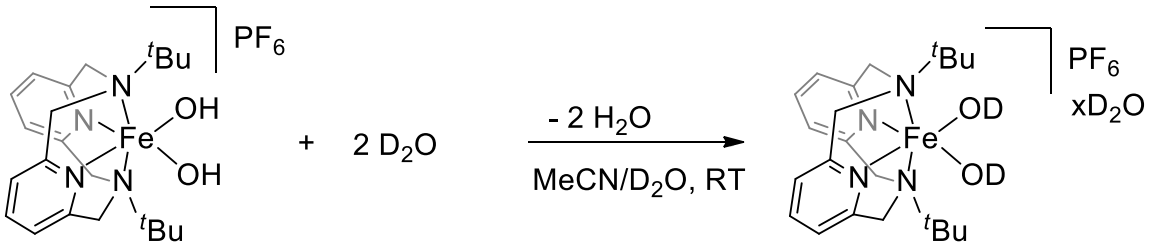

587.35 g/mol 18.02 g/mol 589.35 g/mol

Approach: 82.6 mg (0.14 mmol) $[Fe(L\text{-}N_4{}^tBu_2)(OH)_2]PF_6$ (**14c**)

Under air, **14c** was dissolved in MeCN (5 mL) and ten drops of D_2O were added with a Pasteur pipette. The mixture was dried in vacuo to decrease the concentration of H_2O in the mixture. The residue was again taken up in MeCN (5 mL) and two drops of D_2O were added. Slow diffusion of Et_2O (containing 2 drops of D_2O) at 4°C in the dark yielded an amorphous powder that was washed with freshly distilled Et_2O to obtain the product.

Yield: 56.2 mg, 68 % (calculated for water free $[Fe(L\text{-}N_4{}^tBu_2)(OD)_2](PF_6)$).

Elemental Analysis ($FeC_{22}H_{32}D_2F_6N_4O_2P$ (1), $FeC_{22}H_{32}D_2F_6N_4O_2P\cdot 1D_2O$ (2), $FeC_{22}H_{32}D_2F_6N_4O_2P\cdot 0.5D_2O$ (3)):

	C	H	N
calculated (1)	44.84	5.81	9.51
calculated (2)	43.37	5.96	9.19
calculated (3)	44.09	5.90	9.35
found	44.16	5.72	9.38

The found intermediate water content suggests product inhomogeneity.

IR (ATR, cm^{-1}): 3664, 3635, 3450, 3213, 3101, 3057, 3009, 2973, 2924, 2803, 2700, 2678, 2558, 1604, 1585, 1469, 1439, 1428, 1405, 1379, 1369, 1354, 1292, 1265, 1253, 1229, 1214, 1191, 1165, 1092, 1075, 1045, 1028, 1005, 962, 940, 911, 879, 827, 791, 776, 752, 742, 732, 712, 649, 627, 616, 577, 554, 484, 469.

No structural data could be obtained. For information on representative structural data for the non-deuterated analogue see 5.1.2 and 8.1.33.

8.1.35. Synthesis of [Fe(L-N$_4$^{t}Bu$_2$)(OH)$_2$](PF$_6$) (14c)

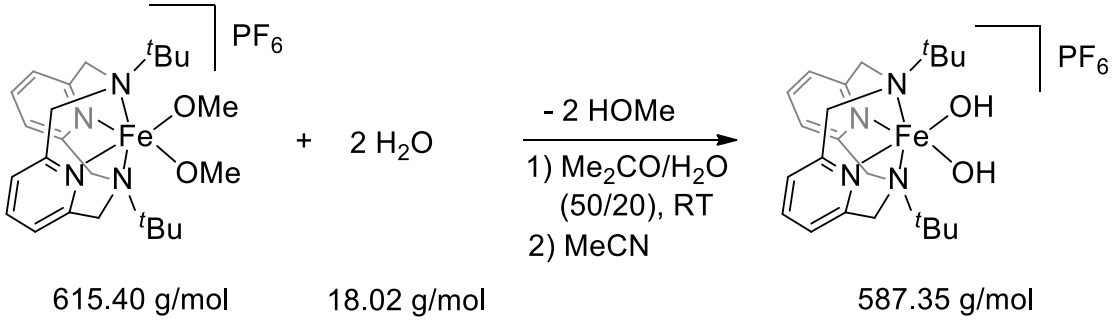

615.40 g/mol 18.02 g/mol 587.35 g/mol

Approach: 151.5 mg (0.25 mmol) [Fe(L-N$_4$^{t}Bu$_2$)(OMe)$_2$] (**4b**)

Under air, **4b** was dissolved in Acetone (50 mL) and water (deionized, 20 mL) was added. The amorphous precipitate was redissolved in MeCN (6 mL) and the solution was filtered to remove any insoluble residues. Slow diffusion of Et$_2$O to the solution yielded a powder that was washed with freshly distilled Et$_2$O to obtain an analytically pure product.

Yield: 75.9 mg, 52 %.

Elemental Analysis (FeC$_{22}$H$_{34}$F$_6$N$_4$O$_2$P):

	C	H	N
calculated	44.99	5.83	9.54
found	44.85	5.70	9.61

^{1}H-NMR(400 MHz, CD$_3$CN, 14) δ(ppm) = 135.90 (br), 97.00 (s), 88.88 (br), 9.05 (br), 1.60 (s), -3.89 (br).

ESI-MS(+): calculated: m/z = 442.2; found m/z = 442.0 (main signal).

Mößbauer parameters (70 K): δ_{IS} = ~0.4 mms^{-1} ΔE_q = >2.2 mms^{-1}. Parameters are preliminary as the signal is very broad and an applied external magnetic field is necessary for a more accurate determination.

For electronic spectroscopy data (MeCN) see 5.1.7. For electrochemical data (MeCN/TBAP) see 5.1.10. No structural data could be obtained.

8.1.36. Synthesis of 2,2,6,6-Tetramethylpiperidin-*N*-hydroxide (TEMPOH)

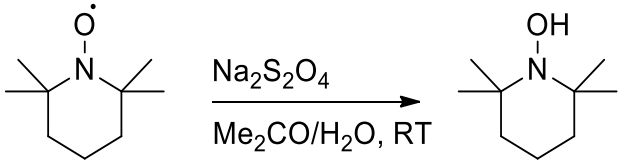

156.14 g/mol 157.14 g/mol

Approach: 1.0 g (6.40 mol) 2,2,6,6-tetramethylpiperidinyl-*N*-oxyl (TEMPO)
1.45 g (8.33 mmol) sodium dithionite

TEMPOH was synthesized according to a modified literature procedure to increase the yield.[101,174] A similar approach had been employed in a previous work by myself.[2] TEMPO was dissolved in a 1:1 (vol/vol) mixture of acetone and deionized water (30 mL). The mixture was degassed by purging the solution with nitrogen through a canula for 15 minutes. All following steps were done under nitrogen atmosphere. After the addition of $Na_2S_2O_4$ the mixture was stirred for 5 min and the volume was reduced until a white precipitate was observed. The slurry was then treated with Et_2O (50 mL) and cooled below the freezing point of water to extract the Et_2O phase with a canula. This was done twice, and the combined organic phases (100 mL) were dried with Na_2SO_4. After filtration and removal of the solvent in vacuo, the raw, colorless product was sublimed under a static oil pump vacuum from a flask at room temperature into a flask cooled with liquid nitrogen to obtain an NMR pure colorless solid.

Yield: 1.0 g, quantitative (Lit 74 – 80 %).[101,174]

^{1}H-NMR (400 MHz, $CDCl_3$) δ = 4.32 (s, 1H, OH), 1.48 (s, 6H, CH_2), 1.13 (s, 12H, CH_3).

EPR (0.2 mmol·L^{-1} in MeCN, 298 K): no signal.

Crystals could be obtained by storage in a flask under mild vacuum in a freezer but were not further investigated.

8.1.37. Synthesis of [Fe(L-N$_4$^{t}Bu$_2$)(OAc)$_2$]

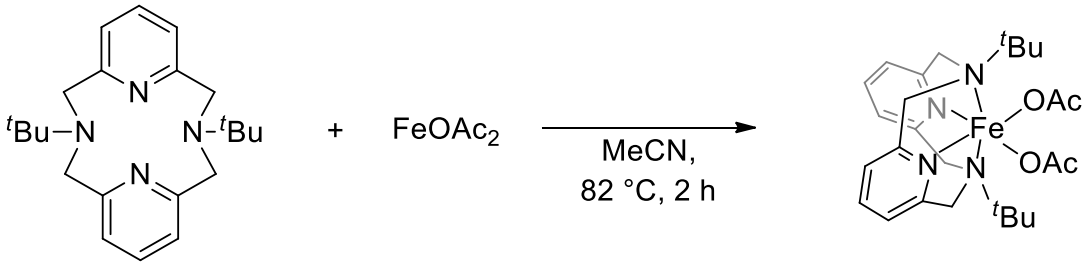

352.26 g/mol 173.93 g/mol 526.22 g/mol

*As an alternative to **5**, [Fe(L-N$_4$^{t}Bu$_2$)(OAc)$_2$] can also be used as precursor to synthesize **4a**, **4b**, and **4c**. Thus, the synthesis and characterization of this new compound is described in the following for completeness, although it was not further discussed in this thesis.*

Approach: 357.4 mg (1.01 mmol) L-N$_4$^{t}Bu$_2$
170.9 mg (0.98 mmol) Fe(OAc)$_2$

Under an atmosphere of nitrogen, L-N$_4$^{t}Bu$_2$ and Fe(OAc)$_2$ were suspended in Acetonitrile (60 mL). The mixture was refluxed for 2 h, then cooled down to room temperature and filtered over celite. The volume of the filtrate was reduced (30 mL). Analytically pure, orange/red crystals could be obtained by diffusion of diethylether into the concentrated solution.

Yield: 344.8 mg (67 %).

Elemental Analysis (FeC$_{26}$H$_{38}$N$_4$O$_4$):

	C	H	N
calculated	59.32	7.28	10.64
found	59.26	7.37	10.65

IR (ATR, cm^{-1}): 2966, 2902, 1598, 1578, 1462, 1435, 1402, 1378, 1351, 1264, 1249, 1227, 1194, 1154, 1079, 1022, 937, 924, 909, 858, 801, 714, 640 (strong bands) only).

UV-vis-NIR (solid ground powder, 300-2000 nm): λ(nm) = 376, 484, 841, ~1800 (broad).

Mößbauer (298 K): δ_{IS} = 1.07 mms^{-1}, ΔE_q = 1.68 mms^{-1}. The sample slowly decomposed during the measurement, giving rise to a minor signal at δ_{IS} = 1.03 mms^{-1}, ΔE_q = 2.48 mms^{-1}. The origin of this is unknown.

For structural data see attachment.

8.2. Reactivity Studies

8.2.1. Spectroscopic Studies Under a Nitrogen Atmosphere

8.2.1.1. General considerations

The reactivity studies under nitrogen atmosphere were all conducted as quantitative experiments with highest precision standards. Because these studies only provide spectroscopic evidence of reaction monitoring experiments, it is important to also consider the methods and instruments employed (section 7.2) for a full comprehension of the procedures. All experiments were done at room temperature if not stated otherwise.

8.2.1.2. Oxidation of 2,2,6,6-Tetramethylpiperidin-*N*-hydroxide (TEMPOH) with 1 Under a Nitrogen Atmosphere

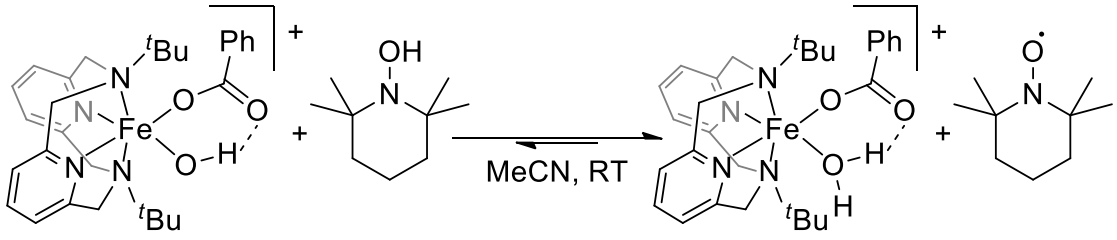

1 TEMPOH **2** TEMPO

EPR reaction monitoring

The reaction mixture was prepared under a nitrogen atmosphere in a glove box. The employed concentrations in these reactivity studies were 5.0 mmol·L^{-1} of **1a** and 5.0 mmol·L^{-1} of CHD in MeCN and the reaction mixture was kept at room temperature. The reaction solution was tempered for 5 minutes at 20 °C to ensure temperature stability during the EPR measurement. The EPR spectrum of the solution was measured after 20 minutes of reaction time to ensure that the reaction mixture had reached equilibrium conditions. A 5 mmol·L^{-1} solution of TEMPO in MeCN (abs., N_2 atmosphere) was measured as a reference to verify quantitative conversion.

ESI-MS reaction monitoring

The reaction mixture was prepared under a nitrogen atmosphere in a glove box. The employed concentrations in this study were 2 mmol·L^{-1} of **1a** and 20 mmol·L^{-1} of TEMPOH in MeCN and the reaction mixture was kept at room temperature. The sample was taken with a 100 μL Hamilton syringe from the reaction solution in the glovebox. The Hamilton syringe with the reaction solution was swiftly carried to the instrument for injection (approx. 30 seconds) to minimize the contact and contamination with air.

8.2.1.3. Oxidation of 2,4,6-Tri(*tert*-butyl)phenol (TTBP) with 1 Under a Nitrogen Atmosphere

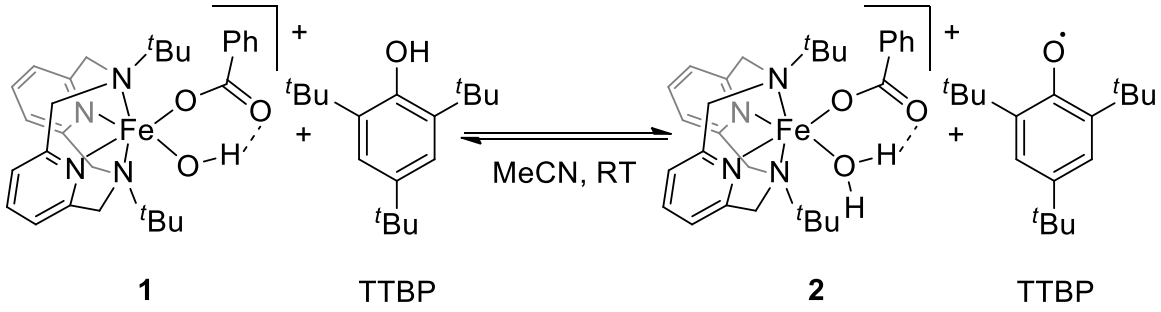

1 TTBP **2** TTBP

EPR equilibrium studies

All reaction mixtures were prepared individually under a nitrogen atmosphere in a glove box. Aliquots of a stock solution of 2,4,6-tri-(*tert*-butyl)phenol in acetonitrile were added to solid compound **1a**, and the resulting solutions were diluted with acetonitrile to render the reaction solutions with the respective concentrations as given in section 2.3.5, Table 11. All reaction solutions were tempered for 5 minutes at 20 °C to ensure temperature stability during the EPR measurement. The EPR spectrum of each reaction solution was measured after 20 minutes of reaction time to ensure that the reaction mixture had reached equilibrium conditions. In initial experiments it was ensured that the intensity remained constant for at least 30 minutes after the first measurement. A 0.2 mmol·L^{-1} solution of TEMPO in MeCN (abs., N_2 atmosphere) was measured as a reference prior to and after the measurement sequence of the equilibrium study. It was ensured that the integral values were identical within the error range. The averaged integral of the two samples was used as a reference value for a 0.2 mmol·L^{-1} concentration of molecules containing one unpaired electron.

ESI-MS reaction monitoring

The reaction solution was prepared as an equimolar mixture of **1a** and TTBP in MeCN under a nitrogen atmosphere in a glove box. The employed concentrations in this study were 0.2 mmol·L^{-1} of **1a** and 0.2 mmol·L^{-1} of TTBP. The sample was taken with a 100 µL Hamilton syringe from the reaction solution in the glovebox. The Hamilton syringe with the reaction solution was swiftly carried to the instrument for injection (approx. 30 seconds) to minimize the contact and contamination with air.

8.2.1.4. Oxidation of 2,4,6-Tri(*tert*-butyl)phenol (TTBP) with 7 Under a Nitrogen Atmosphere

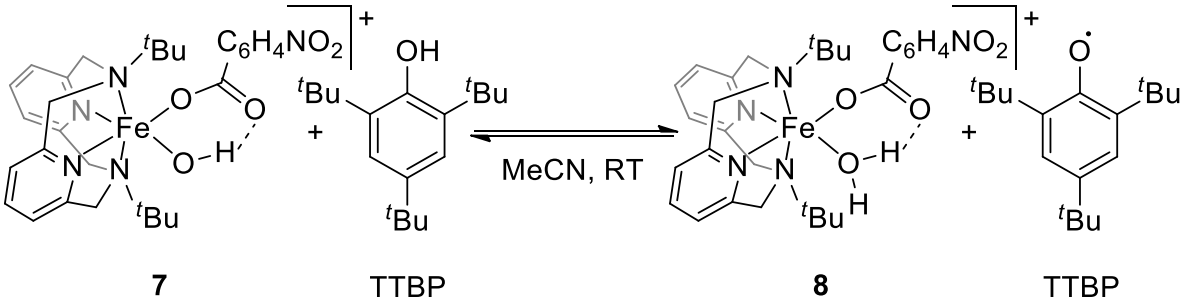

EPR equilibrium studies

All reaction mixtures were prepared individually under a nitrogen atmosphere in a glove box. Aliquots of a stock solution of 2,4,6-tri-(*tert*-butyl)phenol in acetonitrile were added to solid compound **7b**, and the resulting solutions were diluted with acetonitrile to render the reaction solutions with the respective concentrations as given in section 3.3.1, Table 35. All reaction solutions were tempered for 5 minutes at 20 °C to ensure temperature stability during the EPR measurement. The EPR spectrum of each reaction solution was measured after 20 minutes of reaction time to ensure that the reaction mixture had reached equilibrium conditions. In initial experiments it was ensured that the intensity remained constant for at least 30 minutes after the first measurement. A 0.2 mmol·L^{-1} solution of TEMPO in MeCN (abs., N_2 atmosphere) was measured as a reference prior to and after the measurement sequence of the equilibrium study. It was ensured that the integral values were identical within the error range. The averaged integral of the samples was used as a reference value for a 0.2 mmol·L^{-1} concentration of molecules containing one unpaired electron.

8.2.1.5. Oxidation of 1,4-Cyclohexadiene (CHD) to Benzene with 1 Under a Nitrogen Atmosphere

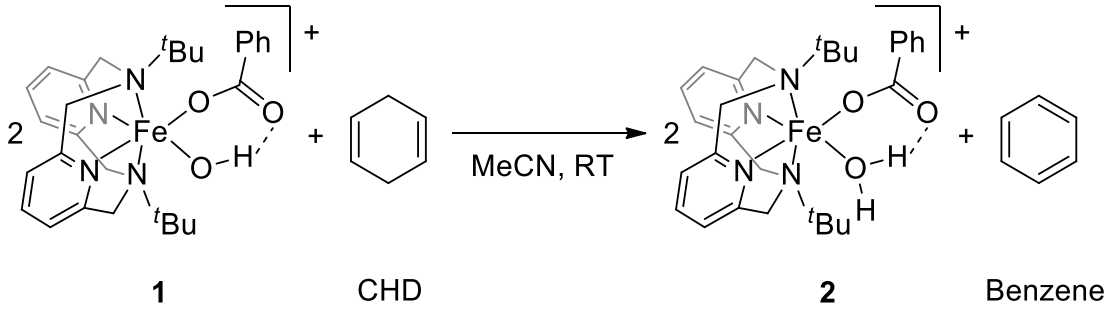

1 CHD **2** Benzene

ESI-MS reaction monitoring

The reaction mixture was prepared under a nitrogen atmosphere in a glove box. The employed concentrations in these reactivity studies were 0.2 mmol·L^{-1} of **1c** and 2 mmol·L^{-1} of CHD in MeCN and the reaction mixture was kept at room temperature. Samples were taken almost daily for 23 days with a 100 μL Hamilton syringe from the reaction flask under nitrogen flow using Schlenk techniques. The Hamilton syringe with the reaction solution was swiftly carried to the instrument for injection (approx. 15 seconds) to minimize the contact and contamination with air. Pseudo-quantitative monitoring was achieved by maintaining the same injection volumes, experimental parameters, and data workup (see methods section for instrument and procedural details) under the assumption of equal flight properties of **1** and **2** or **3**, respectively.

NMR reaction monitoring (as described in chapter 2)

The reaction mixture was prepared in a Young NMR tube under a nitrogen atmosphere in a glove box. The concentrations employed in this study were 40 mmol·L^{-1} of **1c** and 20 mmol·L^{-1} of CHD in MeCN-d3. The CHD was obtained freshly from commercial sources and distilled prior to use to remove any stabilizing agents (BHT) and benzene residues. The benzene content of the distilled CHD was verified to be <1 % via NMR spectroscopy. NMR spectra of the mixture were recorded over the course of 432 h with a 600 MHz spectrometer (see methods section for details) to follow the reaction. After a reaction time of 432 h, a yield of formed benzene was ascertained to be 27 % and additional signals corresponding to **2** were found while signals corresponding to **1** diminished.

NMR reaction monitoring (as described in chapter 3)

The reaction mixture was prepared in a Young NMR tube under a nitrogen atmosphere in a glove box. The concentrations employed in this study were 40 $mmol \cdot L^{-1}$ of **1c** and 20 $mmol \cdot L^{-1}$ of CHD in MeCN-d3. The CHD was obtained freshly from commercial sources and distilled prior to use to remove any stabilizing agents (BHT) and benzene residues. The benzene content of the distilled CHD was verified to be <1 % via NMR spectroscopy. NMR spectra of the mixture were recorded over the course of 332 h with 2 h intervals in the first 94 h before only irregular intervals were sampled with a 600 MHz spectrometer to follow the reaction. After a reaction time of 332 h, a yield of formed benzene was ascertained to be 19 % and additional signals corresponding to **2** were found while signals corresponding to **1** diminished.

8.2.1.6. Oxidation of 1,4-Cyclohexadiene (CHD) to Benzene with 7 Under a Nitrogen Atmosphere

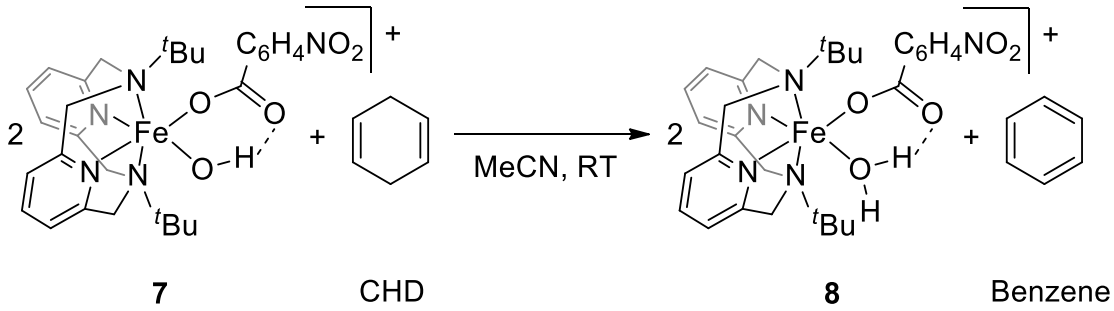

7 CHD **8** Benzene

NMR reaction monitoring

The reaction mixture was prepared in a Young NMR tube under a nitrogen atmosphere in a glove box. The concentrations employed in this study were 40 mmol·L^{-1} of **7b** and 20 mmol·L^{-1} of CHD in MeCN-d3. The CHD was obtained freshly from commercial sources and distilled prior to use to remove any stabilizing agents (BHT) and benzene residues. The benzene content of the distilled CHD was verified to be <1 % via NMR spectroscopy. NMR spectra of the mixture were recorded over the course of 670 h with 2 h intervals in the first 94 h before only irregular intervals were sampled with a 600 MHz spectrometer to follow the reaction. After a reaction time of 332 h (670 h), a yield of formed benzene was ascertained to be 20 % (32 %) and additional signals corresponding to **8** were found while signals corresponding to **7** diminished.

8.2.1.7. Oxidation of 1,4-Cyclohexadiene (CHD) to Benzene with 10 Under a Nitrogen Atmosphere

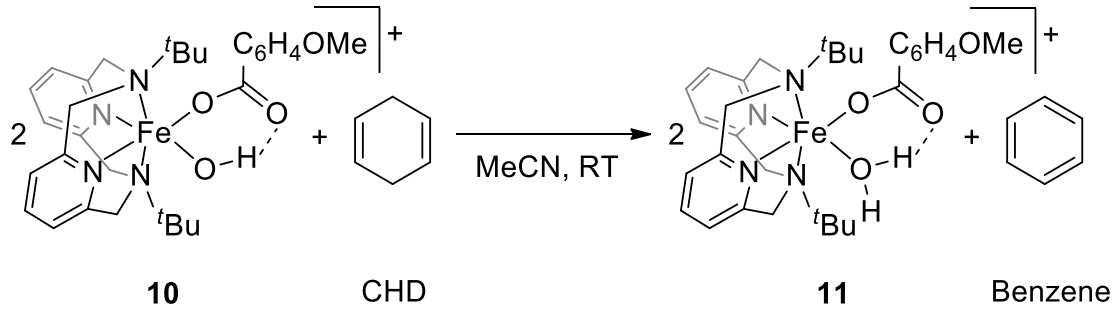

NMR reaction monitoring

The reaction mixture was prepared in a Young NMR tube under a nitrogen atmosphere in a glove box. The concentrations employed in this study were 40 mmol·L^{-1} of **10b** and 20 mmol·L^{-1} of CHD in MeCN-d3. The CHD was obtained freshly from commercial sources and distilled prior to use to remove any stabilizing agents (BHT) and benzene residues. The benzene content of the distilled CHD was verified to be <1 % via NMR spectroscopy. NMR spectra of the mixture were recorded over the course of 502 h with 2 h intervals in the first 94 h before only irregular intervals were sampled with a 600 MHz spectrometer to follow the reaction. After a reaction time of 332 h (502 h), a yield of formed benzene was ascertained to be 20 % (28 %) and additional signals corresponding to **11** were found while signals corresponding to **10** diminished.

8.2.1.8. Oxidation of 9,10-Dihydroanthracene (DHA) to Anthracene with 1 Under a Nitrogen Atmosphere

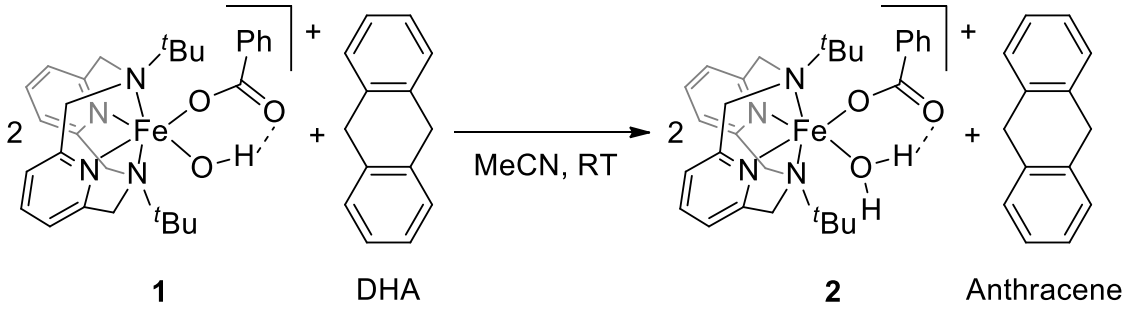

1 DHA **2** Anthracene

ESI-MS reaction monitoring

The reaction mixture was prepared under a nitrogen atmosphere in a glove box. The employed concentrations in these reactivity studies were 0.2 mmol·L^{-1} of **1c** and 2 mmol·L^{-1} of DHA in MeCN and the reaction mixture was kept at room temperature. Samples were taken daily until approximate half conversion was achieved after 120 h. Samples were taken with a 100 μL Hamilton syringe from the reaction flask under nitrogen flow using Schlenk techniques and the syringe with the reaction solution was swiftly carried to the instrument for each injection (approx. 15 seconds) to minimize the contact and contamination with air. Pseudo-quantitative monitoring was achieved by maintaining the same injection volumes, experimental parameters, and data workup (see methods section for instrument and procedural details) under the assumption of equal flight properties of **1** and **2** or **3**, respectively.

NMR reaction monitoring

The reaction mixture was prepared in a Young NMR tube under a nitrogen atmosphere in a glove box. The concentrations employed in this study were 20 mmol·L^{-1} of **1c** and 10 mmol·L^{-1} of DHA in MeCN-d3. The DHA was obtained from commercial sources and used without additional purification. No traces of anthracene were found in the NMR spectrum of this organic educt. NMR spectra of the mixture were recorded over the course of 117.5 h with a 600 MHz spectrometer (see methods section for details) to follow the reaction. After a reaction time of 117.5 h, a conversion of 5 % was found.

8.2.1.9. Self-Exchange Reaction of 1 with 2

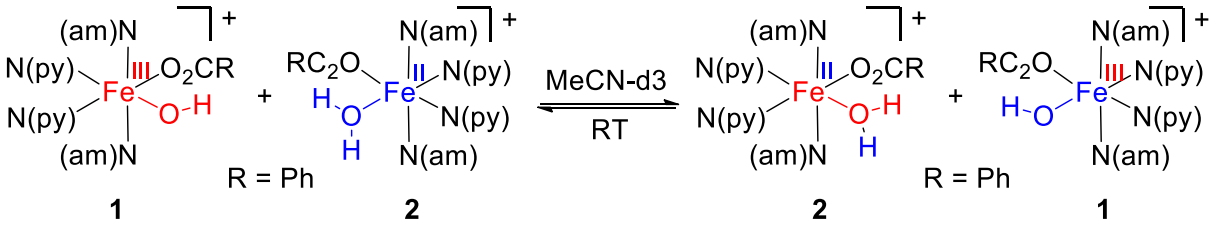

NMR equilibrium studies

The reaction mixture discussed in chapter 3 was prepared in a Young NMR tube under a nitrogen atmosphere in a glove box. The concentrations employed in this study were 20 mmol·L^{-1} of **1c** and 20 mmol·L^{-1} of **2a** in MeCN-d3. NMR spectra of the mixture were recorded with a 600 MHz spectrometer at room temperature (see methods section for more details).

Methodic details for the EXSY-NMR studies are directly described in chapter 4 section 4.3.

8.2.1.10. Pseudo-Self-Exchange Reaction of 1^D with 2

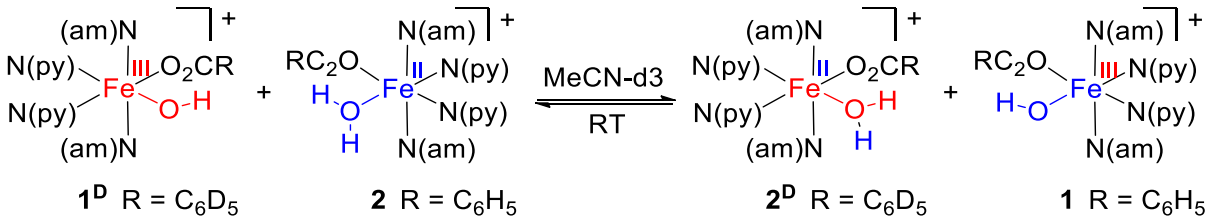

1^D R = C_6D_5 **2** R = C_6H_5 **2^D** R = C_6D_5 **1** R = C_6H_5

NMR equilibrium study

The reaction mixture was prepared in a Young NMR tube under a nitrogen atmosphere in a glove box. The concentrations employed in this study were 20 mmol·L^{-1} of **1^Dc** and 20 mmol·L^{-1} of **2a** in MeCN-d3. NMR spectra of the mixture were recorded with a 600 MHz spectrometer at room temperature (298 K). The initial measurement was recorded after 8 minutes of reaction time, no time-resolved changes in the spectrum were observed in any measurements after longer reaction times. Shorter reaction times were impractical, because of the intrinsic duration of sample preparation and measurement. Measurements were subsequently done at variable temperatures between 293-233 K, then at 303-343 K (each in 10 K increments), at 348 K, and finally at 298 K again to verify the approximate reproducibility of the initial spectrum (neglecting minor decomposition).

8.2.1.11. Pseudo-Self-Exchange Reaction of 1^D with 2^D

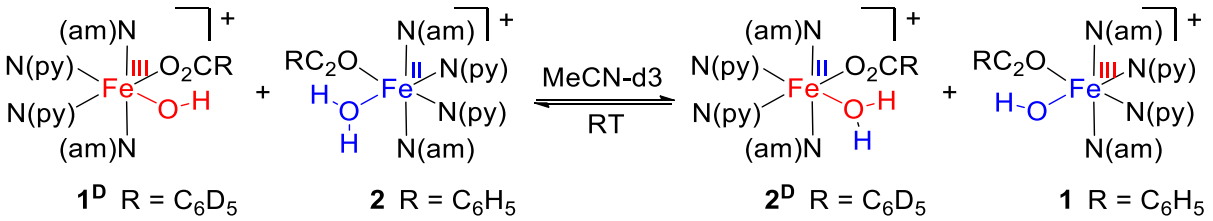

1^D R = C_6D_5 **2** R = C_6H_5 **2^D** R = C_6D_5 **1** R = C_6H_5

NMR equilibrium study

The reaction mixture was prepared in a Young NMR tube under a nitrogen atmosphere in a glove box. The concentrations employed in this study were 20 mmol·L^{-1} of **1^Dc** and 20 mmol·L^{-1} of **2^Da** in a 0.2 mol·L^{-1} solution of MeCN-d3 in MeCN. NMR spectra of the mixture were recorded with a 600 MHz spectrometer at room temperature (298 K). Measurements were subsequently done at variable temperatures (233 K, 238 K, 243 K, 253 K, 263 K, 273 K, 283 K, 298 K, 348 K) and finally at 298 K again to verify the reproducibility of the initial spectrum.

8.2.1.12. Pseudo-Self-Exchange Reaction of 7 with 2

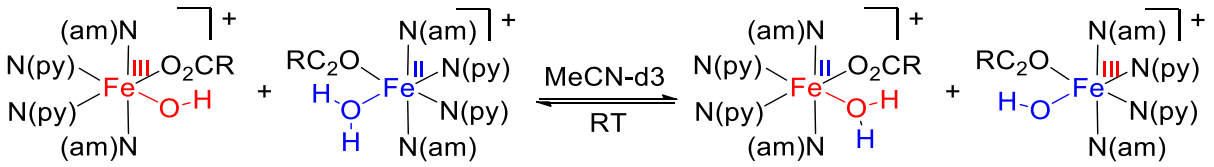

7 R = $C_6H_4NO_2$ **2** R = C_6H_5 **8** R = $C_6H_4NO_2$ **1** R = C_6H_5

NMR equilibrium study

The reaction mixture was prepared in a Young NMR tube under a nitrogen atmosphere in a glove box. The concentrations employed in this study were 20 mmol·L^{-1} of **7b** and 20 mmol·L^{-1} of **2a** in MeCN-d3. NMR spectra of the mixture were recorded with a 600 MHz spectrometer at room temperature.

8.2.1.13. Pseudo-Self-Exchange Reaction of 10 with 2

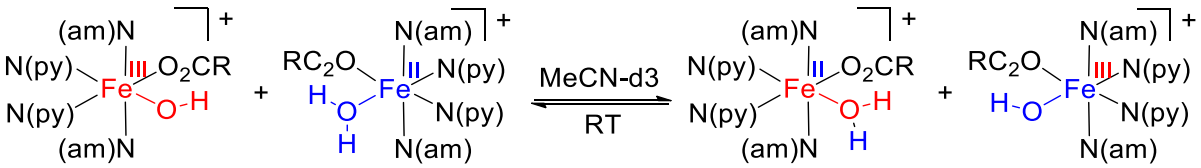

10 R = C_6H_4OMe **2** R = C_6H_5 **11** R = C_6H_4OMe **1** R = C_6H_5

NMR equilibrium study

The reaction mixture was prepared in a Young NMR tube under a nitrogen atmosphere in a glove box. The concentrations employed in this study were 20 mmol·L^{-1} of **10b** and 20 mmol·L^{-1} of **2a** in MeCN-d3. NMR spectra of the mixture were recorded with a 600 MHz spectrometer at room temperature.

8.2.2. Reactivity Studies Under Aerobic Conditions

8.2.2.1. General considerations

Some of the below described studies only provide spectroscopic evidence of reaction monitoring experiments. Thus, it is important to also consider the methods and instruments employed (section 7.2) for a full comprehension of the procedures. All experiments were done at room temperature if not stated otherwise.

8.2.2.2. Oxidation of 2 under Aerobic Conditions

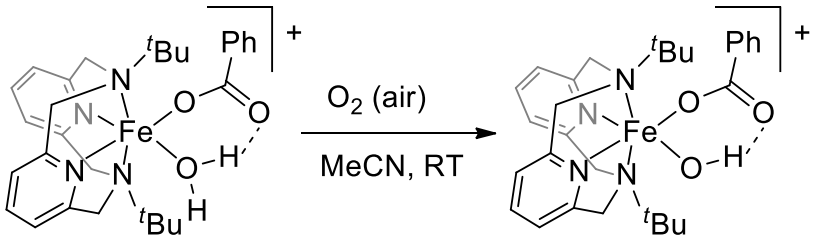

2 **1**

ESI-MS reaction monitoring

A solution of of **2a** in MeCN (0.2 mmol·L^{-1}) was prepared under aerobic conditions to ensure a constant oxygen level in the mixture throughout the reaction. The mixture was stirred for one day under atmospheric conditions and samples were taken with a 100 μL Hamilton syringe after 10, 30, 120, 240, 480, and 1455 min to follow the reaction. The instrument was kept on for the first five measurements to ensure equal conditions, however the instrument had to be switched off overnight and switched on again for the last measurement. Thus, the instrument was kept on for one hour prior to the measurement to ensure the stabilization of all parameters. Pseudo-quantitative monitoring was achieved by maintaining the same injection volumes, experimental parameters, and data workup (see methods section for instrument and procedural details) under the assumption of equal flight properties of **1** and **2** or **3**, respectively. The conversion of **1** to **2** under aerobic conditions was found to be approximately 50 % after 1455 min.

8.2.2.3. Kinetic study of the Reaction of 1 with 2,4,6-Tri(*tert*-butyl)phenol (TTBP)

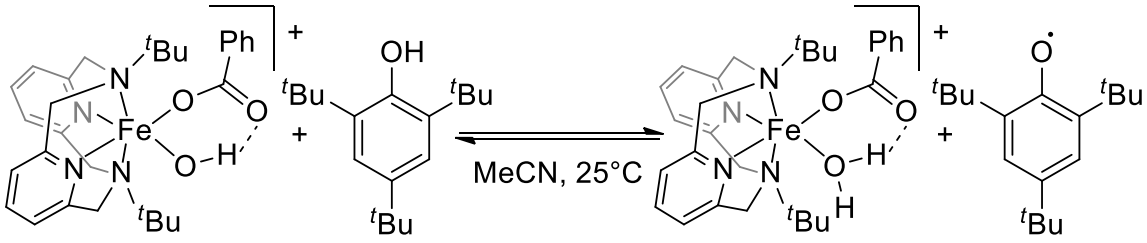

1 TTBP **2** TTBP

UV-Vis reaction monitoring

A solution of TTBP in MeCN (0.5 mL, 10.0 mmol L^{-1}) was added to a solution of **1a** in MeCN (1 mL, 2.0 mmol L^{-1}) in a quartz cuvette under aerobic conditions. The solution in the cuvette was constantly stirred with a magnetic stirring bar and tempered at 25 °C with a Peltier thermostat. Immediately after combining both solutions the measurement was started. The progress of the reaction was followed every 0.5 s for 120 s. From previous studies on the kinetics of the oxidation of **2** under air (see 8.2.2.2) and the reportedly relatively high stability of the 2,4,6-tri(*tert*-butyl)phenoxyl radical even under air it can be assumed that side reactions are much slower than the H-atom abstraction reaction to be investigated.[135]

8.2.2.4. Catalytic Oxidation of 2,4,6-Tri(*tert*-butyl)phenol (TTBP) with 1 Under Aerobic Conditions

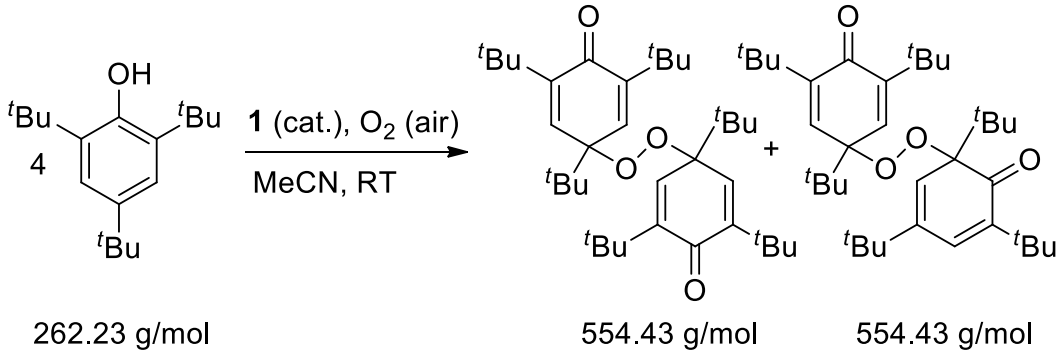

Approach: 52.5 mg (0.2 mmol) 2,4,6-Tri-(*tert*-butyl)phenol (TTBP)
13.8 mg (0.02 mmol) $[Fe(L\text{-}N_4{}^tBu_2)(O_2CPh)(OH)]PF_6$ (**1c**)

Under air, TTBP and **1c** were dissolved in acetonitrile (4 mL). The solution turned from green to dark blue within hours; yellow crystals formed after days. The crystalline material was collected after 19 days and shown to be a mixture of 4,4'-peroxybis(2,4,6-tri(*tert*-butyl)-cyclohexa-2,5-dienone) (**A**) and 2,4,6-tri(*tert*-butyl)-6-((1,3,5-tri(*tert*-butyl)-4-oxocyclohexa-2,5-dien-1-yl)peroxy)cyclohexa-2,4-dienone (**B**).

Yield: 18.5 mg, 35 % (with respect to TTBP).

IR (ATR, cm^{-1}): 2958, 2909, 2866, 1666, 1643, 1483, 1460, 1389, 1362, 1336, 1246, 1214, 1202, 1161, 1106, 1054, 1025, 995, 970, 934, 902, 881, 871, 819, 810, 741, 555, 460.

^{1}H-NMR (400 MHz, $CDCl_3$) δ = 6.87 (d, J = 3.0 Hz, 1 H, ring proton of **B**), 6.81 (d, J = 2.4 Hz, 1 H, ring proton of **B**), 6.69 (s, 4 H, ring protons of **A**), 6.64 (d, *J* = 3.0 Hz, 1 H, ring proton of **B**), 6.08 (d, *J* = 2.4 Hz, 1 H, ring proton of **B**), 1.30 (s, 9 H, protons of ^{t}Bu-groups of **B**), 1.27 (s, 36 H, protons of ^{t}Bu-groups of **A**), 1.26 (s, 9 H, protons of ^{t}Bu-groups of **B**), 1.25 (s, 9 H protons of ^{t}Bu-groups of **B**), 1.19 (s, 9 H protons of ^{t}Bu-groups of **B**), 0.84 (s, 18 H protons of ^{t}Bu-groups of **A** or **B**), 0.80 (s, 18 H, protons of ^{t}Bu-groups **A** or **B**).

Preliminary structural data could be obtained to verify the structural motif and determine connectivity already during my master thesis.[2] Additional attempts to measure crystals obtained from this reaction and refine the structural data also failed because of the large degree of disorder of the isomers. For more information see attachment.

*Note: Parts of these results had been obtained and previously reported in my master thesis but were included in this work for completeness.[2] The reaction of **1** with TTBP was, however, reproduced. The IR spectrum was recorded anew with the Perkin Elmer instrument and the Specac ATR accessory and the XRD and NMR results were verified by remeasurement on a sample obtained during this work.*

8.2.2.5. Oxidation of 9,10-Dihydroanthracene (DHA) to Anthraquinone with 1 Under Aerobic Conditions

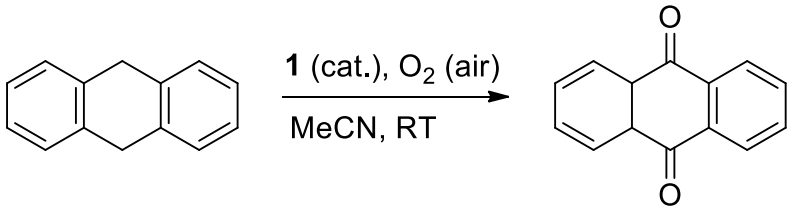

180.09 g/mol 178.08 g/mol

Approach: 90.2 mg (0.51 mmol) 9,10-Dihydroanthracene (DHA)
69.0 mg (0.10 mmol) [Fe(L-N$_4$^{t}Bu$_2$)(O$_2$CPh)(OH)]PF$_6$ (**1c**)

Under air, DHA and **1c** were dissolved in MeCN (10 mL) and kept at room temperature for 7 days in a vial covered with pierced Parafilm©. Within one day, pale, yellow needles crystallized from the solution.

Yield 18.2 mg, 87 % (with respect to **1c**).

IR (ATR, cm^{-1}) 3321, 3074, 1674 (C=O), 1575, 1473, 1452, 1331, 1303, 1283, 1206, 1169, 1098, 968, 936, 893, 818, 808, 720, 691, 620. ^{1}H-NMR (400 MHz, $CDCl_3$) δ = 8.33 (m, AA'BB', 4 H), 7.81 (m, AA'BB', 4 H).

Structural data obtained for the product crystals matched a reported literature structure of Anthraquinone (CCDC reference number 1031904, literature values are given in brackets).[149] T = 150 K, (T = 200 K), a = 15.7165 Å(15.713(6) Å), b = 3.8960 Å (3.921(1) Å), c = 15.7196 Å (15.722(6) Å), $\alpha = \gamma$ = 90° ($\alpha = \gamma$ = 90°) β = 102,476° (β = 102,670(<1)°).

8.2.3. Reactivity Studies Under a Pure Oxygen Atmosphere

8.2.3.1. Oxidation of 9,10-Dihydroanthracene (DHA) to Anthraquinone with 1 Under a Pure Oxygen Atmosphere

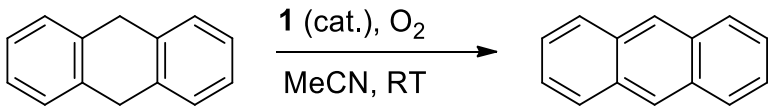

180.09 g/mol 178.08 g/mol

Note: This experiment was described by T. Bonck and is not part of the work done in this thesis. It is only included for completeness, as the previously published work references this experiment.[1,113] Although the purity of the employed catalyst is not ensured, the radical initiator function and the increased rate under a pure oxygen atmosphere is demonstrated with this experiment.

Approach: 195.7 mg (1.09 mmol) 9,10-dihydroanthracene (DHA)
9.6 mg, (0.01 mmol) [Fe(L-$N_4{}^t$Bu$_2$)(O_2CPh)(OH)]BPh_4

9,10-Dihydroanthracene and **1a** were dissolved in MeCN (5 mL) and kept under a pure oxygen atmosphere at room temperature overnight. Pale, yellow needles crystalized from the solution.

Yield: 121.0 mg, 53 % (with respect do DHA).

For more details and analytical data see literature reference.[113]

9. Computational Details

9.1. Spin Density Calculations as described in 2.1.11.

Theoretical calculations were conducted with Tmolex18 4.4.1 and Gaussian® 09.[180,181] Spin density calculations were done by using the "$pointval spindens fmt=cub" command in the control file obtained after the geometry optimization. For the geometry optimization, the structural data were used as starting point and a charge of +1 and a high spin state were assumed accordingly for the complex cations **1** and **2**. Calculations were done using a B3-LYP functional and a def2-TZVP base set. The gridsize was chosen as m5, the convergence criteria was set to 10^{-6} hartree and the gradient norm was set to 10^{-3} hartree/bohr. Further details on the results are provided in the attachment.

9.2. Mechanistic Study as described in 2.4.

The following theoretical calculations were done by J. E. M. N. Klein and M. E. de Waal Malefijt. Computational details are reproduced from the original publication as described by these authors.[1]

Computations were performed using the electronic structure code Gaussian 16.[181] Geometries were optimized using the M06-L functional[182] in combination with the def2-SVP basis set.[183] Weigend's universal fitting basis sets[184] were used for accelerating computations through density fitting.[185] MeCN solvation was mimicked using the PCM solvation model.[186,187] Analytical second derivatives were computed to confirm the minima (no imaginary frequencies) and transition states (single imaginary frequencies). These calculations provided thermal corrections to the Gibbs free energy within the rigid-rotor harmonic oscillator (RRHO) model (unscaled, 298.15 K, 1 atm). To describe the solution state more accurately, a concentration change term of 1.89 kcal mol^{-1} (1 M standard solution state, 298.15 K) was added to each structure.[188] More accurate electronic energies were computed using the PW6B95 functional,[189] Grimme's D3(BJ) dispersion correction,[190] the def2-TZVPP basis set,[184] and the PCM and SMD[191] solvation models (MeCN) at all stationary points. An *ultrafine* grid was used throughout.

For the spin state splitting energies and for the free energies for the reaction between **1** and TTBP calculations electronic energies were also evaluated with the M06-L and B3LYP[192]-D3(BJ) functionals all in combination with the def2-TZVPP basis set and the PCM solvation model (MeCN).

For the analysis of the electron flow for the hydrogen atom abstraction our previously reported procedure was followed.[103,156] The intrinsic reaction coordinates (IRCs).[193] for both the C-H oxidation of CHD and DHA by complex **1** were computed for up to 50 steps in the forward and reverse reactions at the level of theory indicated for geometries above (maxstep=5). For the merged IRCs (reverse and forward directions) KS-wave functions were recomputed in ORCA 4.2.1[194] at the M06-L/def2-SVP level of theory using the CPCM solvation model[187] mimicking the MeCN solvation. Calculations were accelerated using the RI-J approach employing Weigend's universal fitting basis sets.[184] *Grid6* was used throughout. The KS-wave functions obtained were converted into intrinsic bond orbitals (IBOs)[155] using IboView.[156,195] Iboexp = 2 was used throughout.

For more details and tables see supporting information of the original publication "E. Dobbelaar, C. Rauber, T. Bonck, H. Kelm, M. Schmitz, M. E. de Waal Malefijt, J. E. M. N. Klein, and H.-J. Krüger, "Combining Structural with Functional Model Properties in Iron Synthetic Analogue Complexes for the Active Site in Rabbit Lipoxygenase" *Journal of the American Chemical Society* **2021**, 143 (33), 13145-13155, DOI: 10.1021/jacs.1c04422". Copyright 2021 American Chemical Society.[1]

10. Attachment

10.1. Rights & Permissions

This dissertation contains previously published work that has been reproduced (adapted) with permission from “E. Dobbelaar, C. Rauber, T. Bonck, H. Kelm, M. Schmitz, M. E. de Waal Malefijt, J. E. M. N. Klein, and H.-J. Krüger, “Combining Structural with Functional Model Properties in Iron Synthetic Analogue Complexes for the Active Site in Rabbit Lipoxygenase” Journal of the American Chemical Society **2021**, *143* (33), 13145-13155, DOI: 10.1021/jacs.1c04422”. Copyright 2021 American Chemical Society and the supporting information, respectively.

Direct link to the original publication: https://pubs.acs.org/doi/10.1021/jacs.1c04422

The permission license granted by Rightslink© Copyright Clearance Centre on 05. January 2022 for the purpose of including the previously published work into this dissertation is provided on the following page. Because this dissertation is submitted to and remains with RPTU Kaiserslautern-Landau, this page serves as the copy that is to be shared with the university according to Rightslink© Copyright Clearance Centre.

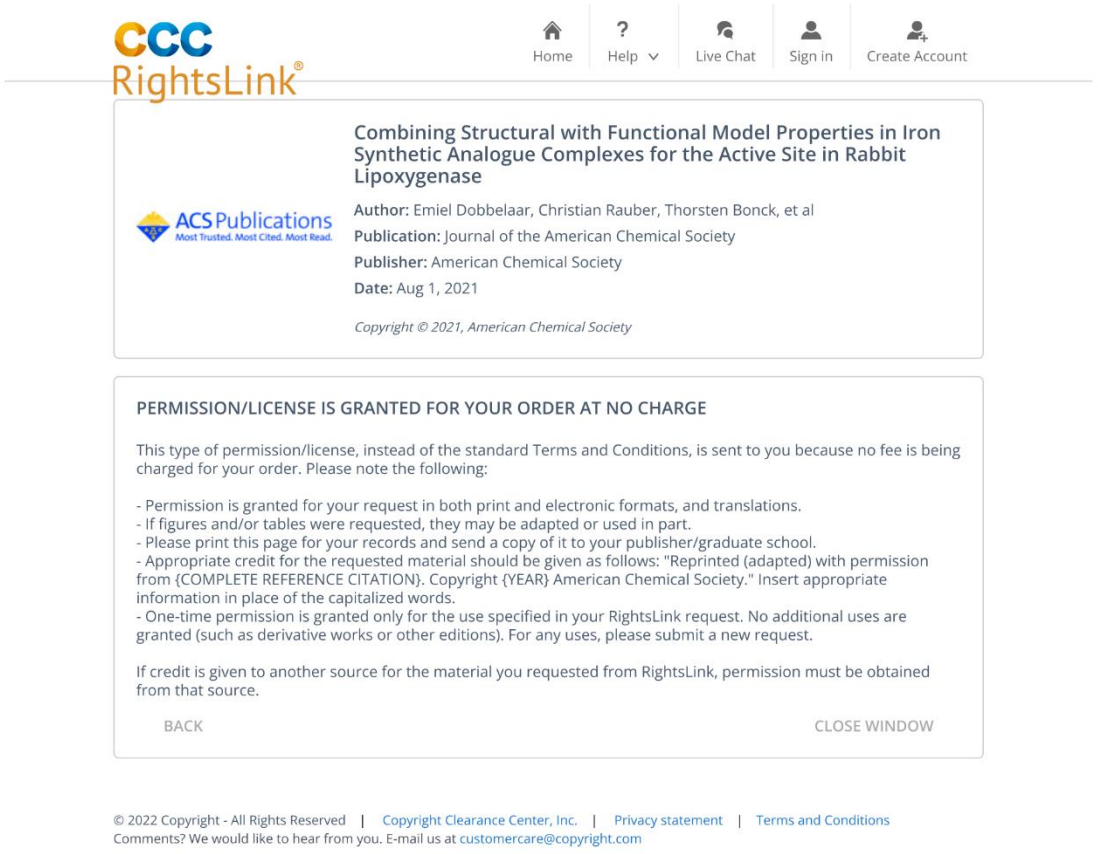

CCC RightsLink®

Home | Help | Live Chat | Sign in | Create Account

ACS Publications
Most Trusted. Most Cited. Most Read.

Combining Structural with Functional Model Properties in Iron Synthetic Analogue Complexes for the Active Site in Rabbit Lipoxygenase

Author: Emiel Dobbelaar, Christian Rauber, Thorsten Bonck, et al
Publication: Journal of the American Chemical Society
Publisher: American Chemical Society
Date: Aug 1, 2021

Copyright © 2021, American Chemical Society

PERMISSION/LICENSE IS GRANTED FOR YOUR ORDER AT NO CHARGE

This type of permission/license, instead of the standard Terms and Conditions, is sent to you because no fee is being charged for your order. Please note the following:

- Permission is granted for your request in both print and electronic formats, and translations.
- If figures and/or tables were requested, they may be adapted or used in part.
- Please print this page for your records and send a copy of it to your publisher/graduate school.
- Appropriate credit for the requested material should be given as follows: "Reprinted (adapted) with permission from {COMPLETE REFERENCE CITATION}. Copyright {YEAR} American Chemical Society." Insert appropriate information in place of the capitalized words.
- One-time permission is granted only for the use specified in your RightsLink request. No additional uses are granted (such as derivative works or other editions). For any uses, please submit a new request.

If credit is given to another source for the material you requested from RightsLink, permission must be obtained from that source.

BACK CLOSE WINDOW

10.2. NMR Spectroscopy

See separate electronic document.

10.3. Structural Data

See separate electronic document.

10.4. Spin Density Calculations

See separate electronic document.

10.5. Author Information (Emiel Dobbelaar)

10.5.1. Curriculum Vitae

Education & Experience:

	Project Manager Material Technologies
12/2022 – now	Freudenberg Technology Innovation SE & Co. KG
	PhD Candidate
01/2019 – 11/2022	TU Kaiserslautern, Germany | Prof. H.-J. Krüger
	M. Sc. Chemistry
10/2016 – 11/2018	TU Kaiserslautern, Germany & UC Dublin, Ireland (11/2017 – 02/2018)
	B. Sc. Chemistry
10/2013 – 03/2017	TU Kaiserslautern, Germany
	Internship Chemical Industry
06/2013 – 08/2013	BASF Polymer Dispersions Research
	High School Graduation
01/2006 – 03/2013	Werner-Heisenberg-Gymnasium (High-School), Germany
08/2004 – 12/2006	German School Helsinki, Finnland
11/2002 – 07/2004	Kurpfalzschule Wachenheim an der Weinstraße, Germany
01/2000 – 10/2002	Swiss School Singapore, Singapore

Honors & Awards: Best Oral Presentation at the Koordinationchemie Tagung (2020), “Deutschlandstipendium” scholarship for gifted and high-achieving students (2017 – 2018).

Research Stays: Argonne National Laboratory /Advanced Photon Source (2018), Los Alamos National High Magnetic Field Laboratory (2018), Queens University Belfast (2018), University College Dublin (2017 – 2018).

Membership and Service: *German Chemical Society (GDCh)* (since 2017) incl. subdivision memberships in macromolecular chemistry (since 2023), sustainable chemistry (since 2020), the Wöhler Vereinigung of inorganic chemistry (since 2020), and the young chemists network (GDCh-JCF) (since 2015). **Service:** Regional chair, regional treasurer, federal chair, and federal board member of GDCh-JCF (2018 – 2021); founder and leader of the GDCh-JCF team sustainability (2020 – 2021), co-founder & federal board member of the Young Inorganic Chemists Group of the Wöhler Vereinigung JuWöV (2021 – 2023); GDCh Sustainability Committee member (2023). *International Younger Chemists Network (IYCN)* (since 2019). **Service:** Board Member and Public Outreach Committee Leader (2021 – 2022), inaugural task force member of the Global Conversation on Sustainability (since 2022). *UNEP major group for children and youth (UNEP MGCY)* (since 2021). **Service:** Founding member and scientific advisor of the Coordination Committee of the Chemicals & Waste Youth Platform (2021 – now). Other Services: Various student representative functions at TU Kaiserslautern (2013 – 2017) and founding of a Scientists for Future (S4F) regional group Kaiserslautern (2019).

10.5.2. Publication List

Research Articles

1. V. B. Jakobsen, E. Trzop, E. Dobbelaar, L. C. Gavin, S. Chikara, X. Ding, M. Lee, K. Esien, H. Müller-Bunz, S. Felton, E. Collet, M. Carpenter, V. S. Zapf* G. G. Morgan*, "Domain Wall Dynamics in a Ferroelastic Spin Crossover Complex with Giant Magnetoelectric Coupling", *J. Am. Chem. Soc.* **2022**, 144, 1, 195–211. DOI: 10.1021/jacs.1c08214

2. E. Dobbelaar, V. B. Jakobsen, E. Trzop, M. Lee, S. Chikara, X. Ding, H. Müller-Bunz, K. Esien, S. Felton, M. A. Carpenter, E. Collet,* G. G. Morgan* and V. S. Zapf*, "Thermal and Magnetic Field Switching in a Two-Step Hysteretic Mn(III) Spin Crossover Compound Coupled to Symmetry Breakings" *Angew. Chem. Int. Ed.* **2022**, 61, e202114021, DOI: 10.1002/anie.202114021, Angew. Chem. **2021**, 10.1002/ange.202114021.

3. E. Dobbelaar, C. Rauber, T. Bonck, H. Kelm, M. Schmitz, M. E. de Waal Malefijt, J. E. M. N. Klein, H.-J. Krüger*, "Combining Structural with Functional Model Properties in Iron Synthetic Analogue Complexes for the Active Site in Rabbit Lipoxygenase", *J. Am Chem. Soc.* **2021**, 143, 33, 13145 – 13155. DOI: 10.1021/jacs.1c04422.

4. V.B. Jakobsen§, S. Chikara§, J-X. Yu, E. Dobbelaar, C. T., Kelly, X. Ding, F. Weickert, E. Trzop, E. Collet, H.-P. Cheng, G. G. Morgan*, V. S. Zapf*, "Giant Magnetoelectric Coupling and Magnetic Field-Induced Permanent Switching in a Spin Crossover Mn(III) Complex", *Inorg. Chem.* **2021**, 60, 6167 – 6175. DOI: 10.1021/acs.inorgchem.0c02789. On the Cover of Inorg. Chem. Vol. 60, 9, 2021. § = equal contributions.

5. V.B. Jakobsen, E. Trzop, L. C. Gavin, E. Dobbelaar, S. Chikara, X. Ding, K. Esien, H. Müller-Bunz, S. Felton, V. S. Zapf, E. Collet*, M. A. Carpenter*, G. G. Morgan*, "Stress-induced Domain Wall Motion in a Ferroelastic Mn3+ Spin Crossover Complex", *Angew. Chem. Int. Ed.* **2020**, 59, 13305 – 13312, DOI: 10.1002/anie.202003041, Angew. Chem. **2020**, 132, 13407 – 13414, 10.1002/ange.202003041.

Opinion Pieces & Interviews

6. E. Dobbelaar*, S. Goher, J. L. Vidal, N. K. Obhi, B. M. B. Felisilda, Y. S. L. Choo, H. Ismail, H. L. Lee, V. Nascimento, R. Al Bakain, M. Ranasinghe, B. L. Davids, A. Naim, N.-A. Offiong, J. Borges,* T. John,* "Towards a Sustainable Future: Challenges and Opportunities for Young Chemists", *Angew. Chem. Int. Ed., invited article, submitted* **2023**.

7. M. Dilanas,§ E. Dobbelaar,§ C. Gerischer,§ A. Haseloer,§ T. John,§ C. Neumeier,§ "Interview with Prof. Dr. Benjamin List - Nobel Laureate in Chemistry 2021", *Chem. Eur. J.* **2022**, 28 (44), e202201236. DOI: https://doi.org/10.1002/chem.202201236 § = equal contributions.

8. J. Richter, E. Dobbelaar*, "Young Chemists Voice in Support of the SDGs", *Chem. Int.* **2022**, 44, 1, 6 – 10. DOI: 10.1515/ci-2022-0103

9. C. Soterío, E. Dobbelaar, S. M. G. Lama, „Becoming a Scientist Means Empowering Oneself to Improve Life", *Chem. Views* **2022**, DOI: 10.1002/chemv.202200003.

10. E. Dobbelaar*, J. Richter, "An Overview of Young Chemists' Expectations Towards the Sustainable Development of the Chemical Sector. Opinions That Matter", *Pure Appl. Chem.* **2022**, 94, 1, 1 – 14. DOI: 10.1515/pac-2021-0602.

10.5.3. Conference Contributions

Oral presentations related to this work:

[1] 9. Promovierendenseminar TU Kaiserslautern, Kaiserslautern, Germany, April **2022**.

[2] JuWöV Sessions, Junge Wöhler Vereinigung (JuWöV) of the German Chemical Society (GDCh), Online, February **2022**.

[3] 24. JCF Frühjahrssymposium, Online, March **2021**.

[4] FrenchBIC 20 2.0, Online, October **2020**.

[5] 16. Koordinationschemie-Treffen, Freiburg, Germany, March **2020**.

Poster presentations related to this work:

[1] 21st Conference on Inorganic Chemistry, Marburg, Germany, **2022**.

[2] EuroBIC-16, Grenoble, France, **2022**.

[3] 15. Koordinationschemie-Treffen, Munich, Germany, March **2019**.

11. References

[1] E. Dobbelaar, C. Rauber, T. Bonck, H. Kelm, M. Schmitz, M. E. de Waal Malefijt, J. E. M. N. Klein, H.-J. Krüger, *J. Am. Chem. Soc.* **2021**, *143*, 13145.

[2] E. Dobbelaar, *Studien zur Synthese und Funktionalität eines Modellsystems der Kaninchen-Lipoxygenase*. Master Thesis, Kaiserslautern, Germany, **2018**.

[3] Pascal Peter, *unpublished results*, Kaiserslautern, Germany, **2023**.

[4] P. Kurz in *Riedel Moderne Anorganische Chemie* (Eds.: P. Kurz, D. Gudat, H.-J. Meyer, C. Janiak), De Gruyter, **2018**, pp. 831–910.

[5] R. Williams, *Coord. Chem. Rev.* **1990**, *100*, 573.

[6] D. Rehder, *Bioinorganic Chemistry*, Oxford University Press, Oxford, **2014**.

[7] K. Schwarz, W. Mertz, *Arch. Biochem. Biophys.* **1959**, *85*, 292.

[8] a) K. R. Di Bona, S. Love, N. R. Rhodes, D. McAdory, S. H. Sinha, N. Kern, J. Kent, J. Strickland, A. Wilson, J. Beaird et al., *J. Biol. Inorg. Chem.* **2011**, *16*, 381; b) J. B. Vincent, *J. Nutrition* **2017**, *147*, 2212; c) M. A. Zoroddu, J. Aaseth, G. Crisponi, S. Medici, M. Peana, V. M. Nurchi, *J. Inorg. Biochem.* **2019**, *195*, 120.

[9] J. J. R. F. Da Silva, R. J. P. Williams, *The biological chemistry of the elements*. *The inorganic chemistry of life*, Oxford Univ. Press, Oxford, **2009**.

[10] John Emsley, *Nature's building blocks*. *BNID 107256*, Oxford University Press, **2011**.

[11] The main topics of bioinorganic chemistry and main aspects of synthetic bioinorganic chemistry described are modified from those described in P. Kurz, *Chapter 5. Bioanorganische Chemie* in *Riedel Moderne Anorganische Chemie*, *De Gruyter*, **2018**.

[12] S. J. Lippard, J. M. Berg, *Principles of bioinorganic chemistry*, University Science Books, Mill Valley, Calif., **1994**.

[13] a) B. List, R. A. Lerner, C. F. Barbas, *J. Am. Chem. Soc.* **2000**, *122*, 2395; b) C. Jin, Z. Chen, S. Shi, Y. Li, S. Liu, S. Wang, H. Wang, C. Chen, *Inorg. Chem.* **2022**, *61*, 12190; c) H. Sardon, *Macromolecules* **2022**, *55*, 3769.

[14] H. U. Sverdrup, M. W. Johnson, R. H. Fleming, *The Oceans, Their Physics, Chemistry, and General Biology*, Prentice-Hall Inc., New York, **1942**.

[15] A. M. James, M. P. Lord, *Macmillan's chemical and physical data*, Macmillan, London, **1992**.

[16] *Geochim. Cosmochim. Acta* **2002**, *66*, 1943.

[17] J. F. Kasting, *Science* **1993**, *259*, 920.

[18] H. D. Holland, *Geochim. Cosmochim. Acta* **2002**, *66*, 3811.

[19] H. Ueda, T. Shibuya, *Minerals* **2021**, *11*, 389.

[20] N. Lane, *Life ascending*. *The ten great inventions of evolution*, Norton, New York, **2009**.

[21] H. Beinert, R. H. Holm, E. Münck, *Science* **1997**, *277*, 653.

[22] T. Cardona, *Heliyon* **2018**, *4*, e00548.

[23] H. D. Holland, *Philos. Trans. R. Soc. Lond., B, Biol. Sci.* **2006**, *361*, 903.

[24] N. Takeno, *Geological Survey of Japan* **2005**.

[25] R. Williams, R. E. M. Rickaby, *A Chemical Account of Evolution*, *Chemistry World* **2012**, online resource: https://www.chemistryworld.com/features/a-chemical-account-of-evolution/5133.article, last checked 08.04.2023.

[26] E. Chi Fru, N. P. Rodríguez, C. A. Partin, S. V. Lalonde, P. Andersson, D. J. Weiss, A. El Albani, I. Rodushkin, K. O. Konhauser, *PNAS* **2016**, *113*, 4941.

[27] M. Sandy, A. Butler, *Chem. Rev.* **2009**, *109*, 4580.

[28] T. W. Lyons, C. T. Reinhard, N. J. Planavsky, *Nature* **2014**, *506*, 307.
[29] a) M. S. W. Hodgskiss, P. W. Crockford, Y. Peng, B. A. Wing, T. J. Horner, *PNAS* **2019**, *116*, 17207; b) A. L. Sessions, D. M. Doughty, P. V. Welander, R. E. Summons, D. K. Newman, *Curr. biol.* **2009**, *19*, R567-74.
[30] S. Takano, M. Tanimizu, T. Hirata, Y. Sohrin, *Nat. commun.* **2014**, *5*, 5663.
[31] N. Zhao, C. A. Enns, *Curr. top. membr.* **2012**, *69*, 67.
[32] R. R. Crichton, M. Charloteaux-Wauters, *Eur. J. Biochem.* **1987**, *164*, 485.
[33] C. C. Philpott, M.-S. Ryu, A. Frey, S. Patel, *Journal biol. chem.* **2017**, *292*, 12764.
[34] A. Stank, D. B. Kokh, J. C. Fuller, R. C. Wade, *Acc. Chem. Res.* **2016**, *49*, 809.
[35] A. Majumdar, S. Sarkar, *Coord. Chem. Rev.* **2011**, *255*, 1039.
[36] J. A. Ibers, R. H. Holm, *Science* **1980**, *209*, 223.
[37] R. H. Holm, E. I. Solomon, *Chem. Rev.* **2004**, *104*, 347.
[38] G. Roelfes, *Acc. Chem. Res.* **2019**, *52*, 545.
[39] D. Lee, S. J. Lippard in *Comprehensive coordination chemistry II*. *From biology to nanotechnology* (Eds.: J. A. McCleverty, T. J. Meyer), Elsevier/Pergamon, Amsterdam, **2004**, pp. 309–342.
[40] a) B. P. Gaber, V. Miskowski, T. G. Spiro, *J. Am. Chem. Soc* **1974**, *96*, 6868; b) G. Winkelmann (Ed.) *CRC Press Revivals*, CRC Press, Boca Raton, FL, **2017**.
[41] a) T. A. Rouault, *Nat. Rev. Mol. Cell Biol.* **2015**, *16*, 45; b) W. H. Orme-Johnson, *Annu. Rev. Biochem.* **1973**, *42*, 159.
[42] M. Paoli, J. Marles-Wright, A. Smith, *DNA Cell Biol.* **2002**, *21*, 271.
[43] E. I. Solomon, S. Goudarzi, K. D. Sutherlin, *Biochem.* **2016**, *55*, 6363.
[44] A. J. Jasniewski, L. Que, *Chem. Rev.* **2018**, *118*, 2554.
[45] M. R. A. Blomberg, T. Borowski, F. Himo, R.-Z. Liao, P. E. M. Siegbahn, *ChemRev.* **2014**, *114*, 3601.
[46] P. C. A. Bruijnincx, G. van Koten, R. J. M. Klein Gebbink, *Chem. Rev.* **2008**, *37*, 2716.
[47] P. L. Roach, I. J. Clifton, V. Fülöp, K. Harlos, G. J. Barton, J. Hajdu, I. Andersson, C. J. Schofield, J. E. Baldwin, *Nature* **1995**, *375*, 700.
[48] J. S. Rieske, D. H. MacLennan, R. Coleman, *Biochem. Biophys. Res. Commun.* **1964**, *15*, 338.
[49] S. M. Barry, G. L. Challis, *ACS Catalysis* **2013**, *3*.
[50] M. I. Flydal, A. Martinez, *IUBMB life* **2013**, *65*, 341.
[51] E. Romero, J. R. Gómez Castellanos, G. Gadda, M. W. Fraaije, A. Mattevi, *Chem. Rev.* **2018**, *118*, 1742.
[52] B. J. Wallar, J. D. Lipscomb, *Chem. Rev.* **1996**, *96*, 2625.
[53] S. Sahu, D. P. Goldberg, *J. Am. Chem. Soc.* **2016**, *138*, 11410.
[54] N. Lehnert, E. I. Solomon, *J. Biol. Inorg. Chem.* **2003**, *8*, 294.
[55] M. M. Abu-Omar, A. Loaiza, N. Hontzeas, *Chem. Rev.* **2005**, *105*, 2227.
[56] W. Kaim, *Bioanorganische Chemie*. *An Introduction and Guide*, John Wiley & Sons Incorporated, New York, **2013**.
[57] J. Cho, S. Jeon, S. A. Wilson, L. V. Liu, E. A. Kang, J. J. Braymer, M. H. Lim, B. Hedman, K. O. Hodgson, J. S. Valentine et al., *Nature* **2011**, *478*, 502.
[58] H. Bataineh, O. Pestovsky, A. Bakac, *Inorg. Chem.* **2016**, *55*, 6719.
[59] F. G. Bordwell, X. M. Zhang, R. Filler, *J. Org. Chem.* **1993**, *58*, 6067.
[60] a) J. Deutscher, P. Gerschel, K. Warm, U. Kuhlmann, S. Mebs, M. Haumann, H. Dau, P. Hildebrandt, U.-P. Apfel, K. Ray, *Chem. Commun.* **2021**, *57*, 2947; b) C. Winslow, H. B. Lee, M. J. Field, S. J. Teat, J. Rittle, *J. Am. Chem. Soc.* **2021**, *143*, 13686.
[61] A. J. Simaan, F. Banse, J. J. Girerd, K. Wieghardt, E. Bill, *Inorg. Chem.* **2001**, *40*, 6538.

[62] J. Hohenberger, K. Ray, K. Meyer, *Nat. Commun.* **2012**, *3*, 720.
[63] H. M. Hüppe, K. Keisers, F. Fink, S. D. Mürtz, A. Hoffmann, L. Iffland, U.-P. Apfel, S. Herres‐Pawlis, *Isr. J. Chem.* **2020**, *60*, 987.
[64] B. J. Gaffney, *Chem. Asian J.* **2020**, *15*, 42.
[65] a) A. Andreou, I. Feussner, *Phytochem.* **2009**, *70*, 1504; b) M. J. Schilstra, G. A. Veldink, J. F. Vliegenthart, *Biochem.* **1994**, *33*, 3974.
[66] R. J. Kuban, R. Wiesner, J. Rathman, G. Veldink, H. Nolting, V. A. Solé, H. Kühn, *Biochem. J.* **1998**, *332 (Pt 1)*, 237.
[67] J. Choi, J. K. Chon, S. Kim, W. Shin, *Proteins* **2008**, *70*, 1023.
[68] S. A. Gillmor, A. Villaseñor, R. Fletterick, E. Sigal, M. F. Browner, *Nat. Struct. Biol.* **1997**, *4*, 1003.
[69] S. Xu, T. C. Mueser, L. J. Marnett, M. O. Funk, *Structure* **2012**, *20*, 1490.
[70] a) I. Ivanov, H. Kuhn, D. Heydeck, *Gene* **2015**, *573*, 1; b) M. E. Newcomer, A. R. Brash, *Prot. Sci.* **2015**, *24*, 298; c) S. Navaratnam, M. C. Feiters, M. Al-Hakim, J. C. Allen, G. A. Veldink, J. Vliegenthart, *Biochim. Biophys. Acta* **1988**, *956*, 70.
[71] R. W. Bryant, J. M. Bailey, T. Schewe, S. M. Rapoport, *J. Biol. Chem.* **1982**, *257*, 6050.
[72] H. Kuhn, S. Banthiya, K. van Leyen, *Biochim. Biophys. Acta* **2015**, *1851*, 308.
[73] R. C. Murphy, M. A. Gijón, *Biochem. J.* **2007**, *405*, 379.
[74] G. Litwack in *Hormones*, Elsevier, **2022**, pp. 195–212.
[75] C. R. Goldsmith, T. D. P. Stack, *Inorg. Chem.* **2006**, *45*, 6048.
[76] M. J. Knapp, K. Rickert, J. P. Klinman, *J. Am. Chem. Soc.* **2002**, *124*, 3865.
[77] P. Li, A. V. Soudackov, S. Hammes-Schiffer, *J. Phys. Chem. Lett.* **2018**, *9*, 6444.
[78] L. Bénisvy, S. Halut, B. Donnadieu, J.-P. Tuchagues, J.-C. Chottard, Y. Li, *Inorg. Chem.* **2006**, *45*, 2403.
[79] L. M. Brines, M. K. Coggins, P. C. Y. Poon, S. Toledo, W. Kaminsky, M. L. Kirk, J. A. Kovacs, *J. Am. Chem. Soc.* **2015**, *137*, 2253.
[80] S. Ogo, S. Wada, Y. Watanabe, M. Iwase, A. Wada, M. Harata, K. Jitsukawa, H. Masuda, H. Einaga, *Angew. Chem. Int. Ed.* **1998**, *37*, 2102.
[81] S. Ogo, R. Yamahara, M. Roach, T. Suenobu, M. Aki, T. Ogura, T. Kitagawa, H. Masuda, S. Fukuzumi, Y. Watanabe, *Inorg. Chem.* **2002**, *41*, 5513.
[82] a) J. Mukherjee, R. L. Lucas, M. K. Zart, D. R. Powell, V. W. Day, A. S. Borovik, *Inorg. Chem.* **2008**, *47*, 5780; b) C. Y. Yeh, C. J. Chang, D. G. Nocera, *J. Am. Chem. Soc.* **2001**, *123*, 1513; c) M. B. Chambers, S. Groysman, D. Villagrán, D. G. Nocera, *Inorg. Chem.* **2013**, *52*, 3159; d) J. Burger, P. Klfers, *Z. Anorg. Allg. Chem.* **1996**, *622*, 1740; e) K. D. Hodges, R. G. Wollmann, S. L. Kessel, D. N. Hendrickson, D. G. van Derveer, E. K. Barefield, *J. Am. Chem. Soc.* **1979**, *101*, 906; f) K. Keshari, M. Bera, L. Velasco, S. Munshi, G. Gupta, D. Moonshiram, S. Paria, *Chem. Sci.* **2021**, *12*, 4418; g) C. E. MacBeth, A. P. Golombek, V. G. Young, C. Yang, K. Kuczera, M. P. Hendrich, A. S. Borovik, *Science* **2000**, *289*, 938; h) S. A. Cook, J. W. Ziller, A. S. Borovik, *Inorg. Chem.* **2014**, *53*, 11029.
[83] R. Çelenligil‐Çetin, P. Paraskevopoulou, R. Dinda, N. Lalioti, Y. Sanakis, A. M. Rawashdeh, R. J. Staples, E. Sinn, P. Stavropoulos, *Eur. J. Inorg. Chem.* **2008**, *2008*, 673.
[84] R. Celenligil-Cetin, P. Paraskevopoulou, R. Dinda, R. J. Staples, E. Sinn, N. P. Rath, P. Stavropoulos, *Inorg. Chem.* **2008**, *47*, 1165.
[85] N. Ortega-Villar, V. M. Ugalde-Saldívar, B. Flores-Pérez, M. Flores-Alamo, J. A. Real, R. Moreno-Esparza, *Inorg. Chim. Acta* **2011**, *375*, 213.
[86] M. J. Drummond, C. L. Ford, D. L. Gray, C. V. Popescu, A. R. Fout, *J. Am. Chem. Soc.* **2019**, *141*, 6639.

[87] H. S. Soo, A. C. Komor, A. T. Iavarone, C. J. Chang, *Inorg. Chem.* **2009**, *48*, 10024.
[88] E. M. Matson, J. A. Bertke, A. R. Fout, *Inorg. Chem.* **2014**, *53*, 4450.
[89] V. Yadav, J. B. Gordon, M. A. Siegler, D. P. Goldberg, *J. Am. Chem. Soc.* **2019**, *141*, 10148.
[90] V. Yadav, R. J. Rodriguez, M. A. Siegler, D. P. Goldberg, *J. Am. Chem. Soc.* **2020**, *142*, 7259.
[91] V. Yadav, M. A. Siegler, D. P. Goldberg, *J. Am. Chem. Soc.* **2021**, *143*, 46.
[92] H. Gao, J. T. Groves, *J. Am. Chem. Soc.* **2017**, *139*, 3938.
[93] a) R. E. Cowley, N. A. Eckert, S. Vaddadi, T. M. Figg, T. R. Cundari, P. L. Holland, *J. Am. Chem. Soc.* **2011**, *133*, 9796; b) C. A. M. Carr, J. P. Klinman, *Biochem.* **2014**, *53*, 2212; c) S. Hu, S. C. Sharma, A. D. Scouras, A. V. Soudackov, C. A. M. Carr, S. Hammes-Schiffer, T. Alber, J. P. Klinman, *J. Am. Chem. Soc.* **2014**, *136*, 8157; d) J. P. Layfield, S. Hammes-Schiffer, *Chem. Rev.* **2014**, *114*, 3466.
[94] J. M. Mayer, *Acc. Chem. Res.* **2011**, *44*, 36.
[95] J. M. Mayer, *Ann. Rev Phys. Chem.* **2004**, *55*, 363.
[96] J. J. Warren, T. A. Tronic, J. M. Mayer, *Chem. Rev.* **2010**, *110*, 6961.
[97] C. F. Wise, R. G. Agarwal, J. M. Mayer, *J. Am. Chem. Soc.* **2020**, *142*, 10681.
[98] J. P. Roth, S. Lovell, J. M. Mayer, *J. Am. Chem. Soc.* **2000**, *122*, 5486.
[99] D. Usharani, D. C. Lacy, A. S. Borovik, S. Shaik, *J. Am. Chem. Soc.* **2013**, *135*, 17090.
[100] E. A. Mader, A. S. Larsen, J. M. Mayer, *J. Am. Chem. Soc.* **2004**, *126*, 8066.
[101] E. A. Mader, E. R. Davidson, J. M. Mayer, *J. Am. Chem. Soc.* **2007**, *129*, 5153.
[102] R. A. Marcus, *J. Phys. Chem.* **1963**, *67*, 853.
[103] J. E. M. N. Klein, G. Knizia, *Angew. Chem. Int. Ed.* **2018**, *57*, 11913.
[104] G. S. Hammond, *J. Am. Chem. Soc.* **1955**, *77*, 334.
[105] Rudolph A. Marcus, *Nobel Lecture* **1992**.
[106] J. M. Tedder, *Angew. Chem. Int. Ed.* **1982**, *21*, 401.
[107] M. G. Evans, M. Polanyi, *Trans. Faraday Soc.* **1938**, *34*, 11.
[108] Ronald P. Bell, *Proc. R. Soc. Lond. A* **1936**, *154*, 414.
[109] R. G. Agarwal, C. F. Wise, J. J. Warren, J. M. Mayer, *Chem. Rev.* **2022**, *122*, 1482.
[110] C. R. Goldsmith, R. T. Jonas, T. D. P. Stack, *J. Am. Chem. Soc.* **2002**, *124*, 83.
[111] a) P. Mulder, H.-G. Korth, D. A. Pratt, G. A. DiLabio, L. Valgimigli, G. F. Pedulli, K. U. Ingold, *J. Phys. Chem. A* **2005**, *109*, 2647; b) M. H. Abraham, P. L. Grellier, D. V. Prior, P. P. Duce, J. J. Morris, P. J. Taylor, *J. Chem. Soc., Perkin Trans. 2* **1989**, 699; c) M. H. Abraham, P. L. Grellier, D. V. Prior, J. J. Morris, P. J. Taylor, *J. Chem. Soc., Perkin Trans. 2* **1990**, 521; d) M. H. Abraham, P. L. Grellier, D. V. Prior, R. W. Taft, J. J. Morris, P. J. Taylor, C. Laurence, M. Berthelot, R. M. Doherty, et al., *J. Am. Chem. Soc.* **1988**, *110*, 8534.
[112] C. Rauber, *Reaktionen von einkernigen Eisen(II)-Benzoat- und KetocarboxylatKomplexen mit molekularem Sauerstof*. Dissertation, Kaiserslautern, Germany, **2008**.
[113] T. Bonck, *Benzoatoeisen(II)- und Benzoatohydroxoeisen(III)-Komplexe mit dem Liganden N,N'-Di-tert-butyl-2,11-diaza[3.3](2,6)pyridinophan als strukturelle und funktionelle Modelle der Lipoxygenase*. Diplomarbeit, Kaiserslautern, Germany, **2011**.
[114] H.-J. Krüger, *2,11-Diaza[3.3](2,6)pyridinophane – A Unique Class of Ligands*. Habilitation Thesis, Hamburg, Germany, **1997**.
[115] H.-J. Krüger, *Coord. Chem. Rev.* **2009**, *253*, 2450.

[116] C. Rauber, *Eisen(II)-Komplexe mit Diazapyridinophan-Liganden – Synthese und Reaktivitätsuntersuchungen mit molekularem Sauerstoff*. Diplomarbeit, Kaiserslautern, Germany, **2003**.
[117] J. R. Khusnutdinova, J. Luo, N. P. Rath, L. M. Mirica, *Inorg. Chem.* **2013**, *52*, 3920.
[118] P. T. Anastas, J. C. Warner, *Green chemistry*. *Theory and practice*, Oxford University Press, Oxford, **2000**.
[119] W. O. Koch, H.-J. Krüger, *Angew. Chem. Int. Ed.* **1996**, *34*, 2671.
[120] R. C. Scarrow, M. G. Trimitsis, C. P. Buck, G. N. Grove, R. A. Cowling, M. J. Nelson, *Biochem.* **1994**, *33*, 15023.
[121] E. Becker, K. Kirchner, K. Mereiter, *Acta Cryst. E* **2009**, *65*, i71.
[122] S. Yahyaoui, W. Rekik, H. Naïli, T. Mhiri, T. Bataille, *J. Solid State Chem.* **2007**, *180*, 3560.
[123] S. F. A. Kettle, *Physical Inorganic Chemistry*. *A Coordination Chemistry Approach*, Springer International Publishing, **1996**.
[124] N. F. Chilton, R. P. Anderson, L. D. Turner, A. Soncini, K. S. Murray, *J. Comp. Chem.* **2013**, *34*, 1164.
[125] P. Gütlich, R. Link, A. Trautwein, *Mössbauer Spectroscopy and Transition Metal Chemistry*. *Fundamentals and Applications*, Springer Berlin Heidelberg, Berlin, Heidelberg, **2011**.
[126] H. D. Lutz, W. Eckers, H. Haeuseler, *J. Mol. Struct.* **1982**, *80*, 221.
[127] G. Kortüm, *Reflexionsspektroskopie*. *Grundlagen, Methodik, Anwendungen*, Springer International Publishing, **1969**, p. 108.
[128] R. Aasa, *J. Chem. Phys.* **1970**, *52*, 3919.
[129] W. R. Hagen, *Biomolecular EPR Spectroscopy*, CRC Press, **2008**.
[130] S. Stoll, A. Schweiger, *J. Magn. Reson.* **2006**, *178*, 42.
[131] G. R. Fulmer, A. J. M. Miller, N. H. Sherden, H. E. Gottlieb, A. Nudelman, B. M. Stoltz, J. E. Bercaw, K. I. Goldberg, *Organomet.* **2010**, *29*, 2176.
[132] M. A. Pavlosky, Y. Zhang, T. E. Westre, Q.-F. Gan, E. G. Pavel, C. Campochiaro, B. Hedman, K. O. Hodgson, E. I. Solomon, *J. Am. Chem. Soc.* **1995**, *117*, 4316.
[133] R. H. Holm, P. Kennepohl, E. I. Solomon, *Chem. Rev.* **1996**, *96*, 2239.
[134] M. J. Nelson, *Biochem.* **1988**, *27*, 4273.
[135] V. W. Manner, T. F. Markle, J. H. Freudenthal, J. P. Roth, J. M. Mayer, *Chem. Commun.* **2008**, 256.
[136] For a reference of the 4,4'-isomer compare to infrared spectral data from the Bio-Rad/Sadtler IR data collection.
[137] C. D. Cook, R. C. Woodworth, *J. Am. Chem. Soc.* **1953**, *75*, 6242.
[138] J. Knaudt, S. Förster, U. Bartsch, A. Rieker, E.-G. Jäger, *Z. Naturforsch. B* **2000**, *55*, 86.
[139] a) K. Omura, *J. Org. Chem.* **1984**, *49*, 3046; b) K. Omura, *J. Org. Chem.* **2008**, *73*, 858.
[140] M. Lucarini, P. Pedrielli, G. F. Pedulli, S. Cabiddu, C. Fattuoni, *J. Org. Chem.* **1996**, *61*, 9259.
[141] G. R. Eaton, S. S. Eaton, D. P. Barr, R. T. Weber, *Quantitative EPR*. *A Practitioners Guide*, Springer Vienna, Vienna, **2010**.
[142] A. Kütt, S. Tshepelevitsh, J. Saame, M. Lõkov, I. Kaljurand, S. Selberg, I. Leito, *Eur. J. Org. Chem.* **2021**, *2021*, 1407.
[143] D. R. Lide (Ed.) *"Dissociation Constants of Organic Acids and Bases", in CRC Handbook of Chemistry and Physics*, CRC Press, Boca Raton, FL, **2005**.
[144] K. Izutsu, *Electrochemistry in nonaqueous solutions*, Wiley-VCH, Weinheim, **2009**.

[145] Y.-R. Luo, *Comprehensive Handbook of Chemical Bond Energies*, CRC Press, **2007**.
[146] I. Alkorta, J. Elguero, R. Gallo, *Open Chem.* **2013**, *11*, 1711.
[147] D. Jiang, W. Hu, M. Chen, Z. Fu, A. Su, B. Yang, F. Mao, C. Zhang, Y. Liu, D. Yin, *Chem. Sus. Chem.* **2020**, *13*, 1785.
[148] For a reference of the anthraquinone 1H-NMR spectrum see *Spectral Database for Organic Compounds (SDBS)*, *National Institute of Advanced Industrial Science and Technology (AIST)*, entry nr. 123, published **1999**-03-31.
[149] Y.-J. Chen, S.-C. Yang, C.-C. Tsai, K.-C. Chang, W.-H. Chuang, W.-L. Chu, V. Kovalev, W.-S. Chung, *CCDC 1031904: Experimental Crystal Structure Determination*, Cambridge Crystallographic Data Centre, **2015**.
[150] For a detailed description of the computational methods used and corresponding references see attachment.
[151] a) D. J. Xiao, E. D. Bloch, J. A. Mason, W. L. Queen, M. R. Hudson, N. Planas, J. Borycz, A. L. Dzubak, P. Verma, K. Lee et al., *Nat. Chem.* **2014**, *6*, 590; b) P. Verma, K. D. Vogiatzis, N. Planas, J. Borycz, D. J. Xiao, J. R. Long, L. Gagliardi, D. G. Truhlar, *J. Am. Chem. Soc.* **2015**, *137*, 5770; c) W.-M. Ching, A. Zhou, J. E. M. N. Klein, R. Fan, G. Knizia, C. J. Cramer, Y. Guo, L. Que, *Inorg. Chem.* **2017**, *56*, 11129.
[152] a) L. Goerigk, S. Grimme, *Phys. Chem. Chem. Phys.* **2011**, *13*, 6670; b) L. Goerigk, A. Hansen, C. Bauer, S. Ehrlich, A. Najibi, S. Grimme, *Phys. Chem. Chem. Phys.* **2017**, *19*, 32184; c) M. Steinmetz, S. Grimme, *Chem. Open.* **2013**, *2*, 115; d) M. M. Quintal, A. Karton, M. A. Iron, A. D. Boese, J. M. L. Martin, *J. Phys. Chem. A* **2006**, *110*, 709.
[153] P. Verma, Z. Varga, J. E. M. N. Klein, C. J. Cramer, L. Que, D. G. Truhlar, *Phys. Chem. Chem. Phys.* **2017**, *19*, 13049.
[154] a) S. Hammes-Schiffer, *J. Am. Chem. Soc.* **2015**, *137*, 8860; b) D. R. Weinberg, C. J. Gagliardi, J. F. Hull, C. F. Murphy, C. A. Kent, B. C. Westlake, A. Paul, D. H. Ess, D. G. McCafferty, T. J. Meyer, *Chem. Rev.* **2012**, *112*, 4016; c) M. H. V. Huynh, T. J. Meyer, *Chem. Rev.* **2007**, *107*, 5004.
[155] G. Knizia, *J. Chem. Theory. Comput.* **2013**, *9*, 4834.
[156] G. Knizia, J. E. M. N. Klein, *Angew. Chem. Int. Ed.* **2015**, *54*, 5518.
[157] F. G. Bordwell, *Acc. Chem. Res.* **1988**, *21*, 456.
[158] H.-B. Guo, F. He, B. Gu, L. Liang, J. C. Smith, *J. Phys. Chem. A* **2012**, *116*, 11870.
[159] P. K. Pal, S. Chowdhury, M. G. B. Drew, D. Datta, *New J. Chem.* **2002**, *26*, 367.
[160] F. E. Mabbs, F. E. Mabbs, D. J. Machin, *Magnetism and transition metal complexes*, Chapman and Hall, London, **1973**.
[161] a) L. P. Hammett, *J. Am. Chem. Soc.* **1937**, *59*, 96; b) in *Studies in Organic Chemistry*, Elsevier, **1994**, pp. 161–209.
[162] J. Shorter, *Chemie in unserer Zeit* **1985**, *19*, 197.
[163] C. L. Perrin, T. J. Dwyer, *Chem. Rev.* **1990**, *90*, 935.
[164] J. J. Warren, J. M. Mayer, *PNAS* **2010**, *107*, 5282.
[165] J. C. Yoder, J. P. Roth, E. M. Gussenhoven, A. S. Larsen, J. M. Mayer, *J. Am. Chem. Soc.* **2003**, *125*, 2629.
[166] K. Nakamoto, *Infrared and Raman spectra of inorganic and coordination compounds*. *Applications in Coordination, Organometallic, and Bioinorganic Chemistry*, John Wiley and Sons, Hoboken (N. J.), **2009**.
[167] A. Kohen, H.-H. Limbach (Eds.) *Isotope effects in chemistry and biology*, Taylor & Francis, Boca Raton, **2006**.

[168] For completeness, it should be stated that a very minor peak found at m/z = 424.0 (1.2 % height of the maximum peak) which could be explained by the presence of either a {[Fe(L-N$_4$^{t}Bu$_2$)]O$_2$[Fe(L-N$_4$^{t}Bu$_2$)}$^{2+}$ or a [Fe(L-N$_4$^{t}Bu$_2$)O]$^+$ cation. However, this cannot be verified, and the contamination is insignificantly small.
[169] S. N. Khattab, A. M. M. El Massry, A. El-Faham, A. Amer, A. A. Bekhit, *J. Heterocycl. Chem.* **2004**, *41*, 387.
[170] H. Eyring, *J. Chem. Phys.* **1935**, *3*, 107.
[171] G. Voss, W. Schramm, *HCA* **2000**, *83*, 2884.
[172] G. M. Sheldrick, *Acta Cryst. C* **2015**, *71*, 3.
[173] G. A. Bain, J. F. Berry, *J. Chem. Educ.* **2008**, *85*, 532.
[174] A. J. Ozinskas, A. M. Bobst, *Helv. Chim. Acta.* **1980**, *63*, 1407.
[175] D. B. G. Williams, M. Lawton, *J. Org. Chem.* **2010**, *75*, 8351.
[176] A. P. G. Kieboom, *Recl. Trav. Chim. Pays-Bas* **1988**, *107*, 685.
[177] W. L. F. Armarego, *Purification of laboratory chemicals*, Butterworth-Heinemann, Kidlington, Oxford, United Kingdom, Cambridge, MA, **2017**.
[178] D. D. Perrin, W. L. F. Armarego, D. R. Perrin, *Purification of laboratory chemicals*, Pergamon Press, Oxford, **1980**.
[179] a) F. Bottino, M. Di Grazia, P. Finocchiaro, F. R. Fronczek, A. Mamo, S. Pappalardo, *J. Org. Chem.* **1988**, *53*, 3521; b) B. Alpha, E. Anklam, R. Deschenaux, J.-M. Lehn, M. Pietraskiewiez, *HCA* **1988**, *71*, 1042.
[180] a) C. Steffen, K. Thomas, U. Huniar, A. Hellweg, O. Rubner, A. Schroer, *J. Comput. Chem.* **2010**, *31*, 2967; b) S. G. Balasubramani, G. P. Chen, S. Coriani, M. Diedenhofen, M. S. Frank, Y. J. Franzke, F. Furche, R. Grotjahn, M. E. Harding, C. Hättig et al., *J. Chem. Phys.* **2020**, *152*, 184107.
[181] M. J. Frisch, G. W. Trucks, H. B. Schlegel, G. E. Scuseria, M. A. Robb, J. R. Cheeseman, G. Scalmani, V. Barone, G. A. Petersson, H. Nakatsuji, X. Li, M. Caricato, A. V. Marenich, J. Bloino, B. G. Janesko, R. Gomperts, B. Mennucci, H. P. Hratchian, J. V. Ortiz, A. F. Izmaylov, J. L. Sonnenberg, D. Williams-Young, F. Ding, F. Lipparini, F. Egidi, J. Goings, B. Peng, A. Petrone, T. Henderson, D. Ranasinghe, V. G. Zakrzewski, J. Gao, N. Rega, G. Zheng, W. Liang, M. Hada, M. Ehara, K. Toyota, R. Fukuda, J. Hasegawa, M. Ishida, T. Nakajima, Y. Honda, O. Kitao, H. Nakai, T. Vreven, K. Throssell, J. A. Montgomery, Jr., J. E. Peralta, F. Ogliaro, M. J. Bearpark, J. J. Heyd, E. N. Brothers, K. N. Kudin, V. N. Staroverov, T. A. Keith, R. Kobayashi, J. Normand, K. Raghavachari, A. P. Rendell, J. C. Burant, S. S. Iyengar, J. Tomasi, M. Cossi, J. M. Millam, M. Klene, C. Adamo, R. Cammi, J. W. Ochterski, R. L. Martin, K. Morokuma, O. Farkas, J. B. Foresman, and D. J. Fox, *Gaussian 16 Rev. B.01* **2016**.
[182] Y. Zhao, D. G. Truhlar, *J. Chem. Phys.* **2006**, *125*, 194101.
[183] F. Weigend, R. Ahlrichs, *Phys. Chem. Chem. Phys.* **2005**, *7*, 3297.
[184] F. Weigend, *Phys. Chem. Chem. Phys.* **2006**, *8*, 1057.
[185] a) B. I. Dunlap, *J. Chem. Phys.* **1983**, *78*, 3140; b) B. I. Dunlap, *J. Mol. Struct.* **2000**, *529*, 37.
[186] G. Scalmani, M. J. Frisch, B. Mennucci, J. Tomasi, R. Cammi, V. Barone, *J. Chem. Phys.* **2006**, *124*, 94107.
[187] J. Tomasi, B. Mennucci, R. Cammi, *Chem. Rev.* **2005**, *105*, 2999.
[188] V. S. Bryantsev, M. S. Diallo, W. A. Goddard, *J. Phys. Chem. B* **2008**, *112*, 9709.
[189] Y. Zhao, D. G. Truhlar, *J. Phys. Chem. A* **2005**, *109*, 5656.
[190] a) S. Grimme, J. Antony, S. Ehrlich, H. Krieg, *J. Chem. Phys.* **2010**, *132*, 154104; b) S. Grimme, S. Ehrlich, L. Goerigk, *J. Comput. Chem.* **2011**, *32*, 1456.
[191] A. V. Marenich, C. J. Cramer, D. G. Truhlar, *J. Phys. Chem. B* **2009**, *113*, 6378.

[192] a) Lee, Yang, Parr, *Phys. Rev. B* **1988**, *37*, 785; b) Becke, *Phys. Rev. A* **1988**, *38*, 3098; c) A. D. Becke, *J. Chem. Phys.* **1993**, *98*, 5648.
[193] a) H. P. Hratchian, H. B. Schlegel (Ed.) *in Theory and Applications of Computational Chemistry (Eds.: G. Frenking, K. S. Kim, G. E. Scuseria)*, Elsevier Science, Amsterdam, **2005**; b) H. P. Hratchian, H. B. Schlegel, *J. Chem. Theor. Comput.* **2005**, *1*, 61; c) H. P. Hratchian, H. B. Schlegel, *J. Chem. Phys.* **2004**, *120*, 9918.
[194] a) F. Neese, *Wiley Interdiscip. Rev. Comput. Mol. Sci.* **2012**, *2*, 73; b) F. Neese, *Wiley Interdiscip. Rev. Comput. Mol. Sci.* **2018**, *8*.
[195] G. Knizia, *http://www.iboview.org*.

Thank You Notes

I would like to thank everyone who supported me over the course of the work done for this thesis. Many people contributed to its success and of course, I cannot name all. However, there are some people that I would like to mention explicitly here:

- *Prof. Dr. Hans-Jörg Krüger*, for giving me the opportunity to pursue this interesting topic in his group and for always being open to spontaneous (sometimes late-hour) discussions of new results.

- *Prof Dr. Antonio Pierik*, for always being there to support me with the operation of the EPR spectrometer and for agreeing to chair the doctoral committee.

- *Prof Dr. Helmut Sitzmann*, for his interest in the work and for agreeing to referee this thesis.

- *Prof. Dr. Johannes Klein*, for the theoretical calculations that represent a valuable contribution to the journal publication that is part of this work.

- *Dr. Markus Schmitz*, for the measurement and work-up of the magnetic data collected on the SQUID magnetometer, his help with various analytical instruments when I had questions, and his engagement in scientific discussions when I asked for his professional opinion.

- *Dr. Harald Kelm*, for the measurement of many X-ray structures and Mößbauer spectra that fundamentally contributed to the understanding of this work, as well for his valuable input to the choice of methods in 2D-NMR spectroscopy.

- *Christiane Müller*, for the measurement of countless paramagnetic and 2D-NMR spectra and the accompanying trials to find suitable methods and parameter settings.

- The analytics department of the organic chemistry department, especially *Birgit Dusch* and *Jana Ellmer*, for the measurement of many valuable elemental analyses.

- *Pascal Peter*, for allowing me to describe and discuss some of his results in chapter 5 which enriched the discussion and interpretation of my own results in this thesis.

- *Caro Hofmann* and *Ina Berwanger*, for always being there when I needed help with administrative tasks and bureaucracy and for going out of their way to make every wish possible.

- My lab mates and very good friends *Alexander Haag* and *Dr. Niklas Bäsch* that were a joy to work with. The atmosphere in the lab could not have been better, I really cherish the memories we made together. Certainly, the lab discussions and some of their ideas also found their way into the results of this thesis.

- All members of the research group Krüger including all project, bachelor, and master students that I supervised that made work in the lab enjoyable.

- My parents *Jan* and *Sarianne*, that made my study and doctorate possible in the first place, as well as my brother *Niels* who also supported me along the way.

- *Janine*, who came into my life during this time, supported me throughout the work, and gave me strength especially during the pandemic lockdowns.

- Anyone I did not mention explicitly who supported me during this time and contributed to the success of this work.